Gas matters: The Molecular and Atomic Gas Budget in Nearby Galaxies from Centers to Outskirts

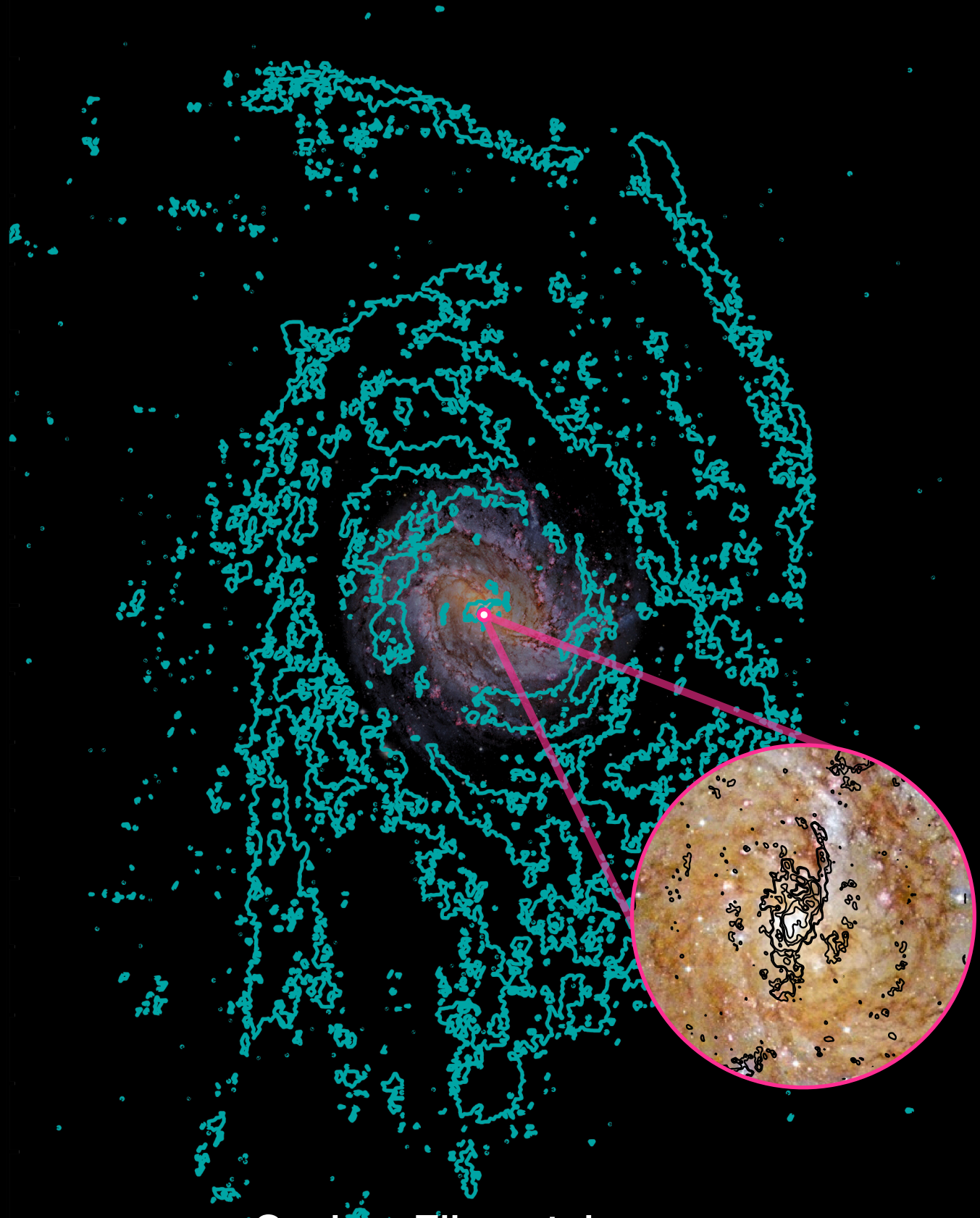

Cosima Eibensteiner

Gas matters: The Molecular and Atomic Gas Budget in Nearby Galaxies from Centers to Outskirts

Dissertation
zur
Erlangung des Doktorgrades (Dr. rer. nat.)
der
Mathematisch-Naturwissenschaftlichen Fakultät
der
Rheinischen Friedrich-Wilhelms-Universität Bonn

von
Cosima Eibensteiner
aus
Salzburg, Österreich

Bonn, July 2023

Angefertigt mit Genehmigung der Mathematisch-Naturwissenschaftlichen Fakultät der Rheinischen Friedrich-Wilhelms-Universität Bonn

1. Gutachter:	Prof. Dr. Frank Bigiel
2. Gutachter:	Prof. Dr. Karl M. Menten
Tag der Promotion:	24.10.2023
Erscheinungsjahr:	2023

When people asked me who my role model was, I always said it was her. She probably wouldn't think so. Through the ups and downs of my family history, she showed me that it's never too late to tackle things. Whether it's moving to a new city with two kids, getting her degree in her early thirties, or marrying the love of her life in her early forties.

To my Mom.

Slow down you're doing fine
You can't be everything you want to be before your time
Although it's so romantic on the borderline tonight
Too bad, but it's the life you lead
You're so ahead of yourself that you forgot what you need
Though you can see when you're wrong
You know you can't always see when you're right
You got your passion, you got your pride
But don't you know that only fools are satisfied?
Dream on, but don't imagine they'll all come true
When will you realize, Vienna waits for you?

Lyrics of the Song "Vienna" by Billy Joel, 1977

Abstract

Hydrogen is the most fundamental component of the baryonic universe, and its various phases have played a key role in its evolution from the Big Bang to the present day. To probe and study these phases of hydrogen in the interstellar medium (ISM) we have to use various direct and indirect diagnostic tools. This thesis deals with two environments that harbor the extremes of hydrogen phases: Centres (consisting of almost all molecular gas) and outskirts (all atomic gas) of nearby disk galaxies. Specifically these are of interest to study because the dynamic processes in the galaxies drive mass flows from the outermost regions replenishing the central regions with fresh material that is converted into molecular gas, fueling ongoing star formation.

Observing multiple molecules in extragalactic space is currently only possible in a small range of environments. This is because species tracing for example dense molecular or shocked gas are faint and thus harder to detect than the bulk molecular gas tracer Carbon Monoxide (CO). Centers of galaxies are one of these rare extragalactic environments and serve as ideal laboratories to study a plethora of molecular line emissions to gain insight into the physical and chemical state of the gas. The first scientific project presents multi-molecular line observations from the *IRAM Plateau de Bure Interferometer* (PdBI) toward the center of the nearby starburst double-barred galaxy NGC 6946. Our results reveal for the first time that an inner smaller bar affects the molecular gas such that the locations of the densest molecular gas material (that is traced by molecules such as HCN, HNC, N_2H^+, or HC_3N) are not necessarily the very centers of the galaxies (i.e. their nuclear region). Furthermore, we find that the star formation rate (SFR) varies within the sub-regions along the bar and show that the SFR efficiency of the dense gas exhibits a different behavior than compared to disk observations. We address the question of whether ratios of molecular line emission can be used as a diagnostic of the physical and chemical state of the gas (temperature and density) and the environment (indicating the presence of an active galactic nucleus) in the center of NGC 6946 and additional 8 galaxy centers (taken from the EMPIRE survey and two high angular resolutions observations). This thesis shows that empirical molecular line diagnostics are a useful tool, but reach their limits and/or cannot be unambiguously interpreted at (sub)kpc scales in nearby galaxy centers.

The atomic gas budget in the outskirts of nearby galaxies and its kinematics on small-scale (turbulent nature of the ISM) and large-scale (disk rotation and mass flow rates) is best explored using the 21 cm H I emission. The second scientific project in this thesis presents the largest *Karl G. Jansky Very Large Array* (VLA) mosaic observations that we combine with *Green Bank Telescope* (GBT) single dish data targeting the super-extended H I disk of the nearby grand design galaxy M 83. We find along the ~50 kpc radial extending H I disk, H I line widths, also called velocity dispersion, greater than inferred from the warm neutral medium (i.e. > 8km s^{-1}) that is expected to be in the outskirts of nearby galaxies. Our analysis reveals that dynamical features (such as rings and spiral arms) have a significant impact on mass flow rate profiles and radial H I velocity dispersion profiles. In particular, this project shows that mass flow rate profiles are highly sensitive to kinematic parameters, in particular inclination thus, such rates should be interpreted with caution.

The third in-progress scientific project addresses the questions of where in nearby galaxies atomic gas transitions to molecular gas (i.e. where their surface densities are approximately equal, $\Sigma_{HI} \approx \Sigma_{H2}$) using new high-quality observations from *More of Karoo Array Telescope* (MeerKAT) together with

Atacama Large Millimeter/submillimeter Array (ALMA), and how the transition ($R_{\rm mol} = \Sigma_{\rm H2}/\Sigma_{\rm HI} = 1$) depends on local conditions, as probed by a range of multi-wavelength observations, across the galaxy disks. Our results reveal that when normalizing the radial extent of H I in 8 nearby galaxies by their optical radius the transition between an H I-dominated and a predominantly H_2-dominated ISM takes place at $0.4\ r_{\rm gal}/r_{25}$. This analysis reveals that the dynamical equilibrium pressure (i.e. the sum of the weight of the ISM due to the self-gravity and due to stellar gravity) tightly correlates with the gas transition, $R_{\rm mol}$. This indicates that the balance between H I and H_2 is primarily determined by the dynamical equilibrium pressure.

Overall, we have gained a detailed picture of molecular and atomic gas tracers, and their diagnostics for physical and chemical processes in individual nearby galaxies. These dissertation projects are advancing future investigations toward a statistical characterization (i.e., a larger sample) of a variety of different nearby galaxy centers and outskirts to improve our understanding of the physics of ISM gas and its role in galaxy evolution.

Zusammenfassung

Wasserstoff ist der grundlegendste Bestandteil des baryonischen Universums, und seine verschiedenen Phasen haben in seiner Entwicklung vom Urknall bis zum heutigen Tag eine wesentliche Schlüsselrolle gespielt. Um diese Phasen des Wasserstoffs im interstellaren Medium (ISM) zu erforschen und zu untersuchen, müssen wir verschiedene direkte und indirekte Diagnoseinstrumente einsetzen. Diese Arbeit befasst sich mit zwei Umgebungen, die die Extreme der Wasserstoffphasen beherbergen: Die Zentren (die fast ausschließlich aus molekularem Gas bestehen) und die Außenbezirke (die ausschließlich aus atomarem Gas bestehen) von nahen Scheibengalaxien. Diese sind von besonderem Interesse, weil die dynamischen Prozesse in den Galaxien Massenströme aus den äußersten Regionen antreiben, die die zentralen Regionen mit frischem Material auffüllen, das auf den Weg dorthin in molekulares Gas umgewandelt wird und die laufende Sternentstehung antreibt.

Die Beobachtung mehrerer Moleküle im extragalaktischen Raum ist derzeit nur in einer kleinen Anzahl von Umgebungen möglich. Der Grund dafür ist, dass Spezies, die z. B. auf dichtes molekulares oder geschocktes Gas hindeuten, schwach sind und daher schwieriger zu erkennen sind als der Massenmolekülgas-Tracer Kohlenmonoxid (CO). Galaxienzentren sind eine dieser seltenen extragalaktischen Umgebungen und dienen als ideale Laboratorien für die Untersuchung einer Vielzahl von Molekülliniemissionen, um Einblicke in den physikalischen und chemischen Zustand des Gases zu gewinnen. Das erste wissenschaftliche Projekt präsentiert Beobachtungen mehrerer Molekülllinien mit dem *IRAM Plateau de Bure Interferometer* (PdBI) im Zentrum der nahen Starburst-Doppelbalkengalaxie NGC 6946. Unsere Ergebnisse zeigen zum ersten Mal, dass ein innerer kleinerer Balken das molekulare Gas beeinflusst, so dass die Orte des dichtesten molekularen Gasmaterials (das durch Moleküle wie HCN, HNC, N_2H^+ oder HC_3N gekennzeichnet ist) nicht notwendigerweise die Zentren der Galaxien sind (d. h. ihre Kernregion). Darüber hinaus stellen wir fest, dass die Sternentstehungsrate (SFR) entlang des Balkens variiert und zeigen, dass die SFR-Effizienz des dichten Gases ein anderes Verhalten zeigt als in den Beobachtungen der ganzen Scheibe von Galaxien.
Wir gehen der Frage nach, ob das Verhältnis der Molekülliniemission als Diagnose des physikalischen und chemischen Zustands des Gases (Temperatur und Dichte) und der Umgebung (Hinweis auf das Vorhandensein eines aktiven galaktischen Kerns) im Zentrum von NGC 6946 und weiteren 8 Galaxienzentren (aus der EMPIRE-Durchmusterung und zwei Beobachtungen mit hoher Winkelauflösung) verwendet werden kann. Diese Arbeit zeigt, dass die empirische Molekülliniendiagnostik ein nützliches Werkzeug ist, aber bei (sub)kpc-Skalen in nahen Galaxienzentren an ihre Grenzen stößt und/oder nicht eindeutig interpretiert werden kann.

Der Haushalt des atomaren Gases in den äußeren Bereichen naher Galaxien und seine Kinematik in kleinen Skalen (turbulente Natur des ISM) und in großen Skalen (Scheibenrotation und Massenflussraten) lassen sich am besten anhand der 21 cm H I Emission erforschen. Das zweite wissenschaftliche Projekt in dieser Arbeit stellt die größten *Karl G. Jansky Very Large Array* (VLA) Mosaikbeobachtungen vor, die wir mit *Green Bank Telescope* (GBT) Single-Dish-Daten kombinieren, die auf die super-ausgedehnte H IScheibe der nahe gelegenen Grand Design Galaxie M 83 abzielen. Entlang der ∼50 kpc radial ausgedehnten H I Scheibe finden wir H I -Linienbreiten, auch Geschwindigkeitsdispersion genannt, die größer sind als die des warmen neutralen Mediums (d.h. $> 8\mathrm{km\ s^{-1}}$), das man in den äußeren Bereichen der nahen Galaxien erwartet. Unsere Analyse zeigt, dass dynamische

Merkmale (wie Ringe und Spiralarme) einen erheblichen Einfluss auf die Massenflussratenprofile und die radialen H I Geschwindigkeitsdispersionsprofile haben. Insbesondere zeigt dieses Projekt, dass Massenflussratenprofile sehr empfindlich auf kinematische Parameter, insbesondere die Inklination, reagieren, so dass solche Raten mit Vorsicht zu interpretieren sind.

Das dritte in Arbeit befindliche wissenschaftliche Projekt befasst sich mit der Frage, wo in nahen Galaxien atomares Gas in molekulares Gas übergeht (d.h. wo ihre Oberflächendichten ungefähr gleich sind, $\Sigma_{\rm HI} \approx \Sigma_{\rm H2}$) unter Verwendung neuer hochwertiger Beobachtungen von *More of Karoo Array Telescope* (MeerKAT) zusammen mit *Atacama Large Millimeter/submillimeter Array* (ALMA), und wie der Übergang ($R_{\rm mol} = \Sigma_{\rm H2}/\Sigma_{\rm HI} = 1$) von den lokalen Bedingungen in den Galaxienscheiben abhängt, was durch eine Reihe von Beobachtungen bei verschiedenen Wellenlängen untersucht wird. Unsere Ergebnisse zeigen, dass bei der Normalisierung der radialen Ausdehnung von H I in 8 nahen Galaxien durch ihren optischen Radius der Übergang zwischen einem H I-dominierten und einem überwiegend H_2-dominierten ISM bei $0.4\, r_{\rm gal}/r_{25}$ stattfindet. Diese Analyse zeigt, dass der dynamische Gleichgewichtsdruck (d. h. die Summe aus dem Gewicht des ISM aufgrund der Eigengravitation und aufgrund der stellaren Schwerkraft) eng mit dem Gasübergang, $R_{\rm mol}$, korreliert. Dies deutet darauf hin, dass das Gleichgewicht zwischen H I und H_2 hauptsächlich durch den dynamischen Gleichgewichtsdruck bestimmt wird.

Insgesamt haben wir ein detailliertes Bild der molekularen und atomaren Gas-Tracer und ihrer Diagnostik für physikalische und chemische Prozesse in einzelnen nahen Galaxien gewonnen. Diese Dissertationsprojekte treiben zukünftige Untersuchungen in Richtung einer statistischen Charakterisierung (d.h. einer größeren Stichprobe) einer Vielzahl verschiedener naher Galaxienzentren und äußeren Bereichen voran, um unser Verständnis der Physik des ISM-Gases und seiner Rolle in der Galaxienentwicklung zu verbessern.

Acknowledgements

I think I've only told one person in my life that they don't always have to apologize. I recently realized that the reason is that she is the only one who has apologized more often than I have. At that time I would have started this Acknowledgments section with the following sentence "Sorry, this might be a long section", but why do I have to apologize for the fact that so many incredible people have accompanied me on this journey? Exactly. So, this will be a long section. Deal with it :)

I would like to thank my supervisor Frank Bigiel for welcoming me into his group in the fall of 2019 and providing me with endless new opportunities and wisdom (not only about science - keyword Bananenweizen). To send me right after two weeks after I arrived in Bonn, on a new adventure full of data reduction in New Mexico, the countless dinners with beer in Harmonie, Fiddlers, or Bönnsch have brought me (among other things) through the following heavy COVID time. Our group dynamic changed a bit during the two years of home office and I only realized at the end of 2022 how important it is for me to be around people while writing papers or observation proposals. I also owe him the opportunity to work in such a great collaboration as PHANGS and to be able to develop myself. Also, since our last visit to Harmonie, I have been able to tie a few things together better while already fully immersed in my thesis, and I am excited to see what the future holds.

I would also like to thank Karl Menten for being the second reviewer of my thesis. We did not have the opportunity to interact much but I have heard from so many PhD students that you are a great supervisor. I remember when I arrived in Bonn and started googling all the professors at AIfA and Max Planck - I was extremely impressed by everything in your CV.

I would also like to thank Florian Bernlochner (also Sebastian Hofferberth) and Heiko Röglin who both agreed to be in my PhD commission. I would also like to thank Jorg Wenniges in the PhD office for his calm and pleasant manner in these stressful last moments.

Ashley Barnes, I can hardly put into words how grateful I am for all you have done. You were an endless scientific help from the beginning and throughout my PhD and always had an ear open for other (mostly more important) things in life. You taught me an infinite amount and I thank you so much for all the quick and spontaneous feedback (especially for this PhD thesis; sent a chapter at 2 am and got feedback right away at 9 am - new record? I think so!). When I've told other PhD students about you, it's always that I'd like to get a little bit of your efficiency coupled with empathy. I also thank you for the support and freaking out after I told you the big news by phone. I'm immensely happy that ESO worked out for you and I see on Instagram that you, Christina, and Nala are doing extremely well.

I would also like to show gratitude for the great and intense support, mentoring, and feedback of my collaborators abroad. I am sure that thanks to them, I am able to continue my research in the academic world. Thank you Eva Schinnerer for all your detailed, extremely helpful, and quick feedback, for your advice, and for our conversation in Nice which opened my eyes. I am deeply impressed by you. Adam Leroy, if I have told others about you, it is that you can motivate me so much after a quick

conversation. Thank you for all your advice and feedback and all the motivation you can transmit via Zoom calls. Thank you Antonio Usero for your attention to technical details and all your help. I will always remember your reaction and mine when I told you that I recreated ALMA in Animal Crossing and you said that you play that game too. Thanks for your funny way, funny videos, and music - fuegos artificiales. Thanks, Erik Rosolowsky for all your superb feedback, for your funny way (especially the dynamic between you and Adam), and for joining in telecons while walking your dog.

I would also like to thank Eric Koch, Maria Jesus Jiménez-Donaire, Jiayi Sun, Miguel Querejeta, and Amy Sardone who have all been incredibly supportive. Especially Maria for sending memes that made my day better, thank you, Amy, for all your wisdom and the talk in Gothenburg that you already told me then that you will leave academia which showed me how much you trust me. Thank you, Jiayi for your ALMA support during the proposal-writing phase and for all your fantastic help and feedback regarding my third project. Thank you Eric and Miguel for your absolutely great feedback regarding my applications when others were highly engaged in analyzing the new PHANGS-JWST data. Eric, I still owe you a beer or two for this. And Miguel I saved the email that you sent me after the Gothenburg conference – thanks for encouraging me. I also want to thank all the other PHANGS members. Special mention goes to Sophia Stuber, Elias Oakes, Sarah Jeffreson, and I-Da Chiang.

At this point, I would also like to thank my collaborators Jürgen Ott and David Meier, who supported me tremendously, especially at the beginning of my PhD. I thank them for a great time in Socorro, for all the wisdom, for the 3-hour crash course private lecture, and for the best burger I ever ate, on the last night of my stay.

Okay, back to Bonn. We started our PhD on the same day, I thank you Jakob for being the best "office buddy". Unfortunately, this was a much too short time as we had to switch to home-office mode after only 6 months. I am incredibly grateful for your support, and our discussions, and I just enjoyed our "alpine club" as Elisabeth used to say. Jakob's friendly and patient way of explaining scientific concepts to his Bachelor's or Master's students is something I would like to see in any scientist. Thank you Ivana, for your kindness, your empathy, your understanding, and for your extremely great help at the beginning of my PhD with all the python packages and scripts that I have never seen before in my life. I will always remember the time when we sat with the laptop at one of Dato's and Sven's legendary home parties on the day of a deadline and afterward closed the laptop and danced like crazy. Thank you for the not-so-simple late-night conversation in Nice and I'm so happy when I see stories on Instagram from you in Paris. I am extremely grateful to have had Johannes as one of the few who fully understood me (no language barriers; ranting about a code in Austrian is just something else). Thank you for your great support and for staying in touch. Our group in Bonn has experienced some changes and I am grateful to have witnessed them, otherwise, I would never have shared an office with Lukas or talked to Dario and Mallory about so many things. Thank you Lukas for your attention to detail. Thank you Dario for your incredibly generous streak, your understanding, your empathy, and your support during my writing phase. Mallory, it's a shame we've known each other for so little. In the month that we were in close contact (because I wasn't writing from home), I just noticed how much we are on the same wavelength. Thank you all for your constant feedback on this work.

Getting through my dissertation required more than academic support, and I have many, many people to thank. People I met in Bonn and people I have known for a long time. I can't begin to express my gratitude and appreciation for their friendship. I want to thank Maude and her hilarious personality which is a rare and unique one that I will really miss. I am extremely grateful for the time spent with Diana, you showed me so many things and all of our conversations in Bonn and in

the US helped me so much. I want to point out our little group – Diana, Maude, and Ivana. Sandra your direct sarcastic way irritated me a bit in the beginning but soon we got along extremely well and I thank you for so many conversations about PhD and other things. I am amazed at how you have mastered your PhD with two children. David A., I can still remember the somewhat funny concert and our conversation afterward where I got to know you even more and I also learned a lot about myself. I think it's a pity that we hardly have contact anymore but I hope you know that I think about our conversations and evenings from time to time.

I would like to thank Christos, Tsan-Ming and Kevin. Thank you for the crazy trekking trip through Patagonia. The W-trek after the conference in Puerta Varas was very special and changed a lot of things (real life hit hard after I came back to Germany). I especially want to thank Christos and Kevin who were there for me, pushed me emotionally and wrote with me on possible applications on the plane. Thank you Kevin for our philosophical and helpful conversation at the water with all the icebergs in the middle of nature at night waiting for Christos and Tsan Ming. They both fell asleep in the tent and I thank you for the funny idea to get ice from the glacier for our Whiskey. I am grateful for your view on life. I am also grateful for Tsan Ming and his way of introducing me to Tawaiin - through food. The best way in my opinion. Thank you Christos for your friendship and daily gossip. The conference in Puerto Varas has also created a friendship between me Arshia and Elena. Thank you Arshia for all your wisdom and support.

I want to thank so many people at AIfA, and hope I won't forget anyone. I thank Prachi, Angie, and Benedetta for our intense and funny conversations, and Abel for all Scooter-related stuff, Toma, Andres, Ben, Yvonne, Ankur, Alex, and Matteo for our lunch and fun conversations from now and then. Thank you, Harim for your kindness. A big shoutout goes to the best (multiple) home parties by Dato and Sven. I want to thank Sabine, Elisabeth, and Andreas for their constant support with travel documents and technical support. I also want to highlight the nice and fun foosball games before lunch.

I especially want to thank the BÖnn group – the "ö" stands for Österreich. Thanks, Niki and Moritz. With you, it was so easy to talk about things that we miss, things that we don't like in Bonn (mostly the food), and things that are just special to us. A very very big thank you to you Niki for being so kind in November, offering to stay at your shared flat for a few weeks while I had all the interviews, applications, and moving stress. I enjoyed our late-night conversations about possible future proposal ideas with ALMA or APEX and I'm deeply grateful that this tied us a bit closer. You are such an empathetic person and I'm thankful for your views and passion for science.

If there's one thing I couldn't have foreseen, it's that for once a late bus can lead to a 'revival' (thanks Covid) of a friendship that became so intense that I'm about to bring Bonn SWB a gift basket. Mary Cruces, what a quick "Hey is everything alright?" can do in November 2022 is incredible. You welcomed me into your "family" and showed me how you make your way through a men-dominated world. I owe you so much and because of you, I have gained so many funny absurd memories. You snuck me into Max Planck and reestablished contacts and friendships. I thank you for all your advice, for the late-night calls, or your request that I use your bathtub to relax while you are at a conference. I just think it's funny that we lived around the corner in the Altstadt for so long and now in my last year in PhD I've sat on your comfy sofa so incredibly often. I still laugh about so many things, be it the moth at the toilet, your facial expression during ChinChin in Cologne, or hiding behind our hair so Andrei doesn't see us laughing. This brings me to the "Family pack", I am so grateful for all the things I could experience with you Mary, Andrei, and Jaswanth.

Andrei, I could not have imagined that you are such a loving and empathetic person. You have your heart in the right place and I felt so sorry for you and your situation and can't even imagine how you

felt about it. War is always bad and watching it put friends in a negative emotional situation just sucks. I hope as soon as Mary and I leave Bonn that you will continue to have as much fun with Jaswanth as we did in our "Family pack".

I have rarely met someone who understands me so quickly and is as empathetic as you, Jaswanth. The one party at Mary's where I introduced myself to you and you said that we already knew each other. Oh COVID. Forgot that we attended one of the IMPRS online courses together in the middle of the pandemic. It was "Efficiency Skills for Scientists" and I can't remember what our task had to do with efficiency, but I had to guide you digitally through Disneyland Paris. It was kind of absurd but we mastered it. That night at Mary's I saw you dancing for the first time and I could feel that it is a strategy to switch off and forget everything around you, just like it is for me. Thank you for the endless long and deep conversations that became so much more. I am infinitely grateful for your tremendous support during my writing phase, your indulgence when I got a weird writing motivation boost in the middle of the night, and for your incredibly good (and spicy, 5 chillis is clearly not not spicy) South Indian dishes.

I would also like to thank Jaswanth for somehow inviting me to a Whatsapp group with many people I didn't know that well before (all from Max Plank). This skiing vacation in Switzerland was something special for me. Thank you Joana, Surya, Jonah, Shilpa, Miquel, and Tim. And again, a big apology for the poor assessment of the slopes for the beginners among us. I especially thank Joana with whom I had such an emotional deep conversation in the hostel in such an absurd situation. Because I wanted to help this stranger in the common room/toilet with my helper instinct (who threw up her soul and didn't even remember us the next day) a conversation arose which led to you inviting me to your wedding quite spontaneously after the skiing vacation. Thank you for so much and I am incredibly proud of you. You will get through all the last hurdles and I am happy that we will both start our new positions on the same day. The same continent - yes.

I want to thank my students Roberto, Josephine Benna, and Sebastian. They showed me once again that I enjoy supervising (well co-supervising) so much and I am beyond grateful and happy for what you all accomplished. Thank you Sebastian for the Virgina guide – I will need that one for sure.

Outside of academia, I would like to thank all the new friends I have made. Thank you Hannah for everything you have done with me and for me. Thank you for our unforgettable spontaneous absurd (I still can't believe it) time in Hawaii. I think pretty much everyone who knows us knows the story of how we got to know each other. I'm absolutely amazed at what a 6-hour random conversation on an airplane can do. Thank you for that. Thank you for your hospitality and thank you for the wonderful stay in Stockholm with you.

Thanks also to my tap dancing friends Armin, Kim, and Petra. Especially Armin, who was always spontaneously ready for a coffee and who accepts my strange behavior (sometimes not answering messages for days), and with whom I can talk about so many things.

I would also like to thank my neighbors. I never thought we would get along so well and do so many things together. Something you would never do with neighbors in Vienna. Thank you, Marie (I finally have to visit you in Heidelberg), Simon for all the evenings with beers, and Lena for all the walks along the Rhein and house cat Momo. I would also like to thank Lukas Fleischmann and his family, Sabine, Andreas, Moritz, Raphael, and his grandparents. I am thankful for the time in Bonn we had together until we parted ways in November.

And now Vienna. Thank you thank you thank you Viktoria Rosenbichler a.k.a. Viki for your kindness and support. I am so thankful to have you as a friend. I can't express my love at all. Thanks

also to Nicole Naber a.k.a. Niki, whom I have been able to call my friend for more than 15 years now. A few months ago there was something that separated us a bit and I hope we can go back to where we used to be – calling weekly and sending postcards. Thanks also to my Vienna-Astro group, Marie, Andreas K., Andreas F., Alice, Alma, Manuel, Sebastian, Michael and Verena.

I am absolutely grateful to be able to continue my research and would like to thank National Science Foundation's National Radio Astronomy Observatory (NRAO) for their fellowship. I am thrilled and am looking forward to my time in Charlottesville.

I could not have undertaken this journey without the support of my family. Thanks to my parents, Petra Menasse-Eibensteiner and Peter Menasse, and Nunu. I thank you for your absolutely great understanding and support, emotionally, financially, and with humor and fun. I am so happy to be able to call you *both* parents. An absolutely big mega big thank you goes to my brother. Nico Eibensteiner. I am deeply impressed by what you have accomplished. I know that you would like to be there for me more often, and I hope you know that I would be as well. Thank you Celeste Eibensteiner for your incredibly calm and positive manner. I'm amazed at how you two manage everything. I also thank Penelope and Jaro Eibensteiner, my niece and nephew. I love you and think of you very, very much. Now, my journey will keep me from being there for you more, but I hope that we will meet often in the US. I love you. Ich möchte mich auch bei meiner Oma Hermine Eibensteiner und Edith bedanken. Besonders die letzen Jahre sind nicht ganz einfach gewesen. Ich bin gespannt was du deinen Freundinnen am Stammtisch erzählt hast an was ich gerade arbeite. Ich liebe dich.

Last but not least, to quote someone I thought I would never quote "I wanna thank me. I wanna thank me for believing in me. I wanna thank me for doing all this hard work" – Snoop Dogg.

List of Publications

Relevant First-Author Publications

The following list indicates the relevant first-author publications that are discussed and presented in this thesis. These thesis culminates in two peer-reviewed and published research publications. In addition, one more manuscript is in preparation for submission to the Astrophysics & Astronomy journal.

1. **Eibensteiner C.**, Barnes A. T., Bigiel F., Schinnerer E., Liu D., Meier D. S., Usero A., Leroy A. K., Rosolowsky E., Puschnig J., Lazar I., Pety J., Lopez L. A., Emsellem E., Bešlić I., Querejeta M., Murphy E. J., den Brok J. S., Schruba A., Chevance M., Glover S. C. O., Gao Y., Grasha K., Hassani H., Henshaw J. D., Jimenez-Donaire M. J., Klessen R. S., Kruijssen J. M. D. Pan, H.-A., Saito T., Sormani M. C., Teng Y.-H., Williams T. G., (2022) , *A 2-3 mm high-resolution molecular line survey towards the centre of the nearby spiral galaxy NGC 6946*, Astronomy & Astrophysics, 659, A173, doi:10.1051/0004-6361/202142624 .

   Author's Contribution: C.E. performed the scientific analysis under the supervision of A.B., F.B., E.S., D.S.M., A.U., A.K.L., E.R., and J.P.; D.L. together with I.L. reduced, calibrated, imaged, and combined the PdBI data with IRAM 30m observations. L.A.L. provided the X-ray data and E.J.M. the 33 GHz continuum observations. The other co-authors helped to interpret the results and provided comments and edits to the final manuscript.

2. **Eibensteiner C.**, F. Bigiel, A. K. Leroy, E. W. Koch, E. Rosolowsky, E. Schinnerer, A. Sardone, S. Meidt, W. J. G de Blok, D. Thilker, D. J. Pisano, J. Ott, A. Barnes, M. Querejeta, E. Emsellem, J. Puschnig, D. Utomo, I. Bešlic, J. den Brok, S. Faridani, S. C. O. Glover, K. Grasha, H. Hassani, J. D. Henshaw, M. J. Jiménez-Donaire, J. Kerp, D. A. Dale, J. M. D. Kruijssen, S. Laudage, P. Sanchez-Blazquez, R. Smith, S. Stuber, I. Pessa, E. J. Watkins, T. G. Williams, and B. Winke, (2023), *Kinematic analysis of the super-extended HI disk of the nearby spiral galaxy M 83*, Astronomy & Astrophysics, 675, A37, doi:10.1051/0004-6361/202245290.

   Author's Contribution: C.E. performed the reduction, calibration, imaging, and combination of VLA and GBT datasets under the supervision of F.B, A.K.L., J.O. A.B., and D.U.; C.E. also performed the scientific analysis under the supervision of F.B, A.K.L., E.W.K., E. R., E.S., A.S, S.M. The other co-authors helped to interpret the results and provided comments and edits to the final manuscript.

3. **Eibensteiner C.**, A.K. Leroy, J. Sun, F. Bigiel, E. Schinnerer, E. Rosolowsky, D.J. Pisano, W. J. G de Blok, and the PHANGS-HI team and PHANGS & MHONGOOSE collaboration, (2023), *MeerKAT HI observations of nearby spiral galaxies: the physical driver of* R_{mol}, in preparation

Author's Contribution: C.E. performed the scientific analysis and wrote the manuscript under the supervision of A.K.L., J.S., F.B. The co-authors E.S., E.R., D.J.P., and W.J.G.B. contributed with discussing the shown results.

Relevant Co-Authored Publications

The following list indicates selected submitted and published work that are complementary and related to the results and analysis presented in this thesis (for a full list see my CV). The author of this dissertation has contributed as a co-author to these papers throughout the duration of the thesis project.

1. Jiménez-Donaire M. J., Usero A., Bešlić I., Tafalla M., Chacón-Tanarro A., Salomé Q., **Eibensteiner C.**, García-Rodríguez A., Hacar A., Barnes A. T., Bigiel F., Chevance M., Colombo D., Dale D. A., Davis T. A., Glover S. C. O., Kauffmann J., Klessen R. S., Leroy A. K., Neumann L., Pan H., Pety J., Querejeta M., Saito T., Schinnerer E., Stuber S., Williams T. G., (2023), *A constant N_2H^+ (1-0)-to-HCN(1-0) ratio on kpc scales*, Astronomy & Astrophysics, 676, L11, doi:10.1051/0004-6361/202347050

   Author's Contribution: C.E. helped with the data analysis and the visualization of key results/plots. C.E. contributed edits that helped to improve the manuscript.

2. den Brok J. S., Bigiel F., Chastenet J., Sandstrom K., Leroy A. K., Usero A., Schinnerer E., Rosolowsky E. W., Koch E. W., Chiang I-Da, Barnes A. T., Puschnig J., Saito T., Bešlić I., Chevance M, Dale D. A., **Eibensteiner C.**, Glover S., Jiménez-Donaire M. J., Teng Yu-Hsuan, and Williams T. G., (2023), *Wide-field CO isotopologue emission and the CO-to-H_2 factor across the nearby spiral galaxy M101*, accepted for publication in Astronomy & Astrophysics

   Author's Contribution: C.E. observed 18/80 hours with the IRAM 30m for this project 160-20, PI: den Brok. C.E. contributed edits that helped to improve the manuscript.

3. Neumann L., Gallagher M. J., Bigiel F., Leroy A. K., Barnes A. T., Usero A., den Brok J. S., Belfiore F., Bešlić I., Cao Y., Chevance M., Dale D. A., **Eibensteiner C.**, Glover S. C. O., Grasha K., Henshaw J. D., Jiménez-Donaire M. J., Klessen R. S., Kruijssen J. M. D., Liu D., Meidt S., Pety J., Puschnig J., Querejeta M., Rosolowsky E., Schinnerer E., Schruba A., Sormani M. C., Sun J., Teng Y.-H. and Williams T. G., (2023), *The ALMOND Survey: Molecular cloud properties and gas density tracers across 25 nearby spiral galaxies with ALMA*, Monthly Notices of the Royal Astronomical Society, 521, 3, doi:10.1093/mnras/stad424.

   Author's Contribution: C.E. contributed edits that helped to improve the manuscript. In addition, C.E. helped with the data analysis and discussed the results and interpretation with the lead author.

4. Barnes A. T., Chandar R., Kreckel K., Glover S. C. O., Scheuermann F., Belfiore F., Bigiel F., Blanc G. A., Boquien M., den Brok J. S., Congiu E., Chevance M., Dale D. A., Deger S., Kruijssen J. M. D., Egorov O. V., **Eibensteiner C.**, Emsellem E., Grasha K., Groves B., Klessen R. S., Hannon S., Hassani H., Lee J. C., Leroy A. K., Lopez L. A., McLeod A. F., Pan H.-A., Sánchez-Blázquez P., Schinnerer E., Sormani M. C., Thilker D. A., Ubeda L., Watkins E. J., Williams T. G., (2022), *Linking stellar populations to H II regions across nearby galaxies. I. Constraining pre-supernova feedback from young clusters in NGC 1672*, Astronomy & Astrophysics, 662, L6, doi:10.1051/0004-6361/202243766.

   Author's Contribution: C.E. contributed edits that helped to improve the manuscript.

5. den Brok J. S., Bigiel F., Sliwa K., Saito T., Usero A., Schinnerer E., Leroy A. K., Jiménez-Donaire M. J., Rosolowsky E., Barnes A. T., Puschnig J., Pety J., Schruba A., Bešlić I., Cao Y., Eibensteiner C., Glover S. C. O., Klessen R. S., Kruijssen J. M. D., Meidt S. E., Neumann L., Tomičić N., Pan H.-A., Querejeta M., Watkins E., Williams T. G., Wilner D., (2022), A CO isotopologue Line Atlas within the Whirlpool galaxy Survey (CLAWS) , Astronomy & Astrophysics, 662, A89, doi: 10.1051/0004-6361/202142247

   Author's Contribution: C.E. contributed edits that helped to improve the manuscript. In addition, C.E. helped with data analysis and discussed in detail the results and interpretation with the lead author.

6. Leroy A. K., Rosolowsky E., Usero A., Sandstrom K., Schinnerer E., Schruba A., Bolatto A. D., Sun J., Barnes A. T., Belfiore F., Bigiel F., den Brok J. S., Cao Y., Chiang I.-D., Chevance M., Dale D. A., **Eibensteiner C.**, Faesi C. M., Glover S. C. O., Hughes A., Jiménez Donaire M. J., Klessen R. S., Koch E. W., Kruijssen, J. M. D., Liu D., Meidt S. E., Pan H.-A., Pety J., Puschnig J., Querejeta M., Saito T., Sardone A., Watkins E. J., Weiss A., Williams T. G., (2022), *Low-J CO Line Ratios from Single-dish CO Mapping Surveys and PHANGS-ALMA*, The Astrophysical Journal, 927, 2, doi:10.3847/1538-4357/ac3490.

   Author's Contribution: C.E. contributed edits that helped to improve the manuscript.

7. Leroy A. K., Schinnerer E., Hughes A., Rosolowsky E., Pety J., Schruba A., Usero A., Blanc G. A., Chevance M., Emsellem E., Faesi C. M., Herrera C. N., Liu D., Meidt S. E., Querejeta M., Saito T., Sandstrom K. M., Sun J., Williams T. G., Anand G. S., Barnes A. T., Behrens E. A., Belfiore F., Benincasa S. M., Bešlić I., Bigiel F., Bolatto A. D., den Brok J. S., Cao Y., Chandar R., Chastenet J., Chiang I.-D., Congiu E., Dale D. A., Deger S., **Eibensteiner C.**, Egorov O. V., García-Rodríguez A., Glover S. C. O., Grasha K., Henshaw J. D., Ho I.-T., Kepley A. A., Kim J., Klessen R. S., Kreckel K., Koch E. W., Kruijssen J. M. D., Larson K. L., Lee J. C., Lopez L A., Machado J., Mayker N., McElroy R., Murphy E. J., Ostriker E. C., Pan H.-A., Pessa I., Puschnig J, Razza A., Sánchez-Blázquez P., Santoro F., Sardone A., Scheuermann F., Sliwa K., Sormani, Mattia C., Stuber, Sophia K., Thilker, David A., Turner, Jordan A., Utomo D., Watkins E. J., Whitmore B., (2021), *PHANGS-ALMA: Arcsecond CO(2-1) Imaging of Nearby Star-forming Galaxies*, The Astrophysical Journal Supplement Series, 257, 2, doi:10.3847/1538-4365/ac17f3.

   Author's Contribution: C.E. contributed to the data reduction and data quality assessment.

8. Bešlić I., Barnes A. T., Bigiel F., Puschnig J., Pety J., Herrera Contreras C., Leroy,A. K., Usero A., Schinnerer E., Meidt S. E., Emsellem E., Hughes A., Faesi C., Kreckel K., Belfiore F. M. C., Chevance M., den Brok J. S., **Eibensteiner C.**, Glover S. C. O., Grasha K., Jimenez-Donaire M. J., Klessen R. S., Kruijssen J. M. D., Liu D., Pessa I., Querejeta M., Rosolowsky E., Saito T., Santoro F., Schruba A., Sormani M. C., Williams T. G., (2021), *Dense molecular gas properties on 100 pc scales across the disc of NGC 3627*, Monthly Notices of the Royal Astronomical Society, 506, 1, doi:10.1093/mnras/stab1776.

   Author's Contribution: C.E. contributed edits that helped to improve the manuscript. In addition, C.E. helped with data analysis and discussed in detail the results and interpretation with the lead author.

Contents

CHAPTER 1

Introduction

> Whenever we look in nature we can see spiral forms in the uncurling fern, the snail, the nautilus shell, the hurricane, the stirred cup of coffee, the water that swirls out of a wash bowl. Perhaps we shouldn't be surprised to see spirals in the great star systems whirling in space. Yet they remain a great, intriguing question.
>
> Cecilia Payne-Gaposchkin

Overview

The centers of galaxies are extreme environments, characterized by strong tidal forces, rapid rotational timescales, high gas density and star formation rates. In contrast, the outskirts of spiral galaxies are low in gas densities and star formation rates. The key link connecting these two environments in disk galaxies is dynamics: driving mass flows from the outermost regions, fueling their centers with fresh material for star formation. This thesis studies the gas of both of these extreme environments with the help of radio observations, that make it possible to constrain some of the key physical and chemical processes that shape and govern the Interstellar Medium (ISM) in these galaxies.

However, before diving into the technical and scientific part of this thesis, key physical concepts need to be introduced. Unless otherwise noted, the primary reference sources in the introductory sections are the textbooks of Unsöld et al. (2002), Schneider (2006), Bennett (2010), Tielens (2010), Draine (2011), Atkins and Friedman (2011), Wilson et al. (2013) and Thompson et al. (2017) and the reviews by Sancisi et al. (2008), Kennicutt and Evans (2012), Krumholz (2015), Klessen and Glover (2016) and Saintonge and Catinella (2022).

1.1 A Brief History of Discoveries

Two seconds ago Johannes Kelper and Galileo Galilei have proven that Earth rotates around the Sun, and not vice versa. Half a minute ago, humanity didn't exist. This timescale arises when we scale the Universe and its currently understood age of 13.8 billion years to a single year. This is known as the

"cosmic calendar" and is widely used in science education and/or outreach to make our Universe's age accessible for the general public ever since Carl Sagan introduced this concept almost 40 years ago (Sagan 1986). The first detection of Radio waves by Karl G. Jansky was roughly three tenths of a second ago – way shorter than an eye blink – and was the birth of Radio Astronomy[1].

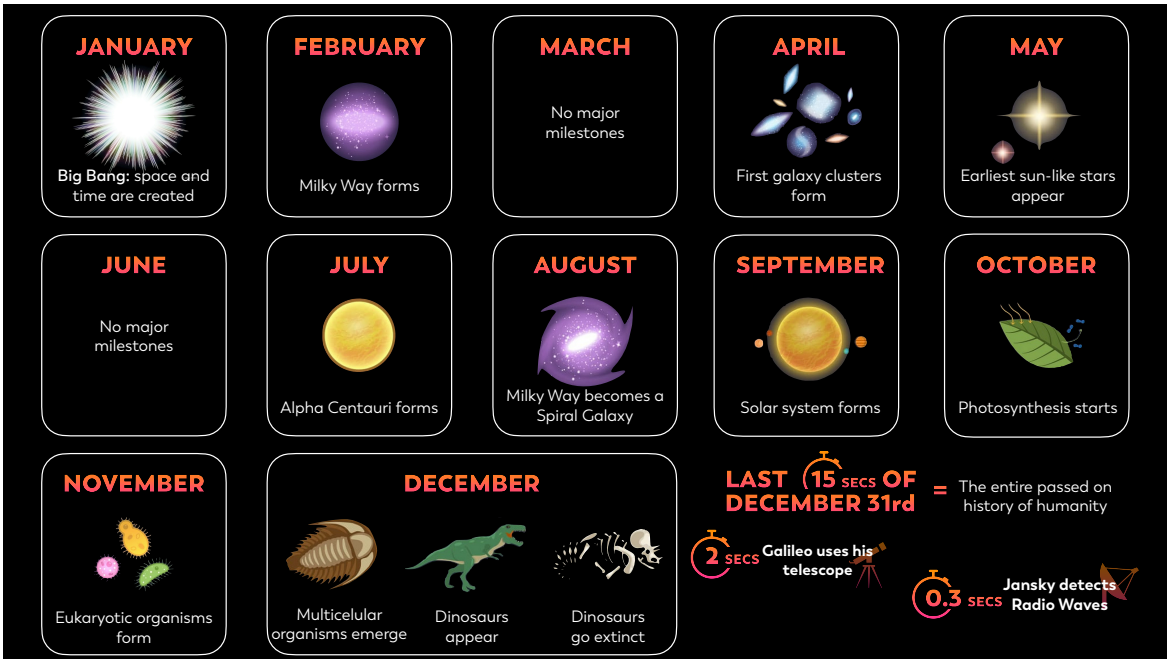

Figure 1.1: **Cosmic calendar**. This representation of the age of the Universe is based on a version by Carl Sagan (Sagan, 1986). The months of March and June are empty because nothing major happens in these months. In other astronomy books, however, the formation of the Milky Way is given for March. This figure is inspired by Star Walk 2[a] and Bennett, 2010. Illustrations are either taken from there or are icons of the presentation software keynote.

[a] https://starwalk.space/en

Figure 1.1 shows that the Big Bang corresponds to the first second of the New Year's Day, and the present time to the last second of December 31st (midnight). In February our Galaxy, the Milky Way, begins to form, in September the Sun and Planets form, on the 26th of December dinosaurs appear, and four days later on December 30th they become extinct. The entire passed on history of humanity to date fits into the last 15 seconds before midnight on New Year's Eve.

The discovery of radio waves – the birth of Radio Astronomy. Jansky was employed by Bell Telephone Laboratories and was in charge of investigating and reducing sources of static interference that affected radio communications over long distances. In 1931, Jansky designed and constructed a large antenna system consisting of several interconnected dipole antennas. This innovative instrument was designed specifically for observing radio waves originating from all directions in the sky. Jansky meticulously scanned the sky with the radio telescope to locate any sources of potential interference.

In the process of his observations, Jansky discovered a strange source of radio waves that did not

[1] This results from the knowledge that the average human lifespan (about 70 years) covers only two tenths of a second of the cosmic calendar and that a blink lasts about one third of a second (Kwon et al. 2013).

originate from human interference, atmospheric thunderstorms, or solar radiation. Extensive analysis revealed that the source was extraterrestrial in nature and originated from the center of the Milky Way. Jansky published his findings in 1933 (Jansky, 1933), pointing to the existence of cosmic radio waves and their potential for studying celestial objects. Despite the importance of his discovery, it took quite some time for the science community to completely understand and embrace the field of Radio Astronomy.

The space between stars is not empty. More than a century and a half ago, the discovery of spectral lines in the optical spectra of emission nebulae were one of the first evidences for the existence of gaseous material between stars, the Interstellar Medium, ISM (Huggins and Miller, 1864; Huggins and Huggins, 1889). Subsequent spectroscopic studies in the early 1930s with improved resolution revealed the inhomogeneous nature of the ISM. In the late 1970s, the ISM was found to consist of distinct phases characterized by different physical and excitation conditions (McKee and Ostriker, 1977). Obtaining an understanding of the interplay between these different phases and constituents of the ISM is crucial to comprehending star formation and galaxy evolution, thus the study of the ISM is key in many areas of astronomy. One of the best approaches to examine the phases of the ISM is with the radio observations of different molecules.

The first detection of Molecules. Ammonia (NH_3) was one of the first molecules detected in the ISM (Cheung et al., 1968). Carbon Monoxide (CO) was detected two years later. Wilson et al., 1970 found intense CO emission from the Orion nebula with the 36 foot NRAO antenna at Kitt Peak, Arizona. The first extragalactic detection of CO was archived in parallel with early Galactic surveys of (Rickard et al., 1975; Solomon and de Zafra, 1975) where they found bright CO emission in the nuclear active galaxies M82 and NGC253. The first ion-molecule was discovered in 1970 and was called 'X-ogen', which was later shown to be HCO^+.

Since then, the number of molecules discovered has increased immensely; six species were found in 1970, 51 ten years later, 85 molecules were discovered in 1990, 130 in 2004, and 170 in 2013. As of early June 2023, 296 molecules are detected[2]. These molecules have shaped our modern understanding of the ISM.

1.2 The Interstellar Medium

> "The thing that is important is the thing that is not seen."
>
> Antoine de Saint-Exupéry, The Little Prince

When we look into the night sky with the naked eye, we see that the space between the stars of our Milky Way is mostly empty. This '' emptiness'' results from our eyes being limited to seeing only visible light. In reality, this '' emptiness'' is filled with interstellar gas, dust, cosmic rays, electromagnetic radiation, interstellar magnetic field, gravitation fields, and (hypothetical) dark matter particles. Altogether this is referred to as the Interstellar Medium (ISM). It makes up on average about 10% of the mass of the baryonic (directly observable) matter in galaxies like the Milky Way and

[2] https://cdms.astro.uni-koeln.de/classic/molecules

represents a fascinating laboratory that allows for studying a wide range of astrophysical phenomena, including for example the processes of star formation, the formation of molecules and their chemistry, and the structure and evolution of galaxies. This thesis deals with the interstellar gas component of the ISM that contains ions, electrons, atoms, and molecules that all exist in the gaseous phase. That is why in the following paragraphs we only focus on this constituent and refer the reader to (Draine, 2011) for more details on the other components.

The gas in the ISM consists to almost its entirety of hydrogen (H) and helium (He); 70% and 28% of the total mass, respectively. The remaining 2% are heavier elements, often referred to by astronomers as *metals*[3]. The gas in its thermal and chemical state covering a wide range of temperatures and densities has been classified into a number of *phases* of the ISM. Studies about the phases of the ISM have seen several paradigm shifts over time.

1.2.1 Phases of the Interstellar Medium

The initial description of the ISM was based on the so-called "Two-phase model" by Field et al. (1969). They showed that under the assumption that the atomic gas in the ISM is in thermal equilibrium that this will result in a wide range of pressures for which there are two thermally stable solutions. This corresponds to a cold, dense gas phase with T~100K known as the Cold Neutral Medium (CNM), and a warm, diffuse gas phase with T~10^4 K known as the Warm Neutral Medium (WNM). In this scenario, gas at intermediate temperatures is thermally unstable and depending on its density will either cool down, leading to an increase in density and eventual incorporation into the CNM or heat up, resulting in a decrease in density and eventual incorporation into the WNM.

Eight years later, this two-phase model was extended by another phase. McKee and Ostriker (1977) found that supernovae in the ISM would create large, ionized bubbles filled with very hot gas with T~10^6 K. This gas would eventually cool down, however, the temperature dependence of the atomic cooling curve at high temperatures is such that the cooling time around T~10^6 K is way longer than that of the temperature range of $10^4 < T < 10^6$ K. Therefore, this hot gas would not be expected to have a wide temperature range, but most of it would be around T~10^6 K. This hot ionized phase of the ISM is today known as the Hot Ionized Medium (HIM).

Another few years went by and evidence for another phase arose due to the discovery of dispersion of radio signals from pulsars (e.g. Reynolds, 1989), and the observed free-free absorption of the Galactic synchrotron background (e.g. Hoyle and Ellis, 1963) This phase is known as the Warm Ionized Medium (WIM) and has a similar density as the WNM.

Last but not least, today, a distinction is made between (i) the dense, molecular gas (MG) of the ISM that is observed to be in the form of discrete molecular clouds and, (ii) the lower density, cold atomic gas (AG) that surrounds molecular clouds and is part of the CNM. Figure 1.2 shows an overview of the phases of the ISM with corresponding typical temperatures and densities (taken from Klessen and Glover, 2016). While the gas in the ISM is often classified based only on these distinct phases (HIM, WNM, WIM, CNM, and MG), the question remaining is how *distinct* these phases truly are.

In the classical model of Field et al. (1969) and the many subsequent models inspired by this model, the CNM and WNM are two completely different phases in pressure equilibrium, and all of the neutral atomic hydrogen (H I) in the ISM belongs to one of these two phases. From observations of H I in

[3] Most chemists will not like that.

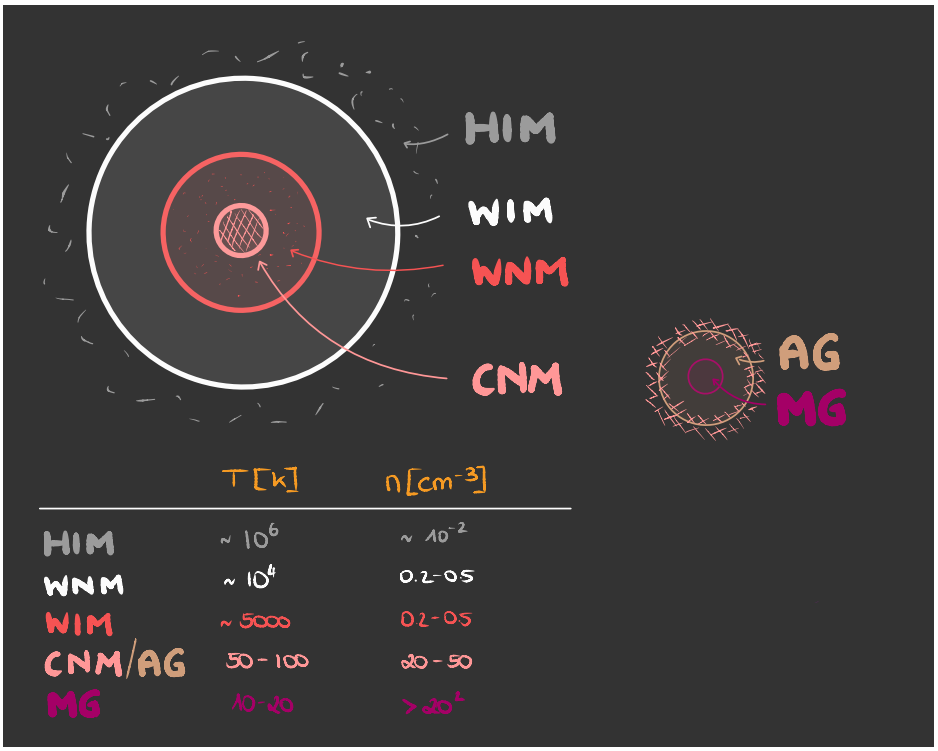

Figure 1.2: **Phases of the Interstellar Medium**. The schematic model showing the Hot Ionized Medium (HIM), Warm Ionized Medium (WIM), Warm Neutral Medium (WNM), and Cold Neutral Medium (CNM) is inspired by McKee and Ostriker (1977). The representation of the Atomic Gas (AG) and the Molecular Gas (MG) is inspired by Klessen and Glover (2016). The temperatures and densities are adapted from Klessen and Glover (2016).

the ISM, however, it appears that the real picture is more complex, as there seems to be a significant fraction of the atomic gas having a temperature between the CNM and WNM solutions (e.g. Wolfire et al., 2003; Roy et al., 2013). This gas cannot be associated with either the CNM or the WNM. That and the inclusion of various phases over the past few years shows that the ISM is far from simple, in fact, the schematic overview in Figure 1.2 is a strong oversimplification since the ISM is highly turbulent. This could cause the mixing together of phases that would otherwise be *distinct* phases of the ISM (see e.g. Seifried et al., 2011). Turbulence is driven by, for example, thermal instability, supernova feedback, and the inflow of gas onto the disk.

1.2.2 Gas Life Cycle in the Interstellar Medium

The development of ISM is like many processes in life - filled with (re-)construction and deconstruction. The so-called gas life cycle, or baryonic life cycle, includes several different types of events that contribute to the evolution and dynamics of gas in galaxies, see Figure 1.3. The cycle begins with a reservoir of gas in the ISM, consisting of a mixture of atomic and molecular hydrogen along with other elements and molecules – a *Diffuse Cloud*. Under favorable conditions, the gas collapses under its own gravity and forms denser regions – *Dense Molecular Clouds*. These clouds predominantly consist of molecular hydrogen and provide the environment for star formation. Within molecular clouds, the

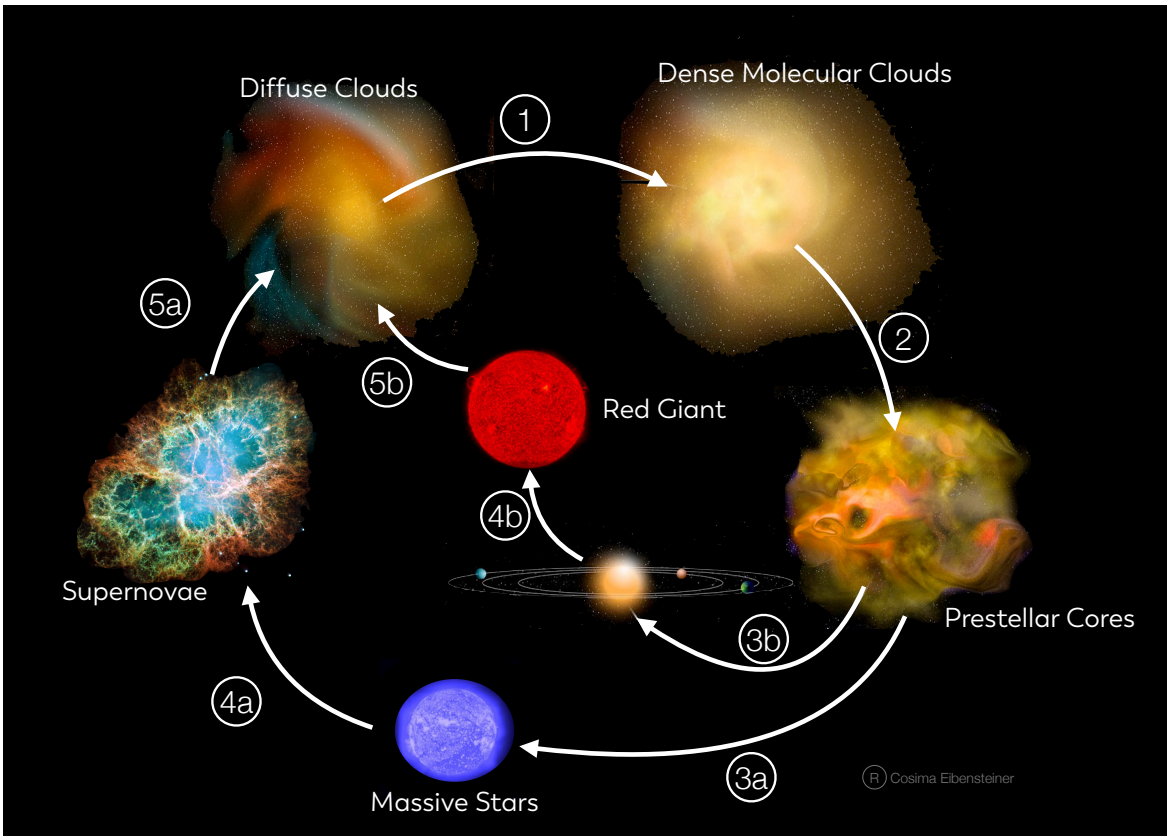

Figure 1.3: **Gas Life Cycle in the ISM.** The individual stages are written out and the processes from one to another stage are indicated with a number. (1) Gas Accretion, (2) Core Formation, (3a) High Mass Star Formation, (4a) Silicon-burning Process, (5a) Feedback, (3b) Low Mass Star Formation, (4b) Run out of Hydrogen Fuel for Nuclear Fusion, (5b) Feedback. Note that the Crab Nebula (between 4a and 5a) is strictly speaking showing the remnants of Supernova 1054. The figure is inspired by Dartois, 2005 and the individual picture credits are: Bill Saxton/NRAO/AUI/NSF; Daniel Huber University of Sydney.

gas undergoes gravitational collapse, leading to the formation of *Protostellar Cores* and subsequent birth of *Low Mass* or *Massive Stars*. When stars form, they release energy and mass back into their surroundings through stellar feedback, such as radiation pressure, stellar winds, and *Supernova* explosions, that can significantly impact the surrounding gas. These processes heat, compress, and disperse the gas, influencing its structure and dynamics. As the feedback processes disperse gas, they contribute to the mixing of different phases of the ISM. This mixing facilitates the redistribution of enriched elements, energy, and momentum throughout the galaxy. Galactic outflows driven by the combined effects of stellar feedback can eject gas from galaxies into the intergalactic medium. Therefore, they play a crucial role in regulating the gas content and star formation activity in galaxies.

1.3 Observing the Interstellar Medium

The entire thesis revolves around the observations of atoms and molecules in the ISM – from (sub)mm to cm wavelength. Therefore, some fundamental concepts relating to the formation and emission of radiation from these will be explained in the course of the chapter.

1.3.1 Spectroscopy and Molecular Basics

Spectroscopy can be described as the measure and interpretation of a spectrum that results from interactions between electromagnetic radiation and matter as a function of the frequency or wavelength of radiation. This thesis makes use of *Radio-Frequency Spectroscopy*. The observed spectra can be used to determine the physical properties of the gas (such as its density, temperature, and ionization state) and its chemical composition. This works with the knowledge of spectroscopic parameters through theoretical work or through measurements in laboratories. In these laboratories, catalogs are created with the goal of assigning various spectral lines (and their energy levels) of astronomical interest to a given species. The two major ones are the Cologne Database for Molecular Spectroscopy (CDMS, Müller et al., 2005) and the Jet Propulsion Laboratory catalogue (JPL, Pickett et al., 1998).

We describe how atoms such as hydrogen emit in Subsection 1.3.6, here we focus on spectral lines of molecules that arise from transitions between discrete energy levels. In general, for molecules, we can distinguish between three types of excitation:

(a) *electronic*; one or more electrons of the molecule get excited. Typical energies of a few eV can be found → this corresponds to lines in the visual or UV wavelength range of a spectrum.

(b) *vibrational*; vibrational state of the two nuclei is responsible for excitation. This is caused by oscillations of the relative positions of nuclei with respect to their positions of equilibrium. Typical energies of $0.1 - 0.01$eV can be found → this corresponds to lines in the infrared part of a spectrum.

(c) *rotational*; state of the two nuclei's rotation around the center of mass is what causes the excitation. Typical energies are $\sim 10^{-3}$eV → this corresponds to lines in the cm and mm wavelength range.

Since this thesis is focusing on cm and mm wavelength ranges, it is obvious that most of the analysis of the excitation involves rotational transitions. For example, for a diatomic molecule, the rotational transition is caused by the change in angular momentum in a molecule that is given as,

$$E_J = \frac{\hbar^2}{2\mu\, R_0^2} J(J+1), \tag{1.1}$$

where $\hbar$ is the reduced Planck constant, μ is the reduced mass, R_0 is the equilibrium separation distance and J is the quantum rotational number.

1.3.2 Radiation

Cosmic radiation is produced by random processes, of which there are three common types: (i) collisions between electrons and protons in a gas, (ii) spiraling of relativistic electrons in a magnetic field, and (iii) transitions between energy levels of an atom or molecule. The types (i) & (ii) generate

radiation over a wide spectrum of frequencies and are called continuum radiation because its frequency spectrum is very broad and featureless. Type (iii) generates a narrow spectrum called a *spectral line*.

The most crucial quantity whenever observational astronomers want to describe radiation is the *specific intensity*, I_ν (also known as spectral intensity or spectral brightness). It is defined by the power $\mathrm{d}P$, describing the energy flow per unit time (i.e. in watts), which is given by (i) an infinitesimal surface area $\mathrm{d}A$ that the radiation travels through, (ii) an angle θ between the incoming ray of radiation and the plane of the surface, (iii) the frequency bandwidth $\mathrm{d}\nu$, and (iv) an infinitesimal solid angle $\mathrm{d}\Omega$,

$$\mathrm{d}P = I_\nu \cos\theta \, \mathrm{d}A \, \mathrm{d}\nu \, \mathrm{d}\Omega \, . \tag{1.2}$$

This equation can be seen as all photons that are collected with a telescope and the *specific intensity* I_ν can be simply expressed as,

$$I_\nu = \frac{\mathrm{d}P}{\cos\theta \, \mathrm{d}A \, \mathrm{d}\nu \, \mathrm{d}\Omega} \quad \left[\mathrm{W\,m^{-2}\,sr^{-1}\,Hz^{-1}}\right]. \tag{1.3}$$

It is, however, often useful to express the specific intensity in units of Kelvin, which is referred to as brightness temperatures, T_B. With Planck's law for radiation, the brightness of a black body radiator at a temperature T, can be expressed as,

$$B_\nu(\nu, T) = \frac{2h\nu^3}{c^2} \frac{1}{e^{h\nu/k_\mathrm{B}T} - 1} \tag{1.4}$$

where k_B is the Botzmann's constant, h is Planck's constant, c is the speed of light and $B_\nu(\nu, T) \equiv I_\nu$. In the case when $h\nu \ll k_\mathrm{B}$, the brightness is given by the Rayleigh-Jeans (RJ) approximation, in which we end up with

$$B_\mathrm{RJ}(\nu, T) = \frac{2\nu^2}{c^2} k_\mathrm{B} T, \tag{1.5}$$

and requires $\nu(\mathrm{GHz}) \ll 20\, T(\mathrm{K})$[4] and would therefore not hold at high frequencies (e.g. millimeter or sub-mm range) and low temperatures. This regime is of interest to many astronomers and Equation 1.5 is proportional to the brightness temperature T_B and can be expressed as,

$$T_\mathrm{B} = \frac{c^2 I_\nu}{2k_\mathrm{B}\nu^2}, \tag{1.6}$$

it is only important to interpret these correctly. Meaning, for

a) low frequencies – like in this thesis studied 1.46 GHz (21cm) H I emission in Chapter 6 and Chapter 7 – Equation 1.6 gives the thermodynamic temperature of the source.

b) higher frequencies, – like in this thesis studied ~87 – 147 GHz (~2 – 3mm)[5] in Chapter 5, T_B is potentially different from a thermodynamic temperature of a black body.

For compact sources, it is common to calculate the integral of the angular surface brightness over the solid angle. This is referred to as the *flux density* $S_\nu$and the total power density from the whole source is

[4] This condition arises when we define the radiation temperature, often used in the mm and sub-mm regime, as $J(T) = (h\nu/k)(1/(e^{h\nu/k_\mathrm{B}T} - 1))$ and plug in the numerical values for k_B and h.

[5] At these frequencies Equation 1.5 is not valid anymore.

$$S_\nu = \int I_\nu \cos\theta \, \mathrm{d}\Omega \left[\mathrm{W\,m^{-2}\,Hz^{-1}}\right]. \tag{1.7}$$

The objects that we observe in this thesis (and almost all other objects out there in space) are usually *very* small in flux densities. It is more practical to scale the flux densities with 10^{-26} leading to a unit that has been named after Karl. G. Jansky – the unit *Jansky* (abbreviated Jy),

$$1\ \mathrm{Jy} = 10^{-26}\ \mathrm{W\ m^{-2}\ Hz^{-1}} = 10^{-23}\ \mathrm{erg\ s^{-1}\ cm^{-2}\ Hz^{-1}}. \tag{1.8}$$

1.3.3 Line Emission

All scientific projects in this thesis focus on studying *line emission* of atoms and/or molecules in nearby galaxies. Line emission occurs whenever an electron undergoes a transition from a high-energy state to a lower-energy state. The energy of the emitted photon equals the differences in energy between the two states. The probability of absorption and emission have been described in Einstein (1917). In the original version, he starts with the canonical state distribution of statistical mechanics in the form of

$$W_n = p_n e^{-\frac{\varepsilon_n}{k_\mathrm{B} T}} \tag{1.9}$$

where k_B is the Boltzmann constant, p_n is a number characteristic of the molecule in the nth quantum state, independent of T, which he calls the statistical "weight" of the state, and ε_n the energy. However, nowadays it is more common to denote the statistical weights as g_n and the energy levels as E_n. Equation 1.9 can be derived from the Boltzmann principle or in a purely thermodynamic way and is the expression of the most extensive generalization of Maxwell's law of distribution of velocities. Einstein (1917) then postulates his hypotheses about the energy transfer through radiation with coefficients that describe the probability of (i) spontaneous emission (ii) absorption and, (iii) stimulated emission. For a two level system labeled as l for *lower* and u for *upper* levels (i)-(iii) have the following form

$$\begin{aligned} &\textbf{(i)}\ \ \mathrm{d}n_l = A_{ul}\, n_u \mathrm{d}t \qquad &&\textbf{(ii)}\ \ \mathrm{d}n_l = -B_{lu}\, n_l\, \rho(\nu)\, \mathrm{d}t \\ &&&\textbf{(iii)}\ \ \mathrm{d}n_l = B_{ul}\, n_u\, \rho(\nu)\, \mathrm{d}t \end{aligned} \tag{1.10}$$

where n_i is the number density of atoms in state i ($\rightarrow\ n_l$ or n_u), and $\rho(\nu)$ is the spectral energy density of the radiation field at frequency ν[6] of the transition. We have A_{ul} in units of $\mathrm{s^{-1}}$, B_{lu} and B_{ul} in units of $\mathrm{cm^2 erg^{-1} s^{-1} sr}$. Consequently, (ii) & (iii) are the results of a radiation field where the energy of the resonator changes due to the fact that the electromagnetic field of the radiation transfers energy to the resonator. The process described in (i) is random and independent of a radiation field.

In the case of thermal equilibrium, we ask for the effective radiation density which must prevail so that the energy transfer between radiation and molecules does not disturb the state distribution of the molecules by virtue of the statistical laws equation (Equation 1.10 and Equation 1.9). That is simply speaking the sum of stimulated emitted photons and the spontaneous emitted photons equals the absorbed photons as,

$$A_{ul} n_u + B_{ul} n_u\, \rho(\nu) = B_{lu} n_l\, \rho(\nu). \tag{1.11}$$

[6] With $\nu = \frac{E_u - E_l}{h}$.

When the transition from a lower level to an upper level is thermalised, then the ratio of the level population follows the Boltzmann distribution as in Equation 1.9,

$$\frac{n_u}{n_l} = \frac{g_u}{g_l} e^{\frac{-h\nu}{k_B T}}, \tag{1.12}$$

where g_l and g_u describe the level degeneracies. T is the excitation temperature (not a real temperature), and when dealing with rotational transitions, it is generally also referred to as the rotational temperature.

In this thesis, we study rotating linear molecules and hydrogen atoms. For rotating linear molecules (for example, CO, see Subsection 1.3.7) we have $g = 2\,J + 1$, where $J = 0, 1, 2, ...$ is the angular-momentum quantum number. Hydrogen atoms have two hyperfine energy levels (their difference yields the 21 cm H I line, see Subsection 1.3.6) with $g_u = 3$ and $g_l = 1$.
Together with Equation 1.12 the Einstein coefficients are related as,

$$\textbf{(i)}\;\; g_l\, B_{lu} = g_u\, B_{ul} \qquad\qquad \textbf{(ii)}\;\; A_{ul} = \frac{2h\nu^3}{c^2}\, B_{ul} \tag{1.13}$$

These are known as the *equations of detailed balance*. They relate the three quantities A_{ul}, B_{lu}, and B_{ul}, therefore all of them can be calculated if only (for example, the spontaneous emission A_{ul}) one is known. Additionally, it shows that B_{ul} must be non-zero, which means that stimulated emission has to take place.

In general, the lowest frequency of line emission depends on the mass and size of the molecule, as $\nu \propto m^{-1} r_e^{-1}$, where r_e describes the equilibrium nuclear separation. This means that large, heavy molecules in cold clouds can be seen at centimeter wavelengths, while smaller and lighter molecules emit at millimeter wavelengths only.

1.3.4 Radiative Transfer

All observations mentioned in this thesis are based on a principle concept – energy transfer in the form of electromagnetic radiation that is propagating through a medium. This is called *radiative transfer*. The interaction with a medium is affected by absorption, emission, and scattering processes of photons. To describe this phenomenon, we consider a beam of radiation with a specific intensity I_ν (see Equation 1.3), emitted with a frequency ν and propagating through matter in a certain direction. Neglecting effects of scattering and the change in amount of radiation received along a path length ds, we can describe it as,

$$\mathrm{d}I_\nu = j_\nu \mathrm{d}s - I_\nu \kappa_\nu \mathrm{d}s \tag{1.14}$$

$$\frac{\mathrm{d}I_\nu}{\mathrm{d}s} = j_\nu - I_\nu \kappa_\nu. \tag{1.15}$$

This *equation of transfer* encompasses two important processes: the increase in radiation via emission – j_ν, the *emission coefficient*[7], and the decrease because of scattering and absorption along the path via absorption of photons – κ_ν, the *absorption coefficient*. Equation 1.15 can be solved for four situations in a straightforward way: (i) for emission only, where $\kappa_\nu = 0$, (ii) for absorption only, where $j_\nu = 0$, (iii) for thermodynamic equilibrium (TE), where the brightness distribution is the Planck function (see Equation 1.4), and (iv) local thermodynamic equilibrium (LTE).

[7] The emission coefficient j_ν is also known as the emissivity

For the fourth case, under LTE conditions, the radiation is assumed to propagate through a uniform medium[8] and j_ν & κ_ν depend on the temperature as it is described through Krichhoff's law as,

$$\frac{j_\nu}{\kappa_\nu} = B_\nu(T). \tag{1.16}$$

The capability of a photon penetrating an absorbing medium along a certain path can be characterized by the optical depth τ_ν, which is given by,

$$\mathrm{d}\tau_\nu = -\kappa_\nu \,\mathrm{d}s\,, \quad \text{or} \quad \tau_\nu = \int_{s_0}^{s} \kappa_\nu\,(\mathrm{s})\,\mathrm{d}s. \tag{1.17}$$

Here is to note that whenever $\tau_\nu \gg 1$ the medium is *optically thick* to the incident radiation and if the opposite is true, $\tau_\nu \ll 1$ then the medium is *optically thin*. The Equation 1.15 can be expressed in terms of τ_ν as,

$$-\frac{1}{\kappa_\nu}\frac{\mathrm{d}I_\nu}{\mathrm{d}s} = \frac{\mathrm{d}I_\nu}{\mathrm{d}\tau_\nu} = I_\nu - B_\nu(T). \tag{1.18}$$

We find then a solution for Equation 1.18 as,

$$I_\nu(s) = I_\nu(0)\mathrm{e}^{-\tau_\nu(s)} + \int_0^{\tau_\nu(\mathrm{s})} B_\nu(T(\tau))\mathrm{e}^{-\tau}\mathrm{d}\tau. \tag{1.19}$$

When we have a isothermal medium, meaning if $T(\tau) = T(s) = \mathrm{T} = \text{constant}$, then Equation 1.19 will turn into,

$$I_\nu(s) = I_\nu(0)\mathrm{e}^{-\tau_\nu(s)} + B_\nu(T)(1 - \mathrm{e}^{-\tau_\nu(s)}). \tag{1.20}$$

Whenever we have a optical thick medium (meaning $\tau \gg 1$), then $\tau_\nu(0) \longrightarrow 0$ and Equation 1.20 reaches the limit and is equal to the Planck function $I_\nu = B_\nu(T)$.

1.3.5 Critical Densities

When we introduced the Einstein coefficient notation in the previous section, we only included transition due to radiative processes. However, in addition, collisions will affect the level populations. These are generally described by the rates for collisional transitions C_{lu} and C_{ul}, both in units of s^{-1}. The detailed balance including C_{lu} and C_{ul} results in,

$$n_l(B_{lu}\overline{I_\nu} + C_{lu}) = n_u(A_{ul} + B_{ul}\overline{I_\nu} + C_{ul}) \tag{1.21}$$

where $\overline{I_\nu}$ is the specific intensity averaged over the line profile and overall directions[9] and the Einstein coefficients A_{ul}, B_{ul}, B_{lu} are described in Equation 1.10. We can express the collisional excitation rates as the product between the density of the collision partner (n_{coll}) and the rate coefficient. The rate coefficient is the average velocity-integrated cross-section denoted as γ in units of $\mathrm{cm}^3\mathrm{s}^{-1}$. Regardless of the equilibrium conditions, the upward and downward collisional rates are related as follows,

[8] That is independent of the material.

[9] The specific intensity averaged over the line profile and overall directions can be expressed as $1/4 \iint I_\nu \phi(\nu)\,\mathrm{d}\nu\,\mathrm{d}\Omega$

$$C_{lu} = \frac{g_u}{g_l} C_{ul} \left(e^{\frac{-h\nu}{k_B T}} \right) \tag{1.22}$$

These rates are known from measurements in laboratories or from quantum chemical calculations, which can be retrieved from the online Leiden Atomic and Molecular Database (LAMDA[10]). Neglecting the effects of the internal and external radiation fields (that is $\overline{I_\nu} = 0$) and under the conditions of an optical thin limit, Equation 1.21 can be expressed as,

$$\frac{n_u}{n_l} = \frac{C_{lu}}{C_{ul} + A_{ul}}. \tag{1.23}$$

Inserting Equation 1.22 reveals,

$$\frac{n_u}{n_l} = \frac{1}{\left(1 + \frac{A_{ul}}{C_{ul}}\right)} \frac{g_u}{g_l} e^{\frac{-h\nu}{k_B T}}, \tag{1.24}$$

and,

$$\frac{n_{\text{crit}}}{n_{\text{coll}}} = \frac{A_{ul}}{C_{ul}} \Longrightarrow n_{\text{crit}} = \frac{A_{ul}}{\gamma_{ul}}, \tag{1.25}$$

this means in turn that $C_{ul} = n_{\text{coll}} \gamma_{ul}$ and n_{crit} is known as the *critical density*. That is the density where the rates of collisional de-excitation equals the rates of radiative de-excitation. This means that for densities that are above n_{crit}, the collisional excitations are efficient for compensating the n_u losses due to de-excitation by spontaneous emission. Consequently, molecules with higher critical densities are used to study regions of denser gas.

1.3.6 Neutral Atomic Hydrogen, HI

Hydrogen is the most abundant element in space and we already know from Subsection 1.2.1 that the gas of the ISM is 70% hydrogen. Two projects in this thesis are studying the neutral atomic hydrogen (H I) that can be detected via the 21-cm line (at a frequency of ~1.42 GHz) that originates in the hyperfine structure splitting of the hydrogen atom due to the interaction between the magnetic moments of the proton and electron within the atom. This hyperfine transition F(1 → 0) in the hydrogen atom represents a flip of the proton and electron spin-configuration from parallel to antiparallel. This transition is *forbidden* (magnetic dipole transition).

Simplified, Figure 1.4 illustrates the proton and electron in a hydrogen atom as charged Miniature golf balls spinning on their own axes (with the Born–Oppenheimer approximation). In the lowest energy state of a hydrogen atom, the proton and electron are spinning in opposite directions. It is possible, however, through collisions with electrons and other atoms, for the hydrogen atom to receive a small amount of energy that aligns the spin of the electron with that of the proton. With the aligned spins, the hydrogen atom is in a slightly excited state. If the electron is left for a very long time of about 10 million years on average, it can spontaneously flip its spin back again to the lower energy configuration. At this spin-flip transition, the energy of the emitted photon is equal to the energy difference between the two spin states of the hydrogen atom. This energy is very small which leads to the long wavelength of 21 cm for the emitted photon. The thought may arise that detecting H I through

[10] https://home.strw.leidenuniv.nl/~moldata/

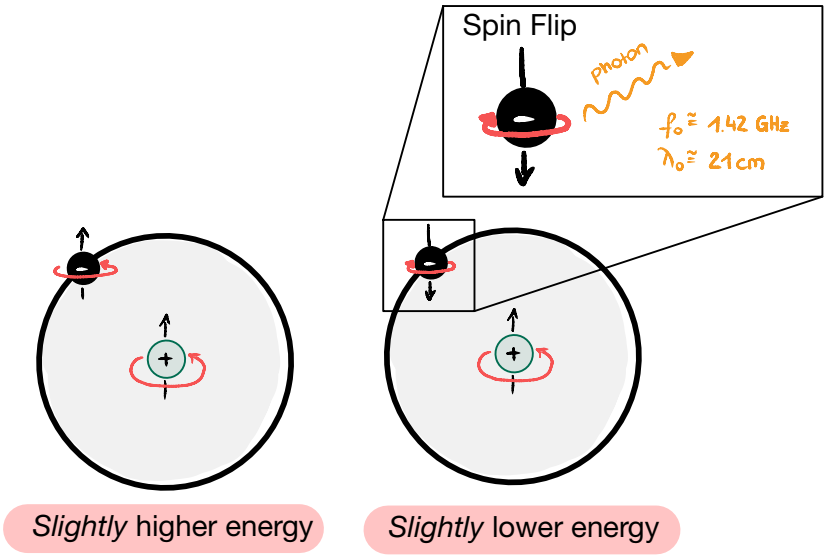

Figure 1.4: **HI spin flip.** (Left) Proton and electron are spinning in the same directions. A hyperfine transition is a consequence of a flip of spin-configuration. (Right) Proton and electron are spinning in opposite directions and a photon is released.

this spin-flip mechanism is almost impossible, though waiting for millions of years for the electron to flip its spin back to the lower energy configuration. However, we need to keep in mind that there is a huge amount of neutral hydrogen atoms in the interstellar medium, some of which are in a slightly excited state at any given time.

Measuring the brightness temperature T_B of H I is linearly related to the H I column density along the line of sight integrated over velocity

$$N_\mathrm{HI}[\mathrm{cm}^{-2}] = 1.82 \cdot 10^{18} \int T_B \, \mathrm{d}v, \tag{1.26}$$

and holds if the radiation is optically thin that is usually the case. Observing the extent of H I gas is one of the most powerful tools in radio astronomy as it traces the kinematics in disk galaxies which gives further insights into the understanding of galaxy evolution. This thesis observes and analyzes H I and studies the kinematics of the nearby galaxy M 83.

1.3.7 Molecular Hydrogen H_2; Carbon Monoxide as the savior

Additionally to H I that we described in the paragraphs before, equally important is the molecular hydrogen phase of the ISM. This thesis analyzes the molecular gas in nearby galaxies (the second and third scientific projects) and that is why we outline here how to observe this particular ISM gas phase.

Molecular hydrogen H_2, the most abundant molecule in space, is symmetric, homo-nuclear, and lacks any dipole moment. Additionally, high temperatures are needed to excite the rotational levels[11] of H_2. The first excited rotational state, $J = 1$, is 175 K above its ground state $J = 0$. The fact that H_2 is a homo-nuclear molecule means that only transitions with $\Delta J = 2$ are permitted, leading to the

[11] Rotational levels are among the other excitation mechanism (i.e. electronic and vibrational) the lowest in energy spacing and therefore easiest to excite.

lowest energy transitions of $J = 2 \rightarrow 0$. The energy spacing depends on the mass of molecules with $m^{-1/2}$ and since H_2 is small in mass, this leads to this large energy spacing of the rotational states.

All of this leads to the fact that H_2 can only be observed in regions of warmer gas. For example, in the vicinity of stars, meaning the process of forming a star already happened. Whenever we want to study star formation regions, the birthplaces of stars, that are associated with the cold ISM (see again Figure 1.2) H_2 is not helpful. Here another molecule can act as a "savior". The second most abounded molecule – Carbon Monoxide (CO). It is related to H_2 via collisions and has rotational transitions that are easily excited even in the gold phase of the gas. Therefore, the CO molecule can be used as an indirect tracer of molecular hydrogen and utilized as a proxy of molecular gas in general.

In more detail, CO can be excited at temperatures of 5.5 K to populate the $J = 1$ state. CO is a heteronuclear molecule and its abundance relative to H_2 is $\sim 10^{-4}$, this makes it possible to observe the $J = 1 \rightarrow 0$ transition (at 115.271 GHz) and higher J transitions that are excited in cold environments of the ISM. From an observer's point of view, it is more convenient to observe the $J = 2 \rightarrow 1$ of CO (at 230.538 GHz) in nearby galaxies (instead of $J = 1 \rightarrow 0$ one). This is because with the current capabilities of ALMA (see Subsection 2.2.4) it allows for a faster observations by a factor of ~ 2 than mapping CO(1-0) due to the line's brightness. In this thesis' third project we use observations of CO(2-1) that were obtained with ALMA.

1.4 Star Formation in Nearby Galaxies

In general, two possible views exists to study the process of star formation namely the microphysics and the macrophysics view (see McKee and Ostriker, 2007, for more details). The microphysics view addresses how individual stars form, deals with questions like whether stars of all dimensions gain most of their mass through the gravitational collapse of a dense core, or searches for the properties of protostellar disks, jets, outflow, and what determines their dynamical evolution. The macrophysics of star formation, on the other hand, approaches the process of forming systems of stars, from clusters to galaxies, and deals with the topics such as the question of why stars form in only a small fraction of the available gas and what defines the mass distribution of forming stars. Another typical question is, what is determining where in the galaxy, in terms of location and the physical state of the ISM, a transformation of its gas content into stars will take place.

This thesis deals with the latter view connected with the attempt to understand its connection to galaxy formation and evolution. In this respect, most of our knowledge of star formation is made up of some kind of scaling relation between the mass of the gas that is believed to form stars and the rate at which that gas is converted to stars – known as the *star formation rate* (SFR).

1.4.1 Star Formation Rate Scaling Relations

The seminal work of Schmidt, 1959 analyzed how atomic gas and stars are distributed in the solar environment and found that the star formation rate is proportional to the square of the gas density. Thirty years, and a second study almost 40 years later, confirmed that with observations of disk-averaged gas surface densities and star formation rate surface density of nearby galaxies (Kennicutt, 1989; Kennicutt, 1998). The tight relationship can be written as,

$$\Sigma_{\rm SFR} \propto \Sigma_{\rm gas}^{N} \tag{1.27}$$

where $\Sigma_{\rm SFR}$ is the SFR surface density, $\Sigma_{\rm gas}$ is the surface density of the total gas (i.e.$\Sigma_{\rm gas} = \Sigma_{\rm HI} + \Sigma_{\rm H_2}$), and N is the power law index, where Kennicutt, 1998 found $N = 1.40 \pm 0.15$ for a sample of ~100 nearby spiral and starburst galaxies. This relation between SFR and gas is known as the *Kennicutt-Schmidt law*. The exact value of the power law depends, however, on which (i) factor is used to convert the observed CO emission to H_2 surface densities[12] and, (ii) tracer is used to infer the SFR and the connected calibration method applied[13]. Overall, because of that, but not only the main reason, N varies in the literature from $N \sim 1-3$ (e.g., Sanduleak, 1969; Hartwick, 1971; Kennicutt, 1989; Buat, 1992).

With the developments of telescopes in the 21st century, it was for the first time possible to resolve the gas and star formation in nearby galaxies. Subsequent studies (see for example, Wong and Blitz, 2002; Leroy et al., 2008; Bigiel et al., 2008; Bigiel et al., 2010a; Schruba et al., 2011) of these spatially resolved quantities changed the picture of the SFR scaling relations. Essentially, the correlation between $\Sigma_{\rm SFR}$ and molecular gas was found to be tighter than the galaxy-averaged correlation to atomic gas first explored by Kennicutt, 1998. Correlations between $\Sigma_{\rm SFR}$ and $\Sigma_{\rm HI}$ only hold in regions where the ISM is completely dominated by atomic gas, but with a very large scatter. In those regions, most likely other parameters such as the metallicity or the stellar mass density affect SFR, which is not the case in inner disks.

1.4.2 Star Formation Rate Tracers

In the thesis' science projects, we use in each project a different technique to trace the SFR. Typically used tracers are near-ultraviolet (NUV), far-ultraviolet (FUV), recombination lines such as Hα emission of galaxies, that measure light from young massive stars (> 8 M$_\odot$), the radiation re-emitted by dust in the infrared (IR) or the thermal free-free part of radio continuum emission that is related to the production rate of ionizing photons. The lifespan of a star is proportional to its mass (via the Kelvin-Helmholtz time scale, $\tau_{\rm th} = \frac{\text{total kinetic energy}}{\text{energy loss rate}} = \frac{2GM^2}{2RL}$[14]), meaning that a star with > 8 M$_\odot$ is short-lived. By extrapolating the rate of young star formation to the entire stellar population using an initial mass function (IMF), which describes the distribution of masses for newly formed stars, it becomes possible to estimate the overall star formation rate.

Radio continuum; Free free emission

Tracers of the number of ionizing photons, specifically free-free radio continuum emission (and hydrogen recombination lines), are often regarded as good indicators of massive star formation. For the first scientific project in this thesis, we use the radio continuum emission at low frequencies that consists of two components: (1) thermal free-free emission which is directly related to the production rate of ionizing photons in HII regions, and (2) non-thermal emission that arises from cosmic ray

[12] This factor is referred to as the X_{CO} *factor* and was assumed as a constant for all galaxies in the majority of SFR-gas relation works. However, nowadays it is known that $X_{\rm CO}$ is lower for starbursts, higher for metal-poor galaxies, and can even vary within galaxies.

[13] In Kennicutt, 1998, he used the H_α luminosities corrected for extinction as a tracer for the SFR. However, one could also use UV, radio continuum, or FIR emission as a SFR tracer. We describe these different tracers in Subsection 1.4.2

[14] In this times scale, G is the gravitational constant, M is the mass and R the radius of the star, and L is the star's luminosity. For example, the Sun's thermal time scale is $\sim 3 \times 10^7$ years.

electrons, positrons which propagate through the magnetized ISM after being accelerated by supernova remnants, or from active galactic nuclei (AGN). Concentrating on the first case only stars more massive than $\sim 8 M_\odot$ are able to produce a measurable ionizing photon flux (see e.g. Murphy et al., 2011; Kennicutt and Evans, 2012).

We do not measure the light from the low-mass stars and because of this reason, they need to be extrapolated. For that, we use the initial mass function (IMF) and a comprehensive set of model predictions for spectrophotometric and related properties of galaxies with active star formation (e.g. `Starburst99`). Using `Starburst99` (Leitherer et al. 1999) together with a Kroupa (2001) IMF[15], together with assumptions of a continuous, constant SFR over ~100 Myr, `Starburst99` stellar population models show a relation between the SFR and the production rate of ionizing photons, $Q(H^0)$ as[16] :

$$\frac{\mathrm{SFR}}{[\mathrm{M}_\odot\ \mathrm{yr}^{-1}]} = 7.29 \times 10^{-54}\ \frac{Q(H^0)}{[\mathrm{s}^{-1}]}\ . \tag{1.28}$$

A continuum map needs to be separated into the (1) thermal free-free and (2) non-thermal (synchrotron) parts of the emission. We denote thermal as $^{\mathrm{T}}$, non-thermal as $^{\mathrm{NT}}$ and the frequency as ν in GHz. The thermal emission scales as,

$$S_\nu^{\mathrm{T}} \propto \nu^{-\alpha^{\mathrm{T}}}, \tag{1.29}$$

and the non-thermal emission as,

$$S_\nu^{\mathrm{NT}} \propto \nu^{-\alpha^{\mathrm{NT}}}. \tag{1.30}$$

To convert the thermal flux into a SFR is then,

$$\frac{\mathrm{SFR}_\nu^{\mathrm{T}}}{[\mathrm{M}_\odot\ \mathrm{yr}^{-1}]} = 4.6\ \times\ 10^{-28} \left(\frac{T_\mathrm{e}}{[10^4\ \mathrm{K}]}\right)^{-0.45} \left(\frac{\nu}{[\mathrm{GHz}]}\right)^{-\alpha^{\mathrm{T}}} \frac{L_\nu^{\mathrm{T}}}{[\mathrm{erg\,s^{-1}\,Hz^{-1}}]}\ , \tag{1.31}$$

where T_e is the electron temperature in units of 10^4 K, ν refers to the frequency in GHz, and L_ν^{T} is the luminosity of the free-free emission at frequency ν in units of $\mathrm{erg\,s^{-1}\,Hz^{-1}}$ written as,

$$\frac{L_\nu^{\mathrm{T}}}{[\mathrm{erg\,s^{-1}\,Hz^{-1}}]} = \frac{L}{[\mathrm{erg\,s^{-1}\,Hz^{-1}}]} \times f_\nu^{\mathrm{T}}\ . \tag{1.32}$$

where f_ν^{T} is the thermal fraction of the radio continuum emission. For completeness, although not studied in this thesis, we also give here the SFR as a function of the non-thermal radio emission that arises from a linear relationship between the total core-collapse supernova rate and the SFR and results in the equation as,

$$\frac{\mathrm{SFR}_\nu^{\mathrm{NT}}}{[\mathrm{M}_\odot\ \mathrm{yr}^{-1}]} = 6.64\ \times\ 10^{-29} \times \left(\frac{\nu}{[\mathrm{GHz}]}\right)^{-\alpha^{\mathrm{NT}}} \frac{L_\nu^{\mathrm{NT}}}{[\mathrm{erg\,s^{-1}\,Hz^{-1}}]}\ . \tag{1.33}$$

An advantage of the SFR calculated based on free-free emission is not subject to the extinction

[15] The Kroupa IMF has a slope of −1.3 for stellar masses between 0.1 and 0.5 $\mathrm{M}_\odot$, and a slope of −2.3 for stellar masses ranging between 0.5 and 100 $\mathrm{M}_\odot$

[16] The following equations are from Murphy et al., 2011.

problems that complicate the estimation of SFR at optical and ultraviolet wavelengths. A caveat is, that the free-free emission is a tracer of high-mass star formation, as it is only sensitive to stars that are able to ionize the surrounding gas and produce an HII region. The SFR based on free-free emission is used in this thesis' first project in Chapter 5 on 150 pc scales.

Far-Ultraviolet, FUV

The Far-Ultraviolet (FUV) part of the electromagnetic spectrum traces the photospheric emission of young stars and is, therefore, one of the most direct indicators of recent star formation (stars formed over the past 10–200 Myr). To convert the FUV intensities into SFR surface densities, we can adopt the conversion of Salim et al., 2007 and divide their coefficient by an extra factor of 1.59 to make the formula appropriate for a Kroupa-type IMF (this has been done in the literature by e.g. Leroy et al. 2008 and Bigiel et al. 2008). This results in:

$$\Sigma_{\mathrm{SFR}}\ [\mathrm{M}_\odot\ \mathrm{yr}^{-1}\ \mathrm{kpc}^{-2}] = 0.86\ \times\ 10^{-28} \times\ I_{\mathrm{FUV}}\ [\mathrm{ergs\ s}^{-1}\ \mathrm{Hz}^{-1}\ \mathrm{kpc}^{-2}] \tag{1.34}$$

Here the effects of internal extinction are neglected, which can be applied to the outer disk of galaxies (see e.g. Bigiel et al., 2010a).

FUV emission can be affected by factors like dust attenuation and the presence of other sources of FUV radiation unrelated to star formation. Therefore, combining FUV observations with data from other wavelengths is often necessary for a more comprehensive assessment of the star formation rate. The FUV emission as a proxy for SFR is used in this thesis' second project in Chapter 6 on 500 pc scales.

Composite Multi-wavelength Tracers

As mentioned in the paragraph before, UV emission is affected by dust attenuation. Therefore, there is a need of combining several tracers which can leverage the advantages of individual SFR calibration methods. One of the prominent combinations, that will be covered in the third scientific topic in this thesis, is the combination of FUV (at 154 nm) and mid-IR (at 22 μm) following Leroy et al., 2019,

$$\Sigma_{\mathrm{SFR}}\ [\mathrm{M}_\odot\ \mathrm{yr}^{-1}\ \mathrm{kpc}^{-2}] = \left(8.9 \times 10^{-2}\, I_{154\,\mathrm{nm}}\ [\mathrm{MJy\ sr}^{-1}] + 3.0 \times 10^{-3}\, I_{22\,\mu\mathrm{m}}\ [\mathrm{MJy\ sr}^{-1}]\right)\ . \tag{1.35}$$

The mid-infrared (mid-IR) possesses several benefits compared to the far-infrared (far-IR). In terms of its physical characteristics, the mid-IR continuum is anticipated to directly respond to incoming radiation. In empirical observations, the presence of warm dust in the mid-IR is closely linked to areas of intense star formation, as supported by studies conducted by Helou et al., 2004 and Relaño et al., 2010. Additionally, the mid-IR demonstrates a lesser contribution from cool dust that is heated by older stars compared to the far-IR. This composite of FUV and mid-IR as a SFR tracer is used in this thesis' third project in Chapter 7 on 1.5 kpc scales.

Challenges of Spatially Resolved SFRs in Nearby Galaxies

The resulting SFR prescriptions implicitly assume that local variations in the stellar-age mix, IMF population, and gas/dust geometry largely average out when the integrated emission of a galaxy is measured.

Kennicutt and Evans, 2012 highlight a hypothetical example where the observers are considered to be observing from the 10 Mpc distant grand design spiral galaxy M 51. If the observer were to target the solar neighborhood in the Milky Way, in a pixel of a size of 100 pc centered on our Sun they would capture no molecular gas and no star formation. However, when they would choose a resolution of 300 pc they would be able to observe the Gould Belt clouds but no SFR (i.e. Hα emission). Increasing the radius to 500 pc would include one of the most active star-forming regions in the galactic neighborhood, Orion with its O stars and HII region. The M 51 observers are then able to measure $\Sigma_{\rm mol} = 0.11 M_\odot$ pc^{-2} but applying the SFR-Hα luminosity relationship from Kennicutt, 1998 they would estimate $\Sigma_{\rm SFR}$ to be a factor of 10 lower than the actual SFR in Orion. The observers would also underestimate the total SFR within 500 pc by a factor of 20 since the other clouds do not produce O stars. This is the case because the Orion cluster is too small to completely populate the IMF. The earliest spectral type within Orion is O7 V, this means that the cluster produces relatively little ionizing luminosity relative to its total mass and SFR.

Under these conditions, whether because the region is small and/or inefficient at forming stars, or because the galaxy as a whole has a low SFR, it is not unusual for studies dealing with low SFRs to be affected by the impact of stochastic sampling, meaning that the stellar IMF is sampled randomly and not completely (see Calzetti, 2013). Stochastic sampling's influence is greater for the most massive stars because we have proportionally fewer massive stars than low-mass stars. From a Kroupa IMF expression, only 11% of all stars, in terms of number, are above 1 $M_\odot$ in mass, even though these stars account for 56% of the total mass.

Strong support for this is provided by the existence of the so-called extended UV (XUV) disks of galaxies, as discovered by GALEX (e.g. the XUV disk of M 83 Thilker et al., 2005). These are bright in UV but faint in Hα. Initially, the hypothesis was that these XUV disks might be the result of peculiar IMFs (for example, lacking massive stars). This was, however, replaced by the realization that the IMF in these regions is stochastically sampled with a low SFR (Goddard et al., 2010). Models by Cerviño et al. (2002) indicate that a cluster of mass $\sim 1 \times 10^4$ $M_\odot$ is undergoing sufficient stochastic sampling so that a scatter in the measured ionizing photon flux of up to 20% can be found. This scatter increases drastically with a decrease in cluster mass, reaching 70% for a cluster mass of $\sim 1 \times 10^3$ $M_\odot$.

This results in a convenient constraint of SFR when an uncertainty of 20% or lower is desired: (i) SFR $\gtrapprox 0.001$ $M_\odot$ yr^{-1} for the use of SFR indicators based on the ionizing photon flux, and (ii) SFR $\gtrapprox 0.0003$ $M_\odot$ yr^{-1} based on the UV (Lee et al., 2009). This thesis' projects deal with linear scales of 150 pc, 500 pc, and 1.5 kpc; in all of these observations, we do not reach the aforementioned limits.

1.4.3 Where do stars form in Nearby Galaxies?

The star-gas-star cycle has continued uninterrupted since the Milky Way was formed. Nevertheless, the newly formed stars are not evenly distributed in the galaxy. In some regions, many more stars seem to form than in others. Whenever we see optical images of a nearby galaxy, we can see much higher concentrations of young, bright, blue stars surrounded by red appearing emission nebulae in the spiral arms of the galaxy. In the radio domain, we can also identify an accumulation of molecular and atomic gas in the spiral arms. So spiral arms contain young stars together with the matter from which new stars are formed.

At first glance, spiral arms appear as if they should move with the stars, however, stars show differential rotation. If stars and spiral arms would move in the same way, the central parts of the arms would have already orbited the galaxy several times in the time, in which the outermost stars orbit once. This difference in the orbital periods would wind up the spiral arms into a dense knot.

This is known as the winding problem. Since we do not observe such tightly wound spiral arms in galaxies, spiral arms are assumed to be rotating waves. Theoretical models indicate that perturbations called density waves are responsible for the spiral arms. As the spiral density waves move through the disk, the changing gravitational forces acting on the stars within the wave cause stars and gas to initially move closer together and subsequently move apart. Simplified, we can imagine it like the traffic behind a slow coach on the highway. Vehicles approaching the coach slow down and drive behind each other. After the vehicles have overtaken the coach, they accelerate again and soon drive again at a greater distance from each other. As a result, there are always a few vehicles crowded behind the coach, even when it is constantly overtaken by a few vehicles. In a density wave, gravity plays the role of the coach, and stars and gas act as vehicles. The stars and gas clouds of a galactic disk are constantly moving "from behind" into and through the spiral arm. What exactly causes the density wave, however, is not yet clear. Density waves are also believed to be the cause of creating bars in barred spiral galaxies where some parts of these central bar-shaped structures are composed of stars. A large accumulation of molecular gas is found at the ends of these bars from which the spiral arms start. These areas are typically referred to as bar ends. This thesis deals with dynamical features such as spiral arms and bars.

Physics at High Angular Resolution in Nearby GalaxieS (PHANGS)

In this thesis, some analyses are based on observations and knowledge from the collaboration Physics at High Angular Resolution in Nearby GalaxieS (PHANGS). In general, PHANGS involves projects to study the small-scale physics of gas, star formation, and stellar feedback, and how these processes are connected to galactic structure and galaxy evolution. It all started with an ALMA Large Program to map the CO emission across the disk of 58 nearby galaxies (PI: E. Schinnerer). Subsequently, additional observations were included which form the PHANGS-ALMA survey that is targeting the CO (2−1) line emission in 90 nearby galaxies (Leroy et al., 2021b). These galaxies are on the SFR-$M_\star$ plane (that is a plot of the star formation rate versus the stellar mass which is commonly used to discuss galaxy evolution) and provide a good sampling of the local "main sequence" of star-forming galaxies. This was followed by observations in other wavelengths, UV with HST (Lee et al., 2022), optical light with MUSE on VLT (Emsellem et al., 2022), infrared with JWST (Lee et al., 2023), and radio waves with VLA and MeerKAT (see Figure 1.5). Currently, for 19 galaxies, all these data of the different wavelengths are available within the PHANGS collaboration. This thesis's scientific projects have drawn immense knowledge from this collaboration (even though technically the galaxies and their observations in the first two projects are not part of the original PHANGS-ALMA sample). The third project of this thesis describes the first PHANGS-MeerKAT survey of three galaxies and lays out the ongoing effort to get the PHANGS-ALMA sample covered with VLA and MeerKAT.

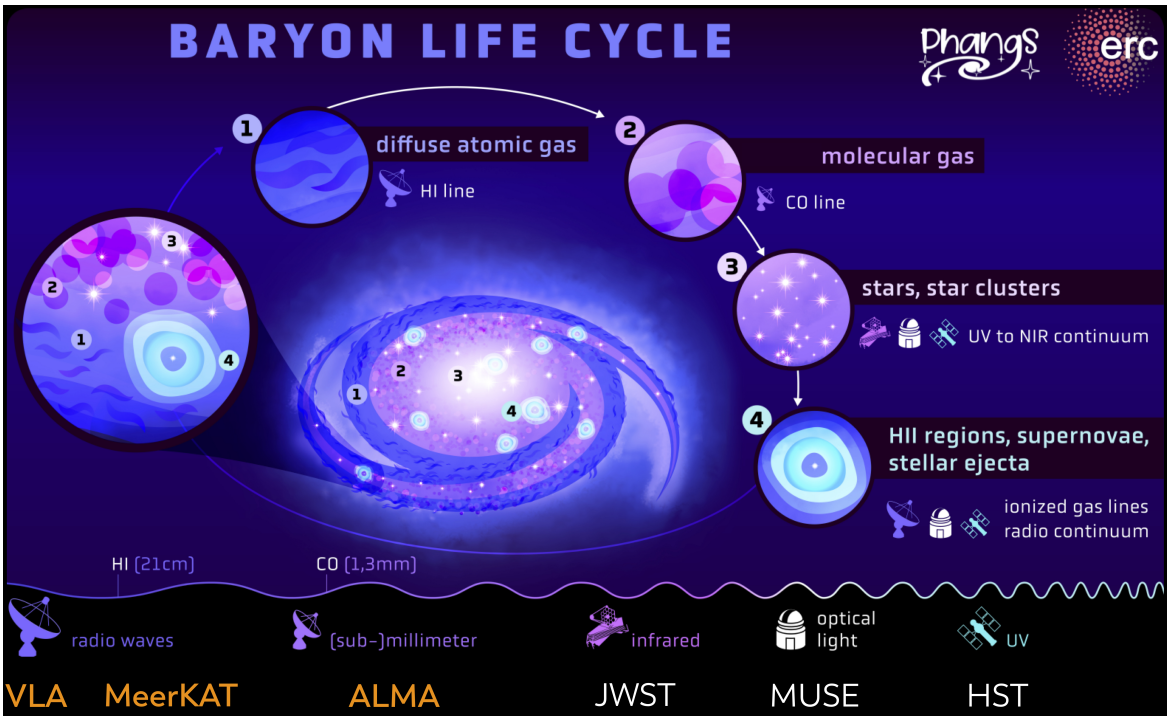

Figure 1.5: **Physics at High Angular Resolution in Nearby Galaxies (PHANGS) and the baryon life cycle.** We show here some of the key interferometers which are used in this thesis as orange (VLA, MeerKAT, ALMA) and they will be described together with interferometers such as NOEMA and single dish telescopes such as IRAM30m and GBT in Section 2.2. This thesis focus is two stages of the baryon life cycle, namely, (1) diffuse atomic gas via the 21 cm H I line and the (2) molecular gas via the CO line and multiple other emission lines in the mm wavelength regime. Image credit: PHANGS collaboration (PI: E. Schinnerer), Design: Daniela Leitner and slightly modified by Cosima Eibensteiner.

1.5 Diagnostic Power of Molecules in Nearby Galaxies

In the first scientific project of this thesis, we analyze a set of molecular emission lines toward the center of the nearby double-barred starburst spiral galaxy NGC 6946. These 2-3 mm lines together with the ancillary 1.3 mm ^{12}CO (2−1) line are used to assess the specific physical and chemical processes in the gas. We outline here some of the covered molecules, important regions of interest, and ratios of molecular emission lines and what they can be used for.

1.5.1 Molecules in Centers of Nearby Galaxies

In the past years, several disk galaxies have been intensively analyzed on ∼100 pc scales across the whole disks with respect to their bulk molecular gas (via CO) or even more recently their HCN emission. However, even for HCN we encounter challenges due to its low brightness, even in the best sources we have so far studied. Investigating multiple molecules in extragalactic environments is currently only possible where they are relatively easy to detect. These are the centers of galaxies, which are ideal laboratories to study a plethora of molecular line emissions.

To illustrate, even in the extremely bright and highly concentrated gas in the centers of galaxies, HCN is about 10 times fainter than CO, and N_2H^+ is about 10 times fainter than HCN; meaning 100

times fainter than CO. Their line brightness is in part due to the different chemistry and therefore the abundance of the molecular lines (and also their excitation condition). Understanding the chemistry of these molecules is important to gain insight into how they can be used as probes for the environment. In the following, we briefly describe this thesis's relevant molecules and outline their formation and destruction pathways.

(1) **HCN and HNC**
HCN, Hydrogen cyanide is one of the molecules that has become increasingly used in nearby galaxy studies in the last two decades. Although here on Earth it is very toxic, smells like almonds, and it is almost impossible to think of associating it with any form of living thing, in space we usually associate denser (compared to CO) molecular gas with where stars are born. Its isomer HNC, hydrogen iso-cyanide does not necessarily share similar chemical or physical properties in interstellar space. It can form through two major pathways via a neutral-neutral reaction (i.e. collisions between molecular species that carry no electrical charge) as,

$$\mathrm{HNC + H \rightarrow HCN + H} \tag{1.36}$$

$$\mathrm{HNC + O \rightarrow NH + CO} \tag{1.37}$$

(e.g. Schilke et al., 1992). The first reaction converts HNC directly into HCN. However, theoretical calculations suggest that both reactions have activation energies too large to contribute at gas temperatures less than several hundred Kelvins (Talbi et al., 1996; Meier and Turner, 2005). Therefore, other reactions, such as,

$$\mathrm{N + CH_2 \rightarrow HCN + H} \tag{1.38}$$

have been suggested (e.g. Goldsmith et al., 1981; Turner et al., 1997), but they are exothermic[17] enough to undergo isomerization upon relaxation, and therefore end up making equal amounts of HNC and HCN (Herbst et al., 2000).

(2) **HCO^+**
The molecule HCO^+, Formylium ion, is thought to be a good tracer of cosmic rays and UV dominated regions in dense gas (e.g. Huettemeister et al., 1995). HCO^+ is believed to be enhanced in regions with young supernova remnants, massive star formation regions, and shocked and dense environments(Dickinson et al., 1980; Wootten, 1981). In dense, quiescent gas HCO^+ forms from proton transfer reactions (i.e. where a proton is removed from one species) of H_3^+ with CO as,

$$\mathrm{H_3^+ + CO \rightarrow HCO^+ + H_2}. \tag{1.39}$$

In diffuse gas or gas in photodissociation regions, HCO^+ has a relatively rapid formation path,

$$\mathrm{C^+ + OH \rightarrow CO^+ + H}, \tag{1.40}$$

followed by,

$$\mathrm{H_2 + CO^+ \rightarrow HCO^+ + H}. \tag{1.41}$$

[17] An exothermic reaction is a reaction in which there is a net release of energy between the energy state of the reactants and the energy state of the products.

HCO^+ has as a critical density nearly an order of magnitude lower than HCN and is therefore considered to be an indicator of gas with densities intermediate between CO and HCN. The formation pathway of HCO^+ leads it to be present in significant amounts in relatively diffuse gas, and because this molecule is an ion, it is more sensitive to collisions with electrons (e.g. Papadopoulos, 2007). In consequence, HCO^+ is able to remain abundant and excited in diffuse gas (Lucas and Liszt, 1996).

(3) **CS**

CS, Carbon monosulfide is the sulfur analog of carbon monoxide and is unstable as a solid or a liquid, but was observed as a gas in both the laboratory and ISM. In regions dominated by UV-radiation, CS can be formed through dissociative recombination of HCS^+[18]

$$HCS^+ + e^- \rightarrow CS + H. \tag{1.42}$$

Another reaction route that becomes important particularly when there is a large SO abundance is,

$$C + SO \rightarrow CS + O. \tag{1.43}$$

Ion-molecular reactions with HCO^+ and with H_3O^+ will destroy CS but will form HCS^+, which in turn can form CS again (Meier and Turner, 2005). At low extinction CS can also be destroyed by photodissociation.

(4) **N_2H^+**

The nitrogen-rich molecule N_2H^+, Diazenylium, is often used in the Milky Way to trace cold and dense regions. N_2H^+ is almost entirely formed through the reaction,

$$N_2 + H_3^+ \rightarrow N_2H^+ + H_2, \tag{1.44}$$

and therefore N_2H^+ is often used as a tracer of N_2 (e.g. Turner, 1995; Benson et al., 1998; Meier and Turner, 2005). In diffuse gas, N_2H^+ is destroyed through dissociative recombination with electrons, and in dark clouds through ion-neutral reactions with CO and O. N_2H^+ is a very selective high-density tracer, as it only efficiently forms once CO is heavily depleted (Meier and Turner, 2005), therefore traces cold, dense gas. In cold, high-density gas, CO freezes out onto the dust grains, eliminating the main N_2H^+ destroyer and making available more H_3^+ to react with N_2 (Caselli and Ceccarelli, 2012). The combined result is a significant enhancement of the N_2H^+ abundance in cold and dense gas. Consequently, N_2H^+ yields a bright emission line in the densest regions of molecular clouds (Caselli et al., 1999; Bergin and Tafalla, 2007), while, in those same regions, carbon-bearing molecules freeze onto dust grains (Tafalla et al., 2002; Bergin and Tafalla, 2007).

(5) **HC_3N**

The formation of HC_3N, Cyanoacetylene, is still unclear. However, the most likely formation process is through a neutral-neutral reaction between C_2H_2 and CN, as

$$C_2H_2 + CN \rightarrow HC_3N + H \tag{1.45}$$

[18] HCS^+ is formed from $S^+ + CH/C_2 \rightarrow CS^+ + H/C$ and $C^+ + SO \rightarrow CS^+ + O$, this is followed by reactions with H_2.

and it is destroyed by photodissociation and through reactions with C^+ (e.g. Turner et al., 1998; Meier and Turner, 2005). It has among the studied molecules the highest critical densities more than an order of magnitude higher than HCN.

(6) **CH_3OH**

The molecule CH_3OH, Methanol, is thought to be a tracer of shocks (e.g. Saito et al., 2017). The reason is that the formation process of CH_3OH in the gas phase is not efficient enough to produce higher amounts of CH_3OH (Lee et al., 1996). The process of, photo-dissociative recombination of $CH_3OH_2^+$, which is formed through a radiative association of CH_3^+ with water molecules H_2O (Turner, 1998) is simply to slow to explain the high amounts and abundances of methanol (Meier and Turner, 2005). Hence, intense CH_3OH emission is believed to arise from a series of hydrogenations of CO on dust grain surfaces under low-temperature conditions (Watanabe et al., 2003). Subsequent to the production on dust, energetic heating mechanisms – shock chemistry – are needed (e.g. Viti et al., 2011; James et al., 2020) to heat the dust and then sublimate CH_3OH into the gas phase. However, methanol emission can also be enhanced in environments without shocks, for example, near massive stars or sources of cosmic rays or X-rays that heat the dust to ∼100 K and evaporate methanol into the gas phase.

(7) **C_2H**

C_2H, Ethynyl, is formed either through the photodissociation of acetylene C_2H_2, or through the dissociative recombination of $C_2H_2^+$ or $C_2H_3^+$ with an electron,

$$C_2H_2^+ + e^- \rightarrow C_2H + H, \tag{1.46}$$

$$C_2H_3^+ + e^- \rightarrow C_2H + 2H/H_2, \tag{1.47}$$

(see Meier and Turner, 2005). That is why, it is believed that C_2H traces diffuse photodissociation regions, where C^+ and UV-photons are abundant. However, C_2H is also destroyed in strong UV fields. Following that, it has been suggested that C_2H can trace star formation in deeply embedded environments, as well as different stages of starbursts (e.g. Li et al., 2012; Martın et al., 2015).

(8) **H_2CO**

The molecule H_2CO, Formaldehyde, forms as,

$$H + CO \rightarrow HCO \tag{1.48}$$

$$HCO + H \rightarrow H_2CO \tag{1.49}$$

(see Woon, 2002). It is widely used as a temperature indicator that is sensitive to warmer (T> 20 K) and denser ($n \sim 10^{4-5}\mathrm{cm}^{-3}$) gas (e.g. Ginsburg et al., 2016; Mangum et al., 2019). H_2CO can be formed in the gas phase as well as on the surface of dust grains (Terwisscha van Scheltinga et al., 2021) and is also a reliable probe of the high-density environs of star formation regions (Mangum et al., 2013).

In general, molecules can indicate various physical or chemical processes, but we must mention here

that each molecule is not a unique tracer of particular processes or sets of physical conditions in a galaxy.

1.5.2 Photodissociation regions and X-ray dominated regions

In this thesis, we use molecular line ratios to distinguish between photodissociation regions (PDRs) and X-ray-dominated regions (XDRs). In the following, we briefly describe them.

PDRs: Ultraviolet photons from O and B stars greatly affect the structure and emission spectra of the interstellar medium. The UV photons of sufficient energy to ionize hydrogen ($h\nu > 13.6$ eV) create a so-called HII region around the star, but lower energy UV photons escape. These far-UV photons (6 eV$< h\nu <$ 13.6 eV) are still energetic enough to photodissociate molecules and ionize atoms with low ionization potentials such as carbon, silicon, and sulfur. Thus, they create a photodissociation region (PDR) just outside the HII region. A 1-D structure of a PDR can be seen in Figure 1.6 (upper panel).

XDRs: X-ray radiation can have a crucial effect on the heating, ionization, and chemical composition of regions known as X-ray dominated regions (XDRs; Maloney et al., 1996). X-ray emission can originate from a variety of sources and processes, including young stellar objects, gas accretion at supermassive black holes, and X-ray binaries. Early seminal studies focused on the effects of X-rays emanating from embedded stellar sources in molecular clouds and the effect of X-rays on the molecular gas within the obscuring torus surrounding Active Galactic Nuclei (AGN). Figure 1.6 (lower panel) shows a 1-D structure of an XDR.

1.5.3 Molecular line ratios

The ratio of different molecular emission lines can be utilized to better understand physical or chemical relationships in nearby galaxies. In project I we mention various ratios among integrated intensities of emission lines and star formation rate tracers. For better guidance, we briefly describe them in the following paragraphs.

(a) $\boldsymbol{I_{\rm HCN}/I_{\rm CO} \propto f_{\rm dense}}$: The integrated intensity of HCN over the integrated intensity of CO is referred to the dense gas fraction $f_{\rm dense}$, so the fraction of gas (above a fixed density) that is denser than gas traced by CO. Various studies of nearby disk galaxy showed that this ratio increases towards galaxy centers (for example, Usero et al., 2015; Bigiel et al., 2016; Gallagher et al., 2018b; Jiménez-Donaire et al., 2019; Bešlić et al., 2021). However, variations of $f_{\rm dense}$ with higher angular resolution and involving other molecules such as HCO^+ or HNC (i.e.) in relation to CO have barely been studied in nearby galaxies.

(b) $\boldsymbol{\Sigma_{\rm SFR}/I_{\rm HCN} \propto {\rm SFE}_{\rm dense}}$: The star formation rate surface density over the integrated intensity of HCN is often referred to as the star formation efficiency[19] of the dense gas $\rm SFE_{dense}$, meaning how efficiently the dense gas is forming stars.

[19] Here we like to note, that the calling $\Sigma_{\rm SFR}/\Sigma_{\rm dense}$ an efficiency is not always liked in the astronomy community. This is because the term 'efficiency' indicates that all of the dense gas (traced for example by HCN) that is available will be used to produce stars and that it has, in reality, a dimension (time^{-1}) that is counterintuitive for an efficiency, which is normally a dimensionless quantity. This is, however, not the real picture. Nevertheless, it has been established to use this term in the context of studying dense gas in nearby galaxies with a word of caution that it is a first-order approximation.

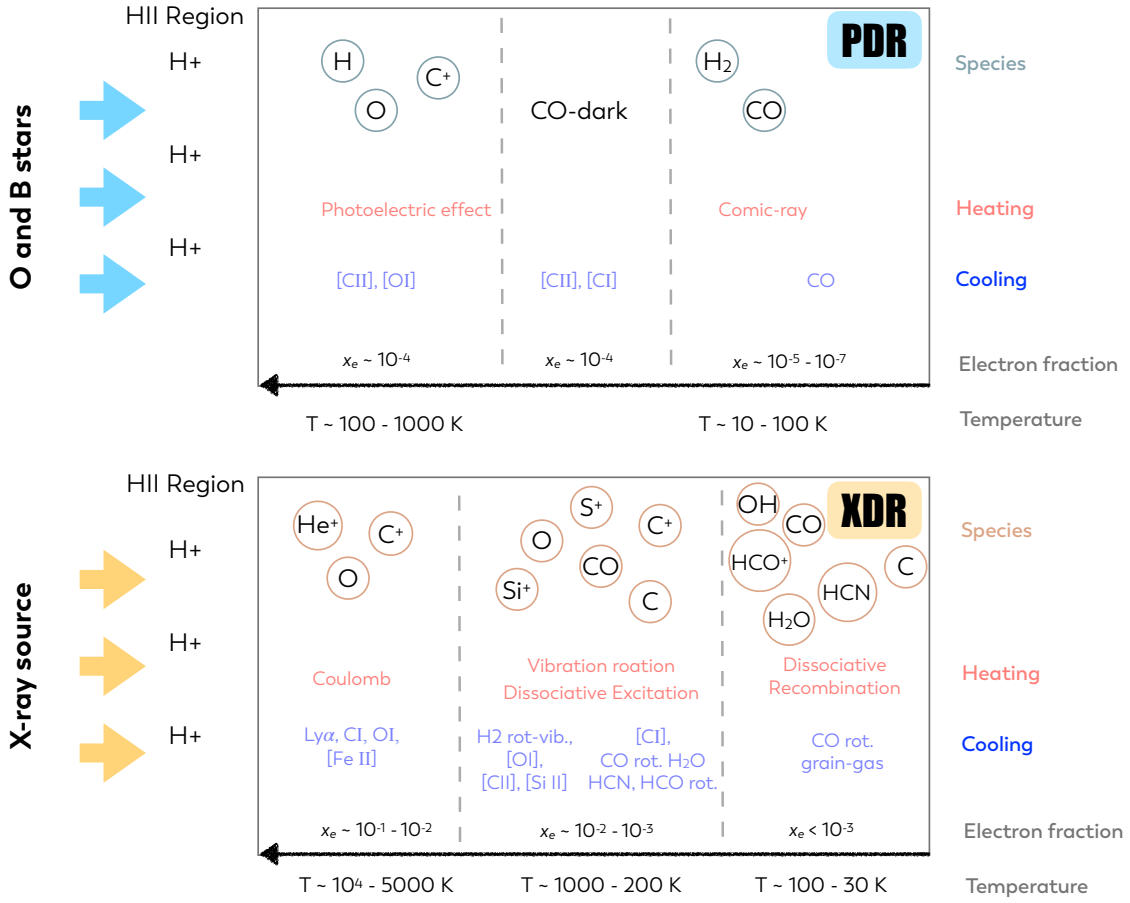

Figure 1.6: **1-D structure of a photodissociation region (PDR) and an X-ray dominated region (XDR).** The top panel shows as a square box of the PDR with decreasing temperature on the x axis. On the left side, we have O and B stars and their FUV flux penetrating through the HII region and into the PDR. The plot reads as follows, for gas at temperatures 100-1000 K, gas is heated by the photoelectric effect on small grains, and cooled by fine-structure lines of [C II] and [O I] with electron fractions of $x_e \sim 10^{-4}$. For higher gas temperatures with 10-100 K, heating is dominated by cosmic-ray and gas-grain heating, and cooling via CO rotational line. In a similar manner, we can read the lower plot, whereas the orange arrows indicate X-rays from the X-ray source. Although we do not go into that much detail within this thesis regarding PDRs and XDRs, these 1-D structures represent their complexity. These plots were inspired by Wolfire et al., 2022 we refer interested readers to their review for more details.

(c) $\boldsymbol{I_{\mathrm{CO\,(2-1)}}/I_{\mathrm{CO\,(1-0)}} \propto R_{21}}$ The ratio between the CO (2−1) and CO (1−0) lines, known as R_{21}, is commonly employed to convert CO (2−1) emission into CO (1−0), which can subsequently be converted into molecular gas mass using the α_{CO} conversion factor. Previous studies have demonstrated that higher R_{21} values are typically observed within the central kpc of individual galaxies (Leroy et al., 2009; Leroy et al., 2013; Koda et al., 2020a; den Brok et al., 2021). However, these studies are not able to resolve variations within the center between different sub-features. Considering the physical aspects, R_{21} is expected to be influenced by several factors, including the temperature and density of the gas, along with the optical depths of the lines (Peñaloza et al., 2018).

(d) $\boldsymbol{I_{\mathrm{HNC}}/I_{\mathrm{HCN}} \propto}$ **kinetic temperatures?**

The abundance ratio of the isomers HCN and HNC indicates a unity value at low temperatures (Schilke et al., 1992; Graninger et al., 2014). The temperature dependence suggests that the ratio is kinetically controlled (Herbst et al., 2000), leading to an expected decrease in the integrated intensity line ratio HNC/HCN at higher temperatures (Pety et al., 2017). However, the sensitivity of this ratio to temperatures in extragalactic sources remains uncertain (e.g. Aalto et al. 2002; Meier and Turner 2005; Meier and Turner 2012). However, a recent study by Hacar et al. (2020) emphasized the strong sensitivity of the HNC/HCN ratio to the gas kinetic temperature (T_{k}) in the Orion star-forming region, bringing renewed attention to this line ratio.

(e) **Ratios among HCN, $\mathrm{HCO^+}$ and HNC**

Theoretical modeling of ratios between $\mathrm{HCO^+}$ and HCN suggested it as a diagnostic tool to distinguish between photon-dissociated regions (PDRs) and X-ray-dominated regions (XDRs) for a given column density of $N \sim 10^{23}$ cm^{-2} in the presence of ionizing radiation (Meijerink and Spaans 2005; Meijerink et al. 2007). In their models, the $\mathrm{HCO^+}$/HCN ratio seems to systematically vary with gas density, the incident ultraviolet and infrared radiation field. Also, mechanical heating and cosmic ray ionization could be possible sources of variations in $\mathrm{HCO^+}$/HCN (Bayet et al. 2010; Meijerink et al. 2011). Including HNC to the analyses, Loenen et al. (2008) claims that in XDRs HNC is always stronger than the HCN line, whereas the inverse trend is seen in PDRs (resulting in line ratios lower than unity). For their analyses they used observations obtained with the IRAM 30-m telescope for the HCN, HNC, $\mathrm{HCO^+}$ line emission of 37 infrared luminous galaxies (Baan et al., 2008) and additional 80 sources from the literature (see Loenen et al. 2008 and references therein); all unresolved measurements. Then they compared the observational data with the predictions of PDR and XDR models (Meijerink et al., 2007) with varying volume densities, ranging from $10^{4.5}$ to $10^{6.0}$ cm^{-3}. Based on that they propose the diagnostic plots shown in Figure 1.7.

1.6 21-cm Line Emission of H I in Nearby Galaxies

The observation of neutral atomic hydrogen (H I) is of great importance because it can tell us more about the kinematics and evolution of galaxies. In this section, we briefly describe the connection between galaxy evolution and cold gas accretion. We highlight some observational phenomena that can serve as indicators of cold gas accretion.

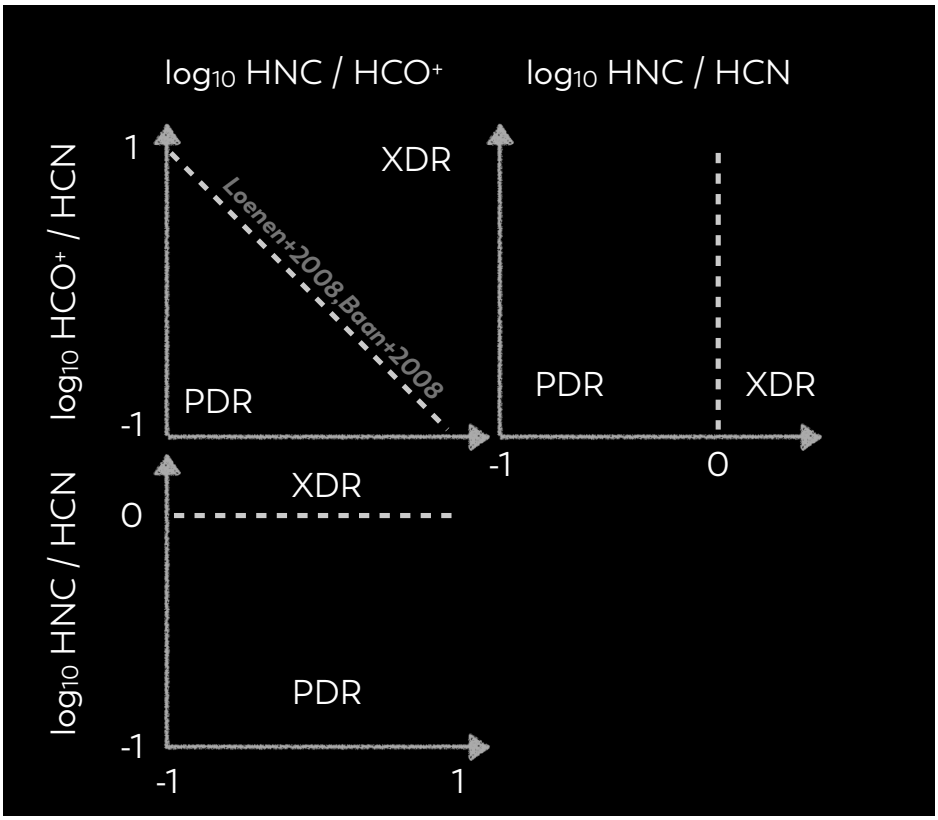

Figure 1.7: **Ratios among HCN, HCO^+ and HNC as a diagnostic tool.** The x and y axis of each panel represent the ratios of two molecules. These plots are the proposed diagnostics to distinguish between a photodissociated region and an X-ray dominated region established in Loenen et al., 2008 and Baan et al., 2008. In this thesis, we apply this to centers of nearby galaxies.

1.6.1 Galaxy evolution: the importance of gas accretion

The universe is in constant change. No state remains. Nothing stays as it is. Even objects the size of a galaxy change: they form, evolve, cluster together, and merge with other galaxies, and in this way some pass away. Galaxies are classified morphologically along the sequence named after the astronomer E. Hubble: Spiral galaxies, barred spiral galaxies, elliptical galaxies, and irregular galaxies. In addition, there are special forms like dwarf galaxies or active galaxies.

Gas accretion is a crucial factor in the formation dynamics of galaxies. The continuous supply of fresh gas is essential for maintaining the ongoing star formation processes. This process of galaxy nurturing by gas infall is thought to continue in the present day. The importance and effects of gas infall on the evolution of disk galaxies have long been recognized, and it is emphasized that it plays a fundamental role in shaping their evolutionary paths. A significant fraction of the baryonic matter in the local universe remains in the intergalactic medium (IGM) and galaxies will grow through a series of infall events, ranging from a few major mergers to a continuous inflow of dwarf galaxies and gas clouds. Especially at lower redshifts, the contribution of gas clouds in the growth process of galaxies becomes more and more important. A direct record of observations demonstrating accretion actually takes place, however, has been difficult to obtain. For the past decades, H I observations provided important insights into the gas content, structure, and kinematics of galaxies, along with information

about their surroundings.

1.6.2 H I in the Outskirts of Nearby Galaxies

Spiral galaxies typically have extended, massive reservoirs of atomic gas that often extend far beyond the inner optical disk. These reservoirs typically reach distances of 2−4 times the optical radius (r_{25}). These extended gas reservoirs play a critical role as potential fuel for star formation in the inner disk.

H I offers the possibility to follow the process of gas accretion from the IGM. This gas flows through diffuse filamentary structures into the circumgalactic medium (CGM) of galaxies and eventually into the galaxy disk itself. The gas entering the galactic halo maintains its cool temperature as it descends onto the disk, consistent with the "cold mode" scenario described in Kereš et al., 2005. This cold accretion mode predominates in environments characterized by lower H I density. From an observational point of view there are possible signs in the structure and kinematic of H I that are indicators of cold gas accretion, these are,

(a) **Interactions, minor mergers and peculiar H I structures around galaxies.** It is believed that these are smoking gun evidences for gas accretion. The remnants of stellar mergers and other faint optical characteristics in the vicinity of galaxies are expressions of the same phenomena found in H I observations.

(b) **Extra-planar gas** is a product of galactic fountains, but must also contain a constituent that resulted from infall or minor mergers. High-Velocity Clouds (HVCs) and filaments in the outskirts are direct evidence for the infall of intergalactic gas.

(c) **Extended and warped outer H I layers** of spiral galaxies can also be a result of infall and provide a source of ongoing supply of fresh gas toward the inner disks.

(d) **Lopsidedness of H I morphology and kinematics** and the asymmetric optical images in many disks could have resulted from recent minor mergers or large-scale cosmological gas accretion.

Phenomena in (a) are thought to be direct evidence of cold gas recreation, however the connection of scenarios described in (b) - (d) and accretion is not completely understood and most of the evidence is indirect. The evidence available from H I observations in the literature[20] suggests that at least 25% of the field galaxies currently or in the recent past have experienced some sort of tidal interaction. The lifetime of the observed features is typically $\sim$ 1 Gyr with H I masses on the order of $10^8 - 10^9$ $M_\odot$. Note that the number of past interactions and mergers could be higher. Taking also the lopsided structure and kinematics as evidence (see (d)), which is also being suggested in optical studies, the consequence would be that more than 50% of today's galaxies have undergone one or more mergers in the recent past.

As for (b), the extra-planar gas consists of two components: one large one from galactic sources and one smaller component which is accreted from the intergalactic medium (IGM). Direct (HVCs in the Milky Way and filaments in external galaxies) and indirect (rotational velocity gradients) evidence of accretion from outside exists. Certainly, it is obvious that the observed extra-planar gas cannot be exclusively and entirely attributed to accretion. This is because, accretion rates would be implausibly high ($\sim$30 $M_\odot yr^{-1}$), and strong observational evidence exists that galactic fountains (i.e. gas outflows induced by Supernovae) take place and play a significant role in forming the halo.

[20] The numbers quoted are from a review by Sancisi et al., 2008 and may have changed slightly since then.

In (c), the gas accretes from satellites or directly from the IGM that settles in the outskirts of the H I disks. These are characterized by spiral features and large-scale warping. They provide a reservoir of gas, from which the gas can slowly migrate to fill up the inner parts of the galaxies.

Phenomena (d), the lopsidedness in the density distribution and disk kinematics seems to be a common phenomenon in spiral galaxies. It is not clear where it comes from or how persistent it is. Minor mergers and tidal interactions were suggested as possible reasons. However, from numerical simulations, it appears that galaxy interactions and mergers are not sufficient enough on their own to explain all the properties of the observed lopsided galaxies, and therefore cosmological accretion of gas on galactic disks has to be responsible. In any case, it seems likely that many of the asymmetries, especially some of those evident in the H I distribution and kinematics, are temporary phenomena and are the result of recent accretion events.

1.7 Scientific Goals and Outline of Thesis

The central regions of galaxies are extreme environments with striking features such as high gas densities and high star formation rates. In contrast, the outer regions of spiral galaxies have lower gas densities and lower star formation rates. The crucial link between these two environments in disk galaxies lies in the dynamics that drive mass flows from the outermost regions and replenish the central regions with fresh material for ongoing star formation. This thesis focuses on studying the gas properties in these two extreme environments using radio observations (see Figure 1.8). These observations provide valuable insights into the fundamental physical and chemical processes that shape and control the interstellar medium in these galaxies. This research provides a deeper understanding of the physical and chemical mechanisms affecting and shaping the ISM in centers and in the outskirts of these galaxies.

The previous chapters introduce the relevant topics that encompass this thesis. Chapter 2 and Chapter 3 will describe the observations and analysis methods that we used. The main part of the thesis can be split into technical and scientific parts. The first includes a project that deals with observations that were re-reduced, calibrated, and imaged with the goal to increase the signal-to-noise ratio (S/N) to check if additional emission lines can be detected. Another technical project deals with the reduction, calibration, and imaging of observations that were later used for scientific analysis. Three scientific projects focus on different scientific questions that we lay out in the following paragraphs. The outline of the thesis is as follows.

TECHNICAL PROJECT I & II

Both of these technical projects are described in Chapter 4. For the first project, we planned to use VLA K band observations to detect Ammonia transition to determine the kinetic temperature at the center of the nearby starburst galaxy NGC 6946. These observations, dating from 2010, were published in Gorski et al., 2018. In their paper, they stated to have detected one transition of Ammonia but left unspecified the reason why the others had not been detected. Accordingly, the task/challenge was to reduce, calibrate, and re-image the data in anticipation of increasing the S/N and discovering more transitions. In Chapter 4 we outline how we reduced and calibrated these observations. The second technical part gives more background about the reduction, flagging, imagining, and correcting for short spacing of scientific project II where we analyzed M83's super extend H I disk.

SCIENTIFIC PROJECT I

The high-resolution molecular line survey towards the center of the Fireworks Galaxy, NGC 6946
Scientific Questions of *Project I*:

- ⋆ How does NGC 6946's small-scale bar affect the molecular line emission?
- ⋆ How do the density tracers (HCN, HCO^+, and HNC) relate to NGC 6946's star formation rate?
- ⋆ In what way do density tracers (HCN, HCO^+, and HNC) and the star formation efficiency of the dense gas depend on resolved environments in the center of NGC 6946?
- ⋆ What do empirical line ratios diagnostics indicate?

Molecular line emission can be used to uncover physical and chemical processes in nearby galaxies. In the past, molecules like HCN were often used in the extragalactic context to trace the denser gas (which is important for star formation) and to study various scaling relations. Other molecules (which

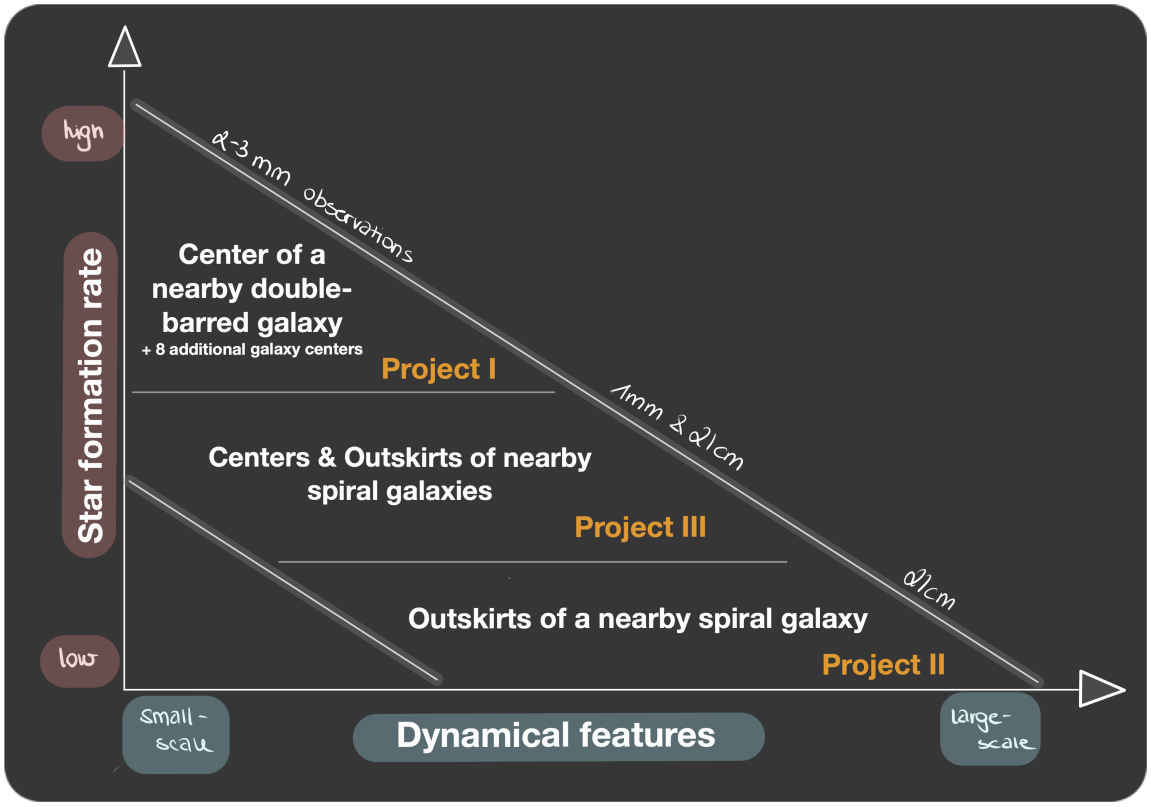

Figure 1.8: **This thesis covers three scientific projects – Project I-III**. We show them in a star formation rate (SFR) - dynamical features (DF) plane. The first project deals with regions of high SFR and small-scale DF – an inner small-scale bar and its effect on molecular line emission (detected in the 2-3mm window). The second project investigates regions of low SFR and large-scale DF – giant spiral arms and connecting branches that can be seen in atomic hydrogen (via the 21cm H I emission). The third project uses observations that indicate regions of both low and high SFR and small-scale and large-scale DF, where we particularly focus on the new observations of the atomic gas content. We investigate the relationship between molecular and atomic gas in these galaxies.

mostly indicate even denser gas) are more difficult to detect because they are much fainter. Galaxy centers are so far the ideal extragalactic laboratories to study them, their relation to other molecules as an indicator of physical processes, and scaling relations to star formation. In this work, we use high-resolution observations that are among the first studies to investigate the effects of the second bar of a double-barred spiral galaxy on molecular emission. Chapter 5 describes and discusses the 132 hours observation of the central $50''$(corresponds to 1.9 kpc) towards the nearby double-barred actively star-forming galaxy NGC 6946. The whole suite of molecular lines gives us one of the most comprehensive, high-resolution ($2 - 4'' \approx 75 - 150$ pc) molecular line data sets for a nearby galaxy center in the northern hemisphere and addresses the aforementioned scientific questions.

SCIENTIFIC PROJECT II

Kinematics of M 83's super-extended HI disk
Scientific Questions of *Project II*:

- ⋆ How is the H I gas surface density distributed in the nearby galaxy M 83?
- ⋆ To what extent does the H I gas surface density, velocity, and velocity dispersion depend on the environment within M 83?
- ⋆ How does the velocity dispersion behave across the whole disk of M 83?
- ⋆ What are the important factors that impact ring-averaged mass flow rates?

The 21cm H I emission line is used to trace the kinematics of galaxies. The H I disks of nearby spiral galaxies are extending far beyond their optical radius, usually 2-4 times the optical radius (r_{25}). Some rare examples can show H I emission extending more than 5 times r_{25} – we call this phenomenon in this work, *super* extended H I disk. The very near grand-design spiral galaxy M 83 is such a candidate. However, studies of such were limited by coarser resolution or not being able to capture the entire disk. In this work, we analyze the super-extended H I disk of M 83 in terms of its kinematics with new VLA observations using a 10-point mosaic covering roughly 1.5 deg^{-2} on the sky, that is nine times the appearance of the moon in the night sky. Chapter 6 describes and discusses the high resolution ($21'' \approx 500$ pc) 40 hours VLA observation across the entire H I disk of M 83 and the combination with single dish GBT observation. This is one of the first data sets of a super-extended H I disk and addresses the aforementioned scientific questions.

SCIENTIFIC PROJECT III

Physical processes driving the conversion of atomic to molecular gas in nearby galaxies
Scientific Questions of *Project III*

- ⋆ How is the atomic and molecular gas distributed in nearby galaxies?
- ⋆ Where do nearby galaxies cross their atomic equals molecular gas (i.e. where $R_{\mathrm{mol}} = \Sigma_{\mathrm{H2}} / \Sigma_{\mathrm{HI}} = 1$) boundary? In other words, where does atomic gas become molecular?
- ⋆ On what physical quantities does R_{mol} depend on?
- ⋆ To what extent do interacting and non-interacting galaxies show different behaviors?

In the previous two projects described in Chapter 5 and Chapter 6 we investigate the physical and chemical mechanisms of molecular and atomic gas, respectively, at the center and outskirts of nearby galaxies. The crucial link between these two environments in disk galaxies is dynamics. It drives mass flows from the outermost regions (atomic gas) and fuels galaxy centers, where it gets converted to molecular gas along the way, with fresh material to form stars. Previous studies investigate where this conversion from atomic to molecular gas happens and analyzed connections to some physical parameters. However, these studies mostly were limited to coarse sensitivity observations, and thus not able to capture the low H I density gas, and/or had not a multi-wavelength suite of ancillary data available. In Chapter 7, we analyze new high-quality and highly sensitive MeerKAT H I observations of the first three PHANGS-MeerKAT galaxies together with five galaxies from the MHONGOOSE collaboration along with high-quality data from the PHANGS-ALMA survey, along with multi-wavelength observations (such as ultraviolet or infrared) to address the science questions.

Chapter 9 gives a brief overview of future projects focusing on both molecular and atomic hydrogen in nearby galaxies, either including important additional tracers and/or increasing the sample size. Finally, Chapter 8 concludes with the key results and findings of this thesis.

CHAPTER 2

Observations

Overview

Astronomers observe a range of wavelengths of the electromagnetic spectrum, and when observing from the ground, some of the incident energy is absorbed by the atmosphere. The places where the atmosphere absorbs little or almost none are called the atmospheric windows, where radiation can pass through the atmosphere of Earth. Figure 2.1 shows exactly that and indicates why radiotelescopes observing in the sub-mm regime need to be built at higher altitudes. In this thesis we study mainly wavelengths of $\lambda = 21$ cm down to shorter wavelengths around $\lambda = 1$ mm.

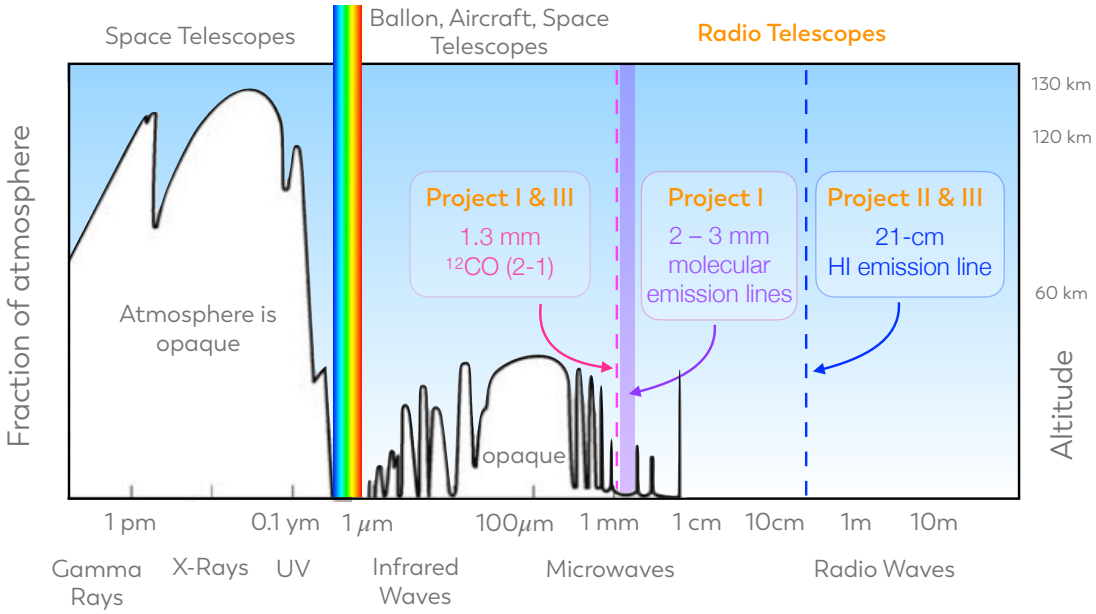

Figure 2.1: **Atmospheric transmission.** Schematic representation of the transmission through the atmosphere of Earth in the electromagnetic spectrum as a function of wavelength. The black curve represents the fraction of the atmosphere and the altitude required to achieve a transmission of 0.5. This means that the atmosphere below the black curve is opaque. We highlight the emission lines studied in this thesis. This figure is inspired by Wilson et al. (2013).

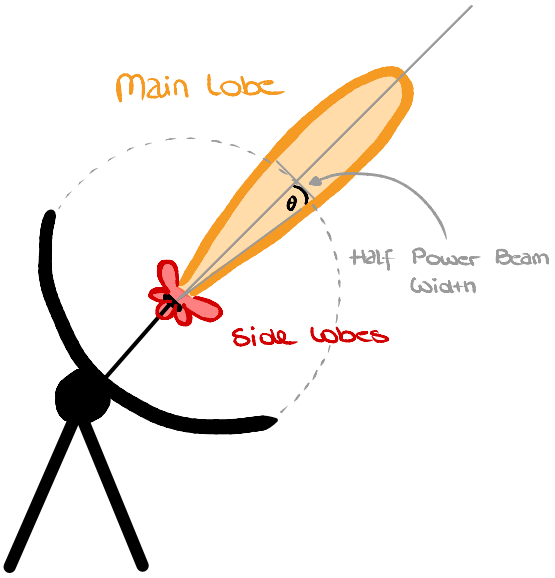

Figure 2.2: **Antenna Power Pattern.** Shown are the main lobe that points in the direction of the source and the side lobes that illustrate the power pattern of an antenna. The dashed semicircle represents, normalized to the signal strength, half of the signal. The angle θ indicates the angle to the pointing axis of the antenna, and Φ is the rotational direction that is perpendicular to the axis. Together they form the antenna power pattern $P(\theta, \Phi)$ in Equation 2.3.

2.1 Observing in the mm-cm regime

Whenever radio astronomers observe an astronomical object, they strive for higher angular resolution and higher sensitivity to detect faint signals. The angular resolution depends on the diameter of a telescope and can be improved by building a larger single dish telescope[1] or simulating a larger telescope by connecting several antennas together. An array of multiple antennas is called an interferometer where the distance of those antennas furthers apart (also called maximum baseline) acts like the diameter. A telescope's diameter provides us information about the area in which the signal is collected, the collecting area (like wider buckets collect more rain). Increasing the collecting area and minimizing the noise (the temperatures of the system) can improve the sensitivity of a telescope. In the following, we describe the basics of a single dish telescope and further explain an interferometer. We refer the reader to Thompson et al., 2017 for a more detailed description.

2.1.1 Telescope fundamentals

Before we start introducing the concept of an interferometer we look into a simpler instrument – a single-dish telescope. The parabolic-shaped antenna collects electromagnetic waves that are reflected and directed into the focal point, and further into the receiver. The telescope is sensitive to radiation from all directions and can therefore be described by its power pattern $\mathrm{P}(\theta, \Phi)$ where the angles θ

[1] Building a larger single dish telescope with acceptable performance is limited to a diameter of about 100 m. Larger dishes will become drastically less accurate about their surface, such that the highest angular resolution achieved with single-dish telescopes at sub-mm wavelengths is $10''$.

and Φ describe the direction with respect to pointing axis in polar coordinates. Essentially, the power pattern (see Figure 2.2) measures the response of the telescope to a point source containing the main beam (the largest lobe), and the sidelobes (the smaller lobes). Describing the main beam lobe as a Gaussian function, the width at half power (the so-called half power beam width, HPBW), or full width at half maximum (FWHM), determines the angular resolution. The resolution θ_{FWHM} depends on the wavelength (or frequency) and the diameter of the telescope (as $\theta \propto \lambda/D$). From Figure 2.2 we also see that the area on which the dish is collecting radiation does not coincide with the geometric area of the dish. The effective collecting area, A_{eff} is defined as,

$$A_{\mathrm{eff}} = \frac{\lambda^2}{\Omega_{\mathrm{A}}} \tag{2.1}$$

where λ is the wavelength and Ω_{A} is the total beam solid angle that can be described as,

$$\Omega_{\mathrm{A}} = \iint_{4\pi} P(\theta, \Phi)\, \mathrm{d}\Omega\,. \tag{2.2}$$

Essentially, it gives the total directivity contributed by the radiation of an ideal isotropic source. Integrating only over the main lobe, we obtain the solid angle of the main beam, Ω_{mb}. The ratio of the total beam solid angle with the main beam is then the main beam efficiency $B_{\mathrm{mb,eff}} = \Omega_{\mathrm{mb}} \,/\, \Omega_{\mathrm{A}}$. The total power received by an antenna in a unit of frequency for unpolarized radiation[2] is characterized by Equation 2.1, the sky brightness distribution $\mathrm{I}(\theta, \Phi)$ and the power pattern of an antenna normalized with respect to its peak as,

$$P_\nu = \frac{1}{2}\, A_{\mathrm{eff}} \int_\Omega I(\theta, \Phi)\, P(\theta, \Phi)\, \mathrm{d}\Omega\,. \tag{2.3}$$

Whenever we want to observe an object with an antenna, we want to determine the emission of this object, which is referred to as the main beam temperature, T_{mb}. This temperature is among other factors related to the temperature of the antenna, T_A. With the brightness, $I(\theta, \Phi)$ being a black body radiator under the Rayleigh-Jeans approximation (see Equation 1.5), together with Equation 2.2, we find the Johnson-Nyquist noise as,

$$P = k_{\mathrm{B}} T. \tag{2.4}$$

This called thermal noise can be used to relate the power per unit frequency of an antenna and T_{A}, as,

$$T_{\mathrm{A}} = A_{\mathrm{eff}} \frac{\nu^2}{c^2} \int_\Omega T(\theta, \Phi)\, P(\theta, \Phi)\, \mathrm{d}\Omega = \frac{1}{\Omega_{\mathrm{A}}} \int_\Omega T(\theta, \Phi)\, P(\theta, \Phi)\, \mathrm{d}\Omega\,. \tag{2.5}$$

Assuming a uniform brightness temperature across the solid angle gives,

$$T_{\mathrm{A}} = \frac{1}{\Omega_{\mathrm{A}}} T \int_\Omega P(\theta, \Phi)\, \mathrm{d}\Phi \Longrightarrow T \tag{2.6}$$

This means that the antenna temperature is equal to this temperature in the Rayleigh-Jeans limit independent of the size of the antenna. This temperature is referred to as the brightness temperature T_{B}. For a source filling just the main beam the temperature is related to the forward beam efficiency, F_{eff} correcting for rearward losses and the main beam efficiency $B_{\mathrm{mb,eff}}$ considering only the main

[2] The factor 1/2 in Equation 2.3 arises from the fact that we considered only unpolarized radiation.

beam lobe, as,

$$T_{\rm mb} = \frac{F_{\rm eff}}{B_{\rm mb,eff}}\, T_{\rm A}, \tag{2.7}$$

where $T_{\rm mb}$ stands for the main beam brightness temperature.

As mentioned earlier, the sensitivity of a telescope depends on the noise temperature that influences the observations. The sum of all these temperatures is known as the system temperature ($T_{\rm sys}$) and depends on,

$$T_{\rm sys} = T_{\rm bg} + T_{\rm sky} + T_{\rm spill} + T_{\rm cal} + T_{\rm rx}\ , \tag{2.8}$$

where $T_{\rm bg}$ is the galactic background temperature, $T_{\rm sky}$ the sky temperature (contribution of atmosphere), $T_{\rm spill}$ is the spillover temperature, $T_{\rm cal}$ is the contribution based on the injected noise, and $T_{\rm rx}$ the receiver noise temperature. Related to that, the radiometer sensitivity equation is given by,

$$\sigma = \frac{T_{\rm sys}}{\sqrt{\Delta\nu\ t_{\rm int}}} \tag{2.9}$$

where $t_{\rm int}$ is the integration time ($\propto\ N\ \Delta t$, for N samples and a integration time step Δt), and $\Delta\nu$ is the spectral resolution. The spectral resolution is given by the maximum bandwidth $\mathrm{Bw}_{\rm max}$, and the spectral channels $N_{\rm chan}$that are required to ensure the Nyquist sampling rate (that is $1/{\rm d}t = 2\ \mathrm{Bw}_{\rm max}$) as,

$$\Delta\nu = \frac{\mathrm{Bw}_{\rm max}}{N_{\rm chan}} = \frac{1}{2\ N_{\rm chan}{\rm d}t} = \frac{1}{2\Delta t}\ . \tag{2.10}$$

The minimum change in antenna temperature that can be confidently detected is usually specified as being greater than or equal to three times the rms value of the noise. Consequently, a line is considered to be detected with certainty if the peak intensity of the line is $> 3\sigma$. The angular resolution is, as said earlier, for a single-dish telescope limited by its geometric diameter. Improving the possible changeable factors in Equation 2.8, for example, $T_{\rm rx}$, can lead to a significant improvement in the sensitivity of a telescope.

2.1.2 Interferometer

One of the most remarkable developments in radio astronomy was the creation of astronomical interferometry in 1946. In that year Ruby Payne-Scott used the sea cliff interferometer she had co-designed with Joseph Pawsey to perform the first radio interferometry for astronomical observations. In the same year, they worked on the first formulation of the idea of aperture synthesis[3]. Although not mentioned enough, Payne-Scott contributed significantly to the theory of radio interferometry.

Essentially, an interferometer consists of an array of separated telescopes (referred to as "antennas" hereafter) that simultaneously observe the same source and measures the interference pattern produced by the apertures, which are related to the source brightness distribution. Observing a source with spatial sky coordinates l and m will give the brightness distribution as $I(l, m)$. With the help of the technique of aperture synthesis, the interferometer is simulating a larger antenna with the exact angular resolution as an instrument the size of the whole array to achieve higher resolution. The high-resolution is governed by the largest distance between two antennas in an array. The distance of a pair of antennas is specified by the spatial frequencies in units of wavelengths referred to as the baseline. This is defined as the separation vector (u, v). Interferometers exploit the rotation

[3] See https://public.nrao.edu/blogs/ruby-payne-scott/

of the Earth, causing the projected baselines to vary and this will result in elliptical tracks in the u-v-coverage[4]. Due to the rotation of the Earth and the differences in the path length between the source and each antenna, variations occur in the relative phases of a signal received by each antenna. The recorded signal of these separated antennas will be correlated and the correlation product $V(u, v)$ is referred to as ''visibility'' with the Fourier coefficients being called the ''visibilities''. The true sky brightness distribution $I(l, m)$ and V are linked via the van Cittert-Zernike theorem (van Cittert, 1934; Zernike, 1938),

$$V(u, v) = \iint I(l, m) \mathrm{e}^{-2\pi i(\theta\ u + \Phi\ v)} \mathrm{d}l \mathrm{d}m \tag{2.11}$$

which states that the correlation product for a single baseline is the Fourier coefficient of the true sky brightness distribution for that baseline.

In Figure 2.3 we see a sketch of a simple interferometer consisting of two antennas. They point toward the same astronomical source and the wavefront from the source in the direction θ reaches the right-hand antenna at a time,

$$\tau_g = \frac{D}{c}\ \sin\theta \tag{2.12}$$

earlier than the left-hand one. τ_g is referred to as the geometric delay, the distance between the two antennas is the baseline D and c is the speed of light. The two signals then get amplified and later undergo *heterodyning*, meaning the mixing of the frequencies with a frequency from a local oscillator (ν_{LO}). Then it will run through the Baseband filter and results in the intermediate frequency (IF). The right-handed antenna gets an arbitrary phase (ϕ_{LO}) added before being mixed, and after mixing is accounted for the geometric delay via τ_i. Then the signals of both antennas that have a phase-offset get correlated and reach the integrater followed by the recorder for storing the data.

For an interferometer, a few of the most important performance metrics are the resolution, the maximum recoverable scales, and the sensitivity. The approximate resolution of an interferometer is related as,

$$\theta_{\mathrm{res,\ interferometer}} = k\frac{\lambda}{D_{\mathrm{max}}}, \tag{2.13}$$

where k is a factor depending on the weighting of the visibilities during inversion (typically ~ 1) and D_{max} is the longest baseline in the array. The approximate maximum recoverable scale (MRS) is related to the minimum baseline as,

$$\theta_{\mathrm{MRS,\ interferometer}} \approx 0.6\frac{\lambda}{D_{\mathrm{min}}}. \tag{2.14}$$

Interferometers are excellent for high resolution studies but one of the most important performance metrics is sensitivity. The radiometer sensitivity equation (Equation 2.9) for an interferometer is given by,

$$\sigma = \frac{T_{\mathrm{sys}}}{\sqrt{N(N-1)\Delta\nu\ t}}. \tag{2.15}$$

Here, $N(N\text{-}1)$ indicates the independent samples for an interferometer with N identical receivers and $N(N\text{-}1)/2$ individual baselines.Analogically, the rms noise of the brightness temperature, σ_{T_B}, in the

[4] The u-v-coverage can be understood as a mask for the Fourier transform of the image. It represents where on the Fourier plane the image was sampled.

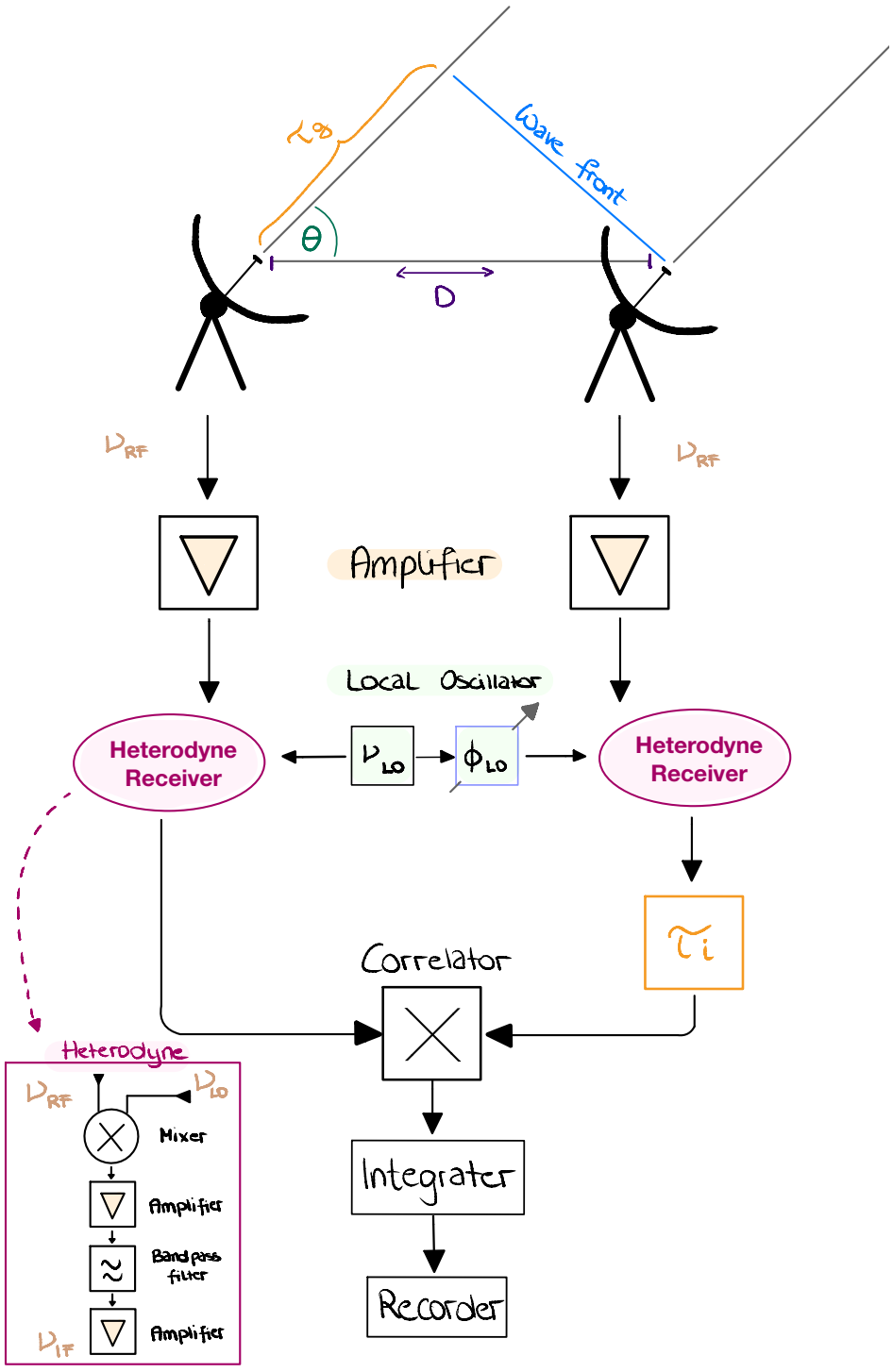

Figure 2.3: **Block diagram for a two antenna interferometer.** A wavefront is received by two antennas with a distance D, one of them with a geometric delay τ_g. The two signals get amplified and the signal from the left antenna enters the *Heterodyne Receiver* together with frequencies of a local oscillator, ν_{LO}. The pink box indicates what occurs in that receiver. The signal from the right antenna will enter the receiver together with ν_{LO} and the phase of the local oscillator, ϕ_{LO}, and will be corrected for the geometric delay. The signal of both antennas will be correlated, and reach the integrator followed by the recorder for storing the data.

RJ limit is related as,

$$\sigma_{T_B} = \frac{2\ k_{\rm B}\ T_{\rm sys}}{A_{\rm eff}\ \Omega_{\rm A,\ Gaussian} \sqrt{N(N-1)\ \Delta\nu\ t}}. \tag{2.16}$$

where, $\Omega_{\rm A,\ Gaussian}$ is the beam solid angle for a Gaussian beam (=1.133 $\theta^2_{\rm HPBW}$). In general, lower values of the system equivalent flux density (SEFD) indicate more sensitive performance and is defined as,

$$\text{SEFD} = \frac{T_{\rm sys}}{G} = \frac{T_{\rm sys}}{A_{\rm eff}\ B_{\rm mb,eff}/(2\ k_{\rm B})}, \tag{2.17}$$

where G is the total antenna gain.

2.2 Telescopes used in this Thesis

This thesis uses observations from various telescopes. The first published project is focusing on the sub-mm, mm regime of the electromagnetic spectrum and makes use of the data from the interferometer PdBI (now known as the NOEMA), and the single-dish telescope called IRAM30m. The second published work and a prior project (that is described in Section 4.1) focus on the cm regime and use observations from the interferometer VLA and the single-dish telescope Green Bank Telescope (GBT). The third project which is in preparation uses the interferometer ALMA and MeerKAT combining observations from mm and cm wavelengths, together with ancillary data taken from space telescopes. The following paragraphs will describe each of these telescopes (starting with the interferometers) and will finish with an overview chart that relates the capabilities of the major interferometers used in this thesis.

Figure 2.4: **VLA.** Me in front of one of VLA's antennas. Image credit: Dr. Kenzie Nimmo.

2.2.1 (Karl G. Jansky) Very Large Array (VLA)

The Very Large Array (VLA) is one of the world's most significant astronomical radio telescopes, located in New Mexico 80 km west of Socorro, and is operated by the National Radio Astronomical Observatory (NRAO). Already built in the 1970s at an elevation of 2 120 m above sea level, it is one of the world's most powerful radio interferometers in terms of science output. The VLA consists of 27 (plus one spare) parabolic antennas, each of them 25 m in diameter. The antennas are oriented in an upside-down "Y-shape" and can be moved to adjust the baselines and thus the u-v-coverage with a maximum baseline of 36 km. Four common configurations are used, named A (the largest) through D (the narrowest, with all dishes within 600 meters of the center point). Each of the antennas uses receivers with frequencies ranging from 74 MHz to 43 GHz.

Building on the excellent observing conditions and existing infrastructure of the VLA site, the next-generation VLA (ngVLA) will be an interferometric array with more than 10 times the sensitivity and spatial resolution of the current VLA (and ALMA), operating at frequencies spanning from $\sim 1.2 - 116$ GHz with baselines spanning across North America and Mexico ($D_{\mathrm{max}} \approx 1000$ km). To this thesis' interest, the ngVLA will enable efficient and rapid observations and analysis of multi-line measurements (e.g. NH_3, ^{13}CO, $C^{18}O$, HCN, HCO^+) in nearby galaxies.

Figure 2.5: **One of VLA's 25m dishes**. On antenna 10, in the background a few other antennas are visible. On that day in October 2019, the array was in its A configuration – the most extended one. Image credit: Dr. Kenzie Nimmo.

2.2.2 *More of* Karoo Array Telescope (MeerKAT)

The *More of* Karoo Array Telescope (MeerKAT, the SKA precursor facility) is located in the Karoo Central Astronomy Advantage Area in South Africa, the largest radio quiet zone on earth which covers an area of around 106 306 km^2. MeerKAT's site is about 450 km northeast of Cape Town in the Northern Cape Province. The interferometer consists of 64 antennas, each of them 13.5 m in diameter, and achieves a maximum baseline of 8 km. Low-noise amplifier and radio receiver technology have significantly improved since the early days of radio astronomy in the 1950s. A few decades ago, sacrificing a fraction of the bandwidth was necessary to minimize system temperature, but now, thanks to new engineering knowledge and technologies allow for the development of low-noise receivers over a full octave or more of bandwidth. This is exactly the strength and exceptional feature of MeerKAT and together with the particular design of MeerKAT's antennas lead to low system temperatures (Lehmensiek and Theron, 2014). This makes it ideally suited to detect low column density H I emission (see e.g. de Blok et al., 2016).

Figure 2.6: MeerKAT located at the Karoo Central Astronomy Advantage Area. Image credit: South African Radio Astronomy Observatory

Figure 2.7: **NOEMA and ALMA.** The northern hemisphere interferometer NOEMA is located in the french alps and the southern hemisphere interferometer ALMA in the north of Chile. The orange circle in the world map indicates from west to east the sites of VLA, GBT, and MeerKAT. All of these telescopes were used in this thesis. Image credits: Clem & Adri Bacri-Normier/ESO, IRAM

2.2.3 Plateau de Bure Interferometer (PdBI) / Northern Extended Millimeter Array (NOEMA)

The NOrthern Extended Millimeter Array (NOEMA) is located at the Plateau de Bure in the French Alps at an altitude of 2550 m and is operated by the Institut de radioastronomie millimétrique (IRAM). NOEMA is the successor of the Plateau de Bure interferometer (PdBI), a six-antenna interferometer that observed from 1988 to 2014. Since 2014 the array got a major upgrade. The last antenna started being fully operational in January 2022, and NOEMA reached its full capabilities and sensitivity with 12 antennas, each of them 15 m in diameter. It is the most powerful radio telescope in the Northern Hemisphere and observes frequencies of 80 to 370 GHz (3 to 0.8 millimeters).

Compared with the PdBI, NOEMA has higher spatial resolution and sensitivity by a factor of 4 and 10, respectively. The antennas can move along two tracks; one in a north-south and the other in an east-west direction. With the `POLYFIX` receiver with a bandwidth of 32 GHz, NOEMA is one of the few radio observatories worldwide that can simultaneously detect and measure a large number of molecular and atomic emission lines.

2.2.4 Atacama Large Millimeter/submillimeter Array (ALMA)

The Atacama Large Millimeter/submillimeter Array (ALMA) is located at 5 000 m altitude on the Chajnantor Plateau in northern Chile and is one of the largest millimeter and sub-millimeter interferometers. ALMA was built between 2004 and 2014 and is the result of an international association between Europe (ESO), North America (NRAO), and East Asia (NAOJ), in collaboration with the Republic of Chile. With 66 antennas ALMA can achieve a maximum baseline of 16 km. The array has 54 12-m and twelve 7-m dishes. The combination of four 12-m dishes with twelve 7-m dishes form the ALMA Compact Array (ACA). Its receivers can detect wavelengths from 8.6 to 0.32 mm equivalent to 35 to 950 GHz in a frequency range separated into ten bands.

2.2.5 IRAM 30-m Telescope and the Green Bank Telescope (GBT)

In this thesis, we use single-dish observations to correct for short spacing (more details in Subsection 4.2.4). The 30m telescope on Pico Veleta at an altitude of 2850 m in the southern Spanish Sierra Nevada is operated by IRAM and was built in the early 1980s. It is one of the largest and most sensitive radio telescopes operating in the millimeter wavelength regime, from 73 to 350 GHz.

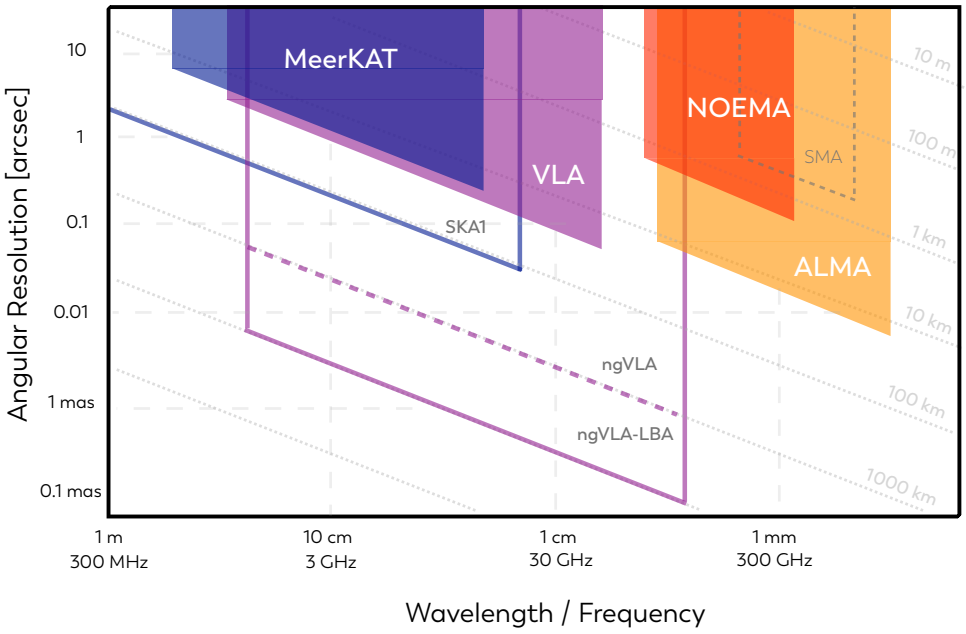

Figure 2.8: **A comparison of interferometers used in this thesis.** Spatial resolution versus frequency set by the maximum baselines. In this thesis, we use the northern hemisphere interferometers VLA and NOEMA, and the southern hemisphere arrays MeerKAT and ALMA. The outlined regions indicate future facilities such as the SKA1 and the next-generation VLA. The Submillimeter Array (SMA) is also indicated as during this thesis we were granted for SMA observations (PI: Eibensteiner). The figure is inspired by Selina et al., 2018.

Figure 2.9: **IRAM 30m and GBT.** Image credit: Cosima Eibensteiner and GBO.

The most commonly used receiver is the Eight MIxer Receiver (EMIR). Past studies also relied on observations made with the HEterodyne Receiver Array (HERA). The EMIR receiver provides spectral coverage with four different bands ranging from 73 to 350 GHz.

The Robert C. Byrd Green Bank Telescope (GBT) in Green Bank, is a 100-m Radio Telescope operated by the Green Bank Observatory. It is the world's largest entirely steerable radio telescope. GBT observes at 0.1–116 GHz frequency range. The panels are made from aluminum manufactured resulting in a high surface accuracy.

2.2.6 Space telescopes: GALEX, Spitzer, WISE, and Chandra

In this thesis, we use ancillary data from space telescopes that help us to understand star formation, stellar surface densities, the fraction of heavier elements known as ''metallicity'', and diffuse emission of X-ray in nearby galaxies.

(1) We use data from Galaxy Evolution Explorer (GALEX) which was a NASA orbiting space telescope designed to observe the universe in ultraviolet wavelengths. We make use of 154 nm observations to infer the star formation.
(2) Observations from the Spitzer Space Telescope (or just Spitzer), are used in this thesis to study stellar surface densities. Spitzer observed near-infrared emission until 2020. We use the 3.6 μm band of Spitzer's Infrared Array Camera (IRAC).
(3) We use Wide-field Infrared Survey Explorer (WISE) data to investigate star formation rates and together with Spitzer data to study stellar surface densities. We use WISE's 3.4 μm and 22 μm bands in this thesis.
(4) To examine diffuse emission of X-ray we use Chandra data, named after the Nobel Prize-winning astrophysicist Subrahmanyan Chandrasekhar.

CHAPTER 3

Analysis Techniques

Overview

In this work, we use a variety of different methods to analyze the various observations from multiple telescopes. In this section, we describe how we store the multi-wavelength data, followed by the interpretation of molecular and atomic line observations through moment maps, line ratios, and dissecting a galaxy into multiple rings to characterize its kinematic behavior.

3.1 Storing Multi-line/wavelength Data

This thesis deals with several emission lines and in most cases additional data from various telescopes. To make sense of this amount of information, two different types of pipelines were used. These are data product pipelines that perform calculations on observations to infer physical data products. For project I and II we used a pipeline called `PyStructure` and for project III we use the PHANGS `Mega-Table` pipeline (published in Sun et al., 2022). Both are based on `IDL` scripts used to obtain bias-free measurements of molecular cloud properties (Rosolowsky and Leroy, 2006).

3.1.1 `PyStructure`

In project I we observe NGC 6946 at different frequencies and therefore, the angular resolutions do not match. With the `PyStructure`[1] we convolve all unprocessed [2] data cubes and ancillary maps (for example the star formation rate tracer) to a common beam size. Here we consider that the convolution kernel of the data is described by a 2D Gaussian function. In project I we deal with 12 molecular emission lines and to be able to compare all of them accordingly, we need to regrid all the data to a common sampling grid. Within this routine, we perform a half-beam-sized hexagonal sampling. Unlike a Cartesian sampling grid, the data points in a hexagonal sampling grid are all equidistant. This provides a more uniform sampling. The oversampling factor $N_{\rm os}$ for a hexagonal grid is smaller,

[1] We uploaded along with the publication of this paper a NGC 6946 version of the `PyStructure` under https://github.com/ceibensteiner/Molecular-Fireworks-in-NGC6946

[2] We mean here that the data cubes are immediately taken as they are after the reduction, calibration, and imaging process. This is different from the method we used in project III

compared to a Cartesian sampling grid, and hexagonal sampling ensures Nyquist sampling. The oversampling factor is described as,

$$N_{\rm os} = (1.13 \cdot \theta^2_{\rm FWHM})/A^{\rm hex}_{\rm pix} \tag{3.1}$$

where $1.13 \cdot \theta^2_{\rm FWHM}$ is the beam area and $A^{\rm hex}_{\rm pix}$ the hexagonal pixel size. The rms of each line is derived from the part of the spectrum without a signal using the mean absolute standard deviation. Our dataset contains very faint emission lines (compared to CO) and therefore we aim to improve the signal-to-noise. The pipeline is creating a 3D mask with voxels that have a value above a certain threshold factor of the line rms. Firstly, two masks are created, a high mask with a high rms threshold and a low mask with a low rms threshold which are combined in the following step. The high mask is expanded into the low mask to recover regions of low rms emission associated with the high rms core. This guarantees that the ultimate mask is free of noise peaks, without omitting a large part of the line voxels. Then the data products described in Subsection 3.2.1 are generated.

3.1.2 `Mega-Table`

For project III we use the `Mega-Table` database construction[3] (described in Sun et al., 2022) which is based on a ''cross-spatial-scale'' analysis framework to connect molecular cloud properties to galactic environmental properties (mostly measured on ~kpc scales), and is inspired by previous works (for example, Sandstrom et al., 2013; Leroy et al., 2016). This routine divides the sky footprint of each galaxy into a set of hexagonal apertures, as illustrated in Figure 3.1. These apertures form a regular tiling in the plane of the sky, with a central aperture positioned right at the galaxy center. Adjacent apertures are separated by a linear distance of 1.5 kpc. The configuration of the hexagonal apertures in the `Mega-Table` method is analogous to the 'solution pixels' used in Sandstrom et al., 2013, except that the apertures do not overlap with each other. The databases published in Figure 3.1 do not include the new MeerKAT H I observations and the additional H I data from the MHONGOOSE collaboration. Additionally, only apertures covering out to a galactocentric radius of 1.5 r_{25}[4] in each galaxy are included. The restriction to 1.5 r_{25} applies to the CO-related analysis, but is not applicable to the H I-related analysis since the H I disks are most of the time much more extended (e.g. M 83 with $5\times$ r_{25}, see project II). For that, we wrote a script that adds relevant information to the existing databases of the relevant galaxies that we analyze in Chapter 7. First, we import the `TessellMegaTable` class of the `Mega-Table` code. We then initialize the Mega-Table by calling the TessellMegaTable class and changing the `tessell_FoV_radius` to $> 5 \times$ r_{25}. After that, we include the provided moment maps (see Subsection 3.2.1) via `calc_image_stats` and add the surface densities with `calc_surf_dens_atom`. In the course of that, we also included new measurements of the dynamical equilibrium pressure P_{DE} into the databases (see Chapter 7 for more details).

3.2 Interpretation of molecular/atomic line observations

In this thesis, we use observations from various telescopes (see Section 2.2). These need to be reduced, calibrated, and imaged (described in detail in Chapter 4). In the end, we have products in the form of

[3] https://github.com/PhangsTeam/MegaTable

[4] r_{25} is the galaxy radius defined by its 25 mag/ arcsec^2 isophote in B band, also known as the optical radius of a galaxy.

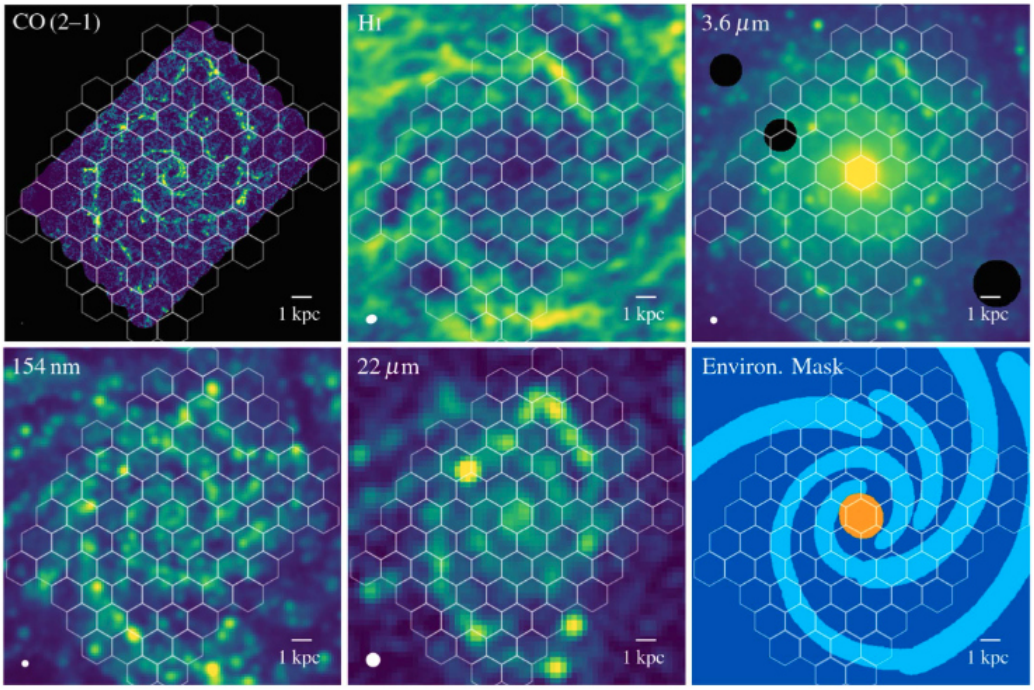

Figure 3.1: **Example of database construction using the `Mega-Table` pipeline**. This figure is adopted from Sun et al., 2022 and shows a subset of the multiwavelength data assembled for the galaxy NGC 628. The top row shows the (i) PHANGS–ALMA CO (2-1) integrated line intensity map (tracing molecular gas), (ii) THINGS VLA HI 21 cm integrated line intensity map (tracing neutral atomic gas), and (iii) S4G Spitzer IRAC 3.6 μm image (tracing stellar mass). The bottom row shows the (iv) GALEX 154 nm image (tracing unobscured star formation), (v) WISE 22 μm image (tracing obscured star formation), and (vi) PHANGS environment mask. The white grids demarcate the hexagonal apertures (1.5 kpc in size). In every panel, the scale bar in the lower right corner indicates the spatial extent of 1 kpc, while the white ellipse in the lower left indicates the size of the beam.

3D data cubes with two spatial x and y, and one frequency or velocity z axis. In this thesis, we reduce these cubes to two axes via several methods to analyze different quantities. We also examine the ratio of integrated intensities of various emission lines, which tell us more about the physical and chemical behavior of the ISM gas (see Subsection 1.5.3). In one of the thesis projects, we use a simplified model to describe the motion of gas in a galaxy (see Subsection 3.2.3).

3.2.1 Moment Maps

The z axis or spectral axis of an astronomical 3D data cube is usually described as a velocity with respect to the rest-frame frequency of an emission line under the use of the Doppler shift. We denote the axis henceforth as (x, y, v). In this work we base our analysis most of the time on 2D data products. It is common practice to produce a mask $M(x, y, v)$ that specifies the voxels[5] that belong to the emission line and the voxels that are only affected by the noise, in order to improve the reliability of the data. In Table 3.1 we summarize some of the data products used in this thesis and how we derived

[5] The word voxel arose analogously to the word ''pixel'', where *vo* stands for ''volume'' (instead of pixel's ''picture'') and *el* stands for ''element''.

them.

Both, the integrated intensity (also called *Moment 0*) and the peak intensity maps describe the strength of an emission line. The first one is created by integrating the cube over the velocity axis and the latter one describes the maximum brightness temperature for a given line of sight. We removed in these processes the information about the line width. Consequently, the integrated intensity map is biased towards broad lines with a low and narrow lines with a high peak.

Especially in the second scientific project of this thesis, we are interested in the kinematics of the gas in nearby galaxies. We examine the line of sight velocities, or the velocity field (also called *Moment 1*). Additionally, we analyze the line width (also called *Moment 2*), the RMS line width, and the effective line width, which are connected to the gas velocity dispersion. Figure 3.2 shows a data cube together with examples of data products.

Table 3.1: Summary of the data products that we used in the thesis' projects. This table is inspired by (Leroy et al., 2021b)

Data Product		Mathematical Expression	Unit
Integrated Intensity	Mom 0	$I(x,y) = \sum_i I_\nu(x,y,\nu_i) M(x,y,\nu_i) \Delta\nu_{\rm chan}$	K km s^{-1}
Peak Intensity	$T_{\rm peak}^{(\star)}$	$I_{\rm peak}(x,y) = \max_{\nu_i}\left[I_\nu(x,y,\nu_i)\right]$	K
LOS Velocity	Mom 1	$V_{\rm los}(x,y) = \frac{\sum_i \nu_i I_\nu(x,y,\nu_i) M(x,y,\nu_i)\Delta\nu_{\rm chan}}{I(x,y)}$	km s^{-1}
Line Width	Mom 2	$\sigma_\nu(x,y) = \frac{\sum_i (\nu_i - V_{\rm los})^2 I_\nu(x,y,\nu_i) M(x,y,\nu_i)\Delta\nu_{\rm chan}}{I(x,y)}$	km s^{-1}
RMS Line Width	$\sqrt{\text{Mom 2}}^{(\star\star)}$	$\sigma_{\sqrt{\rm mom2}}(x,y) = \left\{\frac{\sum_i (\nu_i - V_{\rm los})^2 I_\nu(x,y,\nu_i) M(x,y,\nu_i)\Delta\nu_{\rm chan}}{I(x,y)}\right\}^{1/2}$	km s^{-1}
Effective Line Width		$\sigma_{\rm eff}(x,y) = \frac{I(x,y)}{I_{\rm peak}(x,y)\sqrt{2\pi}}$	km s^{-1}

Notes: $M(x,y,\nu_i)$ is a boolean mask that specifies whether the line is detected or not. $\Delta\nu_{\rm chan}$ denotes the channel width. LOS stands for line-of-sight, RMS means root-mean-square and Mom means Moment. $^{(\star)}$,$^{(\star\star)}$: Also referred to as Moment 8 or 6, respectively (e.g. in CASA's `immoments` task).

3.2.2 Line ratios

In this thesis, we specify the line ratios such that the generally brighter line is in the denominator, while the overall weaker line is in the numerator (except for Project III). We can calculate line ratio maps by only taking integrated intensities above a certain S/N threshold (ϵ) and non-detections are discarded from the line ratio maps,

$$\text{Ratio map} = \frac{I_{\rm line_1}\left[I_{\rm line_1}/\sigma_{\rm line_1} > \epsilon\right]}{I_{\rm line_2}\left[I_{\rm line_2}/\sigma_{\rm line_2} > \epsilon\right]} \begin{cases} \epsilon = 3 & \text{for } \Sigma_{\rm HI} \text{ and } \Sigma_{\rm H_2} \text{ in project III}, \\ \epsilon = 5 & \text{for DGTs in project I}, \\ \epsilon = 15 & \text{for CO in project I}. \end{cases} \tag{3.2}$$

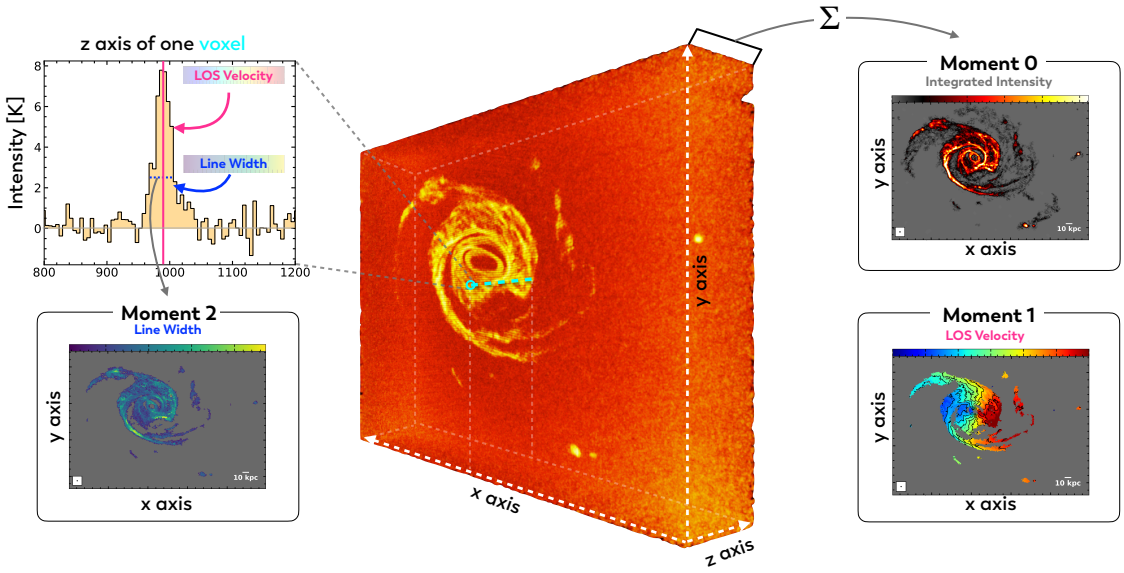

Figure 3.2: **Astronomical Data Cube and example Data Products.** We show here MeerKAT HI observations of the nearby spiral galaxy NGC 1512 (from project III, see also Chapter 7). We label the three axes (x,y,z). Note, that we refer to the z axis as the v axis in Table 3.1. The sum over this axis results in the Moment 0 map. The turquoise line shows the spectral axis for a voxel. We show the corresponding spectrum on the top left. The pink vertical line indicates the line of sight velocity, $V_{\rm los}$ of the line emission relative to the rest frame. The blue line shows the width of the line that results in the Moment 2 map.

DGTs refers to the fainter dense gas tracers such as HCN, HCO^+, and HNC. For most analysis we included non-detections, for example, whenever we explore scaling relations (project I and project III). For the case of no significant detection we replaced the values with the upper limits (2σ in Equation 3.3),

$$\sigma_{\rm line} = \sqrt{n_{\rm chan}} \times \sigma_{\rm rms} \times \Delta v_{\rm chan} \ , \tag{3.3}$$

where this represents the uncertainty that is calculated taking the square root of the number of masked channels ($n_{\rm chan}$) along a line of sight multiplied by the 1σ root mean square ($\sigma_{\rm rms}$) value of the noise and the channel width ($\Delta v_{\rm chan}$). For including the non-detections we need to include the propagated errors ($\sigma_{\rm prop}$). We derive them as,

$$\sigma_{\rm prop} = \frac{|I_{\rm line_1}|}{|I_{\rm line_2}|} \sqrt{\left(\frac{\sigma_{\rm line_1}}{I_{\rm line_1}}\right)^2 + \left(\frac{\sigma_{\rm line_2}}{I_{\rm line_2}}\right)^2} \ , \tag{3.4}$$

using Gaussian error propagation. Whenever the errors are expressed on a logarithmic scale of base 10, we derive them as,

$$\sigma_{\rm log} = \frac{1}{\ln(10)} \cdot \left(\sigma_{\rm prop}/I_{\rm ratio}\right) \approx 0.434 \cdot \left(\sigma_{\rm prop}/I_{\rm ratio}\right) \ . \tag{3.5}$$

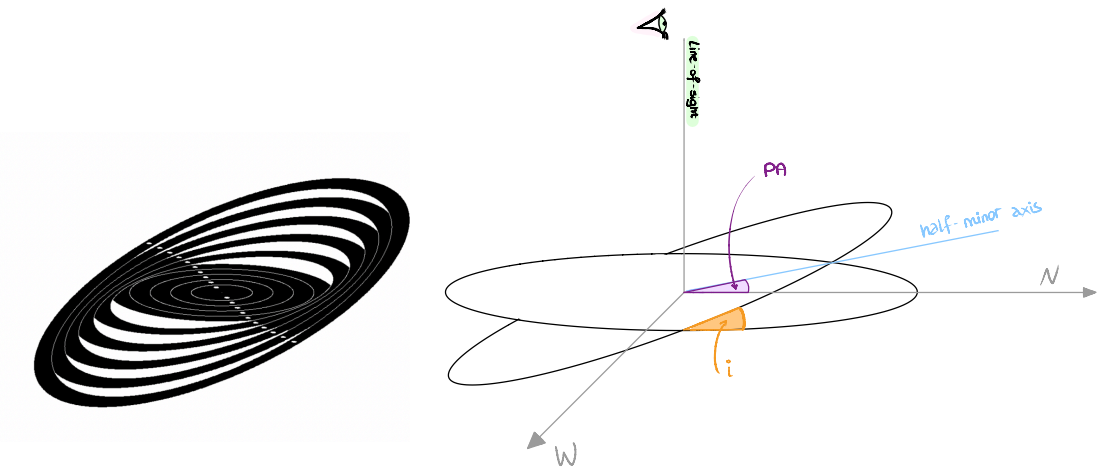

Figure 3.3: **Tilted rings and orientational parameters.** The left panel represents a galaxy separated into tilted rings. The right sketch indicates the inclination i and position angle PA. The position angle is enclosed by the north axis and the half-minor axis (of the projected ellipse; not shown here). The inclination is the angle between the celestial and orbital plane. The left panel is adopted from Garcia-Ruiz (2001) and the right sketch is inspired by Józsa et al. (2007).

3.2.3 Tilted ring models

In Subsection 3.2.1 we showed an example of a velocity field and how to derive it (Moment 1). In the literature it is common whenever we want to analyze one or more galaxies in terms of their kinematics in more detail, to divide them into individual rings, to model them and thereby obtain information about the rotational velocity, the non-circular motions, and the associated presumable inflowing or outflowing mass of gas. The *tilted ring* approach describes a galaxy by a set of rings, each of which has its own inclination i, position angle, systemic velocity $V_{\rm sys}$, center position (x_0, y_0), rotation velocity $V_{\rm rot}$ and radial velocity $V_{\rm rad}$ (see Figure 3.3) and assumes that gas moves in circular orbits within each of these rings[6]. Before we introduce the model it is good to know that we can describe the observed velocities, $V_{\rm los,obs}$ for any position (x, y) on a ring with radius r as,

$$V_{\rm los,obs}(x,y) = V_{\rm sys} + V_{\rm rot}(r)\sin(i)\cos(\theta) + V_{\rm rad}(r)\sin(i)\sin(\theta)\ . \tag{3.6}$$

Here, $V_{\rm sys}$ is the systemic velocity of the galaxy with respect to the observer, and $V_{\rm rot}$ is the rotation velocity. The $V_{\rm los,obs}$ is denoted in sky coordinates (x, y), while the terms on the right side of Equation 3.6 are in the disk coordinate frame (r, θ). These two systems are related as,

$$\cos(\theta) = \frac{-(x-x_0)\sin(\mathrm{PA}) + (y-y_0)\cos(\mathrm{PA})}{r} \tag{3.7}$$

and,

$$\sin(\theta) = \frac{-(x-x_0)\cos(\mathrm{PA}) - (y-y_0)\sin(\mathrm{PA})}{r\cos(i)}, \tag{3.8}$$

[6] The assumption that gas moves in circular orbits only applies for the tilted ring models, but not for the observed velocities (Equation 3.6).

where x_0 and y_0 denote the center coordinates and the position angle (PA) is the angle measured in an anti-clockwise direction between the north direction of the sky and the major axis of the receding half of the galaxy. In project II (see Chapter 6) we adopt tilted ring models from the literature in the form of,

$$V_{\rm los,mdl}(x, y) = V_{\rm sys} + V_{\rm rot}(r)\,\sin(i)\,\cos(\theta), \tag{3.9}$$

thus neglecting radial motions (inflow, outflow). We use literature $V_{\rm rot}(r)$, inclination angle i, and PA values. As a first step, the PA in degrees need to be aligned[7] and convert to radians[8], and i convert to radians. Then we transform from sky coordinates (x,y) to disk coordinate frame (r, θ) via,

$$r_{\rm deprojected} = \sqrt{x_{\rm rot}^2 + \left(\frac{y_{\rm rot}^2}{\cos(i[j])^2}\right)} \tag{3.10}$$

where j denotes each value in the array of the inclination and $x_{\rm rot}$ and $y_{\rm rot}$ are,

$$x_{\rm rot} = -(x[k] - x_0)\,\sin({\rm PA}[j]) + (y[k] - y_0)\,\cos({\rm PA}[j]) \tag{3.11}$$

$$y_{\rm rot} = -(x[k] - x_0)\,\cos({\rm PA}[j]) - (y[k] - y_0)\,\sin({\rm PA}[j])\ . \tag{3.12}$$

Here, x and y are the sky coordinates, meaning the right ascension and declination of each pixel. j denotes each index in the array of the position angle (that needs to have the same shape as the one for $V_{\rm rot}$). With the Equation 3.7 and Equation 3.8 together with Equation 3.10, we get for each pixel k,

$$\cos(\theta)[k] = \frac{-(x[k] - x_0)\,\sin({\rm PA}[j]) + (y[k] - y_0)\,\cos({\rm PA}[j])}{r_{\rm deprojected}[k]} \tag{3.13}$$

$$\sin(\theta)[k] = \frac{-(x[k] - x_0)\,\cos({\rm PA}[j]) - (y[k] - y_0)\,\sin({\rm PA}[j])}{r_{\rm deprojected}[k]i[j]}\ , \tag{3.14}$$

we only calculate these whenever the pixels lay inside the modeled rings. With the solution of Equation 3.7 we are now able to calculate $V_{\rm los,mdl}(x, y)$ and construct a 2D map.

Then, for determining the residual velocities ($V_{\rm res}$), we subtract Equation 3.9 from Equation 3.6, $V_{\rm res}(x, y) = V_{\rm los,obs}(x, y) - V_{\rm los,mdl}(x, y)$ and obtain,

$$V_{\rm res}(x, y) = V_{\rm rad}(r)\,\sin(\theta)\,\sin(i), \tag{3.15}$$

also known as non-circular motions. For studying potential inflowing/outflowing material in a galaxy we aim to get the radial velocities $V_{\rm rad}$ and for that we account for the $\sin(\theta)\,\sin(i)$ term,

$$V_{\rm rad}(r) = \frac{V_{\rm res}(r)}{\sin(\theta)\,\sin(i)}. \tag{3.16}$$

We need to know in which direction a galaxy rotates to correctly interpret the nature of measured radial motions. Because of the geometry of the tilted rings, negative (positive) velocities in $V_{\rm rad}$ are

[7] We needed to align the PA values as, $\rm PA_{aligned}$ = -PA+180

[8] Just as a reminder, to convert from degrees to radians we simply need to multiply the number of degrees by $\pi/180$, or even simpler use the `numpy` function `deg2rad`.

inflow (outflow) motions when a galaxy is rotating clockwise, and they are outflow (inflow) motions when a galaxy is rotating counterclockwise. We make use of the tilted ring approach in this thesis' project II (see Chapter 6).

CHAPTER 4

Reducing and Imaging Radio Observations

Overview

During the course of the thesis, various observations of nearby galaxies were reduced and/or imaged. In the following section, we will describe the process of reducing, calibrating, and imaging the VLA observations that are (i) targeting Ammonia transition in the nearby double-barred spiral galaxy NGC 6946 (in 18.0 – 26.5 GHz, called K-Band), and (ii) targeting H I 21cm emission in the nearby grand design spiral galaxy M 83 (in 1.0 – 2.0 GHz, called L-Band).

The following datasets were reduced and calibrated by the thesis' author (i) K Band VLA observations targeting the central kpc of NGC 6946 (Principle investigator: Emmanuel Momjian), (ii) L Band VLA observations of the extended H I disk of M 83 (Principle investigator: Frank Bigiel), (iii) NOEMA observations of the CO (1−0) isotopologues targeting the central kpc of NGC 6946 (Principle investigator: Cosima Eibensteiner). The datasets (i) and (ii) are described in this section, whereas (iii) will be mentioned in the outlook section of this thesis (see Chapter 9).

4.1 K Band VLA

In this project, we planned to use VLA K band (18.0 – 26.5 GHz) observations to detect Ammonia transition to determine the kinetic temperature at the center of the nearby starburst galaxy NGC 6946. This section will review the physics behind Ammonia as a tracer of kinetic temperature and the initial observations acquired, followed by a justification for new observations taken in 2022.

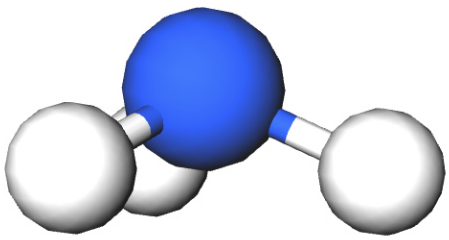

Figure 4.1: **Ammonia.** The structure of Ammonia, NH_3. Taken from molview.org

The observations, dating from 2010, were published in Gorski et al., 2018. In their paper, they stated to have detected one transition of Ammonia but left unspecified the reason why the others had not been detected. Accordingly, the task/challenge was to reduce, calibrate, and re-image the data in anticipation of increasing the signal and detecting more transitions. As is often the case, research is sometimes a roller coaster ride. So was this project, at the beginning of my PhD. In the following sections, it becomes clear that unfortunately, we could not achieve any improvements in data reduction (with the

guidance of Jürgen Ott during the 7th VLA Data Reduction School and months after). Subsequently, we have proposed and received approval for new observations that now observe ~13 hours (on-source time) of the center of NGC 6946 instead of 2 hours. These observations were completed in the fall of 2022 and science ready by the end of 2023 (they are mentioned in the Outlook section; see Chapter 9). In the following sections, we give an overview of the molecule Ammonia NH_3 (described in Subsection 4.1.1), and the observation, reduction, and imaging with the conclusion that new observations are needed to be able to conduct our planned analysis (described in Subsection 4.1.2). This is followed by describing our required brightness sensitivity in Subsection 4.1.3.

4.1.1 Ammonia

Ammonia (NH_3) has a structure of a tetrahedron with a nitrogen atom in one corner and three hydrogen atoms in the other corners (see Figure 4.1). It is possible for the nitrogen atom to tunnel through the plane formed by the three hydrogen atoms. Because of this, the degeneracy of the symmetric peak levels (J, K) is canceled at $J > 0$, splitting the energy levels into doublets. The transitions between these levels are referred to as "inversion lines" and they directly depend on the rotational states of Ammonia. Measuring the intensity of an inversion line, we can thus determine the number of NH_3 molecules in a given rotational state. Changes in population between the different K ladders are driven solely by collisions, and all $(J > K, K)$ states decay rapidly to the metastable $J = K$ levels. Consequently, the distribution of all (J, J) states is a result of the energetics of collisions and is described in terms of a Boltzmann distribution at a temperature T but are almost independent of density. Together with large velocity gradient (LVG) models, it is possible to estimate kinetic temperatures with reasonable precision (e.g. Ho and Townes, 1983; Walmsley and Ungerechts, 1983; Menten and Walmsley, 1985; Ott et al., 2005; Ott et al., 2011; Lebrón et al., 2011; Mangum et al., 2013; Gorski et al., 2017; Gorski et al., 2018). The NH_3 lines are sensitive to the entire range of temperatures ranging from ~10 to ~1000 K, independent of density variations (see e.g. Gorski et al., 2018). This makes ammonia an excellent thermometer.

Ammonia thermometry studies of nearby galaxy centers have shown that high kinetic temperatures (50 to >250K) can be generated by both cosmic rays and mechanical (turbulent) heating processes (e.g. Mangum et al., 2013; Gorski et al., 2018). The central molecular zone of our own Galaxy appears to be different in this regard: The discrepancy between dust and gas temperatures at moderately high density ($10^5 cm^{-3}$) is better explained by mechanical heating (Ginsburg et al., 2016). Although this is still a subject of active debate (Henshaw et al., 2022). Moreover, the uniformity of the temperature distribution of NGC 253 and IC 342 shows that shocks and photon-dominated regions (PDR) do not cause variations in the temperature of the dense molecular ISM over sub-kpc scales (Gorski et al., 2017; Gorski et al., 2018).

4.1.2 The observation, reduction, and imaging

The observations were carried out in November 2010 and aimed to target continuum and multiple Ammonia transitions in K (21.7-22.7 GHz and 23.6-24.6 GHz) and Ka (27.0-28.0 GHz and 36.1-37.1 GHz) frequency bands using these back in the days new capabilities of the EVLA (see Table 4.1). The initial proposal (VLA/10B-161) included observing six galaxies: Arp220, IC342, M83, NGC6946, NGC253, and NGC2146. Within this very first project[1] our focus was the nearby starburst galaxy

[1] This project did not lead to a publication and thus is not mentioned in the Introduction

NGC 6946 and starting with the K Band observations. In the course of the 7th VLA Data Reduction school and in the following months this dataset was reduced, calibrated, imaged, and analyzed.

Table 4.1: The Ammonia transitions that we were aiming to detect in the VLA K-Band observations.

Ammonia transition	Frequency [GHz]		Resolved QNs	E_L [K]
NH_3 (1,1)	23.694	v=0	1(1)0a- 1(1)0s	22.1
NH_3 (2,2)	23.722	v=0	2(2)0a- 2(2)0s	63.3
NH_3 (3,3)	23.870	v=0	3(3)0a- 3(3)0s	122.4
NH_3 (4,4)	24.139	v=0	4(4)0a- 4(4)0s	199.4

In general a measured signal can be affected by a variety of effects that we need to correct (i.e. calibrate). Since the data is from 2010, it was not possible to run the standard VLA pipeline[2] for calibration. Therefore, we decided to perform the calibration steps individually. For this purpose, a script was created that performs the steps shown in Figure 4.2 (similar to the pipeline). Essentially, we started by converting the ALMA Science Data Model (ASDM) observation into a CASA visibility file, the so-called MeasurementSet (MS). This is followed by a first inspection of the MS file via the `CASA` tasks `listobs`, `antpos`, `plotms` and `plotweather`. Then, we need to correct for the

(i) *Antenna Position* – The antennas in an array will be moved around for different configurations. Whenever the antennas in the array are offset from their location a baseline solution will help to accurately give their position. These offsets from the actual positions are published a couple of days subsequent to the observations and saved in a machine-readable table that can be accessed with CASA. This step essentially checks to see if there are offsets, and if so, they are applied;

(ii) *Gaincurve and Efficiencies* – In general, the gain curve describes the way in which each antenna performs depending on the elevation, for each receiver band;

(iii) *Opacity* – The corrections of opacity are usually applied for high-frequency (including K-Band) observations. In these frequency ranges the atmospheric opacity will affect the flux density scale if the sources and calibrators are observed at different elevations. Observational opacity is calculated using a seasonal model as well as data from weather stations;

These three corrections (i) - (iii) are done via the CASA task `gencal`. The next step is the set up a *Flux Density Model* to compare the flux of the flux calibrator that we observed with the model of the flux calibrator. Then these models can be scaled to the exact frequency of the observations at a later stage (via `fluxscale`). This is followed by the calibration of the

(a) *Delays* – The delay is the linear slope of phase across frequency. Here we are solving for simple antenna-based delays (parameter gaintype = 'K') via FFTs of the spectra on baselines to the reference antenna;

(b) *Phase* – In this step we correct for decorrelation. Whenever the bandpass calibrator is strong we can do the phase-only solution (parameter calmode='p') per integration time (parameter solint='int');

(c) *Bandpass* – Now we can calculate the bandpass calibration solution. Determines the amplitude and phase as a function of frequency for each spectral window containing more than one channel. We derive the solution per integration time (parameter solint='int');

[2] The standard VLA pipeline is recommended for observations after 2013. One of the reasons is that it is unable to recognize the old structure of the observations which contained different used scan IDs and corresponding tags.

These calibration steps are done via the CASA tasks `gencal` for (a) and (b) and `bandpass` for (c). Since the calibration tables are incremental, the previous ones must be 'carried' along (e.g. gaintable =['antpos.cal', 'gaincurve.cal', 'opacity.cal', 'delays.cal', 'bpphase.gcal'] for the `bandpass` solution command). After checking the Calibration Solutions via `plotms` (and if necessary flagging some data) we can proceed with the Gain Calibration where we solve for the antenna-based phase and amplitude gain calibration. Because of the fact that the phase is changing on a much shorter timescale than the amplitude, we will solve for them individually.

(1) *Integration Length Solution* – Here we are carrying out the short timescale (integration, parameter solint = '`int`') phase (parameter calmode = '`p`') solution.

(2) *Scan Length Solution* – In this step we are deriving the longer timescale (by scan, parameter solint = '`inf`') phase (parameter calmode = '`p`') solution.

(3) *Amplitude Calibration* – Here we are solving for longer interval (by scan, parameter solint = '`inf`') amplitude (parameter calmode = '`ap`') solution.

After these steps, we scale the amplitude calibration to match the flux density model with `fluxscale`. Subsequent to plotting the solutions and inspecting them we can apply the calibrations to the different sources – Gain/Phase Calibrator, Bandpass Calibrator and Flux Calibrator[3]. Now we have reached the *"Major" Flagging Stage*, where we carefully check all calibration solutions and flag (i.e. delete) corrupted data. After that, we start directly with a second run. For this, it is advisable to rename the previous calibration tables, e.g. with an extension like "firstround.cal". Then we can `split` out the target fields, identify the continuum and subtract it via `uvcontsub`, and finally the data is ready to image.

After the calibration part, we imaged the individual spectral windows where each of the Ammonia transitions is located. The process of imaging will be explained in Subsection 4.2.2. The results are shown in Figure 4.3 for NH_3(1-1), NH_3(2-2), NH_3(3-3), and Figure 4.4 for the whole K-Band. In both of these images, it is obvious that we did not detect these transitions with high significance (or at all). Thus, following our science goals with this dataset is not possible. Figure 4.5 shows, however, that we indeed could confirm the detection of the Water (H_2O) and Methanol (CH_3OH) Masers[4].

4.1.3 The need for new observations

Our goal is to increase the surface brightness sensitivity to the previous C-Configuration VLA observations, which targeted NGC 6946 in K-Band (Gorski et al., 2018) to be able to detect multiple Ammonia transitions. That is why we proposed for new K-Band VLA observations (PI: Cosima Eibensteiner, 25 hours of total time) that were finished observed in September 2022, and will be processed and science ready by the end of 2023. With these D-Configuration observations, we increased the surface brightness sensitivity by a factor of 10 (requires an rms brightness of 0.025 K), thus we will be able to detect even the fainter lines of Ammonia (e.g. 4,4).

We come to these conclusions by estimating the brightness temperature of an NH_3 transition J' from an existing transition J as follows:

[3] This is done with the parameter gaintable =['antpos.cal', 'gaincurve.cal', 'opacity.cal', 'delays.cal', 'bandpass.bcal', 'intphase.gcal', 'amp.gcal', 'flux.cal'], and the parameter gainfield=['', '', '', '8', '8','6','6','6'] for the FLux Calibrator.

[4] Maser stands for Microwave Amplification by Stimulated Emission of Radiation.

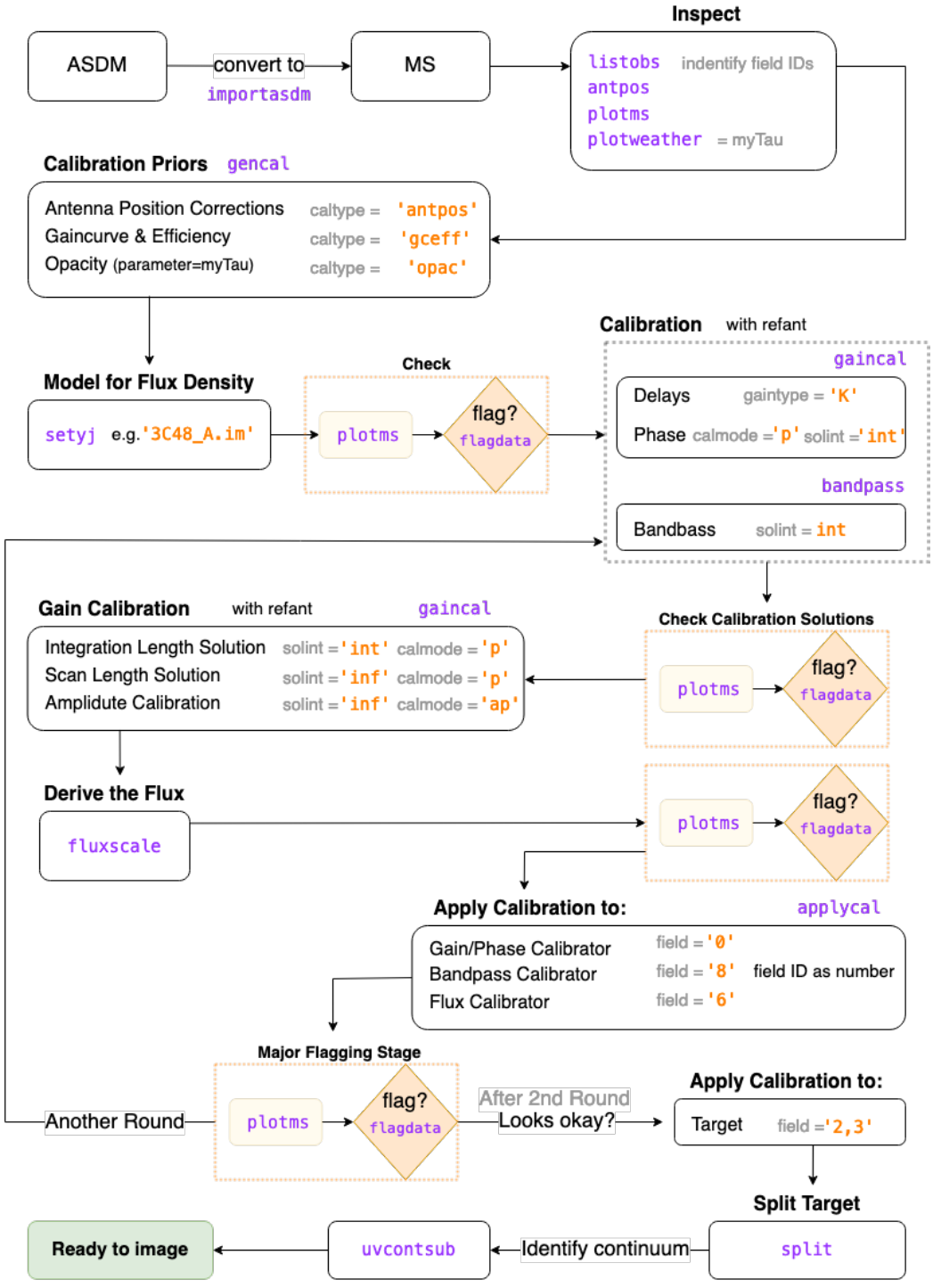

Figure 4.2: A flow chart showing how we reduced and calibrated the VLA K-Band observations of a project from 2010 (VLA pipeline did not work on this dataset). CASA tasks are colorized in purple and the parameters that we chose are in orange.

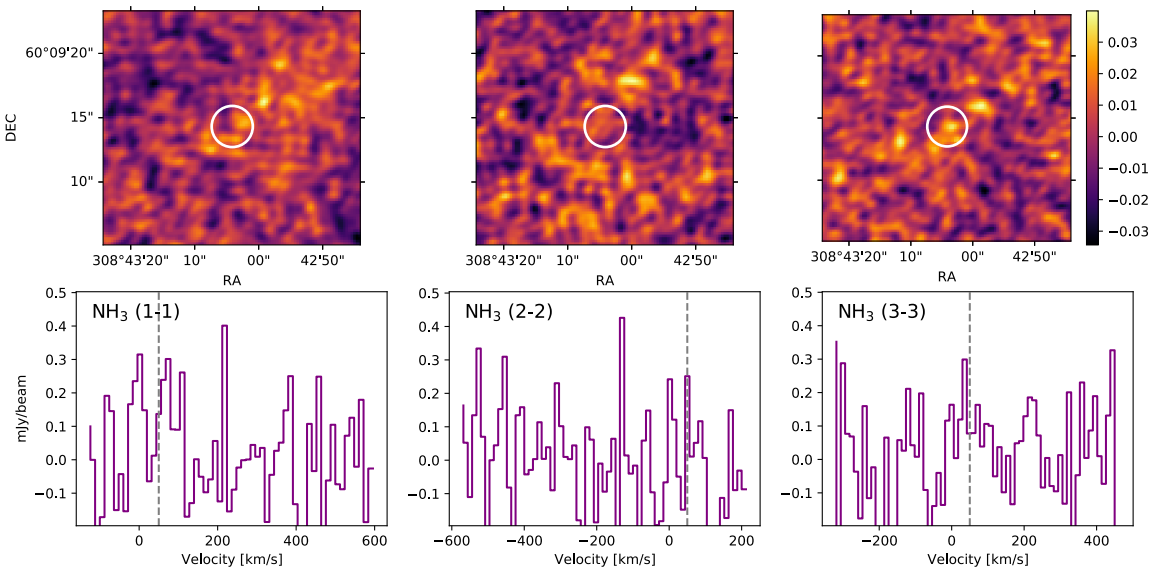

Figure 4.3: **Ammonia, NH_3.** We show here the observations from the project VLA/10B-161. The upper panels show the moment maps of NH_3(1-1), NH_3(2-2), and NH_3(3-3) with a white circle showing the region (position of NGC6946's center) where we extracted the spectra. The lower panels show the corresponding spectra in units of mJy/beam. These overall show, that we were not able to detect either of these lines with great confidence. Neither did we detect NH_3(4-4) (not shown here).

1) Under the assumption that the gas is optically thin, the column density of the upper state can be calculated from the brightness temperature $T_{\rm mb}$, frequency ν, and angular momentum quantum numbers J, K as,

$$N_u(J,K) = \frac{7.73\times10^{13}}{\nu}\frac{J(J+1)}{K^2}\int T_{mb}d\nu \tag{4.1}$$

The integral of $T_{\rm mb}d\nu$ is the integrated brightness temperature in units of K km/s. We assume that differences in excitation temperatures between states are negligible $(J = K) \rightarrow {\rm N}_u(J,J)$.

2) We obtain

$$\int T_{\rm mb}d\nu = 21.8{\rm K\ km\ s^{-1}} \tag{4.2}$$

for NH_3 (3,3) from Gorski et al., 2018 at $1''$ resolution. Additionally to that, for further calculations, we assume a linewidth of 20 km s^{-1} and a representative rotational temperature, $T_{\rm rot}$, of 40 K.

3) Then we use,

$$\frac{N_u(J',J')}{N_u(J,J)} = \frac{g'(2J'+1)}{g(2J+1)}\exp\left(\frac{-\Delta E}{T_{JJ'}}\right), \tag{4.3}$$

where ΔE is the difference in energy between J and J' states in Kelvin, and g and g' are the statistical weight of the NH_3 species. $g = 1$ for para-NH_3 where J is not $3n$, and $g = 2$ for ortho-NH_3, where $J = 3n$ with the (0,0) state belonging to ortho-NH_3 [5]. We know $N_u(J,J)$ from

[5] This means, for example, for NH_3(1,1) and NH_3(2,2) $g = 1$ and for NH_3(3,3) $g = 2$.

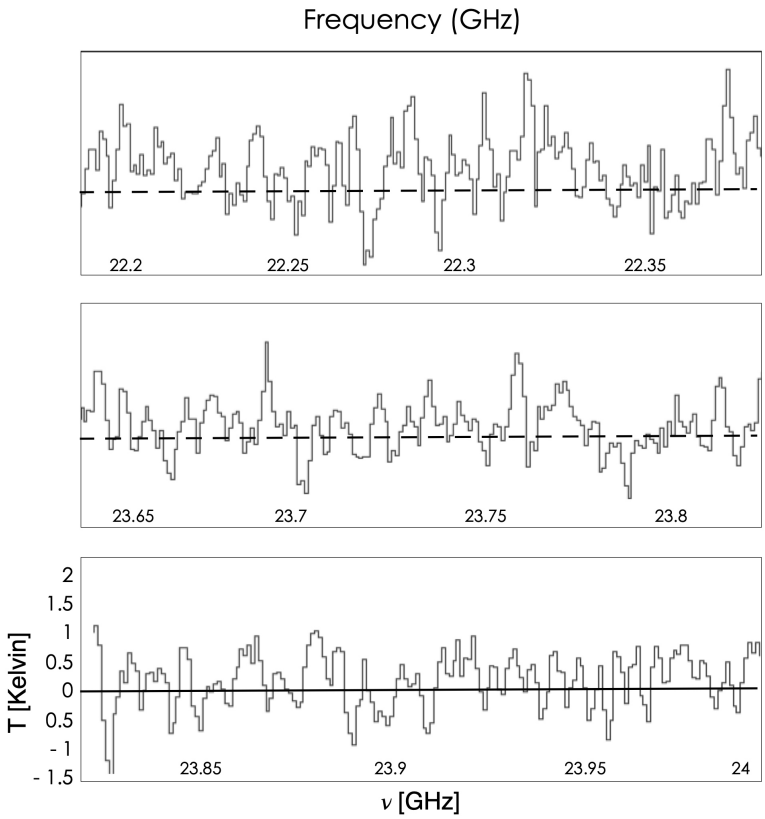

Figure 4.4: **The whole K-Band.** This shows the spectra over the whole K-Band from project VLA/10B-161 in units of Kelvin (y axis) and GHz (x axis) extracted from the same region that we highlighted as white circles in Figure 4.3.

Equation 4.1, which is the column density of the upper inversion state of the (J, J) transition in cm^{-2}, and can calculate $N_u(J', J')$ via,

$$N_u(J', J') = \frac{g'(2J'+1)}{g(2J+1)} \exp\left(\frac{-\Delta E}{T_{JJ'}}\right) N_u(J, J). \tag{4.4}$$

4) We then get,

$$\int T'_{\mathrm{mb}} \mathrm{d}\nu = \frac{N_u(J', J')}{\frac{7.73\times10^{13}}{\nu} \frac{J'(J'+1)}{J'^2}} \,. \tag{4.5}$$

5) The last step is to divide $\int T'_{\mathrm{mb}} d\nu$ by the linewidth (see step 2) to get the brightness temperature in kelvin, T_{mb}.

Taking ν and E_L from Table 4.1 together with the above-mentioned steps reveals predicted brightness temperatures of 1.87 K for NH_3(1,1), 1.49 K for NH_3(2,2), 0.11 K for NH_3(4,4).
Towards NGC 6946 the (1,1) and (2,2) transitions were detected using GBT (Mangum et al., 2013), and as already mentioned the (3,3) transition at higher resolution using the VLA (Gorski et al., 2018) (see Figure 4.6). The proposed resolution of $4''$ is well-matched with the data described in Chapter 5.

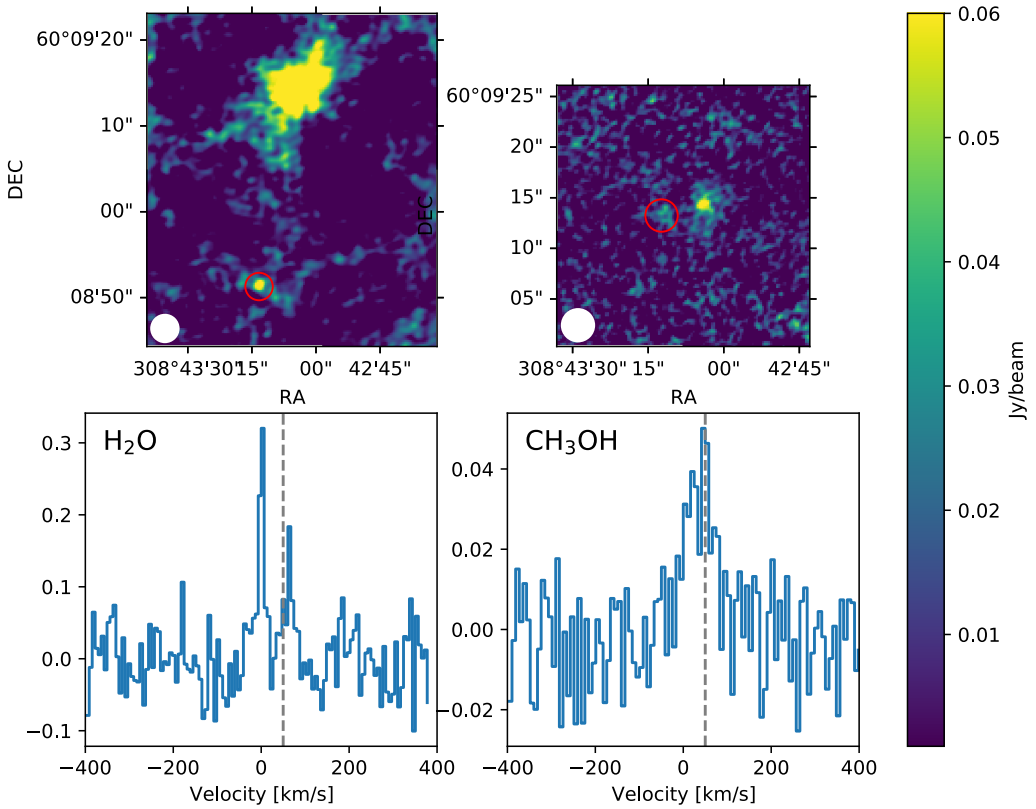

Figure 4.5: **Water (H_2O) and Methanol (CH_3OH) Masers.** The red circle at the channel maps show the position of the detected Masers that were published in Gorski et al., 2018. After reducing the same dataset we checked as a proof of concept if these Masers are also detected in our version of images. Here, the continuum was not subtracted, since the Masers are located far off the center which is the main source of continuum emission.

Once this new dataset is reduced, calibrated, and imaged it will enable us to 1.) resolve Ammonia emission from the lower levels (1,1) and (2,2) that were seen with the GBT and 2.) detect transitions emerging from higher energy levels where the environment is more extreme (hotter and/or denser). With an on-source time of 13 hours, we predict that the combined high sensitivity and resolution of the new observations will allow us to detect all the previously detected transitions of NH_3, along with even higher transitions up to (4,4) - crucial for allowing for an accurate constraint on the kinetic temperature on sub-kpc scales.

4.2 L Band VLA

This technical part of the thesis led to a publication (see Chapter 6) where we analyzed M83's extend HI disk. Within this section, we provide some background regarding the reduction, flagging, imagining, and correcting for short spacing. These observations were carried out with the dual-polarization L-band of the VLA from February 2014 through January 2015 (for ~40 hours with three hybrid

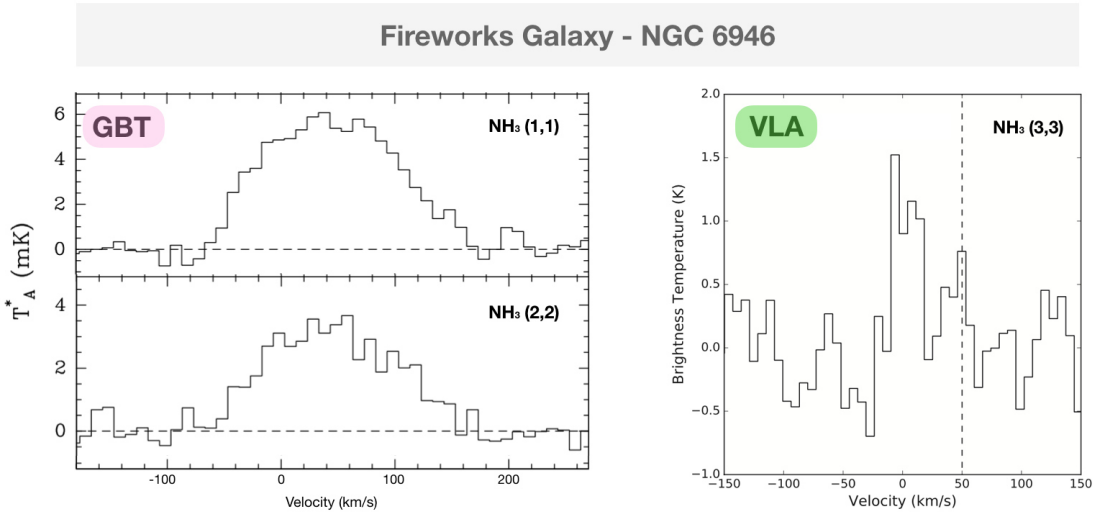

Figure 4.6: Detection of Ammonia towards NGC 6946 with the Green Bank Telescope (GBT) and Very Large Array (VLA). Spectra are adopted from Mangum et al., 2013 and Gorski et al., 2018.

configurations, D north C (DnC), C north B (CnB), and B north A (BnA)) to map the 21-cm emission of neutral hydrogen over the entire super-extended disk of the nearby galaxy M 83. For that, we used a ten-point mosaic (i.e. pointing the VLA in 10 different directions to be able to cover the whole disk of M 83). Unlike in the K-band observations, for this project, we were able to run the VLA pipeline for each of the 22 measurement sets. After that, a second round of calibration was performed. We produce various diagnostic plots and flagged corrupted data (described in Subsection 4.2.1). We imaged the data using CASA's task `tclean` selecting the deconvolution approach `multiscale` and applied auto-masking (described in Subsection 4.2.2) together with the `mosaic` gridding algorithm (described in Subsection 4.2.3). To account for the missing short-spacing we used CASA's task `feather` together with the python package `uvcombine` (described in Subsection 4.2.4). This reveals that single-dish data are needed even for interferometric observations, including compact configurations.

4.2.1 Flagging – Diagnostic Plots

Within this thesis project, we had to remove problematic data (i.e. flagging) that appeared in a few channels. We mostly flagged horizontal and vertical stripes (fringes) and radio frequency interference (RFI). In the following paragraphs, we describe typical 'recipes' for how to flag for horizontal and vertical stripes or possible-RFI with `plotms` and `flagdata`.

Fringes Flagging

1. Plotting the amplitude (amp) versus the uv distance (uvdist) of the target (10 targets/pointings for M83) colored by antenna baselines.
2. As a next step we are looking for spikes and locating/identifying for example their scan ID, baseline, and polarization (LL, RR).
3. For documentation purposes and repeatability it is advisable to put this info into a textfile.
4. Flag them using `flagdata`

5. Repeat steps 2 to 4 until satisfied.
6. As a next step we do imaging to see if the fringes have cleared out.
7. Repeat steps 2 to 6 until satisfied.
8. Whenever we flag the calibrator data, we need to redo the calibration and imaging.

Possible-RFI Flagging

We often find spikes in the plot amplitude versus channel but not all baselines, correlations, and scans are affected. This can create fringing at certain frequencies that are affected by RFI. Flagging only the affected channel is probably not a good approach if that channel is associated with H I emissions.

1. We check whether only one of the correlations is affected. Usually, the RR correlation is affected.
2. Next, we run through each scan and iterate over the antenna (or running through each baseline which is, however, super time-consuming). To make it faster, we can just plot phasecal's scan and flag the scan before and after (that correspond to target scans).
3. We flag scans and antennae affected by RFI (put this list in flagtemplate).
4. Checking whether we are missing something, for example, `plotms` again, but can be plotted for the entire scan and antenna.
5. Repeat steps 2 to 4 until satisfied.
6. Whenever we flag the calibrator data, we need to redo the calibration and imaging.

4.2.2 Deconvolution - CLEAN

Before an image can be used for scientific purposes, it must be *cleaned*. The *dirty image*[6] can contain diffraction structures like fringes or side lobes. During the process of cleaning, these are removed using a suitable deconvolution technique. One of the most used and successful deconvolving procedures in synthesis imaging is the iterative CLEAN Algorithm developed by Högbom in the year 1974 (Högbom, 1974). Essentially, it begins with the dirty image and defines a *model* that is empty before cleaning where in the end the cleaned components are saved. Subtracting the cleaned components from the original dirty image gives the *residual image*. For that to work, the CLEAN Algorithm demands an accurate synthesized beam (i.e. dirty beam) to distinguish between real structures and artifacts originating from the side lobes in the dirty image. The algorithm works as follows:

Step 1) The first step is to find the position and value of the peak of the highest absolute intensity in the dirty image I_{D}.

Step 2) On this position the dirty beam I_{B} multiplied by the peak strength and a damping factor (also known as loop gain) will be subtracted.

Step 3) The first two steps will be repeated until the remaining peaks are less than a user-specified level.

Step 4) One of the last steps is to convolve the point source model accumulated in all iterations with an idealized clean beam B_{C} which is an elliptical Gaussian fitted to the central lobe of the dirty beam.

Step 5) Last but not least the residuals of the dirty image will be added to the clean image to get a realistic background.

[6] The dirty image is the synthesized intensity function.

The dirty image $I_{\rm D}$ represents the inverse Fourier transform of the gridded (and weighted) observed visibilities. Or simplified, the dirty image is the sky brightness convolved with the dirty beam, as,

$$I_{\rm D} = B_{\rm D} * I. \tag{4.6}$$

The dirty beam $B_{\rm D}$ is the response to a synthetic point source. Finding now a solution for I, the on-sky distribution, of this convolution equation represents a deconvolution. The algorithm will start with an initial approximation $I_0 = 0$. At the nth iteration, it searches for the largest value in the residual map

$$I_n = I_D - B_D * I_{n-1}. \tag{4.7}$$

Subsequently, a delta function[7] is centered at the location of the largest residual flux.The response of an antenna to the delta function, the dirty beam, is then subtracted from I_{n-1} to get I_n. Iteration proceeds until a user-specified value N is met. The resulting map is denoted as I_N, and the position of each delta function is stored as "clean component". Every clean component is convolved with the clean beam $B_{\rm C}$ A proper clean beam $B_{\rm C}$ should have the following characteristics: (i) a uniform Fourier Transform within the sampled region of (u, v) space, (ii) a Fourier Transform that approaches 0 as fast as possible outside the sampled (u, v) region, and (iii) no effects from negative sidelobes larger than the noise level.

Finally, a clean image is produced when the final residual map is added to the approximate solution,

$$[\text{clean image}] = I_N * B_{\rm C} + [I_D - B_D * I_N]. \tag{4.8}$$

The algorithm converges to one solution (out of many) if the following conditions are satisfied (Schwarz, 1978): (i) a symmetric beam, (ii) a non-negative Fourier transform of the dirty beam, and (iii) no spatial frequencies should be present in the dirty map that are not also present in the dirty beam. More details can be found in Schwarz, 1978. This algorithm is implemented in CASA's task `tclean`.

Multiscale

In this project, we use the deconvolution `multiscale` approach in the CASA's task `tclean`. The MultiScale Clean approach (Cornwell, 2008) smooths the residual image to multiple scale sizes where the rule of thumb states α = [0, 2×beamsize, 5×beamsize], and then adding larger scales up to the maximum scale that the interferometer can image. In principle, for each scale α_q the algorithm will calculate scale-convolved residual denoted as I_R in Cornwell, 2008,

$$\alpha = m(\alpha) \times I_R \tag{4.9}$$

and calculating the bias via

$$S(\alpha) = 1 - 0.6 \times \alpha/\alpha_{\rm max}. \tag{4.10}$$

For each pair of scales α_p, α_q the algorithm calculates the cross term as,

$$B_{\rm D} \times m(\alpha_p) \times m(\alpha_q), \tag{4.11}$$

[7] A delta function describes a function or distribution over the real numbers that has a value equal to zero everywhere except at zero and whose integral over the whole real line is equal to one.

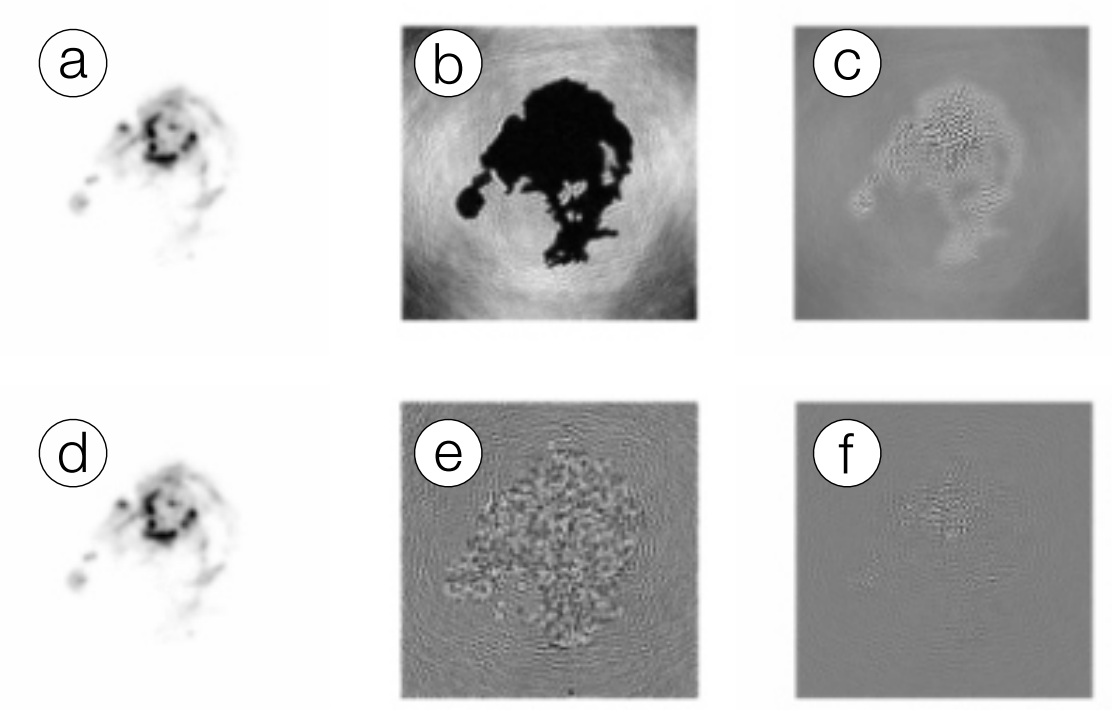

Figure 4.7: **Comparison of deconvolution methods.** Deconvolution of simulated VLA observations of the 'M31' image adopted from Cornwell, 2008. (a) Högbom CLEAN restored image, (b) Högbom CLEAN residual image, (c) Högbom CLEAN error image, (d) Multi-Scale CLEAN restored image, (e) Multi-Scale CLEAN residual image, and (f) Multi-Scale CLEAN error image.

where B_{D} denotes again the dirty beam. Then the algorithm will find the location and scale at which the peak occurs and adds this multiscale component to the model image. Next a scaled, smoothed, shifted point spread function (PSF) from all residual images is subtracted. This procedure continues until either the maximum of I_R^{α} < threshold is reached or, the maximum number of components are identified. The last steps are to convolve the current model by the clean beam and add the residuals to get a restored image.

Figure 4.7 shows a comparison of the Högbom and Multiscale algorithm. It shows the restored images, and residuals, along with the error pattern that is calculated by subtracting the model image as smoothed with the appropriate clean beam. Immediately present, the structure in the residual is quite obvious in the Högbom version and shows that in this case, the multiscale approach does a better job. This is because the residuals show little correlation with the source structure. An additional advantage of multiscale is that, for extended emission, multiscale is much faster than Högbom (a factor of 2 for the example shown in Figure 4.7 described in Cornwell, 2008).

Automasking

Currently "auto-multithresh" is the automasking algorithm available in CASA's task `tclean`. In essence, the algorithm generates clean masks automatically during the deconvolution process by applying flux density thresholds to the residual image. It uses a top-down approach to create masks: it

utilizes the residual images in order to find significant peaks, and then expands the mask to incorporate the emission related to these peaks down to the lower signal-to-noise ratio (see e.g. Kepley et al., 2020). In this project, we restricted the deconvolution using exactly this approach.

In this algorithm, the mask is updated at the start of a minor cycle based on the current residual image. The algorithm uses multiple thresholds based on the user-defined noise and sidelobe levels in the residual image to determine what emission to mask. Auto-multithresh also has the ability to remove small mask regions that are unlikely to be true astronomical emissions. The `sidelobethreshold` and `noisethreshold` subparameters control the initial masking of the image. The `sidelobethreshold` specifies the minimum sidelobe level to be masked, while the `noisethreshold` specifies the minimum signal-to-noise level to be masked. The threshold used for masking is the greater of the two values that are calculated for each sidelobe cycle based on the rms values of the noise and sidelobes in the current residual image. For imaging the extended HI disk of M 83 we used `sidelobethreshold` = 0.75, `noisethreshold` = 3.0, `lownoisethreshold` = 2.0, `negativethreshold` = 0.0, `min-beamfrac` = 0.1, `growiterations` = 75. The detailed algorithm is presented in Kepley et al., 2020[8].

4.2.3 Interferometric Mosaicing

The limitations of observing extended sources with an interferometric array are not a new issue. For most objects in the sky, two kinds of constraints must be considered in order to obtain comprehensive coverage of the extended structure: (1) The source may contain structures with spatial frequencies smaller than the shortest baseline ($\delta > \lambda/B_{min}$), so that the interferometer is incapable of imaging them, (2) The angular extent of the source may be large relative to the primary beam of a single antenna ($\delta > \lambda/D$), where D is the diameter of the single antenna of the interferometric array. In this case, a single pointing fails to image the entire structure. The solution to the latter limitation is interferometric mosaicing (e.g. Holdaway, 1999), meaning a measurement that consists of multiple pointings.

Mosaicing approaches exist, such as a linear combination of the individual pointings (Holdaway, 1999), a joint deconvolution of the pointings (Sault et al., 1996), or adding the visibility measurements of individual pointings to obtain what is called a dirty mosaic. For the linear method, the interferometric mosaic is made of multiple individual single-point observations, each of them treated separately for imaging and deconvolution. The concatenation of all the adjusted point observations results in an interferometric mosaic. The concatenation is linear, taking into account the proper weights for the primary beam. The joint deconvolution approach demands a combined dirt image and a combined dirt beam. Here, mosaicing occurs during deconvolution.

For this project, we used the parameter `gridder=''mosaic''` within CASA's task `tclean`. It uses polynomial models to construct azimuthally symmetric beams per antenna that are transformed into baseline convolution functions and used for gridding. The algorithm applies direction-dependent, time-variable, and baseline-dependent corrections during gridding in the visibility domain, by computing the appropriate gridding convolution kernel to use along with the imaging weights.

Deconvolution generally interpolates the missing information in the (u, v) domain. However, the extrapolated information for spatial scales smaller than the shortest measured distance is uncertain. Mosaicing can reduce the shortest distance to $d - D/2$, where d is the size of the shortest baseline and

[8] The summary of the algorithm can be found here: https://casadocs.readthedocs.io/en/latest/notebooks/synthesis_imaging.html#Automasking.

D is the size of a single antenna in the array. But regardless of the mosaicing method, the center of the (u, v) coverage is still incomplete. This is especially important when a large-scale structure is present. Correcting for short-spacing correction, that is, combining the interferometric data with that from a single dish provides this missing information.

4.2.4 Short Spacing; The Need for Single Dish Observations

The shortest baseline that an interferometer can cover depends on the size of its dishes, so the central part of the (u, v) coverage is never sampled. This deficit of coverage at low spatial frequencies causes interferometers to be insensitive to large angular scales. This is known as the short spacing problem. The majority of existing approaches for performing the SSC operate in the Fourier (spatial frequency) domain. Among these methods, the most widely used approach for combining the deconvolved interferometric data cube with the single-dish data cube is probably *feathering*.

Feathering

Feathering is the technique of combining a Single Dish (SD) observation with interferometric observation of the same field in the Fourier (spatial frequency) domain weighted by the spatial frequency response of each observation. The aim of this is to reconstruct the emission from the source at all spatial scales, spanning from the small spatial scales (measured by the interferometer) to the large-scale structures (measured by the SD). Essentially feathering does the following: (i) Using the Fourier transformation of the SD beam to taper (meaning down weight) the central regions of the interferometric (u, v) coverage, (ii) combining the SD and tapered interferometric data in the spatial frequency domain, and (iii) obtaining the combined image via an inverse Fourier transformation. Feathering requires that the spatial frequencies of the SD and the interferometric data overlap to some extent (see Figure 4.9).

The effects of missing short-spacing corrections are shown in Figure 4.8. Whenever we observe with an interferometer that is not capturing the short spacing in the spatial frequencies we will end up with negative bowls in the image domain. In this project, we used CASA's task `feather` to combine SD with interferometric data. Prior to this, however, we looked for the correct Single Dish Scaling Factor (parameter `sdfactor`) used to scale the SD image (see Section 4.2.4) to get it to the same scale as the interferometer data. Essentially, it is a change in the flux scale of the SD image. After that we prepare the individual images for feathering, meaning converting them from brightness temperature units to Jy/beam.

Single Dish Scaling Factor with uvcombine

To quantify the scaling factor, we use a distribution-based method on the (u, v)-amplitudes where the spatial coverage of the VLA and SD data overlap. For that, we use the `uvcombine` package (Koch and Ginsburg, 2022) and examine the distributions of the SD amplitudes, the VLA amplitudes, and their ratio across all channels. The ratio between the SD and VLA amplitudes is following a Cauchy distribution and the logarithm of these ratios of amplitudes can be fitted to this distribution. Then, the scaling factor is the location of the peak of this distribution. Figure 4.10 is adopted from the appendix of Eibensteiner et al., 2023 (see also Chapter 6) and shows the distribution of the amplitudes across all

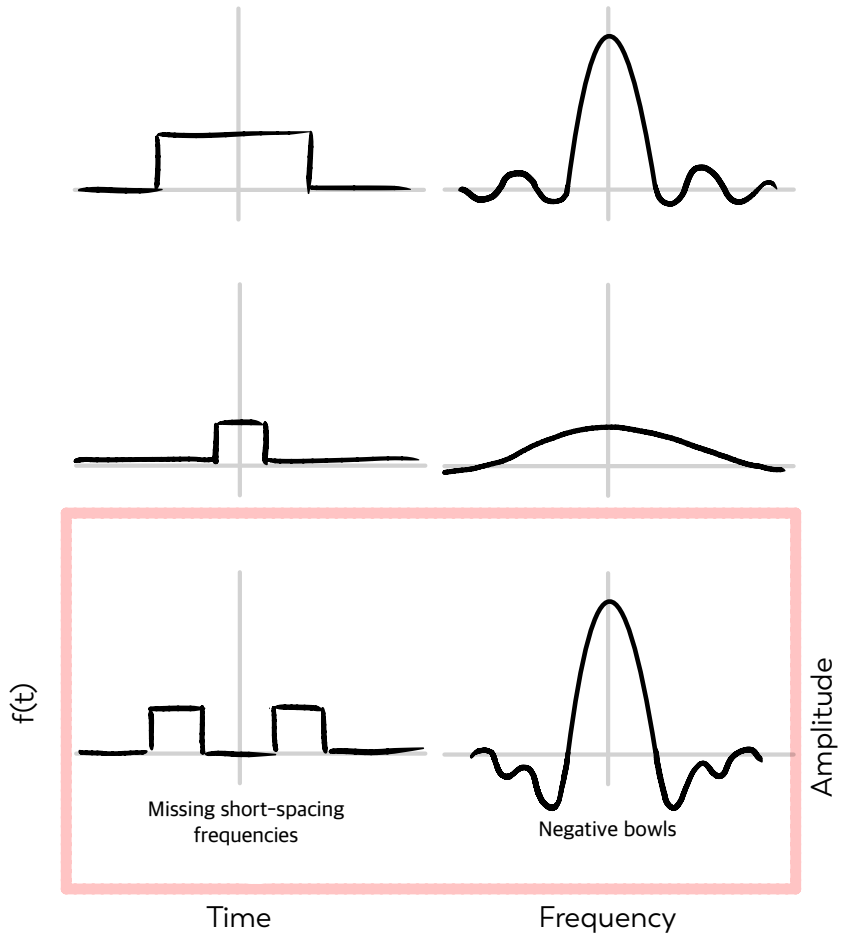

Figure 4.8: The effects of missing short-spacing frequencies. The left column shows the box functions in the spatial frequency domain, whereas the right column shows their corresponding Fourier transformation. However, we focus on the functions marked in pink: The left one is showing a simplified (u, v) coverage of an interferometer, where the central region is not sampled. The right one is the corresponding Fourier transformation which is a sinc function with pronounced negative amplitudes referred to as *negative bowls*. This sketch is inspired by Braun and Walterbos, 1985.

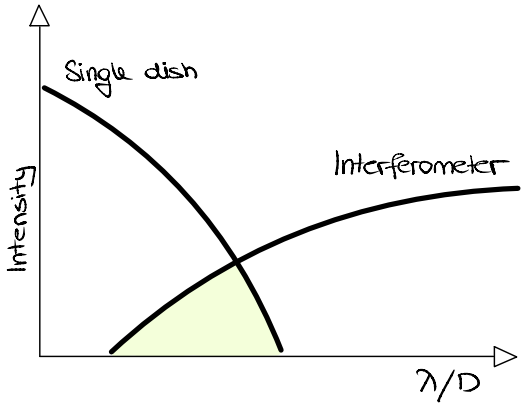

Figure 4.9: **Overlap for typical single dish and interferometric observations**. Schematic view of the intensity against spatial scales and the overlap region between the single dish and interferometer observations. The overlap region (yellow colored) corresponds to spatial scales, to which both instruments are sensitive.

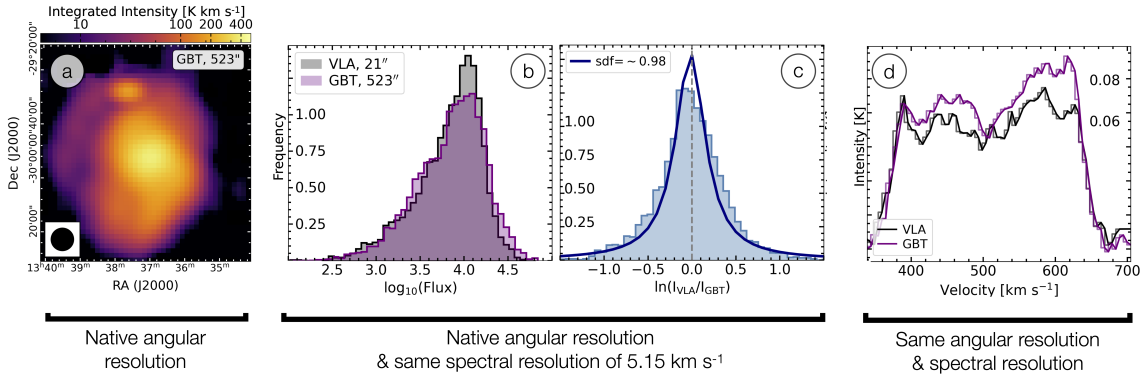

Figure 4.10: **Image combination.** Adopted from Eibensteiner et al., 2023. Panel (a) shows the integrated intensity maps of the GBT observation at native angular resolution. (b) Shows the distribution of the flux of the single dish (SD) and VLA data at matched spectral resolution (that is, we regridded the VLA to the GBT spectral resolution). (c): We used the `uvcombine` python package to find the single dish scaling factor (sdf; blue line). The ratio of the low-res and high-res observations results in a Cauchy distribution. We fit the log of the ratio to a Cauchy distribution (blue histogram) and its mean is then an estimate for the scaling factor. (d): The spectra of the VLA and GBT observation at matched angular and spectral resolution (that is, we gaussian convolve and regridded the VLA to the GBT angular and spectral resolution).

channels and the best-fit Cauchy distribution. For our VLA observation, we use Green Bank Telescope (GBT) SD data to correct for short spacing.

Applying a maximum likelihood approach and using the ratios from all channels, we find a scaling factor of 0.982 ± 0.003 for the GBT data. Assuming that the absolute flux uncertainties are $\sim 10\%$, the scaling factor from the distribution fit is consistent with a factor of 1. Therefore, we did not apply a scaling factor to the GBT data before feathering.

In the end we find a total flux for the VLA cube of 5.2×10^4 K and 6.6×10^4 K for the feathered one (VLA plus GBT). This difference emphasizes that single-dish data are needed even for interferometric observations, including compact configurations.

CHAPTER 5

Molecular Fireworks: A high-resolution molecular lines survey towards the center of the Fireworks Galaxy, NGC 6946

A 2–3 mm high-resolution molecular line survey towards the centre of the nearby spiral galaxy NGC 6946

C. Eibensteiner, A. T. Barnes, F. Bigiel, E. Schinnerer, D. Liu, D. S. Meier, A. Usero, A. K. Leroy, E. Rosolowsky, J. Puschnig, I. Lazar, J. Pety, L. A. Lopez, E. Emsellem, I. Beslic, M. Querejeta, E. J. Murphy, J. den Brok, A. Schruba, M. Chevance, S. C. O. Glover, Y. Gao, K. Grasha, H. Hassani, J. D. Henshaw, M. J. Jimenez-Donaire, R. S. Klessen, J. M. D. Kruijssen, H.-A. Pan, T. Saito, M. C. Sormani, Y.-H. Teng, and T. G. Williams

2022, A&A, 659, A173, 24 pp. (DOI: 10.1051/0004-6361/202142624)

Overview

In this work, we observed the central 50″(corresponds to 1.9 kpc) for 132 hours across the 1 – 3 mm window with the IRAM Plateau de Bure Interferometer (PdBI). Our goal is to assess the physical and chemical structure of the molecular gas of the inner few kpc of NGC 6946. The observations were carried out from 2002 to 2009 and two molecular lines were published in Schinnerer et al., 2006; Schinnerer et al., 2007. This project presents the whole suite of molecular lines giving us one of the most comprehensive, high-resolution (2 – 4″≈ 75 – 150 pc) molecular line data sets for a nearby galaxy center in the northern hemisphere.

NGC 6946 is a prime target since it is one of the nearest face-on large spiral galaxies (D~7.7 Mpc; Anand et al., 2018) in the northern hemisphere. This galaxy is a double-barred actively star-forming galaxy and leads the list of observed supernovae in any galaxy, which has led to its name *Fireworks Galaxy*. While studies exist that investigate individual extragalactic central molecular zones, they often have complex morphologies that are hard to interpret. NGC 6946 has the advantage of having a morphologically well-characterized galaxy center and a face-on orientation which makes it possible to investigate for the first time the effect of resolved sub-regions of an inner small-scale bar on molecular

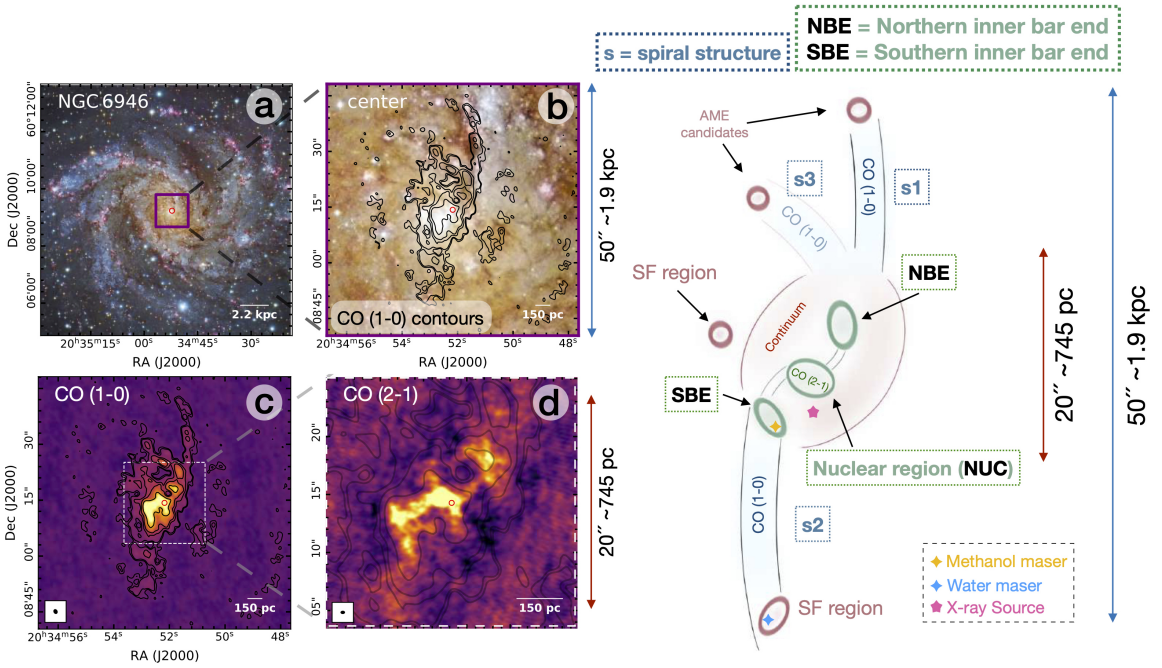

Figure 5.1: **Observation towards the center of NGC 6946.** *Left panels:* (a) three color optical image, with the region we observed drawn as a purple box, (b) CO (1−0) emission shown in contours levels of 60, 90, 200, 300, 600 K km s^{-1}, and are repeated on all panels for comparison, (c) integrated CO (1−0) emission, (d) CO (2−1) emission towards the inner 20″ shown as color scale; *Sketch (right):* We denote here all observed features. In this work, we particularly focus on the inner 20″and the regions associated with the inner small-scale bar (modeled in Schinnerer et al., 2006 and shown in green color): the southern inner bar end (SBE), the nuclear region (NUC), and the northern inner bar end (NBE). We denote in the sketch for completeness other observed features. Red colors indicate continuum emission and the identified star formation (SF) regions and potential anomalous microwave emission (AME) candidates (Linden et al., 2020). Blue colors show the three spiral structures (s1, s2, and s3), and the blue marker at the end of s2 indicates the location of a water maser. The orange marker presents the location of the methanol maser detected in SBE (Gorski et al., 2018). Optical image credits: NASA, ESA, STScI, R. Gendler, and the Subaru Telescope (NAOJ). This figure is a modified version of figure 1 in Eibensteiner et al., 2022.

line emission and star formation, along with scaling relationships of star formation rate and variations of molecular line ratios as diagnostics of the physical state of the molecular gas.

The following work was published in the Journal A&A in 2022. The paper Eibensteiner et al., 2022 is provided in its entirety in original form in Appendix A. I performed all of the analysis steps presented in the paper myself, receiving helpful advice and suggestions from a wider group of co-authors to improve certain aspects of the methodology. The following sections provide a detailed review of the relevant scientific questions that were raised as part of the project.

5.1 Covered Molecular Lines

In this work, we detect spectral lines from ten molecules: ^{12}CO, HCN, HCO$^+$, HNC, CS, HC_3N, N_2H^+, C_2H, CH_3OH, and H_2CO. We detect two transitions for ^{12}CO, CS, HC_3N, and CH_3OH, resulting in a total of 14 molecular emission lines. We show some of their properties in Table 5.1.

Table 5.1: Summary of the molecular lines detected towards the center of NGC 6946.

	Molecules	Transition	$\nu_{\rm rest}$	$\nu_{\rm obs}$	$E_{\rm u}$	$n_{\rm H_2}$ ($\epsilon_{\rm max}$)	$n_{\rm eff}$	Reference
			[GHz]	[GHz]	[K]	[cm^{-3}]	[cm^{-3}]	
	(1)	(2)	(3)	(4)	(5)	(6)	(7)	(8)
3 mm	C_2H	$N = (1–0), J = 3/2–1/2$	87.316	87.302	4.19			this work
	HCN	(1–0)	88.632	88.617	4.25	2×10^5	4.5×10^3	this work
	HCO^+	(1–0)	89.188	89.173	4.28	4×10^4	5.3×10^2	this work
	HNC	(1–0)	90.664	90.648	4.35	1×10^5	2.3×10^3	this work
	HC_3N	(10–9)	90.979	90.964	16.69		4.3×10^4	this work
	N_2H^+	(1–0)	93.174	93.158	4.47		5.5×10^3	this work
	CH_3OH	$J_K = 2_0–1_0$	96.741	96.725	6.96			this work
	CS	(2–1)	97.980	97.965	7.10		1.2×10^4	this work
	^{12}CO	(1–0)	115.271	115.252	5.53	1×10^2		S1 & S2
2 mm	CH_3OH	$J_K = 3_0–2_0$	145.100	145.073	18.80			this work
	HC_3N	(16–15)	145.561	145.534	41.27			this work
	p-H_2CO	$N = (2–1), J = 0/2–0/1$	145.603	145.576	10.48		6.3×10^4	this work
	CS	(3–2)	146.969	146.942	14.11		3.3×10^4	this work
1.3 mm	^{12}CO	(2–1)	230.538	230.499	16.59	1×10^3		S2

Notes: (1–2): Molecular lines with their transition ordered by their rest frequencies[a]; (3–4): Rest and observational frequencies; (5): Upper energy levels (6): Minimum density at which the emissivity of the line reaches 95% of its peak value for $T = 25$ K (see table 2 within Leroy et al. 2017 and references therein); (7): Taken from Shirley 2015 (table 1, for 20 K), and have been defined by radiative transfer modelling as the density that results in a molecular line with an integrated intensity of 1 K km s^{-1}; (8): References, S1 = Schinnerer et al., 2006 and S2 = Schinnerer et al., 2007

[a] Throughout this chapter, for simplicity, we refer to the transitions of C_2H as (1-0), of CH_3OH as (2-1) and (3-2), and of H_2CO as (2-1)

In Figure 5.2 we show their integrated intensity maps after convolving each of the molecular emission lines to a common resolution of 4″that corresponds to 150 pc. On each of the 14 panels we overplotted the contours of CO (1–0) emission in red, that reflects the spiral structures (blue colors in the sketch of Figure 5.1). At first glance we see in Figure 5.2 that the 14 molecular emission lines show different distributions in their integrated intensities towards the inner 50″ of NGC 6946. They also show differences in their peaks in integrated intensities (indicated by the yellow hexagons). In the case of the strongest molecular lines, such as CO (1–0), CO (2–1), HCN (1–0), HCO^+ (1–0) and HNC (1–0) in our dataset, distinct regions are clearly observed, and their integrated intensities peak in the nuclear region (NUC, the central few hexagons).

5.2 The effects of the small-scale bar

NGC 6946 is a double-barred galaxy and the appearance of the distribution of ^{12}CO in NGC 6946's inner 20″could be explained with modeling effort by an inner small-scale bar (see Schinnerer et al., 2006). This small-scale bar has a radius of ~250 pc (projected into the galaxy plane). In our work, we analyzed the effects of the small-scale bar on molecular line emission and the star formation rate. For that, we associated individual hexagons to the regions of NUC, SBE, and NBE as seen in the right panel of Figure 5.3.

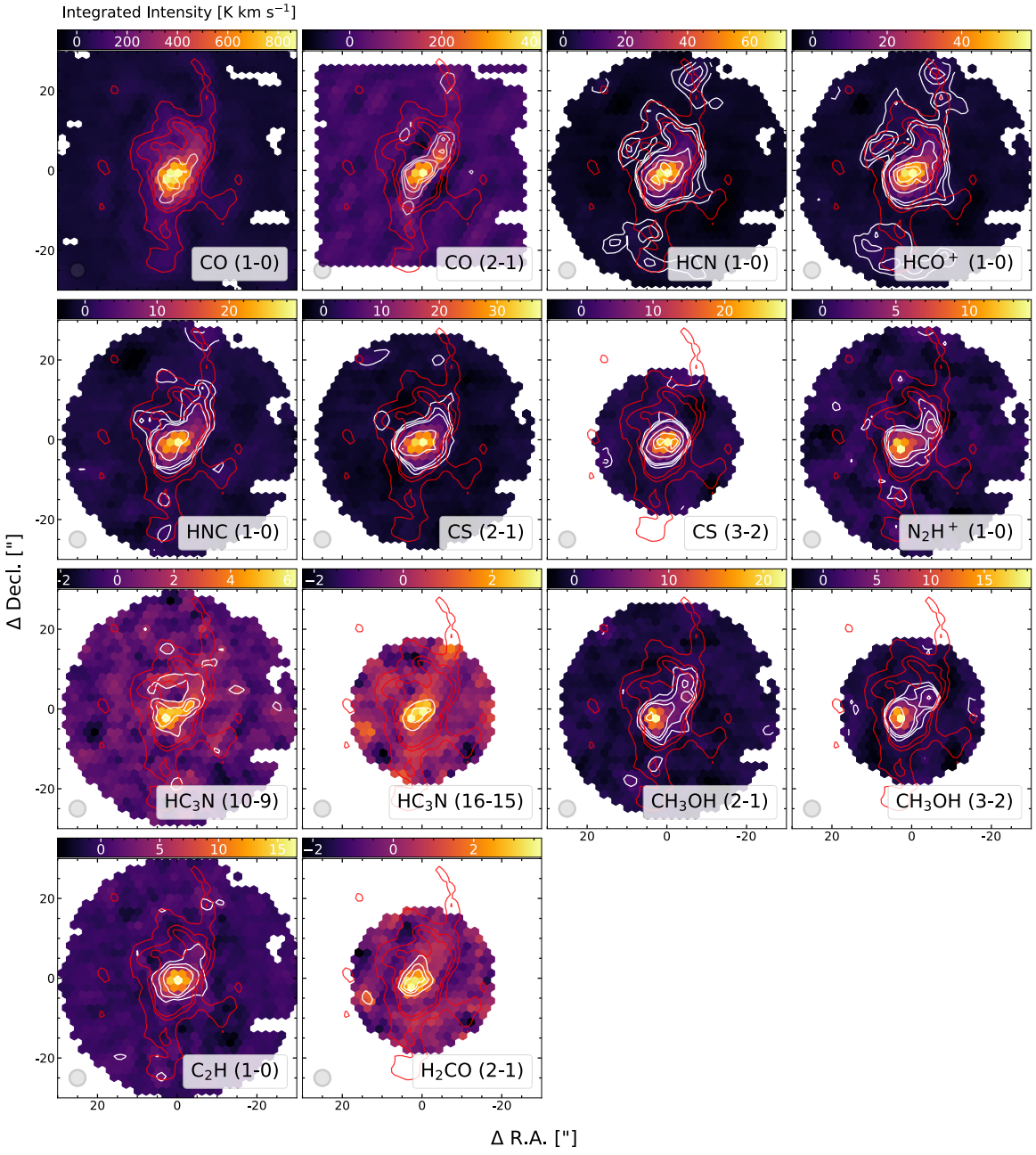

Figure 5.2: **Integrated intensity maps for 14 molecular emission lines at a common resolution of $4'' \approx 150$ pc.** The maps were created using a hexagonal sampling technique. The grey shaded circle in the lower left corner marks the beam size and the red contours show CO (1−0) S/N levels of 30, 60 and 90. The white contours in the first panel show S/N levels of 200 and 300, and in the second panel S/N levels of 30, 60 and 90. The following panels (from HCN to H_2CO (2−1)) show S/N levels of 3, 6, 9, 30, 60 and 90. The colorbar indicates the integrated intensity of each line in units of K km s^{-1}. Figure taken from Eibensteiner et al., 2022.

As shown in Figure 5.2, the strongest emission lines peak in their integrated intensity in NUC. However, the situation differs for molecular species with higher effective critical densities ($n_{\rm eff}$).

Notably, CS (3−2) and C_2H (1−0) exhibit concentrated emission primarily within the inner 5″ in radius. Having a look again on Figure 5.2 with the knowledge of where the SBE and NBE are located, interestingly, HC_3N (10−9), N_2H^+ (1−0), CH_3OH (2−1) and CH_3OH (3−2) do not display their highest integrated intensities at the central position, but rather at the SBE. It is noteworthy that, despite the higher $n_{\rm eff}$ values of CS maps compared to N_2H^+ (1−0), the former does not exhibit a peak in the SBE, whereas the latter does. We note that the different distributions of molecular emissions may not solely result from density variations, but could also be influenced by temperature changes (potentially driven by embedded star formation), affecting both excitation and abundance patterns.

We detect in the southern inner bar end higher SFR in combination with shock tracers (e.g. CH_3OH (3k–2k)) and higher concentration of denser gas (e.g. HCN (1−0)) than in the northern inner bar end.

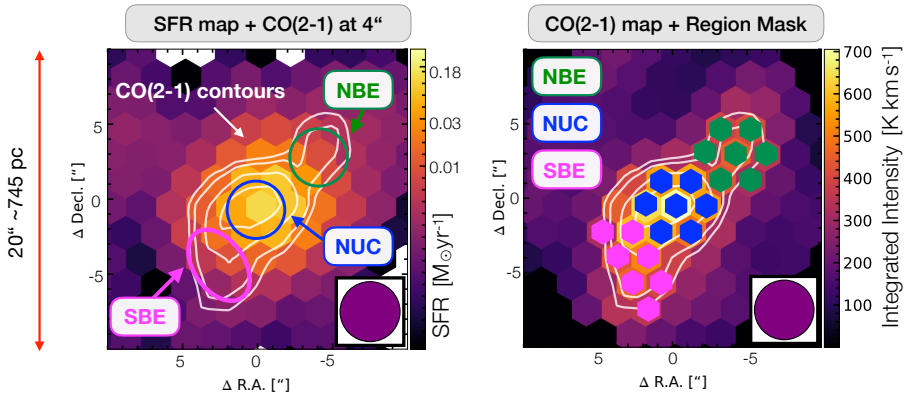

Figure 5.3: **Star formation rate map and region mask.** *Left:* SFR map at 4″ ≈ 150 pc resolution on hexagonal grid with white contours of CO (2−1) integrated intensities. For the SFR map we used the thermal part of the 33 GHz continuum emission at 2″.12 × 1″.70 resolution. Overploted are the identified regions – nuclear region (NUC), northern and southern inner bar end (NBE and SBE). *Right:* The region mask shows the chosen hexagonal points in colors of green for the NBE, blue for the NUC, and pink for SBE. To each of the regions we associate – equivalent to our beam size of 4″ – seven individual lines of sight (hexagonal points). In the background, we show the integrated intensity map of CO (2−1) at 4″ resolution. This figure is a modified version of figure 4 in Eibensteiner et al., 2022.

5.3 Star formation scaling relations

We focused on a sub-sample of the 14 molecular emission lines. Namely, we focus on those molecular lines where we found single-dish observations to correct for short spacing to ensure a correct interpretation. These are CO (1−0), CO (2−1) HCN (1−0), HCO^+ (1−0), and HNC (1−0). We investigated how

(i) the dense gas tracers (HCN, HCO^+, and HNC) relate to the star formation rate surface density ($\Sigma_{\rm SFR}$)

(ii) the dense gas fraction ($f_{\rm dense}$) respond to the integrated intensity of CO (2−1), and

(iii) the star formation efficiency ($\rm SFE_{dense}$) respond to the integrated intensity of CO (2−1).

We take the integrated intensity of CO (2−1) as an indicator of mean volume density as many previous studies (e.g. Leroy et al., 2016; Sun et al., 2018; Gallagher et al., 2018b).

To put it right up front, we find for relations (i) and (ii) behaviors as expected from previous studies, however, this is not the case for (iii). In detail, for (i) we expect a positive correlation between the dense gas tracers and $\Sigma_{\rm SFR}$ (as it has been shown using HCN in e.g. Gao and Solomon, 2004). We find exactly that with the addition that the integrated intensity of the molecular line with the lowest effective critical density ($n_{\rm eff}$) shows the strongest correlation ordered as HCO^+ < HNC < HCN. So essentially, we find the strongest correlation for HCO^+ with $\rho \sim 0.95$.

For (ii) we expect that the dense gas fraction $f_{\rm dense}$ increase towards the center as it has been observed towards many galaxies using HCN over CO (e.g. Usero et al., 2015; Bigiel et al., 2016; Jiménez-Donaire et al., 2019; Bešlić et al., 2021) along with models predicting a positive correlation between the volume density and $f_{\rm dense}$ (see Padoan et al., 2014). We explore the $f_{\rm dense}$ versus integrated intensity of CO (2−1) for all three dense gas tracers and find that they increase towards the nuclear region (NUC) and that the dense gas fraction using HNC shows the strongest correlation with $\rho \sim 0.66$. Additionally, the order in the slopes (β) and correlation coefficients (ρ) do not follow the order of $n_{\rm eff}$. Instead, they show the order of $\beta_{\rm HNC} > \beta_{\rm HCO^+} > \beta_{\rm HCN}$. One possible explanation for this behavior could be attributed to anomalous excitation of one of the species. For instance, it could involve IR pumping affecting the HCN and HNC levels, or potentially peculiar filling factors that contribute to the observed phenomenon.

For (iii) we expect $\rm SFE_{dense}$ to decrease towards the center, as it has been observed towards other galaxy centers using $\Sigma_{\rm SFR}$ and HCN and to drop with the integrated intensity of CO (2−1). We find exactly the opposite behavior. We show this in Figure 5.4 where $\rm SFE_{dense}$ *increases* towards the NUC, having higher $\rm SFE_{dense}$ values in NUC relative to the rest of the center. That is contrary to the trends found in Gallagher et al., 2018a and Jiménez-Donaire et al., 2019 over the whole disks of nearby galaxies. These studies, however, could not resolve the sub-structures of NGC 6946's center (the inner bar with the regions NUC, SBE, and NBE). Their resolution was about 1 kpc which would be as if all of the individual points shown in Figure 5.4 are averaged resulting in one data point.

5.4 Molecular line ratios at sub/kpc-scales

Previous studies suggest that the ratio of different molecular emission lines can be used as a diagnostic to assess the physical and/or chemical state of molecular gas. As part of this project, we analyzed molecular line ratios of

(i) CO (2−1)/CO (1−0) denoted as R_{21}
(ii) HNC/HCN, and
(iii) ratios between HCN, HCO^+, and HNC.

We explore (i) only towards NGC 6946, but for (ii) and (iii) we include observations from eight additional nearby galaxies centers (from the IRAM-30m EMPIRE survey, Jiménez-Donaire et al., 2019) and for the line ratio diagnostic plots in (iii) we additionally include high-resolution observations of M 51 from Querejeta et al., 2016 as well as NGC 3627 from Bešlić et al., 2021).

R_{21}

Previous studies analyzed R_{21} across the disks of nearby galaxies and found higher R_{21} values in their centers (e.g. Leroy et al., 2009; Koda et al., 2020b; den Brok et al., 2021; Yajima et al., 2021). However,

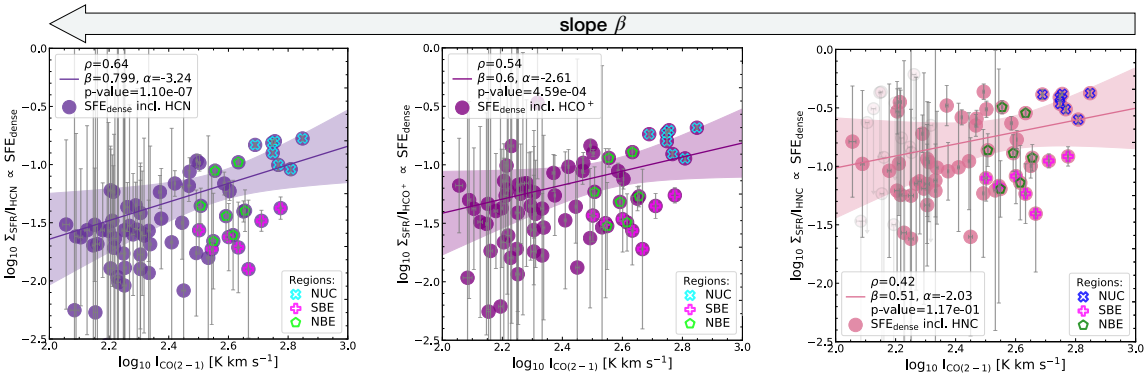

Figure 5.4: **Correlation plots ordered by their slope, β.** The slope increases from right to left (indicated by the grey arrow above). Dark purple colors show HCN, purple HCO^+, and pink HNC. We show in all three panels integrated intensity of CO (2−1) – an indicator of the mean volume density – versus the ratio of Σ_{SFR} with the dense gas tracers – a spectroscopic tracers of SFE_{dense}. The fits (accounting for upper limits) are shown as solid lines surrounded by 3σ confidence intervals (shaded regions of corresponding colors). Absolute uncertainties are plotted on each data point, which are generally small towards the regions NUC, NBE, and SBE. We find the highest uncertainties in the outskirts in our Σ_{SFR} map. Correlations including HNC result in 58 significant sight lines and 15 upper limits (denoted as light pink markers). We display in each panel Pearson's correlation coefficient and the power-law slope, intercept, and p-value. This figure is a modified version of figure 6 in Eibensteiner et al., 2022 only showing one row of scaling relations.

these studies could not resolve sub-structures with their galaxy centers. With our observations, we can explore for the first time R_{21} variations in the galaxy center where we can resolve regions of the inner bar. Higher R_{21} values could be related to denser gas and/or warmer gas with higher temperatures. We find strong variations of R_{21} in the inner 20″ of NGC 6946 ranging from 0.4 – 0.8. Surprisingly, we find higher values of R_{21} towards the northern inner bar end, NBE, than the NUC; despite the higher Σ_{SFR} in the SBE compared to the NBE. One possible interpretation for this could be the presence of denser gas in the NBE. However, our RADEX modeling analysis does not indicate a significant increase in higher density within the NBE compared to the NUC or the SBE. The ambiguous nature of this behavior raises an open question that requires further exploration.

HNC/HCN

Comparing the integrated intensities between HNC and HCN, are thought to be sensitive to gas kinetic temperatures, T_k as this temperature dependence has been first observed in the Orion Molecular Cloud 1 (OMC-1) in Schilke et al., 1992. Ever since then, it has been debated whether a ratio between these isomers could really be linked to kinetic temperatures (see e.g. Aalto et al., 2002; Meier and Turner, 2012) and recently it came back into consideration (Hacar et al., 2020). Essentially, Hacar et al., 2020 demonstrated a strong sensitivity of the HNC/HCN ratio to T_k, comparing the ratio with observations of the lower inverse transitions of NH_3. They described T_k by a two-part linear function for two conditions (their equation 3). We apply their equation to infer T_k and compare it with the literature values not only for NGC 6946 but also for the eight additional galaxy centers from the EMPIRE survey.

To put it right up front, an unambiguous determination of the kinetic temperature is in general challenging but we find that the HNC/HCN ratio results in low inferred T_k in galaxy centers (up to a factor of 7 lower than with other temperature estimate techniques). In detail, we find for NGC 6946 T_k(HCN/HNC) of ∼ 27 K for the NUC and slightly higher temperatures for the NBE ∼ 31 K and the

SBE~ 32 K. Using the ratio of the lower transition of NH_3, NH_3 $(1,1)/NH_3$ $(2,2)$, Mangum et al., 2013 found T_k ~47±8 K for NGC 6946. That is a factor of ~ 2 higher than the one inferred using T_k(HNC/HCN). For galaxy centers such as NGC 253, the difference is a factor of ~ 7 (warm and hot component of $T_{k,warm} > 50$ K and $T_{k,hot} > 300$ using H_2CO as a temperature tracer Mangum et al., 2019; or $T_{k,warm} > 75$ K and $T_{k,hot} > 150$ using NH_3 as a temperature tracer). For the EMPIRE centers we find for almost all kiloparsec-sized centers $T_{k,warm} < 50$. We speculate that the isomer ratio may not be a reliable probe of kinetic temperature for large-scale extragalactic regions, especially in the vicinity of galaxy centers where high optical depths, complex chemistry, AGN activity, and additional excitation mechanisms can play significant roles.

Ratios between HCN, HCO^+ and HNC

In the inner kpc of galaxies, gas clouds experience high levels of radiation originating from various sources such as active galactic nuclei (AGN), which emit intense X-rays with energies exceeding 1 keV. Additionally, radiation from starburst regions, predominantly composed of O and B stars, can also contribute to the radiation field. The presence of excessive X-ray emission has the potential to disrupt the thermal and chemical equilibrium of the surrounding ISM, subsequently impacting molecular line emissions. As outlined in detail in Subsection 1.5.3, the ratios of HCN, HCO^+, and HNC were proposed to be a diagnostic tool to distinguish between a photon-dominated region (PDR) and an X-ray dominated region (XDR) (Meijerink and Spaans, 2005; Meijerink et al., 2007; Baan et al., 2008; Loenen et al., 2008).

In Figure 5.5 we investigate these diagnostic plots proposed to visually discriminate between XDR and PDR in the central 20″towards NGC 6946 (circle markers). In all these diagnostic plots (panels a–d), NGC 6946 is in the PDR regime. For NGC 6946 there is no clear evidence for an AGN and with ancillary X-ray data from Chandra we do not find any X-ray sources that are strong enough to could trigger an XDR. The star markers in Figure 5.5 show the kpc-sized central regions of the EMPIRE galaxies and *all* of them lie in the PDR regime. We would expect that for galaxies hosting an AGN, the situation looks different. The galaxies NGC 3627, NGC 5055, and M51 are known to host an AGN classified as LINER (Goulding and Alexander, 2009, star markers with red contours) and are still located in the PDR regime. We find no strong enhanced HCN emission relative to HCO^+ towards these three galaxy centers that would 'move' them to the XDR regime of the diagnostic plots. One reason could be that the EMPIRE AGNs are faint and their effects are diluted when averaging over 1 kpc regions. Therefore, we include available high-resolution observations for NGC 3627 and M51, but again they lie in the PDR regime. This suggests that this ratio might not be ideal to diagnose the presence of an AGN (which would indicate an XDR) in galaxies on kpc/sub-kpc scales.

5.5 Summary and Conclusions

In this paper, we analyzed high-resolution multi-molecule observations towards the inner 50″(1.9 kpc) of the nearby double-barred starburst galaxy NGC 6946, also known as the Fireworks Galaxy. As for the main scientific questions, we arrive at the following answers,

- ⋆ **How does NGC6946's small-scale bar affect the molecular line emission?**
  NGC 6946 is a double-bared nearby galaxy and its inner smaller bar is 250 pc in radius. In our observations, we can distinguish individual sub-regions associated with the inner smaller bar: the nuclear region (NUC), and the southern and northern inner bar ends (SBE and NBE). We

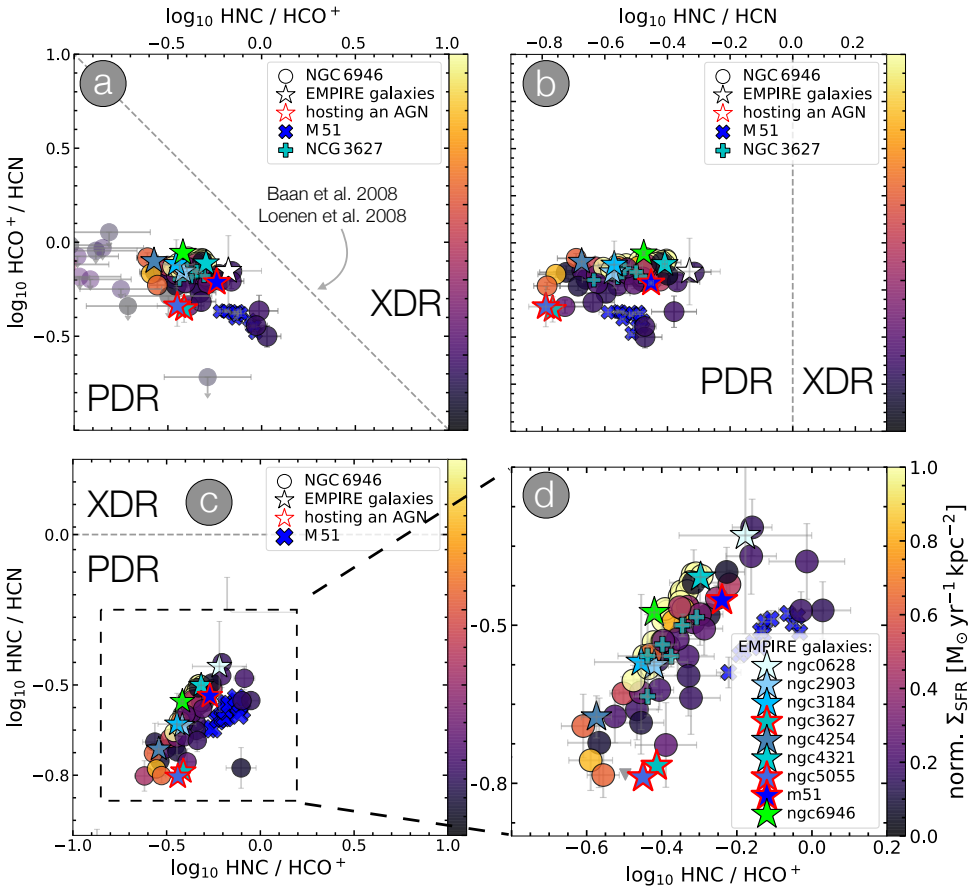

Figure 5.5: **Diagnostic plots using integrated line ratios of HCN, HNC and HCO^+ versus each other.** *Left panels:* (a): Integrated HCO^+/HCN versus HNC/HCO^+ ratios. (b): Integrated HCO^+/HCN versus HNC/HCN ratios. (c): Integrated HNC/HCN versus HNC/HCO^+ ratios. The grey dashed lines mark the border between XDR and PDR (Baan et al., 2008; Loenen et al., 2008). Circles indicate reliable values (S/N > 5) and upper limits for the central 20″ ≈ 745 pc towards NGC 6946. Stars show the EMPIRE galaxies and stars with red contours present galaxy centers hosting an AGN (Goulding and Alexander, 2009). For two of them, we find ancillary data: the cross shaped markers show the ∼4″ (≈ 166 pc) M 51 observations (Querejeta et al. 2016) and the ∼2″ (≈ 100 pc) NGC 3627 observations (Bešlić et al. 2021); (d): The enclosed integrated HNC/HCN versus HNC/HCO^+ with the kpc-sized centers of the EMPIRE survey (see Jiménez-Donaire et al. 2019 for details). NGC 6946 and the EMPIRE galaxies are in the PDR regime in all panels. Interestingly, EMPIRE galaxies harboring an AGN do not show an enhancement of HCN as suggested in many studies (see text for a discussion). This figure is a modified version of figure 8 in Eibensteiner et al., 2022 only showing the PDR-XDR diagnostic plots.

find that the molecular emission lines tracing the densest gas (compared to HCN), for example, by N_2H^+ (1−0) and shocks traced, for example, by CH_3OH (2−1) are more concentrated in the SBE than in the NUC or NBE. The small-scale bar affects the molecular gas such that the locations of the densest molecular gas material are not necessarily the very centers of the galaxies. Furthermore, the increased star formation rate found suggests that shocks and denser gas are responsible for this scenario.

⋆ **How do the density tracers (HCN, HCO^+, and HNC) relate to star formation rate of NGC 6946?**
Previous studies showed a relationship between HCN and Σ_{SFR}. In our study, we find among our molecules the strongest correlation between HCO^+ (1−0) and Σ_{SFR}, with a Pearson's correlation coefficient of 0.95. Additionally, we identify a relationship between the correlation coefficient (ρ) and the effective critical density (n_{eff}) of the dense gas tracers. This opens up the possibility to investigate whether we observe similar trends in other extragalactic CMZs.

⋆ **In what way do density tracers (HCN, HCO^+, and HNC) and the star formation efficiency of the dense gas depend on resolved environments in the center of NGC 6946**?
The dense gas fraction fits do not follow the order of n_{eff}, instead, they show the order of $\beta_{HNC} > \beta_{HCO^+} > \beta_{HCN}$. The strongest correlation among our mean volume density versus different f_{dense} is $I_{CO(2-1)}$ versus HNC/CO (2−1) with ρ ∼0.76. We find the highest f_{dense} values in the NUC.

We find that SFE_{dense} increases with increasing gas surface density (i.e. $I_{CO\,(2-1)}$ emission) within the inner ∼ 1 kpc of NGC 6946, contrary to the opposite trends found within low-resolution observations covering the whole disk (Gallagher et al., 2018a; Jiménez-Donaire et al., 2019). The reason for this is that we are able to resolve structures within this region, such as the nuclear region (NUC; inner ∼ 0.15 kpc) where we find for the first time SFE_{dense} enhancements relative to the rest of the center, namely the SBE, and NBE. This once again demonstrates the influence of the small-scale bar and opens up avenues for studying a variety of different extragalactic CMZs to determine if we can observe similar behavior once we are able to resolve individual substructures.

⋆ **What do empirical molecular line ratio diagnostics indicate?**
We investigated ratios in the form of (i) CO (2−1)/CO (1−0) denoted as R_{21}, (ii) HNC/HCN, and (iii) ratios between HCN, HCO^+, and HNC.

We investigate R_{21} for the first time on sub-kpc scales towards a nearby double-barred galaxy center. We find R_{21} variations in the center. Essentially, we find higher R_{21} in NBE (∼0.7) than in the NUC or SBE (∼0.65 and ∼0.62). The cause of this could be more dense gas in the NBE. However, we find no increase in higher density in the NBE (compared to NUC or SBE via RADEX modeling). This ambiguous behavior remains an open question.

We speculate that the isomer ratio is not an accurate probe for kinetic temperatures for (sub-)kiloparsec sized extragalactic regions. This is because, if the prescription of Hacar et al., 2020 can be applied here, the HCN/HNC ratio results in low T_k (<50 K, for NGC 6946 as well as for six EMPIRE galaxies, IC 342 and NGC 253) which is up to a factor of 7 lower compared to other existing T_k measurements (NH_3 or H_2CO).

We find that the HCO^+/HCN ratio might not be a unique indicator to diagnose AGN activity in galaxies at (sub-)kiloparsec scales. The reason for this is that the diagnostic diagrams for the center of NGC 6946 favor a PDR, and together with EMPIRE galaxy centers, we find that those galaxies that have an active galactic nucleus (AGN) fall within the PDR range in these diagnostic diagrams. For two of these AGN galaxies, we find higher resolution observations (∼100pc for NGC 3627 and ∼166pc for M51), again erroneously suggesting a PDR.

In summary, empirical molecular line diagnostics are a useful tool, but reach their limits and/or cannot be unambiguously interpreted at (sub)kpc scales in nearby galaxies. Higher resolution

observations and/or observations of additional indicators for calibration (e.g. NH_3 observations to compare with HNC/HCN) could become of immense importance in this context.

This project serves as an interesting template for future high-resolution extragalactic central molecular zone studies (with telescopes such as ALMA, NOEMA, VLA, ngVLA). Altogether, in this study, I showed the importance of analyzing molecular lines to better understand galaxy centers and their dynamical features such as stellar bars and spiral arms, and how they regulate local gas physics.

CHAPTER 6

Kinematics of M 83's super-extended HI disk

Kinematic analysis of the super-extended HI disk of the nearby spiral galaxy M 83

C. Eibensteiner, F. Bigiel, A. K. Leroy, E. W. Koch, E. Rosolowsky, E. Schinnerer, A. Sardone, S. Meidt, W. J. G de Blok, D. Thilker, D. J. Pisano, J. Ott, A. Barnes, M. Querejeta, E. Emsellem, J. Puschnig, D. Utomo, I. Bešlic, J. den Brok, S. Faridani, S. C. O. Glover, K. Grasha, H. Hassani, J. D. Henshaw, M. J. Jiménez-Donaire, J. Kerp, D. A. Dale, J. M. D. Kruijssen, S. Laudage, P. Sanchez-Blazquez, R. Smith, S. Stuber, I. Pessa, E. J. Watkins, T. G. Williams, and B. Winkel

2023, A&A, 675, A37, 24 pp. (DOI: 10.1051/0004-6361/202245290)

Overview

In this work, we observed the nearby grand-design spiral galaxy M 83 for 40 hours using the VLA in different configurations (BnA, CnB, and, DnC) to detect the 21cm H I emission. For that, we needed to use a 10-point mosaic to fully cover M 83's H I disk. The field of view of our observations is ~1.5 deg^2, or nine times the appearance of the moon in the night sky. Our goal is to investigate M83's extended H I disk in terms of its small-scale (turbulent nature of the ISM) and large-scale (disk rotation) kinematics. The observations were carried out from 2014 to 2015 and we combined them with single dish GBT observations to account for short spacing. This project presents the combined observations allowing us for the first time to analyze H I at high resolution ($21''\approx$ 500 pc) across the entire disk of M 83.

M 83 is a nearby grand-design spiral galaxy and is known to have compared to other galaxies a very extended H I disk – we call it *super* extended H I disk (with r > 5 × r_{25}). While previous studies could identify and study the H I gas of M 83, they were limited by coarser resolution or not being able to capture the entire disk. These new VLA observations allow us to study both, the radial and environmental dependence of velocity dispersion across the whole disk of M 83, and analyze velocity fields and mass flow rate profiles which is an important ingredient to understanding how star formation is fueled across galaxies.

The following work was published in the Journal A&A in 2023. The paper Eibensteiner et al., 2023 is provided in its entirety in original form in Appendix B. I performed the reduction, imaging, feathering, and all of the analysis steps presented in the paper myself, receiving helpful advice and suggestions from a wider group of co-authors to improve certain aspects of the methodology. The

following sections provide a detailed review of the relevant scientific questions that were raised as part of the project.

6.1 Distribution of HI in M 83 – a super-extended HI disk

In this work, we observed the nearby grand-design spiral galaxy M 83 using the VLA in different configurations targeting the 21cm H I emission. We detect significant H I emission until a galactocentric radius of ∼ 50 kpc that is more than five times its optical disk radius ($r_{\mathrm{gal,H\,I}} > 5 \times r_{25}$). In Figure 6.1 we see the super extended H I disk of M 83 at 21″resolution that corresponds to 500 pc. Along with that, we see M 83's companion dwarf irregular galaxy UGCA 365. We find that H I gas is concentrated towards the central disk of M 83 which is surrounded by H I emission that follows a ring-like structure extending to a galactocentric radius of ∼ 16 kpc. The most prominent features in the outskirts of M 83 are the southern and northern spiral-like structures. Based on Figure 6.1 we defined different regions: The *central disk* where we find an averaged H I column density of 6.28×10^{20} cm^{-2}, the *ring* that surrounds the central disk, the prominent *northern arm* and *southern arm*. In the southwest, we detect significant H I emission with spots of enhanced column densities – we refer to this region as the *southern area*.

6.2 Impact of environment and dynamical features on physical parameters

M 83 has prominent environmental features that were not always detected in previous observations (see e.g. Walter et al., 2008; Bigiel et al., 2010b) or the resolution was too coarse to investigate the turbulent nature of H I across the whole disk (see e.g. Heald et al., 2016; Koribalski et al., 2018). In this work, we are able to analyze the environmental features central disk, ring, southern area, and southern and northern arm in terms of their

(i) H I surface density, Σ_{HI} in $\mathrm{M}_{\odot}\,\mathrm{pc}^{-2}$
(ii) H I velocity dispersion, σ in $\mathrm{km\,s}^{-1}$
(iii) H I line of sight velocity, V_{los} in $\mathrm{km\,s}^{-1}$
(iv) residual velocity, V_{res} in $\mathrm{km\,s}^{-1}$

We get the values for (iv) by subtracting the outputs of a tilted ring model analysis from Heald et al., 2016 from our observations (i.e. observed velocity field). The model assumes that the gas moves in circular orbits, which in turn leads to a residual velocity after subtraction – also known as non-circular motions. In Figure 6.2 we show the distributions of each quantity for each environment. We masked each individual area by eye based on the emission seen in Figure 6.1 after applying a S/N cut (S/N =3). In more detail, to create a mask for the central disk and the ring we applied a radius cut ($\mathrm{r_{gal}}$ = 8.1 kpc and $\mathrm{r_{gal}}$ = 16 kpc, respectively) in the plane of the disk. The gap between the central disk and the ring seen in the left panel of Figure 6.2 represents lines of sight that were difficult to assign to a specific region and thus were not included in a region. The two arms and the southern area were chosen by applying a cut in right ascension (R.A.) and declination.

The second column of Figure 6.2 shows the distributions for (i) Σ_{HI}, the third for (ii) σ, the fourth for (iii) V_{los} and the fifth for (iv) V_{res} . We find that Σ_{HI} and σ decrease with galactocentric radius from the central disk to the outermost outskirt region, the northern arm. For V_{los} and V_{res} we find that the

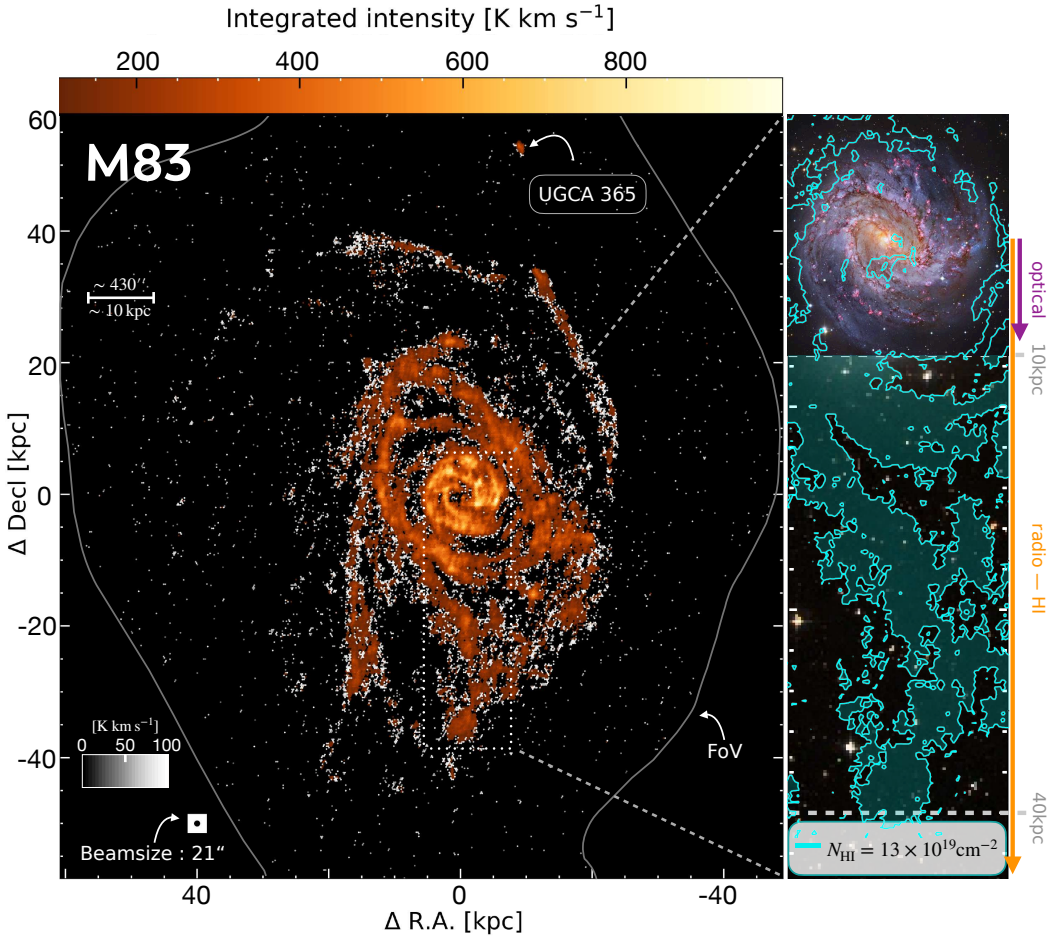

Figure 6.1: **The integrated intensity map for H I emission across the super-extended disk of M 83 at a resolution of 21″.** The field of view represents ~ 1.5 deg^2 or nine times the appearance of the moon in the night sky. The black circle in the lower left corner marks the beam size of 21″ (≈500 pc). The black to white colorbar indicates integrated intensities from 0 – 100 K km s^1 and the orange to yellow integrated intensities above 101 K km s^1. We denote the companion galaxy UGCA 365 which in projection is ~55 kpc away from the center of M 83. To the right, we show the enclosed optical disk (r_{25}~8 kpc) overlaid with H I column density contour ($N_{HI} = 13 \times 10^{19}$ cm^{-2}) extending over a radius of ~40 kpc. For visualization reasons, we show unfilled N_{HI} contours for the high resolution optical image. Beyond 10 kpc we show filled N_{HI} contours. The white line surrounding M 83 shows the field of view (FoV) (i.e. the full mosaic coverage) of the VLA observation. (optical image credits: CTIO/NOIRLab/DOE/NSF/AURA, M. Soraisam; Image processing: Travis Rector, Mahdi Zamani & Davide de Martin; low resolution background > 10 kpc: DSS2). This figure is taken from Eibensteiner et al., 2023.

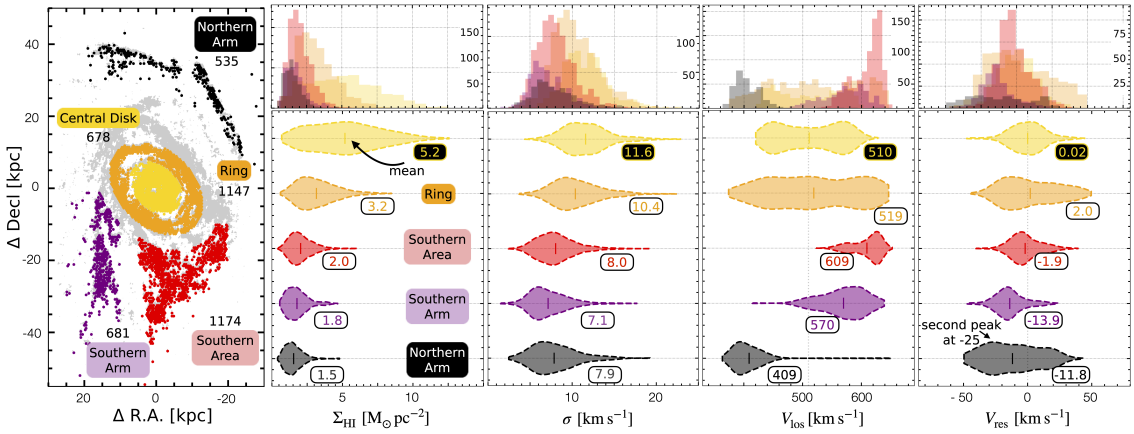

Figure 6.2: **Environmental differences in velocities, H I gas surface density and velocity dispersion in M 83.** *Mask:* Colors represent the regions: Central disk, ring, southern area, northern arm, and the southern arm. We note the total sightlines for each of the regions. The grey colors in the background show the H I column density contours ($N_{HI} = 13 \times 10^{19}$ cm^{-2}) that we show in Figure 6.1. *Violin plots:* Each violin represents the distribution of each quantity in a region defined in the mask. We set the kernel density estimation (KDE) to compute an empirical distribution of each quantity to 200 points. The columns on the x axis show from left to right the H I gas surface density Σ_{HI}, the line width σ (here, the effective line width), the observed velocities V_{los}, and the last residual velocities V_{res}. We show the mean value of the observed quantity for each violin. The long tails seen for example in the V_{los} violin for the northern arm are representing the presence of one discrepant value. This figure is taken from Eibensteiner et al., 2023

central disk and ring region can be well described by the tilted ring model as their distributions of V_{los} look very symmetric and the mean of V_{res} is close to zero. This is different for the other environmental regions. The V_{los} values of the southern area are on the receding side (i.e., > 510 km s^{-1}, marked by the gray dashed horizontal line), but only show small mean deviations to circular motions of $\langle V_{res} \rangle = -1.9$ km s^{-1}. Significant deviations from circular motions can be seen in the outermost regions, the southern and northern arms, as they show $\langle V_{res} \rangle$ values of -13.9 km s^{-1} and -11.8 km s^{-1}, but their means in V_{los} are on the receding and approaching side, respectively. The distribution of V_{res} values towards the northern arm represents a change in residual velocities along the arm. We found this "inflection point" (i.e. the location where $V_{res} \approx 0$)in observed velocities along the northern arm to be the point where the arm diverges in two different directions. We speculate that one of these directions is a 20 kpc long possible connecting branch to the dwarf galaxy UGCA 365. Its distance to us is similar to that of M 83 within the given uncertainty; 5.25±0.42 Mpc (Karachentsev et al. 2007). This connecting branch is a clear result of the dynamical interaction of M 83 with UGCA 365.

6.3 The H I velocity dispersion across the whole disk of M 83

Numerous observations have demonstrated that the H I velocity dispersion (i.e. the width of the H I emission line) contains valuable information regarding a variety of factors such as temperature, turbulence, and unresolved mass motions. As a result, it is very sensitive to feedback processes, energy, and the physical state of the gas (e.g. Tamburro et al., 2009; Ianjamasimanana et al., 2015; Mogotsi et al., 2016; Romeo and Mogotsi, 2017; Koch et al., 2018; Ianjamasimanana et al., 2015; Oh et al.,

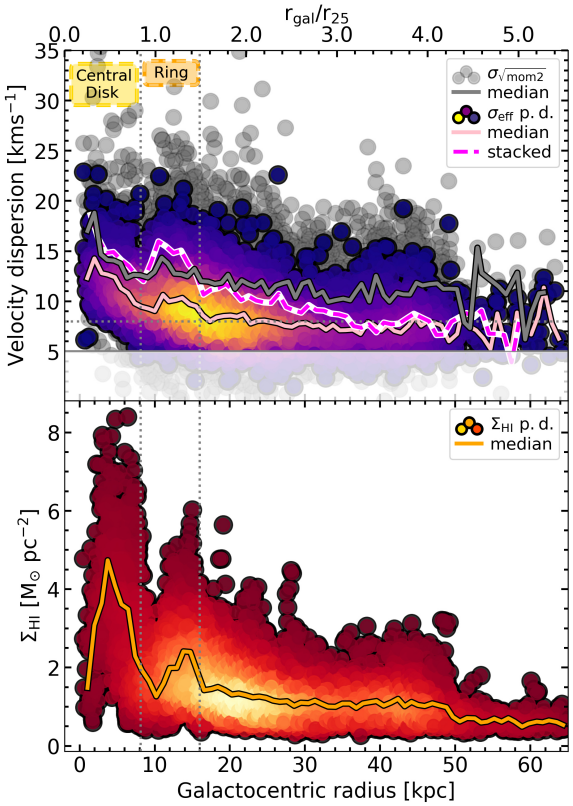

Figure 6.3: **Radial profile of the velocity dispersion, σ, and the H I gas surface density Σ_{HI}.** We also show the point density of σ and Σ_{HI} for individual lines of sight (circular points; the color coding reflects a linear density distribution, where the highest density is shown in yellow). *Top panel*: We compare here the effective width (σ_{eff} purple-to-yellow scatter points) and the square root of the moment 2 ($\sigma_{\sqrt{mom2}}$ grey points) approaches to estimate the velocity dispersion across the whole disk of M 83. We show the median for $\sigma_{\sqrt{mom2}}$ (grey solid line), the median for σ_{eff} (pink solid line), and the results after stacking σ_{eff} (pink-white dashed line). We see in all three cases enhanced velocity dispersion in the central disk and in the ring (indicated by the dashed vertical lines at 8.1 kpc and 16 kpc). The horizontal dashed line indicates the 8 km s^{-1} . *Bottom panel:* The profile of the H I gas surface density shows an enhancement of H I gas in the ring. This is similar to the velocity dispersion profiles. This figure is taken from Eibensteiner et al., 2023

2022). As part of this work, we analyzed and compared different methods of deriving the H I velocity dispersion, namely,

(a) the effective width, σ_{eff}, usually used to study cooling and the physics of the ISM
(b) the square root of the moment 2, $\sigma_{\sqrt{mom2}}$, usually used for studies dealing with dynamics and large-scale evolution,

where (a) is less sensitive to noise, but will mischaracterize line profiles that significantly deviate from a single Gaussian, on the other hand (b) is more sensitive to noise but has been found to over-estimate line widths (e.g. Mogotsi et al., 2016; Koch et al., 2018). In Figure 6.3 we show the H I velocity dispersion across the whole disk of M 83 indicated by three different radial profiles: the median of $\sigma_{\sqrt{mom2}}$, and the median and stacked values of σ_{eff}. Regarding the environments towards M 83, we find that all three profiles show, in addition to the center, enhanced velocity dispersion in the ring; an indicator that the atomic gas in the ring region seems to be more turbulent than in the outer regions. The same behavior arises in the Σ_{HI} radial profile shown in the bottom panel.

From a methodological point of view, we find that the profile for $\sigma_{\sqrt{mom2}}$ shows higher line width values than the one for σ_{eff}. The stacked profile of σ_{eff} on the other hand yields an alternative behavior. We find that the stacked values are higher than the median values until a galactocentric radius of ~40 kpc and then approach the lower values of the median. Altogether, the different line width approaches show similar trends but are offset by ~3 km s^{-1} between σ_{eff} and $\sigma_{\sqrt{mom2}}$, and 2 km s^{-1} between σ_{eff} and stacked σ_{eff} (taking the mean between the differences until r_{gal} = 40 kpc).

Across the whole disk of M 83, all three profiles show line widths greater than ~ 8 km s^{-1} (marked as the horizontal dashed line in Figure 6.3) over a super large galactocentric radius range until $r_{\rm gal} \sim 50$ kpc. In general, the bulk of the gas in the outskirts of galaxies is expected to be in the form of the warm neutral medium (WNM). According to Wolfire et al., 2003, the WNM is not expected to have a thermal velocity dispersion larger than 8 km s^{-1}. This is because the WNM temperature does not drop below 6000−7000 K which corresponds to a line width of ∼8 km s^{-1}. That said, it means that we observe velocity dispersions slightly larger than thermal until $r_{\rm gal} \sim 50$ kpc. We need to be careful in interpreting the exact values of the velocity dispersion presented in Figure 6.3. The caution arises from the presence of multiple peaks in individual spectra, particularly in the central disk. Therefore, it may not be entirely appropriate to relate these values exclusively to a thermal linewidth. Nevertheless, it shows to a first order that linewidths are larger than thermal across the super-extended H I disk of M 83.

In this work, we have investigated whether there is evidence for an increase in velocity dispersion associated with ongoing star formation, as we would expect if turbulent motions were driven by feedback. M 83 has an extended UV (XUV) disk (Thilker et al. 2005) and we compare our velocity dispersion map and FUV emission from Bigiel et al., 2010b as an indicator of star formation. We find towards sub-regions in the ring at the location with the highest FUV emission the lowest H I velocity dispersion. In a model combining both star formation feedback and radial transport, Krumholz et al., 2018 have shown that turbulence in galaxy disks can be driven by star formation feedback, radial transport, or a combination of both. Thus, the increased velocity dispersion we found in some regions in M 83 cannot be explained by star formation (because we found no one-to-one correspondence between recent star formation and increased velocity dispersion), suggesting that radial transport may be the cause.

6.4 Mass flow rates in M 83 and their sensitivity of initial kinematic parameters

Mass flows - inflow and outflow - play a crucial role in the galaxy evolution processes. They supply galaxies with fresh, new star-forming material. As part of this work, we investigate common techniques used in the literature (e.g. Di Teodoro and Peek, 2021) to estimate average radial mass flow rates for M 83. We derive them as,

$$\frac{\dot{M}_{\rm HI}(r)}{[\mathrm{M}_\odot\ \mathrm{yr}^{-1}]} = \frac{2\pi\, r}{[\mathrm{pc}]} \frac{\Sigma_{\rm HI}(r)}{[\mathrm{M}_\odot\ \mathrm{pc}^{-2}]} \frac{V_{\rm rad}(r)}{[\mathrm{pc\ yr}^{-1}]}, \tag{6.1}$$

where we use the radial velocity profile $V_{\rm rad}(r)$ and H I surface density profile $\Sigma_{\rm HI}(r)$ to obtain H I mass flow rate profiles. To get radial velocities, $V_{\rm rad}$, we use Equation 3.16. We find within

- the central disk: (i) at radii ∼2 kpc evidence of outflowing-material with mass flow rates of ∼1 M$_\odot$ yr^{-1} and (ii) at r∼5.5 kpc inflowing-material of ∼2 M$_\odot$ yr^{-1},
- towards the ring: (iii) out-flowing material of order ∼10 M$_\odot$ yr^{-1} at radii of r∼14 kpc.

The found mass flow rates toward the central disk are in agreement with previous studies. Essentially, observations using MUSE found indications of an ionized outflow (at the same location as (i) Della Bruna et al., 2022). At larger radii studies of CO (2−1) and the Hα line found streaming motions

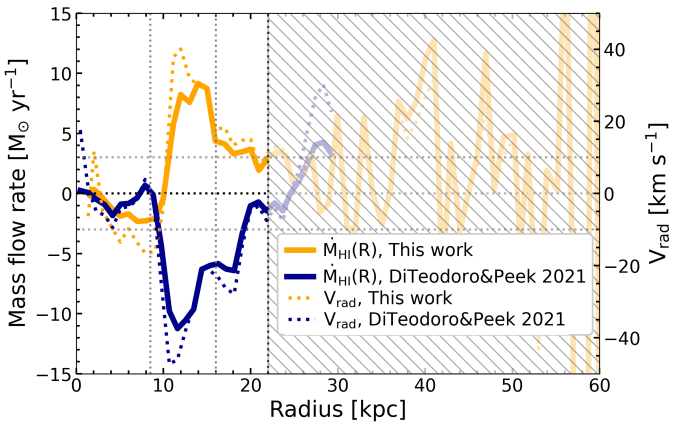

Figure 6.4: **Mass flow rates across the disk of M 83.** We show the mass flow rate of this work (orange) and the mass flow rate using different initial parameters (blue). The dashed lines show $V_{\rm rad}$. Negative (positive) values mean inflow (outflow). Within the ring region, we find the opposite trend of mass flow rates. This figure is taken from Eibensteiner et al., 2023

along the optical spiral arm (at the same location as (ii); Lundgren et al., 2004; Fathi et al., 2008). We find no correspondence in the literature for the possible out-flowing material in the ring region (iii).

We compare our mass flow rate profile with another set of kinematic parameters of M 83 from a tilted ring model by Di Teodoro and Peek, 2021 in Figure 6.4. We fit them with the same procedure as we did with the kinematic parameters from Heald et al., 2016 and calculate the mass flow rate using Equation 6.1. The two profiles in Figure 6.4 are drastically different. In the ring region, they even indicate the opposite trend – in-flowing material. Di Teodoro and Peek, 2021 found a lower inclination of $i = 40$ deg compared to our used $i = 48$ deg. These differences lead to a flip in the inferred flow direction; from outflow to inflow. This demonstrates how challenging it is to unambiguously determine inflow/outflow rates. Even at inclinations far from face-on, the chosen inclination can have a large impact on the inferred mass flow rate. Mass flow rates are sensitive to the inclination and position angle, to the extent that inflows can even flip sign. However, relying solely on the "circular motion + axisymmetric radial motion" model may not guarantee an accurate estimation of the true inflow rate if the $V_{\rm rot}$ + $V_{\rm rad}$ model is not precise. That is why the values mentioned above should be considered with caution, though we point out that they do represent our best guess at the H I mass flow rates and directions in M 83.

6.5 Summary and Conclusions

In this paper, we analyzed one of the largest VLA H I mosaics combined with GBT single dish data of a nearby galaxy. These observations target the super-extended H I disk of the nearby grand design galaxy M 83. As for the main scientific questions, we arrive at the following answers,

- ⋆ **How is the H I gas surface density distributed in the nearby galaxy M 83?**
  In our field of view of ∼ 1.5 deg^2 (or nine times the appearance of the moon in the night sky), we detect significant H I emission until a radius of ∼50 kpc. The most prominent features in Figure 6.1 are the northern extended arm, the southern arm, and the ring surrounding the central disk. We find an “inflection point” in observed velocities along the northern arm and speculate a possible connecting branch to the dwarf irregular galaxy UGCA 365, that deviates from the general direction of the northern arm; a clear sign of dynamical interaction between M 83 and

UGCA 365.

- ⋆ **To what extent does the H I gas surface density, velocity, and velocity dispersion depend on the environment within M 83?**
  For that, we defined environmental regions of M 83: central disk, ring, southern area, and southern and northern arm. We find that the H I gas surface density and the velocity dispersion ($\Sigma_{\rm HI}$ and σ) decrease with galactocentric radius – from the central disk to the northern arm. To analyze non-circular motions (i.e. residual velocities) we used tilted ring models and find that both the residual velocities ($V_{\rm res}$) and the line of sight velocity ($V_{\rm los}$) can be well described by this model towards the central disk and ring region, while the southern and northern arm deviate from the circular motion model.

- ⋆ **How does the velocity dispersion behave across the whole disk of M 83?**
  We examined the radial dependence of velocity dispersion across the whole disk of M 83 and found an enhanced velocity dispersion in its ring region (surrounding its optical disk). Quite surprisingly, using FUV data to trace star formation, we did not find enhanced FUV emission where the H I velocity dispersion is enhanced. The anti-correlation with star formation might actually suggest that radial transport rather than star formation could be the reason for enhanced velocity dispersions in the outskirts of M 83. Over the entire disk of M 83, up to a radius of $r_{\rm gal} \sim 50$ kpc, we find line widths larger than thermal (i.e., line widths exceeding $\sim 8\ {\rm km\,s^{-1}}$).

- ⋆ **What are the important factors that impact ring-averaged mass flow rates?**
  With a simplified method to derive average mass flow rate profiles, we find in the central disk indications for (i) outflow and (ii) inflow, and in the ring region (iii) out-flowing material. These overall agree with the literature. We then compare our mass flow profile with another set of kinematic parameters from a titled ring model (from Di Teodoro and Peek, 2021), which we use to determine a second mass flow profile. The latter looks completely different from ours, in such a way that it becomes clear that a difference of only 8° in inclination will flip the signs of flow direction. That means that the out-flowing material in the ring becomes in-flowing material. To summarize, ring-averaged mass flow rates are highly sensitive to inclination angles and therefore the values reported in the literature should be taken with caution.

To summarize, in this paper, I showed that dynamical features (such as rings and spiral arms) have a significant impact on mass flow rate profiles and radial H I velocity dispersion profiles. I showed, in particular, that mass flow rate profiles are highly sensitive to kinematic parameters, especially inclination, and thus, such rates should be interpreted with caution.

CHAPTER 7

Physical processes driving the conversion of atomic to molecular gas in nearby galaxies

MeerKAT HI observations of nearby spiral galaxies: the physical driver of $R_{\rm mol}$

C. Eibensteiner, A.K. Leroy, J. Sun, F. Bigiel, E. Schinnerer, E. Rosolowsky, D.J. Pisano, W. J. G de Blok
and the PHANGS-HI team and PHANGS & MHONGOOSE collaboration

in preparation

Overview

The two projects presented in Chapter 5 and Chapter 6 investigated the physical and chemical mechanisms of molecular and atomic gas, respectively, at the center and outskirts of nearby galaxies. The crucial element that connects these two environments in disk galaxies is dynamics. It drives mass flows from the outermost regions (atomic gas) and fuels galaxy centers (where it gets converted to molecular gas) with fresh material to form stars. In this third scientific project, we investigate where the atomic gas becomes molecular ($\Sigma_{\rm HI} \approx \Sigma_{\rm H2}$) in nearby galaxies using new high-quality observations from MeerKAT and ALMA, for H I and CO, respectively. We define the transition from atomic to molecular dominated phase similar to other studies as $R_{\rm mol} = \Sigma_{\rm H2}/\Sigma_{\rm HI} = 1$ and measure how $R_{\rm mol}$ depends on local conditions in the galaxy disks supported by multi-wavelength observations.

The following chapter consists of the current manuscript *MeerKAT HI observations of nearby spiral galaxies: the physical driver of* $R_{\rm mol}$, which is in preparation and will be submitted to A&A. Throughout the text, we indicate parts/analysis that will be included before the submission to A&A as *italic purple* text.

7.1 Introduction

Our understanding of the formation and evolution of galaxies is connected to the accretion of cold gas from the circumgalactic medium. This gas cools down and forms first atomic hydrogen (H I), and then molecular hydrogen (H_2), which eventually collapses under gravitational instability and

forms new stars. Feedback from star formation is important to consider in this aspect including photo-dissociation of H_2 into H I due to radiation emitted by young stars; the reason why H I is not only an intermediate gas phase/stage of star formation but also one of its products. All this shows that the atomic-to-molecular gas ratio (in this work we define it as $R_{\rm mol} = \Sigma_{\rm H2}/\Sigma_{\rm HI}$; i.e. molecular over atomic gas surface densities) is highly relevant to the evolution of the interstellar medium (ISM) for star formation in galaxies, from local environments in the Milky Way to distant cold gas reservoirs in high redshift systems.

Atomic gas reservoirs are massive, extended, and often surround spiral galaxies usually far beyond the inner optical disk (2-4 $\times$ r_{25} , where r_{25} is the optical radius; e.g. Wang et al. 2016 or even 5 $\times$ r_{25}; e.g. Eibensteiner et al. 2023). The majority of gas in galaxy disks is H I gas, but star formation occurs in H_2 gas. The current abundance of molecular gas in galaxies reflects a balance between cloud formation and destruction, with both large-scale dynamical processes and small-scale ISM physics playing important roles (e.g., see Dobbs et al., 2014; Sternberg et al., 2014). On large scales, both theory and observations show that the mean pressure or density of the ISM affects the molecular-to-atomic gas ratio (e.g., Elmegreen, 1989; Wong and Blitz, 2002; Blitz and Rosolowsky, 2004; Blitz and Rosolowsky, 2006; Leroy et al., 2008; Ostriker et al., 2010; Sun et al., 2020a) as do large-scale dynamical features such as spiral shocks (Dobbs et al., 2014). Locally, metallicity and gas column density combine to affect the amount of shielding H I needs for molecular gas to become dominant (Krumholz and Burkert, 2010; Wolfire et al., 2010; Sternberg et al., 2014; Schruba et al., 2018).

A few studies have been conducted in an attempt to answer the question of what influences the molecular gas fraction in the Milky Way and in nearby galaxies. Already Elmegreen (1989) suggested that the ISM midplane pressure from dynamical equilibrium models determines the balance of the molecular and atomic phases of the ISM. They find that this pressure term is tightly related to the fraction of molecular gas and thus influences the fraction of ISM in the dense star-forming phase. Follow-up studies (e.g. Wong and Blitz 2002; Blitz and Rosolowsky 2006; Leroy et al. 2008; Sun et al. 2020a) examined this and found as well a tight relationship. Similar to the work in Sun et al. (2020a), we refer to this term as the "dynamical equilibrium pressure" ($P_{\rm DE}$) throughout this work. H I represents the limiting factor in the above-mentioned analyses; in terms of resolution and sensitivity. With upcoming and improved observations, the question arises whether $R_{\rm mol}$ may be determined by other physical quantities (e.g. star formation rate surface density, metallicity, radiation field).

Many of the key required data have been assembled for a large set of galaxies in the context of the PHANGS[1] surveys (see, Leroy et al., 2021a; Leroy et al., 2021b; Emsellem et al., 2022; Sun et al., 2022) to revisit this experiment. One of the missing pieces is high-quality H I observations. In this work, we fill this gap with new high-quality H I observations towards eight nearby galaxies that are also in the PHANGS-ALMA sample supported by available comprehensive multi-wavelength data.

In this project, we analyze new H I observations taken with MeerKAT (the SKA precursor facility, Jonas and MeerKAT Team 2016) towards eight nearby galaxies and present the first comparison of new high-quality MeerKAT and ALMA observations to measure $R_{\rm mol}$. MeerKAT is the most sensitive centimeter-wavelength interferometer in the southern hemisphere. A few decades ago it was necessary to sacrifice a fraction of the bandwidth to minimize the system temperature, but today, thanks to new engineering knowledge and technologies, it is possible to develop low-noise receivers over a full octave or more of bandwidth. This is precisely the strength and special feature of MeerKAT and, together with the special design of the MeerKAT antennas, leads to low system temperatures (Lehmensiek and

[1] www.phangs.org

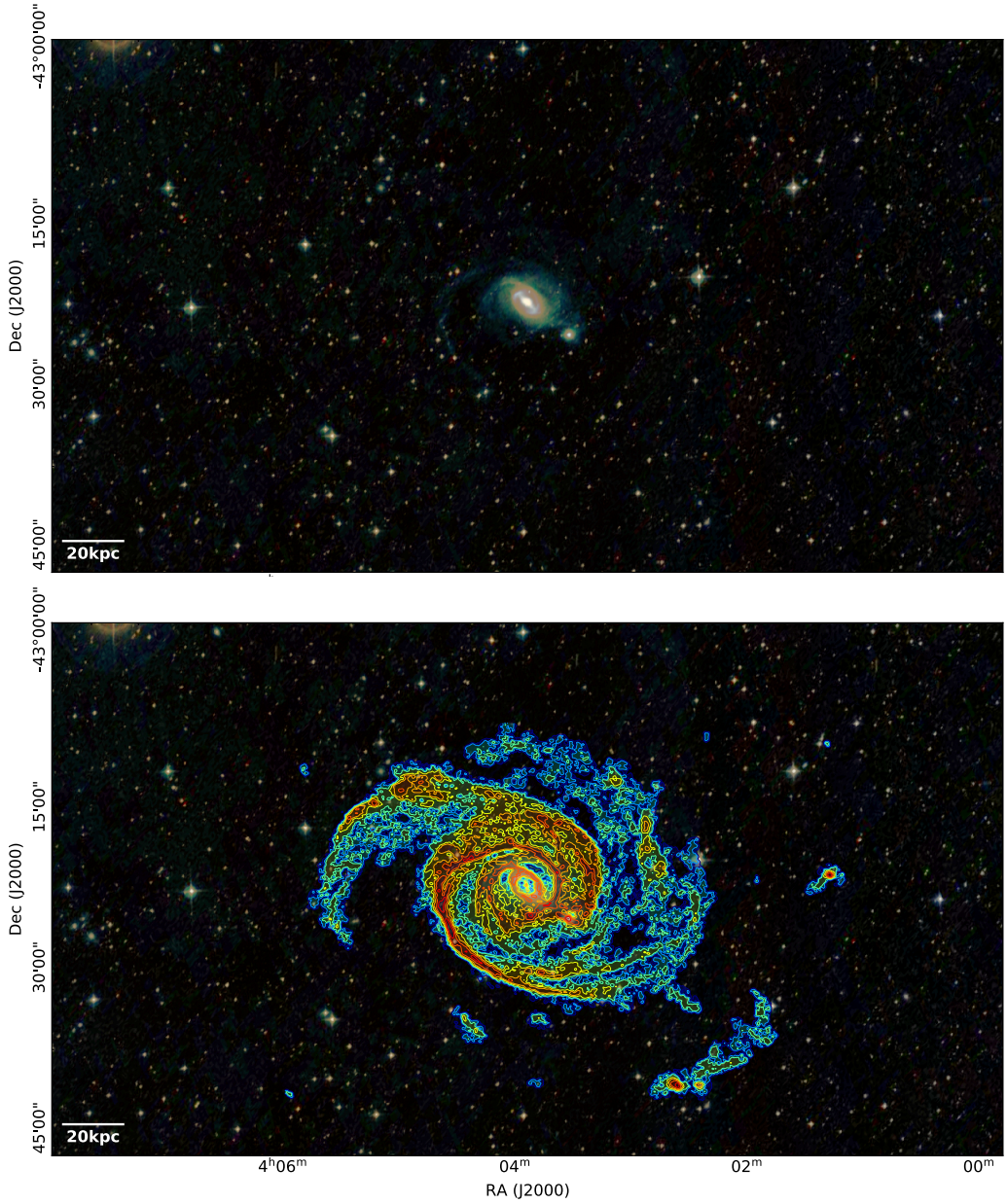

Figure 7.1: *Top*: Three color image showing NGC 1512 and NGC 1510 in the optical (image credits: DSS2). The scale bar on the lower left corner indicates 20 kpc. *Bottom*: Same as above but overlayed with contours of H I emission.

Theron, 2014). The total MeerKAT antenna gain is ~2.8 K/Jy and the system temperature is ~18 K for the L band (856–1712 MHz) which makes it ideally suited to detect low column density H I emission (see e.g. de Blok et al., 2016).

In this work, we measure how the molecular gas fraction ($R_{\rm mol}$) depends on local conditions in the galaxy disk. We conduct new measurements of $R_{\rm mol}$ for 8 MeerKAT+ALMA data sets and compare these to the total gas surface density ($\Sigma_{\rm gas}$), the star formation rate surface density ($\Sigma_{\rm SFR}$), the stellar

Table 7.1: Properties of our compiled dataset, NGC 1512, NGC 4535, and NGC 7496 (from PHANGS-MeerKAT; this work) and IC1954, NGC 1566, NGC 1672, NGC 3511, and NGC 5068 (from MHONGOOSE, de Blok et al. 2016). We provide in columns from left to right the galaxy name, morphological type (Morph.), central right ascension (RA) and declination (Dec.), distance (Dist.), effective radius ($R_{\rm eff}$), optical radius (r_{25}), inclination (i), position angle (P.A.), stellar scale length ($l_\star$), the total mass of stars ($M_\star$), and global star formation rate (SFR).

Galaxy	Morph.	RA	Dec	Dist.	$R_{\rm eff}$	r_{25}	i	P.A.	$l_\star$	$M_\star$	SFR
		[°]	[°]	[Mpc]	[kpc]		[°]	[°]	[kpc]		
	(1)	(2)	(3)	(4)	(5)	(6)	(7)	(8)	(9)	(10)	(11)
IC 1954	Sb	52.522	-52.074	12.8	2.4	5.6	57.1	63.4	1.5	9.7	-0.4
NGC 1512	SB(r)ab	60.976	- 43.349	18.8	4.8	23.1	42.5	261.9	6.2	10.7	0.1
NGC 1566	SABb	65.002	- 54.938	17.7	3.2	18.6	29.5	214.7	3.9	10.8	0.7
NGC 1672	Sb	71.427	- 59.247	19.4	3.4	17.4	42.6	134.3	5.8	10.7	0.9
NGC 3511	SABc	165.238	-22.817	13.9	3.0	12.3	75.1	256.8	2.4	10.4	0.1
NGC 4535	SAB(s)c	188.585	8.198	15.8	6.3	18.7	44.7	179.7	3.8	10.5	0.3
NGC 5068	Sc	199.728	-21.039	5.2	2.0	5.7	35.7	342.4	1.3	9.4	-0.6
NGC 7496	SBb	347.447	-43.428	18.7	3.8	9.1	35.9	193.7	1.5	10.0	0.4

Notes: (1): The morphological classifications are from HyperLEDA (Makarov et al., 2014). (2–3): Central positions are taken from Salo et al., 2015. (4): Source distances are taken from Anand et al., 2021. (5): $R_{\rm eff}$ contains half of the stellar mass of the galaxy and is taken from (Leroy et al., 2021b). (6): r_{25} is based on the radial position of the isophote at 25 mag arcsec^{-2} and is taken from (Leroy et al., 2021b). (7–8): From Lang et al., 2020, based on PHANGS CO(2–1) kinematics. (9): The stellar scale length taken from (Leroy et al., 2021b). (10–11): Derived by Leroy et al. (2021b), using *GALEX* UV and *WISE* IR photometry, following a similar methodology to Leroy et al., 2019. $M_\star$ in units of [log($M_\odot$)], and SFR in units of $M_\odot$ yr^{-1}

surface density (Σ_*), the dynamical equilibrium pressure ($P_{\rm DE}$), and metallicity (Z($r_{\rm gal}$)).

7.2 MeerKAT 21-cm maps to compare with PHANGS-ALMA CO

In this work, we analyze new H I observations taken with MeerKAT (the Square Kilometre Array (SKA) precursor facility, Jonas and MeerKAT Team 2016) towards the first eight nearby galaxies that are also in the PHANGS-ALMA sample and therefore have multi-wavelength data available. Three of the eight galaxies are from the ongoing efforts from the PHANGS collaboration to cover the PHANGS-ALMA sample with MeerKAT (cycle0 observations, described in this work). We include five more galaxies from the MeerKAT HI Observations of Nearby Galactic Objects - Observing Southern Emitters (MHONGOOSE) sample (de Blok et al. 2016).

7.2.1 New MeerKAT 21-cm observations of three galaxies

The observations were carried out using the South African MeerKAT radio telescope. The data of NGC 1512, NGC 4535, and NGC 7496 were taken between 11 April 2021 and 14 June 2021 for two times 3.5 hours for each galaxy. We chose a velocity resolution of 5.5 km s^{-1} (26.123 kHz) and a bandwidth of 856 MHz corresponding to 860 km s^{-1}, which is well suited to resolve the H I line and cover the full range of 21-cm emission from each galaxy.

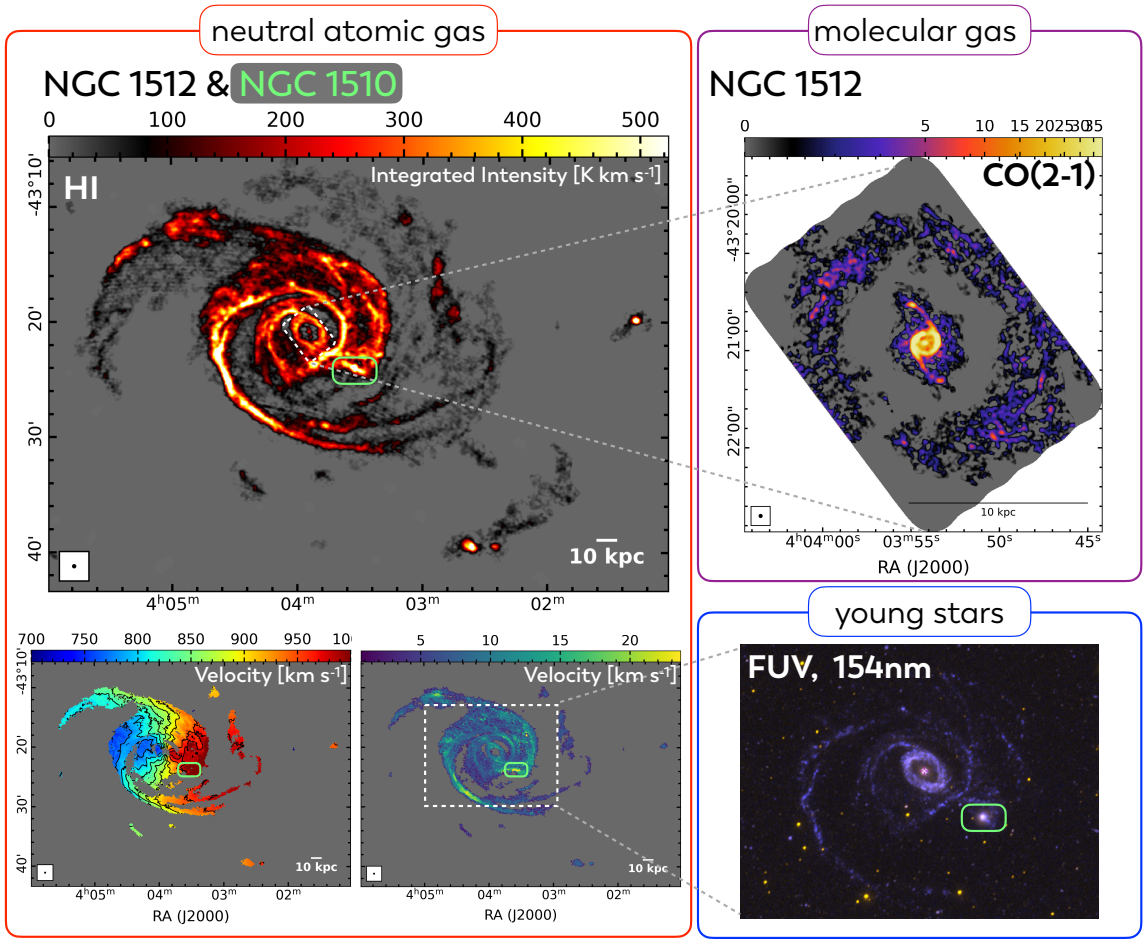

Figure 7.2: Example of a multi-wavelength view of one of our galaxies within our sample – NGC 1512. *Left in red frame:* MeerKAT H I observations showing on top the integrated intensity map in units of K km s^{-1} (moment 0) and bottom left the velocity field (moment 1) and the velocity dispersion (moment 2). *Right top in purple frame:* ALMA observations of CO(2-1) from PHANGS-ALMA (Leroy et al., 2021b) showing an integrated intensity map. *Right bottom in blue frame:* GALEX observation of FUV at 154 nm. The green rectangle shows the location of the interacting galaxy NGC 1510.

Table 7.2: Properties of our imaged dataset.

Galaxy	Beam		$\Delta v_{\rm chan}$	rms	P.c.
	[″]	[kpc]	[km s^{-1}]	[mJy/beam]	
	(1)	(2)	(3)	(4)	(5)
IC 1954	15.2	0.94	1.4	0.508	M
NGC 1512	15	1.36	5.5	0.219	P-M
NGC 1566	12.7	1.08	1.4	0.178	M
NGC 1672	15.4	1.44	1.4	0.499	M
NGC 3511	14.3	1.30	1.4	0.570	M
NGC 4535	15	1.14	5.5	0.275	P-M
NGC 5068	13.4	0.34	1.4	0.169	M
NGC 7496	15	1.35	5.5	0.200	P-M

Notes: (1–2): The size of the beam in angular and linear scales (adopting distances based on Table 7.1). (3): The channel width, i.e. spectral resolution. (4): Root mean square (rms) noise. (5): Project codes: P-M = PHANGS-MeerKAT (cycle 0 observation); *this work*. M = MHONGOOSE (de Blok et al., 2016). To be able to compare these galaxies, we sample all of them on a hexagonal sampling grid with 1.5 kpc (driven by the worst linear resolution in our sample, NGC 1672) sized apertures.

Reduction

The observations of NGC 1512, NGC 4535, and NGC 7496 were reduced using the `IDIA` calibration pipeline[2]. Briefly, the data were put through an initial flagging stage, to eliminate regions of known persistent radio frequency interferences (RFI), known bad antennas, and very liberal flagging to eliminate the strongest RFI. This was followed by an initial round of continuum calibration, followed by a second round of automated flagging to flag the fainter RFI visible after a single round of calibration. The data are then processed through one final round of continuum calibration. The calibrated target was then put through 2 rounds of phase-only self-calibration, using a pyBDSF mask to constrain the deconvolution to avoid artifacts.

Imaging

We then ran the calibrated data for the galaxies NGC 1512, NGC 4535, and NGC 7496 through a standard PHANGS product creation suite (similar to Leroy et al. 2021a; PHANGS-ALMA pipeline v3.0[3] using `CASA 5.7.0-134`), building noise cubes, strict masks at each resolution, and combined native+15″+30″+60″broad masks. The `PHANGS pipeline` essentially uses the `multiscale` clean (with scales of 0, 30, 100, and 300 ″) followed by a more closely restricted single scale clean. We set robust = 0.5 and pblimit = 0.125 during imaging.

Prior to that, we used an order 1 baseline to subtract the continuum in the uv-data, excluding the region around the spectral line in the galaxy itself. The bandpass calibration or selfcal produced some spectral curvature for some of the bright sources that could not be fitted with an order-1 uv continuum subtraction. Rather than do anything more aggressive, we blanked the images in regions where a significant continuum was detected in the line-free channels after cleaning. In other words: we picked

[2] https://idia-pipelines.github.io/docs/processMeerKAT

[3] https://github.com/akleroy/phangs_imaging_scripts

the line-free channels manually and flagged all regions where S/N > 5 in the integrated map, allowing either positive or negative signal (i.e. we flagged absorption-like features too), then we also blanked a couple of regions manually. This did not overlap the galaxy in any case. The biggest visible imaging artifacts remaining come from what looks like a bright source off to the southeast of NGC 7496 which shows some low-level artifacts. However, this is not enough to affect the overall noise, and therefore we continue.

After the galaxies NGC 1512, NGC 4535, and NGC 7496 were imaged using `CASA 5.7.0-134` with `robust`=0.5, we rounded the beam, which inflates to a bit coarser resolution but also really improves the signal-to-noise (S/N). The resulting angular resolution for the beam-rounded images is $12'' - 15.0''$. The noise is $\sim 0.7 - 0.8$ K in the central part of the primary beam for all targets at this resolution. It will be possible to make higher resolution images with adjusted weighting in the future, however, for our analysis, a resolution of $\sim 15''$ that corresponds to $\sim$1.5 kpc is sufficient.

7.2.2 Observations from MHONGOOSE

The galaxies IC1954, NGC 1566, NGC 1672, NGC 3511, and NGC 5068 are part of the MHONGOOSE sample (de Blok et al., 2016). Each galaxy was observed for 5.5 hours as part of the MHONGOOSE survey. Each of the tracks consists of 10 mins of observing time on one of the primary calibrators J1939-6342 or J0408-6545. This is then followed by five cycles of two mins on a phase calibrator and $\sim$ 55 mins on the target galaxy. We used the `c856M4k_n107M` correlator mode, allowing for a 32k-narrow-band and a 4k-wide-band to be used simultaneously. The narrow-band mode has 32768 channels of 3.265 kHz each, giving a total bandwidth of 107 MHz. The data were binned by two channels leading to a measurement set with a channel width of 6.53 kHz (1.4 km s^{-1}).

Reduction

The data were processed using the publicly available CARACal data reduction pipeline[4]. The pipeline flags calibrators for RFI, derives and applies the cross-calibration, and flags the target. This is followed by self-calibration using the continuum. After applying the self-calibration solutions, the sky model derived in these steps is subtracted from the measurement set. A second round of uv-plane continuum subtraction using the line-free channels is then used to remove any residual continuum.

Imaging

Data cubes at various resolutions and weightings were created using `wsclean`. Lower-resolution cubes were used to produce clean masks for the higher resolution cubes using the SoFiA-2 source finder. The data presented here use a robustness parameter of 0.5 and 1.5, resulting in an average beam size of $11''$ and $30''$ respectively. Moment maps were created using SoFiA-2 using the smooth+clip algorithm. We used spatial kernels at 0 and 1 times the beam size and spectral kernels of 0, 9, and 25 channels. In all cases, a source finding threshold of 4 sigma was used. A reliability value of 0.8 was used, but we found that in most cases this had little impact as the signal was well separated from the noise.

[4] https://github.com/caracal-pipeline/caracal

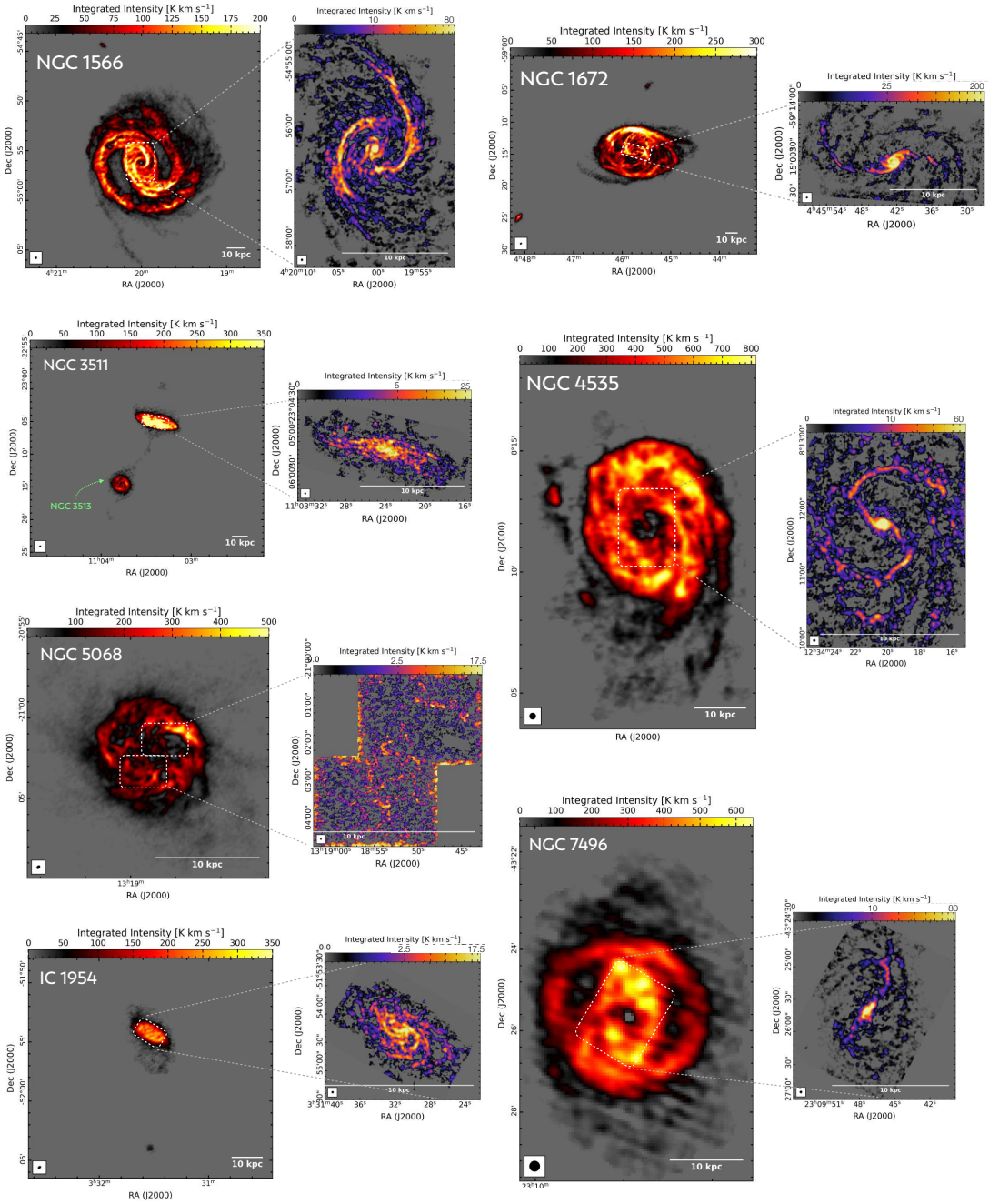

Figure 7.3: The integrated intensity maps (moment 0) for H I emission and CO(2-1) across the disks of our sample of eight (excluding NGC 1512, see Figure 7.2) nearby spiral galaxies. The corresponding beam sizes are visible in the left bottom corner of each map. The white contours on the MeerKAT H I map represents the field of view of the ALMA CO (2−1) observations, that we show to the right side of each galaxy.

7.3 Derivation of physical quantities

Our goal in this work is to make new measurements of the H2-to-HI ratio, $R_{\rm mol}$, and to compare this to a series of local environmental factors that should, theoretically, have a bearing on the balance of atomic and molecular gas in each part of each galaxy. Within this work, we use a variety of different physical quantities such as the atomic gas surface density ($\Sigma_{\rm HI}$), molecular gas surface density ($\Sigma_{\rm H2}$), stellar surface density (Σ_{*}), star formation rate surface density ($\Sigma_{\rm SFR}$), dynamical equilibrium pressure ($P_{\rm DE}$), metallicity (Z'), total gas surface density ($\Sigma_{\rm gas}$), the FUV+WISE based star formation surface density as a proxy of UV radiation field emission, and, the ratio between the dynamical equilibrium pressure and the UV radiation field ($P_{\rm DE}$ / $\Sigma_{\rm SFR}$) as a proxy for G_0/n.

We extract measurements in a set of 1.5 kpc hexagonal apertures[5] that completely tile the sky footprint of each galaxy. This is the same sampling scheme used in Sun et al. 2022 and allows us to leverage a rich set of existing measurements made available by that work (see, for example, Figure 7.4). Below we briefly describe how we derive various physical properties. We refer interested readers to Sun et al. 2022 for more information.

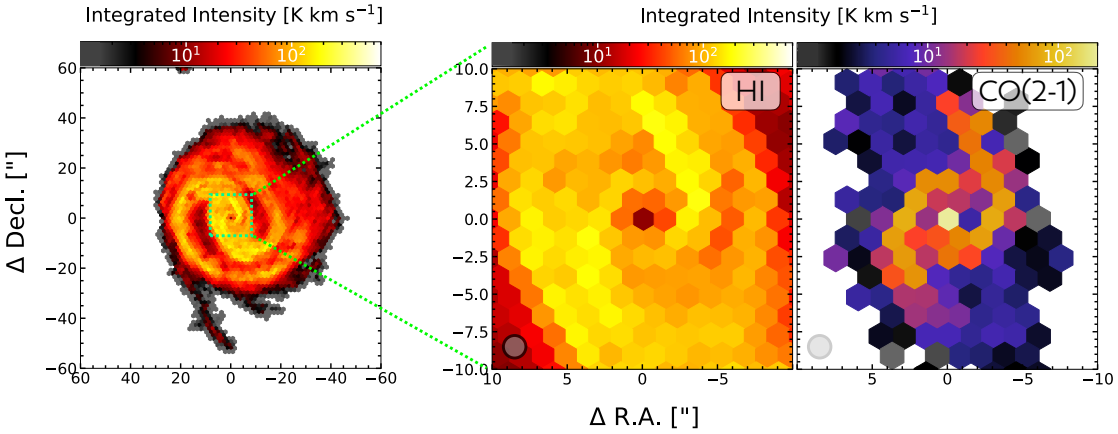

Figure 7.4: Integrated intensity maps after hexagonal sampling. The left plot shows the overall H I disk of NGC 1566. The right two panels show the enlarged versions of the green rectangle at matched field of view. We show here hexagonal apertures (1.5 kpc in size) of H I and CO(2-1) whereas the circle in the lower left corner indicates the size of the beam.

7.3.1 Atomic gas surface density

Assuming optically thin H I emission, we convert $I_{\rm HI}$ from the new MeerKAT observations and MHONGOOSE sample (see Section 7.2) to atomic gas surface density $\Sigma_{\rm HI}$ via,

$$\Sigma_{\rm HI}\ [{\rm M}_\odot\ {\rm pc}^{-2}] = 2.0 \times 10^{-2}\ I_{\rm HI}\ [{\rm K\ km\ s}^{-1}]\ \cos(i)\ . \tag{7.1}$$

Here $\Sigma_{\rm HI}$ includes the (extra 35%) mass of helium and heavier elements. The cos (i) term accounts for galaxy inclination taken from Table 7.1. In the future, these new maps will yield additional constraints on the inclination and the PA angle (for example, Laudage, in prep. for NGC 1512, NGC 4535, and NGC 7496).

[5] We chose 1.5 kpc sized hexagonal apertures because 1.5 kpc represent one linear resolution element of our H I observations.

7.3.2 Molecular gas surface density

We estimate the molecular gas mass surface density, Σ_{H2}, from the CO integrated intensity taken from the PHANGS-ALMA survey (Leroy et al., 2021b) via,

$$\Sigma_{H2}\ [\mathrm{M_\odot\ pc^{-2}}] = \alpha_{CO(1\text{–}0)}\ R_{21}^{-1}\ I_{CO}\ [\mathrm{K\ km\ s^{-1}}]\ \cos(i)\ . \tag{7.2}$$

For the CO line ratio (R_{21}) and CO (1–0)-to-H_2 conversion factor ($\alpha_{CO(1\text{–}0)}$) we adopted $R_{21} = 0.65$ from (den Brok et al., 2021; Leroy et al., 2022) and use a metallicity-dependent α_{CO} prescription as described in Sun et al. (2020b) as $\alpha_{CO(1\text{–}0)} = 4.35\ Z'^{-1.6}\ \mathrm{M_\odot\ (K\ km\ s^{-1}\ pc^2)^{-1}}$, where Z' is the inferred local gas phase abundance normalized to the solar value (see Subsection 7.3.8). Again, Σ_{H2} includes the (extra 35%) mass of helium and heavier elements. The same cos (i) inclination correction from Equation 7.2 also applies here.

7.3.3 Total gas surface density and molecular gas fraction

We estimate the total gas surface density, Σ_{gas} from the sum of Equation 7.1 and Equation 7.2 as,

$$\Sigma_{gas}\ [\mathrm{M_\odot\ pc^{-2}}] = \Sigma_{HI} + \Sigma_{H_2}. \tag{7.3}$$

We estimate the molecular gas fraction, R_{mol} = H_2-to-H I , by taking the ratio as,

$$R_{mol} = \frac{\Sigma_{H2}\ [\mathrm{M_\odot\ pc^{-2}}]}{\Sigma_{HI}\ [\mathrm{M_\odot\ pc^{-2}}]} \tag{7.4}$$

For this work, the molecular gas fraction is only measured where we detect both, Σ_{H2} and Σ_{HI}. In a forthcoming paper, we will include upper limits in H I and plan to include stacking techniques that will recover fainter CO and H I emissions.

7.3.4 Star formation rate surface density

We make use of star formation rate (SFR) surface density Σ_{SFR} maps from the z0mgs survey (Leroy et al. 2019). They estimated the SFR surface density by using a combination of ultraviolet (UV) observations from the Galaxy Evolution Explorer (GALEX; Martin et al. 2005) and mid-infrared (mid-IR) observations from the Wide-field Infrared Survey Explorer (WISE; Wright et al. 2010). For all galaxies we use the SFR maps with the combination FUV 154 nm (GALEX) + mid-IR 22 μm (WISE4) that were calculated as follows,

$$\begin{aligned}\Sigma_{SFR}\ [\mathrm{M_\odot\ yr^{-1}\ kpc^{-2}}] = \Big(&8.9\times10^{-2}\ I_{154\,nm}\ [\mathrm{MJy\ sr^{-1}}] \\ &+3.0\times10^{-3}\ I_{22\,\mu m}\ [\mathrm{MJy\ sr^{-1}}]\Big)\cos i\ .\end{aligned} \tag{7.5}$$

The calibration assumes a Chabrier IMF (Chabrier, 2003) via its anchoring to the models by Bruzual and Charlot, 2003 of integrated galaxies by Salim et al., 2016; Salim et al., 2018. *In an updated future version of this manuscript we will use new calibration methods (see Belfiore et al., 2023) and we will also include Hα based star formation rate surface density measurements using the PHANGS-MUSE dataset (see Emsellem et al., 2022).*

7.3.5 Stellar surface density

We use the stellar mass surface density Σ_* maps computed with the technique utilized for sources in the PHANGS-ALMA survey (Leroy et al., 2021b). The Σ_* estimate is based on near-infrared emission observations at 3.6 μm (IRAC1 on Spitzer, from the S^{4}G survey; Sheth et al. 2010) or 3.4 μm (WISE1, from the z0MGS project; Leroy et al. 2019). The final stellar mass is then derived from the NIR emission using a mass-to-light ratio, $\Upsilon_{3.4\,\mu m}$, that depends on the regional specific star formation rate SFR/$M_\star$,

$$\Sigma_*[\mathrm{M}_\odot\ \mathrm{pc}^{-2}] = 350 \left(\frac{\Upsilon_{3.4\,\mu m}}{0.5}\right) I_{3.6\,\mu\mathrm{m}}\ [\mathrm{MJy\ sr}^{-1}]\ \cos(i)\ . \tag{7.6}$$

7.3.6 Dynamical equilibrium pressure

In general, the dynamical equilibrium pressure is an approximation of the pressure in the ISM, which arises primarily from the gravity of the gas (atomic and molecular) and stars. We derive the kpc-scale dynamical equilibrium pressure, P_{DE}, in the same way as in Sun et al. 2020a that are based and build on works from Spitzer, 1942; Elmegreen, 1989; Wong and Blitz, 2002; Blitz and Rosolowsky, 2004; Blitz and Rosolowsky, 2006; Leroy et al., 2008; Ostriker et al., 2010; Kim et al., 2011; Kim et al., 2013. We calculate P_{DE} under the assumptions that (i) the distribution of gas and stars in a galaxy disk are treated as isothermal fluids in a plane-parallel geometry, (ii) the (single component) gas disk scale height is much smaller than the stellar disk scale height, (iii) gravity due to dark matter can be neglected since it represents only a minor component in the inner disk (the relevant region where we can calculate P_{DE}) of massive galaxies. P_{DE} can then be expressed as the sum of the weight of the ISM due to the self-gravity (see e.g. Spitzer, 1942; Elmegreen, 1989) and the weight of the ISM due to stellar gravity (see e.g. Spitzer, 1942; Blitz and Rosolowsky, 2004):

$$P_{\mathrm{DE}}\ [\mathrm{K\,cm}^{-3}] = \left(\frac{\pi\, G}{2}\Sigma_{\mathrm{gas}}^2 + \Sigma_{\mathrm{gas}}\sqrt{2G\rho_*}\sigma_{\mathrm{gas,z}}\right)/k_{\mathrm{B}}\ . \tag{7.7}$$

Here, Σ_{gas} it the total gas surface density (see Subsection 7.3.3). ρ_* is the stellar mass volume density near the disk midplane that we can describe as,

$$\rho_* = \frac{\Sigma_*}{0.54\ R_*}. \tag{7.8}$$

This is under the assumption of an isothermal density profile along the vertical direction and a fixed stellar disk flattening ratio $\mathrm{R_*/H_*} = 7.3$, where $\mathrm{R_*}$ is the radial scale length of the stellar disk and $\mathrm{H_*}$ its height. We take $\mathrm{R_*}$ for each galaxy in our sample from Leroy et al., 2021b. Sun et al., 2020a compared this way of calculating ρ_* with a flared disk geometry and found that this scenario gives lower P_{DE} values. In Equation 7.7, $\sigma_{\mathrm{gas,z}}$ is the mass-weighted average velocity dispersion of the molecular and atomic phase (see equation 14 in Sun et al. 2020a). Following Sun et al., 2020a we adopt a fixed σ_{atom} of 10 km s^{-1} and set $\sigma_{\mathrm{mol}} = \sigma_{\mathrm{atom}}$ (taken from Leroy et al. 2008). According to Sun et al., 2020a the assumption of a fixed σ_{atom} leads to generally higher P_{DE}. For both, ρ_* and σ_{atom} the resulting deviation lies within 0.2 dex. These are minor differences and therefore should not have too much of an impact, which is why in this work we (i) take a fixed stellar disk flattening ratio, and (ii) fix σ_{atom}.

7.3.7 Proxy for UV radiation field and G_0/n

We use the star formation rate surface density, $\Sigma_{\rm SFR}$ as a proxy of the UV radiation field emission as in the inner disk (where we detect both, $\Sigma_{\rm H2}$ and $\Sigma_{\rm HI}$) most of the radiation field is captured by the dust-reradiated emission. As we pointed out previously, including stacking techniques that will recover fainter CO and H I emission is planned for a future paper[6]. And we additional take another proxy,

$$\Sigma_{\rm SFR}\,[{\rm M_\odot\ yr^{-1}\ kpc^{-2}}] \propto G_0 \Longrightarrow \frac{\Sigma_{\rm SFR}\,[{\rm M_\odot\ yr^{-1}\ kpc^{-2}}]}{P_{\rm DE}\ [{\rm K\,cm^{-3}}]} \propto \frac{G_0}{n} \tag{7.9}$$

Here, G_0 is the radiation field and n is the number density in cm^{-3}.

7.3.8 Metallicity

Following Sun et al., 2022, we use in this work the scaling relations to get the general trends of metallicity variation across our sample of eight galaxies. We assume a global galaxy mass–metallicity relation (Sánchez et al., 2019) and a fixed radial metallicity gradient within each galaxy (Sánchez et al., 2014), that gives,

$$\log_{10}Z'(r_{\rm gal}) = \log_{10}Z'(r_{\rm e}) - 0.1\frac{r_{\rm gal}}{r_{\rm e}}\,, \tag{7.10}$$

with,

$$\log_{10}Z'(r_{\rm e}) = 0.04 + 0.01\left(\log_{10}\frac{M_\star}{M_\odot} - 11.5\right)\exp\left(-\log_{10}\frac{M_\star}{M_\odot} + 11.5\right)\,. \tag{7.11}$$

$Z'(r_{\rm e})$ is the local gas-phase abundance at $r_{\rm gal} = r_{\rm e}$ normalized by the solar value [12 + log (O/H) = 8.69] and $Z'(r_{\rm gal})$ is the normalized abundance at arbitrary $r_{\rm gal}$. $M_\star$ is the galaxy's global stellar mass under the assumption of a Chabrier IMF (Chabrier, 2003). Note that these scaling relations are appropriate for abundance measurements adopting the O3N2 calibration in Pettini and Pagel (2004). For more details see the Appendix in Sun et al., 2022. *In an updated future version of this manuscript we will also include metallicity measurements of individual HII regions for the galaxies that are in the PHANGS-MUSE sample (see Emsellem et al., 2022; Groves et al., 2023). These are NGC 1512, NGC 1566, NGC 1672, NGC 5068 and NGC 7496.*

7.4 The sample

In this work we use a compiled dataset that contains new observations from the MeerKAT telescope targeting the galaxies NGC 1512, NGC 4535, and NGC 7496 from the first results of the PHANGS-MeerKAT survey and together with the galaxies IC1954, NGC 1566, NGC 1672, NGC 3511, and NGC 5068 from the MHONGOOSE survey (de Blok et al. 2016) form a sample of nine nearby (D = 5.2 − 19.4 Mpc) spiral galaxies (see Table 7.1). These nine galaxies are part of the PHANGS-ALMA survey (Leroy et al., 2021b) and have archival multi-wavelength observations available. In the following, we shortly describe each galaxy shown in Figure 7.3 and give a brief literature overview.

- **IC 1954**: From the H I map we see strong H I emission (> 250 K km s^1) that extends ~5 kpc in radius and surrounded by fainter emission (~50 K km s^1). The CO map reveals some spiral

[6] Here, we could use the integrated intensity of the FUV emission, $I_{\rm FUV}$ as a proxy of the UV radiation field emission as these are very sensitive for outer disk studies with the combination of lower extinction.

arm-like structures. Apart from the properties mentioned in Table 7.1, relatively little is known about the H I content of this galaxy.

- **NGC 1512**: We highlight the barred, double-ring galaxy NGC 1512 in Figure 7.2. Its H I distribution reflects the ring like structuring of the gas, which can also be seen in the CO map. More astonishing, however, are the two gigantic (more than 160 kpc in length[7]) spiral arms and the prominent disturbances of the H I emission in the southern part of the inner 20 kpc caused by the interacting low-mass dwarf companion NGC 1510. The southern arm is at larger galactic radii somehow split into three sub-arms. The northern arm, on the other hand, is clumpier in structure and seems to follow only in one direction (i.e. no splitting into sub-arms). The distribution of the H I gas and kinematics of this system has also been studied by Koribalski and López-Sánchez, 2009 using the Australia Telescope Compact Array (ATCA). However, our map shows much more details due to the higher resolution of the MeerKAT observations (our $15''$ compared to a synthesized beam size of $\approx 88''$ from ATCA). In addition to the splitting of the southern arm, our map shows in the south and east additional clumps of H I emission. These were characterized as tidal dwarf galaxies (TDG) by Koribalski and López-Sánchez, 2009 who named them simply NGC 1512-south and NGC 1512-west, both showing clear signs of star formation. In our H I map, however, NGC 1512-south is showing two separate emission clumps. Following the nomenclature we name them NGC 1512-south-a and NGC 1512-south-b. Within the PHANGS collaboration a detailed kinematic study of this H I disk together with the ones from NGC 4535 and NGC 7496 (marked as P-M in Table 7.2) are underway (Laudage et al. 2023, in prep.).

- **NGC 1566**: In H I two remarkably prominent spiral arm-like features are visible with corresponding "inter-arm" regions. Both of these arms are winding clockwise, somehow forming a natural extension to the arms seen in CO. There is a beam-sized H I hole in the center, where the gas becomes mostly molecular. NGC 1566, also known as the "Spanish Dancer", is an active galaxy classified as Seyfert 1 (Combes et al., 2014). Within the MHONGOOSE collaboration a detailed study of this H I disk is under way (Maccagni et al. 2023, in prep.).

- **NGC 1672**: From the H I map it is hard to identify clear arm-like features. The H I gas seems to be more randomly distributed, however, we find higher integrated intensities along the northern edge of the H I disk. Also, regions within the field of view of the CO observations show higher integrated intensities (i.e. > 300 K km s^{-1}) at two regions that seem to be the intersections between a bar and the beginning of two spiral arm-like features – the bar ends. NGC 1672 is known to have a strong bar with $2.4'$ in length, which corresponds to 13.5 kpc at a distance of 19.4 Mpc. These bar ends are only faintly detected in CO. High-resolution optical imaging data from the Hubble Space Telescope (HST) reveal four spiral arms with many HII regions and vigorous star formation along them (e.g. Jenkins et al. 2011; Barnes et al. 2022)

- **NGC 3511**: The H I map shows no clear signs of spiral arm-like features. In CO, two very diffuse, thick, and patchy spiral arms are apparent. The galaxy NGC 3513 is about 10 arcminutes away from NGC 3511. A filamentary structure with low integrated intensity between both galaxies speculatively seems to connect them. Both galaxies have similar distance estimates of 14.19 Mpc (taken from the MHONGOOSE sample table).

[7] We roughly measure the length of a spiral arm as $30'$ long which translates at NGC 1512's distance of 18.8 Mpc to ~160 kpc.

- **NGC 4535**: The H I map reveals a compact emission forming a disk of ~20 kpc in radii. In the outskirts, two spiral arm-like structures are present which are forming (similar to the ones in NGC 1566, but not as prominent) a natural extension to the ones seen in CO.

- **NGC 5068**: The H I disk of NGC 5068 has a diameter of ~10 kpc and shows no clear sign of spiral arm-like structures. NGC 5068 is classified as Sc, is the closest galaxy with a distance of ~5.2 Mpc, and has the lowest total molecular gas mass and the lowest star formation rate in our sample (see Table 7.1). Apart from the properties mentioned in this table, relatively little is known about this galaxy. Within the MHONGOOSE collaboration a detailed study of this H I disk is under way (Healy et al. 2023, in prep.).

- **NGC 7496**: NGC 7496's appearence in H I is somewhat different compared to the other galaxies. Its H I map reveals an inner compact disk that is surrounded by a symmetric ring-like structure that could be the extensions of the inner two spiral arms. These spiral arm like features are best visible in the CO map.

7.5 Results

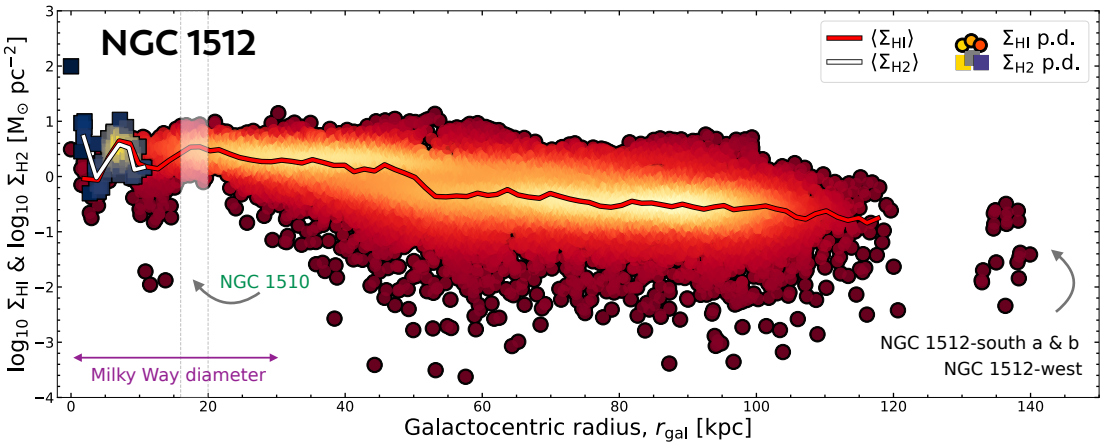

Figure 7.5: Radial extent of H I and CO in NGC 1512. We compare here the radial extent of the CO emission with the H I emission. The scatter points show each individual sight line, i.e. aperture of 1.5 kpc. The red-to-yellow color scale shows the point density of $\Sigma_{\rm HI}$ and the dark-blue to yellow shows the point density of $\Sigma_{\rm H2}$. We see that H I extends until $r_{\rm gal}$ ~ 120 kpc (that is $5 \times r_{25}$ or 4 times the diameter of the Milky Way, indicated as a purple arrow). We indicate the approximate $r_{\rm gal}$ range where NGC 1510 sits. The clumps NGC 1512-south-a, NGC 1512-south-b, and NGC 1512-west are ~ 140 kpc from the center of NGC 1512.

In this section we present the results from the MeerKAT and ALMA observations of eight nearby galaxies (from the PHANGS and MHONGOOSE collaborations). Figure 7.2 and Figure 7.3 show the H I and CO moment maps of our sample. In this section, we describe the radial extent of H I and CO emission (see Figure 7.5 - Figure 7.7 and Figure 7.8). Using ancillary data (described in Section 7.3) we analyze $R_{\rm mol}$ scaling relations (see Figure 7.9).

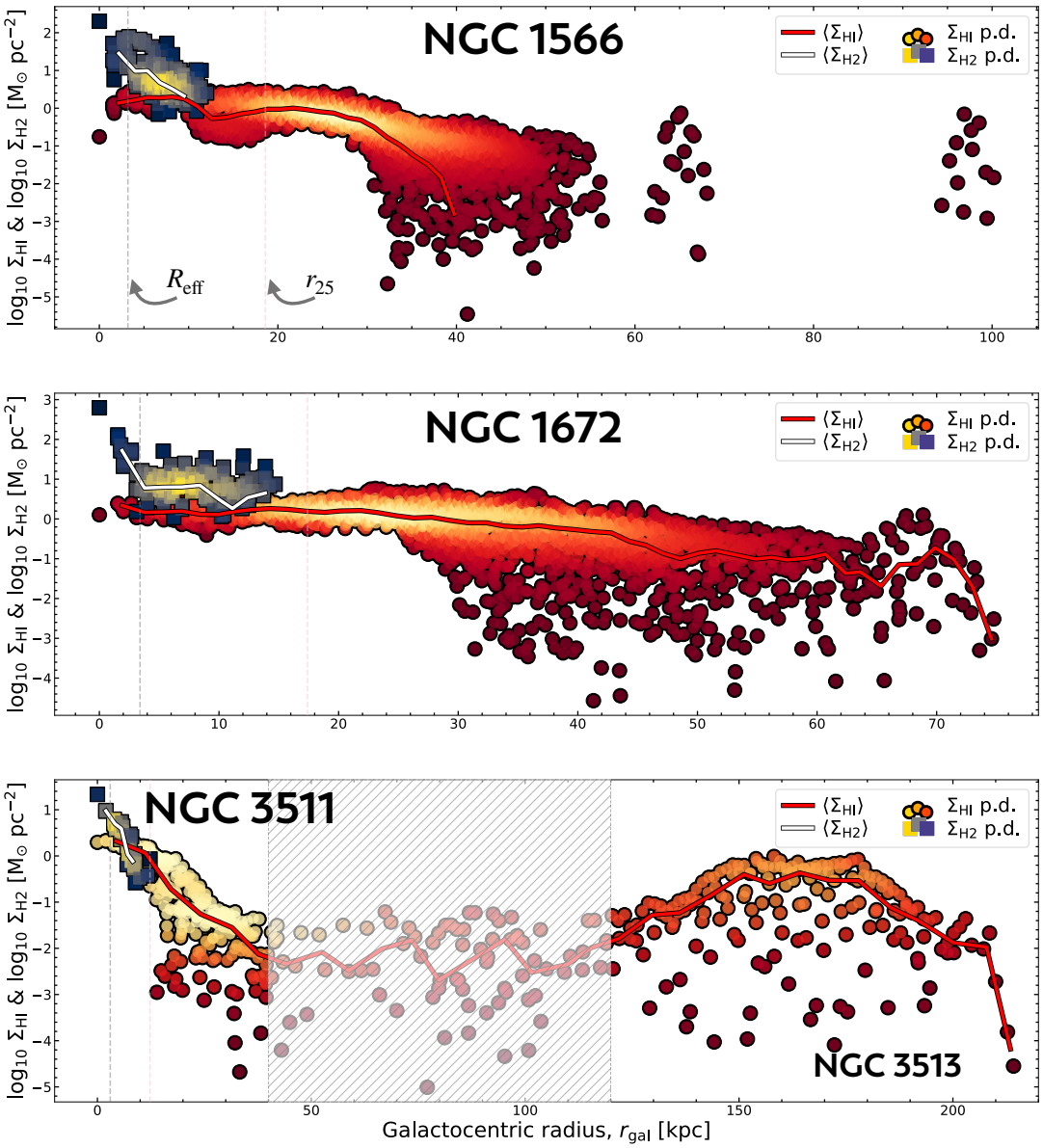

Figure 7.6: Radial extent of H I and CO in NGC 1566, NGC 1672 and NGC 3511. Here we indicate additionally $R_{\rm eff}$ and r_{25} as grey and pink vertical dashed lines, respectively (taken from Table 7.1). *Top:* We note here two additional clumps outside of NGC 1566's main H I disk. *Middle:* Toward NGC 1672 we see an increase of H I emission at $r_{\rm gal} \sim 70$ kpc, that is the region of an additional H I clump in the south-east to NGC 1672 (see also Figure 7.3). *Bottom:* The hatched region from $r_{\rm gal}$= 40-120 kpc indicates the region of the filament structure, that can be seen in the moment map, which gives the impression of connecting NGC 3511 and NGC 3513.

7.5.1 Radial extent of atomic and molecular gas

In Figure 7.5, Figure 7.6 and Figure 7.7 we show the radial extent of $\Sigma_{\rm HI}$ and $\Sigma_{\rm H2}$ together with their point densities. We are binning $\Sigma_{\rm HI}$ and $\Sigma_{\rm H2}$ in galactocentric bins of 1.5 kpc width (the size of our hexagonal apertures). The white and red lines thus represent the average within a given bin defined by

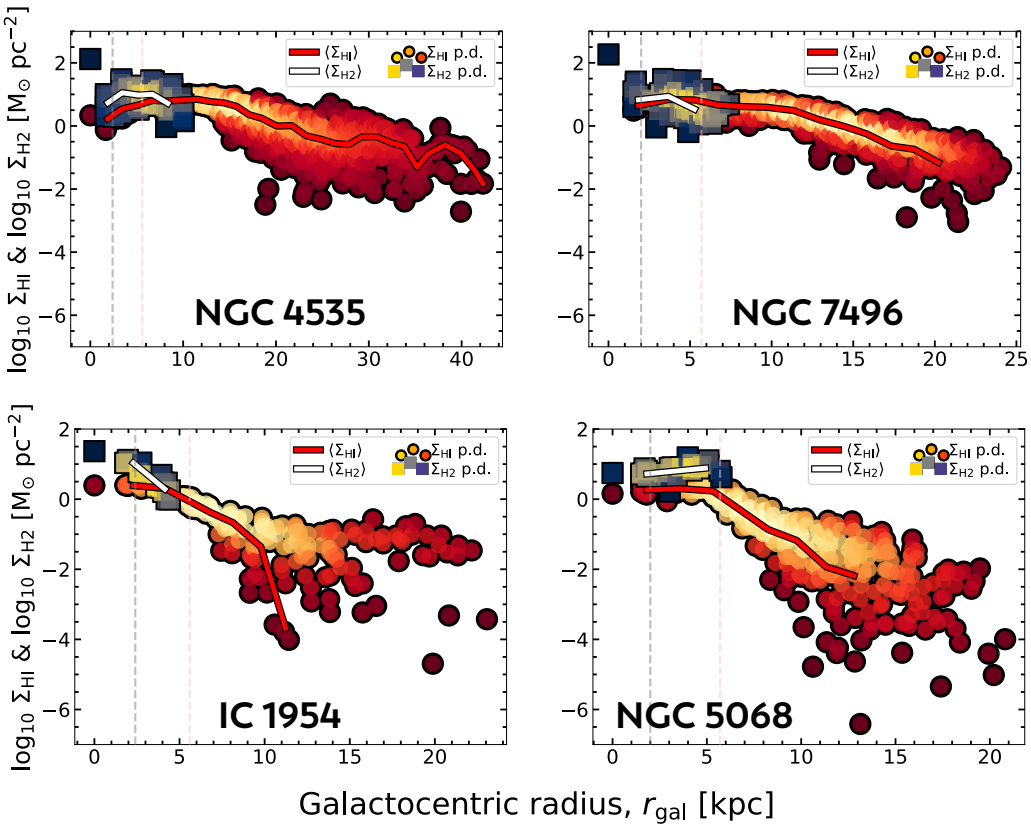

Figure 7.7: Radial extent of H I and CO in NGC 4535, NGC 7496, IC 1954 and NGC 3511 with their corresponding $R_{\rm eff}$ and r_{25} indicated as vertical dashed lines. These galaxies have the smallest H I disk extend in our sample, and do not exhibit special H I characteristics.

the structure parameters (Table 7.1). For our sample, we find a range of maximum radial extent of $\Sigma_{\rm HI}$ of $r_{\rm gal,max}$ ~20 − 120 kpc, and for $\Sigma_{\rm H2}$ we find $r_{\rm gal,max}$ ~5 − 18 kpc. The H I emission extends on average 5 times more than the CO emission (see also Table 7.3).

Almost all of our galaxies show in their central 1.5 kpc sized region higher $\Sigma_{\rm H2}$ than $\Sigma_{\rm HI}$. The galaxy that stands out the most regarding its central region is NGC 1566 with a difference of ~3 orders of magnitude. We do not detect any H I emission in the inner 1.5 kpc for NGC 7496. This can also be seen in the moment map in Figure 7.3.

The strongest radial decrease in $\Sigma_{\rm HI}$ is visible for the galaxies IC 1954, NGC 3511, and NGC 5068; almost 3 orders of magnitude. On the other hand, NGC 1672 and to some degree, NGC 1512 show the flattest behavior of $\Sigma_{\rm HI}$. In the panel for NGC 1512, we see at $r_{\rm gal}$ ~8 kpc an increase in $\Sigma_{\rm HI}$ and $\Sigma_{\rm H2}$, which is the location of the ring-like feature that can be seen in Figure 7.2.

Carefully inspecting each individual galaxy reveals additional clumps, dips, or peaks at larger $r_{\rm gal}$, and/or companion galaxies. We sorted the galaxies by their extent in H I. In Figure 7.5 showing NGC 1512, H I extends out to $r_{\rm gal}$ ~ 120 kpc (that is $5 \times r_{25}$ or 4× the diameter of the Milky Way, indicated as a purple arrow). NGC 1512's interacting companion sits at the grey shaded $r_{\rm gal}$ range. The clumps NGC 1512-south-a, NGC 1512-south-b, and NGC 1512-west are ~ 140 kpc from the

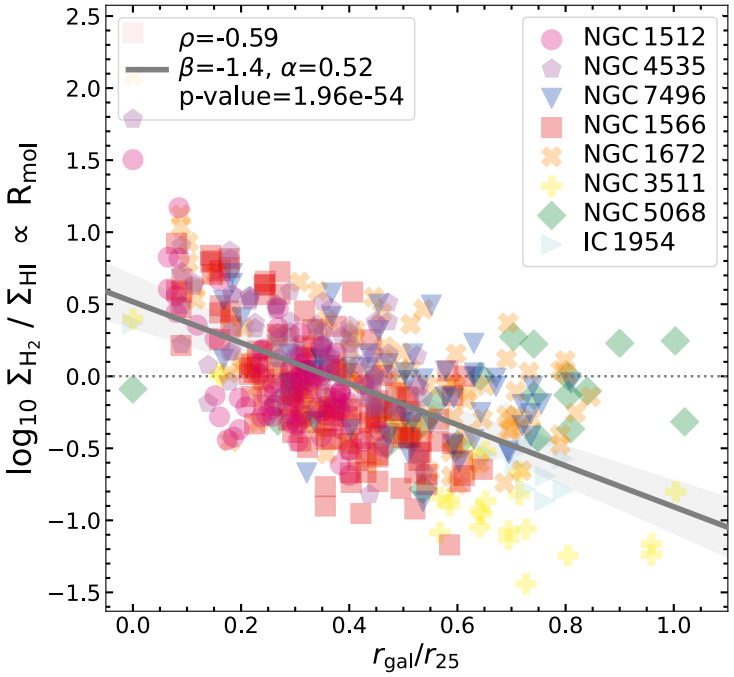

Figure 7.8: $R_{\rm mol}$ against the normalized radius $r_{\rm gal}/r_{25}$. The region below the dotted horizontal line can be viewed as dominated by $\Sigma_{\rm HI}$, and the region above that line by $\Sigma_{\rm H2}$. The grey line shows a fit for all the galaxies that crosses the $R_{\rm mol}$=1 boundary at ~0.4 $r_{\rm gal}/r_{25}$.

center of NGC 1512. The clumps NGC 1512-south-a and NGC 1512-south-b were previously detected as one whole clump by Koribalski and López-Sánchez, 2009 (they named it NGC 1512-south). In Figure 7.6 we show the radial extent of NGC 1566, NGC 1672, and NGC 3511 together with their values of $R_{\rm eff}$ and r_{25} taken from Table 7.1. For NGC 1566 H I extends until $r_{\rm gal}$ ~ 55 kpc with two additional clumps at $r_{\rm gal}$ ~ 65 kpc and $r_{\rm gal}$ ~ 97 kpc. For NGC 1672 H I extends until $r_{\rm gal}$ ~65 kpc with a crossover to the region of the south-east clump. The H I extent in NGC 3511 is dominated by other features besides the steep decline in $\Sigma_{\rm HI}$. The hatched region indicates the filamentary structure with low integrated intensity, followed by the companion galaxy NGC 3513. In Figure 7.7 we show the galaxies in our sample that have the least extended H I disk and/or do not exhibit special characteristics such as clumps or connection branches. IC 1954, NGC 5068 and NGC 7496 show an maximal H I extent of ~25 kpc, whereas NGC 4535 reaches $r_{\rm gal}$~40 kpc.

We aim to know where in our galaxies the overall molecular gas surface density is equal to the atomic gas one. That is the boundary where either H I or H_2 dominates. To compare galaxies at different distances and stellar masses, it is common to normalize the galactocentric radius ($r_{\rm gal}$) with r_{25}. In Figure 7.8 we show $R_{\rm mol}$ versus $r_{\rm gal}/r_{25}$. The rainbow-colored symbols show individual 1.5 kpc apertures of each galaxy. The gray linear regression fit in the form $\log(y) = \beta \times \log(x) + \alpha$, shows the correlation of $R_{\rm mol}$ and $r_{\rm gal}/r_{25}$ across all galaxies. The fit crosses the $\Sigma_{\rm H2}/\Sigma_{\rm HI}$= 1 boundary (in log scale indicated as a horizontal line at 0) at ~0.4 $r_{\rm gal}/r_{25}$. However, looking at individual galaxies, such as NGC 1512, or NGC 7496, it becomes evident that for these objects $\Sigma_{\rm HI}$ dominates already at a smaller $r_{\rm gal}/r_{25}$. In the discussion, we also present another method to determine this transition.

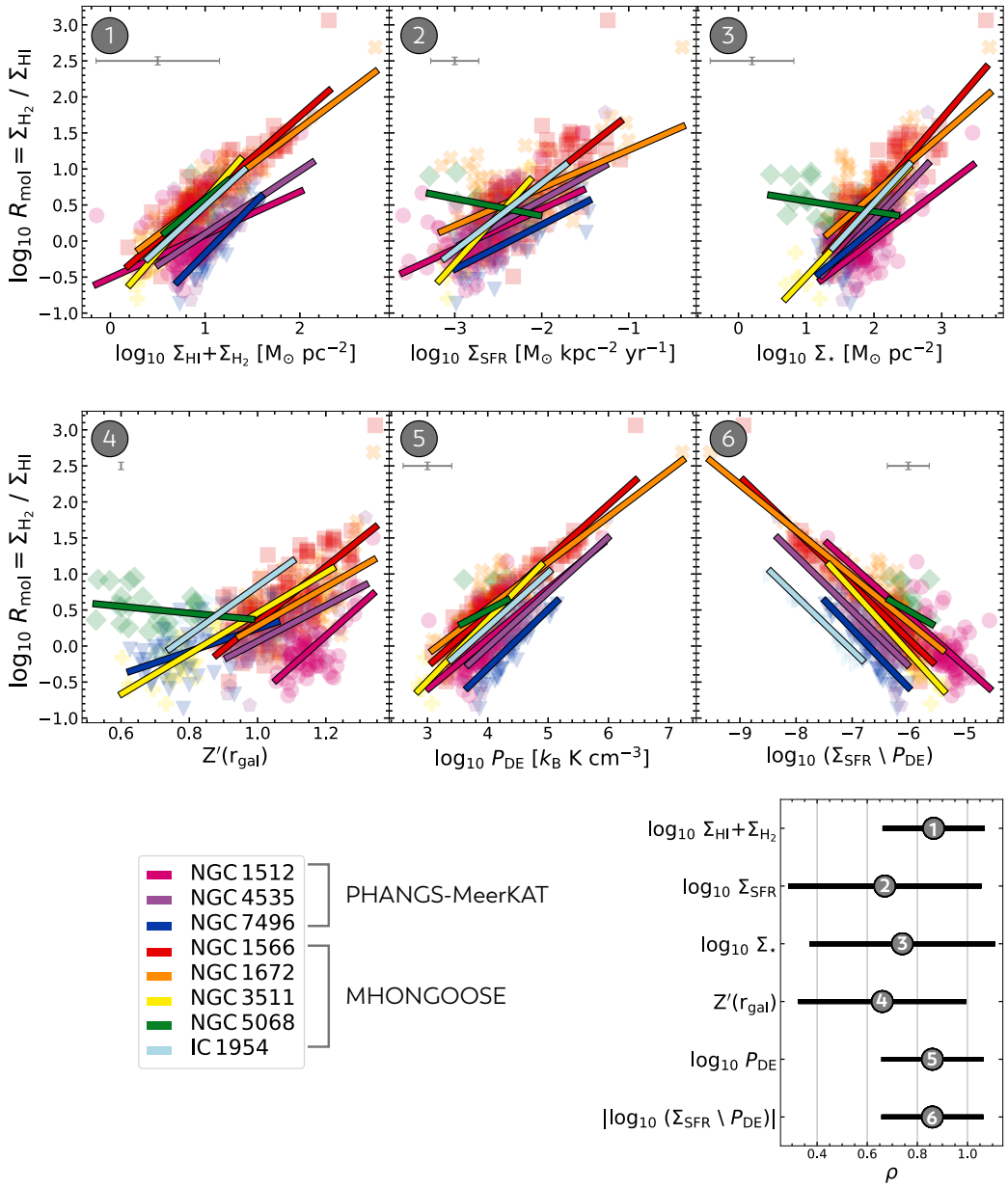

Figure 7.9: $R_{\rm mol}$ scaling relations. The numbered panels show linear regression fits between $\log_{10}$ $\Sigma_{\rm H2}$ /$\Sigma_{\rm HI}$ against six different physical quantities that we derived in Section 7.3, (1) $\Sigma_{\rm gas}$, (2) $\Sigma_{\rm SFR}$, (3) Σ_{*}, (4) Z', (5) $P_{\rm DE}$, and (6) $\Sigma_{\rm SFR}$/ $P_{\rm DE}$. Each color represents one galaxy. The lower right panel represents the range of Pearson ρ and the mean ρ for all galaxies for each individual fitted quantity shown in panels (1) - (6). Here, only for visualization purposes, we show the positive ρ values for (6). All of the properties of the presented linear regression fits are listed in Table 7.5 and Table 7.6.

Table 7.3: Radial extent of our sample

Galaxy	$r_{gal,max}$ CO(2-1) [kpc] (1)	$r_{gal,max}$ H I [kpc] (2)	R_{eff} (3)	r_{25} (4)
IC 1954	5	25	× 10	× 4.5
NGC 1512	10	120	× 25	× 5.0
NGC 1566	12	55	× 17	× 3.0
NGC 1672	18	75	× 22	× 4.3
NGC 3511	13	40	× 13	× 3.3
NGC 4535	11	45	× 7	× 2.4
NGC 5068	6	20	× 10	× 3.5
NGC 7496	8	25	× 7	× 2.7
Average	10	51	× 14	× 3.6

Notes: (1–2): The maximum value in galacocentric radius (r_{gal}) for CO(2-1) and H I, for each galaxy. (3): The value that R_{eff} corresponds to H I. For example, for NGC 1512 it takes 25 times R_{eff} to reach 120 kpc. (4): The value that r_{25} corresponds to H I. For example, for NGC 1512 it takes 5 times r_{25} to reach 120 kpc. Values of both, R_{eff} and r_{25} are taken from Table 7.1.

7.5.2 R_{mol} scaling relations

In this work, we want to investigate how the molecular gas fraction, R_{mol}, depends on the local conditions in galaxy disks. For this purpose, we focus on the regions in the galaxies where we detect both Σ_{HI} and Σ_{H2}. We show the scaling relations of R_{mol} against six physical quantities (Σ_{gas}, Σ_{SFR}, Σ_{*}, P_{DE}, P_{DE}/Σ_{SFR}, and Z'(r_{gal})) in Figure 7.9 for all galaxies. Our sample spans almost 4 orders of magnitude in R_{mol}. The rainbow-colored markers show the individual apertures in all galaxies. Among them, we see a spread of $\log(x)$ of ~3 dex in panels Σ_{gas}, Σ_{SFR}, Σ_{*}, and Z', ~3 dex in P_{DE}, and P_{DE}/Σ_{SFR}.

We show linear regression fits in the form of $\log(y) = \beta \times \log(x) + \alpha$. We find for most of the galaxies moderate[8] sub-linear (i.e. $\beta < 1$) correlations between $\log_{10}$ Σ_{H2}/Σ_{HI} and log(x) (see Table 7.5). There are a few notable exceptions. For correlations between $\log_{10}$ R_{mol} and (i) Σ_{SFR} we find only for NGC 3511 a linear relation, (ii) Σ_{*} the galaxies NGC 1566, NGC 3511, and IC 1954 show a tight (i.e. $\rho > 0.7$) linear relation, (iii) P_{DE} all galaxies except NGC 5068 show a tight correlation, (iv) Z' (r_{gal}) all galaxies except NGC 5068 show a linear correlation, (v) Σ_{gas} all galaxies except NGC 4535 show a linear correlation, (vi) Σ_{SFR}/P_{DE} NGC 1566 and IC 1954 both show a tight linear correlation. We discuss these exceptions in Subsection 7.6.2

The lowest right panel shows the ranges of Pearson ρ (black line) and the median ρ of all galaxies (grey circular marker). We find the highest median ρ value for P_{DE} with $\langle\rho\rangle = 0.86$, followed by Σ_{gas} with $\langle\rho\rangle = 0.85$.

[8] Here we refer to a moderate correlation if ρ lies in the range of 0.5 – 0.7.

7.6 Discussion

In this section, we discuss the finding that $P_{\rm DE}$ tightly correlates with $R_{\rm mol}$ (see Figure 7.9) in our sample, indicating that the balance between H I and H_2 is primarily determined by the dynamical equilibrium pressure, and compare it with literature values. We further examine conditions at $R_{\rm mol}$ = 1, where above or below this transition, either H I or H_2 dominates the ISM in nearby galaxies. We also investigate potential differences in physical quantities between interacting and non-interacting galaxies.

7.6.1 Dynamical Equilibrium Pressure and $R_{\rm mol}$

In panel 5 of Figure 7.9 and in Table 7.5 we find a tight, positive correlation between $P_{\rm DE}$ and the molecular gas fraction in our sample (with $\langle\rho\rangle$ = 0.86). This suggests that among our studied physical quantities $P_{\rm DE}$ is potentially the most influential driver of $R_{\rm mol}$.

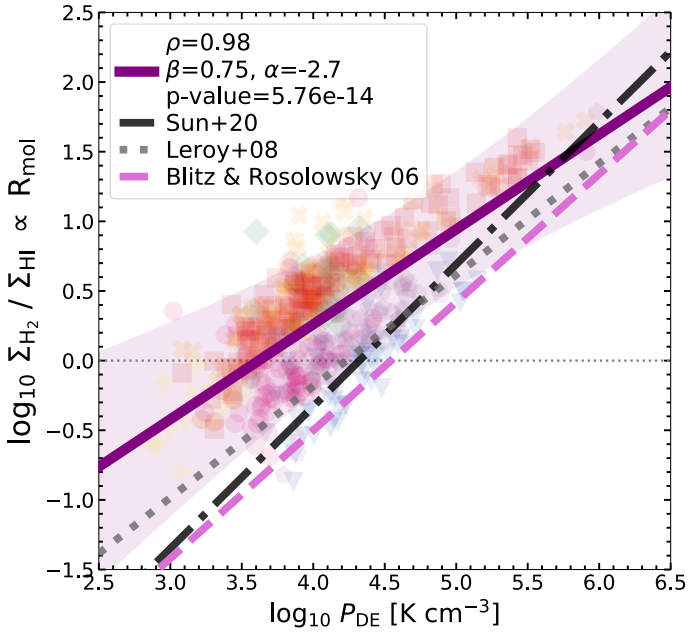

Figure 7.10: $R_{\rm mol}$ against $P_{\rm DE}$. Shown here is an enlarged version of panel 5 from Figure 7.9, however, here the fit was performed over the entire sample (purple line) with the corresponding 3σ confidence interval (purple shaded region). The black, grey, and pink lines show literature fits adopted from Sun et al., 2020b; Leroy et al., 2008; Blitz and Rosolowsky, 2004. We explain possible reasons for the slight offset of our fit to the literature ones in the text.

Wong and Blitz (2002) and Blitz and Rosolowsky (2006) report a strong (with power-law indices of 0.8 and 0.92) correlation between the $\Sigma_{\rm H2}$ / $\Sigma_{\rm HI}$ and the midplane hydrostatic pressure mostly where $\Sigma_{\rm H2} > \Sigma_{\rm HI}$. Blitz and Rosolowsky, 2006 found this relation over three orders of magnitude for 14 galaxies. Leroy et al. (2008) showed that this relation extends to the regime where H I dominates the ISM. However, they stated that the fits between the molecular gas fraction and the midplane hydrostatic pressure are reflected by the covariant behavior of, for example, the radius, Σ_*, and the midplane hydrostatic pressure where each of these quantities could be used to predict $\Sigma_{\rm H2}$ / $\Sigma_{\rm HI}$.

A study by Sun et al. (2020a) reveals P_{DE} values in the range of $10^3 - 10^6$ K cm^{-3} for massive star-forming galaxies similar to our targets. This range is consistent with our P_{DE} values determined in this work. This agrees with the estimated dynamical equilibrium pressure in the solar neighborhood which is ~10^4 (Elmegreen, 1989). Sun et al. (2020a) found a moderate positive correlation between P_{DE} and R_{mol}, however, with Spearman's rank correlation coefficient of $\rho = 0.58$. With our better quality H I data, we see an even stronger (or tighter) correlation with $\langle\rho\rangle = 0.86$ (i.e. the median over all the individual ρ for each galaxy, see Table 7.5). This overall agrees with previous studies (Wong and Blitz, 2002; Blitz and Rosolowsky, 2006; Leroy et al., 2008), although they used a different CO-to-H_2 conversion factor, stellar mass-to-light ratio, and stellar disk geometry.

In Figure 7.10 we show R_{mol} against P_{DE} for our galaxies together with the aforementioned literature fits (from Blitz and Rosolowsky, 2004; Leroy et al., 2008; Sun et al., 2020b). The purple line shows a fit over all of our nine galaxies, which yields an even tighter relationship (with ρ=0.98, β=0.75, α=-2.7, and p-value=5.76E-14). Our fit is slightly offset to the other ones. The literature ones are within our 3σ confidence interval for $R_{mol} > 1$. In Sun et al., 2020b the R_{mol}-P_{DE} plane was shown for 28 galaxies, using older H I observations to infer R_{mol} and P_{DE}. We compared those galaxies that overlap with our sample (NGC 1512, NGC 4535, NGC 7496, NGC 1672 and NGC 3511) with the measurements for R_{mol} and P_{DE}. We find that they are reasonably similar to the new measurements and therefore are not the cause of this discrepancy. However, other PHANGS galaxies that are included in the Sun et al. (2020b)'s study are in the low R_{mol}, low P_{DE} regime and appear to affect the fit. Conversely, galaxies that fall in the low R_{mol} and low P_{DE} range may be missing from our sample. In a forthcoming paper, we will include stacking techniques that will recover fainter CO and H I emissions that will have an impact on the R_{mol} - P_{DE} fit.

7.6.2 Other physical quantities

From a global view (i.e. the median ρ of all eight galaxies) the lower right panel in Figure 7.9 shows that P_{DE} correlates best with R_{mol}. However, looking at individual galaxies, we find two 'outliers' that are responsible for the wide ranges of ρ values for Σ_{SFR}, Σ_*, and Z'(r_{gal}). One galaxy – NGC 5068 – seems to show different slopes and exhibits negative ρ values in R_{mol}versus all of the three aforementioned quantities. This can be attributed to the relatively weak CO emission from this target and consequently the low S/N of the PHANGS-ALMA CO map. This low S/N could introduce biases in measuring R_{mol} and could explain the different behavior seen in the fits. IC 1954, on the other hand, shows high ρ values (i.e., $\rho > 0.9$) in all these relations. This is a simple, isolated, pure disk galaxy, so the R_{mol} is mostly driven by the radial variation of physical conditions rather than galaxy morphological structures or interactions. Our literature overview in Section 7.4 showed that this galaxy is almost unexplored and thus, relatively little is known about the gas properties of this galaxy.

In spiral galaxies, the transition between an Σ_{HI}-dominated and a predominantly Σ_{H2}-dominated ISM takes place at a characteristic value for most quantities. In Table 7.3 we list the conditions at the $R_{mol} = 1$ (i.e. where $\Sigma_{HI} \approx \Sigma_{H2}$). For each galaxy, we measured the median of the quantity in question over all hexagonal apertures where $\Sigma_{H2} \approx$ 0.8-1.2 Σ_{HI}. We show the median transition value along with the 1σ scatter among our galaxies. At $R_{mol} = 1$ the baryon mass budget is dominated by stars $\Sigma_* \approx 39.72$ M$_\odot$ pc^{-2} while the total gas is $\Sigma_{gas} \approx 4.14$ M$_\odot$ pc^{-2}. The dynamical equilibrium pressure corresponds to 4.9×10^3. We note that some of these values are different from the ones quoted in Table 7.3 taken from Leroy et al., 2008. For example, their median value of P_{DE} is one order of magnitude higher than ours. However, looking at the individual galaxies we find median values in the

Table 7.4: Conditions at $R_{\rm mol}$ = 1, where $\Sigma_{\rm HI} \approx \Sigma_{\rm H2}$

Quantity	Median	Scatter	Leroy et al., 2008
	(1)	(2)	(3)
$r_{\rm gal}/r_{25}$	0.54	0.12	0.43
$\Sigma_{\rm gas}$ [$M_\odot$ pc^{-2}]	4.14	0.97	14
$\Sigma_{\rm SFR}$ [$M_\odot$ pc^{-2}]	1.86E-3	4.2E-4	-
Σ_* [$M_\odot$ pc^{-2}]	39.72	13.31	81
$P_{\rm DE}$ [K cm^{-3}]	4.9×10^3	0.34	2.3×10^4

Notes: (1): Following Leroy et al., 2008 we measure the quantity for each galaxy overall apertures in each galaxy where $\Sigma_{\rm H2}$= 0.8 − 1.2 $\Sigma_{\rm HI}$, and take the median. (2): The corresponding 1σ scatter. (3): Literature median values using observations from the THINGS and HERACLES surveys.

range of $P_{\rm DE} = 2.8 \times 10^3 - 2.1 \times 10^4$ K cm^{-3}, where the upper end of this range is in agreement with the literature value. Additionally, as mentioned earlier, we may be missing galaxies that fall in the low $R_{\rm mol}$ and low $P_{\rm DE}$ range from our sample.

We also note the difference between our found median value of 0.54 $r_{\rm gal}/r_{25}$ (see Table 7.4 where we measured the median value where $\Sigma_{\rm H2}$= 0.8 − 1.2 $\Sigma_{\rm HI}$) compared to our determined 0.40 $r_{\rm gal}/r_{25}$ value by performing a linear regression fit. Overall, different methodologies affect the values quoted in Table 7.3 by ∼ 20%. These include the choice of using apertures or rings, to interpolate, using the mean or median. Therefore, our $r_{\rm gal}/r_{25}$ values estimated from fitting and taking the median in the $\Sigma_{\rm H2} \approx$ 0.8-1.2 $\Sigma_{\rm HI}$ range are with the margin of error (1σ) and the choice of methodology.

7.6.3 Differences in interacting and non-interacting galaxies?

Figure 7.2 shows a prominent example of an interacting galaxy – NGC 1512 interacting with NGC 1510. In our sample we have another galaxy that is potentially interacting with one close-by companion; NGC 3511 with NGC 3513. Apart from these two galaxies all of the other galaxies are non-interactive ones. Blitz and Rosolowsky, 2006 observed a different behavior of pressure between interacting and non-interacting galaxies. The question arises now whether we find among these two galaxies compared to the other six galaxies different signatures in $P_{\rm DE}$, or in other physical quantities.

What both galaxies have in common are their relatively low global values in star formation rate (∼0.1 log($M_\odot$); see Table 7.1) in our sample. The second panel in Figure 7.9 – $R_{\rm mol}$ against $\Sigma_{\rm SFR}$ – does not show a particularly different behavior of NGC 1512 (pink line) and NGC 3511 (yellow line) than the non-interactive galaxies in our sample. This holds also for all the other physical quantities, including the dynamical equilibrium pressure. However, our sample of a total of eight galaxies of which only two are interacting is not statistically significant.

7.6.4 Next required steps

With upcoming MeerKAT and/or high-resolution VLA H I observations of additional nearby galaxies targeted by the PHANGS project that have multi-wavelength data available[9], a natural next step is to perform this analysis on the full sample. This will allow us to further investigate how global galaxy properties (stellar mass, star formation rate, or morphology) impact the conversion from atomic to

[9] The availability of CO observations is required to calculate for example $P_{\rm DE}$, see Subsection 7.3.6, Equation 7.7.

molecular gas. Additionally, we will be able to further explore, the differences between interacting and non-interacting galaxies and what effect a different choice of CO-to-H_2 conversion factor has on the $R_{mol} - P_{DE}$ relation, and whether the strong correlation between R_{mol} and P_{DE} holds for a larger sample of galaxies.

7.7 Conclusion

In this work, we have examined which physical mechanism is responsible for the determination of the molecular gas fraction ($R_{mol} = \Sigma_{H2}/\Sigma_{HI}$). For that, we used a multi-wavelength approach together with new observations of eight nearby galaxies taken with the MeerKAT telescope (PHANGS-MeerKAT, this work + MHONGOOSE from de Blok et al., 2016). We performed our analysis in a way that we averaged each quantity (Σ_{H2}, Σ_{HI}, Σ_{gas}, Σ_{SFR}, Σ_*, Z'(r_{gal}), P_{DE}, and Σ_{SFR} / P_{DE}) over a 1.5 kpc hexagon region (following Sun et al. 2022). We find the following results:

1) We present new MeerKAT H I observations towards the three nearby spiral galaxies NGC 1512, NGC 4535, and NGC 7496 (PHANGS-MeerKAT) at 15″angular resolution, together with additional observations towards five nearby galaxies IC1954, NGC 1566, NGC 1672, NGC 3511, and NGC 5068 (MHONGOOSE); see Figure 7.1, Figure 7.2 and Figure 7.3. Their H I distribution shows gigantic spiral arms (in NGC 1512, NGC 1566, and NGC 4535), splitting into sub-arms (in NGC 1512), compact disks (in NGC 3511 and IC 1954), ring-like structures (in NGC 7496 and a smaller one in NGC 1512), or additional clumps (in NGC 1512 and NGC 1566).
2) We detect on average significant H I emission out to a radius of ~51 kpc, which is 5 times more than the extent of CO emission (see Figure 7.5, Figure 7.6, and Figure 7.7). In terms of r_{25}, we find H I emission $2.7 - 5.0 \times r_{25}$ (see Table 7.3). The R_{mol} - r_{gal}/r_{25} fit crosses the $R_{mol} = 1$ border (where $\Sigma_{HI} \approx \Sigma_{H2}$, indicated as grey horizontal line in Figure 7.8) at 0.4 r_{gal}/r_{25}.
3) To understand how R_{mol} responds to the local conditions in each galaxy, we investigate scaling relations with various physical parameters. We examine scaling relations of R_{mol} and the total gas surface density (Σ_{gas}), the star formation rate surface density (Σ_{SFR}), the stellar surface density (Σ_*), the dynamical equilibrium pressure (P_{DE}), a proxy for the ratio of the radiation field and density, and the metallicity (Z'(r_{gal})). Among all of these fits R_{mol} - P_{DE} shows the tightest correlation with a median Pearson ρ of each galaxy's Pearson ρ of $\langle\rho\rangle = 0.86$ (see Figure 7.9, Table 7.5 and Table 7.6).
4) A relationship between R_{mol} and P_{DE} has been found in previous studies (e.g. Blitz and Rosolowsky, 2004; Leroy et al., 2008; Sun et al., 2020b). Similar to these studies we perform a fit over all galaxies (see Figure 7.10), which yields for our sample an even tighter relationship with $\rho = 0.98$. We explain the slight offset of our fit to the literature ones with the fact that we may be missing galaxies that fall in the low R_{mol} and low P_{DE} range from our sample. Upcoming observations will increase the sample size and thus allow for further investigation.
5) We examine the transition between an H I-dominated and a predominantly H_2-dominated ISM that takes place at a characteristic value for most quantities. We find that at $R_{mol} = 1$ the baryon mass budget is dominated by stars $\Sigma_* \approx 40\ M_\odot\ pc^{-2}$ while the total gas is $\Sigma_{gas} \approx 4\ M_\odot\ pc^{-2}$ (see Table 7.3).
6) A different behavior of the pressure between interacting and non-interacting galaxies has been shown in past studies (e.g. Blitz and Rosolowsky, 2006). In our sample, NGC 1512 interacts with NGC 1510 and potentially NGC 3511 with its close-by companion NGC 3513. We do not

Table 7.5: $R_{\rm mol}$ (log(y)) scaling relations and correlation coefficients (ρ) for the discussed physical quantities $\Sigma_{\rm gas}$, $\Sigma_{\rm SFR}$, and Σ_* (log(x)) for each galaxy.

log(x)	ngc	ρ Pearson (1)	$\langle\rho\rangle$ (2)	β slope	α intercept	p-value
	1512	0.41		0.60	-0.51	2.19e-04
	4535	0.60		0.88	-0.78	1.73e-10
	7496	0.84		1.30	-1.50	2.99e-15
$\Sigma_{\rm gas}$	1566	0.92	0.85	1.10	-0.56	4.31e-55
	1672	0.89		0.99	-0.42	1.74e-40
	3511	0.95		1.50	-0.91	2.71e-19
	5068	0.61		1.10	-0.51	8.89e-04
	1954	0.98		1.20	-0.72	1.43e-14
	1512	0.49		0.56	1.60	2.83e-05
	4535	0.57		0.66	1.90	1.25e-08
	7496	0.75		0.62	1.50	9.13e-10
$\Sigma_{\rm SFR}$	1566	0.77	0.67	0.95	2.70	6.75e-26
	1672	0.59		0.53	1.80	9.06e-12
	3511	0.85		1.30	3.70	2.64e-10
	5068	-0.34		-0.24	-0.13	1.32e-01
	1954	0.95		0.93	2.70	1.02e-10
	1512	0.72		0.71	-1.40	1.25e-13
	4535	0.76		0.99	-1.70	8.39e-19
	7496	0.62		0.78	-1.40	5.72e-07
Σ_*	1566	0.88	0.74	1.10	-1.60	1.48e-42
	1672	0.69		0.82	-0.99	1.75e-17
	3511	0.90		1.00	-1.50	2.19e-14
	5068	-0.26		-0.15	0.71	2.01e-01
	1954	0.93		1.00	-1.50	2.47e-09

Notes: (1): Pearson ρ for individual fits for for each galaxy. (2): The median Pearson ρ for all galaxies for each log(x).

find a significantly different behavior than the non-interactive galaxies in our sample among all of our physical quantities.

Table 7.6: R_{mol} (log(y)) scaling relations and correlation coefficients (ρ) for the discussed physical quantities Z'(r_{gal}), P_{DE}, and $\Sigma_{\mathrm{SFR}}/P_{\mathrm{DE}}$ (log(x)) for each galaxy.

log(x)	ngc	ρ Pearson (1)	$\langle\rho\rangle$ (2)	β slope	α intercept	p-value
	1512	0.67		4.20	-4.90	1.47e-11
	4535	0.65		2.50	-2.40	2.24e-12
	7496	0.52		1.60	-1.30	6.22e-05
Z'(r_{gal})	1566	0.75	0.66	3.80	-3.50	9.27e-25
	1672	0.58		2.70	-2.40	8.38e-12
	3511	0.88		2.80	-2.40	3.74e-13
	5068	-0.20		-0.47	0.83	3.19e-01
	1954	0.91		3.40	-2.60	3.19e-08
	1512	0.67		0.70	-2.70	3.10e-11
	4535	0.76		0.76	-3.10	7.63e-19
	7496	0.82		0.81	-3.50	2.29e-14
P_{DE}	1566	0.96	0.86	0.75	-2.50	2.26e-70
	1672	0.90		0.64	-2.00	1.6e-43
	3511	0.94		0.86	-3.10	1.2e-18
	5068	0.36		0.44	-1.30	7.2e-02
	1954	0.98		0.75	-2.70	5.7e-14
	1512	-0.67		-0.70	-3.80	3.1e-11
	4535	-0.76		-0.76	-4.80	7.6e-19
	7496	-0.82		-0.81	-5.40	2.2e-14
$\Sigma_{\mathrm{SFR}}/P_{\mathrm{DE}}$	1566	-0.96	-0.85	-0.75	-4.40	2.26e-70
	1672	-0.90		-0.64	-3.50	1.67e-43
	3511	-0.94		-0.86	-5.20	1.23e-18
	5068	-0.36		-0.44	-2.20	7.23e-02
	1954	-0.98		-0.75	-5.30	5.76e-14

Notes: (1): Pearson ρ for individual fits for for each galaxy. (2): The median Pearson ρ for all galaxies for each log(x).

CHAPTER 8

Conclusion

Overview

This thesis investigates the centers and outskirts of nearby galaxies in terms of their molecular and atomic gas, respectively, and how they affect star formation, show environmental differences due to dynamical features, and shape and govern the ISM in these galaxies.

The thesis contains two technical and three scientific projects. The technical parts describe **(1)** the efforts of increasing the signal of observations targeting Ammonia and **(2)** the reduction, calibration, imaging, and feathering tasks for a dataset that was later published as part of one of the scientific projects. The three scientific projects describe **(3)** high-resolution multi-molecular emission line observations towards the inner 50″ of the nearby double-barred starburst galaxy NGC 6946 and the analysis of star formation rate scaling relations and ratios of molecular lines, **(4)** the large and small-scale kinematic analysis of the outskirts of the nearby grand design galaxy M 83 – it's super-extended H I disk, and **(5)** the new MeerKAT H I observations that were used to study where the atomic gas gets converted into molecular gas in nearby galaxies.

(1) & (2) Reduction, calibration, imaging, and feathering

Chapter 4 investigates Ammonia observations and whether it is possible to increase the signal in this data set. We show that this is not possible and requested new observation (future project, see Chapter 9). Another project describes the reduction, imaging and feathering of Very Large Array and Green Bank Telescope observations of H I emission towards M 83. We find a total flux for the VLA cube of 5.2×10^4 K and 6.6×10^4 K for the feathered one (VLA plus GBT). This difference emphasizes that single-dish data are needed even for interferometric observations, including compact configurations.

(3) The high-resolution molecular line survey towards the center of NGC 6946, the Fireworks Galaxy

Our understanding of star and planet formation, a fundamental challenge in astrophysics, is still largely unresolved. Molecular gas, which serves as fuel for star formation, plays a critical role in the evolution of galaxies. While progress has been made in understanding star formation in galactic disks, our knowledge of the process in galaxy centers remains limited. However, improving our

understanding is critical because these centers contribute substantially (10-100%) to the total star formation in galaxies.

Chapter 5 presents the results from the published study analyzing high-resolution multi-molecular line observations towards the inner 50″(1.9 kpc) of the nearby double-barred starburst galaxy NGC 6946, also known as the Fireworks Galaxy. As part of the project, we studied for the first time the effect of a small-scale bar on molecular line emission and star formation. With the wealth of molecular line emission data, we address various science questions to assess the physical and chemical structure of gas in NGC 6946's center and its inner smaller bar that is 250 pc in radius.

We find that the small-scale bar affects the molecular gas such that the locations of the densest molecular gas material are not necessarily the very centers of the galaxies. In more detail, higher molecular mean density and higher star formation rates correlate with the shock tracers in the southern bar end. Furthermore, we show that the star formation efficiency of the dense gas (SFE_{dense}) exhibits a different behavior than expected from large-scale disk observations; SFE_{dense} increases with increasing integrated intensity of CO (2−1). The reason for this is that for the first time, we are able to resolve sub-structures and study star formation rate scaling relations in these $\sim$ 150 pc scale environments.

Adding ancillary dense gas observations of 8 nearby galaxies to our analysis, we speculate that (i) the ratio of the molecules HCN and HNC is not an accurate probe for kinetic temperatures for sub-kpc and kpc sized extragalactic regions, and (ii) the HCO+/HCN ratio might not be a unique indicator for AGN activity in galaxies at these scales. This is because the galaxies, although hosting an AGN, are in the photon-dominated region of the diagnostic diagrams (rather than the X-ray-dominated region where we would expect them to be). That means empirical molecular line diagnostics are a useful tool, but reach their limits and/or cannot be unambiguously interpreted at (sub)kpc scales in nearby galaxies. Higher resolution observations and/or observations of additional indicators for calibration (e.g. NH_3 observations to compare with HNC/HCN) could become of immense importance in this context.

In summary, this survey serves as an interesting template for future high-resolution extragalactic central molecular zone studies. Altogether, in this study, we showed the importance of analyzing molecular lines to better understand galaxy centers and their dynamical features such as stellar bars and spiral arms, and how they regulate local gas physics.

(4) Kinematics of M 83's super-extended HI disk

The study of galaxy evolution, formation, and dynamics is a fundamental and active area of research in modern astrophysics. An important aspect of these processes is the accretion of cold gas from the intergalactic medium (IGM). Studying the kinematics of neutral hydrogen (H I) in nearby galaxies provides a valuable opportunity to study and gain insight into these phenomena.

Chapter 6 presents the published results of one of the largest VLA H I mosaics combined with GBT single dish data of a nearby galaxy. These observations target the super-extended H I disk of the nearby grand design galaxy M 83 to investigate the kinematics of H I gas.

In this work, we investigate M 83's super-extended H I disk (out to $r_{gal} > 50$ kpc), including analyzing velocity fields and mass flow rate profiles. While examining the radial and environmental dependence of velocity dispersion across the whole disk of M 83, we find an enhanced velocity dispersion in its ring region (surrounding its optical disk). Surprisingly, using GALEX FUV data to trace star formation, we do not find enhanced FUV emission where the H I velocity dispersion is enhanced. The anti-correlation with star formation might suggest that radial transport rather than star formation could be the reason for enhanced velocity dispersions in the outskirts of M 83.

Careful examining M 83's velocity field revealed an "inflection point" in observed velocities along the northern extended arm with a possible connecting branch to the dwarf irregular galaxy UGCA 365, that deviates from the general direction of M 83's northern arm; a clear result of dynamical interaction of M 83 with UGCA 365.

Moreover, we model a radial mass flow rate profile and compared it with literature mass flow rates, showing that kinematic parameters (such as inclination) have a strong impact on these profiles. Although mass inflow is one of the most important processes feeding star formation, tilted-ring models (2D or 3D) as the basis for deriving such profiles, are strongly sensitive to initial parameters (such as estimation of kinematic parameters in warped or flaring H I disks at large radii). For some radii this can even flip signs of the inflow/outflow rate. While the upper limits for mass flow rates in the optical disk region ($\sim$1 $M_\odot$ yr^{-1}) agree with prior work, our extended analysis also includes larger radii and we find substantial inflow e.g. in the ring region ($\sim$10 $M_\odot$ yr^{-1}).

To summarize, we show with this study that dynamical features (such as rings and spiral arms) have a significant impact on mass flow rate profiles and radial H I velocity dispersion profiles. In particular, we show that mass flow rate profiles are highly sensitive on kinematic parameters, in particular inclination thus, such rates should be interpreted with caution.

(5) Where and what drives the conversion of atomic to molecular gas in nearby galaxies

The crucial connection between centers and outskirts in disk galaxies is dynamics. It drives mass flows from the outermost regions (atomic gas) and fills galaxy centers (where it gets converted to molecular gas) with fresh material to form stars.

In Chapter 7 we present an in-progress manuscript of the new high-quality MeerKAT H I observations towards the three nearby spiral galaxies NGC 1512, NGC 4535, and NGC 7496 (PHANGS-MeerKAT) at 15″angular resolution, together with additional observations towards five nearby galaxies (from the MHONGOOSE survey). Paired with high-quality CO observations (from PHANGS-ALMA) along with multi-wavelength data, we investigate which physical mechanism is responsible for atomic gas to become molecular ($R_{\rm mol} = \Sigma_{\rm H2}/\Sigma_{\rm HI}$).

We detect on average significant H I emission out to a radius of $\sim$50 kpc, which is 5 times further out than the extent of CO emission. In terms of r_{25} (i.e. the optical radius), we find H I emission $2.7-5.0 \times r_{25}$. Normalizing the radial extend of H I in nearby galaxies by their optical radius ($r_{\rm gal}/r_{25}$), we find that the $R_{\rm mol}$ - $r_{\rm gal}/r_{25}$ fit crosses the $R_{\rm mol} = 1$ border (where $\Sigma_{\rm HI} \approx \Sigma_{\rm H2}$) at 0.4 $r_{\rm gal}/r_{25}$.

We investigate how $R_{\rm mol}$ responds to the local conditions in each of our galaxies. We examine scaling relations of $R_{\rm mol}$ and various physical quantities and find that the dynamical equilibrium pressure fit over all galaxies, yields for our sample a very tight relationship with $\rho = 0.98$. This indicates that the balance between H I and H_2 is primarily determined by the dynamical equilibrium pressure. We do not find a different behavior of the pressure between interacting and non-interacting galaxies in our sample, as shown in previous studies. The transition between an H I-dominated and a predominantly H_2-dominated ISM takes place at a characteristic value for most quantities. We find that at $R_{\rm mol} = 1$ the baryon mass budget is dominated by stars $\Sigma_* \approx 40\ M_\odot\ {\rm pc}^{-2}$ while the total gas is $\Sigma_{\rm gas} \approx 4\ M_\odot\ {\rm pc}^{-2}$.

In summary, the atomic gas gets converted into molecular gas at roughly 0.4 $r_{\rm gal}/r_{25}$ across our sample of eight galaxies. One of the key parameters determining the conversion is the dynamical equilibrium pressure.

CHAPTER 9

Outlook

> One never notices what has been done; one can only see what remains to be done
>
> Marie Curie

Overview

The previous chapters in this thesis have shown in detail that through a variety of different observations and analyses, the physics and chemistry of gas in nearby galaxies can be studied and determined in great detail. The investigations of this thesis have provided remarkable results and at the same time lay further building blocks for future projects. Overall, we can either study objects as precisely as possible, and/or extend our analysis to a larger sample. In the following, we list projects that correspond to both of these approaches with the goal of understanding the molecular and atomic gas in nearby galaxies and their connection to various physical processes in more detail.

9.1 Extragalactic Central Molecular Zones

Our understanding of the formation process of stars and planets is one of the most fundamental unsolved problems in contemporary astrophysics. Molecular gas plays an important role in the evolution of galaxies, as it is the fuel for star formation. While we have made great progress in understanding star formation in galactic disks (e.g. Kennicutt and Evans, 2012), our understanding of the star formation process in galaxy centers is much poorer. Improving this is essential since they contribute 10–100% of the overall star formation in galaxies (Kormendy and Kennicutt, 2004), host extreme star formation events (e.g. young massive clusters, starbursts), challenge various proposed star formation models and can represent major sites of feedback to the circumgalactic medium (e.g. Veilleux et al., 2020).

The Central Molecular Zone (CMZ) in the Milky Way is the closest starting point to studying the physical properties of gas and star formation in an extreme environment. However, our position within the disk impedes our ability to obtain a clear view of the overall physical properties of the ISM, resulting, for example, in the 3-D geometry of the CMZ remaining unclear as three possible

scenarios could explain this morphology (explained in detail in the review by Henshaw et al., 2022). Additionally, far from being a starburst, it is still debated why the CMZ appears to be dramatically underproducing stars.

Therefore, inner regions of nearby galaxies – sometimes referred to as *extragalactic CMZs* – are ideal test sites to study the key physical properties of molecular gas under “face-on conditions" and to link back our gained knowledge to the Milky Way, but also to use as templates for high-redshift galaxies which host similarly extreme conditions (e.g. Hodge and da Cunha, 2020).

9.1.1 A multiple molecular line study

A handful of individual extragalactic CMZ studies exist that leverage the state-of-the-art interferometers such as ALMA, VLA, SMA, or NOEMA to use emission from multiple molecular lines to characterize the physical state of the ISM. However, studies are rare that combine observations from several of these telescopes and exploit their different capabilities (i.e., observations at a range of frequencies that probe multiple types of molecules). Additionally, for example, the complex environment (i.e. line-of-sight confusion due to inclination) in most centers limits direct morphological comparison/matching between star formation and gas location.

Chapter 5 presents the 14 molecular emission lines that were observed using the Plateau de Bure Interferometer (PdBI) for one of the closest and brightest northern hemisphere face-on nearby spiral galaxy centers – NGC 6946. With recent observations using the VLA, NOEMA, and SMA interferometers we gathered a comprehensive molecular dataset of > 20 molecular lines[1], that trace different physical states of the molecular ISM (see Figure 9.1) that will provide insights into the physical and kinematic structure of an extragalactic CMZ along with its chemistry at Giant Molecular Cloud (GMC) scales.

In Chapter 5 we discussed proposed concepts to infer the kinetic temperature ($T_{\rm kin}$) from a ratio of molecular line emission that according to our analysis might not be applicable to (sub-)kpc sized region in extragalactic environments. Furthermore, we only focused on a sub-sample of molecular gas and did not investigate the different tracers in terms of their kinematical aspect.

9.1.2 The key missing ingredient: kinetic temperatures

One key missing ingredient, essential for accurately modeling a comprehensive molecular data set is the kinetic temperature. Radiative transfer models often assume generic values and therefore molecular gas temperatures represent a major source of uncertainty in such models. Our VLA K-Band observations at GMC scales targeting Ammonia (NH_3) will solve this. Because the relative strengths of the inversion transitions of NH_3 strongly depend on the temperature of the gas via the Boltzmann equation but are almost independent of density, makes the NH_3 inversion transitions one of the favored temperature probes in the Milky Way and beyond (see Section 4.1). Such an analysis is rare in extragalactic environments because it requires a significant investment in observing time.

The VLA NH_3 observations will allow us to answer how variations in kinetic temperature in different environments (e.g., inner bar ends or distinct regions) are related to local star formation

[1] The exact number of detected molecular emission lines will be able to state after all observations are reduced and imaged. As we expect some additional emission lines to be detected that are covered with our observations, the number of 20 serves as a lower limit.

MOLECULAR DATA SET

Line	ν [GHz]	Ref	Status
C_2H 1(3,2)-0(1,2)	87.316	PdBI	published
HCN (1-0)	88.632		
HCO^+ (1-0)	89.188		
HNC (1-0)	90.664		
HC_3N (10-9)	90.979		
N2H+ (1-0)	93.174		
CH_3OH (2_0-1_0)	96.741		
^{12}CS (2-1)	97.980		
^{12}CO (1-0)	115.271		

Line	ν [GHz]	Ref	Status
CH_3OH (3_0-2_0)	145.100	PdBI	published
HC_3N (16-15)	145.561		
p-H_2CO 2(0,2)-1(0,1)	145.603		
^{12}CS (3-2)	146.969		
^{12}CO (2-1)	230.538		
NH_3 (1,1)	23.694	VLA	Observed
NH_3 (2,2)	23.723		
NH_3 (3,3)	23.870		
NH_3 (4,4)	24.139		

Line	ν [GHz]	Ref	Status
$C^{18}O$ (2-1)	219.56	SMA	Observed
^{13}CO (2-1)	220.40		
^{12}CO (2-1)	230.54		
^{12}CO (3-2)	345.79		
$C^{18}O$ (1-0)	109.782	NOEMA	Reduced
^{13}CO (1-0)	110.201		

Figure 9.1: **Overview of our molecular data set for future projects.** Molecular lines towards the central region of one of the nearest face-on large spiral galaxies in the Northern Hemisphere, NGC 6946 at ~2 – 4″ (PdBI, published in Eibensteiner et al., 2022, PI: E. Schinnerer), at ~4″ (VLA, PI: C. Eibensteiner; observed), at ~3.5″ (SMA, PI: C. Eibensteiner; observed) and at ~2.5″ (NOEMA, PI: C. Eibensteiner; reduced) angular resolution. The various molecular lines all trace different physical states of the molecular ISM

activity (using, for example, the free-free component of the 33 GHz continuum emission as an indicator of star formation rate) and the distribution of dense or shocked gas.

9.1.3 An accurate picture of molecular gas physics

Observations of CO isotopologues help to unravel physical processes such as excitation temperatures, abundances, and optical depth of the molecular gas. Observations of ^{12}CO (1–0), ^{13}CO (1–0), C^{18}O (1–0), ^{12}CO (2–1), ^{13}CO (2–1), C^{18}O (2–1), and ^{12}CO (3–2) at GMC scales (~2-4″) using new observations from NOEMA and SMA (together with the published ^{12}CO (1–0)) together with the robust kinetic temperature estimates (from above) will allow us to accurately quantify the aforementioned physical properties of the molecular gas in an active star-forming CMZ.

The concept behind it is that ratios of optically thin tracers such as ^{13}CO and C^{18}O trace the relative abundance of the two isotopologues within the Milky Way (e.g. Langer and Penzias, 1990) and in extragalactic environments (e.g. Cormier et al., 2018). While this has been a standard analysis in the Milky Way for more than 20 years, it is still almost untouched in the extragalactic domain. This is due to the fact that detecting these faint lines is challenging. Additionally, they offer the opportunity to trace abundance variations due to chemistry or stellar nucleosynthesis (Davis, 2014).

To constrain the optical depth of the gas, the gas column and volume densities of the molecular gas (e.g. Pineda et al., 2008) we can use the ratio of optically thin (e.g. C^{18}O) to optically thick lines (e.g ^{12}CO). Ratios between the ^{12}CO (1–0), ^{12}CO (2–1), and ^{12}CO (3–2) transitions are tracers of CO excitation. Finally, we can use large velocity gradient (LVG) radiative transfer models (e.g. RADEX; a non-LTE radiative transfer code[2]) to relate the observed CO isotopologues intensities to further physical properties (e.g. $n_{\rm H2}$ and $T_{\rm kin}$).

[2] RADEX assumes a homogeneous medium and uses radiative transfer equations based on the escape probability formalism to find a converged solution for the excitation temperature and level population.

Applying the gained knowledge to the full molecular dataset:
The accurate radiative modeling efforts will open up the scientific investigations of all (> 20) molecular lines allowing us to conduct analyses that are common practice in the Milky Way.

(a) Measuring the relative intensities of lines with a wide range of effective critical densities enables us to study different gas densities among different environments (e.g. bar ends).
(b) With derived kinetic temperatures from NH_3 we can test, for example, the HNC/HCN temperature sensitivity framework of Hacar et al. (2020) that has been found in the Milky Way towards the Orion star-forming region.
(c) Chemistry depends on the environment and can affect the abundance of each species (e.g. van Dishoeck, 2014). Comparisons of species that are typically locked within ices, but liberated by shocks, such as HNCO[3] and CH_3OH, will allow us to investigate regions of high energy dynamics (e.g. star formation and feedback Meier et al., 2008). The distribution of the shock tracers can also be compared to the line widths and hence linked to the kinematics/dynamics of the CO lines as well as to star formation rate and molecular gas excitation.

9.1.4 Expanding the extragalactic CMZs sample

Building on this analysis, we could extend it to further extragalactic CMZs, selected from, for example, CO (2−1) observations of extragalactic CMZs in the PHANGS collaboration (targeted with ALMA). A first step would be to get Ammonia observations at high angular resolution[4] with the VLA for those targets that can be observed with VLA[5]. This would provide the foundation and starting point for accurate modeling of the physics of molecular gas in these extragalactic CMZs.

The future is even brighter. With the future new generation VLA (ngVLA), it will be possible to efficiently and rapidly observe and analyze multi-line measurements in nearby galaxies (e.g. NH_3, ^{13}CO, $C^{18}O$, HCN, HCO^+). This opens the prospect of statistical characterization of a variety of different extragalactic CMZs that will revolutionize our understanding of molecular gas physics and its role in star formation.

9.2 Atomic Gas in the Outskirts of Galaxies

The evolution, formation, and dynamics of galaxies is one of the fundamental ongoing research in modern astrophysics. Cold gas accretion from the IGM plays a crucial role in these processes. Exploring the kinematics of H I in nearby galaxies offers the possibility to tackle down these phenomena. Further kinematic analyses of super-extended disks, requires further high resolution high quality observations of possible nearby candidates. Also, individual sub-regions within nearby galaxies, for example, H I rings or connecting branches, are interesting possibilities to analyze the kinematics of H I gas at high spectral and spatial resolution and their relation to turbulent mechanism in the outskirts of disk galaxies. Within the PHANGS collaboration further high sensitive observations of H I are planned (status: to be imaged) which we can use for an extension of the third scientific project,

[3] We expect to detect HNCO in the NOEMA observational setup.
[4] Or, additionally Formaldehyde, which is also commonly used in the Milky Way as a kinetic temperature tracer with ALMA
[5] A majority of the PHANGS-ALMA galaxies are southern hemisphere nearby galaxies that are impossible to observe with a northern hemisphere interferometer.

increasing our sample size from 8 to 18 nearby galaxies. Connecting to the investigation of where and what drives the conversion of atomic to molecular gas, a natural next step is to compare observations with simulations. In summary, we continue studying disk kinematics, rotation and the turbulent nature of the atomic interstellar medium and its role in star formation.

9.2.1 High-resolution view of sub-regions in interesting environmental regions of H I disks with the VLA

Based on the results described in Chapter 6 (and Chapter 7) we want to exploit VLA's capacity to conduct high resolution (mostly A-configuration) observations of interesting sub-regions in nearby spiral galaxies. For example, M83's ring region (region 4 in figure 7; see Appendix B) or the inflection point (region 1) to investigate the nature of turbulence (i.e. velocity dispersion) with sufficient angular and spectral resolution to further explore whether H I turbulence it is driven by star formation feedback, radial transport, or a combination of both (e.g. Krumholz et al., 2018). Another interesting source for a follow up high angular and spectral resolution study would be the interacting galaxies NGC 1512 and NGC 1510.

9.2.2 Extending the current sample

In this whole thesis, we focused on nearby spiral galaxies that are on the main sequence of the Σ_{SFR} – $M_{\star}$ plane as shown in Figure 9.2. Possible avenues are extending this thesis' studies to lower or higher star formation regimes, as in observing early-type galaxies or mergers, respectively. Another possible area of the extension is to the lower stellar mass regime, the atomic-dominated dwarf galaxies. This would allow us to "transfer" a sample like PHANGS, which is designed to study star formation in galaxies, into a sample to study galaxy evolution at high resolution.

The interferometers ALMA and MeerKAT, both located in the southern hemisphere, are not able to observe northern hemisphere galaxies (e.g. NGC 6946 in Chapter 5 that we observed with PdBI, the precursor of NOEMA). Therefore, the PHANGS-ALMA sample contains mostly southern hemisphere galaxies. Another possible step would be to intensively use interferometers like VLA and NOEMA to obtain H I and CO maps for these northern nearby targets.

9.2.3 Low H I low column densities

The above mentioned H I related projects require gathering the observations first. An immediate H I project is to extend the investigation described in Chapter 7 to the MeerKAT cycle 1 highly sensitive observations (thus capturing low H I low column densities, see also Subsection 2.2.2) of additional 10 nearby PHANGS galaxies once they are ready for science (see also purple markers in Figure 9.2). Currently, they are imaged within our collaboration and are expected to be ready to use by the end of 2023 the latest. Together with high-quality data from ALMA it will enable us a better statistical sample and allows us to quantify new physical properties (e.g. star formation rates derived from the PHANGS-MUSE or PHANGS-JWST observations) responsible for converting atomic to molecular gas (analyses that we conducted in Chapter 7). Moreover, we plan to include stacking to recover faint CO emission that we use as our molecular gas tracer.

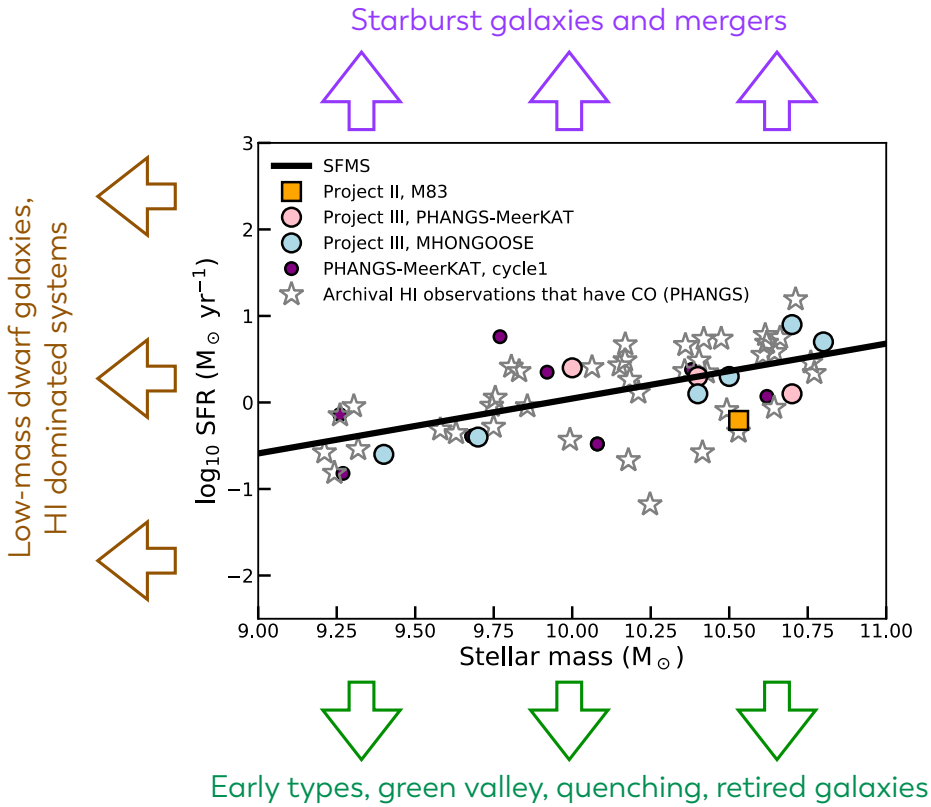

Figure 9.2: **H I observations in nearby galaxies in the SFR-$M_\star$ plane.** We show the star formation main sequence (SFMS) together with the observations described in Chapter 6 (orange square) and Chapter 7 (pink and blue circular markers). The purple markers show highly sensitive MeerKAT H I observations (capturing low H I column densities) within the PHANGS collaboration that are currently imaged. Star markers show PHANGS-VLA and archival H I observations. The next logical step is to (i) perform our analysis including the cycle1 MeerKAT data, and (ii) extend our parameter space to higher and lower star formation rates and lower stellar masses, examining different types of galaxies.

9.2.4 Comparison to simulations of disk galaxies

Our observations and further efforts of exploring the transition of atomic to molecular gas in nearby galaxies, can be compared with simulations that are able to produce Milky Way like maps of H I and CO. This is the case for example in Jeffreson et al., 2020, where they performed high-resolution simulations of three Milky Way-like disk galaxies with the moving-mesh[6] hydrodynamics code Arepo. That would allow us to compare (i) velocity dispersion along the galactocentric radius (analysis mentioned in Chapter 6), (ii) where in a galaxy gas becomes molecular (i.e. $R_{\rm mol} = \Sigma_{\rm H2}/\Sigma_{\rm HI}$ in Chapter 7), and (iii) the correlation of $R_{\rm mol} = \Sigma_{\rm H2}/\Sigma_{\rm HI}$ to the dynamical equilibrium pressure (i.e. $P_{\rm DE}$ in Chapter 7).

[6] In this scenario, a solid material follows the mesh deformation. The movement of a boundary can therefore be considered as bending or punching of the original object. Undeformed and deformed solid objects share the same mass, but the total amount of fluid in a area whose boundaries deform can change.

Appendix

APPENDIX A

A 2-3 mm high-resolution molecular lines survey towards the centre of the nearby spiral galaxy NGC 6946

The paper *Eibensteiner al. A&A (2022), 659, A173* is reproduced below in its original form with permission by ESO.

A&A 659, A173 (2022)
https://doi.org/10.1051/0004-6361/202142624

Astronomy & Astrophysics

A 2–3 mm high-resolution molecular line survey towards the centre of the nearby spiral galaxy NGC 6946⋆

C. Eibensteiner[1], A. T. Barnes[1], F. Bigiel[1], E. Schinnerer[2], D. Liu[3], D. S. Meier[4,5], A. Usero[6], A. K. Leroy[7], E. Rosolowsky[8], J. Puschnig[1], I. Lazar[9], J. Pety[10,11], L. A. Lopez[7], E. Emsellem[12,13], I. Bešlić[1], M. Querejeta[6], E. J. Murphy[14], J. den Brok[1], A. Schruba[3], M. Chevance[15], S. C. O. Glover[16], Y. Gao[17,18], K. Grasha[19], H. Hassani[8], J. D. Henshaw[2], M. J. Jimenez-Donaire[6], R. S. Klessen[16,20], J. M. D. Kruijssen[15], H.-A. Pan[21], T. Saito[2], M. C. Sormani[16], Y.-H. Teng[22], and T. G. Williams[2]

(Affiliations can be found after the references)

Received 9 November 2021 / Accepted 20 December 2021

ABSTRACT

The complex physical, kinematic, and chemical properties of galaxy centres make them interesting environments to examine with molecular line emission. We present new 2−4″ (∼75−150 pc at 7.7 Mpc) observations at 2 and 3 mm covering the central 50″ (∼1.9 kpc) of the nearby double-barred spiral galaxy NGC 6946 obtained with the IRAM Plateau de Bure Interferometer. We detect spectral lines from ten molecules: CO, HCN, HCO^+, HNC, CS, HC_3N, N_2H^+, C_2H, CH_3OH, and H_2CO. We complemented these with published 1 mm CO observations and 33 GHz continuum observations to explore the star formation rate surface density Σ_{SFR} on 150 pc scales. In this paper, we analyse regions associated with the inner bar of NGC 6946 – the nuclear region (NUC), the northern (NBE), and southern inner bar end (SBE) and we focus on short-spacing corrected bulk (CO) and dense gas tracers (HCN, HCO^+, and HNC). We find that HCO^+ correlates best with Σ_{SFR}, but the dense gas fraction (f_{dense}) and star formation efficiency of the dense gas (SFE_{dense}) fits show different behaviours than expected from large-scale disc observations. The SBE has a higher Σ_{SFR}, f_{dense}, and shocked gas fraction than the NBE. We examine line ratio diagnostics and find a higher CO(2−1)/CO(1−0) ratio towards NBE than for the NUC. Moreover, comparison with existing extragalactic datasets suggests that using the HCN/HNC ratio to probe kinetic temperatures is not suitable on kiloparsec and sub-kiloparsec scales in extragalactic regions. Lastly, our study shows that the HCO^+/HCN ratio might not be a unique indicator to diagnose AGN activity in galaxies.

Key words. galaxies: ISM – ISM: molecules – galaxies: individual: NGC 6946

1. Introduction

The study of star-forming regions within galaxy centres is of particular interest, as the extreme conditions within these regions are thought to greatly influence their host giant molecular cloud (GMC) populations, and, thus, the stellar populations that they may form. For example, the inner few kiloparsecs of galaxies typically have higher average gas and stellar densities, gas temperatures, levels of turbulence and magnetic field strengths relative to their discs. All of these characteristics have direct implications for the physical, dynamical and chemical properties of the star-forming 'dense'[1] molecular gas within systems (see e.g. McKee & Ostriker 2007; Lada et al. 2010, 2012; Longmore et al. 2013; Klessen & Glover 2016).

Molecular gas is denser in centres than is typically inferred within disc star-forming regions; the cause of this are strong compressive tidal forces, frequent molecular cloud interactions, short dynamical timescales, constant feeding of material via, for example, bars (e.g. Schinnerer et al. 2006, 2007), and feedback from both young and old stars (e.g. Kruijssen et al. 2019; Chevance et al. 2020a,b; Barnes et al. 2020a) along with energetic phenomena within the galaxy centres (e.g. AGN; Combes et al. 2013; Querejeta et al. 2016) and this should favour star formation. However, it is seen both within the Milky Way (e.g. Kruijssen et al. 2014; Barnes et al. 2017) and inferred at centres of nearby galaxies (e.g. Gallagher et al. 2018a; Jiménez-Donaire et al. 2019) that the gas over-density required to form stars is also higher. Averaged over the galaxy population (and thereby presumably over episodic variations, e.g. Krumholz et al. 2017), centres show an apparent deficit of star formation despite their large quantities of dense molecular gas (e.g. Bigiel et al. 2015; Usero et al. 2015; Jiménez-Donaire et al. 2019 among others). For a complete understanding of star formation, the study of these complex environments present in galaxy centres is crucial.

Observations and simulations of a Milky Way-like galaxy suggest that large-scale bars (a few kiloparsecs) could be responsible for a molecular gas mass build-up in the central few hundred parsecs (e.g. Díaz-García et al. 2020; Renaud et al. 2015; Emsellem et al. 2015; Sormani & Barnes 2019; Sormani et al. 2020). The overlap between the end of those large-scale bars and the spiral arms are – in addition to the centre – active star-forming regions coupled with enhanced dense gas, for example the bar ends of NGC 3627 (Beuther et al. 2017; Bešlić et al. 2021). Secondary small-scale bars (a few hundred parsecs) of double barred galaxies (e.g. Erwin 2011) were intensively studied through photometric analysis (e.g. Méndez-Abreu et al. 2019; de Lorenzo-Cáceres et al. 2020). However, secondary

⋆ Based on observations carried out with the IRAM Plateau de Bure Interferometer (PdBI). IRAM is supported by INSU/CNRS (France), MPG (Germany) and IGN (Spain).

[1] The majority of the discussed studies throughout this work, observed the base transitions of molecules such as HCN and HCO^+, which become excited at effective critical densities of $n > 3 \times 10^3$ cm^{-3} (e.g. Shirley 2015). This is then typically referred to in the literature as 'dense gas', relative to the density of gas traced by CO ($n \approx 10^2$ cm^{-3}).

Article published by EDP Sciences

small-scale bars (we refer to them as 'inner bar' in this work) have been hardly observed with emission from multiple rotational molecular line transitions. This leads us to question if we would find also enhanced molecular line emission (indicating increased gas volume densities) and/or star formation activity at the inner bar ends compared to the surrounding environment (i.e. as with larger scale galactic bars). And how does this relate to the increased dense gas fraction ($f_{\rm dense}$), and yet decreased dense gas star formation efficiency (SFE$_{\rm dense}$), typically observed in galaxy centres.

The emission from rotational molecular line transitions observed within the radio domain is typically used to study the aforementioned properties of the molecular interstellar medium (ISM). Studies conducted over the past several decades found that emission of high-critical-density tracers, such as Hydrogen Cyanide (HCN), Formylium ion (HCO^+), Carbon Monosulfide (CS), and Diazenylium (N_2H^+) are prevalent across galaxy centres, suggesting the presence of large amounts of 'dense' molecular gas (Mauersberger et al. 1989; Mauersberger & Henkel 1989, 1991; Nguyen et al. 1992; Solomon et al. 1992; Helfer & Blitz 1993). More recently, higher angular resolution observations have allowed the study of dense gas content of individual centres of galaxies on sub-kiloparsec scales (e.g. Schinnerer et al. 2007; Pan et al. 2015; Tan et al. 2018 for NGC 6946; Martín et al. 2015 for NGC 253; Murphy et al. 2015 for NGC 3627; Salak et al. 2018 for NGC 1808; Querejeta et al. 2019 for M 51; Bemis & Wilson 2019 for NGC 4038 and NGC 4039; Callanan et al. 2021 for M 83).

Galaxy centres also have a rich and diverse chemistry that could be used to probe the environmental conditions of gas beyond just the density (e.g. Morris & Serabyn 1996; Belloche et al. 2013; Rathborne et al. 2015; Barnes et al. 2019; Petkova et al. 2021 for the Milky Way; Meier & Turner 2005 for IC 342; Meier & Turner 2012 for Maffei 2; Aladro et al. 2013 for NGC 1068; Meier et al. 2015; Leroy et al. 2018; Krieger et al. 2020; Holdship et al. 2021 for NGC 253; Martín et al. 2015 for NGC 1097; Henkel et al. 2018 for NGC 4945). These studies used molecular line ratio diagnostics to investigate the physics and chemistry of the ISM in these extreme environments. But many open questions still remain, such as: how the location of active formation of young massive stars correlate with that of the various molecular line tracers, or, what the ratios between molecular lines indicate about temperature, excitation and density structure in the gas.

NGC 6946 is an ideal candidate to study the effect of large and small scale bars on the dense gas and chemistry through molecular line emission. NGC 6946 has beside its large-scale stellar bar with a length of 100−120″ (≈3.7−4.5 kpc) (Regan & Vogel 1995; Menéndez-Delmestre et al. 2007; Font et al. 2014), a small-scale bar (see below), and is one of the nearest large double-barred spiral galaxies ($D \approx 7.72$ Mpc; see Table 1). It does not seem to host an AGN (see Sect. 6.3) and leads the list of observed supernovae in a nearby galaxy disc (10 supernovae[2]), which has led to its name Fireworks Galaxy.

In this work, we study the inner 50″ ≈ 1.9 kpc of NGC 6946, which has previously been the target for many multi-wavelength observations which we can use to compare to, and build upon, for our analysis. We use ancillary 33 GHz continuum data (Murphy et al. 2018; Linden et al. 2020) to obtain the SFR from the free-free emission part to compare dense gas, total molecular gas, and extinction-free estimates of recent star formation

Table 1. Properties of NGC 6946.

Parameter	Value	Notes
Morphology	SAB(rs)cd	(1)
Nuclear type	Star-forming, H II	(2)
Age of starburst	7−20 Myr	(3)
Distance	7.72 Mpc	(4)
Linear scale	37 pc/arcsec	
Inclination	33°	(5)
PA major axis	242°	(6)
PA minor axis	152°	(6)
$V_{\rm LSR}$	50 km s^{-1}	(7)
Dynamical centre		(7)
RA (J2000)	20:34:52.35	
Dec (J2000)	+60:09:14.58	
Inner bar		
Length	6.5−8″	(7)
NBE, RA	20:34:51.71	This work
NBE, Dec	+60:09:17.21	This work
SBE, RA	20:34:52.67	This work
SBE, Dec	+60:09:11.53	This work

Notes. (1) de Vaucouleurs et al. (1991); (2) Goulding & Alexander (2009); (3) Engelbracht et al. (1996); (4) Anand et al. (2018); they applied the tip of the red giant branch method to measure the distance to NGC 6946. The brightest red giant stars in the outer regions of NGC 6946 were adopted as standard candles. Research on NGC 6946 carried out before 2018 used smaller values for its distance, ranging from 5 Mpc (e.g. Schinnerer et al. 2006) to about 7 Mpc (e.g. Murphy et al. 2011). Where necessary, we convert measurements from the literature to our adopted distance. (5) de Blok et al. (2008); (6) Crosthwaite (2002); (7) Schinnerer et al. (2006).

across the inner star-forming centre of NGC 6946. In the sketch in Fig. 1, we see in green colours three distinct regions in ^{12}CO (2−1) (hereafter CO(2−1)). The appearance of these three features as an S-shaped structure have been explained with modelling efforts in Schinnerer et al. (2006). To do so, they obtained a three-dimensional representation of the luminosity and mass distribution of the galaxy using the multi-Gaussian expansion (MGE) method (see e.g. Emsellem et al. 2003). They then inferred the corresponding axisymmetric gravitational potential by using the Poisson equation and assuming a constant mass-to-light ratio, which is then perturbed by adding a ∼kpc bar-like structure to the MGE potential (as in Emsellem et al. 2003). They showed that their model reproduces the observed (straight) ∼kpc gas lane morphologies, when applying an inner bar with a radius of ∼250 pc (or 6.5−8″ projected into the galaxy plane) with a pattern speed $\Omega_{\rm p}$ of 510−680 km s^{-1} kpc^{-1}. They concluded that molecular gas flows inwards from the outer disc, shaping and driving the evolution of the centre of NGC 6946. Therefore, we refer to their 'clumps' as the bar ends of the inner bar (see green ellipses in the sketch of Fig. 1). This allows us to study different regions in the centre: (a) the nuclear region – NUC, (b) the northern inner bar end – NBE, and (c) the southern inner bar end – SBE, which we refer to as abbreviated above throughout this work.

In this work we present a suite of lines observed across the 1−3 mm IRAM Plateau de Bure Interferometer (PdBI) window [PI: E. Schinnerer] to assess the physical and chemical structure of the inner ∼50″ of NGC 6946 (see Fig. 2). This gives us one of the most comprehensive, high resolution (2−4″ ≈ 75−150 pc) molecular line data set for a nearby galaxy centre in the northern

[2] http://cbat.eps.harvard.edu/lists/Supernovae.html

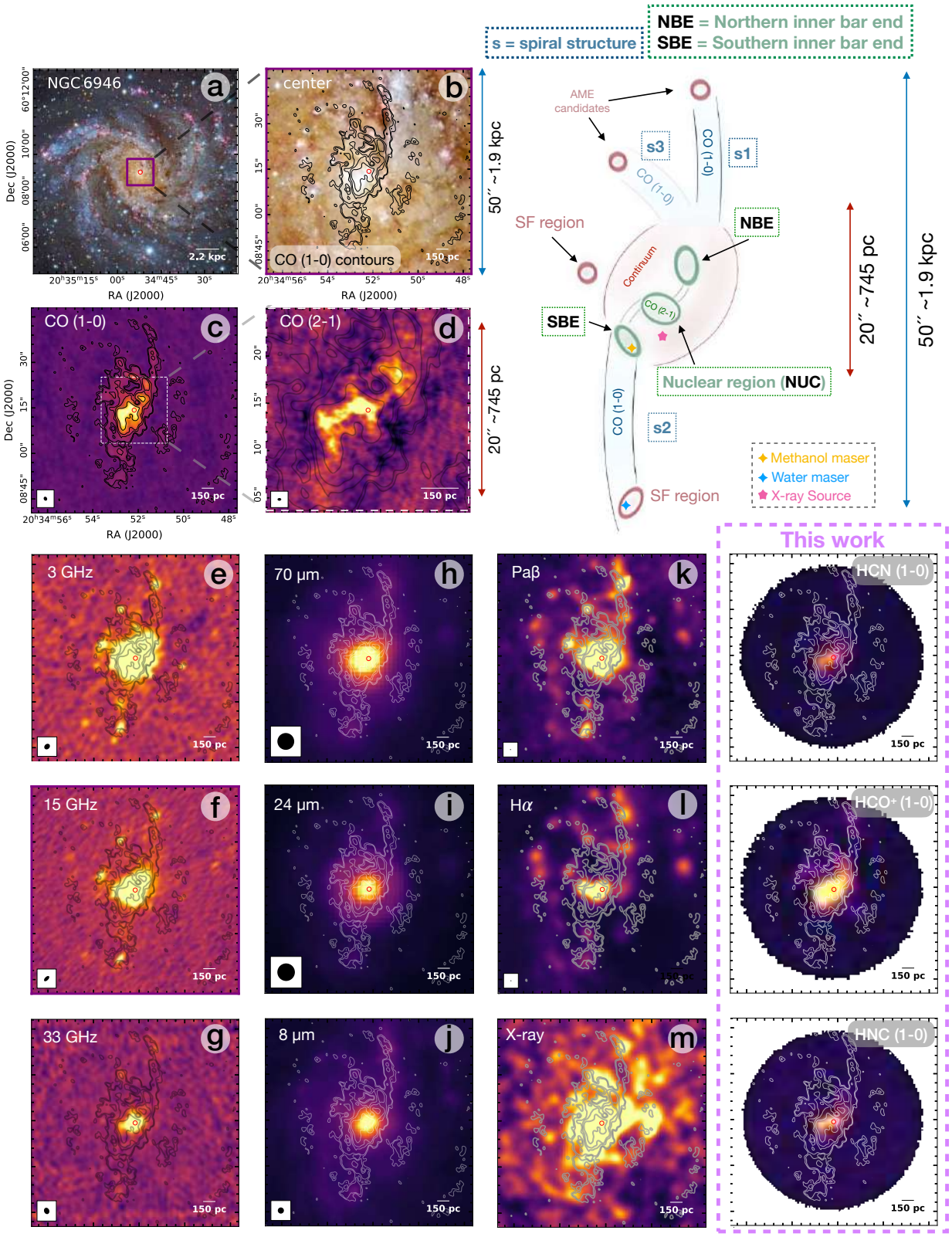

Fig. 1. Gallery of the multi-wavelength observation towards the centre of NGC 6946. *Left panels*: (*a*) three colour optical image, with the region of interest drawn as a purple box, (*b*) CO(1−0) emission shown in contours levels of 60, 90, 200, 300, 600 K km^{-1} s^{-1}, and are repeated on all panels for comparison, (*c*) integrated CO(1−0) emission, (*d*) CO(2−1) emission towards the inner 20″ shown as colour scale; sketch (*right*): denoting all observed features (see Sect. 2.4 for an overview), (*e*)–(*g*) continuum emission, (*h*)–(*j*) infrared emission and (*k*)–(*m*) hydrogen recombination lines and X-ray emission (see Table A.1 for references of all observations shown). The *rightmost column* shows integrated intensity maps of three of our fourteen detected emission lines for comparison. Optical image credits: NASA, ESA, STScI, R. Gendler, and the Subaru Telescope (NAOJ).

Table 2. Summary of the molecular lines in our compiled data set towards the centre of NGC 6946.

	Molecules		$\nu_{\rm rest}$	$\nu_{\rm obs}$	$E_{\rm u}$	$n_{\rm H_2}$ ($\epsilon_{\rm max}$)	$n_{\rm eff}$	Project code	Setup
			[GHz]	[GHz]	[K]	[cm^{-3}]	[cm^{-3}]		
	(1)	(2)	(3)	(4)	(5)	(6)	(7)	(8)	(9)
	C_2H	$N = (1-0), J = 3/2-1/2$	87.316	87.302	4.19			Q059+R02C	A
	HCN	(1−0)	88.632	88.617	4.25	2×10^5	4.5×10^3	Q059+R02C+P069	A
	HCO^+	(1−0)	89.188	89.173	4.28	4×10^4	5.3×10^2	Q059+R02C	A
	HNC	(1−0)	90.664	90.648	4.35	1×10^5	2.3×10^3	Q059+R02C	C
3 mm	HC_3N	(10−9)	90.979	90.964	16.69		4.3×10^4	R09F	C
	N_2H^+	(1−0)	93.174	93.158	4.47		5.5×10^3	R09F	C
	CH_3OH	$J_K = 2_0-1_0$	96.741	96.725	6.96			Q059+R02C	B
	CS	(2−1)	97.980	97.965	7.10		1.2×10^4	R09F+S08E	B
	^{12}CO	(1−0)	115.271	115.252	5.53	1×10^2		M032	D
	CH_3OH	$J_K = 3_0-2_0$	145.100	145.073	18.80			S02A	B
	HC_3N	(16−15)	145.561	145.534	41.27			S02A	B
2 mm	p-H_2CO	$N = (2-1), J = 0/2-0/1$	145.603	145.576	10.48		6.3×10^4	S02A	B
	CS	(3−2)	146.969	146.942	14.11		3.3×10^4	S02A	B
1.3 mm	^{12}CO	(2−1)	230.538	230.499	16.59	1×10^3		M032+P069	One mm

Notes. (1) and (2) Molecular lines with their transition ordered by their rest frequencies; Throughout the paper, for simplicity, we refer to the transitions of C_2H as (1−0), of CH_3 OH as (2−1) and (3−2), and of H_2CO as (2−1). (3) and (4) Rest and observational frequencies. (5) Upper energy levels. (6) Minimum density at which the emissivity of the line reaches 95% of its peak value for $T = 25$ K (see Table 2 within Leroy et al. 2017 and references therein). (7) Taken from Shirley (2015) (Table 1, for 20 K), and have been defined by radiative transfer modelling as the density that results in a molecular line with an integrated intensity of 1 K km s^{-1}. (8) and (9) PdBI project code and setup. A = configuration C and D; B = configuration A, B, C, D; C = configuration B, C, D.

hemisphere. In this first of a series of papers, we present the observations and especially focus on the short-spacing corrected bulk (CO) and dense gas tracers (HCN, HCO^+, and HNC).

This paper is structured as follows: In Sect. 2, we present how the PdBI observations were taken, calibrated and imaged, along with information of the ancillary observations used within this work and how we convert observational measurements to physical quantities. Section 3 shows the results and Sect. 4 the discussion of our extended data set. In Sect. 5, we show the results from our short-spacing corrected data set focusing on the nuclear region and inner bar ends. In Sect. 6, we discuss line ratio diagnostics of the short-spacing corrected data set and possible implications for spectroscopic studies of other galaxy centres.

2. Observations and ancillary data

2.1. PdBI observations and data reduction

The Plateau de Bure Interferometer (PdBI) was used to image molecular lines at 1.3 to 3 mm using a single pointing focusing on the central 50″ of NGC 6946 for a total of 132 h from 2002 to 2009. Eight high-resolution spectral windows were used in each observation, each offering a bandwidth of 160 MHz and channel width of 2.5 MHz (i.e. 9 km s^{-1} at 87 GHz). The data, acquired from multiple observations (project codes: Q059, R02C, R09F, S02A, R09F, S08E, P069, M032 and S02A; PI: Schinnerer), were split between five spectral setups at reference frequencies of ∼87 GHz (setup A), ∼97 GHz (setup B), ∼92 GHz (setup C), ∼115 GHz (setup D) and ∼230 GHz (setup one mm). We identified in the spectral setup A: $C_2H(1-0)$, $HCO^+(1-0)$ and HCN(1−0), in setup B: $CH_3OH(2-1)$, CS(2−1), $CH_3OH(3-2)$, $HC_3N(16-15)$, $H_2CO(2-1)$ and CS(3−2), in setup C: HNC(1−0), $HC_3N(10-9)$ and $N_2H^+(1-0)$, in setup D: CO(1−0), in setup one mm: CO(2−1) (see Table 2). The primary beam FWHM ranges from ∼57″ at 87 GHz to ∼43″ at 115 GHz and ∼22″ at 230 GHz. The spectral window of each molecular line was centred on the redshifted frequency of the line assuming a systemic velocity of 50 km s^{-1} for NGC 6946 (Schinnerer et al. 2006). The imaged width in each spectral window is the velocity width at zero level of the CO(1−0) line (300 km s^{-1}, matching the Full Width at Zero Intensity of the HI line seen by THINGS in Walter et al. 2008) plus 50 km s^{-1} on each side of the line centre. These data were all calibrated and imaged using `GILDAS`[3]. For the bandpass calibration, observations of the bright quasars 3C 454.3, 2145+067, 0923+392 and 3C 273 have been used. The phase and amplitude calibrators were either both 2037+511 and 1928+738 or one of them. These calibrators were observed every 20 min. Most of the observations compared MWC 349 observations with its IRAM flux model to calibrate the absolute flux scale. We expect an accuracy of the flux calibration of about 5% at 3 mm and a typical antenna aperture efficiencies of about 25 Jy K^{-1} at 3 mm, and 28 Jy K^{-1} at 2 mm data.

The continuum emission has been combined with the `UV MERGE` task after excluding the line channels. The spectral lines were resampled to 10 km s^{-1} for all the lines during the creation of UV tables in the `GILDAS CLIC` environment. The continuum has been subtracted in the $u-v$ plane with the above continuum $u-v$ table extracted from all line-free channels with the `UV SUBSTRACT` task before the imaging. Imaging of the visibilities used natural weighting, where each visibility is weighted by the inverse of the noise variance, as this maximises the sensitivity. The field of view of each image is twice the primary beam with pixel sizes 1/4 of the synthesised beam major axis FWHM size (ranging from 0.4″ × 0.29″ to 2.0″ × 1.7″ and 3.6″ × 2.9″, see Table 3).

`Cleaning` was performed with a preconstructed clean mask which has been produced similar to the signal identification methodology used in `CPROPS` (Rosolowsky & Leroy 2006; Rosolowsky et al. 2021; Leroy et al. 2021) using the high resolution (∼1″) CO(1−0) PdBI data without short-spacing correction (Schinnerer et al. 2006). Following Leroy et al. (2021; for the PHANGS-ALMA survey), the clean mask creation includes the following steps: (a) convolving the CO(1−0) beam from ∼1″

[3] `http://www.iram.fr/IRAMFR/GILDAS`

Table 3. Properties of the PdBI only data set.

	Native resolution		Characteristics at 4″ resolution							
	Beam size	PA	$I_{\rm line}$	$T_{\rm peak}$	Noise	S/N	Ratios with			
Molecules	[″]	[°]	[K km s^{-1}]	[K]	[K km s^{-1}]		CO(2−1)	CO(1−0)	HCN	$\Sigma_{\rm SFR}$
(1)	(2)	(3)	(4)	(5)	(6)	(7)	(8)	(9)	(10)	(11)
^{12}CO (1−0)	1.36 × 1.11	26	748.04	8.80	2.85	262.72	2.52	1.00	13.04	8.31E+01
^{12}CO (2−1)	0.40 × 0.29	91	296.40	4.75	2.20	134.56	1.00	0.40	5.17	3.29E+01
HCN (1−0)	2.61 × 2.12	97	57.35	0.62	0.71	80.65	0.19	0.08	1.00	6.37E+00
HCO$^+$ (1−0)	3.45 × 2.83	−101	47.94	0.53	0.52	92.43	0.16	0.06	0.84	5.31E+00
HNC (1−0)	2.45 × 2.00	62	22.06	0.32	0.62	35.66	0.07	0.03	0.38	2.45E+00
CS (2−1)	1.89 × 1.60	97	29.39	0.40	0.72	40.57	0.01	0.04	0.51	3.26E+00
CS (3−2)	1.98 × 1.76	−180	21.07	0.30	0.28	76.00	0.07	0.03	0.37	2.34E+00
N_2H^+ (1−0)	2.39 × 1.96	65	6.43	0.21	0.49	13.02	0.02	0.01	0.11	7.14E−01
HC_3N (10−9)	2.41 × 1.98	64	4.06	0.09	0.68	5.93	0.01	0.01	0.07	4.51E−01
HC_3N (16−15)	2.02 × 1.77	339	2.25	0.08	0.39	5.72	0.01	0.01	0.04	2.50E−01
CH_3OH (2k−1k)	1.89 × 1.59	98	7.15	0.27	0.66	10.77	0.02	0.01	0.12	7.95E−01
CH_3OH (3k−2k)	1.98 × 1.76	−17	6.12	0.28	0.55	11.09	0.02	0.01	0.11	6.80E−01
C_2H (1−0), 3/2−1/2	3.54 × 2.84	77	12.78	0.14	0.72	17.76	0.04	0.02	0.22	1.42E+00
H_2CO (2−1)	1.99 × 1.75	343	2.29	0.08	0.35	6.61	0.01	0.01	0.04	2.54E−01

Notes. We arranged the PdBI only data set as in Fig. 3 and show them at their native and best-common 4″ ≈ 150 pc spatial resolution. Column (1) Molecules and their transitions. (2) and (3) Characteristics of the native resolution observation. (4)−(11) We quote the mean for the central sight line, i.e. aperture of 4″ ≈ 150 pc. (4) Integrated intensity. (5) Peak temperature of the spectrum. (6) Root mean square (rms) noise. (7) Signal to noise. (8)−(11) Ratios of molecular species with CO, HCN and $\Sigma_{\rm SFR}$. The $I_{\rm line}/\Sigma_{\rm SFR}$ ratio results in units of K km s^{-1}/($M_\odot$ yr^{-1} kpc^{-2}).

to a coarser resolution of 33″ and smoothing along the spectral axis with a boxcar function with a width of 20 km s^{-1}; (b) selecting peak pixels for each channel which have a S/N of at least 4; (c) expanding each peak down to a S/N of 2; (d) binary-dilating 4 channels along the spectral axis to account for edge effect. This produces a clean mask that covers all possible CO signal regions and ensures that the cleaning of other molecular gas tracers is less affected by noisy, no-signal regions outside the mask. The typical rms per channel observed is ≈2 mJy beam^{-1}.

Before being used in the deconvolution, the clean mask was regridded to match the astrometry of the dirty cube of each line. After imaging and deconvolution we corrected for the primary beam attenuation. We provide the observational characteristics of the PdBI only data in Table 3 (and show the channel maps in Figs. A.3–A.14).

Given that these data have different u−v coverage, we built a homogenised product by imaging only the visibilities that are within the u−v coverage of the CO(1−0) PdBI data, that is 11.5 to 153.8 kλ. We do this to match the spatial scales of the CO data. This has been done using a `GILDAS` script where we loop through all the visibilities and flag the ones outside the CO(1−0) u−v range by assigning negative weights to them. Then the `UV TRIM` function was used to discard the flagged data.

Interferometric observations are insensitive to emission with low spatial frequencies due to the lack of the shortest baselines. For the short-spacing correction, we utilise IRAM 30 m observations. We use data of the EMIR Multiline Probe of the ISM Regulating Galaxy Evolution (EMPIRE; Jiménez-Donaire et al. 2019) survey which observed in the 3−4 mm regime, in particular, HCN across the whole disc of nine nearby spiral galaxies, among them NGC 6946. For the purpose of short-spacing correction (SSC) we use their 33″ resolution HCN(1−0), HCO$^+$(1−0) and HNC(1−0) maps. For the CO(2−1) observations, we use data from the HERA CO-Line Extragalactic Survey (HERACLES) (Leroy et al. 2009). For the remaining PdBI detected molecules we do not find public single-dish data with a significant S/N[4], therefore, no SSC was feasible for them.

SSC has been done in `GILDAS` in its `MAPPING` environment. Before performing SSC on the data available, we ensured that the 30 m data used the same projection center and spectral grid as the interferometric data, before applying the `UVSHORT` task. This produces pseudo-visibilities that fill the short-spacings before imaging and deconvolution (see Rodriguez-Fernandez et al. 2008; Pety et al. 2013 for details). We summarise the observational characteristics of the SSC + u−v trim data in Table 4.

In summary, within this work we make use of the following data sets: PdBI only, which includes 14 molecular emission lines, and SSC + u−v trim, which includes five molecular emission lines.

2.2. Integrated intensity maps

As a next step, we converted our PdBI only and SSC + u−v trim data cubes from units of Jy beam^{-1} to brightness temperature, $T_{\rm b}$, measured in Kelvin. Our observations include emission lines from a wavelength range of 1 to 3 mm which results in various spatial resolutions. We convolved our data to a common beam size of 4″ (corresponding to 150 pc at 7.72 Mpc distance) and sampled the integrated intensities onto a hexagonal grid. The grid points are spaced by half a beam size to approximately Nyquist sample the maps. This approach has the advantage that the emission lines can be directly compared.

To improve the signal-to-noise ratio (S/N) we applied a masking routine for the determination of the integrated intensity maps. We used the bright CO(1−0) emission line as a prior for masking and produced two S/N cuts: a low S/N mask ($S/N > 2$) and a high S/N mask ($S/N > 4$). Subsequently, the high S/N mask is expanded into connected voxels in the low S/N mask,

[4] We note that the 3 mm emission lines of C_2H, N_2H^+, and HC_3N were covered by EMPIRE, but not included in the public release.

Table 4. Properties of the SSC + $u-v$ trim data set.

	Characteristic after SSC			Characteristic at 4″ resolution				Ratios with			
	Beam size	PA	Recov. flux	$I_{\rm line}$	$T_{\rm peak}$	Noise	S/N				
Molecules	[″]	[°]	[%]	[K km s^{-1}]	[K]	[K km s^{-1}]		CO(2−1)	CO(1−0)	HCN	$\Sigma_{\rm SFR}$
(1)	(2)	(3)	(4)	(5)	(6)	(7)	(8)	(9)	(10)	(11)	(12)
^{12}CO (1−0)	1.37 × 1.12	25	52.8	892.75	9.33	3.60	247.75	1.52	1.00	13.13	97.46
^{12}CO (2−1)	0.96 × 0.90	−160	25.2	587.38	6.36	2.24	262.39	1.00	0.65	8.64	64.13
HCN (1−0)	2.90 × 2.57	93	60.2	67.97	0.67	0.58	116.90	0.12	0.07	1.00	7.42
HCO$^+$ (1−0)	3.62 × 3.07	82	53.2	54.74	0.57	0.51	106.57	0.09	0.06	0.81	5.98
HNC (1−0)	2.90 × 2.57	55	68.1	25.16	0.34	0.62	40.52	0.04	0.03	0.37	2.75

Notes. We show the short-spacing corrected and $u-v$ trimmed data set at their native and best-common 4″ ≈ 150 pc spatial resolution. Column (1) Molecules and their transition. (2)−(4) Characteristics after the short-spacing correction at their native resolution and recovered flux compared to PdBI only data set (see Table 3). (5)−(12) We quote the mean for the central sight line, i.e. aperture of 4″ ≈ 150 pc. (5) Integrated intensity. (6) Peak temperature of the spectrum. (7) Root mean square (rms) noise. (8) Signal to noise. (9)−(12) Ratios of molecular species with CO, HCN and $\Sigma_{\rm SFR}$. The $I_{\rm line}/\Sigma_{\rm SFR}$ ratio results in units of K km s^{-1}/($M_\odot$ yr^{-1} kpc^{-2}).

and the integrated intensity is determined by integrating along the velocity axis for each of the individual sight lines multiplied by the channel width, $\Delta v_{\rm chan}$, of 10 km s^{-1}:

$$I = \sum_{n_{\rm chan}} T_{\rm b} \times \Delta v_{\rm chan}. \quad (1)$$

The uncertainty is calculated taking the square root of the number of masked channels ($n_{\rm chan}$) along a line of sight multiplied by the 1σ root mean square ($\sigma_{\rm rms}$) value of the noise and the channel width:

$$\sigma_I = \sqrt{n_{\rm chan}} \times \sigma_{\rm rms} \times \Delta v_{\rm chan}. \quad (2)$$

We calculate $\sigma_{\rm rms}$ over the signal-free part of the spectrum using the `astropy` (Astropy Collaboration 2013, 2018) function `mad_std` that calculates the median absolute deviation and scales it by a factor of 1.4826. This factor results from the assumption that the noise follows a Gaussian distribution. We show the integrated intensity maps of the PdBI only data in Fig. 2.

2.3. Ancillary data

We include ancillary data for investigating the central regions of NGC 6946 and analysing the relationship of our detected molecules to star formation rate (SFR) tracers. We also compare NGC 6946 with other galaxy centers. Therefore, we include (1) 33 GHz continuum emission, (2) EMPIRE dense gas observations of eight additional galaxy centres (angular resolution of 33″ ≈ 1 kpc), (3) high resolution resolution dense gas observations of M 51 (∼4″ ≈ 166 pc) and NGC 3627 (∼2″ ≈ 100 pc), and (4) 0.5−7.0 keV X-ray observations of NGC 6946.

2.3.1. SFR tracers

Tracers of the number of ionizing photons, specifically free-free radio continuum emission and hydrogen recombination lines, are often regarded as good indicators of massive star formation. The radio continuum emission at low frequencies consists of two components: (1) thermal free-free emission directly related to the production rate of ionizing photons in H II regions and (2) non-thermal emission arising from cosmic ray electrons or positrons which propagate through the magnetised ISM after being accelerated by supernova remnants or from AGN. Concentrating on the first case, only stars more massive than ∼8 $M_\odot$ are able to produce a measurable ionising photon flux (see e.g. Murphy et al. 2012; Kennicutt & Evans 2012).

For NGC 6946 we find recently published 33 GHz continuum emission, which best match with the angular resolution of our molecular data set (∼2.1″ angular resolution, see Figs. 1g and 4). These data are from Very Large Array (VLA) observations within the Star Formation in Radio Survey (SFRS; Murphy et al. 2018; Linden et al. 2020). In this work, we use the (1) thermal free-free emission of the 33 GHz continuum emission as a SFR tracer (see below). We discuss the reasons why we preferred 33 GHz and check for consistency in the Appendix A.

2.3.2. Calibration of the SFR

The calibration of a variety of SFR indicators has been described in detail by Murphy et al. (2011). They used `Starburst99` (Leitherer et al. 1999) together with a Kroupa (2001) initial mass function (IMF). This type of IMF has a slope of −1.3 for stellar masses between 0.1 and 0.5 $M_\odot$, and a slope of −2.3 for stellar masses ranging between 0.5 and 100 $M_\odot$. Together with their assumptions of a continuous, constant SFR over ∼100 Myr, their `Starburst99` stellar population models show a relation between the SFR and the production rate of ionizing photons, $Q(H^0)$, as:

$$\frac{\rm SFR}{[M_\odot\,{\rm yr}^{-1}]} = 7.29 \times 10^{-54}\,\frac{Q(H^0)}{[{\rm s}^{-1}]}. \quad (3)$$

For the 33 GHz continuum map, we need to separate the (1) thermal free-free and (2) non-thermal (synchrotron) parts of the emission. The thermal emission (denoted by T) scales as $S_\nu^{\rm T} \propto \nu^{-\alpha^{\rm T}}$, where ν refers to the frequency in GHz. To convert the thermal flux into a SFR, we follow Eq. (11) from Murphy et al. (2011):

$$\frac{{\rm SFR}_\nu^{\rm T}}{[M_\odot\,{\rm yr}^{-1}]} = 4.6 \times 10^{-28} \left(\frac{T_{\rm e}}{[10^4\,{\rm K}]}\right)^{-0.45} \times \left(\frac{\nu}{[{\rm GHz}]}\right)^{-\alpha^{\rm T}} \frac{L_\nu^{\rm T}}{[{\rm erg\,s^{-1}\,Hz^{-1}}]}, \quad (4)$$

where $T_{\rm e}$ is the electron temperature in units of 10^4 K, ν refers to the frequency in GHz, and $L_\nu^{\rm T}$ is the luminosity of the free-free emission at frequency ν in units of erg s^{-1} Hz^{-1}.

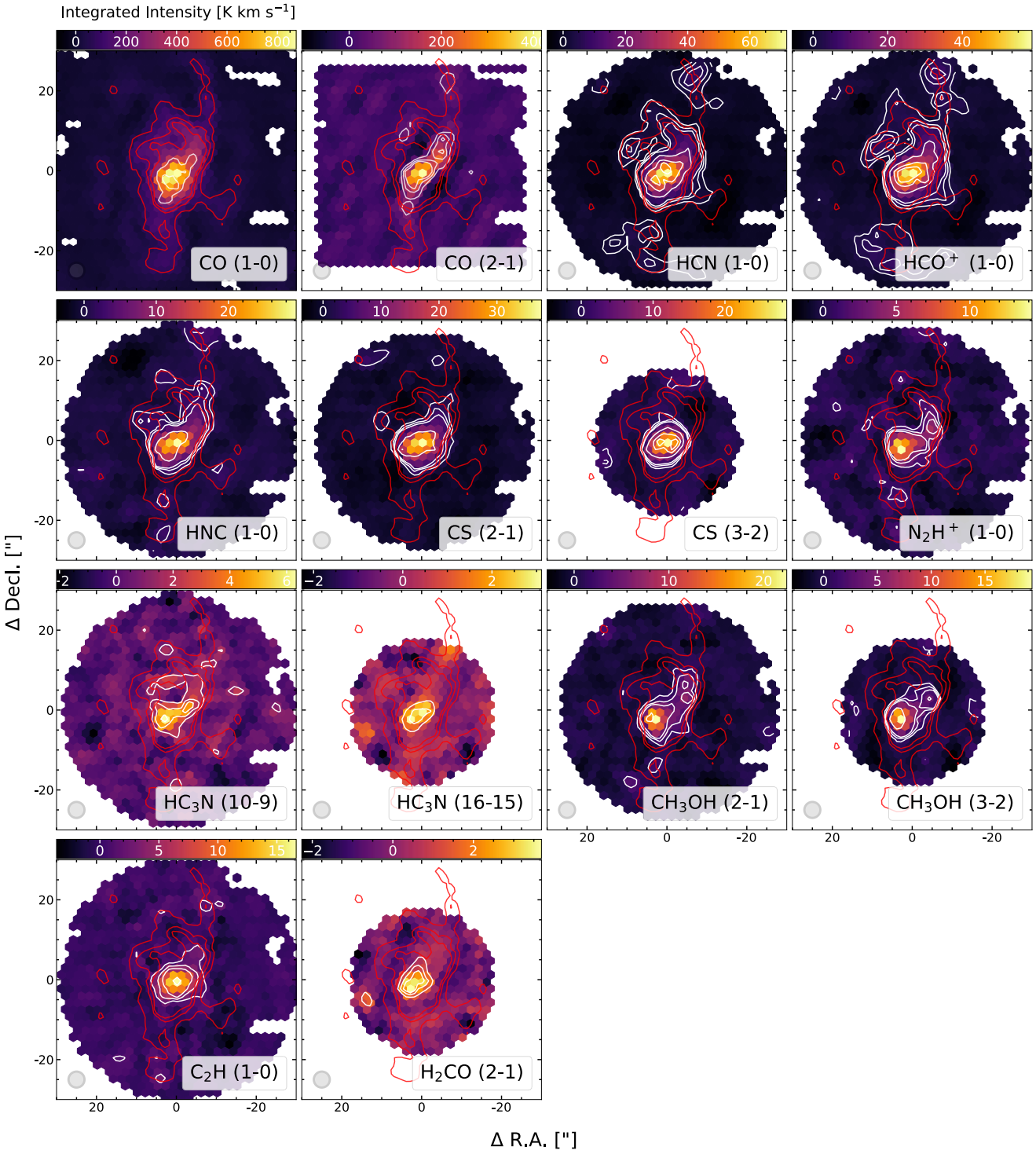

Fig. 2. Integrated intensity maps (moment 0) for 14 molecular emission lines at a common resolution of 4″ ≈ 150 pc. The maps were created using a hexagonal sampling with half a beam spacing, where CO(1−0) was used as a mask. The grey shaded circle in the lower left corner marks the beam size and the red contours show CO(1−0) S/N levels of 30, 60 and 90. The white contours in the *first panel* show S/N levels of 200 and 300, and in the *second panel* S/N levels of 30, 60 and 90. The following panels (from HCN to $H_2CO(2-1)$) show S/N levels of 3, 6, 9, 30, 60 and 90. The colourbar indicates the integrated intensity of each line in units of K km s^{-1}. See Table 1 for the properties of this data set.

We adopt $\alpha^{\mathrm{T}} = 0.1$ and a thermal fraction of $f^{\mathrm{T}}_{33\,\mathrm{GHz}} = 0.62$ (as in Murphy et al. 2011 for the nucleus of NGC 6946) and calculate the luminosity of the thermal free-free emission at frequency ν:

$$\frac{L^{\mathrm{T}}_{\nu}}{[\mathrm{erg\,s^{-1}\,Hz^{-1}}]} = \frac{L}{[\mathrm{erg\,s^{-1}\,Hz^{-1}}]} \times f^{\mathrm{T}}_{33\,\mathrm{GHz}}. \quad (5)$$

Together with $T_{\mathrm{e}} = 0.42$ in units of 10^4 K (again as in Murphy et al. 2011 for the nucleus of NGC 6946) and Eq. (5) we can solve Eq. (4) and get a $\mathrm{SFR}^{\mathrm{T}}_{33\,\mathrm{GHz}}$ map in units of $M_{\odot}\,\mathrm{yr}^{-1}$. We discuss the mean values within 150 pc sized apertures (i.e. the 4″ working resolution) containing the NUC, SBE, or NBE regions in Sect. 4. In this work, we also use SFR surface

densities ($\Sigma_{\rm SFR}$) in units of $M_\odot\,{\rm yr}^{-1}\,{\rm kpc}^{-2}$ for scaling relations in Sect. 5.2. We define $\Sigma_{\rm SFR}$ as:

$$\frac{\Sigma_{\rm SFR}}{[M_\odot\,{\rm yr}^{-1}\,{\rm kpc}^{-2}]} = \frac{{\rm SFR}_{33\,{\rm GHz}}}{[M_\odot\,{\rm yr}^{-1}]}\left(\frac{\Omega}{[{\rm kpc}^{-2}]}\right)^{-1}, \quad (6)$$

where Ω is:

$$\frac{\Omega}{[{\rm kpc}^{-2}]} = \left(\pi\left[\frac{\theta_{\rm bmaj}}{[{\rm arcsec}]}\left(\frac{d}{[{\rm kpc}]}\,\psi^{-1}\right)\right]\times\left[\frac{\theta_{\rm bmin}}{[{\rm arcsec}]}\left(\frac{d}{[{\rm kpc}]}\,\psi^{-1}\right)\right]\right)\times[(4\,\ln(2))]^{-1}. \quad (7)$$

Here, $\theta_{\rm bmaj}$ and $\theta_{\rm bmin}$ are the major and minor axis of the beam in arcsec, d the distance to NGC 6946 in kpc and ψ is the factor to convert from rad to arcsec (i.e. $(3600\times180)/\pi$).

2.3.3. Molecular gas mass and depletion time

The molecular gas mass surface density can be estimated from the CO(1−0) line emission in our data set. Given that H_2 is the most abundant molecule, the conversion of CO emission to molecular gas mass surface density is related to the CO-to-H_2 conversion factor $\alpha_{\rm CO}$. We adopt a fixed conversion factor $\alpha_{\rm CO} = 0.39\,M_\odot\,{\rm pc}^{-2}\,({\rm K\,km\,s}^{-1})^{-1}$ corrected for helium (Sandstrom et al. 2013; from their Table 6 for the centre of NGC 6946). This low, central $\alpha_{\rm CO}$ value of NGC 6946 (a factor ∼10 lower than the canonical Milky Way value of $4.36\,M_\odot\,{\rm pc}^{-2}\,({\rm K\,km\,s}^{-1})^{-1}$; see Bolatto et al. 2013) agrees with other studies (e.g. Cormier et al. 2018; Bigiel et al. 2020) and will not affect the main results in this paper. Then we convert the CO(1−0) integrated intensity, $I_{\rm CO}^{1-0}$, to the molecular gas mass surface density, $\Sigma_{\rm mol}$, via:

$$\frac{\Sigma_{\rm mol}}{[M_\odot\,{\rm pc}^{-2}]} = \alpha_{\rm CO}\,\frac{I^{1-0}_{\rm CO,\,150\,pc}}{[{\rm K\,km\,s}^{-1}]}\,\cos(i). \quad (8)$$

Here, $I^{1-0}_{\rm CO,\,150\,pc}$ stands for $I^{1-0}_{\rm CO}$ convolved to 150 pc (4″) FWHM and the cos(i) factor corrects for inclination. We note, that the conversion from observed to physical quantity is subject to uncertainties for example, the low-J transition of ^{12}CO is known to be optically thick and does not necessarily peak in the 1−0 transition in many environments. These, together, may result in a less accurate CO to H_2 conversion, particularly towards starburst or AGN regions, yet this is most likely still secondary compared to the uncertainty on the $\alpha_{\rm CO}$ (e.g. due to metallicity). The ratio of the two profiles $\Sigma_{\rm mol}/\Sigma_{\rm SFR}$ is the molecular gas depletion time, the time it takes (present day) star formation to deplete the current supply of molecular gas:

$$\frac{\tau^{\rm mol}_{\rm depl,\,150\,pc}}{[{\rm yr}^{-1}]} = \frac{\Sigma_{\rm mol}}{[M_\odot\,{\rm pc}^{-2}]}\left(\frac{\Sigma_{\rm SFR}}{[M_\odot\,{\rm yr}^{-1}\,{\rm kpc}^{-2}]}\times\frac{\gamma}{[{\rm kpc}^2\,{\rm pc}^{-2}]}\right)^{-1}. \quad (9)$$

Here, γ stands for the conversion factor to get from $\rm kpc^{-2}$ to $\rm pc^{-2}$. Equation (9) implies that all the molecular gas traced by CO will turn into star formation fuel which is an overestimate. We use CO to define $\tau^{\rm mol}_{\rm depl,\,150\,pc}$ because we later compare it to literature values that used the same method to calculate $\tau^{\rm mol}_{\rm depl}$; this does not affect the main results of this work.

2.3.4. EMPIRE dense gas data, high-resolution M 51 and NGC 3627 data

In Sect. 6 we discuss line ratio diagnostic plots of the dense gas tracers HCN, HCO^+ and HNC. To compare NGC 6946 with other galaxy centres, we use available observations of additional eight galaxy centres covered in the EMPIRE survey (Jiménez-Donaire et al. 2019). Those data products have a common angular resolution of 33″ (≈1 kpc). For the analysis in Sect. 6.3 we also include high resolution observations of the dense gas tracers for: (i) M 51 and (ii) NGC 3627. The M 51 short-spacing corrected observations have an angular resolution of ∼4″ (≈166 pc) and their reduction are described in Querejeta et al. (2016). We used the same technique as for the NGC 6946 observations described in Sect. 2.2 to sample the data on a hexagonal grid and produce integrated intensity maps with a common angular resolution of 4″. We have also done this for the NGC 3627 observations, which have an angular resolution of ∼2″ (≈100 pc); their short-spacing correction and reduction are described in Bešlić et al. (2021).

2.3.5. X-ray

We also compare our observations to *Chandra* ACIS-S observations (ObsIDs 1054 and 13435) from 2001 (PI: S. Holt; Holt et al. 2003) and 2012 (PI: C. Kochanek) totalling 79 ks. We reduced the data using the *Chandra* Interactive Analysis of Observations (`ciao`) Version 4.9 and produced exposure-corrected images using the `ciao` command *merge_obs*. Point sources were identified using *wavdetect* on the merged, broad-band (0.5−7.0 keV) image and were removed with *dmfilth* to create the X-ray image shown in Sect. 6.3. We also show a version of the X-ray diffuse, hot gas that has been smoothed with a Gaussian kernel (FWHM of 3) in Fig. 1m.

2.4. Multi-wavelength gallery of the central region of NGC 6946

Figure 1 shows a compilation of the various observations towards the inner 50″ ≈ 1.86 kpc of NGC 6946 (see Table A.1 for details on the observations). The centre appears to have several branches that connect to the outside environment. The two more pronounced spiral-like structures running north and south (extending 50″) are most apparent in ^{12}CO(1−0) (published in Schinnerer et al. 2006) (c) and to some extent also in the infrared emission (h)–(j). Another spiral-like structure could be presumed from these observations. Preceding studies even assumed four spiral features (Regan & Vogel 1995), which are not apparent in this CO map. The sketch on the top right shows the two prominent spiral-like structures and the third presumable one as blue coloured arcs.

The red coloured ellipse in the sketch (extending 20″ ≈ 750 pc) denotes the radio continuum emission (e)–(g). In the 70 μm, 24 μm, 8 μm, Paβ, Hα and X-ray emission (h)–(m), we likewise find emission in this region. In maps (e)–(m), however, no substructures are visible within the red ellipse due to high saturation or limited angular resolution. In contrast to that, CO(2−1) reveals the nuclear region and two additional features to the north and south, illustrated as green ellipses in the sketch (central ∼10″ ≈ 372 pc). Schinnerer et al. (2006) showed with dynamical models that the structures of CO(2−1) can be explained with an inner bar (first observed and proposed via FIR by Elmegreen et al. 1998). The two inner bar ends (NBE and SBE) are connected to the nuclear region by straight gas lanes

running along a position angle of PA ∼ 40°. Those regions are also bright in emission in HCN, HCO^+ and HNC (see Sect. 3).

The four additional red ellipses in the sketch, most visible in the continuum emission (e)–(f), were identified by Linden et al. (2020). The southern two are associated with star formation (SF) regions and the northern two are suggested to be anomalous microwave emission (AME) candidates (Linden et al. 2020). The exact mechanism causing AMEs is not entirely understood, but the most promising explanation is that they occur due to small rotating dust grains in the ISM (see the review on AMEs by Dickinson et al. 2018). One of the techniques to identify AMEs is to investigate the 33 GHz/Hα flux ratio (Murphy et al. 2018). Larger ratios of 33 GHz flux to Hα line flux would arise by an excess of non-thermal radio emission (see Fig. 4 in Murphy et al. 2018; ratios of $\sim 10^9$). Using 7″ apertures in diameter for the two AME candidates we find 33 GHz/Hα ratios of $\sim 10^9$ expected for AME emission. This would confirm them being AME candidates.

Within the southern SF region, at the end of the CO(1−0) southern spiral structure, Gorski et al. (2018) found a water maser (H_2O (6_{16}−5_{23}) at 22.235 GHz) and within the southern inner bar end two methanol masers (CH_3OH (4_{-1}−3_0) at 36.169 GHz), marked as blue and orange stars in the sketch. The water maser is associated with one of the identified SF regions of Linden et al. (2020). Water masers can be in general variable on timescales of a few weeks and could indicate YSOs or AGB stars (Palagi et al. 1993). Billington et al. (2020) showed within the Milky Way the relationship between dense gas clumps and water masers. The location of the water maser matches well with the SF region seen in the Hα and 33 GHz maps.

3. Results – Molecules in different environmental regions in the centre of NGC 6946

We investigate how the molecular species in our data set spatially vary in the inner kiloparsec of NGC 6946. Our compiled data set contains 14 molecular emission lines obtained with the IRAM PdBI covering the inner 50″ ≈ 1.9 kpc of NGC 6946, which are summarised in Table 3. Their intensity maps can be seen in Fig. 2 showing the integrated intensities for the detected molecular lines.

3.1. The substructures in the inner kiloparsec of NGC 6946

In every map of Fig. 2 we detect significant emission in the inner 10″ ≈ 375 pc. We note that we have for the first time detected ethynyl C_2H(1−0), cyanoacetylene HC_3N(10−9) and HC_3N(16−15) in the inner kiloparsec of NGC 6946. All other molecules have been detected previously, mostly at lower resolution (e.g. ∼30″ HNC(1−0) and N_2H^+(1−0): Jiménez-Donaire et al. 2019; 25″ and 17″ CH_3OH(2−1), CH_3OH(3−2), H_2CO(2−1): Kelly et al. 2015; 8″ HCO^+(1−0): Levine et al. 2008; 1″ HCN(1−0): Schinnerer et al. 2007).

The spiral structures. We see several branches that seem to be connected to the outside environment. The two more prominent spiral-like structures are best visible in the integrated intensity map of CO(1−0) tracing the bulk molecular gas. For comparison with the other molecular species, we plot red contours of CO(1−0) with S/N levels of 30, 60, 90 showing the spirals to the north and south in all of the 14 maps. The white S/N contours of HCN(1−0), HCO^+(1−0) and HNC(1−0) overlap with the northern spiral structure (labeled as 's1' in the sketch in Fig. 1). The southern spiral (s2) is visible in HCN(1−0), HCO^+(1−0), HNC(1−0) and N_2H^+(1−0). We denoted a third spiral (s3), which is present in HCN(1−0), HCO^+(1−0), HNC(1−0), N_2H^+(1−0), CS(2−1) and CH_3OH(2−1).

Table 5. Spatial distribution comparison of the molecular species.

	s1	s2	s3	NBE	SBE	NUC
^{12}CO (1−0)	✓	✓	✓	✓	✓	✓^{p}
^{12}CO (2−1)	✓	✓	✓	✓	✓	✓^{p}
HCN (1−0)	✓	✓	✓	✓	✓	✓^{p}
HCO^+ (1−0)	✓	✓	✓	✓	✓	✓^{p}
HNC (1−0)	✓	✓	✓	✓	✓	✓^{p}
CS (2−1)	✗	✗	✓	✓	✓	✓^{p}
CS (3−2)	✗	✗	✗	✓	✓	✓^{p}
N_2H^+ (1−0)	✗	✓	✓	✓	✓^{p}	✓
HC_3N (10−9)	✗	✗	✓	✓	✓^{p}	✓
HC_3N (16−15)	✗	✗	✗	✗	✓^{p}	✓
CH_3OH (2k−1k)	✗	✗	✓	✓	✓^{p}	✓
CH_3OH (3k−2k)	✗	✗	✗	✓	✓^{p}	✓
C_2H (1−0), 3/2−1/2	✗	✗	✗	✓	✓	✓^{p}
H_2CO (2−1)	✗	✗	✗	✗	✓^{p}	✓

Notes. The comparison is based on their $S/N > 5$ peaks in the integrated intensity maps (see Fig. A.2). We consider the three spiral structures (s1–s3), the inner bar ends (NBE and SBE) and the nuclear region (NUC). ✓ denotes that we find within this region a $S/N > 5$ detection, ✗ not; ✓^{p} refers to the location of the peak/maximum in integrated intensity in the inner 50″ ≈ 1.9 kpc.

The inner bar and nuclear region. Already inferred in the sketch in Fig. 1 from the native resolution CO(2−1) data, we know the location of the inner bar ends (NBE and SBE) and the nuclear region (NUC), and are able to investigate them with our other molecular emission lines. Considering only the integrated intensities with $S/N > 5$ in each of the maps in Fig. 2, we see that the small-scale distributions of molecular species vary in these environments and that they do not necessarily peak at the same locations (see Table 5).

While in the strongest lines, CO(1−0), CO(2−1), HCN(1−0), HCO^+(1−0) and HNC(1−0), all these regions are evident and their integrated intensities are peaking in the NUC, the situation becomes different for molecular species with higher effective critical densities[5]. In particular, CS(3−2) and C_2H(1−0) show emission concentrated to the inner 5″ in radius. Contrary to that, the highest integrated intensities are not peaking at the very centre for HC_3N(10−9), N_2H^+(1−0), CH_3OH(2−1) and CH_3OH(3−2). Their peaks in emission are in the southern inner bar end. Interestingly, in the CS maps we do not see a peak in the SBE, although their $n_{\rm eff}$ is higher than N_2H^+ which peaks in the SBE. Of course, the different distributions of the molecular emissions may not be a direct result of the density difference, but also temperature (e.g. driven by the embedded star formation) that could drive both excitation and abundance variations. Table 5 compares the spatial distribution of various molecular species.

3.2. Molecular line profiles towards the nuclear region and what they are indicating

Figure 3 shows the spectra of all the detected molecules for the central sight line (4″ ≈ 150 pc aperture). For visualisation pur-

[5] The effective critical densities, $n_{\rm eff}$, are defined in Table 2.

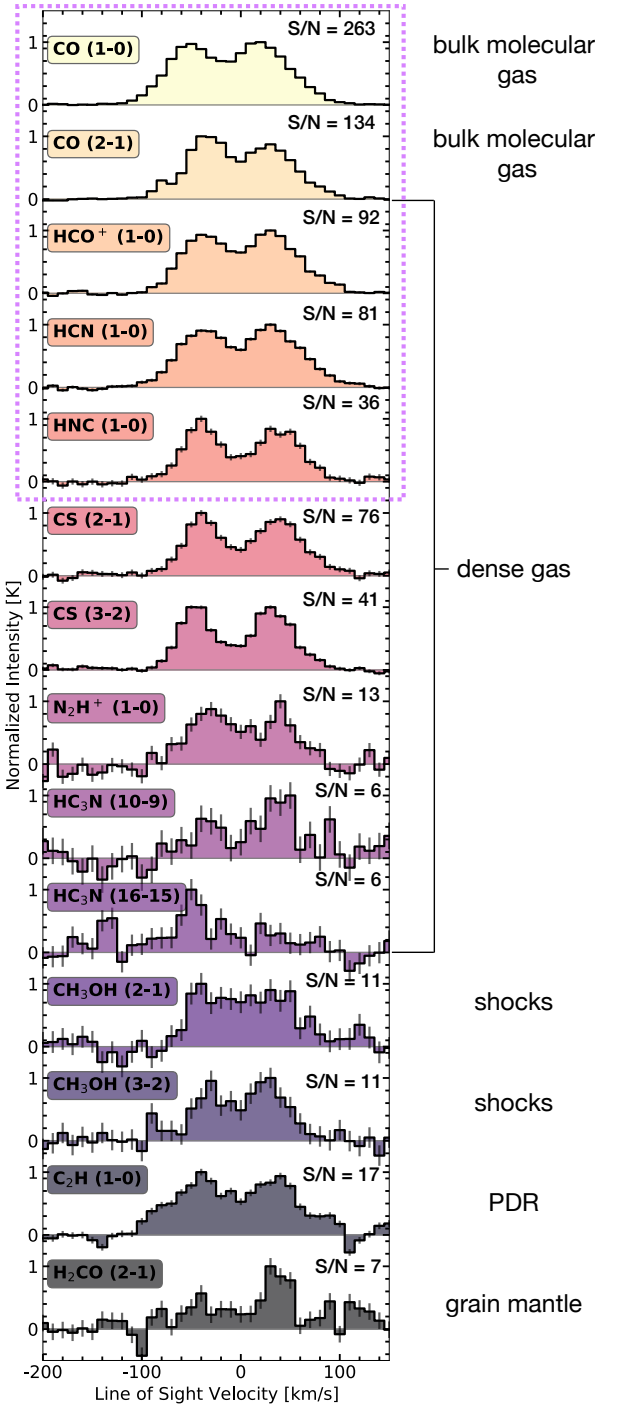

Fig. 3. Spectra of fourteen emission lines. We show the spectra of all the emission lines detected within this survey for the central sight line, i.e. aperture of 4″ ≈ 150 pc. The pink dotted rectangle shows the ones we use for discussing line ratio diagnostic plots later in this work (Sect. 6). We normalise all of them to the maximum value in their spectra. The right-hand side indicates what each molecule could be tracing according to literature (we refer the reader to the cautionary statements Sect. 3.2). Within each group we ordered the spectra by their S/N (see Table 3).

poses we normalised them to the maximum value in their spectra. We investigate what the molecular species in our data set reveal about the physical state of the molecular gas at the centre of NGC 6946.

CO is tracing the bulk molecular gas content and its line brightness is up to a factor of 14 higher than other molecular lines within this work (see Table 3). Relative to CO, molecules such as HCN are tracing denser gas, as they get excited at effective densities of $n \gtrsim 10^3$ cm^{-3}. As we go up in $n_{\rm eff}$, HNC, N_2H^+, CS and HC_3N are potentially tracing even denser molecular gas. This means, HC_3N is tracing the densest molecular gas in our data set. The spectrum in Fig. 3, however, shows that HC_3N has in the central 150 pc the lowest S/N among all our molecular emission lines (S/N of 6). However, as we could see in Table 5, their maximum integrated intensities are located in the SBE, and there we find a S/N of 11 and 36.

Among our molecular species, there are some that reveal more about the chemistry of the gas. The formation path of ethynyl (C_2H) is favoured in PDRs by the reaction of C^+ with small hydrocarbons and additionally through photodissociation of C_2H_2 (Meier & Turner 2005, and references therein). This means enhanced C_2H in PDRs associated with massive hot cores indicates hidden star formation (Martín et al. 2015; Harada et al. 2018). Recently, Holdship et al. (2021) showed in the nucleus of NGC 253 that high abundances of C_2H can be caused by a high cosmic ray ionization rate. We detect $C_2H(1-0)$ towards the nuclear region of NGC 6946 and the line shows similar to CO and dense gas tracers a broad line profile ($FWHM \sim 200$ km s^{-1}) including two peaks.

Strong methanol (CH_3OH) emission is considered a tracer of shocks (e.g. Saito et al. 2017). The reason for this is the formation process of CH_3OH in the gas phase is not efficient enough to produce higher amounts of CH_3OH (Lee et al. 1996). Intense CH_3OH emission is believed to arise from a series of hydrogenations of CO on dust grain surfaces under a low-temperature condition (Watanabe et al. 2003). After production on dust, it needs energetic heating mechanisms – shock chemistry – (e.g. Viti et al. 2011; James et al. 2020) to heat the dust and then sublimate CH_3OH into the gas phase. However, methanol emission can also be enhanced in non-shocked environments, such as towards massive stars or sources of cosmic ray or X-rays that heat the dust to ∼100 K and allow methanol to evaporate into the gas phase. In our data set, both methanol transitions are stronger in their line brightness than the faintest dense gas tracers – N_2H^+ and HC_3N. Also, both methanol tracers have their maximum integrated intensity peaks in the SBE, where their ratios with CO are higher ($I_{CH_3OH}/I_{CO(2-1)}$). Methanol is also known to be a good kinetic temperature probe (e.g. Beuther et al. 2005). Furthermore, para-H_2CO transitions can also be used as a temperature indicator which is sensitive to warmer ($T > 20$ K) and denser ($n \sim 10^{4-5}$ cm^{-3}) gas (e.g. Ginsburg et al. 2016; Mangum et al. 2019). H_2CO can be formed in the gas phase as well as on the surface of dust grains (e.g. Terwisscha van Scheltinga et al. 2021). In our data set, $H_2CO(2-1)$ is one of the faintest lines with $S/N \sim 7$ towards the nuclear region.

We note, however, that each molecule is not a unique tracer of a particular process or sets physical conditions in a galaxy. To highlight this point, $C_2H(1-0)$, for example, in the Milky Way is a tracer of PDRs, yet in NGC 1068 or NGC 253 it is tracing a completely different type of gas (García-Burillo et al. 2017; Holdship et al. 2021). In NGC 1068 it appears to trace a turbulent extended interface between outflows and ISM, yet in NGC 253 it appears to trace the dense gas that is subject to enhanced cosmic-ray ionization rates. Modelling can shed some light on the interpretation, and will be the subject of future work.

Schinnerer et al. (2006) found that the profiles of $CO(1-0)$ and $CO(2-1)$ are double peaked in NGC 6946. In Fig. 3 we also notice double-peaked profiles in the spectra of $HCN(1-0)$, $HCO^+(1-0)$, $HNC(1-0)$, $CS(2-1)$, $CS(3-2)$, $HC_3N(10-9)$,

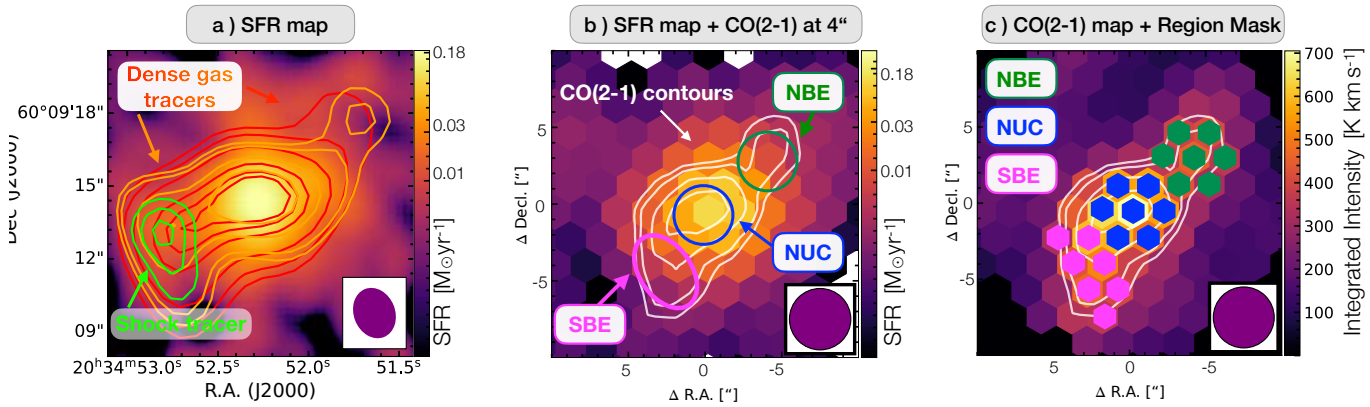

Fig. 4. Star formation rate map and region mask. *Panel a*: SFR map with red, orange and green contours of HCN(1−0), HNC(1−0) and $CH_3OH(3-2)$ integrated intensities (we used the thermal part of the 33 GHz continuum emission at $2\farcs12 \times 1\farcs70$ resolution; see Sect. 2.3.2 for SFR calibration). *Panel b*: SFR map at $4'' \approx 150$ pc resolution on hexagonal grid with white contours of CO(2−1) integrated intensities. Overploted are the identified regions – nuclear region, northern and southern inner bar end. *Panel c*: the region mask showing the chosen hexagonal points in colours of green for the northern inner bar end, blue for the nuclear region and pink for the southern inner bar end. To each of the regions we associate – equivalent to our beam size of 4″ – seven individual lines of sight (hexagonal points). In the background we show the integrated intensity map of CO(2−1) at 4″ resolution. We detect in the southern inner bar end higher SFR in combination with shock tracers (e.g. CH_3OH (3k−2k)) and higher concentration of denser gas (e.g. HCN(1−0)) than in the northern inner bar end.

$N_2H^+(1-0)$, $C_2H(1-0)$, $CH_3OH(2-1)$ and $CH_3OH(3-2)$. These could be due to galactic orbital motions or in/outflows in the central $4'' \approx 150$ pc. A more detailed analysis of the kinematics and dynamics of these spectral features are not discussed in this paper but it is planned for a future publication.

In Fig. 3 we denote the peak S/N and what condition each of the molecules can potentially indicate on the right-hand side.

4. The environmental variability of the star formation rate in NGC 6946

We seek answers to how the molecular lines in our data set relate to the current star formation rate (SFR) and if the different environments vary in their SFR on 150 pc scales, or if they have similar characteristics in this respect. We show a map of SFR in panel a of Fig. 4 with contours of tracers of denser gas HCN(1−0) and HNC(1−0), and shock tracer $CH_3OH(3-2)$ at their native resolution (see Table 2). SFR is peaking at the very centre and drops towards the NBE and SBE.

To further investigate these differences and the correlations between SFR and the molecular lines in our data set, we convolve the SFR map in units of $M_\odot\,\mathrm{yr}^{-1}$ to our working resolution of $4'' \approx 150$ pc and sampled it onto a hexagonal grid to match with our integrated intensity maps[6]. The white contours in panel b of Fig. 4 show the CO(2−1) emission indicating the three distinct features – the nuclear region (NUC) and the northern and southern inner bar ends (NBE and SBE). Since integrated intensities of our dense gas tracers are higher in the SBE than in NBE, we expect to find higher SFR in SBE.

In the following we quote SFR values for the NUC, SBE and NBE which have been averaged over these 150 pc sized regions.

As expected, we find the highest SFR within the NUC, $0.089\,M_\odot\,\mathrm{yr}^{-1}$. But we see differences in the other two regimes: higher SFR in the SBE than in NBE, 0.013 and $0.006\,M_\odot\,\mathrm{yr}^{-1}$, respectively[7]. This agrees with our extended molecular data set, where we find that molecules representing even denser gas, such as $N_2H^+(1-0)$ or $HC_3N(10-9)$, reach a maximum in their integrated emission in SBE. Additionally we find the shock tracer CH_3OH peaking in their integrated intensities in SBE. This suggests that maybe weak shocks lead to a higher SFR in the SBE compared to the NBE.

The inner bar ends also differ in their molecular masses, as already noted by Schinnerer et al. (2006). We find in our 150 pc sized apertures using Eq. (8) molecular gas mass surface densities (Σ_{mol}) of $\approx 189 \pm 0.26\,M_\odot\,\mathrm{pc}^{-2}$ in the NBE and $\Sigma_{\mathrm{mol}} \approx 236 \pm 5.09\,M_\odot\,\mathrm{pc}^{-2}$ in the SBE. We find that the bar ends have a molecular gas depletion time ($\tau^{\mathrm{mol}}_{\mathrm{depl,\,150\,pc}}$) that is a factor of 10 higher than NUC; the highest in the SBE $\tau^{\mathrm{mol}}_{\mathrm{depl,\,150\,pc}} \approx 3.05 \times 10^8$ yr (which is rather short, see discussion below).

Towards the NUC we find that stars are formed at a rate of $0.089\,M_\odot\,\mathrm{yr}^{-1}$ over the past ∼10 Myr[8] which translates into $0.89 \times 10^6\,M_\odot$ of recently formed stars. We find $\Sigma_{\mathrm{mol}} \approx 298 \pm 1.98\,M_\odot\,\mathrm{pc}^{-2}$ and at the current SFR it will take $\tau^{\mathrm{mol}}_{\mathrm{depl,\,150\,pc}} \approx 3.43 \times 10^7$ years to deplete the present supply of molecular gas. This is shorter (factor of $\sim 10^2$) than found by previous studies on ∼kpc scales, for example a median $\Sigma_{\mathrm{mol}} \sim 2.2$ Gyr for the HERACLES galaxies in Leroy et al. (2013), or 1.1 Gyr in Usero et al. (2015). These studies used a Milky Way-like α_{CO} value (a factor of 10 smaller), which is however, not applicable for NGC 6946 (see e.g. Sandstrom et al. 2013; Bigiel et al. 2020 and Sect. 2.3.3). The bar ends have a depletion time of a factor of 10 higher than NUC, and if we calculate $\tau^{\mathrm{mol}}_{\mathrm{depl,\,150\,pc}}$ with a MW value, we would also get into the Gyr range for the bar ends (i.e. ≈1.6 Gyr for NBE and ≈3.3 Gyr for SBE). This demonstrates the importance of adopting a proper α_{CO} factor. The nuclear region of NGC 6946 was studied in terms of its SFR by e.g. Meier & Turner (2004), Schinnerer et al. (2007) and

[6] We do this also with our Σ_{SFR} map in units of $M_\odot\,\mathrm{yr}^{-1}\,\mathrm{kpc}^{-2}$ to calculate star formation efficiencies of the dense molecular gas (see Eq. (8)).

[7] We calculate the uncertainties for these SFR values using the uncertainty 33 GHz map and apply the equations as in Sect. 2.3.2. We then get over a 4″ region a SFR uncertainty of $\pm 1.35 \times 10^{-3}\,M_\odot\,\mathrm{yr}^{-1}$.

[8] Recall that the approximate age sensitivity of the thermal fraction of the 33 GHz continuum emission as a SFR tracer is ∼10 Myr.

Tsai et al. (2013) using different SFR indicators over different spatial scales.

For example, Schinnerer et al. (2007) found within a 3″ × 3″ square box region a SFR of ∼0.18 $M_\odot\,\mathrm{yr}^{-1}$ using Paα, 6 cm and 3 mm continuum as SFR tracers[9]. We find with our 33 GHz based star formation in the same region a SFR of ∼0.11 $M_\odot\,\mathrm{yr}^{-1}$, that is slightly lower than that of Schinnerer et al. (2007).

We remind the reader that the SFR we calculate is based on free-free emission, which is not subject to the extinction problems that complicate the estimation of SFR at optical and ultraviolet wavelengths. The free-free emission is a tracer of high-mass star formation, as it is only sensitive to stars that are able to ionise the surrounding gas and produce an H II region. However, we have to mention some uncertainties with this SFR. A different choice of initial mass function[10], or stellar population models during the calibration of 33 GHz (see Sect. 2.3.2), could introduce a systematic offset in the derived SFR but this should not vary from region to region. The parameter T_e in Eq. (4) has an impact of at most ∼7% on the SFR and regional variations in the thermal fraction, f^T, are likely to be too small to explain the observed variations in SFR among the bar ends (see e.g. Sect. 4.1 in Querejeta et al. 2019). Another factor that could potentially vary from region to region is the escape fraction of ionising photons (i.e. which part is absorbed in a region outside the 150 pc aperture and therefore does not contribute to the observed free-free emission). However, these uncertainties probably do not explain the factor of 2 higher SFR in the SBE than in the NBE.

5. Results – Line ratios and relationships among molecular species

Molecular line ratios open up the possibility to investigate the physical and chemical state of the ISM. Integrated line ratios among certain molecules were proposed to provide insights into the environment (e.g. $\mathrm{HCO^+/HCN}$; Loenen et al. 2008), the temperatures (HCN/HNC; Hacar et al. 2020) and density variations (e.g. line ratio pattern to CO; Leroy et al. 2017). The question can be asked whether we see differences between the inner bar ends and the nuclear region, and if these line ratio diagnostics hold for an extragalactic extreme environment like the centre of NGC 6946. For a meaningful analysis of the line ratios and their relationships, we need to correct the interferometric data for missing short-spacing information. Therefore, we use the five emission lines (CO(1−0), CO(2−1), HCN, $\mathrm{HCO^+}$ and HNC) for which single-dish observations were available (see Table 4). The line ratios are calculated from integrated line intensities in units of $\mathrm{K\,km\,s^{-1}}$ throughout the entire paper and we refer to them simply as 'line ratio'.

5.1. Ratios of integrated intensities

In Fig. 5 we show line ratio maps for our SSC + u−v trim data set (see Table 4). We specify the line ratios such that the generally brighter line is in the denominator, while the overall weaker line is in the numerator. The line ratio maps were calculated by only taking integrated intensities with $S/N > 5$ for the fainter dense gas tracers (DGTs: HCN, $\mathrm{HCO^+}$ and HNC) and $S/N > 15$ for the bulk molecular gas tracers (CO); non-detections were discarded

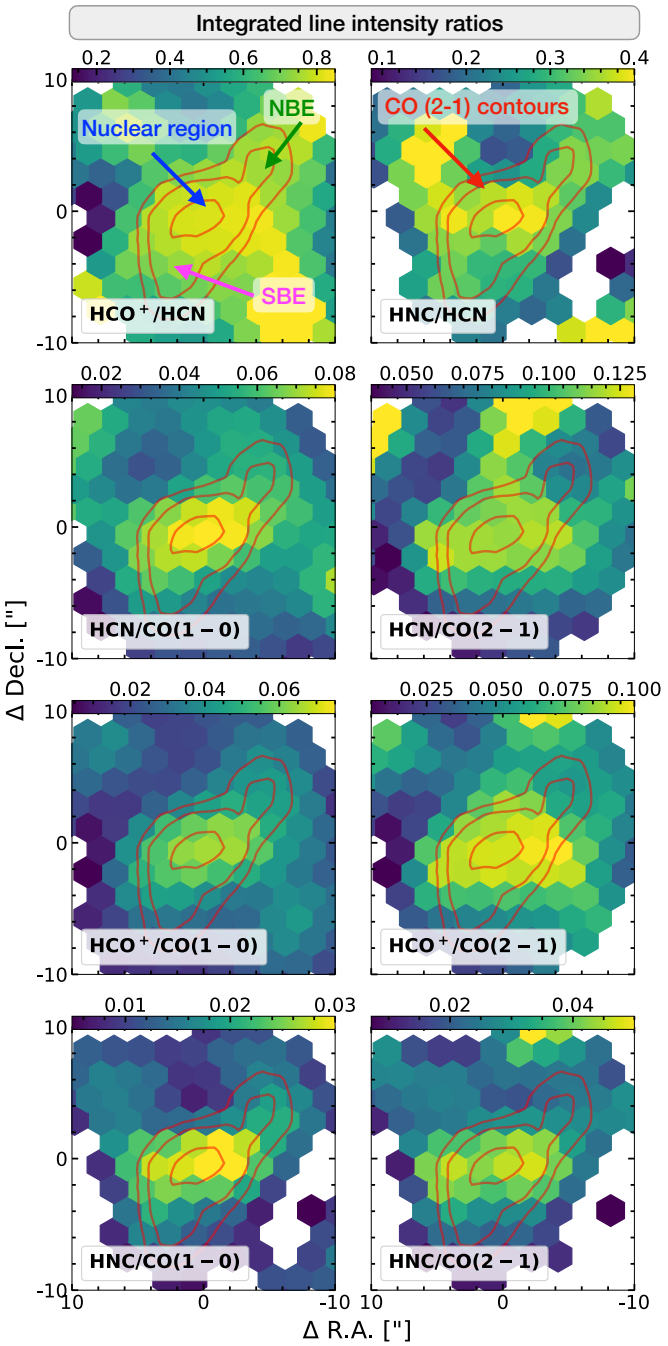

Fig. 5. Line ratio maps of the central 20″. We show the line ratio maps for the central 20″ ≈ 750 pc. We overplot on each map contours of the CO(2−1) integrated intensity map in red and denote the features associated with the inner bar (see Fig. 4 for the region mask).

from the line ratio maps:

$$\text{Ratio map} = \frac{I_{\mathrm{line}_1}\,[I_{\mathrm{line}_1}/\sigma_{\mathrm{line}_1} > \epsilon]}{I_{\mathrm{line}_2}\,[I_{\mathrm{line}_2}/\sigma_{\mathrm{line}_2} > \epsilon]} \begin{cases} \epsilon = 5 & \text{for DGTs,} \\ \epsilon = 15 & \text{for CO.} \end{cases} \quad (10)$$

In the next section, we include non-detections in our analysis. For the case of no significant detection we replaced the values with the upper limits (2σ in Eq. (2)) and include the propagated errors (σ_prop). We derive them as:

$$\sigma_\mathrm{prop} = \frac{|I_{\mathrm{line}_1}|}{|I_{\mathrm{line}_2}|}\sqrt{\left(\frac{\sigma_{\mathrm{line}_1}}{I_{\mathrm{line}_1}}\right)^2 + \left(\frac{\sigma_{\mathrm{line}_2}}{I_{\mathrm{line}_2}}\right)^2}. \quad (11)$$

[9] They adopted a distance of 5.5 Mpc to NGC 6946 for their SFR calculations. We have re-scaled their value to the distance of 7.7 Mpc using a factor of 1.8, see Appendix A.1.

[10] As well as any potential stochasticity due to IMF sampling.

The errors are expressed on a logarithmic scale of base 10 as:

$$\sigma_{\log} = \frac{1}{\ln(10)} \times \left(\sigma_{\rm prop}/I_{\rm ratio}\right) \approx 0.434 \times \left(\sigma_{\rm prop}/I_{\rm ratio}\right). \quad (12)$$

In Fig. 5 the line ratio maps for the central 20″ ≈ 750 pc show differences in line ratios between the environments NUC, SBE and NBE. In the following we report straight mean values over these regions by applying the mask in Fig. 4. The ratios HCO^+/HCN and HNC/HCN both show values below unity in all three regions; and over the entire field of view. In both cases, the ratio to HCN is greater in the NUC than in the SBE or NBE.

Looking at the NUC reveals values of 0.81 ± 0.01 and 0.37 ± 0.01 for HCO^+/HCN and HNC/HCN, respectively. Ratios to CO indicate higher values in the SBE than in NBE; best visible in the case of HNC/CO(2−1). We discuss the implications of these line ratios in Sects. 6.2–6.4.

5.2. The relationship between molecular lines and SFR surface density

In this section we investigate how our molecular species correlate with $\Sigma_{\rm SFR}$ and how the dense gas fraction traced by HCN/CO (we investigate also HCO^+/CO and HNC/CO) responds to the integrated intensity of CO (an indicator of the mean volume density, see below). We study how these quantities relate to conditions in the centre of NGC 6946. Figure 6 shows the relationships we investigate.

We characterise scaling relations by including upper limits and measurement errors, using the hierarchical Bayesian method described in Kelly (2007). This approach is available as a python package: `linmix`[11]. It performs a linear regression of y on x while having measurement errors in both variables and being able to account for non-detections (upper limits) in y. The regression assumes a linear relationship in the form of:

$$\log(y) = \beta \times \log(x) + \alpha, \quad (13)$$

where β is the slope, and α is the y-intercept[12]. We find Pearson's correlation coefficients ρ of the data sets for each fitted relationship, and the 3σ confidence intervals are estimated via Markov chain Monte Carlo (MCMC). For a detailed description we refer to Kelly (2007). We provide all the correlations in Table 6.

Dense molecular gas traced by, e.g., HCN emission, has been observed to correlate with SFR (e.g. Gao & Solomon 2004; Lada et al. 2010, 2012). Kauffmann et al. (2017) showed that HCN traces more extended gas and therefore can have an impact on the observed SF trends in galaxies (also see e.g. Pety et al. 2017; Barnes et al. 2020a). Krumholz & Thompson (2007) showed that star formation correlates with any line with a critical density comparable to the median molecular cloud density. Therefore, we expect to see positive correlations between $\Sigma_{\rm SFR}$ and the surface density of HCN, HCO^+ and HNC. In our observations this is confirmed with the additional characteristic that the molecular line with the lowest effective critical density ($n_{\rm eff}$) shows the strongest correlation ($n_{\rm eff}$ ordered as HCO^+ < HNC < HCN; see Table 2). HCO^+ shows the strongest ($\rho \sim 0.95$, see Table 6 for uncertainties of ρ) correlation with a slope of $\beta = 1.55$ and a small intrinsic scatter:

$$\log(\Sigma_{\rm SFR}) = 1.55 \pm 0.11 \times \log(I_{\rm HCO^+}) - 1.91 \pm 0.15. \quad (14)$$

[11] https://linmix.readthedocs.io/en/latest/index.html

[12] We specify the covariance between the measurement errors in x and y (xycov parameter) and set $K = 2$.

We note that our slopes are all higher ($\beta > 1$) than those found at global scales ($\beta < 1$; e.g. Gao & Solomon 2004; Krumholz & Thompson 2007). We speculate that this is due to two contributing factors. Firstly, in this work we are focussing on the centre of NGC 6946 (central 20″ ≈ 745 pc), and not the whole galaxy disc. Hence, this could be due to the limited dynamic range in environmental conditions we are including within the analysis – that is focussing on the densest and most actively star-forming gas within the galaxy. Secondly, this could be a result of the resolution obtained with our PdBI observations. At around 150 pc, we are close to resolving individual discrete star-forming and/or quiescent regions, which could result in the different slope compared to lower resolution studies that include an average on small scale conditions within each sample point; somewhat akin to following a branch of the tuning fork within the recent 'uncertainty principle for star formation' framework (Kruijssen et al. 2018, 2019; Chevance et al. 2020a; Kim et al. 2021).

The dense gas fraction, $f_{\rm dense}$[13], usually traced by the integrated intensity of HCN(1−0) over CO, has been observed to increase towards the centres of galaxies (e.g. Usero et al. 2015; Bigiel et al. 2016; Gallagher et al. 2018a; Jiménez-Donaire et al. 2019; Jiang et al. 2020; Bešlić et al. 2021). In turbulent cloud models, increasing the mean volume density of a molecular cloud results in a shift of the gas density distribution to higher densities (e.g. Federrath & Klessen 2013). In addition, the velocity dispersion (or Mach number) widens the density PDF, which causes a larger fraction of the mass to be at higher gas densities. Combined, these increase the fraction of gas above a fixed density (e.g. the effective critical density of HCN), and consequently, these models predict a positive correlation between the volume density and $f_{\rm dense}$ (see Padoan et al. 2014 for a review). Such trends are, in particular, interesting to study within galaxies centres environments thanks to their higher average densities and broader (cloud-scale) line widths compared to typical disc star-forming regions (e.g. Henshaw et al. 2016; Krieger et al. 2020). In the following we use the integrated intensity of CO(2−1) as an indicator of the mean volume density (Leroy et al. 2016; Sun et al. 2018; Gallagher et al. 2018b, see also Sect. 6.4) and explore the dense gas fraction using HCN, HCO^+ and HNC. All three $f_{\rm dense}$ versus CO(2−1) fits in Fig. 6 present sub-linear power-law indices (i.e. $\beta < 1.0$). We find that the correlations are weakest for the dense gas fraction using HCN ($\rho \sim 0.39$) and strongest for HNC/CO(2−1) ($\rho \sim 0.66$):

$$\log\left(\frac{I_{\rm HNC}}{I_{\rm CO(2-1)}}\right) = 0.76 \pm 0.13 \times \log\left(I_{\rm CO(2-1)}\right) - 1.63 \pm 0.16. \quad (15)$$

The particular order in the slopes and correlation coefficients do not follow the order of $n_{\rm eff}$ as given in Shirley (2015). Instead, they show the order of $\beta_{\rm HNC} > \beta_{\rm HCO^+} > \beta_{\rm HCN}$ (see second row in Fig. 6). Possible explanations for this behaviour could be anomalous excitation for one of the species, for example IR pumping of HCN and HNC levels and/or peculiar filling factors. The star formation efficiency of dense gas ($\rm SFE_{dense}$) – the ratio of SFR to the integrated intensity of HCN(1−0) – has been observed to decrease towards galaxy centres (same studies as above). This is because the critical overdensity (relative to the mean density) is higher due to the higher Mach number, but also that the absolute critical density (i.e. that obtained from the above line ratios) is higher due to the higher (1) mean density and (2) Mach number (in the context of the CMZ of the

[13] In this work, we take the CO(2−1) data for our $f_{\rm dense}$ estimates because they have a higher S/N and better quality than CO(1−0).

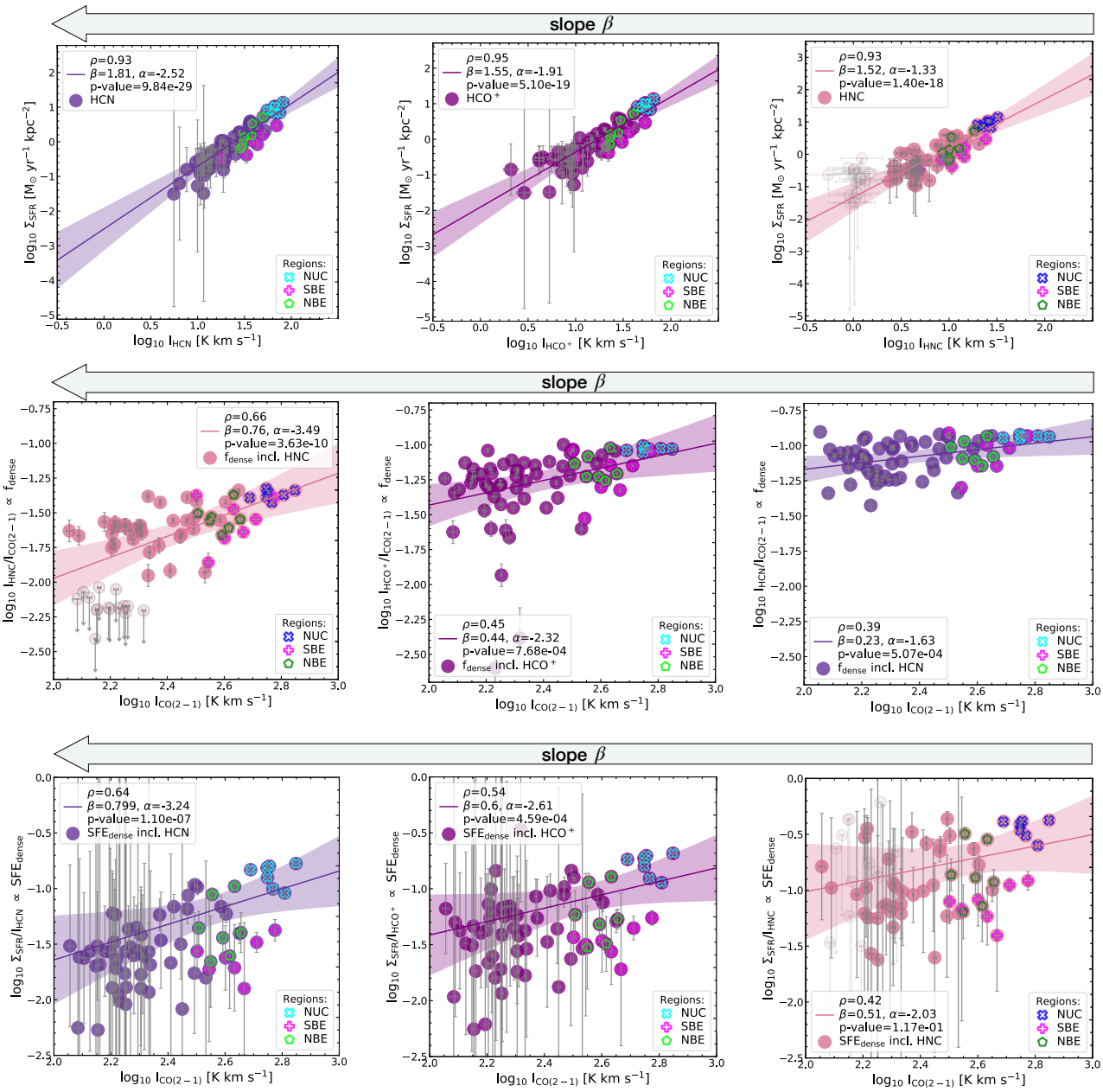

Fig. 6. Correlation plots ordered by their slope, β. Dark purple colours show HCN, purple HCO^+ and pink HNC. *Top row*: integrated intensities of the dense gas tracers (ordered by their slope, β) versus Σ_{SFR}. *Middle row*: integrated intensity of CO(2−1) – an indicator of the mean volume density – versus the line ratio with CO(2−1) – a spectroscopic tracers of f_{dense}. *Bottom row*: integrated intensity of CO(2−1) – an indicator of the mean volume density – versus the ratio of Σ_{SFR} with the dense gas tracers – a spectroscopic tracers of SFE_{dense}. The `linmix` fits (accounting for upper limits) are shown as solid lines surrounded by 3σ confidence intervals (shaded regions of corresponding colours). Absolute uncertainties are plotted on each data point, which are generally small towards the regions NUC, NBE and SBE. We find the highest uncertainties in the outskirts in our Σ_{SFR} map. Correlations including HNC result in 58 significant sight lines and 15 upper limits (denoted as light pink markers). We display in each panel Pearson's correlation coefficient and the power-law slope, intercept and p-value (see Table 6).

Milky Way, see e.g. Kruijssen et al. 2014). Hence, as the mean density of a molecular cloud approaches n_{eff} of the molecular line, the line's intensity will increasingly trace the bulk mass of the cloud, and not exclusively the overdense, star-forming gas; in effect reducing the apparent SFE. From that we would expect to see SFE_{dense} to drop with $I_{CO(2-1)}$ ($\propto$volume density) as it has been observed over the disc regions of galaxies (e.g. Gallagher et al. 2018a; Jiménez-Donaire et al. 2019). We use the ratio of Σ_{SFR} to the integrated intensities of the dense gas tracers as SFE_{dense}, and find a different picture of SFE_{dense} with galactocentric radius – increasing towards the NUC; as it shows higher efficiencies in the NUC than in the bar ends (see third row in Fig. 6). We find a moderate[14], approximately linear correlation between Σ_{SFR}/I_{HCN} and $I_{CO(2-1)}$. The other two SFE_{dense} measurements show weak sub-linear relationships with $\rho \sim 0.46$ and $\rho \sim 0.19$ for ratios using HCO^+ and HNC, respectively. We find that SFE_{dense} increases with increasing $I_{CO(2-1)}$, contrary to the trends found by Gallagher et al. (2018a), Jiménez-Donaire et al. (2019). The reason for that could be the special environment

[14] Here we refer to a moderate correlation if ρ lies in the range of 0.5–0.7.

Table 6. Scaling relations and correlation coefficients for the central 20″ ≈ 745 pc of NGC 6946 at 150 pc scale.

log(y)	log(x)	β slope	α intercept	ρ Pearson (1)	p-value	Scatter (2)	Cov(log(x),log(y))
Σ_{SFR}	HCN	1.81 ± 0.13	−2.52 ± 0.20	0.93 ± 6.6E−04	9.84E−29	0.04	9.75
Σ_{SFR}	HCO^+	1.55 ± 0.11	−1.91 ± 0.15	0.95 ± 1.7E−02	5.10E−19	0.04	8.24
Σ_{SFR}	HNC	1.52 ± 0.14	−1.33 ± 0.14	0.93 ± 1.1E−02	1.40E−18	0.07	3.30
Σ_{SFR}	CO(1−0)	2.46 ± 0.22	−6.56 ± 0.60	0.89 ± 2.2E−03	7.90E−23	0.06	112.00
Σ_{SFR}	CO(2−1)	1.93 ± 0.22	−4.68 ± 0.54	0.80 ± 2.4E−03	5.90E−16	0.09	68.70
HCN/CO(2−1) ∝ f_{dense}	CO(2−1)	0.23 ± 0.06	−1.63 ± 0.16	0.39 ± 3.4E−04	5.07E−04	0.01	0.01
HCO^+/CO(2−1) ∝ f_{dense}	CO(2−1)	0.44 ± 0.11	−2.32 ± 0.26	0.45 ± 6.5E−04	7.68E−04	0.03	0.02
HNC/CO(2−1) ∝ f_{dense}	CO(2−1)	0.76 ± 0.13	−3.49 ± 0.31	0.66 ± 8.5E−08	3.63E−10	0.03	0.04
Σ_{SFR}/HCN ∝ SFE_{dense}	CO(2−1)	0.80 ± 0.22	−3.24 ± 0.56	0.64 ± 2.9E−01	1.10E−07	0.04	0.04
Σ_{SFR}/HCO^+ ∝ SFE_{dense}	CO(2−1)	0.60 ± 0.20	−2.61 ± 0.52	0.54 ± 3.2E−01	4.59E−04	0.04	0.03
Σ_{SFR}/HNC ∝ SFE_{dense}	CO(2−1)	0.51 ± 0.24	−2.03 ± 0.62	0.42 ± 2.8E−01	1.17E−01	0.05	0.02

Notes. (1) We perform a Monte Carlo analysis perturbing the x and y data points to get the uncertainty of ρ. (2) The regression intrinsic scatter.

of NGC 6946 (inner bar) and/or the different used SFR tracers (we use the free-free emission of 33 GHz continuum compared to Hα + 24 μm and total infrared). Also the above studies could not resolve the inner bar of NGC 6946 (Jiménez-Donaire et al. 2019, angular resolution of 33″ ≈ 1 kpc) or NGC 6946 was not in the nearby disc galaxy sample (Gallagher et al. 2018a). However, we notice, as expected, that stronger correlations in f_{dense} result in weaker correlations in SFE_{dense} and vice versa (e.g. $I_{HNC}/I_{CO(2-1)}$ with ρ = 0.76 ± 0.13 and Σ_{SFR}/I_{HNC} with ρ = 0.51 ± 0.24; see Table 6).

6. Implications for spectroscopic studies of other galaxies – from bulk molecular gas to dense gas

Here we discuss some of the common integrated line ratios in more detail and what they can be used for. We compare our high-resolution (150 pc) integrated line ratios of dense gas tracers towards the central region of NGC 6946 with available dense gas tracers from the EMPIRE survey, which include eight additional galaxy centers. It is worth noting that the central regions in the EMPIRE sample are ∼1 kpc sized areas which result in one data point per galaxy (see Jiménez-Donaire et al. 2019 for more details). Nevertheless, it provides us with an understanding of how NGC 6946 compares to other centers.

6.1. R_{21} variations in the nuclear region and inner bar ends

The CO(2−1)-to-CO(1−0) line ratio, R_{21}, is widely used to convert CO(2−1) emission to CO(1−0), which then can be further converted via the α_{CO} conversion factor to the molecular gas mass. It has been shown that higher R_{21} values are expected within the central kpc in individual galaxies (Leroy et al. 2009, 2013; Koda et al. 2020). The same trend has been found by den Brok et al. (2021) and Yajima et al. (2021) studying a galaxy sample. NGC 6946 is in both of the aforementioned studies. They find within the central kpc region R_{21} ∼ 0.7 (at an angular resolution of 33″ ∼ 1 kpc; den Brok et al. 2021 using the EMPIRE sample) and R_{21} ∼ 1.1 (angular resolution of 17″ ∼ 0.6 kpc; Yajima et al. 2021). However, these studies are not able to resolve variations within the centre between different subfeatures. From a physical point of view, R_{21} should depend on the temperature and density of the gas, as well as on the optical depths of the lines (e.g. Peñaloza et al. 2018). Therefore, understanding how R_{21} varies in response to the local environment also has the prospect of providing information about the physical conditions of the molecular gas.

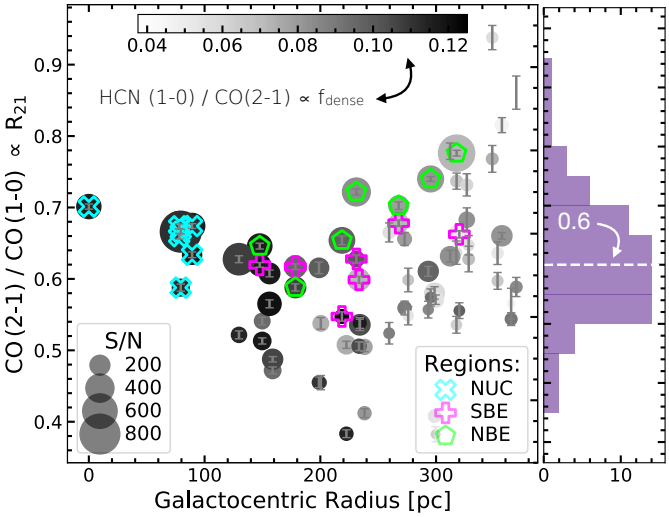

Fig. 7. R_{21} against galactocentric radius. The circular shaped markers represent all of the R_{21} values for the central 20″ ≈ 745 pc coloured by their f_{dense}. The different sizes show their varying signal-to-noise ratio in CO(2−1). Additionally, we overplot the contours of the three different regions: The cyan colour refers to the nuclear region (NUC), the green to the northern bar end (NBE) and the magenta to the southern bar end (SBE). Along the galactocentric radius, we find in the centre higher R_{21} values, an initial steady decrease followed by a gradual increase. R_{21} towards NBE is higher than expected (more in Sect. 6.1).

With our higher resolution (4″ ≈ 150 pc) observations we are able to resolve smaller-scale structures and thus have the opportunity to investigate variations of R_{21} within the centre. In Fig. 7 we show R_{21} against galactocentric radius, highlighting NUC, NBE and SBE in different colours.

We see along the galactocentric radius, in the centre higher R_{21} values, an initial steady decrease followed by a gradual increase. We find average R_{21} of 0.65 ± 2E−3 within NUC and even lower values in the southern end of the bar R_{21} = 0.62 ± 3E−2 (see Table 7). Interestingly, however, we observe higher R_{21} values towards the northern end of the bar (R_{21} = 0.70 ± 3E−2) compared to the NUC (factor of ∼1.08), despite the higher Σ_{SFR} in the SBE compared to the NBE (see Sect. 4). The reason for a higher R_{21} value could be related to denser

Table 7. Summary of the characteristics of the nuclear region and inner bar ends of NGC 6946 based on the analyses in this work.

	Unit	NUC	NBE	SBE	Section	Notes
$I_{CO(1-0)} \propto$ bulk mol. gas	[K km s^{-1}]	892.75 ± 2.43	565.91 ± 2.23	705.35 ± 2.25	Section 3	
$I_{CO(2-1)} \propto$ bulk mol. gas	[K km s^{-1}]	587.38 ± 1.51	388.65 ± 0.86	438.52 ± 1.68	Section 3	
$I_{HCN} \propto$ dense gas	[K km s^{-1}]	67.96 ± 0.39	35.19 ± 0.37	40.12 ± 0.36	Section 3	
$I_{CH_3OH} \propto$ shock	[K km s^{-1}]	7.15 ± 0.45	5.17 ± 0.40	11.53 ± 0.35	Section 3	(1)
$I_{CH_3OH}/I_{CO} \propto f_{shocked}$	[%]	2.43 ± 0.24	2.98 ± 0.34	8.85 ± 0.50	Section 3	(1)
SFR	[$M_\odot$ yr^{-1}]	8.9E−2 ± 1.33E−3	6.0E−3 ± 1.33E−3	1.3E−3 ± 1.33E−3	Section 4	
Σ_{mol}	[$M_\odot$ pc^{-2}]	298.07 ± 1.98	188.95 ± 0.26	235.50 ± 5.09	Section 4	
$\Sigma_{mol}/\Sigma_{SFR} \propto \tau^{mol}_{depl,\,150\,pc}$	[yr^{-1}]	3.43E+7	1.46E+8	3.05E+8	Section 4	
$I_{HCN}/I_{CO} \propto f_{dense}$	[%]	11.56 ± 0.11	9.07 ± 0.15	9.00 ± 0.14	Section 5.2	
$I_{HNC}/I_{CO} \propto f_{dense}$	[%]	4.27 ± 0.11	2.94 ± 0.11	2.89 ± 0.12	Section 5.2	
$\Sigma_{SFR}/I_{HCN} \propto SFE_{dense}$		0.13 ± 3E−3	0.05 ± 7E−3	0.02 ± 7E−3	Section 5.2	(2)
$I_{CO(2-1)}/I_{CO(1-0)} \propto R_{21}$		0.65 ± 2E−3	0.70 ± 3E−3	0.62 ± 3E−3	Section 6.1	
I_{HNC}/I_{HCN}		0.37 ± 0.01	0.32 ± 0.01	0.31 ± 0.01	Section 6.2	
T_k	[K]	27.19 ± 0.06	31.19 ± 0.09	31.99 ± 0.11	Section 6.2	(3)
I_{HCO^+}/I_{HCN}		0.81 ± 0.01	0.76 ± 0.01	0.70 ± 0.01	Section 6.3	
n_{H2}	[cm^{-3}]	$10^{3.7-4.1}$	$10^{3.3-4.1}$	$10^{3.4-4.2}$	Section 6.4	

Notes. We quote the mean values over each region that are equivalent to our beam size of 4″ ≈ 150 pc. NUC = Nuclear Region; NBE = northern inner bar end; SBE = southern inner bar end. (1) Taken from our extended molecular data set – PdBI only. CH_3OH is the (2k−1k) transition and CO the (2−1) transition. (2) In units of K km s^{-1}/($M_\odot$ yr^{-1} kpc^{-2}). (3) If the Hacar et al. (2020) framework holds valid in NGC 6946; see detailed discussion in Sect. 6.2.

gas and/or warmer gas with higher temperatures. We colour-code points in Fig. 7 by their HCN(1−0)/CO(2−1) line ratio ($\propto f_{dense}$) and find them showing higher f_{dense} towards the NUC. Furthermore, we would expect to observe higher HCN-to-CO ratios towards the NBE. However, we do not see an increase in the denser gas in the NBE, suggesting a different physical driver for the increased R_{21} in the NBE. We analyse the three regions regarding their molecular gas density in more detail in Sect. 6.4.

In summary, we find higher R_{21} values towards one of the inner bar ends of NGC 6946 compared to the nuclear region. If substructures such as small-scale bar ends are to be observed and analysed, R_{21} may possibly deviate in a minimal way from the kpc-sized R_{21} values from the literature.

6.2. HNC/HCN: sensitive to kinetic temperatures in extragalactic environments?

In interstellar space, isomers do not necessarily share similar chemical or physical properties. HNC (hydrogen iso-cyanide) and HCN (hydrogen cyanide) isomers are both abundant in cold clouds, but at temperatures exceeding ∼30 K, HNC begins to be converted to HCN by reactions with atomic H. These isomers exhibit an abundance ratio of unity at low temperatures (Schilke et al. 1992; Graninger et al. 2014). A major study to understand this ratio, which was focused on the galactic SF region Orion Molecular Cloud 1 (OMC-1), was carried out by Schilke et al. (1992). They found that the HNC/HCN ratio is ∼1/80 in the direction of Orion Kleinmann-Low (Orion-KL) but increases to 1/5 in regions with lower temperatures near Orion-KL. In the coldest OMC-1 regions, the ratio rises further to 1. The temperature dependence suggests that the ratio must be kinetically controlled (Herbst et al. 2000), so that the integrated intensity line ratio HNC/HCN should decrease at higher temperatures (Pety et al. 2017).

Whether this ratio is sensitive to temperatures in extragalactic sources is uncertain (e.g. Aalto et al. 2002; Meier & Turner 2005, 2012). For example, Meier & Turner (2005) found a kinetic temperature for the centre of IC 342 using the HCN/HNC ratio and the empirical relation of Hirota et al. (1998) of a factor of 2 less than the dust temperature and the kinetic temperature of the gas using CO(2−1) and ammonia (NH_3). They suggested that there might be an abundant dense component in IC 342 that is significantly cooler and more uniform than the more diffuse CO, but this was not consistent with the similar distribution of CO, HNC and HCN, unless such a dense component directly follows the diffuse gas. Alternatively, they assumed that this line relationship might not capture temperature, for the nuclear region of IC 342. Also Aalto et al. (2002) find overluminous HNC in many of the most extreme (and presumably warm) (U)LIRGs and suggest that its bright emission cannot be explained by the cool temperatures demanded.

Recently, however, this line ratio has come back into focus. Hacar et al. (2020) demonstrated the strong sensitivity of the HNC/HCN ratio to the gas kinetic temperature, T_k, again towards the Orion star-forming region. They compared the line ratio with NH_3 observations (Friesen et al. 2017) and derived T_k from their lower inversion transition ratio $NH_3\,(1,1)/NH_3\,(2,2)$. In particular, they found that T_k can be described by a two-part linear function for two conditions (we show only Eq. (3) in Hacar et al. 2020):

$$T_k\,[\mathrm{K}] = 10 \times \frac{I_{HCN}}{I_{HNC}} \quad \text{for} \quad \frac{I_{HCN}}{I_{HNC}} \leq 4. \tag{16}$$

However, since the $NH_3\,(1,1)/NH_3\,(2,2)$ transitions are only sensitive to $T_k \lesssim 50$ K (see e.g. Fig. 1 of Mangum et al. 2013), the calibration shown above only represents the low temperature regime. The challenge of apply such concepts in nearby galaxies is that the concentrations of dense gas studied by Hacar et al. (2020) in the local Milky Way environment (i.e. Orion) are very compact (∼0.1−1 pc; Lada & Lada 2003), and representative of solar neighbourhood environmental conditions (e.g. chemistry, and average densities, Mach numbers and kinetic temperatures). Achieving such a resolution is currently extremely difficult in an extragalactic context (e.g. 1 pc = 0.025″ at the distance of the NGC 6946), potentially limiting our capability to determine kinetic temperatures (e.g. when using H_2CO;

see Mangum et al. 2019 and below). That said, galaxy centres present an ideal regime in which to focus our efforts. As densities similar to the concentrations observed within local star-forming regions are not compact, but can span (nearly) the entire CMZ (so up to 100 pc), leading to luminous and, importantly, extended HCN and HNC emission (Longmore et al. 2013; Rathborne et al. 2015; Krieger et al. 2017; Petkova et al. 2021). Hence, testing this temperature probe within galaxy centres overcomes the requirement for such extremely high-resolution observations, and should be possible with ∼100 pc scale measurements presented in this work.

We find in the nuclear region of NGC 6946 a mean HNC/HCN ratio of ∼0.37. For the bar ends we find lower ratios: ∼0.31 for NBE and ∼0.32 for the SBE (see Table 7). Jiménez-Donaire et al. (2019) reported over kpc-scales a ratio of ∼0.31. There are no other ratios of HNC and HCN in the literature for a comparison, since HNC has hardly been observed towards NGC 6946. If we assume that the ratio of HCN and HNC traces kinetic temperature and adopt the Hacar et al. (2020) relation[15], then we would infer a T_k(HCN/HNC) of ∼27 K for the NUC. For the bar ends we calculate slightly higher temperatures of ∼31 K and ∼32 K (on 4″ ≈ 150 pc scales). Meier & Turner (2004) predict T_k ∼ 20–40 K (for $n_{H_2} = 10^3$ cm^{-3}) based on CO and its isotopologues using a large velocity gradient (LVG) radiative transfer model (building on the models presented in Meier et al. 2000). Including HCN into their LVG models, favoured higher T_k (∼90 K) and n_{H_2} (∼10^4–$10^{4.5}$ cm^{-3}), but these numbers are sensitive to whether ^{13}CO and HCN trace the same gas component. With the inverse transition of NH_3, Mangum et al. (2013) found T_k ∼ 47 ± 8 K (using the NH_3 (1, 1)/NH_3 (2, 2) ratio) which is a factor of ∼2 higher than our inferred T_k (HNC/HCN). The higher excitation NH_3 (2, 2)/NH_3 (4, 4) ratio, which monitors $T_k \lesssim 150$ K, was not yet detected towards NGC 6946 (Mangum et al. 2013; Gorski et al. 2018). Those studies already showed that an unambiguous determination of the kinetic temperature is challenging.

Comparing our obtained T_k (HNC/HCN) to typical T_k measurements towards the central molecular zone (CMZ) in the Milky Way, reveals higher gas temperatures in the CMZ ($T_k > 40$ K; Ao et al. 2013; Ott et al. 2014; Ginsburg et al. 2016; Krieger et al. 2017). Investigating individual CMZ clouds, Ginsburg et al. (2016) used para-H_2CO transitions as a temperature tracer which is sensitive to warmer ($T_k > 20$ K) and denser (n ∼ 10^{4-5} cm^{-3}) gas. They determined gas temperatures ranging from ∼60 to >100 K. We know from extragalactic studies that high kinetic temperatures (50 to >250 K) can be produced by both cosmic ray and mechanical (turbulent) heating processes (Mangum et al. 2013; Gorski et al. 2018). The CMZ of our own Galaxy seems to be different in this respect where the mismatch between dust and gas temperature at moderately high density (n ∼ 10^{4-5} cm^{-3}) is better explained by mechanical heating (Ginsburg et al. 2016). However, it is not clear what might be the reason for observing low T_k in an environment where we expect mechanical heating processes.

Compared to the better studied extragalactic nuclear source NGC 253, Mangum et al. (2019) found kinetic temperatures on 5″ ≈ 85 pc scales of $T_k > 50$ K using ten transitions of H_2CO, while on scales <1″ (∼17 pc) they measure $T_k > 300$ K. Using NH_3 as a thermometer indicates the presence of a warm and hot component with $T_k = 75$ K and $T_k > 150$ K, respectively (Gorski et al. 2018; Pérez-Beaupuits et al. 2018). The reported HCN/HNC ratio over the whole nucleus is ∼1, which if Hacar et al. (2020) were true would imply T_k(HNC/HCN) ∼ 10 K. This is in contrast to the aforementioned warm component a factor of 7 lower. It indicates that this ratio provides no reliable information about T_k in the extragalactic region of NGC 253.

We find for the eight kpc-sized galaxy centers in the EMPIRE sample – using Eq. (16) – T_k (HNC/HCN) lower than 50 K for almost all galaxies[16]. NGC 3627 and NGC 5055 exhibit higher kinetic temperatures, 58 K and 61 K, respectively. Bešlić et al. (2021) found towards NGC 3627 on 100 pc scales (using the same framework) lower T_k (HNC/HCN) of ∼34 K.

In summary, the HNC/HCN ratio results in low inferred kinetic temperatures in galaxy centres ($T_k < 50$ K) if Hacar et al. (2020) prescription can be applied. However, in the absence of other accurate kinetic temperature measurements (with NH_3 or H_2CO) against NGC 6946 and the EMPIRE galaxies, we speculate that the isomer ratio is not a suitable T_k probe for large sized extragalactic regions, and, in particular, towards galaxy centres that can also have high optical depths and complex chemistry (also AGN activity and prominent additional excitation mechanisms). A comparison with similarly high resolution observations towards a galaxy centre using kinetic temperatures derived from ammonia emission would be worthwhile to further investigate the HNC/HCN temperature sensitivity framework of Hacar et al. (2020).

6.3. Examining ratios among HCN, HCO$^+$ and HNC as a diagnostic of AGN state

Clouds of gas in the inner kpc of galaxies are exposed to intense radiation, which can emanate from an active galactic nucleus (AGN), seen as hard X-rays with $E > 1$ keV; from starburst regions, dominated by radiation of O and B stars; or from both. Excess of X-ray emission affects the thermal and chemical balance of the surrounding ISM, which in turn could influence molecular line emission (see below). The centre of NGC 6946 exhibits no clear indication for the presence of an AGN. Holt et al. (2003) studied the distribution of the X-ray emission over the full disc of NGC 6946 and found several low-luminosity point-like sources, one of which coincides with the dynamical centre determined by Schinnerer et al. (2006).

Theoretical modelling of ratios between HCO$^+$ and HCN suggested it as a diagnostic tool to distinguish between photon-dominated regions (PDRs) and X-ray-dominated regions (XDRs) for a given column density of N ∼ 10^{23} cm^{-2} in the presence of ionizing radiation (Meijerink & Spaans 2005; Meijerink et al. 2007). In their models the HCO$^+$/HCN ratio seems to systematically vary with gas density, the incident ultraviolet and infrared radiation field. Also mechanical heating and cosmic ray ionization could be possible sources of variations in HCO$^+$/HCN (Bayet et al. 2010; Meijerink et al. 2011). Including HNC to the analyses, Loenen et al. (2008) claims that in XDRs HNC is always stronger than the HCN line, whereas the inverse trend is seen in PDRs (resulting in line ratios lower than unity). For their analyses they used observations obtained with the IRAM 30-m telescope for the HCN, HNC, HCO$^+$ line emission of 37 infrared luminous galaxies (Baan et al. 2008) and additional 80 sources from the literature (see Loenen et al. 2008 and references therein); all unresolved measurements. Then they compared the observational data with the predictions of PDR

[15] The equation in Hacar et al. (2020) uses HCN over HNC (HCN/HNC), therefore we have for e.g. NUC = 1/0.37 = 2.7.

[16] For NGC 3627, NGC 4254 and NGC 5055 we had to take for the calibration the second part of the two-part linear function in Hacar et al. (2020).

and XDR models (Meijerink et al. 2007) with varying volume densities, ranging from $10^{4.5}$ to $10^{6.0}$ cm^{-3}.

A low HCO$^+$/HCN ratio was proposed as the signature of an AGN. Since studies of galaxies hosting an AGN have found evidence for enhanced emission from HCN, relative to HCO$^+$ (e.g. Kohno et al. 2001; Imanishi et al. 2007; Davies et al. 2012). Recently, however, this statement has been under discussion, for example, in Privon et al. (2020). They investigated *NuSTAR* hard X-ray emission together with literature HCO$^+$ and HCN observations and found no correlation between the HCO$^+$/HCN ratio and the X-ray to IR luminosity ratio or the AGN luminosity. Thus, observing enhanced HCN relative to HCO$^+$ against a galaxy centre is not convincingly linked to currently observed AGN activity.

We now apply the PDR versus XDR framework by Baan et al. (2008) and Loenen et al. (2008) to our observed dense gas tracers towards the centre of NGC 6946 and investigate *Chandra* X-ray observations.

We see from the top panels of Fig. 5 that the HCO$^+$/HCN and HNC/HCN ratios exhibit values lower than unity in all three regions (see Table 7). In Fig. 8 we investigate the diagnostic plots proposed by Baan et al. (2008) and Loenen et al. (2008) to visually discriminate between XDR and PDR by comparing the line ratios between HCO$^+$, HCN and HNC in the central 20″ ≈ 745 pc towards NGC 6946. In all these diagnostic plots (panels a–d), NGC 6946 is in the PDR regime. Panel d could indicate a linear relationship between HNC/HCN and HNC/HCO$^+$. We see $\log_{10}$(HNC/HCN) in the range of −0.80 to −0.25 and $\log_{10}$(HNC/HCO$^+$) between −0.70 and +0.10. We investigate which mechanism could cause the observed ranges of line ratios. For this purpose we run the Meijerink & Spaans (2005) models for the PDR case. In particular, we investigate two scenarios: (i) fixing the radiation field ($G_0 = 10^2$) with varying densities ranging of $n = 10^5$–10^6 cm^{-3}, and (ii) fixing the density ($n = 10^{5.5}$ cm^{-3}) with varying radiation field[17] of $G_0 = 10^2$–10^5 (see panel i and ii in Fig. 8). For the first scenario, we find consistent ratios for $n \sim 10^{5.25}$–$10^{5.75}$ cm^{-3}, but the predicted ratios span a narrow range (from $\log_{10}$(HNC/HCO$^+$ = −0.25 to +0.10) compared to the observations (red shaded areas). On the other hand, $\log_{10}$(HNC/HCN) remains rather constant. In the second case, $\log_{10}$(HNC/HCO$^+$) decreases roughly linearly with G_0, from −0.2 to −0.7. This corresponds quite well to our observed ranges. From this we conclude that the scatter we observe in $\log_{10}$(HNC/HCO$^+$) (panel d) is mainly due to variations in the radiation field strength, with smaller ratios for stronger radiation fields. From all these diagnostic plots (panels a–d), it seems that the centre of NGC 6946 is dominated by photons (PDR) rather than X-rays (XDR).

For NGC 6946 – as mentioned above – there is no clear evidence for an AGN. In the following we investigate whether there are X-ray sources that are strong enough to trigger an XDR, although the diagnostic diagrams favour a PDR. The *Chandra* X-ray map (0.5–7.0 keV) in counts towards the central 20″ of NGC 6946 shows us that most of the diffuse X-ray emission is coming from a region not associated with the NUC, SBE and NBE (see Fig. 8). The stronger of the two detected X-ray sources near NUC by Holt et al. (2003) (shown as black crosses) is ∼2″ away from the dynamical centre position (shown as red circle). They find a flux of 2.8×10^{-13} erg s^{-1} cm^{-2} and classified its hardness as 'medium' (see their Table 2 for SourceID 45). Scaling this flux to our working resolution results in 4.53×10^{-3} erg s^{-1} cm^{-2}[18]. This is similar to the lowest values in Meijerink et al. (2007). This suggests that the brightest X-ray source might affect the gas within a beam scale, but hardly beyond that.

Interestingly, all the kpc-sized central regions of the EMPIRE galaxies in Fig. 8 lie in the PDR regime. Their $\log_{10}$(HNC/HCN) ratios are in the same range as those observed for NGC 6946. On the other hand, $\log_{10}$(HNC/HCO$^+$) varies only from −0.60 to −0.20. The galaxies NGC 3627, NGC 5055 and M 51 are known to host an AGN classified as LINER (Goulding & Alexander 2009) and are still located in the PDR regime in Fig. 8. There is no strong enhanced HCN emission relative to HCO$^+$ towards these three galaxy centres which would 'move' them to the XDR regime of the diagnostic plots. The fact that they do not lie within the XDR region of Loenen et al. (2008) could be because: (a) their models are not quantitatively accurate; (b) the EMPIRE AGNs are faint and their effects are diluted when averaging over 1 kpc regions; and (c) a different model that does not require the significant variations in the line ratio to be driven by a PDR or XDR (e.g. Viti 2017). We test the dilution effects in a way that we include available high-resolution dense gas observations of M 51 and NGC 3627 (i.e. ∼4″ ≈ 166 pc from Querejeta et al. 2016 and ∼2″ ≈ 100 pc from Bešlić et al. 2021, respectively; see Sect. 2.3). For both, we show line ratios for the central beam size; they are all in the PDR regime. From that we speculate that the diagnostic plots shown in Fig. 8 and in particular the HCO$^+$/HCN line ratio might not be a unique indicator to diagnose the presence of an AGN in galaxies on kpc/sub-kpc scales. This finding is consistent with the previous studies by Privon et al. (2020) and Li et al. (2021).

6.4. Density variations at the inner bar ends and nuclear region

Already in Fig. 2 we saw that the CO(1–0) and CO(2–1) emission is spatially more extended than HCN(1–0), HCO$^+$(1 – 0) or HNC(1–0), which could be a sign that the CO lines trace a lower density regime. That said, line intensities depend not only on density, but also on optical depth, elemental abundance variations and IR pumping (see e.g. Shirley 2015; Barnes et al. 2020b), and all of these effects can thus drive the relative line intensity ratios.

Leroy et al. (2017) analysed how changes in the sub-beam density distributions affect the beam-averaged line emissivity, by applying non-LTE radiative transfer models coupled with a parametrised density probability distribution. They found that the strength of tracer emission for dense gas is more sensitive to changes in gas density than for example CO. More precisely, the line can still be emitted at densities below the critical density, but with lower efficiency. As a result, a small increase in gas density can significantly increase the efficiency of the emission. This is not the case for lines with a lower critical density (e.g. bulk molecular gas tracer – CO). The density of the gas exceeds the critical density, so varying the gas density does not significantly affect the efficiency of the emission.

We investigate the scenario from Leroy et al. (2017) that line ratios can reflect changes in density distributions. In Fig. 9 we investigate the dependence of the observed molecular line ratios. The colourbar shows the integrated intensity of CO (an indicator of the volume density at cloud scales Leroy et al. 2016;

[17] $G_0 = 10^2$ and $G_0 = 10^5$ are the default minimum and maximum G_0 in their model outputs.

[18] Assuming the source is point-like, we scale the flux by $(D/d)^2$, where D is the distance to NGC 6946 and d is the distance from the X-ray source, 2″.

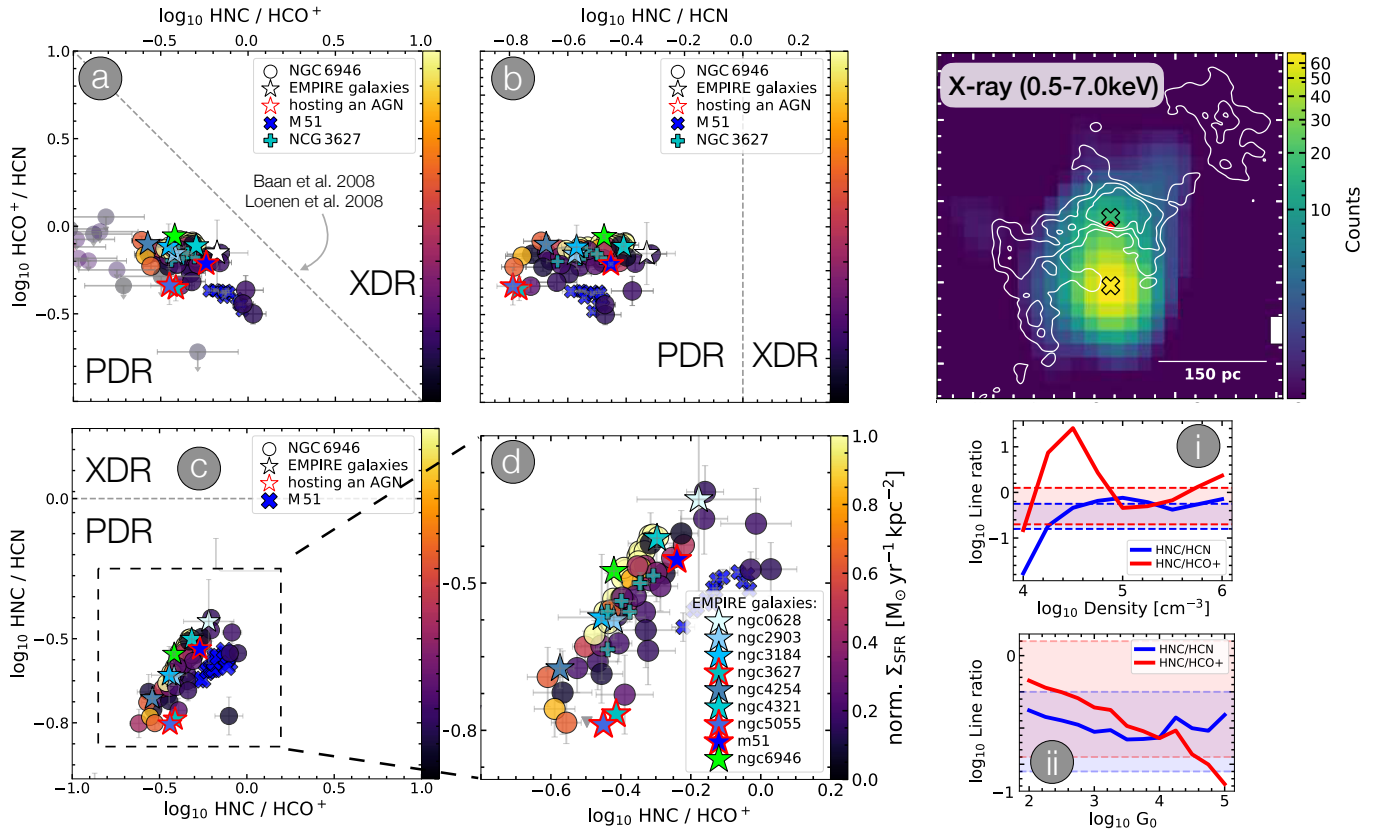

Fig. 8. Diagnostic plots using integrated line ratios of HCN, HNC and HCO^+ versus each other. *Left panels:* (*a*): integrated HCO^+/HCN versus HNC/HCO^+ ratios. (*b*): integrated HCO^+/HCN versus HNC/HCN ratios. (*c*): integrated HNC/HCN versus HNC/HCO^+ ratios. The grey dashed lines marks the boarder between XDR and PDR (Baan et al. 2008; Loenen et al. 2008). Circles indicate reliable values ($S/N > 5$) and upper limits for the central $20'' \approx 745$ pc towards NGC 6946. Stars show the EMPIRE galaxies and stars with red contours present galaxy centres hosting an AGN (Goulding & Alexander 2009). For two of them we find ancillary data: the cross shaped markers show the $\sim 4''$ ($\approx$166 pc) M 51 observations (Querejeta et al. 2016) and the $\sim 2''$ ($\approx$100 pc) NGC 3627 observations (Bešlić et al. 2021). (*d*): the enclosed integrated HNC/HCN versus HNC/HCO^+ with the kpc-sized centres of the EMPIRE survey (see Jiménez-Donaire et al. 2019 for details). NGC 6946 and the EMPIRE galaxies are in the PDR regime in all panels. Interestingly, EMPIRE galaxies harbouring an AGN do not show an enhancement of HCN as suggested in many studies (see text for a discussion). We run (Meijerink & Spaans 2005) PDR models for the observed ranges of line ratios (blue and red shaded areas) by (i) fixing the radiation field and (ii) fixing the density. The red and blue lines show the model output (more in text). The colours in (*a–d*) indicate Σ_{SFR}. We have normalised them to the mean Σ_{SFR} value and find no trend with the integrated line ratios. *Upper right panel*: X-ray 0.5–7.0 keV in counts for NGC 6946 with integrated CO(2–1) contours on top. The black crosses mark the positions of the detected X-ray sources by Holt et al. (2003) which are not strong enough to trigger a XDR.

Sun et al. 2018) towards the 150 pc sized NUC, NBE and SBE (see Fig. 4; we take the mean over the 7 hexagonal points). The upper panel shows on the *y*-axis logarithmic molecular line ratios with CO(2–1). At first glance, within NUC we find line ratios being enhanced by at least 20% compared to the inner bar ends. Identifying ratio variations by eye in the two bar ends is challenging. The lower panel shows the relative differences. Here we divide for example HCN/CO by the mean HCN/CO of all the 3 regions. We ordered them by their flaring appearance. We see the trend is not monotonic with n_{eff}, instead they show an order of HCN < HCO^+ < HNC; that is the order of decreasing intensity. We find that the highest ratios are associated with NUC (purple marker), except for the CO(1–0)/CO(2–1) ratio. Comparing the two bar ends we find (i) higher ratio values towards the SBE (orange marker) for ratios including CO(1–0) and HCN, (ii) higher ratio values towards the NBE (brown markers) for ratios including HCO^+ and HNC and, (iii) that the highest differences between the SBE and NBE is ~10% which are ratios including CO(1–0) and HCO^+. The HCO^+ intensity in the SBE seems to be under-luminous compared to the other two environments. The HNC intensity provides the largest dynamic range, with the highest value seen in the NUC and the lowest one in the SBE.

We compare the observed line ratios of CO, HCN, HCO^+ and HNC in the three regions using radiative transfer models to estimate the mass-weighted mean gas density. From the temperature analyses (see Sect. 6.2) we would expect potential higher densities in the bar ends, whereas from the R_{21} examinations (see Sect. 6.1) we would anticipate higher molecular densities in the NBE than in the SBE. Furthermore, from our derived Σ_{SFR} (see Sect. 4 and Table 7) we would expect higher molecular gas densities in the SBE than in the NBE. For that purpose we use the radiative transfer code `Dense Gas Toolbox` (Puschnig 2020) which is based on the approach by Leroy et al. (2017) including that emission lines emerge from an isothermal ensemble of gas densities that follow a log-normal distribution (with or without power-law tail) in combination with `RADEX` calculations (van der Tak et al. 2007). It works as follows: (i) Using Bayesian inference, model parameters (i.e. temperature and density) are inferred from a number of integrated input line

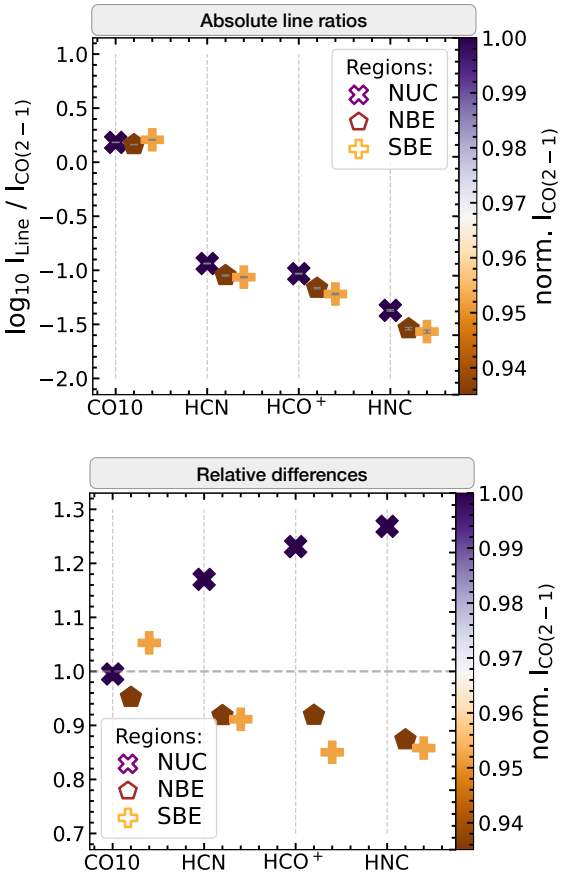

Fig. 9. Line ratios for the nuclear region and inner-bar ends. *Top*: scatter plot showing the mean line ratios of the 7 hexagonal points for each molecule on the *y*-axis with respect to CO(2−1). For visualisation purpose we spaced the markers along the *x*-axis. The different shapes of the markers present the defined regions. The colourbar shows the normalised CO(2−1) integrated intensity to the mean CO(2−1) value. We plot the propagated errors in grey and find that they are very small. For the ratios we applied a signal-to-noise cut (see Sect. 5.1). *Bottom*: the relative differences of the line ratios with respect to the mean of the line ratios among the different regions (linear-scale).

intensities. (ii) The assumed fixed line optical depths and abundances are calibrated through observations of the EMPIRE survey (Jiménez-Donaire et al. 2019, which includes NGC 6946). (iii) Then it solves for line emissivities in each density bin which are calculated using expanding-sphere escape probabilities (large velocity gradient approximation) as implemented in `RADEX` (van der Tak et al. 2007). (iv) Given the estimated kinetic temperature in Sect. 6.2, we are assuming a fixed temperature of 30 K. A more detailed description of the `Dense Gas Toolbox` will be provided in Puschnig et al. (in prep.). The models suggest that the density in NUC is highest with a mass-weighted mean density of $\sim 10^{4.0}$ cm^{-3}, while the lowest one is found in the NBE with a value of $\sim 10^{3.7}$ cm^{-3}.

In summary, these models broadly agree with our empirical findings of Fig. 9. The higher mass-weighted mean densities in the SBE agree with the enhanced $\Sigma_{\rm SFR}$ in the SBE (compared to the NBE). However, the model results do not explain the elevated R_{21} in NBE (see Fig. 7) and, therefore, an additional physical mechanism has to be responsible for it. A note of caution is appropriate, as the mass-weighted mean density differences found among the three regions are of small magnitude and might not be significant in conjunction with the model assumptions (see Table 7). For example, the kinetic temperature in the model is fixed and the same for the two bar ends and the nuclear region. An accurate measurement of kinetic temperatures on parsec scales could unveil the duality of the bar ends.

7. Conclusion

In this paper we present the high-resolution (2−4″ ≈ 75−150 pc at 7.7 Mpc distance) IRAM PdBI multi-molecule observation towards the inner 50″ ≈ 1.9 kpc of the Fireworks Galaxy, NGC 6946 (see Fig. 1). Our compiled data set includes a total of 14 detected molecular lines in the mm-wavelength range. For the analyses in this paper, we convolve our molecular lines to a common beam size of 4″, and analyse three distinct environmental regions associated with the inner bar of NGC 6946: the nuclear region (NUC), the northern inner bar end (NBE) and the southern inner bar end (SBE) (see Fig. 4 for mask and Table 7). We find the following results:

(1) We report the first detection of $C_2H(1-0)$, $HC_3N(10-9)$ and $HC_3N(16-15)$ towards NGC 6946.

(2) The different lines show distinct morphology. More extended emission is seen with CO(1−0), CO(2−1) (associated with bulk molecular gas), $HCO^+(1-0)$, HCN(1−0) and HNC(1−0). The latter three are typically used to trace denser gas. We find that even denser gas (e.g. as seen by $N_2H^+(1-0)$) and shocks (e.g. as seen by $CH_3OH(2-1)$) are more concentrated in the SBE than in the NUC or NBE (see Fig. 2).

(3) We discover a higher star formation rate (SFR) in the SBE. Shocks and denser gas in this bar end could possibly enhance star formation compared to the lower SFR in NBE.

We use our *u*−*v* trimmed and short-spacing corrected data set (SSC + *u*−*v* trim data) which includes CO(1−0), CO(2−1), HCN(1−0), $HCO^+(1-0)$ and HNC(1−0) to investigate how they relate to $\Sigma_{\rm SFR}$ and how the dense gas fraction ($f_{\rm dense}$) and the star formation efficiency ($\rm SFE_{dense}$) respond to the integrated intensity of CO(2−1) (an indicator of mean volume density).

(4) We find among our molecules that $HCO^+(1-0)$ correlates best with $\Sigma_{\rm SFR}$, with Pearson's correlation coefficient $\rho \sim 0.95$. Additionally, we find a relation of ρ to the effective critical density ($n_{\rm eff}$) of the dense gas tracers.

(5) The dense gas fraction fits do not follow the order of $n_{\rm eff}$, instead they show the order of $\beta_{\rm HNC} > \beta_{\rm HCO^+} > \beta_{\rm HCN}$. The strongest correlation among our mean volume density versus different $f_{\rm dense}$ is $I_{\rm CO(2-1)}$ versus HNC/CO(2−1) with $\rho \sim 0.76$.

(6) We find that $\rm SFE_{dense}$ increases with increasing gas surface density (i.e. $I_{\rm CO(2-1)}$ emission) within the inner ∼1 kpc of NGC 6946, contrary to the opposite trends found within low-resolution observations covering the whole disc (Gallagher et al. 2018a; Jiménez-Donaire et al. 2019). The reason for this is that we are resolving structures within this region, such as the nuclear region (NUC; inner ∼0.15 kpc) that appears to exhibit $\rm SFE_{dense}$ enhancements relative to the rest of the centre.

We test line ratio diagnostic plots and compare our high-resolution (150 pc) dense gas tracer towards NGC 6946 with those of eight other galaxy centres in the EMPIRE survey (angular resolution of 33″ ∼ 1 kpc) and discuss implications for other galaxy centre studies.

(7) From previous studies higher CO(1−0) to CO(2−1) (R_{21}) values are expected in the inner kiloparsec compared to their disc. We find R_{21} variations in the centre; higher R_{21}

in NBE (∼0.7) than in the NUC or SBE (∼0.65 and ∼0.62). The reason for this could be, for example, denser gas that is in the NBE. However, we do not find an increase of higher $f_{\rm dense}$ in NBE (see Fig. 7 and Table 7).

(8) Whether the ratio between HCN and HNC is temperature dependent has been discussed by several authors in the past. We speculate that the isomer ratio is not an accurate probe for kinetic temperatures for kiloparsec and sub-kiloparsec sized extragalactic regions. This is because, if the prescription of Hacar et al. (2020) can be applied here, the HCN/HNC ratio results in low $T_{\rm k}$ (<50 K, for NGC 6946 as well as for six EMPIRE galaxies, IC 342 and NGC 253) which is up to a factor of 7 lower compared to other existing $T_{\rm k}$ measurements (NH_3 or H_2CO).

(9) The observed HCO^+/HCN ratios have been proposed to be a diagnostic tool to distinguish between XDR and PDR. The diagnostic plots for the centre of NGC 6946 favour a PDR. We find that an X-ray source about 2″ away from the dynamical centre does not affect the molecular gas properties in the nucleus. However, when we include the EMPIRE galaxy centres in our analysis, we find that those galaxies that have an active galactic nucleus (AGN) fall within the PDR range in these diagnostic diagrams. We find for two of these AGN host galaxies higher resolution observations (∼100 pc for NGC 3627 and ∼166 pc for M 51) which also lay in the PDR regime. Thus, the HCO^+/HCN ratio might not be a unique indicator to diagnose AGN activity in galaxies at (sub-)kiloparsec scales. This ambiguity is consistent with recent studies (see Fig. 8 and Sect. 6.3).

(10) Molecular line ratios may reflect changes in the (unresolved) gas density distributions (Leroy et al. 2017). The ratios to CO, show enhanced line ratios within the NUC compared to the inner bar ends. $HCO^+(1-0)$ in NBE seems to be under-luminous compared to the NUC and SBE. On the other hand, HNC provides the largest dynamic range, with the highest values in the NUC and the lowest in the SBE (see Fig. 9). We compared that with radiative transfer models and find mass-weight mean densities of $\sim 10^{3.7-4.3}$ cm^{-3} for the NUC, while the NBE shows the lowest mean density of $\sim 10^{3.3-4.1}$ cm^{-3}. The higher mean densities in the SBE compared to the NBE agree with the higher integrated line intensities and the enhanced SFR in the SBE.

This study reflects the importance of analysing molecular lines to better understand galactic centres. Also, it shows that bar ends in galaxies can vary in their dense gas fraction, star formation rate, integrated line ratios and molecular gas densities. In future work we follow up on the investigation of shocks, the densest gas tracers in our extended data set and examine the kinematic and dynamic of the inner bar in more detail.

Acknowledgements. We would like to thank the anonymous referee for their insightful comments that helped improve the quality of the paper. C.E. gratefully acknowledges funding from the Deutsche Forschungsgemeinschaft (DFG) Sachbeihilfe, grant number BI1546/3-1. F.B., A.B., I.B., J.P. and J.d.B. acknowledge funding from the European Research Council (ERC) under the European Union's Horizon 2020 research and innovation programme (grant agreement No. 726384/Empire). E.S., D.L., H.A.P., T.S. and T.G.W. acknowledge funding from the European Research Council (ERC) under the European Union's Horizon 2020 research and innovation programme (grant agreement No. 694343). I.L. acknowledges funding from the Deutsche Forschungsgemeinschaft (DFG) Sachbeihilfe, grant number SCHI 536/11-1. M.C. and J.M.D.K. gratefully acknowledge funding from the Deutsche Forschungsgemeinschaft (DFG) in the form of an Emmy Noether Research Group (grant number KR4801/1-1) and the DFG Sachbeihilfe (grant number KR4801/2-1), and from the European Research Council (ERC) under the European Union's Horizon 2020 research and innovation programme via the ERC Starting Grant MUSTANG (grant agreement number 714907). H.H. acknowledges the support of the Natural Sciences and Engineering Research Council of Canada (NSERC), funding reference number RGPIN-2017-03987 and the Canadian Space Agency funding reference 21EXPUVI3. SCOG and RSK acknowledge financial support from the German Research Foundation (DFG) via the collaborative research center (SFB 881, Project-ID 138713538) 'The Milky Way System' (subprojects A1, B1, B2, and B8). They also acknowledge funding from the Heidelberg Cluster of Excellence 'STRUCTURES' in the framework of Germany's Excellence Strategy (grant EXC-2181/1, Project-ID 390900948) and from the European Research Council via the ERC Synergy Grant 'ECOGAL' (grant 855130). The work of AKL is partially supported by the National Science Foundation under Grants No. 1615105, 1615109, and 1653300. J.P. acknowledges support from the Programme National "Physique et Chimie du Milieu Interstellaire" (PCMI) of CNRS/INSU with INC/INP co-funded by CEA and CNES. M.Q. acknowledges support from the Spanish grant PID2019-106027GA-C44, funded by MCIN/AEI/10.13039/501100011033. E.R. acknowledges the support of the Natural Sciences and Engineering Research Council of Canada (NSERC), funding reference number RGPIN-2017-03987. T.S. acknowledges funding from the European Research Council (ERC) under the European Union's Horizon 2020 research and innovation programme (grant agreement No. 694343). M.C.S. acknowledges financial support from the German Research Foundation (DFG) via the collaborative research center (SFB 881, Project-ID 138713538) "The Milky Way System" (subprojects A1, B1, B2, and B8). A.U. acknowledges support from the Spanish grants PGC2018-094671-B-I00, funded by MCIN/AEI/10.13039/501100011033 and by "ERDF A way of making Europe", and PID2019-108765GB-I00, funded by MCIN/AEI/10.13039/501100011033. Y.-H.T. acknowledges funding support from NRAO Student Observing Support Grant SOSPADA-012 and from the National Science Foundation (NSF) under grant No. 2108081. Y.G. acknowledges support by National Key Basic R&D Program of China (2017YFA0402704), NSFC grants 11861131007 and 12033004.

References

Aalto, S., Polatidis, A. G., Hüttemeister, S., & Curran, S. J. 2002, A&A, 381, 783
Aladro, R., Viti, S., Bayet, E., et al. 2013, A&A, 549, A39
Anand, G. S., Rizzi, L., & Tully, R. B. 2018, AJ, 156, 105
Ao, Y., Henkel, C., Menten, K. M., et al. 2013, A&A, 550, A135
Astropy Collaboration (Robitaille, T. P., et al.) 2013, A&A, 558, A33
Astropy Collaboration (Price-Whelan, A. M., et al.) 2018, AJ, 156, 123
Baan, W. A., Henkel, C., Loenen, A. F., Baudry, A., & Wiklind, T. 2008, A&A, 477, 747
Barnes, A. T., Longmore, S. N., Battersby, C., et al. 2017, MNRAS, 469, 2263
Barnes, A. T., Longmore, S. N., Avison, A., et al. 2019, MNRAS, 486, 283
Barnes, A. T., Longmore, S. N., Dale, J. E., et al. 2020a, MNRAS, 498, 4906
Barnes, A. T., Kauffmann, J., Bigiel, F., et al. 2020b, MNRAS, 497, 1972
Bayet, E., Awad, Z., & Viti, S. 2010, ApJ, 725, 214
Belloche, A., Müller, H. S. P., Menten, K. M., Schilke, P., & Comito, C. 2013, A&A, 559, A47
Bemis, A., & Wilson, C. D. 2019, AJ, 157, 131
Beuther, H., Thorwirth, S., Zhang, Q., et al. 2005, ApJ, 627, 834
Beuther, H., Meidt, S., Schinnerer, E., Paladino, R., & Leroy, A. 2017, A&A, 597, A85
Bešlić, I., Barnes, A. T., Bigiel, F., et al. 2021, MNRAS, 506, 963
Bigiel, F., Leroy, A. K., Blitz, L., et al. 2015, ApJ, 815, 103
Bigiel, F., Leroy, A. K., Jiménez-Donaire, M. J., et al. 2016, ApJ, 822, L26
Bigiel, F., de Looze, I., Krabbe, A., et al. 2020, ApJ, 903, 30
Billington, S. J., Urquhart, J. S., König, C., et al. 2020, MNRAS, 499, 2744
Bolatto, A. D., Wolfire, M., & Leroy, A. K. 2013, ARA&A, 51, 207
Callanan, D., Longmore, S. N., Kruijssen, J. M. D., et al. 2021, MNRAS, 505, 4310
Chevance, M., Kruijssen, J. M. D., Hygate, A. P. S., et al. 2020a, MNRAS, 493, 2872
Chevance, M., Kruijssen, J. M. D., Vazquez-Semadeni, E., et al. 2020b, Space Sci. Rev., 216, 50
Combes, F., García-Burillo, S., Casasola, V., et al. 2013, A&A, 558, A124
Cormier, D., Bigiel, F., Jiménez-Donaire, M. J., et al. 2018, MNRAS, 475, 3909
Crosthwaite, L. P. 2002, PASP, 114, 929
Davies, R., Mark, D., & Sternberg, A. 2012, A&A, 537, A133
de Blok, W. J. G., Walter, F., Brinks, E., et al. 2008, AJ, 136, 2648
de Lorenzo-Cáceres, A., Méndez-Abreu, J., Thorne, B., & Costantin, L. 2020, MNRAS, 494, 1826
den Brok, J. S., Chatzigiannakis, D., Bigiel, F., et al. 2021, MNRAS, 504, 3221
de Vaucouleurs, G., de Vaucouleurs, A., Corwin, H. G., Jr., et al. 1991, Third Reference Catalogue of Bright Galaxies (New York: Springer)
Díaz-García, S., Moyano, F. D., Comerón, S., et al. 2020, A&A, 644, A38
Dickinson, C., Ali-Haïmoud, Y., Barr, A., et al. 2018, New Astron. Rev., 80, 1
Elmegreen, D. M., Chromey, F. R., & Santos, M. 1998, AJ, 116, 1221
Emsellem, E., Goudfrooij, P., & Ferruit, P. 2003, MNRAS, 345, 1297

Emsellem, E., Renaud, F., Bournaud, F., et al. 2015, MNRAS, 446, 2468
Engelbracht, C. W., Rieke, M. J., Rieke, G. H., & Latter, W. B. 1996, ApJ, 467, 227
Erwin, P. 2011, Mem. Soc. Astron. It. Suppl., 18, 145
Federrath, C., & Klessen, R. S. 2013, ApJ, 763, 51
Font, J., Beckman, J. E., Zaragoza-Cardiel, J., et al. 2014, MNRAS, 444, L85
Friesen, R. K., Pineda, J. E., Rosolowsky, E., et al. 2017, ApJ, 843, 63
Gallagher, M. J., Leroy, A. K., Bigiel, F., et al. 2018a, ApJ, 858, 90
Gallagher, M. J., Leroy, A. K., Bigiel, F., et al. 2018b, ApJ, 868, L38
Gao, Y., & Solomon, P. M. 2004, ApJS, 152, 63
García-Burillo, S., Viti, S., Combes, F., et al. 2017, A&A, 608, A56
Ginsburg, A., Henkel, C., Ao, Y., et al. 2016, A&A, 586, A50
Gorski, M., Ott, J., Rand, R., et al. 2018, ApJ, 856, 134
Goulding, A. D., & Alexander, D. M. 2009, MNRAS, 398, 1165
Graninger, D. M., Herbst, E., Öberg, K. I., & Vasyunin, A. I. 2014, ApJ, 787, 74
Hacar, A., Bosman, A. D., & van Dishoeck, E. F. 2020, A&A, 635, A4
Harada, N., Sakamoto, K., Martín, S., et al. 2018, ApJ, 855, 49
Helfer, T. T., & Blitz, L. 1993, ApJ, 419, 86
Henkel, C., Mühle, S., Bendo, G., et al. 2018, A&A, 615, A155
Henshaw, J. D., Longmore, S. N., Kruijssen, J. M. D., et al. 2016, MNRAS, 457, 2675
Herbst, E., Terzieva, R., & Talbi, D. 2000, MNRAS, 311, 869
Hirota, T., Yamamoto, S., Mikami, H., & Ohishi, M. 1998, ApJ, 503, 717
Holdship, J., Viti, S., Martín, S., et al. 2021, A&A, 654, A55
Holt, S. S., Schlegel, E. M., Hwang, U., & Petre, R. 2003, ApJ, 588, 792
Imanishi, M., Nakanishi, K., Tamura, Y., Oi, N., & Kohno, K. 2007, AJ, 134, 2366
James, T. A., Viti, S., Holdship, J., & Jiménez-Serra, I. 2020, A&A, 634, A17
Jiang, X.-J., Greve, T. R., Gao, Y., et al. 2020, MNRAS, 494, 1276
Jiménez-Donaire, M. J., Bigiel, F., Leroy, A. K., et al. 2019, ApJ, 880, 127
Kauffmann, J., Goldsmith, P. F., Melnick, G., et al. 2017, A&A, 605, L5
Kelly, B. C. 2007, ApJ, 665, 1489
Kelly, G., Viti, S., Bayet, E., Aladro, R., & Yates, J. 2015, A&A, 578, A70
Kennicutt, R. C., & Evans, N. J. 2012, ARA&A, 50, 531
Kennicutt, R. C., Jr., Armus, L., Bendo, G., et al. 2003, PASP, 115, 928
Kennicutt, R. C., Calzetti, D., Aniano, G., et al. 2011, PASP, 123, 1347
Kessler, S., Leroy, A., Querejeta, M., et al. 2020, ApJ, 892, 23
Kim, J., Chevance, M., Kruijssen, J. M. D., et al. 2021, MNRAS, 504, 487
Klessen, R. S., & Glover, S. C. O. 2016, Saas-Fee Advanced Course, 43, 85
Koda, J., Sawada, T., Sakamoto, K., et al. 2020, ApJ, 890, L10
Kohno, K., Matsushita, S., Vila-Vilaró, B., et al. 2001, in The Central Kiloparsec of Starbursts and AGN: The La Palma Connection, eds. J. H. Knapen, J. E. Beckman, I. Shlosman, & T. J. Mahoney, ASP Conf. Ser., 249, 672
Krieger, N., Ott, J., Beuther, H., et al. 2017, ApJ, 850, 77
Krieger, N., Bolatto, A. D., Leroy, A. K., et al. 2020, ApJ, 897, 176
Kroupa, P. 2001, MNRAS, 322, 231
Kruijssen, J. M. D., Longmore, S. N., Elmegreen, B. G., et al. 2014, MNRAS, 440, 3370
Kruijssen, J. M. D., Schruba, A., Hygate, A. P. S., et al. 2018, MNRAS, 479, 1866
Kruijssen, J. M. D., Schruba, A., Chevance, M., et al. 2019, Nature, 569, 519
Krumholz, M. R., & Thompson, T. A. 2007, ApJ, 669, 289
Krumholz, M. R., Kruijssen, J. M. D., & Crocker, R. M. 2017, MNRAS, 466, 1213
Lada, C. J., & Lada, E. A. 2003, ARA&A, 41, 57
Lada, C. J., Lombardi, M., & Alves, J. F. 2010, ApJ, 724, 687
Lada, C. J., Forbrich, J., Lombardi, M., & Alves, J. F. 2012, ApJ, 745, 190
Lee, H. H., Bettens, R. P. A., & Herbst, E. 1996, A&AS, 119, 111
Leitherer, C., Schaerer, D., Goldader, J. D., et al. 1999, ApJS, 123, 3
Leroy, A. K., Walter, F., Bigiel, F., et al. 2009, AJ, 137, 4670
Leroy, A. K., Walter, F., Sandstrom, K., et al. 2013, AJ, 146, 19
Leroy, A. K., Hughes, A., Schruba, A., et al. 2016, ApJ, 831, 16
Leroy, A. K., Usero, A., Schruba, A., et al. 2017, ApJ, 835, 217
Leroy, A. K., Bolatto, A. D., Ostriker, E. C., et al. 2018, ApJ, 869, 126
Leroy, A. K., Hughes, A., Liu, D., et al. 2021, ApJS, 255, 19
Levine, E. S., Helfer, T. T., Meijerink, R., & Blitz, L. 2008, ApJ, 673, 183
Li, F., Wang, J., Gao, F., et al. 2021, MNRAS, 503, 4508
Linden, S. T., Murphy, E. J., Dong, D., et al. 2020, ApJS, 248, 25
Loenen, A. F., Spaans, M., Baan, W. A., & Meijerink, R. 2008, A&A, 488, L5
Long, K. S., Winkler, P. F., & Blair, W. P. 2019, ApJ, 875, 85
Longmore, S. N., Bally, J., Testi, L., et al. 2013, MNRAS, 429, 987
Mangum, J. G., Darling, J., Henkel, C., et al. 2013, ApJ, 779, 33
Mangum, J. G., Ginsburg, A. G., Henkel, C., et al. 2019, ApJ, 871, 170
Martín, S., Kohno, K., Izumi, T., et al. 2015, A&A, 573, A116
Mauersberger, R., & Henkel, C. 1989, IAU Circ., 4889, 1
Mauersberger, R., & Henkel, C. 1991, A&A, 245, 457
Mauersberger, R., Henkel, C., Wilson, T. L., & Harju, J. 1989, A&A, 226, L5
McKee, C. F., & Ostriker, E. C. 2007, ARA&A, 45, 565
Meier, D. S., & Turner, J. L. 2004, AJ, 127, 2069
Meier, D. S., & Turner, J. L. 2005, ApJ, 618, 259
Meier, D. S., & Turner, J. L. 2012, ApJ, 755, 104
Meier, D. S., Turner, J. L., & Hurt, R. L. 2000, ApJ, 531, 200
Meier, D. S., Walter, F., Bolatto, A. D., et al. 2015, ApJ, 801, 63
Meijerink, R., & Spaans, M. 2005, A&A, 436, 397
Meijerink, R., Spaans, M., & Israel, F. P. 2007, A&A, 461, 793
Meijerink, R., Spaans, M., Loenen, A. F., & van der Werf, P. P. 2011, A&A, 525, A119
Méndez-Abreu, J., de Lorenzo-Cáceres, A., Gadotti, D. A., et al. 2019, MNRAS, 482, L118
Menéndez-Delmestre, K., Sheth, K., Schinnerer, E., Jarrett, T. H., & Scoville, N. Z. 2007, ApJ, 657, 790
Morris, M., & Serabyn, E. 1996, ARA&A, 34, 645
Murphy, E. J., Condon, J. J., Schinnerer, E., et al. 2011, ApJ, 737, 67
Murphy, E. J., Bremseth, J., Mason, B. S., et al. 2012, ApJ, 761, 97
Murphy, E. J., Dong, D., Leroy, A. K., et al. 2015, ApJ, 813, 118
Murphy, E. J., Dong, D., Momjian, E., et al. 2018, ApJS, 234, 24
Nguyen, Q. R., Jackson, J. M., Henkel, C., Truong, B., & Mauersberger, R. 1992, ApJ, 399, 521
Ott, J., Weiß, A., Staveley-Smith, L., Henkel, C., & Meier, D. S. 2014, ApJ, 785, 55
Padoan, P., Federrath, C., Chabrier, G., et al. 2014, in Protostars and Planets VI, eds. H. Beuther, R. S. Klessen, C. P. Dullemond, & T. Henning, 77
Palagi, F., Cesaroni, R., Comoretto, G., Felli, M., & Natale, V. 1993, A&AS, 101, 153
Pan, H.-A., Kuno, N., Koda, J., et al. 2015, ApJ, 815, 59
Peñaloza, C. H., Clark, P. C., Glover, S. C. O., & Klessen, R. S. 2018, MNRAS, 475, 1508
Pérez-Beaupuits, J. P., Güsten, R., Harris, A., et al. 2018, ApJ, 860, 23
Petkova, M. A., Kruijssen, J. M. D., Kluge, A. L., et al. 2021, MNRAS, submitted [arXiv:2104.09558]
Pety, J., Schinnerer, E., Leroy, A. K., et al. 2013, ApJ, 779, 43
Pety, J., Guzmán, V. V., Orkisz, J. H., et al. 2017, A&A, 599, A98
Privon, G. C., Ricci, C., Aalto, S., et al. 2020, ApJ, 893, 149
Puschnig, J. 2020, https://doi.org/10.5281/zenodo.3686329
Querejeta, M., Schinnerer, E., García-Burillo, S., et al. 2016, A&A, 593, A118
Querejeta, M., Schinnerer, E., Schruba, A., et al. 2019, A&A, 625, A19
Rathborne, J. M., Longmore, S. N., Jackson, J. M., et al. 2015, ApJ, 802, 125
Regan, M. W., & Vogel, S. N. 1995, ApJ, 452, L21
Renaud, F., Bournaud, F., Emsellem, E., et al. 2015, MNRAS, 454, 3299
Rodriguez-Fernandez, N., Pety, J., & Gueth, F. 2008, Single-dish Observation and Processing to Produce the Short-spacing Information for a Millimeter Interferometer, IRAM Memo 2008-2
Rosolowsky, E., & Leroy, A. 2006, PASP, 118, 590
Rosolowsky, E., Hughes, A., Leroy, A. K., et al. 2021, MNRAS, 502, 1218
Saito, T., Iono, D., Espada, D., et al. 2017, ApJ, 834, 6
Salak, D., Tomiyasu, Y., Nakai, N., et al. 2018, ApJ, 856, 97
Sandstrom, K. M., Leroy, A. K., Walter, F., et al. 2013, ApJ, 777, 5
Schilke, P., Walmsley, C. M., Pineau Des Forets, G., et al. 1992, A&A, 256, 595
Schinnerer, E., Böker, T., Emsellem, E., & Lisenfeld, U. 2006, ApJ, 649, 181
Schinnerer, E., Böker, T., Emsellem, E., & Downes, D. 2007, A&A, 462, L27
Shirley, Y. L. 2015, PASP, 127, 299
Solomon, P. M., Downes, D., & Radford, S. J. E. 1992, ApJ, 387, L55
Sormani, M. C., & Barnes, A. T. 2019, MNRAS, 484, 1213
Sormani, M. C., Tress, R. G., Glover, S. C. O., et al. 2020, MNRAS, 497, 5024
Sun, J., Leroy, A. K., Schruba, A., et al. 2018, ApJ, 860, 172
Tan, Q.-H., Gao, Y., Zhang, Z.-Y., et al. 2018, ApJ, 860, 165
Terwisscha van Scheltinga, J., Hogerheijde, M. R., Cleeves, L. I., et al. 2021, ApJ, 906, 111
Tsai, C.-W., Turner, J. L., Beck, S. C., Meier, D. S., & Wright, S. A. 2013, ApJ, 776, 70
Usero, A., Leroy, A. K., Walter, F., et al. 2015, AJ, 150, 115
van der Tak, F. F. S., Black, J. H., Schöier, F. L., Jansen, D. J., & van Dishoeck, E. F. 2007, A&A, 468, 627
Viti, S. 2017, A&A, 607, A118
Viti, S., Jimenez-Serra, I., Yates, J. A., et al. 2011, ApJ, 740, L3
Walter, F., Brinks, E., de Blok, W. J. G., et al. 2008, AJ, 136, 2563
Watanabe, N., Shiraki, T., & Kouchi, A. 2003, ApJ, 588, L121
Yajima, Y., Sorai, K., Miyamoto, Y., et al. 2021, PASJ, 73, 257

[1] Argelander-Institut für Astronomie, Universität Bonn, Auf dem Hügel 71, 53121 Bonn, Germany
e-mail: eibensteiner@astro.uni-bonn.de
[2] Max Planck Institut für Astronomie, Königstuhl 17, 69117 Heidelberg, Germany

[3] Max-Planck-Institut für Extraterrestrische Physik, Giessenbachstraße 1, 85748 Garching, Germany
[4] New Mexico Institute of Mining and Technology, 801 Leroy Place, Socorro, NM 87801, USA
[5] National Radio Astronomy Observatory, PO Box O, 1003 Lopezville Road, Socorro, NM 87801, USA
[6] Observatorio Astronómico Nacional (IGN), C/ Alfonso XII 3, 28014 Madrid, Spain
[7] Department of Astronomy, The Ohio State University, 4055 McPherson Laboratory, 140 West 18th Avenue, Columbus, OH 43210, USA
[8] 4-183 CCIS, University of Alberta, Edmonton, Alberta T6G 2E1, Canada
[9] Centre for Astrophysics Research, School of Physics, Astronomy and Mathematics, University of Hertfordshire, College Lane, Hatfield AL10 9AB, UK
[10] Institut de Radioastronomie Millimétrique (IRAM), 300 Rue de la Piscine, 38406 Saint Martin d'Hères, France
[11] LERMA, Observatoire de Paris, PSL Research University, CNRS, Sorbonne Universités, 75014 Paris, France
[12] European Southern Observatory, Karl-Schwarzschild Straße 2, 85748 Garching bei München, Germany
[13] Univ. Lyon, Univ. Lyon1, ENS de Lyon, CNRS, Centre de Recherche Astrophysique de Lyon UMR5574, 69230 Saint-Genis-Laval, France
[14] National Radio Astronomy Observatory (NRAO), 520 Edgemont Road, Charlottesville, VA 22903, USA
[15] Astronomisches Rechen-Institut, Zentrum für Astronomie der Universität Heidelberg, Mönchhofstraße 12-14, 69120 Heidelberg, Germany
[16] Universität Heidelberg, Zentrum für Astronomie, Institüt für Theoretische Astrophysik, Albert-Ueberle-Strasse 2, 69120 Heidelberg, Germany
[17] Department of Astronomy, Xiamen University, Xiamen, Fujian 361005, PR China
[18] Purple Mountain Observatory, Chinese Academy of Sciences (CAS), Nanjing 210023, PR China
[19] Research School of Astronomy and Astrophysics, Australian National University, Canberra, ACT 2611, Australia
[20] Universität Heidelberg, Interdisziplinäres Zentrum für Wissenschaftliches Rechnen, INF 205, 69120 Heidelberg, Germany
[21] Department of Physics, Tamkang University, No. 151, Yingzhuan Rd., Tamsui Dist., New Taipei City 251301, Taiwan
[22] Center for Astrophysics and Space Sciences, University of California San Diego, 9500 Gilman Drive, La Jolla, CA 92093, USA

Appendix A: Star formation rates

In this work, we used the 33 GHz continuum emission as a SFR tracer. We also found published 15 GHz and Hα observations in comparable angular resolution of our molecular data set (2″; see Table A.1). We chose the 33 GHz over the 15 GHz as a SFR tracer because the 33 GHz observations are: (1) higher in sensitivity (9.72 compared to 21.44 mK, Linden et al. 2020), and (2) probe less non-thermal emission (38% compared to 63%, see Equations below). We did not use extinction corrected Hα data (from Kessler et al. 2020) for our main SFR in this paper because: (1) they used 2″ sized apertures across the whole galaxy covering the bright Hα emitting regions (1σ threshold in Hα) for the extinction correction (using Paβ) and those apertures do not fully cover the inner kpc of NGC 6946, and (2) causes them to miss a handful of heavily attenuated regions in the centre of NGC 6946 (see Fig. 2 in Kessler et al. 2020).

In the following we check the consistency of our SFR derived from the 33 GHz thermal part of the radio continuum emission with the thermal part of the 15 GHz as a $\Sigma_{\rm SFR}$ tracer (observations from Murphy et al. 2018; Linden et al. 2020) for the inner kpc-sized region of NGC 6946.

1. *33 GHz continuum:* Using 33 GHz for the inner 1 kpc gives us a mean $\Sigma_{\rm SFR}$ of 0.792 $M_\odot\,{\rm yr}^{-1}\,{\rm kpc}^{-2}$.
2. *15 GHz continuum:* Before we can use Eq. (4), we first have to compute the thermal fraction ($f^{\rm T}$) at 15 GHz. We recall that we denote thermal as $^{\rm T}$, non-thermal as $^{\rm NT}$ and the frequency as ν. Knowing that $S_\nu^{\rm T} \propto \nu^{-\alpha^{\rm T}}$ with $\alpha^{\rm T} \sim 0.1$ and $S_\nu^{\rm NT} \propto \nu^{-\alpha^{\rm NT}}$ with $\alpha^{\rm NT} \sim 0.74$ (from Murphy et al. 2011 for the nucleus of NGC 6946), we find:

$$f^{\rm T}_{15\,{\rm GHz}} = \left(\frac{f^{\rm T}_{33\,{\rm GHz}}}{\frac{S^{\rm T}_{33\,{\rm GHz}}}{S^{\rm NT}_{33\,{\rm GHz}}}}\right) \times \left(\frac{S^{\rm T}_{15\,{\rm GHz}}}{S^{\rm NT}_{15\,{\rm GHz}}}\right). \tag{A.1}$$

   We take as in Section 2.3.2 $f^{\rm T}_{33\,{\rm GHz}} = 0.62$ and find using Eq. (A.1) that $f^{\rm T}_{15\,{\rm GHz}} = 0.37$. Now we are able to calculate $L_{\nu^{\rm T}}$ (Eq. (5)) and use Eq. (4) to convert the thermal fluxes into a SFR and further to $\Sigma_{\rm SFR}$. Within the central kpc-sized region we get a mean $\Sigma_{\rm SFR}$ of 0.774 $M_\odot\,{\rm yr}^{-1}\,{\rm kpc}^{-2}$.

We conclude, that the $\Sigma_{\rm SFR}$ for the inner kpc derived from 33 GHz and 15 GHz are within the margin of error (~1σ).

A.1. Correcting for distance

Schinnerer et al. (2007) found within a 3″ × 3″ region a SFR of ~0.1 $M_\odot\,{\rm yr}^{-1}$ adopting a distance of 5.5 Mpc. Using 33 GHz as a SFR tracer and taking the same distance and region, we get 0.06 $M_\odot\,{\rm yr}^{-1}$. Adopting the updated distance to NGC 6946 of 7.72 Mpc results in 0.11 $M_\odot\,{\rm yr}^{-1}$. This is only a factor of 1.8 higher.

Table A.1. References of the data shown in Fig. 1.

Panel in Fig. 1	λ, L	Instrument	Res.	Survey, Reference
(a, b)	optical	HST, Subaru		NASA, ESA, STScI, R. Gendler and the Subaru Telescope (NAOJ)
(c)	115 GHz	PdBI	1.4″	Schinnerer et al. (2006)
(d)	230 GHz	PdBI	0.4″	Schinnerer et al. (2006)
(e)	3 GHz	VLA	2.0″	SFRS, Murphy et al. (2018), Linden et al. (2020)
(f)	15 GHz	VLA	2.1″	SFRS, Murphy et al. (2018), Linden et al. (2020)
(g)	33 GHz	VLA	2.1″	SFRS, Murphy et al. (2018), Linden et al. (2020)
(h)	70 μm	*Herschel*/PACS	5.5″	KINGFISH, Kennicutt et al. (2011)
(i)	24 μm	*Spitzer*/MIPS	5.7″	SINGS, Kennicutt et al. (2003)
(j)	8 μm	*Spitzer*/IRAC	2.0″	SINGS, Kennicutt et al. (2003)
(k)	Paβ	HST	2.0″	Kessler et al. (2020)
(l)	Hα	3.5-m WIYN telescope	2.0″	Long et al. (2019), Kessler et al. (2020)
(m)	*X*-ray	*Chandra*		ObsIDs 1054 and 13435, Holt et al. (2003)

Notes: To overlay the contours of CO data on the optical images, we used `http://nova.astrometry.net/`

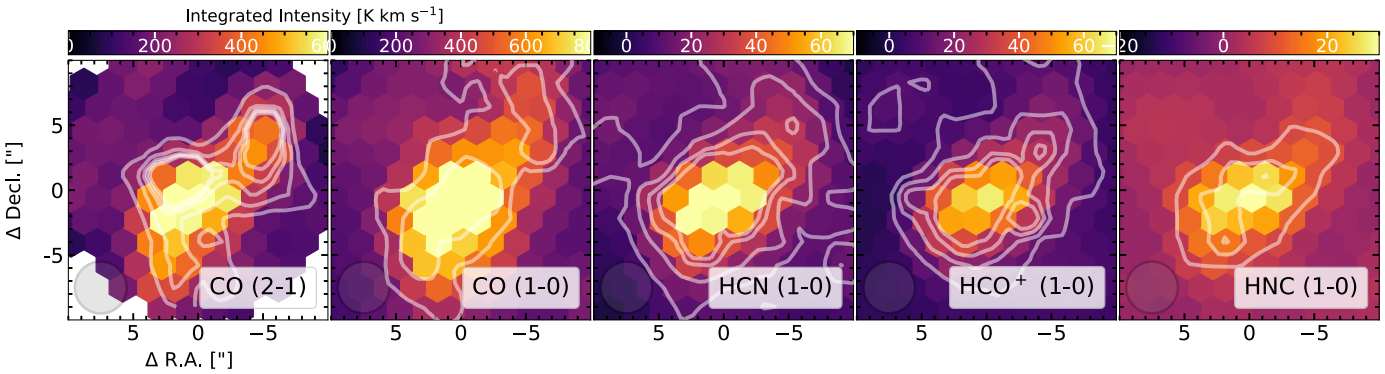

Fig. A.1. SSC + uv trim integrated intensity maps: The way of presenting the data is done as in Figure 2. Here, however, we performed a u–v cut and corrected for the short-spacing using available EMPIRE data for the three typical dense gas tracers. In the first two panels we show contours of 200, 300σ and in the remaining three panels contours of 3, 6, 9, 30, 60, 90σ.

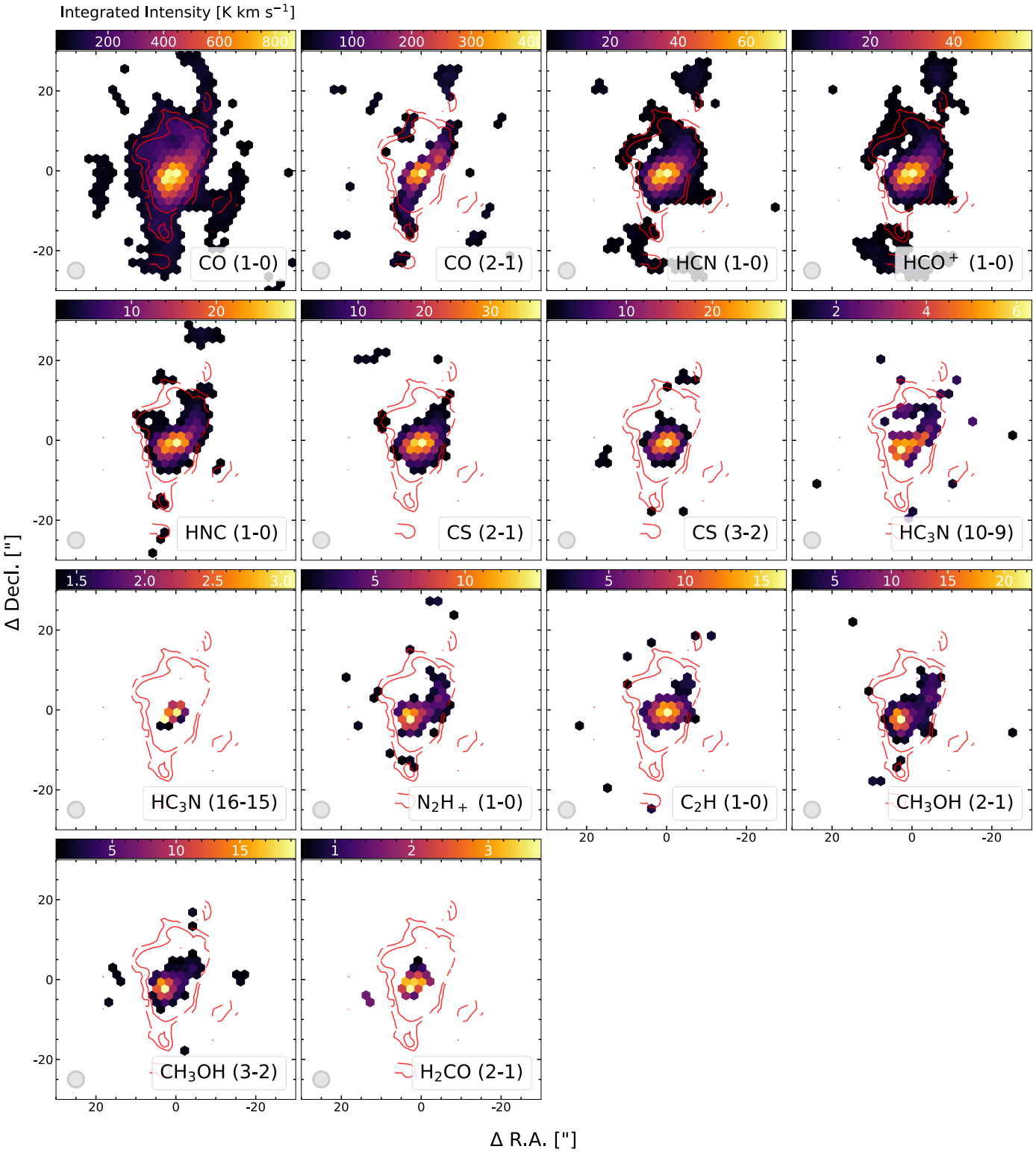

Fig. A.2. Same as Figure 2 but only showing hexagonal points with S/N > 25 for CO(1−0) and CO(2−1), and with S/N > 5 for all other lines.

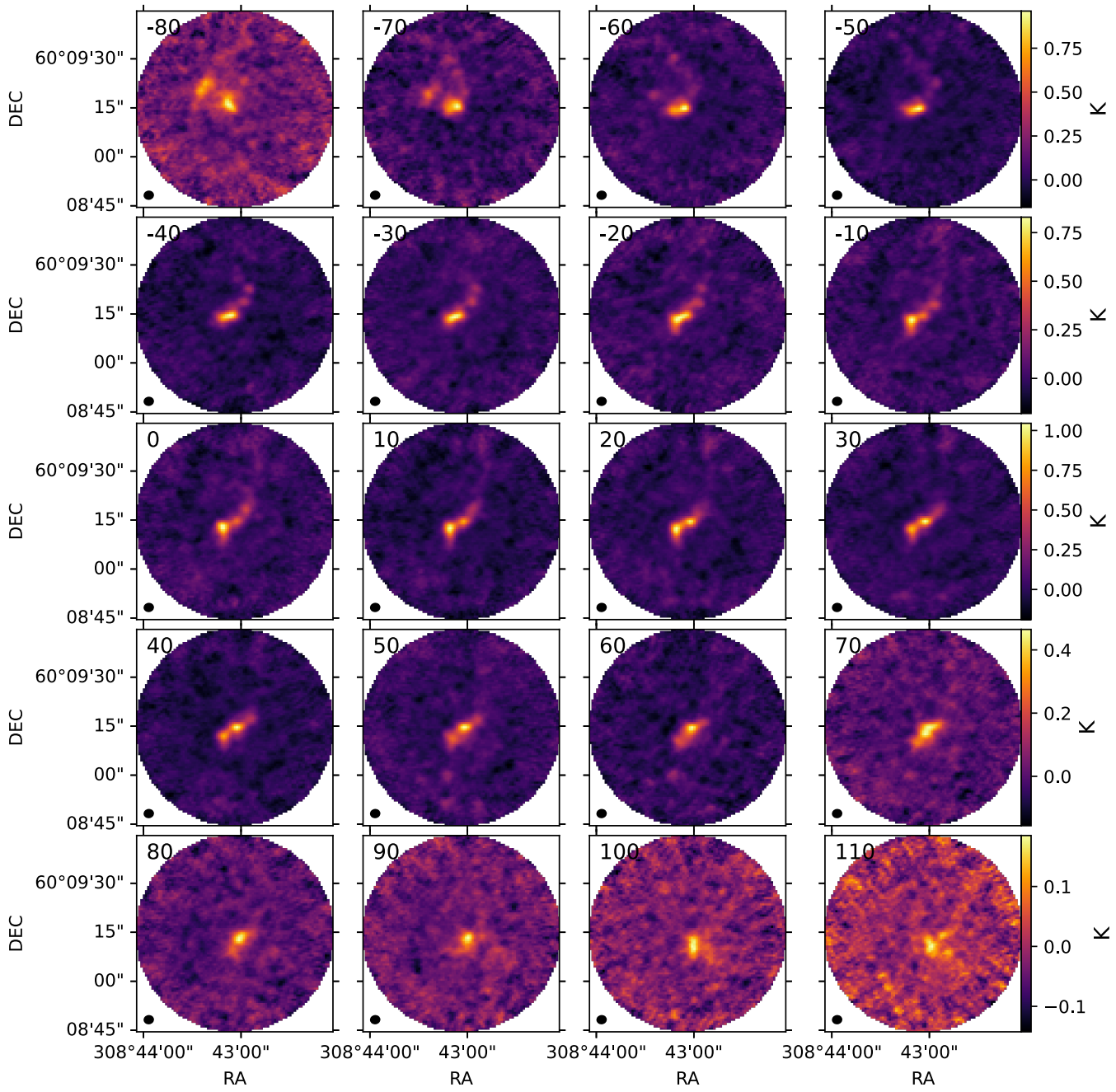

Fig. A.3. HCN channel maps, from −80 to 110 km s^{-1}.

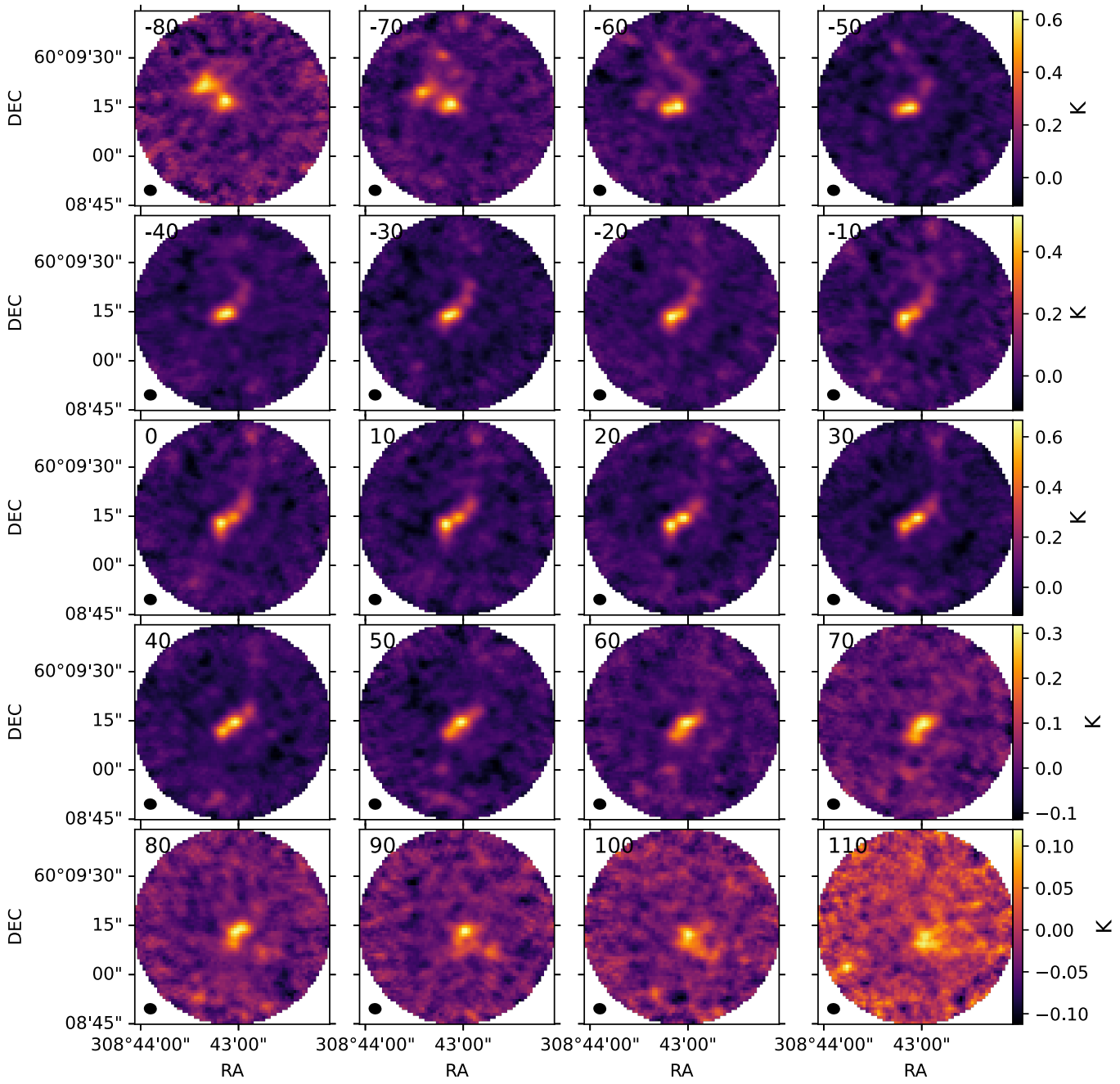

Fig. A.4. HCO^+ channel maps, from −80 to 110 km s^{-1}.

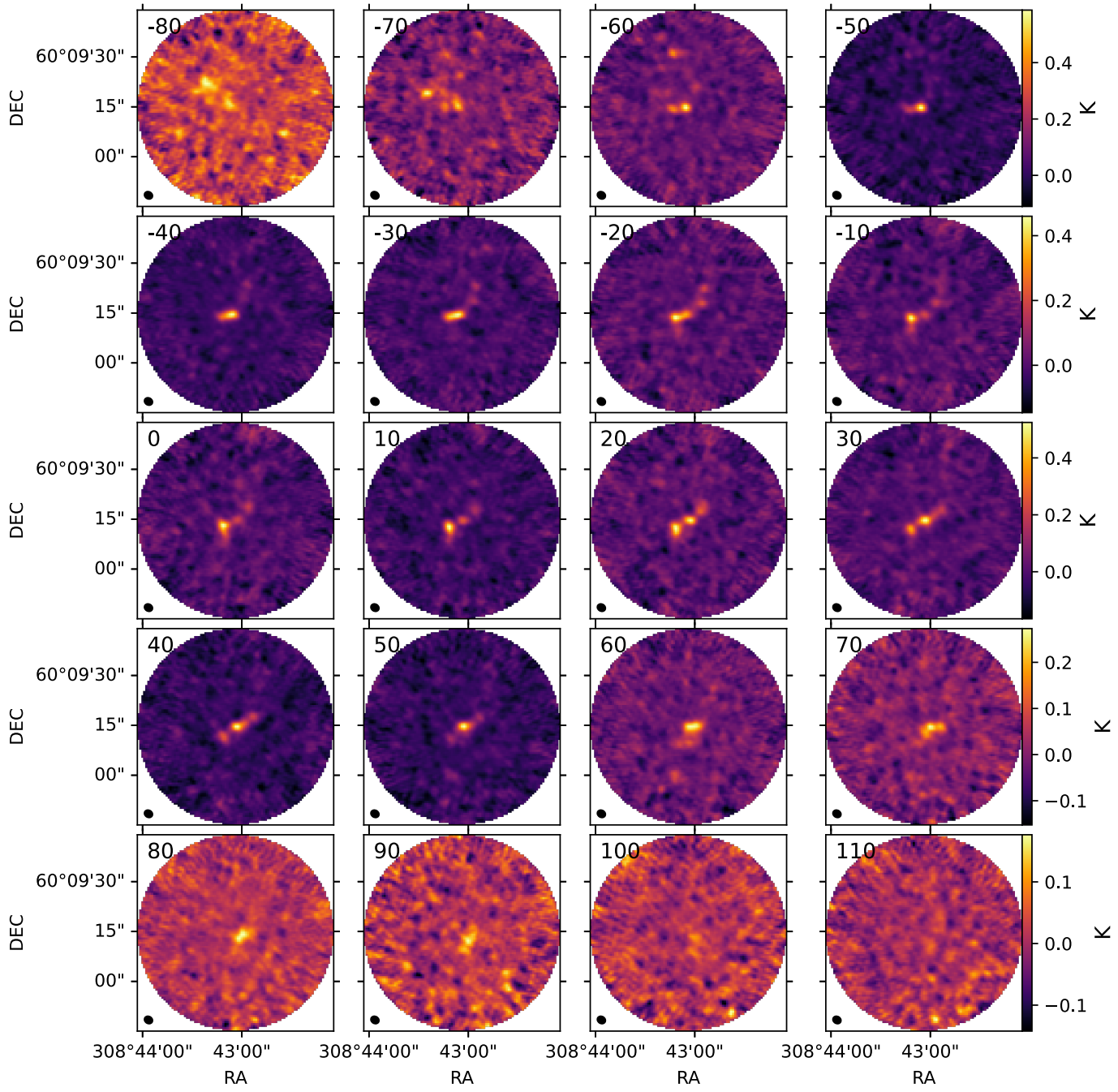

Fig. A.5. HNC channel maps, from -80 to 110 km s^{-1}.

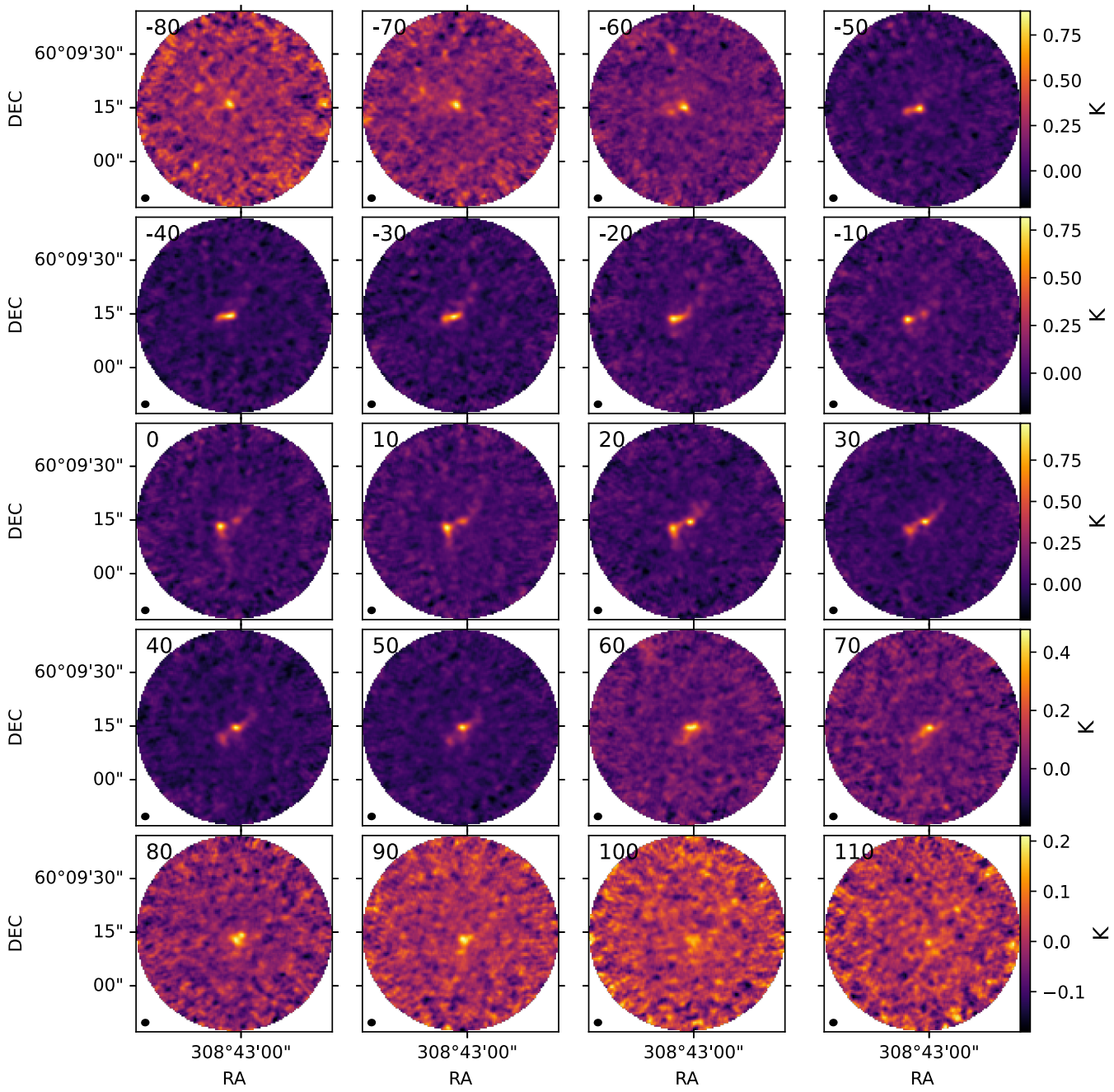

Fig. A.6. CS(2-1) channel maps, from -80 to 110 km s^{-1}.

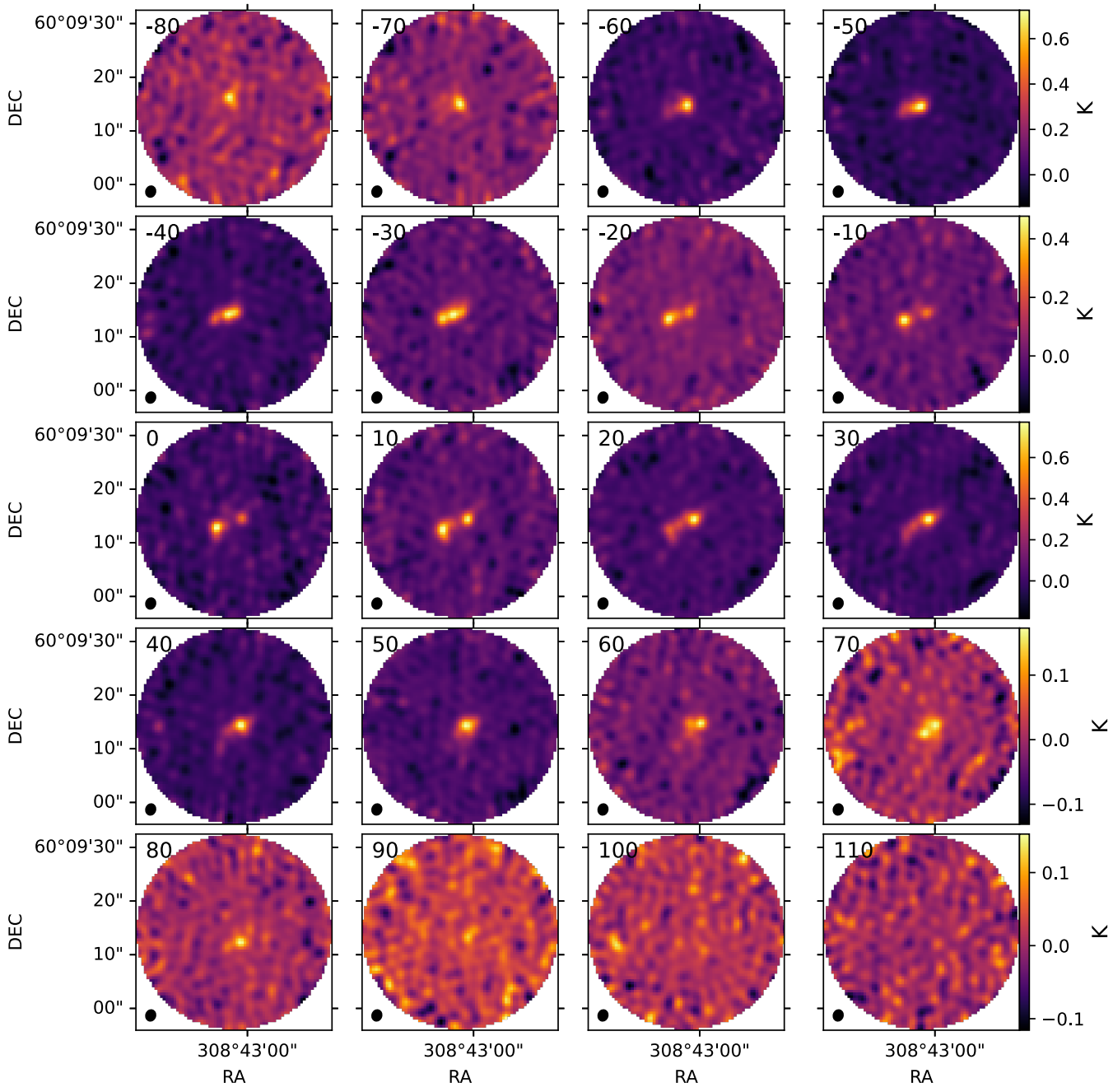

Fig. A.7. CS(3-2) channel maps, from -80 to 110 km s^{-1}.

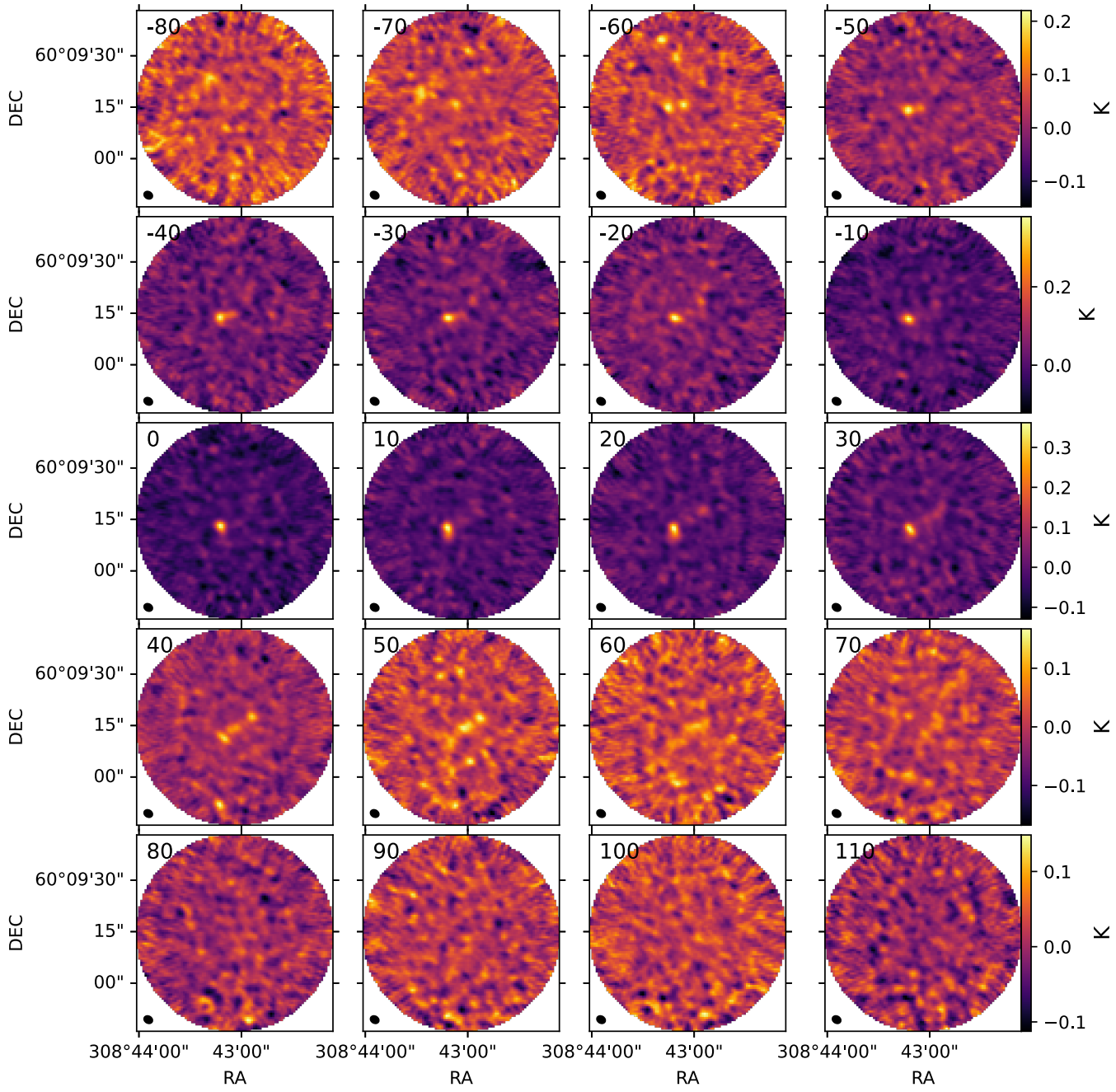

Fig. A.8. N_2H^+ channel maps, from -80 to 110 km s^{-1}.

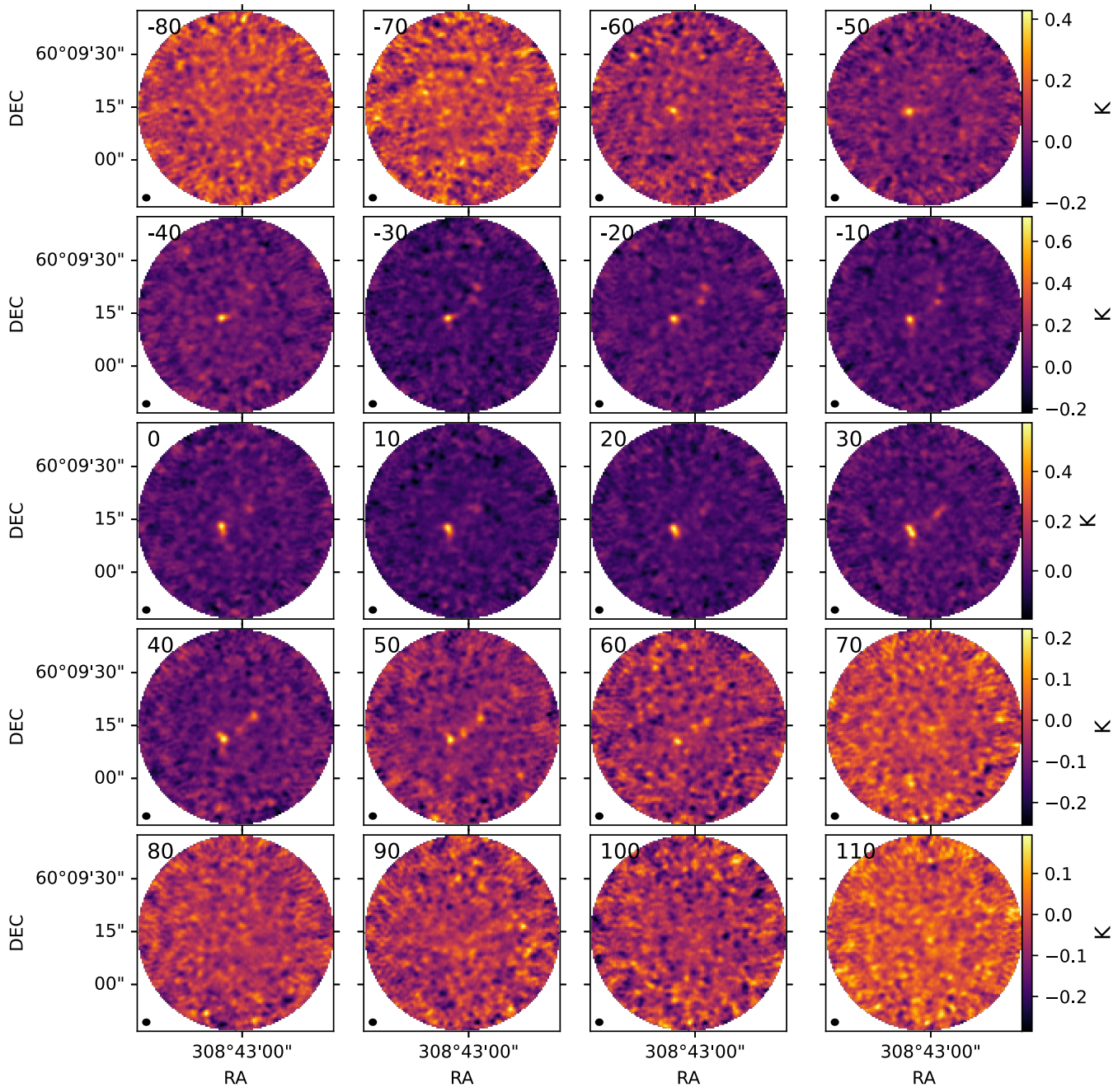

Fig. A.9. CH_3OH(2k-1k) channel maps, from -80 to 110 km s^{-1}.

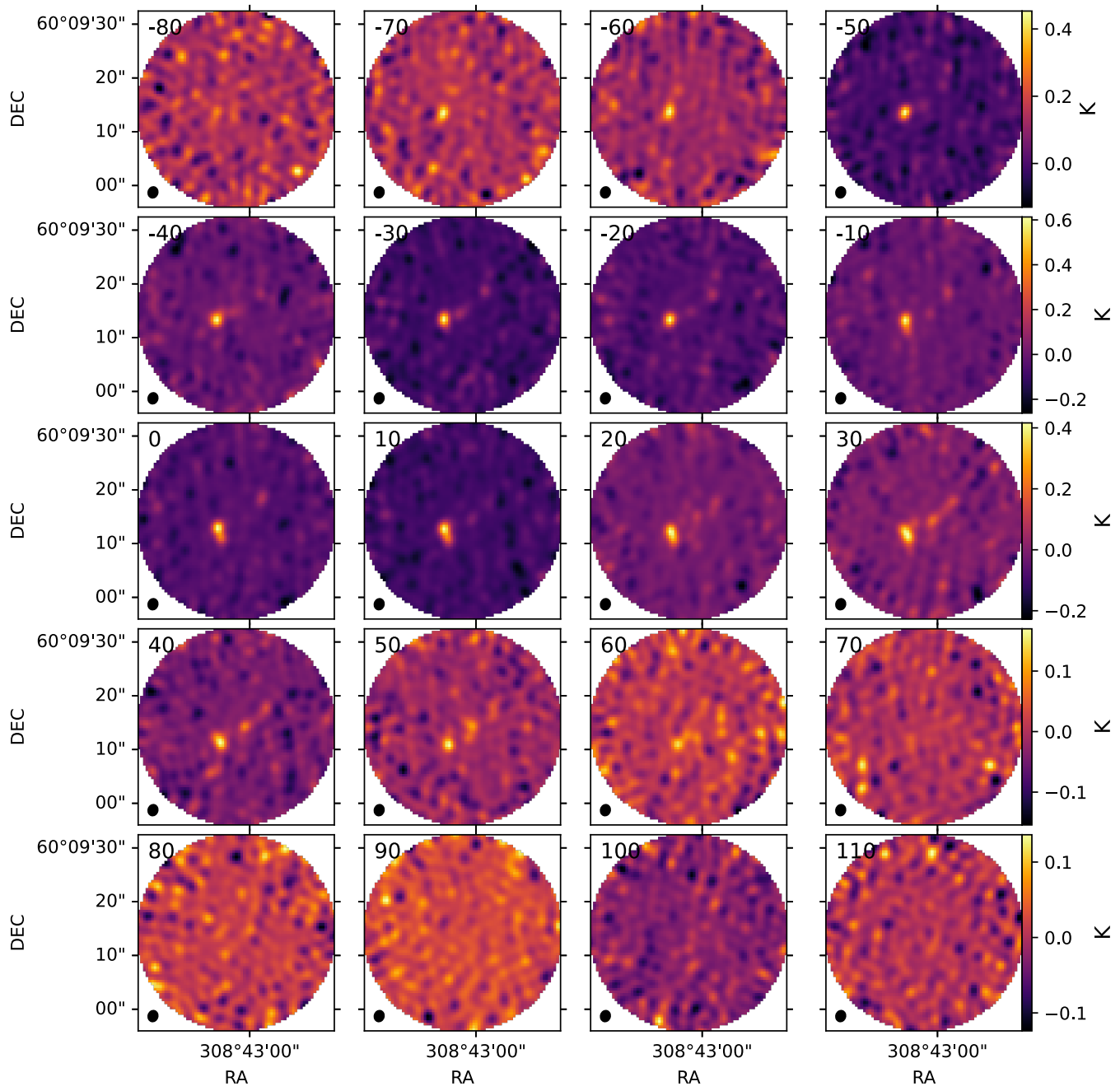

Fig. A.10. CH_3OH(3k-2k) channel maps, from -80 to 110 km s^{-1}.

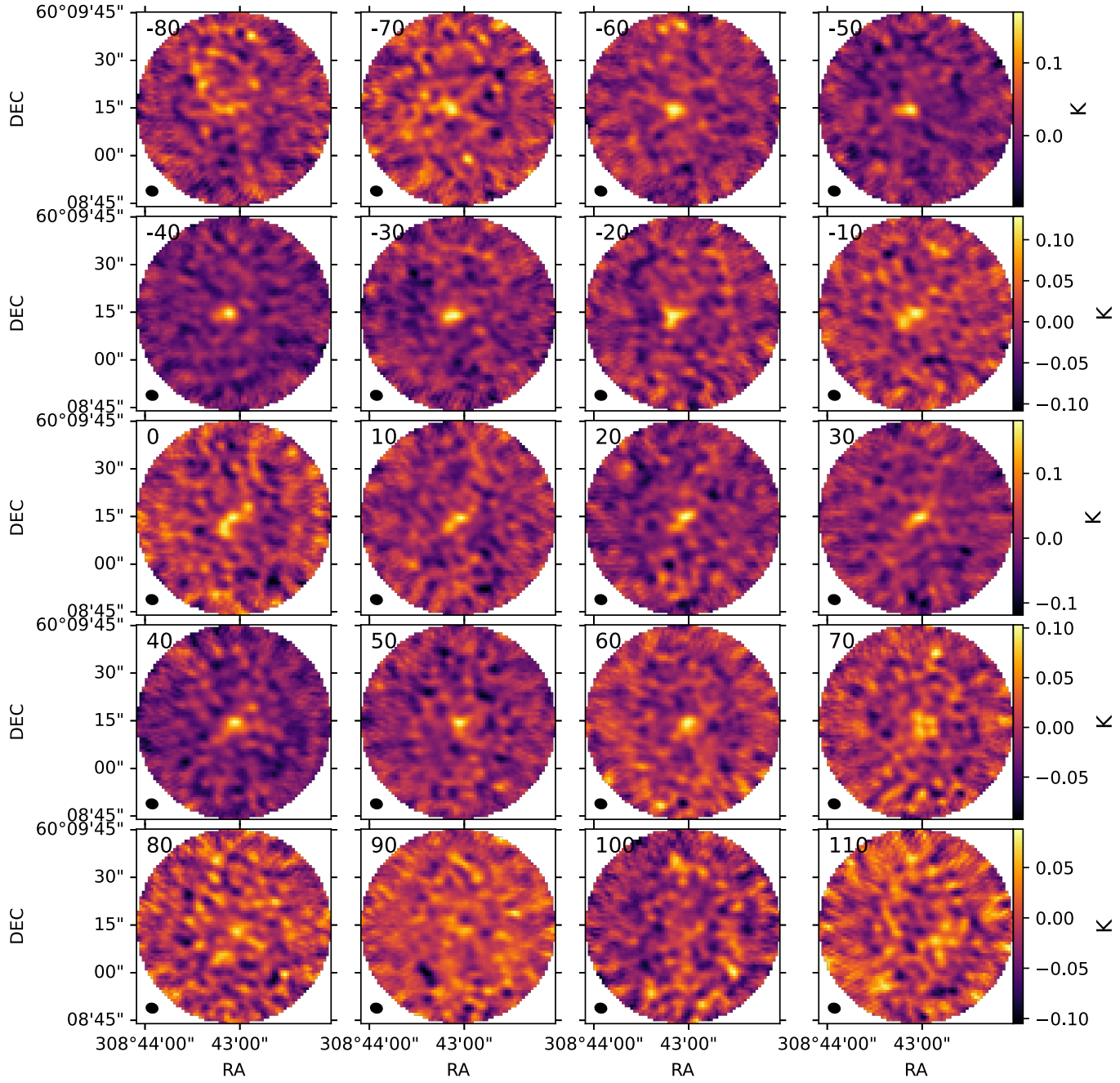

Fig. A.11. C_2H(1-0) channel maps, from -80 to 110 km s^{-1}.

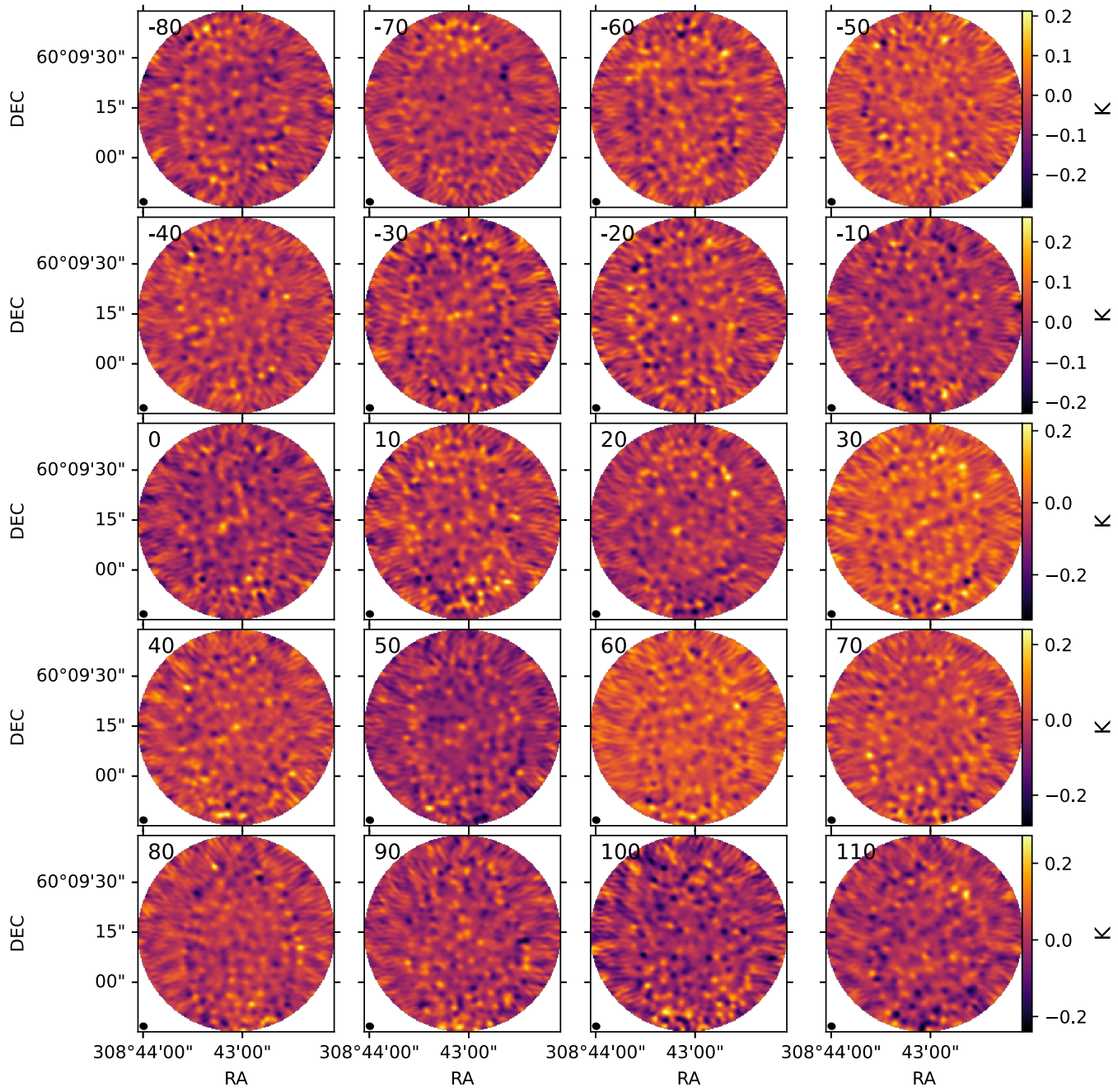

Fig. A.12. HC_3N(10-9) channel maps, from -80 to 110 km s^{-1}.

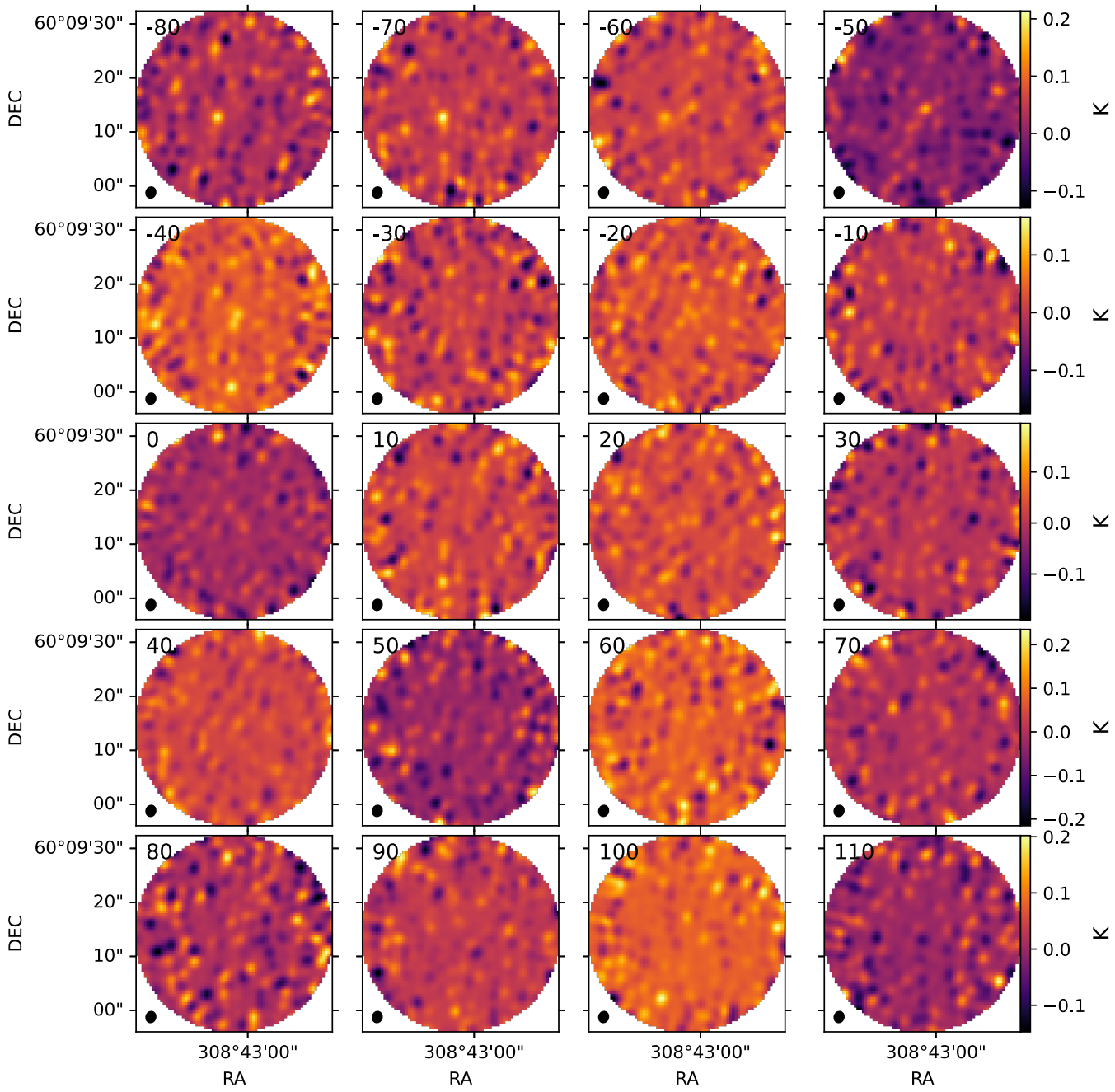

Fig. A.13. HC_3N(16-15) channel maps, from -80 to 110 km s^{-1}.

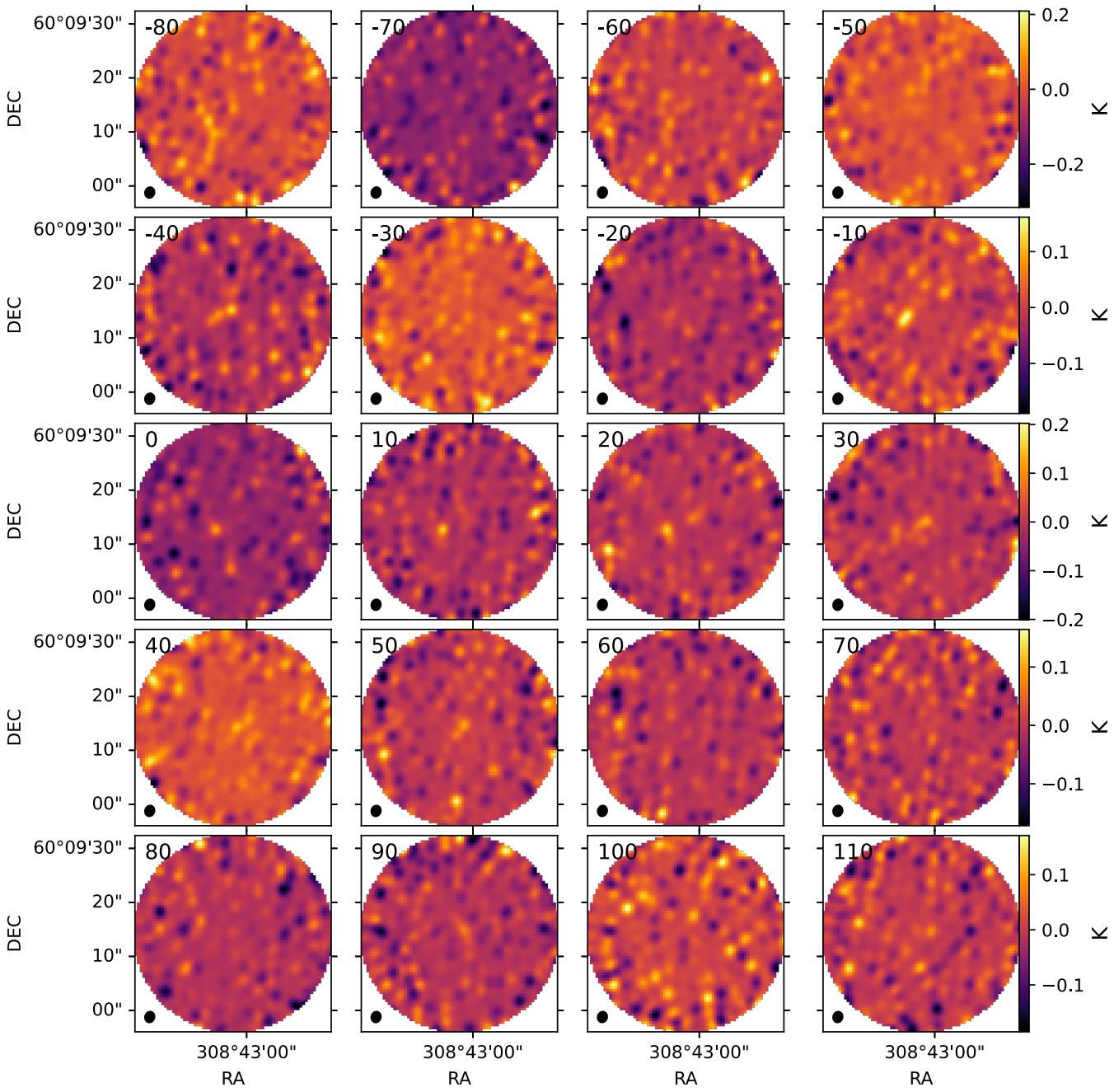

Fig. A.14. $H_2CO(2\text{-}1)$ channel maps, from -80 to 110 km s^{-1}.

APPENDIX B

Kinematic analysis of the super-extended HI disk of the nearby spiral galaxy M 83

The paper *Eibensteiner al. A&A (2023), 675, A37* is reproduced below in its original form with permission by ESO.

A&A 675, A37 (2023)
https://doi.org/10.1051/0004-6361/202245290

Astronomy & Astrophysics

Kinematic analysis of the super-extended H I disk of the nearby spiral galaxy M 83⋆,⋆⋆

C. Eibensteiner[1], F. Bigiel[1], A. K. Leroy[2], E. W. Koch[3], E. Rosolowsky[4], E. Schinnerer[5], A. Sardone[2], S. Meidt[6], W. J. G de Blok[7,8,9], D. Thilker[10], D. J. Pisano[11,12,13], J. Ott[14], A. Barnes[1,15], M. Querejeta[16], E. Emsellem[15,17], J. Puschnig[1], D. Utomo[18], I. Bešlić[1], J. den Brok[1], S. Faridani[1], S. C. O. Glover[19], K. Grasha[20], H. Hassani[4], J. D. Henshaw[14,21], M. J. Jiménez-Donaire[15], J. Kerp[1], D. A. Dale[22], J. M. D. Kruijssen[23], S. Laudage[1], P. Sanchez-Blazquez[24], R. Smith[19], S. Stuber[14], I. Pessa[14], E. J. Watkins[25], T. G. Williams[26], and B. Winkel[27]

(Affiliations can be found after the references)

Received 24 October 2022 / Accepted 24 March 2023

ABSTRACT

We present new H I observations of the nearby massive spiral galaxy M 83 taken with the JVLA at 21″ angular resolution (≈500 pc) of an extended (∼1.5 deg^2) ten-point mosaic combined with GBT single-dish data. We study the super-extended H I disk of M 83 (∼50 kpc in radius), in particular disk kinematics, rotation, and the turbulent nature of the atomic interstellar medium. We define distinct regions in the outer disk (r_{gal} > central optical disk), including a ring, a southern area, a southern arm and a northern arm. We examine H I gas surface density, velocity dispersion, and noncircular motions in the outskirts, which we compare to the inner optical disk. We find an increase of velocity dispersion (σ_v) toward the pronounced H I ring, indicative of more turbulent H I gas. Additionally, we report over a large galactocentric radius range (until r_{gal} ∼ 50 kpc) where σ_v is slightly larger than thermal component (i.e., >8 km s^{-1}). We find that a higher star-formation rate (as traced by far UV emission) is not necessarily always associated with a higher H I velocity dispersion, suggesting that radial transport could be a dominant driver for the enhanced velocity dispersion. Furthermore, we find a possible branch that connects the extended H I disk to the dwarf irregular galaxy UGCA 365 and that deviates from the general direction of the northern arm. Lastly, we compare mass flow rate profiles (based on 2D and 3D tilted ring models) and find evidence for outflowing gas at r_{gal} ∼ 2 kpc, inflowing gas at r_{gal} ∼ 5.5 kpc, and outflowing gas at r_{gal} ∼ 14 kpc. We caution that mass flow rates are highly sensitive to the assumed kinematic disk parameters, in particular to inclination.

Key words. ISM: kinematics and dynamics – radio lines: galaxies – galaxies: groups: individual: M 83

1. Introduction

The massive, extended atomic gas reservoirs that often surround spiral galaxies usually extend far beyond the inner optical disk (2−4 × r_{25}, where r_{25} is the optical radius; e.g., Wang et al. 2016). These reservoirs may eventually serve as the fuel for star formation in the inner disk and may represent a key component for facilitating accretion from the circumgalactic medium (CGM) and cosmic web (see, e.g., review by Sancisi et al. 2008). However, the details of star formation in outer disks, the origin, the nature of turbulence (traced for example by H I velocity dispersion), and, perhaps most importantly, radial gas flows all remain topics in need of more study.

Observing the extent of neutral atomic hydrogen (H I) gas is important, as it traces the kinematics in disk galaxies, which give further insights into the understanding of galaxy evolution. The 21-cm line emission of H I is often used to examine either disk kinematics and rotation on large scales (e.g., de Blok et al. 2008; Heald et al. 2011; Schmidt et al. 2016; Oman et al. 2019; Di Teodoro & Peek 2021) or the turbulent nature of the interstellar medium (ISM) on small scales (e.g., Tamburro et al. 2009; Ianjamasimanana et al. 2012, 2015; Mogotsi et al. 2016; Koch et al. 2018). In the first case, H I traces the process of gas accreting from the intergalactic medium that flows through diffuse filamentary structures into the CGM of galaxies and further onto the galaxy disk (e.g., Kereš et al. 2005). The gas entering the halo remains cool as it falls onto the disk (i.e., the cold mode scenario in Kereš et al. 2005). This cold accretion dominates in the lower H I density environments (e.g., White & Frenk 1991; Kereš et al. 2005; Tumlinson et al. 2017). In the second case, H I is used to analyze velocity profiles and line widths (i.e., H I velocity dispersion) in order to interpret the thermal states of the optically thin warm neutral medium (WNM; as one of the two phases predicted by models from, e.g., Field et al. 1969; Wolfire et al. 1995, 2003; Bialy & Sternberg 2019). This approach has been found to be valid down to 100 pc scales (e.g., Koch et al. 2021), for example, from emission and absorption studies in the Large and Small Magellanic Cloud (Stanimirovic et al. 1999; Jameson et al. 2019).

The exact amount of H I gas in the outskirts of nearby galaxies was analyzed in Pingel et al. (2018) and Sardone et al. (2021). Pingel et al. (2018) analyzed and compared four galaxies out of 24 total sources of the Hydrogen Accretion in LOcal GAlaxies Survey (HaloGAS; see Heald et al. 2011 for the survey paper) made with Green Bank Telescope (GBT) observations. The authors found that the H I mass fraction below

⋆ A copy of the combined datacube is available at the CDS via anonymous ftp to cdsarc.cds.unistra.fr (130.79.128.5) or via https://cdsarc.cds.unistra.fr/viz-bin/cat/J/A+A/675/A37

⋆⋆ Based on observations carried out with the *Karl G. Jansky* Very Large Array (VLA). The National Radio Astronomy Observatory is a facility of the National Science Foundation operated under cooperative agreement by Associated Universities, Inc.

Table 1. Properties of M 83, NGC 5236.

Parameter	Value	Notes
Morphology	SAB(s)c	(1)
RA (J2000)	204.2538 deg	(2)
Dec (J2000)	−29.8658 deg	(2)
Distance	5.16 ± 0.41	(3)
Linear scale	25 pc/arcsec	
D_{25}	11.7 arcmin	(4)
r_{25}	∼8 kpc	(4)
$\log_{10}$ SFR	0.62 $M_\odot$ yr^{-1}	(5)
$\log_{10} L_{CO}$	8.84 K km s^{-1} pc^2	(6)
Adopted parameters:		
Inclination	48°	(7)
PA	225°	(7)
V_{sys}	510 km s^{-1}	(7)
V_{rot}	62 km s^{-1}	(7)
H I mass of:		This work
Central disk	1.1×10^9 $M_\odot$	(8)
Ring	1.9×10^9 $M_\odot$	
Southern area	1.8×10^9 $M_\odot$	
Southern arm	0.7×10^9 $M_\odot$	
Northern arm	0.5×10^9 $M_\odot$	

Notes. (1): de Vaucouleurs et al. (1991). (2): Wang et al. (2016). (3): Karachentsev et al. (2007). (4): Walter et al. (2008). We convert to physical units using the distance mentioned in this table. (5): Adopted from Leroy et al. (2019) using the FUV and WISE4 Band. (6): CO luminosity using CO(2-1) from the PHANGS-ALMA survey, Leroy et al. (2021). (7): Kinematic parameters from Heald et al. (2016) that we use in this work and describe in Sect. 2.6.1. We quote here the ones for the central tilted ring. (8): The total H I mass of each region is calculated including single dish observations.

H I column densities of $N_{HI} = 10^{19}$ cm^{-2} (i.e., diffuse H I gas) is on average 2%. Furthermore, their GBT observations of NGC 925 revealed a detection of ∼20% more H I than observations done with the Very Large Array (VLA) as part of The H I Nearby Galaxy Survey (THINGS; Walter et al. 2008). This finding underscores, among other aspects, that the THINGS VLA interferometric observations require a correction for missing short-spacing observations. Sardone et al. (2021) studied 18 out of a total of 30 nearby disk and dwarf galaxies of the MeerKAT H I Observations of Nearby Galactic Objects: Observing Southern Emitters (MHONGOOSE; see de Blok et al. 2016 for the survey paper) and found that 16 out of the 18 observed galaxies have 0.02 to three times additional H I mass outside of their optically bright disks.

The nearby ($D = 5.16$ Mpc) grand-design spiral galaxy M 83 (also known as NGC 5236; see Table 1) is massive, favorably oriented ($i = 48°$), and associated with active star formation (see Table 1), which has made it a classic target of several studies of the H I in outer portions of disk galaxies (e.g., Huchtmeier & Bohnenstengel 1981; Tilanus & Allen 1993; Miller et al. 2009). Moreover, M 83 was one of the first galaxies where the tilted ring analysis was performed (Rogstad et al. 1974, see their Fig. 8). Sensitive, wide-area H I imaging of M 83 has revealed its highly extended, structured disk as well as a northern spiral arm-like structure (e.g., Heald et al. 2016; Koribalski et al. 2018). However, previous high-resolution interferometric observations (see e.g., Walter et al. 2008; Bigiel et al. 2010a) have been restricted to single central pointing with the VLA (0.5° primary beam). In this paper, we present a ten-field mosaic using the VLA with an angular resolution of 21″ (∼500 pc) corrected for short-spacing using GBT observations (see Sect. 2.3).

The aim of this paper is to study the large- and small-scale kinematics of the H I in M 83's outskirts ($r_{gal} > r_{25}$). To this end, we look at individually defined regions and compare their H I properties to the central (optical) disk. We search for deviations from pure circular motions and asymmetries in the outskirts. We examine radial trends in velocity dispersion and environmental differences between the defined regions. We also highlight the effects of different kinematic parameters (based on 2D and 3D tilted ring models) on average radial mass flow rates and tilted ring modeling in general.

The paper is structured as follows: In Sect. 2 we describe how the VLA observations were taken, calibrated, and imaged along with how we convert observational measurements into physical quantities. In Sect. 3, we present the distribution of H I across M 83, its velocity field, and environmental differences of H I (H I gas surface density, Σ_{HI}) and kinematic parameters (H I velocity dispersion, line-of-sight velocities, and residual velocities). In Sect. 4, we discuss the environmental dependence of the observed H I velocity dispersion along with the northern extended arm of M 83 and M 83's possible interaction with a nearby dwarf irregular galaxy UGCA 365. In Sect. 5, we show upper limits for average radial mass flow rates (based on 2D and 3D tilted ring models), discuss the limitations, and compare the mass flow rates to those from the literature.

2. Observations, data reduction, and products

2.1. Observations

The observations of M 83 were carried out with the VLA. We obtained a ten-point mosaic using the dual-polarization L-band of the VLA to map the 21-cm emission of neutral hydrogen over the entire super-extended disk of the nearby galaxy M 83 (see Figs. 1 and 2). Most of the data were taken February 2014 through January 2015 for approximately 40 hours over the course of 22 runs (project codes: 13B-196, 14B-192, PI: F. Bigiel). We used the VLA in three hybrid configurations, D north C (DnC), C north B (CnB), and B north A (BnA), to ensure good u–v coverage despite M83's southern declination. We chose a time split for the configurations similar to THINGS' observing strategy (see Table 2). We chose a velocity resolution of 0.5 km s^{-1} and a bandwidth of 4 MHz corresponding to 860 km s^{-1}, which is well suited to resolve the H I line and cover the full range of 21-cm emission from the galaxy with enough bandwidth for continuum subtraction. At the beginning of each observing session, we observed the bandpass calibrator 3C286 for approximately ten minutes. Observations were then set up so that two of the ten mosaic pointings were observed in succession for ten minutes each. The sessions were followed by observations of the gain calibrator (J1331-2215). During each session, the gain calibrator was observed six times. We show a summary of our observations in Table 2.

2.2. Reduction

The VLA pipeline implemented in CASA (McMullin et al. 2007; version: 5.4.2-8.el6) was used without Hanning smoothing, as recommended by the VLA pipeline guide[1], for each of the

[1] https://science.nrao.edu/facilities/vla/data-processing/pipeline

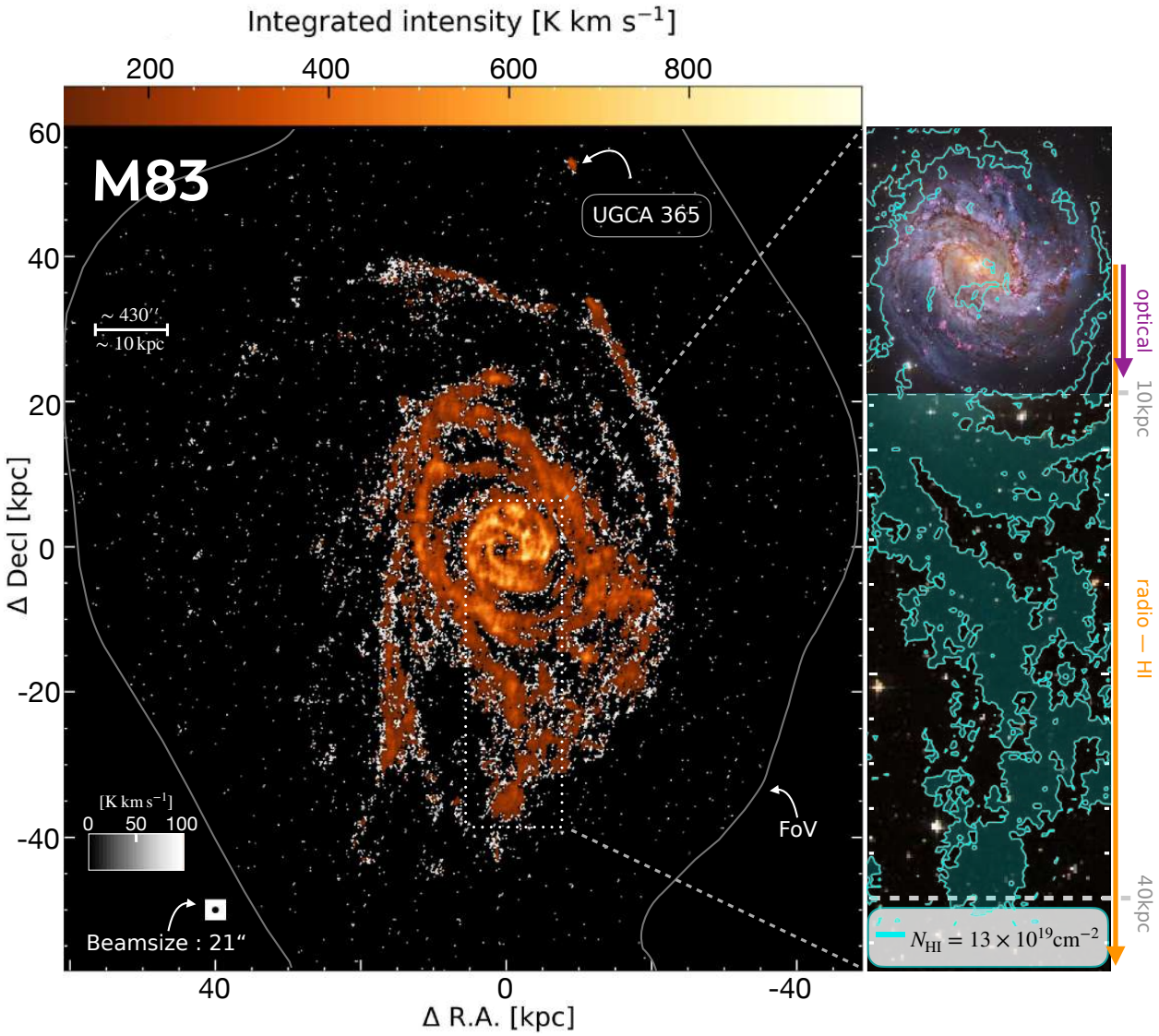

Fig. 1. Integrated intensity map (moment 0) for H I emission across the disk of M 83 at a resolution of 21″. The black circle in the lower left corner marks the beam size of 21″ (≈500 pc). The black to white colorbar indicates integrated intensities from 0–100 K km s^1 and the orange to yellow integrated intensities above 101 K km s^1. We denote the companion galaxy UGCA 365 which in projection is ∼55 kpc away from the center of M 83. To the right, we show the enclosed optical disk ($r_{25} \sim 8$ kpc) overlaid with H I column density contour ($N_{HI} = 13 \times 10^{19}$ cm^{-2}) extending over a radius of ∼40 kpc. For visualization reasons, we show unfilled N_{HI} contours for the high resolution optical image. Beyond 10 kpc we show filled N_{HI} contours. The white line surrounding M 83 shows the field of view (FoV; i.e. the full mosaic coverage) of the VLA observation. (optical image credits: CTIO/NOIRLab/DOE/NSF/AURA, M. Soraisam; Image processing: Travis Rector, Mahdi Zamani & Davide de Martin; low resolution background >10 kpc: DSS2).

science blocks. The flagging summary showed us that one to a maximum of two antennas were completely flagged for some science blocks. As a next step, we reduced the data to include only the spectral window (spw) where the H I emission is located (rest-frequency ∼1.420 GHz) using the CASA task `split`. This was followed by producing various diagnostic plots with a focus on the calibrator sources and applying additional data flagging (e.g., spikes of radio frequency interference or baselines) by hand using the CASA task `flagdata`.

We then ran a standard calibration script where we calibrated the flux, bandpass, and gain using `gaincal`. As the calibrators did not show any discrepancies, we merged all science blocks via the CASA function `concat`. This resulted in a measurement set containing only the H I spw with the target field scans (ten pointing). During our first run of a test `tclean`, we noticed horizontal and vertical stripes in the channels around the local standard of rest velocity of 380 km s^{-1}. We carried out several additional rounds of manual flagging to identify and remove corrupted baselines. We inspected amplitudes and phases for the data from all baselines by eye, finding some corrupt baselines that we flagged.

2.3. Imaging

To create "images" of our VLA observation, we used the CASA task `tclean`, which combines multiple arrays, and deconvolved using the `multiscale` clean algorithm (Cornwell 2008). We used the `mosaic` gridding algorithm and weighed the u–v data according to the Briggs scheme with a robustness parameter $r = 0.5$, which balances spatial resolution and surface

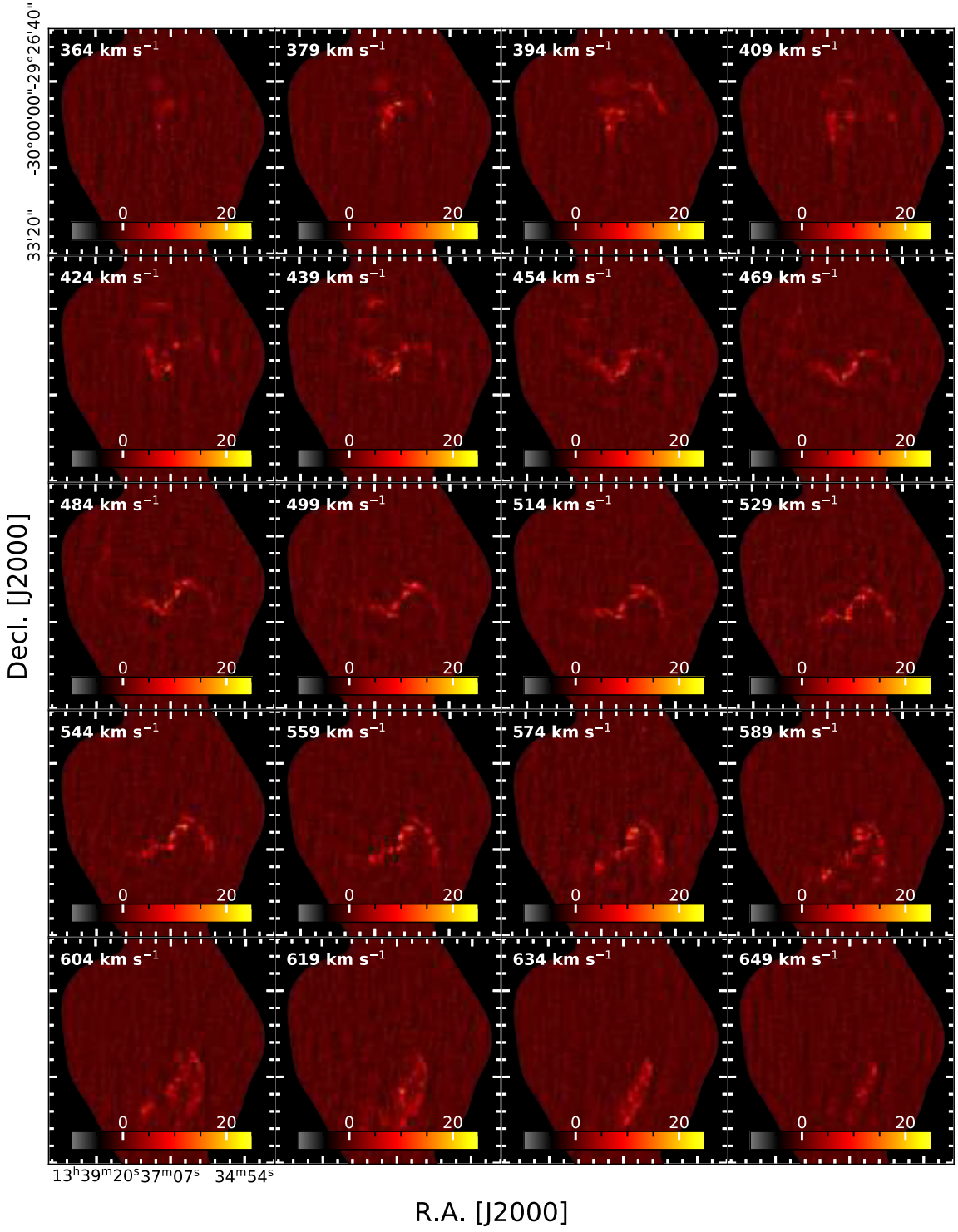

Fig. 2. Channel maps of our VLA+GBT data. The line-of-sight velocity of the shown channels is displayed on the upper left corner of each panel and the colorbar is shown in units of K. For visual purpose we only show every third 5.0 km s^{-1} channel (i.e. we do not integrate over channels). The companion galaxy UGCA 365 is detected in the velocity channels 559 km s^{-1} and 574 km s^{-1}. We show all channels in the appendix (see Appendix B).

brightness sensitivity. We tried several settings (for example, (i) restoringbeam = 15″ with cell = 5″ and (ii) restoringbeam = 21″ with cell = 7″) and found that a resolution of 21″ (restoringbeam = 21.0) and a spectral resolution of 5 km s^{-1} (see Table 3) provides a good compromise between resolution and noise. Since our observations have more integration time and substantially better surface brightness sensitivity in the D-configuration data, our choice of weighting naturally produced a synthesized beam size that is comparable to the D-configuration beam (46″; see Table 3). We restricted the deconvolution by using a clean mask derived from CASA's automasking scheme (Kepley et al. 2020) with the following

Table 2. Summary of our VLA *H* I observation across M 83.

	$\nu_{\rm rest}$ [MHz]	Project codes	Sessions	Gain/phase calibrator	Bandpass/flux calibrator	Config.	$\theta_{\rm HPBW}$ [″]	Obs. time per config. [min]	Total obs. time [min]	Total on source [min]
	(1)	(2)	(3)	(4)	(5)	(6)	(7)	(8)	(9)	(10)
H I	1420.4058	13B-194	17	J1311-2216	1331+305=3C286	BnA	4.3	378	2406	1444
		and		and		CnB	14	516		
		14B-192	5	J1316-3338		DnC	46	1512		

Notes. Column (1): Observational frequency. (2–3): The project codes and the corresponding number of observation sessions (PI: F. Bigiel). (4): The sources we used to calibrate the gain (amplitude and phase). (5): The source we used to perform the bandpass (flux and delay) calibration. (6–10): We quote here the outputs using `analysisUtils` after we have flagged our data: (7): Estimates of the synthesized beamwidth taken from the manual for the VLA observational status summary 2013B (see https://science.nrao.edu/facilities/vla/docs/manuals/oss2013B/performance/resolution) (8): Time of the observation per configuration. (9): Total observation time. (10): Total on source time.

Table 3. Properties of our imaged and feathered dataset.

	Beam [″]	Beam [pc]	$\Delta v_{\rm chan}$ [km s^{-1}]	$I_{\rm HI}$ [K km s^{-1}]	$\sigma_{\rm HI}$ [K km s^{-1}]	S/N	$T_{\rm peak}$ [K]	Noise [K km s^{-1}]	$V_{\rm los}$ [km s^{-1}]	$\sigma_{V\rm los}$ [km s^{-1}]	Ratio with FUV
	(1)	(2)	(3)	(4)	(5)	(6)	(7)	(8)	(9)	(10)	(11)
H I	21	483	5	991	32	31	30	1.6	570	1.3	9.5×10^{-4}

Notes. Columns (1–2): The size of the beam in angular and linear scales (adopting a distance of 4.75 Mpc). (3): The channel width, i.e. spectral resolution. (4–11): We quote the quantities for the sight line with the highest H I integrated intensities, i.e. for an aperture of 21″ ≈ 500 pc (see Table 4 for the mean, the 16th and 84th percentiles of some of these quantities): (4): Integrated intensity. (5): Uncertainty of integrated intensity (6): Signal to noise. (7): Peak temperature of the spectrum. (8): Root mean square (rms) noise. (9): Line of sight velocity, i.e. first-moment. (10): Uncertainty of the first-moment. (11): Ratio of $I_{\rm HI}$ with FUV which results in units of K km s^{-1}/(mJy arcsec^{-2}). These are GALEX FUV observations that have been published in Bigiel et al. (2010a).

sub-parameters: sidelobethreshold = 0.75, noisethreshold = 3.0, lownoisethreshold = 2.0, negativethreshold = 0.0, minbeamfrac = 0.1, growiterations = 75. In order to increase the S/N to be sensitive to emission even where the line is faint, we averaged several channels, resulting in a spectral resolution of $\Delta_{\rm v} = 5.0\,{\rm km\,s^{-1}}$. The typical rms per channel observed is ≈3 mJy beam^{-1}.

The H I in M 83 is extended compared to the primary beam of the VLA. As a result, subsequent to deconvolution, the interferometric VLA data needed to be combined with single-dish data to correct for the insensitivity of the interferometer to the extended emission. We used the GBT single-dish data obtained as part of the GBT-THINGS project (project GBT11A-055; see for example the maps in Pisano 2014). The GBT data were taken on 6, 12, and 26 March 2011. Either 3C147 or 3C295 was observed as a primary flux calibrator before mapping four square degrees around M 83. We derived a $T_{\rm cal}$ value of 1.55 K in both polarizations that we used for all observations. We used the GBT spectrometer with a 50 MHz bandwidth for observing in a frequency-switching mode with a 10 MHz throw while making a basket-weave map in RA and Dec. While data were taken with frequency-switching, we used the edge four integrations as an "off" position to calibrate the maps. These correspond to 6.7 arcmin on each edge. Since the extent of M 83 is less than two degrees and the map shows no subtracted H I emission, we find that these are clean "off" positions. A second order polynomial was fit to the spectra over an emission-free region to remove residual baseline structure. Data were boxcar smoothed to 5.15 km s^{-1} resolution before being imaged with (AIPS). A fourth order polynomial was removed from the final cube the `SDGRD` task in the Astronomical Image Processing System.

We combined the GBT map with the mosaic interferometer data using the `CASA` task `feather`. Some of the emission is very extended and had to be recovered by feathering, so the pixel statistics often reflect this extended emission. Before performing this task, we used the `uvcombine` python package (Koch & Ginsburg 2022) to find the correct single-dish scaling factor (sdfactor). We used an sdfactor of 1.0 (see Fig. A.1). We regarded lines of sight separated by more than a VLA synthesized beam as being statistically independent. However, because of the feathering process, the noise in the GBT data may have led to weak but spurious correlations up to scales approaching the GBT beam of 523″. Since the surface brightness of the noise in the GBT map is small compared to the VLA data and our results do not depend heavily on the statistical independence of the VLA data, we note this as a caution and proceed. We show properties of the feathered data in Table 3. In Fig. 3, we show the spectra of the VLA and the feathered VLA (VLA plus GBT) cubes after we converted them into units of Kelvin. We found a total flux for the VLA cube of 5.2×10^4 K and 6.6×10^4 K for the feathered one (VLA plus GBT). This difference emphasizes that single-dish data are needed even for interferometric observations, including compact configurations. For comparison we also show in Fig. 3 the spectra over the same field of view from The Local Volume H I Survey (LVHIS; Koribalski et al. 2018 with the Australia Telescope Compact Array – ATCA at ∼113″ ≈ 2.62 kpc scales) and KAT7 observations (seven-dish MeerKAT precursor array; Heald et al. 2016 at ∼230″ ≈ 5.33 kpc scales), which were sampled on the same spectral axis grid. We observed that the KAT7 agrees well with the VLA plus GBT spectra, while LHVIS only agrees on the receding side (i.e., >510 km s^{-1}). The spectra of VLA plus GBT highlights a significant fraction of emission that we see with the addition of the GBT observation.

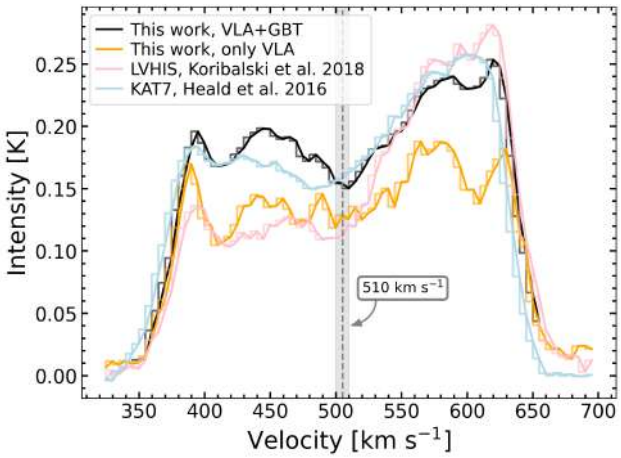

Fig. 3. Global H I profile of M 83 from our VLA observations (orange) and the results of feathering the VLA with the GBT observations (black). The systemic velocity appropriate for the centre of the galaxy is indicated with the vertical grey dashed line at 510 km s^{-1} (see also Table 1). We also show H I observations of the same FoV of M 83 from LVHIS (Koribalski et al. 2018) and KAT7 (Heald et al. 2016) that we have sampled on the same spectral axis grid at their native angular resolution.

2.4. Data products

After feathering, the data were resampled onto a hexagonal grid with a grid size matching the beam size. This ensured that the resampled measurements are mostly independent. This resulted in 50 574 sightlines separated by a beam size. To improve the S/N, we applied a masking routine based on the methodology introduced by Rosolowsky & Leroy (2006). To this end, we first identified pixels with a high S/N ($S/N \geq 4$) and a low S/N ($S/N \geq 2$). As a next step, the identified high S/N regions were iteratively grown to include adjacent, moderate S/N regions as defined by the low S/N mask. In this way, we recovered the more extended two-sigma detection that belongs to a four-sigma core. Only pixels detected with an $S/N \geq 3$ (where the signal represents the integrated intensity; see next paragraph) were used in subsequent analysis. In this work, we made use of the data products described in the following paragraphs.

The integrated intensity map was created from the masked data cube by integrating along the velocity axis for each of the individual sightlines v multiplied by the channel width $\Delta v_{\rm chan}$ of 5 km s^{-1}:

$$I_{\rm HI}\,[{\rm K\,km\,s^{-1}}] = \sum_{n_{\rm chan}} I_v\,[{\rm K}]\,\Delta v_{\rm chan}\,[{\rm km\,s^{-1}}]. \quad (1)$$

The uncertainty was calculated by taking the square root of the number of the included channels along a line of sight multiplied by the 1σ root mean squared value of the noise and the channel width: $\sigma_{\rm HI} = \sqrt{n_{\rm chan}} \times \sigma_{\rm rms} \times \Delta v_{\rm chan}$. We calculated $\sigma_{\rm rms}$ over the signal-free part of the spectrum using the `astropy` (Astropy Collaboration 2013, 2018) function `mad_std` that calculates the median absolute deviation and scales it by a factor of 1.4826. This factor results from the assumption that the noise follows a Gaussian distribution. For further analysis[2] we focused only on significant detections of $S/N = I_{\rm HI}/\sigma_{\rm HI} > 3$, resulting in 5539 sightlines separated by a beam size.

[2] We used this $S/N > 3$ criterion to construct $V_{\rm los}$, $V_{\rm res}$, σ and $\Sigma_{\rm HI}$.

We converted the H I 21-cm intensity ($I_{\rm HI}$) to the H I gas surface density, $\Sigma_{\rm HI}$, via:

$$\Sigma_{\rm HI}\,[M_\odot\,{\rm pc^{-2}}] = 0.015\,I_{\rm HI}\,[{\rm K\,km\,s^{-1}}]\,\cos(i). \quad (2)$$

This conversion was used by Bigiel et al. (2010b, among many others), and results in a hydrogen mass surface density and neglects heavy elements. The cos(i) factor corrects for inclination (see Table 1). We derived the H I column density via:

$$N_{\rm H\,I}\,[{\rm cm^{-2}}] = 1.82 \times 10^{18}\,I_{\rm HI}\,[{\rm K\,km\,s^{-1}}]. \quad (3)$$

Our aim with the use of velocity fields was to obtain an accurate characterization of the dynamics in a galaxy. For this purpose, each pixel was assigned a velocity that represents the average line-of-sight velocity of the gas. However, this is not trivial, and multiple approaches have been used in the literature that differ from one another, each with some advantages and disadvantages (see de Blok et al. 2008 for a discussion on peak velocity fields, Gaussian profiles, multiple Gaussian profiles, and Hermite h3 polynomials methods). In this work, the first moment we took for the observed velocity field can be expressed as follows:

$$V_{\rm los}[{\rm km\,s^{-1}}] = \frac{\sum I_v[{\rm K}]\,v\,[{\rm km\,s^{-1}}]\,\Delta v_{\rm chan}[{\rm km\,s^{-1}}]}{I_{\rm HI}[{\rm K\,km\,s^{-1}}]}. \quad (4)$$

We used the width of the H I emission line to trace the velocity dispersion ($\sigma_{\rm v}$) along each line of sight. Several methods exist to estimate the width of an emission line: fitting the line profiles with a simple Gaussian function or Hermite polynomials or calculating the second moment. In this work, we calculated the velocity dispersion $\sigma_{\rm v}$ following the (i) effective width, $\sigma_{\rm eff}$, approach used in, for example, Heyer et al. (2001), Leroy et al. (2016), and Sun et al. (2018):

$$\sigma_{\rm eff}\,[{\rm km\,s^{-1}}] = \frac{I_{\rm HI}\,[{\rm K\,km\,s^{-1}}]}{T_{\rm peak}\,[{\rm K}]\,\sqrt{2\pi}}. \quad (5)$$

We divided the velocity-integrated intensity by the peak brightness temperature, $T_{\rm peak}$. We then converted this value to the standard intensity-weighted velocity dispersion by dividing it by $\sqrt{2\pi}$ – the conversion constant for a Gaussian profile. This definition of σ has the advantage that it is less sensitive to noise, but it will mis-characterize line profiles that significantly deviate from a single Gaussian.

We did not subtract the finite channel width (i.e., line broadening caused by the instrument) as it is done, for example, for extragalactic CO observations (e.g., Sun et al. 2018). The usual finite correction factor will overcorrect given that 5 km s^{-1} $\approx$ the WNM thermal width.

We also calculated σ_v with (ii) the square root of the second moment:

$$\sigma_{\sqrt{\rm mom2}}\,[{\rm km\,s^{-1}}] = \left\{\frac{\sum I_v\,[{\rm K}]\,({\rm v}\,[{\rm km\,s^{-1}}] - V_{\rm los}\,[{\rm km\,s^{-1}}])^2}{\sum I_v\,[{\rm K}]}\right\}^{1/2}. \quad (6)$$

We compare (i) $\sigma_{\rm eff}$ and (ii) $\sigma_{\sqrt{\rm mom2}}$ in Sect. 4.1.

2.5. Radial profiles – Binning and stacking

Throughout this work, we make use of radial profiles, binning in galactocentric rings of 1 kpc width (roughly twice the beam size of 500 pc). Each point in these profiles thus represents the average within a given ring defined by the structure parameters (Table 1).

In order to average ("stack") spectra within a given ring, we aligned the spectra to the peak velocity (see e.g., Jiménez-Donaire et al. 2019; Bešlić et al. 2021; or for H I related science Koch et al. 2018, who discussed different stacking approaches, i.e., different definitions of the line center $V_{\rm rot}$, $V_{\rm cent}$, and $V_{\rm peak}$). We created stacks again in ∼1 kpc-wide galactocentric rings.

2.6. Tilted ring kinematics

H I rotation curves are most commonly derived from velocity fields. The quantity that is accessible through observations is the line-of-sight velocity ($V_{\rm los}$). To infer the rotational velocities of the gas in the disk from measurements of $V_{\rm los}$, we had to utilize a specific model that could be fitted to the data.

The "tilted ring" approach describes a galaxy by a set of rings, each of which has their own inclination i, position angle, systemic velocity $V_{\rm sys}$, center position (x_0, y_0), and rotation velocity $V_{\rm rot}$. Under the assumption that the gas moves in circular orbits within each ring, we could then describe $V_{\rm los,obs}$ for any position (x, y) on a ring with radius r as:

$$V_{\rm los,obs}(x,y) = V_{\rm sys} + V_{\rm rot}(r)\sin(i)\cos(\theta) + V_{\rm rad}(r)\sin(i)\sin(\theta). \quad (7)$$

The inclination i of the disk together with the azimuthal angle θ and the radius r form a polar coordinate frame.

2.6.1. Adopted tilted ring model for M 83

Several kinematic parameters for M 83 exist in the literature. However, the rotation curve that extends the farthest and is readily available was published in Heald et al. (2016) and uses KAT7 (the seven-dish MeerKAT precursor array) observations with an angular resolution of ∼230″≈5.33 kpc. Since H I in M 83 extends far in our observations, this is the best suited rotation curve that involves the northern and southern arms of M 83 (see Sect. 3.1). In addition, Heald et al. (2016) performed several tilted ring models explicitly for this galaxy, which strengthens our selection of this rotation curve over others. They used the Groningen Image Processing System (GIPSY) task `rotcur` to construct a rotation curve ($V_{\rm rot}$) using a ring width of 100″. For that, they set the radial velocity component ($V_{\rm rad}$) to zero, which reduces Eq. (7) to the first two terms. Heald et al. (2016) found at radii beyond 1000″ ∼ 23 kpc, an opposite deviation of the modeled approaching and receding rotation curves. To account for this, they used $V_{\rm sys}$ = 510 km s^{-1} for r < 23 kpc and $V_{\rm sys}$ = 500 km s^{-1} for r > 23 kpc. In this work, we adopt their resulting kinematic parameters from this approach (see also discussion in Sect. 5.1).

To get a modeled velocity map ($V_{\rm los,mdl}$), we used their rotation curve ($V_{\rm rot}(r)$), their constant inclination angle of 48°, and, their position angles, which vary from 225.0° for the central ring to 158.6° for the outermost ring:

$$V_{\rm los,mdl}(x,y) = V_{\rm sys} + V_{\rm rot}(r)\sin(i)\cos(\theta). \quad (8)$$

Here, $V_{\rm sys}$ is the systemic velocity of the galaxy with respect to the observer, and $V_{\rm rot}$ is the rotation velocity. The $V_{\rm los,mdl}$ is denoted in sky coordinates (x, y), while the terms on the right side of Eq. (8) are in the disk coordinate frame (r, θ). These two systems are related:

$$\cos(\theta) = \frac{-(x-x_0)\sin({\rm PA}) + (y-y_0)\cos({\rm PA})}{r} \quad (9)$$

and $\sin(\theta)$ from Eq. (7) as:

$$\sin(\theta) = \frac{-(x-x_0)\cos({\rm PA}) - (y-y_0)\sin({\rm PA})}{r\cos(i)}, \quad (10)$$

where x_0 and y_0 denote the center coordinates and the position angle is the angle measured counter-clockwise between the north direction of the sky and the major axis of the receding half of the galaxy. We then used Eq. (8) to get $V_{\rm los,mdl}$. For the purpose of showing $V_{\rm los,mdl}$ maps (and $V_{\rm res}$ maps, see next paragraph), we interpolated the space between the rings (see Fig. 11) and applied a simple mask to only show $V_{\rm los,mdl}$ values that match with our observed S/N masked velocity field (i.e., we ignored data outside the mask).

2.6.2. Residual velocities and radial velocities

To determine the residual velocities ($V_{\rm res}$), we subtracted Eq. (8) from Eq. (7), $V_{\rm res}(x,y) = V_{\rm los,obs}(x,y) - V_{\rm los,mdl}(x,y)$ and obtained:

$$V_{\rm res}(x,y) = V_{\rm rad}(r)\sin(\theta)\sin(i). \quad (11)$$

To get radial velocities ($V_{\rm rad}$), we only took $V_{\rm res}$ values within each tilted ring (i.e., we did not use the $V_{\rm res}$ map where we interpolated between the gaps) and accounted for the $\sin(\theta)\sin(i)$ term:

$$V_{\rm rad}(r) = \frac{V_{\rm res}(r)}{\sin(\theta)\sin(i)}. \quad (12)$$

Knowing in which direction a galaxy rotates is required to correctly interpret the nature of measured radial motions. Negative (positive) velocities in $V_{\rm rad}$ are inflow (outflow) motions when a galaxy is rotating clockwise, and they are outflow (inflow) motions when a galaxy is rotating counterclockwise. Under the assumption that spiral galaxies spin with their arms trailing in the direction of rotation, the winding of the extended H I arms reveal that M 83 rotates clockwise. Therefore, $V_{\rm rad} < 0$ indicates inflow and $V_{\rm rad} > 0$ indicates outflow for M 83.

3. Results

In this section, we present the results derived from our H I observations toward M 83 (integrated intensity map and velocity fields, Figs. 1 and 4) and analyze how the super-extended H I disk of M 83 compares to its optical central disk. To do this, we applied a simple environmental mask by visually separating these regions (see Fig. 5), as it allowed us to distinguish between (i) the central disk, (ii) ring, (iii) southern area, (vi) southern arm, and (v) northern arm.

3.1. Distribution of H I in M 83

In Fig. 1 we show the integrated H I intensity map of M 83 that extends over one degree in the sky. The H I emission toward the central optical disk is ∼8.1 kpc in radius and shows the highest integrated intensities. The right panel in Fig. 1 shows an optical image of M 83's central disk with H I column densities in cyan contours. These contours extend up to a radius of 50 kpc (approximately four times the size of the optical disk).

The central disk is surrounded by H I emission that follows a ring-like structure that extends to a galactocentric radius of ∼16 kpc. The most prominent features in the outskirts of M 83 are the southern and northern spiral-like structures seen already

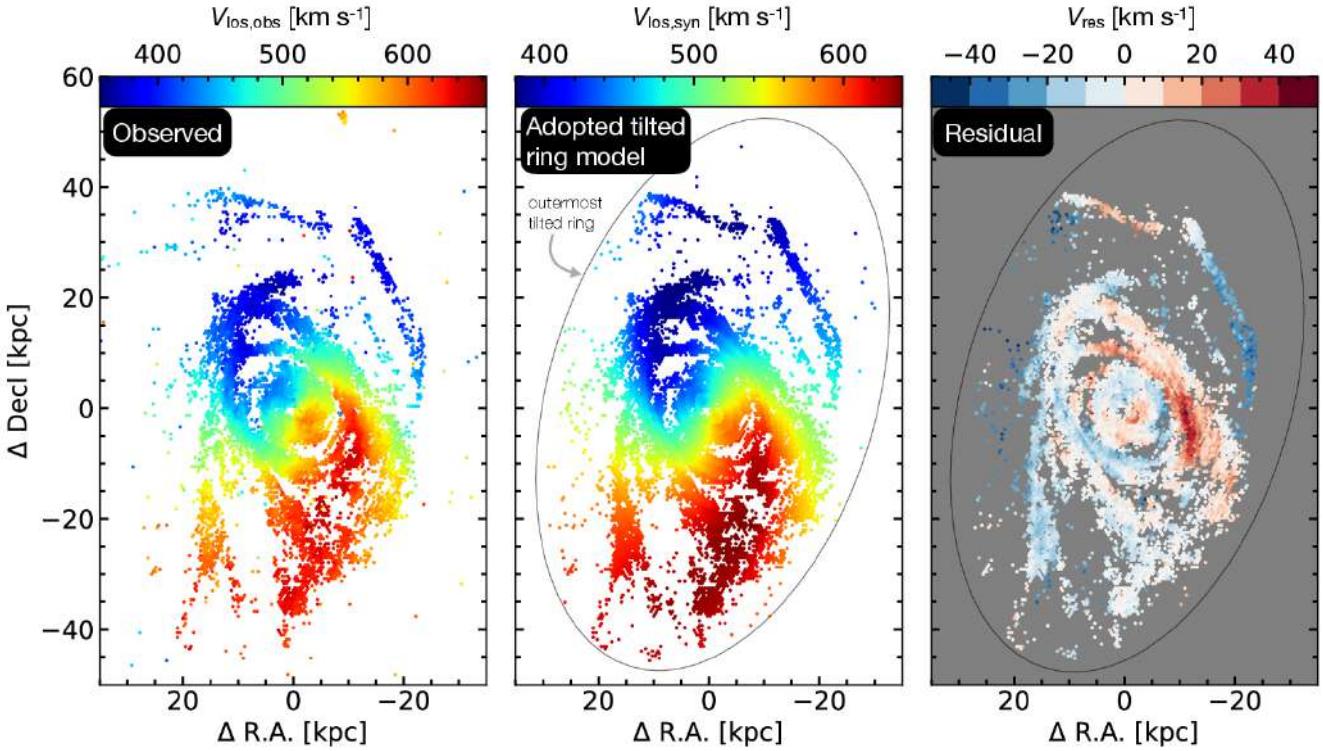

Fig. 4. Observed, adopted, and residual velocity maps. Observed: velocity field of M 83 using our VLA H I observations. The blue colors represent the approaching and the red is the receding side of the H I galaxy disk. Adopted tilted ring model: constructed velocity field using V_{sys}, V_{rot}, i, and position angle of the tilted ring model by Heald et al. (2016). The green colors represent the systemic velocity of ∼510 km s^{-1} for the inner ∼23 kpc in galactocentric radius and ∼500 km s^{-1} beyond (see Sect. 2.6.1). The tilting results in gaps between the rings, which we interpolated for the presentation of these maps (2d interpolation, see Fig. 11). We had to restrict our field of view to the model outputs (i.e. the outermost tilted ring). Residual: The difference between the observed velocities and the modeled velocities; in the range of −40 to 40 km s^{-1}.

in previous studies (e.g., Bigiel et al. 2010a; Heald et al. 2016). Our field of view (gray solid line in Fig. 1) allowed us to also detect the nearby companion galaxy cataloged as UGCA 365, which is 5.25 ± 0.43 Mpc in distance (the red giant branch – TRGB – measurements; Karachentsev et al. 2007). We measured that this dwarf irregular galaxy is ∼50 kpc in projected distance from the center of M 83 and has in our map a diameter of 88″ (≈2 kpc). This is a factor of two smaller than what has been found by Heald et al. (2016). We found an H I mass of $M_{HI} = 6.1 \times 10^5\ M_\odot$, which differs from the quoted H I mass in Heald et al. 2016, who find $M_{HI} = 2.7 \times 10^7\ M_\odot$. We attribute this difference to the fact that our VLA observations are not as sensitive as the KAT-7 data. This companion galaxy was faintly detected in the GBT observations (see Fig. C.1).

Throughout this work, we refer to different regions: the central disk, where we found an averaged H I column density of 6.28×10^{20} cm^{-2}; the ring that surrounds the central disk; and the prominent northern arm and southern arm. In the southwest, we detected significant emission with spots of enhanced column densities; we refer to this region as the southern area.

3.2. Velocity fields

In this work, we analyze observed and modeled first-moment maps to examine noncircular motions. The observed velocities, $V_{los,obs}$, in the first panel of Fig. 4 range from 357 to 661 km s^{-1}, where 510 km s^{-1} is the systemic velocity (shown as green colors, see also Table 1) for the inner ∼23 kpc in the galactocentric radius and ∼500 km s^{-1} beyond (see Sect. 2.6.1). The central disk shows symmetric velocity behaviors that are typical for gas moving in circular motions. However, this symmetry breaks at larger radii. The ring already presents differences in the systemic velocity and the corresponding approaching and receding velocities, as the symmetry axis is no longer the major and minor axis of the central disk. The northern arm only shows approaching velocities, whereas the southern arm shows a transition from systemic to receding velocities along the arm direction. Both of the arms are winding clockwise, similar to the spiral arms seen in the central (optical) disk from, for example, CO observations (e.g., Koda et al. 2020).

The second panel of Fig. 4 shows the line-of-sight velocity field implied by the Heald et al. (2016) tilted ring model (we used their V_{rot}, i, and position angle for each tilted ring; we describe the procedure and our motivation to use this set of kinematic parameters in Eq. (8) and Sect. 2.6.1). The field of view was restricted to the model outputs, meaning that we neglected everything beyond the outermost tilted ring (including the northern companion galaxy UGCA 365). In this map, we observed lower approaching velocities toward the beginning of the northern arm and higher receding velocities in the southern area compared to the observed velocities.

The third panel in Fig. 4 shows the residual velocities, V_{res}. The highest V_{res} values are indicated with dark red or dark blue colors in the third panel in Fig. 4. We found values of ∼40 km s^{-1} in the southwest of the ring along with ∼−10 km s^{-1} on the eastern side. The southern area and southern arm are shown in white to light-blue colors indicating a V_{res} of ∼0−10 km s^{-1}. The northern arm shows negative and positive V_{res} values, whereas the kink of the arm (inflection point; see Sect. 4.2) has V_{res}

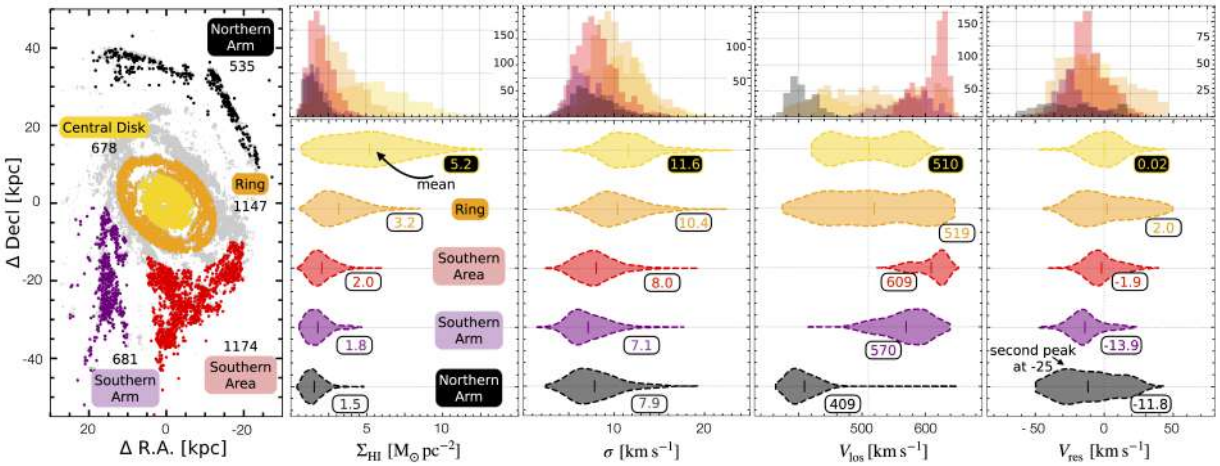

Fig. 5. Environmental differences in velocities, H I gas surface density and velocity dispersion in M 83. Mask: colors represent the different regions: central disk, ring, southern area, northern arm and the southern arm. We note the total sightlines for each of the regions. The grey colors in the background show the H I column density contours ($N_{HI} = 13 \times 10^{19}$ cm^{-2}) that we showed in Fig. 1. Violin plots: each violin represents the distribution of each quantity in a region defined in the mask. We set the kernel density estimation (KDE) to compute an empirical distribution of each quantity to 200 points. The columns on the x axis show the H I gas surface density Σ_{HI}, the second the line width σ_{eff}, the observed velocities V_{los}, and the last residual velocities V_{res}. The mean value of the observed quantity is reported for each violin. The long tails seen for example in the V_{los} violin for the northern arm represents that there is one discrepant value.

$\sim$0 km s^{-1}. Additionally, we found at the end of the northern arm a "blob" of negative V_{res} values of ~ -30 km s^{-1}.

3.3. Environmental differences in velocities, H I gas surface density, and velocity dispersion

We analyzed different environmental regions in more detail, as shown in Fig. 5. We did this by masking each individual area by eye based on the emission seen in Fig. 1 after applying an S/N cut ($S/N = 3$)[3]. This resulted in the following total number of sightlines separated by a beam size for each region: for the central disk = 678, ring = 1147, southern area = 1174, southern arm = 681, and northern arm = 535. In the following paragraphs, we examine the environmental dependence of Σ_{HI}, σ, V_{los}, and V_{res} in M 83 shown in Fig. 5.

The second column of Fig. 5 shows the H I surface density. Overall, this quantity decreases with galactocentric radius from the central disk to the outermost outskirt region – the northern arm. We found the highest mean Σ_{HI} in the central disk: 5.2 $M_\odot$ pc^{-2}. The ring, southern area, and southern arm showed a mean Σ_{HI} of 3.2 $M_\odot$ pc^{-2}, 2.0 $M_\odot$ pc^{-2}, and 1.8 $M_\odot$ pc^{-2}, respectively. The northern arm exhibited a mean Σ_{HI} of 1.5 $M_\odot$ pc^{-2}, which is more than a factor of approximately three lower than the central disk. The overall trend of decreasing Σ_{HI} with r_{gal} in M 83 agrees with previous studies (e.g., Bigiel et al. 2010a).

The third column of Fig. 5 shows to the first order that the means of the velocity dispersion (using σ_{eff}, the effective width; see Eq. (5)) decrease with r_{gal}. Upon closer examination, it became clear that the northern arm has a slightly higher mean line width than the southern arm. However, the overall distributions of these two regions appear reasonably similar. Higher values in σ_{eff} could be attributed to multiple components and/or wider components. This way of measuring the velocity dispersion does not distinguish between these possibilities (see discussion in Sect. 4.1). The overall trend of decreasing σ with r_{gal} agrees with previous studies (e.g., Tamburro et al. 2009 and see our discussion in Sect. 4.1).

The last two columns of Fig. 5 show the line of sight and the residual velocities (i.e., V_{los} and V_{res}). In general, the central disk is well described by the tilted ring model (that assumes circular motions), as the distribution of V_{los} looks very symmetric and the mean of V_{res} is close to zero ($\langle V_{los} \rangle = 0.02$ km s^{-1}). The mean value of 510 km s^{-1} is the same as what was used for systemic velocity in the tilted ring model (until a radius of $\sim$23 kpc; see Sect. 2.6.1). The ring region is still relatively well characterized by this model, with deviations from pure circular motions of $\langle V_{res} \rangle = 2.0$ km s^{-1}. Also, the southern arm has low mean deviations of $\langle V_{res} \rangle = -1.9$ km s^{-1}; however, the mean V_{los} values are on the receding side (i.e., >510 km s^{-1}, gray dashed horizontal line). The outermost regions, the southern and northern arms, show significant deviations from circular motions. They exhibit $\langle V_{res} \rangle$ values of -13.9 km s^{-1} and -11.8 km s^{-1}, but their means in V_{los} are on the receding and approaching side, respectively. The distribution of V_{res} values toward the northern arm represents a change in velocities along the arm (we discuss this in Sect. 4.2).

We show for each quantity the mean as well as the 16th and 84th percentiles in Table 4. This table already contains values of the I_{HI}-far ultraviolet (FUV) ratio for each region. We discuss a visual comparison of FUV emission (as a tracer of the star-formation rate) and velocity dispersion later in the paper (see Sect. 4.1). Table 4 reveals that the central disk has the smallest I_{HI}/FUV values (i.e., 7.32×10^5 K km s^{-1}/(mJy arcsec^{-2})). The ring shows the largest values, and I_{HI}/FUV then decreases with r_{gal}.

4. Discussion

In this section, we study the radial dependence of the velocity dispersion (obtained with three different methods) and H I surface density and how it changes beyond the central disk. We

[3] The central disk and the ring were masked by a radius cut (r_{gal} = 8.1 kpc and r_{gal} = 16 kpc, respectively) in the plane of the disk. The gap between the central disk and the ring represents lines of sight that were difficult to assign to a specific region, and thus they were not included in a region. The two arms and the southern area were selected with a cut in RA and declination.

Table 4. Properties of environmental regions in M 83.

Region (1)	$\langle I_{\rm HI}\rangle$ [K km s^{-1}] (2)	$\langle N_{\rm HI}\rangle$ [10^{20} cm^{-2}] (3)	$\langle \Sigma_{\rm HI}\rangle$ [$M_\odot$ pc^{-2}] (4)	$\langle \sigma_{\rm eff}\rangle$ [km s^{-1}] (5)	$\langle V_{\rm los}\rangle$ [km s^{-1}] (6)	$\langle V_{\rm res}\rangle$ [km s^{-1}] (7)	$\langle I_{\rm HI}/{\rm FUV}\rangle$ [10^5] (8)
Central disk	$345.2^{514.9}_{161.8}$	$6.3^{9.4}_{2.9}$	$5.2^{7.7}_{2.4}$	$11.6^{13.9}_{9.1}$	$510.2^{573.6}_{447.6}$	$0.0^{12.1}_{-12.9}$	$7.3^{13.1}_{2.0}$
Ring	$210.3^{300.1}_{123.0}$	$3.8^{5.5}_{2.2}$	$3.2^{4.5}_{1.8}$	$10.4^{13.1}_{7.8}$	$519.1^{609.1}_{435.1}$	$2.0^{27.5}_{-19.9}$	$35.2^{51.2}_{18.3}$
Southern area	$135.7^{189.0}_{85.6}$	$2.5^{3.4}_{1.6}$	$2.0^{2.8}_{1.3}$	$8.0^{5.9}_{10.1}$	$609.4^{578.4}_{631.3}$	$-1.9^{-12.6}_{10.3}$	$31.8^{44.2}_{21.5}$
Southern arm	$118.4^{163.8}_{70.8}$	$2.2^{2.9}_{1.3}$	$1.8^{1.1}_{2.5}$	$7.1^{5.2}_{9.3}$	$569.6^{527.2}_{604.9}$	$-13.9^{-23.9}_{-3.2}$	$27.9^{38.9}_{17.9}$
Northern arm	$102.7^{141.6}_{61.3}$	$1.9^{2.6}_{1.1}$	$1.5^{0.9}_{2.1}$	$7.9^{5.4}_{10.2}$	$408.9^{385.7}_{428.4}$	$-11.8^{-33.6}_{15.1}$	$25.9^{36.1}_{15.8}$

Notes. (1): Defined environmental regions in M 83: Central disk, ring, southern area, southern and northern arm. (2–8): We show the mean, the 16th, and 84th percentiles of each quantity for each region. (2): H I integrated intensity. (3): H I column density. (4): H I surface density. (5): H I effective line width. (6): L.o.s velocity. (7): Residual velocity. (8): Ratio of H I over the GALEX FUV map shown in Fig. 7. This results in units of K km s^{-1}/(mJy arcsec^{-2}).

further examine possible reasons for broader H I profiles and discuss the extended H I structure of M 83 and its companion UGCA 365.

4.1. H I velocity dispersion in the outskirts of M 83

Multiple observations have shown that the H I velocity dispersion encodes information on a combination of temperature, turbulence, and unresolved bulk motions and is thus sensitive to feedback and energetics and the physical state of the gas (e.g., Tamburro et al. 2009; Ianjamasimanana et al. 2015; Mogotsi et al. 2016; Romeo & Mogotsi 2017; Koch et al. 2018; Oh et al. 2022). In the upper panel of Fig. 6, we show the radial profile of the velocity dispersion across the whole disk of M 83. Overall the velocity dispersion decreases with galactocentric radius, similar to the trend we found in Fig. 5. This agrees also with studies where it was shown that $\sigma_{\rm v}$ decreases with $r_{\rm gal}$ across local disk galaxies (e.g., Tamburro et al. 2009). However, in our radial profile, a peak of velocity dispersion is evident in the region of the ring, which we marked with two vertical dashed lines.

In Fig. 6, we make a comparison between three radial profiles obtained with different methods that are commonly used in the literature. We first compare the effective-width approach ($\sigma_{\rm eff}$ colorized markers; see Eq. (5)) with the square root of the second moment ($\sigma_{\sqrt{\rm mom2}}$, gray markers; see Eq. (6)) and show their corresponding profile (gray and pink solid lines). Though $\sigma_{\rm eff}$ is used to study cooling and the physics of the ISM, for studies dealing with dynamics and large-scale evolution, using $\sigma_{\sqrt{\rm mom2}}$ is more appropriate. We additionally show the velocity dispersion profile where we stacked the $\sigma_{\rm eff}$ values (pink-whited dashed line; see Sect. 2.5 for a description of the binning and stacking techniques). We found that the profiles for $\sigma_{\sqrt{\rm mom2}}$, $\sigma_{\rm eff}$, and stacking $\sigma_{\rm eff}$ all show, in addition to the center, enhanced velocity dispersion in the ring. The same behavior arose in the $\Sigma_{\rm HI}$ radial profile shown in the bottom panel of Fig. 6.

From Fig. 6, it is immediately apparent that the profile of $\sigma_{\sqrt{\rm mom2}}$ has a higher velocity dispersion than that of $\sigma_{\rm eff}$. However, the stacked profile shows an alternative behavior: being greater than the median values until $r \sim 40$ kpc and then approaching the lower values of the median. Overall, the different approaches show similar trends but are offset by $\sim$3 km s^{-1} between $\sigma_{\rm eff}$ and $\sigma_{\sqrt{\rm mom2}}$ and 2 km s^{-1} between $\sigma_{\rm eff}$ and stacked $\sigma_{\rm eff}$ (taking the mean between the differences until $r_{\rm gal}$ = 40 kpc). Koch et al. (2018) analyzed the differences between these methods in more detail, and they demonstrate that the deviation in $\sigma_{\sqrt{\rm mom2}}$ from the stacked profiles is a strong indication for multiple velocity components in some lines of sight. An analysis toward M 31 and M 33 (Koch et al. 2021) finds more than 50% of the lines of sight have more than one Gaussian in a spectrum, suggesting that multi-Gaussian profiles can be a source of discrepancy. This has also been found in various other nearby galaxy surveys (Warren et al. 2012; Stilp et al. 2013a,b). An examination of the masked ring region reveals some of these features (see Appendix B). A by-eye estimate suggests that more than one-third of the over 1000 lines of sight in the ring have more than one component. A more sophisticated fitting of individual spectra is beyond the scope of this paper and is limited by our need to increase the S/N via smoothing of the data to 5 km s^{-1} channels (see Sect. 2.3). Nevertheless, $\sigma_{\rm eff}$ and $\sigma_{\sqrt{\rm mom2}}$ show an enhancement in velocity dispersion in the ring.

Line widths of $\sim$6–10 km s^{-1} have been observed in the outskirts of galaxies (e.g., Tamburro et al. 2009 using the second-moment approach). At pressures that are typical for disk galaxies, the interstellar atomic gas has two phases at which it can remain in stable thermal equilibrium (e.g., Field et al. 1969; Wolfire et al. 1995, 2003). These two phases correspond to the cold neutral medium (CNM) and the WNM with temperatures of $\sim$100 K and $\sim$8000 K, respectively. The cold neutral gas emits lines with a characteristic line width of $\sim$1 km s^{-1}, while the warm neutral gas has a line width of $\sim$8 km s^{-1}. Tamburro et al. (2009) found spectral lines broader than $\sim$8 km s^{-1} in the THINGS galaxies and interpreted them to have been broadened by turbulent motions. However, as mentioned in the previous paragraph, the second-moment approach has been found to overestimate line widths (e.g., Mogotsi et al. 2016; Koch et al. 2018).

The bulk of the gas in the outskirts of galaxies is expected to be in the form of WNM (see e.g., Dickey et al. 2009, who find a CNM fraction of $\sim$15–20% out of $r \sim 25$ kpc in the Milky Way). The WNM temperature does not drop below $\sim$5000 K (corresponding to $\sigma \sim 6$ km s^{-1}) and is typically closer to 6000–7000 K (see e.g., Wolfire et al. 2003). Accordingly, the WNM is not expected to have a thermal velocity dispersion larger than 8 km s^{-1}. We found that the velocity dispersion is higher than the thermal WNM line width (i.e., greater than 8 km s^{-1}; marked as the horizontal dashed line in Fig. 6) for both $\sigma_{\sqrt{\rm mom2}}$ and $\sigma_{\rm eff}$. This agrees with past studies (e.g., Tamburro et al. 2009; Koch et al. 2018; Utomo et al. 2019). Our observations, however, highlight the large galactocentric radius range where we found a shallow decrease in

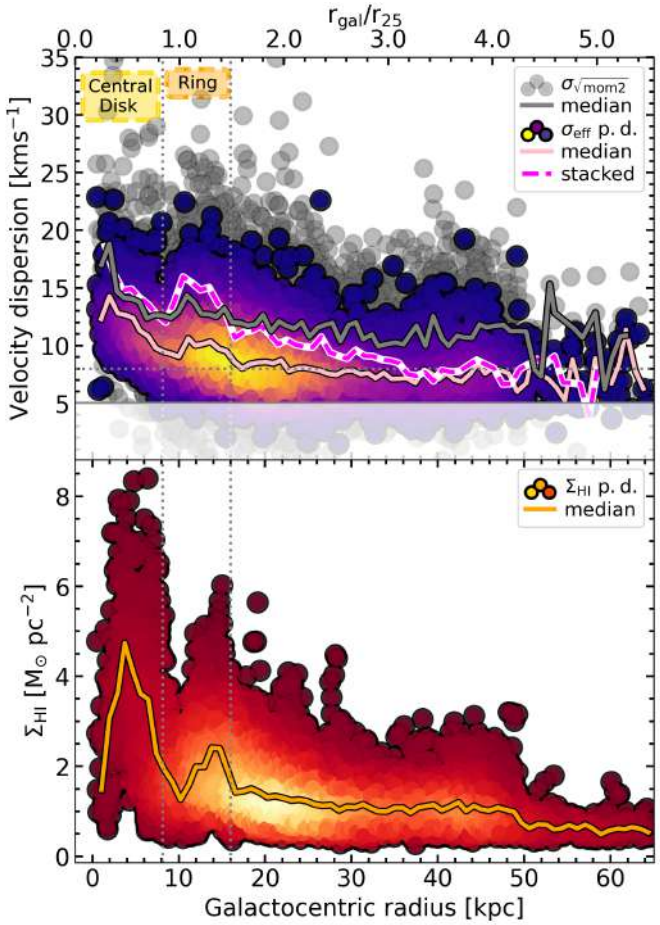

Fig. 6. Radial profile of the velocity dispersion, σ_v, and the H I gas surface density Σ_{HI}, together with the point density of σ_v and Σ_{HI} for individual lines of sight (circular points; the color-coding reflects a linear density distribution, where the highest density is shown in yellow). Top panel: We compare here the effective width (σ_{eff} purple-to-yellow scatter points) and $\sqrt{mom2}$ ($\sigma_{\sqrt{mom2}}$ grey points) approaches to estimate the velocity dispersion across the whole disk of M 83. We show the median for $\sigma_{\sqrt{mom2}}$ (grey solid line), the median for σ_{eff} (pink solid line), and the results after stacking σ_{eff} (pink-white dashed line). We see in all three cases enhanced velocity dispersion in the central disk and in the ring (indicated by the dashed vertical lines at 8.1 kpc and 16 kpc). The horizontal dashed line indicates the 8 km s^{-1} limit that we discuss in Sect. 4.1. Bottom panel: The profile of the H I gas surface density shows an enhancement of H I gas in the ring. This is similar to the velocity dispersion profiles.

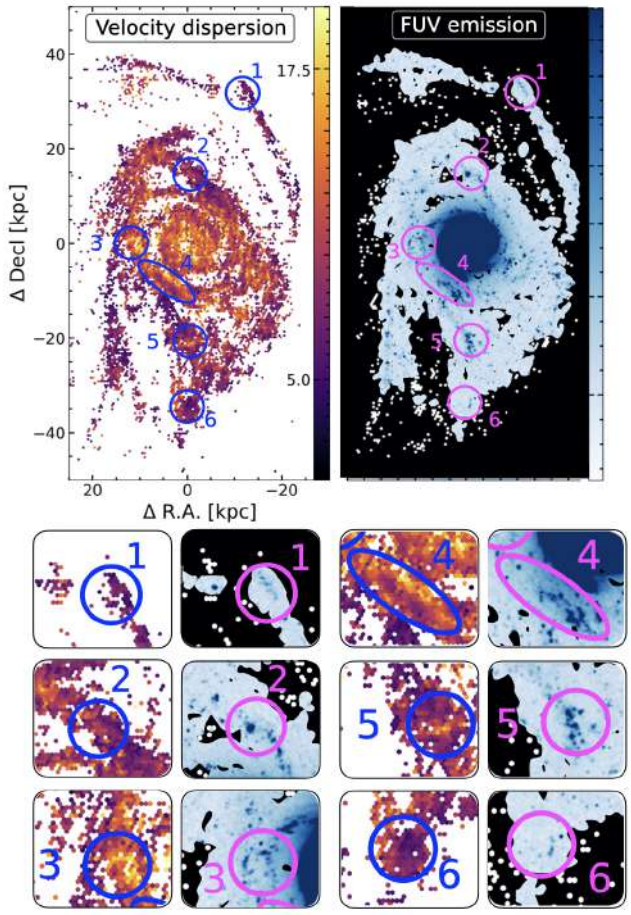

Fig. 7. Velocity dispersion and FUV emission. Visual inspection of spatial correlation of velocity dispersion (σ_{eff} the colorbar represents units of km s^{-1}) and FUV emission as an indicator of star formation (in units of mJy arcsec^{-2}). The FUV emission is the same GALEX FUV map as shown by Bigiel et al. (2010a). We defined 6 individual sub-regions in the ring, southern area, southern and northern arm, based on where we see either stronger FUV emission or enhanced velocity dispersion. See Sect. 4.1 for the discussion on the different regions.

velocity dispersion that is slightly larger than thermal equilibrium – until $r_{gal} \sim 50$ kpc. The exact values of the velocity dispersion shown in Fig. 6 should be taken with caution since individual spectra in our observations show multiple peaks (especially in the central disk) and associating those values with a purely thermal line width may not be appropriate.

We investigated whether there is evidence for an enhancement in velocity dispersion that is connected to ongoing star formation, as would be expected if turbulent motions were driven by feedback. The M 83 galaxy has an extended UV (XUV) disk (Thilker et al. 2005) where a tight spatial correlation between H I and FUV emission has been found (Bigiel et al. 2010a). Using Bigiel et al.'s FUV map, we could see within the ring peaks of the FUV emission. Figure 7, reveals however, at visual inspection of the spatial correlation of velocity dispersion and FUV emission (as an indicator of star formation) toward sub-regions in the ring (region 4) that the lowest H I velocity dispersion exists at locations with the highest FUV emission. Furthermore, regions labeled as 1, 2, 4, 5, and 6 in Fig. 7 show peaks in their FUV emission but no strong velocity dispersion. Region 3 shows stronger FUV emission and enhanced velocity dispersion; however, these quantities do not perfectly spatially correlate. This indicates that, at least at face value, there is no immediate one-to-one correspondence between recent star formation and enhanced velocity dispersion.

Whether the cause of higher velocity dispersion is feedback (from star formation) or gravity-driven turbulence (gravitational instabilities) is still a matter of debate (see e.g., discussion by Krumholz & Burkhart 2016). Some authors in the literature have found that high velocity dispersion is well correlated with regions of active star formation. However, Krumholz & Burkhart (2016) argue that the correlation itself may be explained by the fact that galaxies with more gas tend to have both higher velocity dispersion and more star formation. In a model combining both star formation feedback and radial transport, Krumholz et al. (2018) have shown that turbulence in galaxy disks can be driven by star formation feedback, radial transport, or a combination

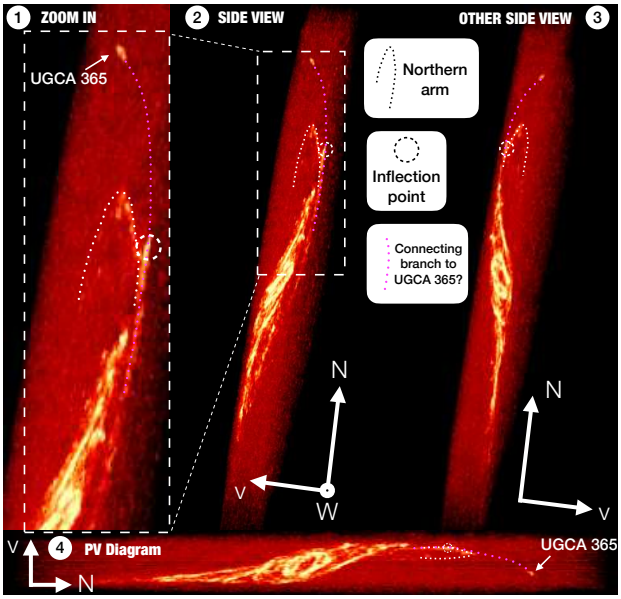

Fig. 8. Intensity map of M 83 from different angles showing the northern arm in a 3D viewer tool (see Sect. 4.2). In the two left plots, the arrow pointing west is directed towards us. In the right plot, it is pointing away from us. The northern orientation is the same in both plots. The v direction indicates the velocity axis over which we integrate for the integrated intensity map shown in Fig. 1. The white doted line shows the direction of the northern arm, while the pink dotted line shows the ~20 kpc long speculative connecting branch to UGCA 365.

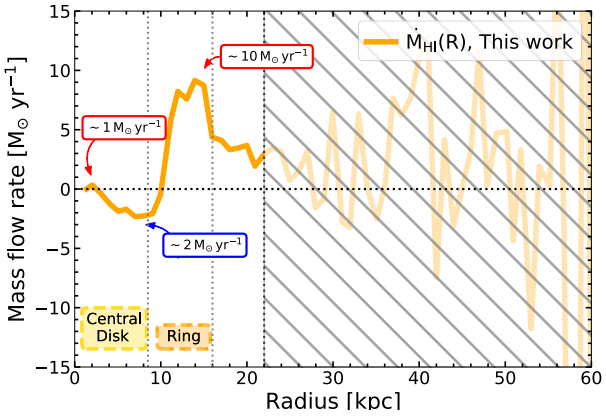

Fig. 9. Mass flow rates. Negative (positive) values mean inflow (outflow). We indicate the vertical line where the symmetry in our observed velocities is no longer valid and thus inferred the mass flow rates (beyond galactocentric radius of 23 kpc). We denote the approximate mass flow rates. The peaks and dips are indications in which radial bin in M 83 gas moves to the previous or following radial bin.

of both. Our observational analysis of M 83 shows no clear correlation with star formation, suggesting that radial transport (e.g., Schmidt et al. 2016) could be the reason for enhanced velocity dispersion in the outskirts of M 83.

4.2. The extended H I structure and the companion UGCA 365

The sharp edges of the H I gas distribution, especially in the southern and northern parts of the extended H I disk, were already noticed by Heald et al. 2016 (see their Fig. 17). They consider that this is due to photoionization or ram pressure from the intergalactic medium and specifically ruled out technical issues.

The prominent northern extended arm of M 83 emerges from its western part that curves 180° around to the east. This can be seen best in the observations of Heald et al. (2016) and Koribalski et al. (2018), serving as evidence that M 83 may have interacted or merged with another smaller galaxy. In our observations the eastern part of the extended arm is not detected, and the irregular galaxy NGC 5264 is not in our field of view (see Figs. B.1 and C.1). Koribalski et al. (2018) mentioned a clump marking a kink in the northwest side of the arm. We also observed it and refer to it as the "inflection point" because it is also visible in the velocity and residual maps where the velocities change[4], and we witnessed enhanced FUV emission at this location (see region 1 in Fig. 7). We marked this inflection point in Fig. 8 along with the northern arm. In the enclosed snapshot made using a 3D viewer tool[5], the dwarf irregular galaxy UGCA 365 can be seen in the northernmost region of our field of view (~55 kpc north of the center of M 83). Its TRGB distance is similar to that of M 83 within the given uncertainty: 5.25 ± 0.42 Mpc (Karachentsev et al. 2007). Koribalski et al. (2018) noted that both, the stellar and the gas distribution show some extension to the southeast along the minor axis of the galaxy and suggested that it may be due to tidal interaction with M 83. In Fig. 8, we denote a ~20 kpc-long speculative connecting branch between the inflection point and UGCA 365. We detected a faint H I emission close to the inflection point in the direction of this branch. The inflection point is best seen in panel 2 as well as in the zoomed-in version, where it appears to deviate from the general direction of the northern arm. In general, these panels show the warped nature of M 83's super-extended H I disk.

5. Upper limits for average radial mass flow rates in M83

Mass flows – inflow and outflow – play an important role in the process of the evolution of a galaxy. For example, mass flows fuel the inner central molecular zones with fresh, new star-forming material (e.g., Kormendy & Kennicutt 2004 or Henshaw et al. 2022 for the central molecular zone of the Milky Way). In this section, we discuss mass flow rates, their limitations, and how they depend on initial disk parameters.

5.1. Mass flow profile – A simple view

For average mass flow rate profiles across the H I disk in M 83, we used a simplified approach presented, for example, in Di Teodoro & Peek (2021):

$$\frac{\dot{M}_{\rm HI}(r)}{[M_\odot\ {\rm yr}^{-1}]} = \frac{2\pi\, r}{[{\rm pc}]} \frac{\Sigma_{\rm HI}(r)}{[M_\odot\ {\rm pc}^{-2}]} \frac{V_{\rm rad}(r)}{[{\rm pc\ yr}^{-1}]}, \quad (13)$$

where the radial velocity profile $V_{\rm rad}(r)$ and H I surface density profile $\Sigma_{\rm HI}(r)$ are used to obtain H I mass flow rate profiles.

[4] The exact velocity values at the inflection point depend on the assumed orientation and the $V_{\rm rot}$ values. For this reason, velocity gradients are not discussed.

[5] Glnemo2; https://projets.lam.fr/projects/glnemo2/wiki/, Lambert (2012)

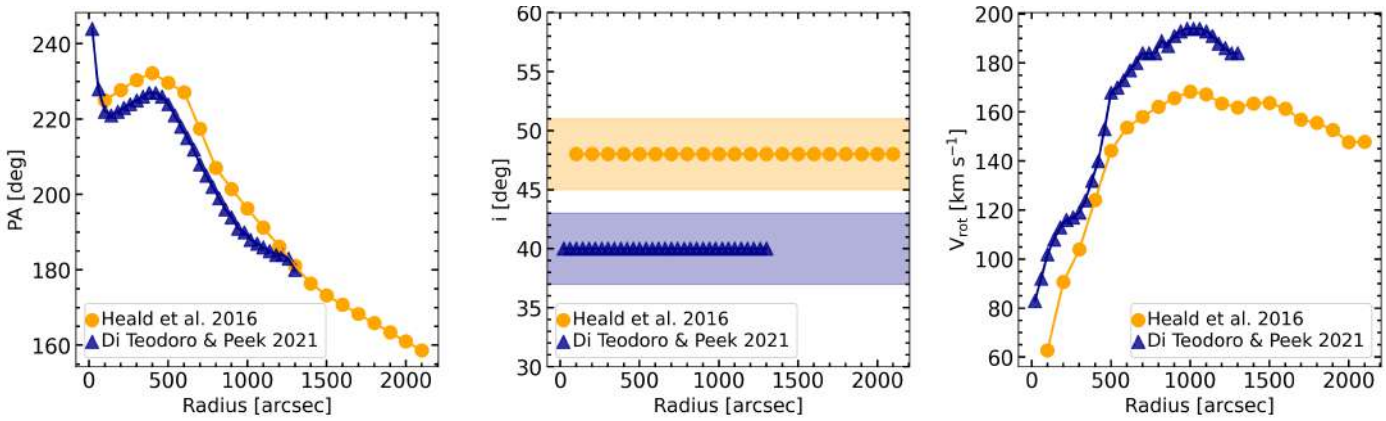

Fig. 10. Parameter comparison. In orange we show the kinematic parameters we used in this work for the velocity field shown in Sect. 3.2. In Sect. 5.2 we investigate how different initial parameters affect mass flow rates using the approach from Di Teodoro & Peek (2021) using their own set of parameters for M 83 (blue markers).

To get radial velocities, $V_{\rm rad}$, we used Eq. (12). We restate that $V_{\rm rad} < 0$ indicates inflow and $V_{\rm rad} > 0$ indicates outflow for M 83 (see Sect. 2.4).

We show the mass flow rate profile in Fig. 9, and also note the radial range of the central disk and ring. Heald et al. (2016) noticed that beyond a radius of ∼22 kpc (they quote 1000″) the approaching and receding side rotation curves differ, and thus, they should not be overinterpreted. Therefore, we shaded the region where the gas distribution and kinematics are no longer symmetric (i.e., deviation from pure circular motions).

Based on Eq. (13), we found within the central disk (i) at radii ∼2 kpc evidence of outflowing material with mass flow rates of ∼1 $M_\odot$ yr^{-1} and (ii) at $r \sim 5.5$ kpc inflowing material of ∼2 $M_\odot$ yr^{-1}. We found indications of (iii) outflowing material of the order ∼10 $M_\odot$ yr^{-1} at radii of $r \sim 14$ kpc, that is the ring (see mask in Fig. 5). In this region, we also found higher residual velocities. Moreover, using the $V_{\rm los,obs}$ map, we found enhanced velocity dispersion compared to the edges of the central disk of ∼20 km s^{-1} in that same ring region (median value; $\sigma_{\rm eff}$ and $\sigma_{\sqrt{\rm mom2}}$, see Fig. 6).

5.2. Initial parameters and their impact on ring-averaged mass flow rates

Multiple variants of tilted ring codes exist in the literature, for example, the 2D fitter GIPSY task `rotcur` (Begeman 1989) and the 3D fitter `BBarolo` (Di Teodoro & Fraternali 2015) and `FAT` (Kamphuis et al. 2015). After running these codes, the next step is often to interpret the noncircular motions and relate them, for example, to flow motions and/or interactions with a companion galaxy. M 83 provides one of the best cases, as it has different kinematic parameters available in the literature.

In Fig. 10, we show another recently published set of kinematic parameters of M 83, which includes position angle, inclination, $V_{\rm rot}$, and $V_{\rm rad}$ with observations from LVHIS using `BBarolo` (by Di Teodoro & Peek 2021; extracted from their appendix Fig. 15 for M 83, also known as NGC 5236). That is the same work from which we adopted the simplified method to derive mass flow rates (see Eq. (13)). Their tilted rings, however, only extend to $r_{\rm gal} = 30$ kpc and therefore do not include the southern and northern extended arms. We show the resulting residual velocity maps of both sets of kinematic parameters and how we interpolated the tilted rings (only for visual purposes) in Fig. 11. When comparing the two $V_{\rm res}$ maps, we saw no great difference in the inner disk. In the residual map of Di Teodoro & Peek (2021), the deviations of the circular motions in the ring region are smaller than in the one of Heald et al. (2016). In the southern area, we observed the opposite behavior: higher deviations of circular motions in the $V_{\rm res}$ map of Di Teodoro & Peek (2021). We took Di Teodoro & Peek's kinematic parameters shown in Fig. 10 and fit them with the same procedure we used for the kinematic parameters from Heald et al. (2016; see Sect. 2.4). After the fitting, we again calculated the mass flow rate using Eq. (13).

We show the two average radial mass flow rate profiles in Fig. 12. What is immediately noticeable is that the two are drastically different. In the ring region, they even indicate the opposite trend – inflowing material. Di Teodoro & Peek (2021) found a lower inclination, $i = 40°$ compared to $i = 48°$. The differences in position angle shift the minor axis, and with the lower inclination, they led to a flip in the inferred flow direction: from outflow to inflow. Additionally, also using LVHIS observations, Kamphuis et al. (2015) derived kinematic parameters using 3D fitting `FAT` and obtained an inclination value of $i = 40.3°$[6] for M 83. In other words, Kamphuis et al. (2015) and Di Teodoro & Peek (2021) found similar lower values for the inclination than Heald et al. (2016).

However, Heald et al. (2016) also determined kinematic parameters using the THINGS data (presented by de Blok et al. 2008) and obtained higher values for the inclination, $i = 46°$. For this purpose, they used the 2D fitting routine `rotcur`. This higher inclination value and the one derived from the KAT7 observations (i.e., $i = 46°$ and $i = 48°$, respectively) agree better with the isophote orientations in the optical disk.

This is a good demonstration of how challenging it is to unambiguously determine inflow and outflow rates. The inclination depends on whether the kinematics are fitted with 2D or 3D tilted rings (`BBarolo` tends to fit incliniations 10° lower than 2D fitters; Di Teodoro & Fraternali 2015). Even at inclinations that are far from being face on, the chosen inclination can have a large impact on the inferred mass flow rate. Mass flow rates are sensitive to inclination and position angle to the extent that inflows can even flip signs. At the same point, mass flow rates seem not to be sensitive to the employed 3D fit (adopted

[6] We do not show the calculated mass flow rates for the inclination value given in Kamphuis et al. (2015), as they did not provide any tables or radial plots for their position angles from which we would be able to extract them.

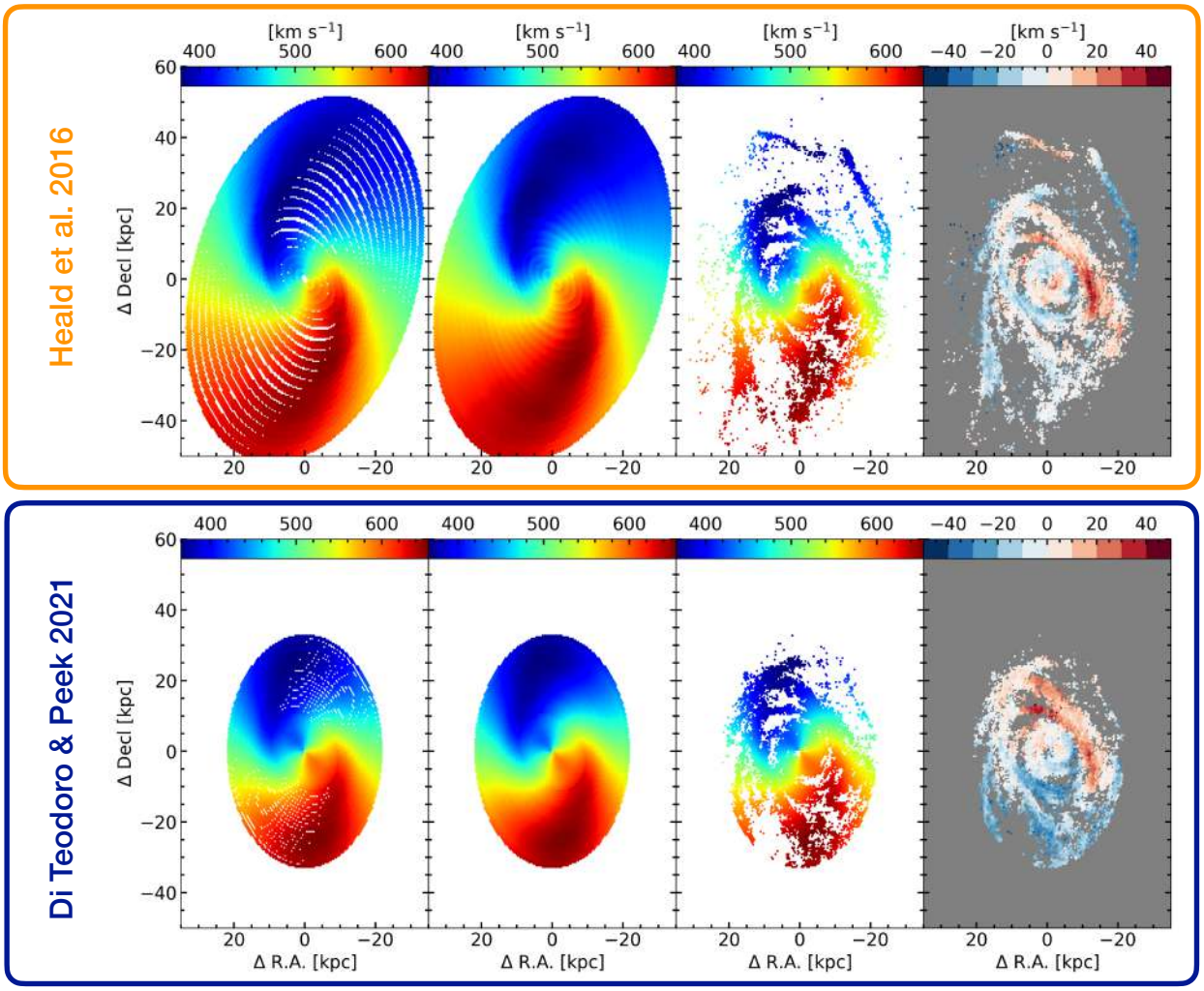

Fig. 11. Comparison of residual maps. Here we compare the modeled and residual maps ($V_{\rm los,mdl}$ and $V_{\rm res}$) of different initial parameters (shown in Fig. 10) that we obtained by using Eq. (8). Upper row: the tilted rings using (Heald et al. 2016) model outputs that are based on their KAT7 observations and using `rotcurv`. For visualisation reasons, we interpolated the gaps using the `scipy` function 2d interpolation. For further analysis we focus on the tilted-ring frame. Lower row: the tilted rings using (Di Teodoro & Peek 2021) model outputs that are based on LVHIS observations and using `BBarolo`. The field of view is restricted to their $V_{\rm rot}$ parameters. Therefore the southern and northern arm are not evident in the residual map.

by Di Teodoro & Peek 2021) or 2D fit (used here). Also, "circular motion plus axisymmetric radial motion" (see Eq. (7)) is not guaranteed to yield the true inflow rate if the $V_{\rm rot}$ + $V_{\rm rad}$ model is not accurate. For these reasons, the values given in Figs. 9 and 12 should be considered with caution, though we point out that they do represent our best guess at the H I mass flow rates and directions in M 83.

In the velocity fields (Fig. 4) and in Fig. 8, we witnessed the warped nature of M83's super-extended H I disk. The position angle twists by almost 90° from the orientation of the central disk. As mentioned by Heald et al. (2016), this shift in isovelocity was accounted by letting the $v_{\rm sys}$ parameter change in their models (which we adopted in this work; see Sect. 2.6.1). However, it has been shown that bar streaming motions are hard to neglect when analyzing mass flow rates toward the Milky Way's central molecular zone (e.g., Kim et al. 2012; Sormani et al. 2015; Sormani & Barnes 2019; Tress et al. 2020) or in nearby galaxies (e.g., Erroz-Ferrer et al. 2015; Salak et al. 2019). The M 83 galaxy is cataloged as SAB(s)c (see Table 1) – in between the classifications of a barred spiral galaxy and an unbarred spiral galaxy. The bar within M 83's central disk is the main reason for the gas inflow seen at $r \sim 5.5$ kpc; thus, the inferred inflow rates at these radii might be underestimated. However, both mass flow rate profiles shown in Fig. 12 are consistent for these small radii that cover the bar.

5.3. Interpreting mass flow rates in M 83

Keeping the uncertainties in mind, the following discussion is based on an approximation of the upper limits of the mass flow rates in M 83. We compare our results (presented in Fig. 9) to multi-wavelength literature studies (i.e., further evidence for mass flows) to interpret our findings.

Starting from the very center of M 83, a study identified signatures of inflowing gas toward its inner circumnuclear ring (~130 pc in radius) using ALMA HCN(1–0) and HCO^+(1–0) observations (Callanan et al. 2021). Recently published results toward M 83's optical disk using Multi-unit spectroscopic explorer (MUSE) observations have shown indications of outflowing ionized gas (Della Bruna et al. 2022). This flow

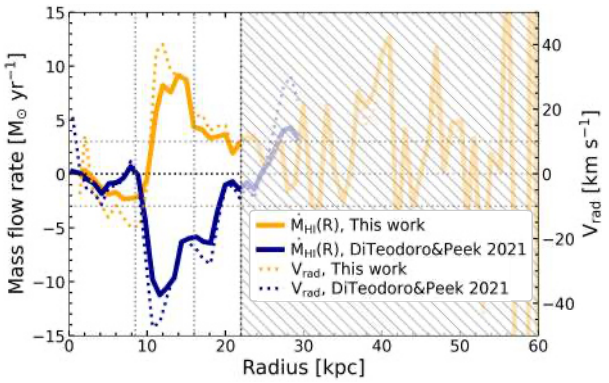

Fig. 12. Mass flow rate of this work (orange) and mass flow rate using different initial parameters as shown in Fig. 10 (blue). The dashed lines show $V_{\rm rad}$. Negative (positive) values mean inflow (outflow). Within the ring region we find the opposite trend of mass flow rates. We discuss the reasons for this in Sect. 5.2.

is east of M 83's nucleus and ∼1.2 kpc[7] in size. This could be consistent with our H I observations indicating an outflow at a galactocentric radius of ∼2 kpc.

The kinematics over the whole central optical disk of M 83 have been studied, for example, in Lundgren et al. (2004) and Fathi et al. (2008). Lundgren et al. (2004) found molecular streaming motions along the spiral arms when using CO(2–1) and CO(1–0) observations. These motions start at $r_{\rm gal} \sim 5.6$ kpc[8] toward M 83's center. This observation agrees with our potential (ii) inflow at $r \sim 5.5$ kpc. Fathi et al. (2008) confirmed this spiral inflow using Fabry-Perot observations of the Hα line across the inner ∼2.3 kpc of the central disk, capturing this inflow down to a few tens of parsecs from the dynamical nucleus of M 83. For the possible outflowing material in the outermost region at radii of $r_{\rm gal} \sim 14$ kpc, we found no correspondence in the literature.

From a theoretical point of view, gas is most likely to first accrete onto galaxies at larger radii and then move radially toward the inner disk to feed star formation (e.g., Ho et al. 2019). Cosmological hydrodynamical simulations of Milky Way-like galaxies have shown expected gas inflow of a few km s^{-1} within the inner optical disk that reaches ∼10 km s^{-1} in the outskirts (e.g., Trapp et al. 2022). Trapp et al. (2022) also found that the gas accumulates at the disk edge and then decreases in average radial speed and increases in column density. Observations also show similar inflow velocities of a few km s^{-1}. For example, Wong et al. (2004) decomposed H I and CO velocity fields of concentric elliptical rings into a third-order Fourier series for seven nearby spiral galaxies. Schmidt et al. (2016) performed a Fourier decomposition of velocity fields for ten THINGS galaxies. Both of these studies found ring-averaged radial inflow velocities of 5−10 km s^{-1} and 5−20 km s^{-1}, respectively, though they used methods different from those in this study. In these models and observations, radial velocities of more than 40 km s^{-1} have not been observed.

In our ring region in M 83, the high values (see right y axis in Fig. 12) are most likely due to differences in the adopted inclination values. The mass inflow rate is strongly dependent on the determined geometry of a galaxy, and therefore, it is hard to make clear estimates of how many solar masses are transported to M83's central disk. However, we observed ≈1.9×10^9 $M_\odot$ of gas at a distance of 16 kpc[9] from the center with a circular orbital period of 4.46×10^3 Myr[10]. To reach inflow rates of 10 $M_\odot$ per year would require infall on a timescale of ∼2.0×10^4 Myr, which is four times that of an orbital time or 0.7 of a free fall time[11].

6. Conclusion

In this paper, we have investigated the super-extended H I disk of M 83 based on ten pointing VLA observations at 21″ (≈500 pc) angular resolution. We found the following:

- We detected significant H I emission until a radius of ∼50 kpc. The most prominent features in Fig. 1 are the northern extended arm, the southern arm, and the ring surrounding the central disk.
- To investigate noncircular motions, we adopted tilted-model outputs from Heald et al. (2016) based on KAT7 observations. We find the highest deviations to be from pure circular motion in the ring (see Fig. 4).
- We examined environmental differences in velocities ($V_{\rm los}$ and $V_{\rm res}$), atomic gas surface density ($\Sigma_{\rm HI}$), and velocity dispersion (σ). To that end, we defined independent regions: central disk, ring, southern area, southern arm, and northern arm. Based on Fig. 5, we find that overall $\Sigma_{\rm HI}$ and σ decrease with galactocentric radius, in agreement with prior work. The distribution of $V_{\rm res}$ toward the ring and northern arm shows a second peak of −25 km s^{-1}.
- We examined the radial and environmental dependence of velocity dispersion across the whole disk of M 83. We analyzed the velocity dispersion, σ, using the effective-width ($\sigma_{\rm eff}$) and second-moment ($\sigma_{\sqrt{\rm mom2}}$) approaches (see Fig. 6). We find enhanced velocity dispersion in the ring as well as in the central disk using both techniques. This indicates that the atomic gas in the ring region seems to be more turbulent than in the outer regions.
- We compared σ with FUV emission to trace recent star formation. We did not find enhanced FUV emission where we found enhanced H I velocity dispersion. This anticorrelation with star formation suggests that radial transport could be the reason for enhanced velocity dispersion in the outskirts of M 83 (see Fig. 7).
- We found an "inflection point" in the observed velocities along the northern arm and speculate a possible connecting branch to the dwarf irregular galaxy UGCA 365 that deviates from the general direction of the northern arm (see Fig. 8).
- We used a simplified model to obtain a radial mass flow rate profile and compared it with the mass flow rates in the literature. We showed that kinematic parameters have a strong impact on these profiles. Although mass inflow is one of the most important processes feeding star formation, tilted ring models (2D or 3D) as the basis for deriving such profiles, are strongly sensitive to initial parameters (see e.g., Fig. 12). Furthermore, warped or flaring H I disks or distinct features at large radii further complicate the derivation of the kinematic parameters. To investigate this in more detail, more sophisticated models are needed to correctly determine the kinematics of this extended structure.

[7] We use here and in the following a distance of 5.16 Mpc, the same mentioned in Table 1, to get physical scales.
[8] See their Fig. 8 with the maximal radial extent of 4′.
[9] Assuming that the ring mass (with average surface density ∼3 $M_\odot$/pc^2 adopted from Fig. 5) is distributed over an 8 kpc-wide area (i.e., the width of the ring, $r_{\rm gal}$ = ∼8−16 kpc).
[10] By taking the average $V_{\rm rot}$ at the ring radius ∼160 km s^{-1} from Fig. 10.
[11] If we take $t_{\rm orb} \sim 6\ t_{\rm ff}$; see Eq. (E).

– In agreement with recent studies, we find within the central disk hints of inflowing material close to the nuclear region and outflowing material in the outer areas of the central disk.

Acknowledgements. We would like to thank the anonymous referee for their insightful comments that helped improve the quality of the paper. CE gratefully acknowledges funding from the Deutsche Forschungsgemeinschaft (DFG) Sachbeihilfe, grant number BI1546/3-1. CE, FB, AB, IB, JdB and JP acknowledge funding from the European Research Council (ERC) under the European Union's Horizon 2020 research and innovation programme (grant agreement No.726384/Empire). The work of AKL is partially supported by the National Science Foundation under Grants No. 1615105, 1615109, and 1653300. ER acknowledges the support of the Natural Sciences and Engineering Research Council of Canada (NSERC), funding reference number RGPIN-2017-03987. TGW acknowledges funding from the European Research Council (ERC) under the European Union's Horizon 2020 research and innovation programme (grant agreement No. 694343). JMDK gratefully acknowledges funding from the European Research Council (ERC) under the European Union's Horizon 2020 research and innovation programme via the ERC Starting Grant MUSTANG (grant agreement number 714907). COOL Research DAO is a Decentralised Autonomous Organisation supporting research in astrophysics aimed at uncovering our cosmic origins. SCOG acknowledges funding from the European Research Council via the ERC Synergy Grant "ECOGAL – Understanding our Galactic ecosystem: From the disk of the Milky Way to the formation sites of stars and planets" (project ID 855130), from the Deutsche Forschungsgemeinschaft (DFG) via the Collaborative Research Center (SFB 881 – 138713538) "The Milky Way System" (subprojects A1, B1, B2 and B8) and from the Heidelberg Cluster of Excellence (EXC 2181 – 390900948) "STRUCTURES: A unifying approach to emergent phenomena in the physical world, mathematics, and complex data", funded by the German Excellence Strategy. MQ acknowledges support from the Spanish grant PID2019-106027GA-C44, funded by MCIN/AEI/10.13039/501100011033. KG is supported by the Australian Research Council through the Discovery Early Career Researcher Award (DECRA) Fellowship DE220100766 funded by the Australian Government. HH acknowledges the support of the Natural Sciences and Engineering Research Council of Canada (NSERC), funding reference number RGPIN-2017-03987 and the Canadian Space Agency funding reference 21EXPUVI3. EW is funded by the Deutsche Forschungsgemeinschaft (DFG, German Research Foundation) – Project-ID 138713538 – SFB 881 ("The Milky Way System", subproject P2). WJGdB received funding from the European Research Council (ERC) under the European Union's Horizon 2020 research and innovation programme (grant agreement No 882793 'MeerGas'). D.J.P. is supported through the South African Research Chairs Initiative of the Department of Science and Technology and National Research Foundation and acknowledges partial support from NSF CAREER grant AST-1149491. This work is based on observations carried out with the *Karl G. Jansky* Very Large Array (VLA) and the Green Bank Telescope (GBT). The National Radio Astronomy Observatory is a facility of the National Science Foundation operated under cooperative agreement by Associated Universities, Inc. The Green Bank Observatory is a facility of the National Science Foundation operated under cooperative agreement by Associated Universities, Inc. This work is based in part on observations made with the Galaxy Evolution Explorer (GALEX). GALEX is a NASA Small Explorer, whose mission was developed in cooperation with the Centre National d'Etudes Spatiales (CNES) of France and the Korean Ministry of Science and Technology. GALEX is operated for NASA by the California Institute of Technology under NASA contract NAS5-98034. Software: `NumPy` (Harris et al. 2020), `SciPy` (Virtanen et al. 2020), `Astropy` (Astropy Collaboration 2018), `pandas` (The pandas development team 2021), `Matplotlib` (Hunter 2007), `CASA` (CASA Team 2022), `BBarolo` (EdT & Oman 2021), `rotcur` (Begeman 1989), radio-astro-tools (`uvcombine`) (Koch & Ginsburg 2022), `glnemo2` (https://projets.lam.fr/projects/glnemo2/wiki/) `astrometry` (https://nova.astrometry.net/)

References

Astropy Collaboration (Robitaille, T. P., et al.) 2013, A&A, 558, A33
Astropy Collaboration (Price-Whelan, A. M., et al.) 2018, AJ, 156, 123
Begeman, K. G. 1989, A&A, 223, 47
Bešlić, I., Barnes, A. T., Bigiel, F., et al. 2021, MNRAS, 506, 963
Bialy, S., & Sternberg, A. 2019, ApJ, 881, 160
Bigiel, F., Leroy, A., Seibert, M., et al. 2010a, ApJ, 720, L31
Bigiel, F., Leroy, A., Walter, F., et al. 2010b, AJ, 140, 1194
Callanan, D., Longmore, S. N., Kruijssen, J. M. D., et al. 2021, MNRAS, 505, 4310
CASA Team (Bean, B., et al.) 2022, PASP, 134, 114501
Cornwell, T. J. 2008, IEEE J. Sel. Top. Signal Proc., 2, 793
de Blok, W. J. G., Walter, F., Brinks, E., et al. 2008, AJ, 136, 2648
de Blok, W. J. G., Adams, E. A. K., Amram, P., et al. 2016, Proc. MeerKAT Science: On the Pathway to the SKA, 25-27 May, 2016 Stellenbosch, South Africa (MeerKAT2016), online at https://pos.sissa.it/cgi-bin/reader/conf.cgi?confid=277, 7
Della Bruna, L., Adamo, A., Amram, P., et al. 2022, A&A, 660, A77
de Vaucouleurs, G., de Vaucouleurs, A., Corwin, H. G. J., et al. 1991, Third Reference Catalogue of Bright Galaxies
Dickey, J. M., Strasser, S., Gaensler, B. M., et al. 2009, ApJ, 693, 1250
Di Teodoro, E. M., & Fraternali, F. 2015, MNRAS, 451, 3021
Di Teodoro, E. M., & Peek, J. E. G. 2021, ApJ, 923, 220
EdT, & Oman, K. 2021, https://doi.org/10.5281/zenodo.5510565
Erroz-Ferrer, S., Knapen, J. H., Leaman, R., et al. 2015, MNRAS, 451, 1004
Fathi, K., Beckman, J. E., Lundgren, A. A., et al. 2008, ApJ, 675, L17
Field, G. B., Goldsmith, D. W., & Habing, H. J. 1969, ApJ, 155, L149
Harris, C. R., Millman, K. J., van der Walt, S. J., et al. 2020, Nature, 585, 357
Heald, G., Józsa, G., Serra, P., et al. 2011, A&A, 526, A118
Heald, G., de Blok, W. J. G., Lucero, D., et al. 2016, MNRAS, 462, 1238
Henshaw, J. D., Barnes, A. T., Battersby, C., et al. 2022, ArXiv e-prints [arXiv:2203.11223]
Heyer, M. H., Carpenter, J. M., & Snell, R. L. 2001, ApJ, 551, 852
Ho, S. H., Martin, C. L., & Turner, M. L. 2019, ApJ, 875, 54
Huchtmeier, W. K., & Bohnenstengel, H. D. 1981, A&A, 100, 72
Hunter, J. D. 2007, Comput. Sci. Eng., 9, 90
Ianjamasimanana, R., de Blok, W. J. G., Walter, F., & Heald, G. H. 2012, AJ, 144, 96
Ianjamasimanana, R., de Blok, W. J. G., Walter, F., et al. 2015, AJ, 150, 47
Jameson, K. E., McClure-Griffiths, N. M., Liu, B., et al. 2019, ApJS, 244, 7
Jiménez-Donaire, M. J., Bigiel, F., Leroy, A. K., et al. 2019, ApJ, 880, 127
Kamphuis, P., Józsa, G. I. G., Oh, S. H., et al. 2015, MNRAS, 452, 3139
Karachentsev, I. D., Tully, R. B., Dolphin, A., et al. 2007, AJ, 133, 504
Kepley, A. A., Tsutsumi, T., Brogan, C. L., et al. 2020, PASP, 132, 024505
Kereš, D., Katz, N., Weinberg, D. H., & Davé, R. 2005, MNRAS, 363, 2
Kim, W.-T., Seo, W.-Y., Stone, J. M., Yoon, D., & Teuben, P. J. 2012, ApJ, 747, 60
Koch, E., & Ginsburg, A. 2022, Astrophysics Source Code Library [record ascl:2208.014]
Koch, E. W., Rosolowsky, E. W., Lockman, F. J., et al. 2018, MNRAS, 479, 2505
Koch, E. W., Rosolowsky, E. W., Leroy, A. K., et al. 2021, MNRAS, 504, 1801
Koda, J., Sawada, T., Sakamoto, K., et al. 2020, ApJ, 890, L10
Koribalski, B. S., Wang, J., Kamphuis, P., et al. 2018, MNRAS, 478, 1611
Kormendy, J., & Kennicutt, Jr., R. C. 2004, ARA&A, 42, 603
Krumholz, M. R., & Burkhart, B. 2016, MNRAS, 458, 1671
Krumholz, M. R., Burkhart, B., Forbes, J. C., & Crocker, R. M. 2018, MNRAS, 477, 2716
Lambert, J. C. 2012, in Astronomical Data Analysis Software and Systems XXI, eds. P. Ballester, D. Egret, & N. P. F. Lorente, ASP Conf. Ser., 461, 897
Leroy, A. K., Hughes, A., Schruba, A., et al. 2016, ApJ, 831, 16
Leroy, A. K., Sandstrom, K. M., Lang, D., et al. 2019, ApJs, 244, 24
Leroy, A. K., Schinnerer, E., Hughes, A., et al. 2021, ApJs, 257, 43
Lundgren, A. A., Olofsson, H., Wiklind, T., & Rydbeck, G. 2004, A&A, 422, 865
McMullin, J. P., Waters, B., Schiebel, D., Young, W., & Golap, K. 2007, in Astronomical Data Analysis Software and Systems XVI, eds. R. A. Shaw, F. Hill, & D. J. Bell, ASP Conf. Ser., 376, 127
Miller, E. D., Bregman, J. N., & Wakker, B. P. 2009, ApJ, 692, 470
Mogotsi, K. M., de Blok, W. J. G., Caldú-Primo, A., et al. 2016, AJ, 151, 15
Oh, S.-H., Kim, S., For, B.-Q., & Staveley-Smith, L. 2022, ApJ, 928, 177
Oman, K. A., Marasco, A., Navarro, J. F., et al. 2019, MNRAS, 482, 821
Pingel, N. M., Pisano, D. J., Heald, G., et al. 2018, ApJ, 865, 36
Pisano, D. J. 2014, AJ, 147, 48
Rogstad, D. H., Lockhart, I. A., & Wright, M. C. H. 1974, ApJ, 193, 309
Romeo, A. B., & Mogotsi, K. M. 2017, MNRAS, 469, 286
Rosolowsky, E., & Leroy, A. 2006, PASP, 118, 590
Salak, D., Noma, Y., Sorai, K., et al. 2019, PASJ, 71, S16
Sancisi, R., Fraternali, F., Oosterloo, T., & van der Hulst, T. 2008, A&ARv, 15, 189
Sardone, A., Pisano, D. J., Pingel, N. M., et al. 2021, ApJ, 910, 69
Schmidt, T. M., Bigiel, F., Klessen, R. S., & de Blok, W. J. G. 2016, MNRAS, 457, 2642
Sormani, M. C., & Barnes, A. T. 2019, MNRAS, 484, 1213
Sormani, M. C., Binney, J., & Magorrian, J. 2015, MNRAS, 449, 2421
Stanimirovic, S., Staveley-Smith, L., Dickey, J. M., Sault, R. J., & Snowden, S. L. 1999, MNRAS, 302, 417
Stilp, A. M., Dalcanton, J. J., Warren, S. R., et al. 2013a, ApJ, 765, 136
Stilp, A. M., Dalcanton, J. J., Skillman, E., et al. 2013b, ApJ, 773, 88
Sun, J., Leroy, A. K., Schruba, A., et al. 2018, ApJ, 860, 172
Tamburro, D., Rix, H. W., Leroy, A. K., et al. 2009, AJ, 137, 4424

The pandas development team 2021, https://github.com/pandas-dev/pandas
Thilker, D. A., Bianchi, L., Boissier, S., et al. 2005, ApJ, 619, L79
Tilanus, R. P. J., & Allen, R. J. 1993, A&A, 274, 707
Trapp, C. W., Kereš, D., Chan, T. K., et al. 2022, MNRAS, 509, 4149
Tress, R. G., Sormani, M. C., Glover, S. C. O., et al. 2020, MNRAS, 499, 4455
Tumlinson, J., Peeples, M. S., & Werk, J. K. 2017, ARA&A, 55, 389
Utomo, D., Blitz, L., & Falgarone, E. 2019, ApJ, 871, 17
Virtanen, P., Gommers, R., Oliphant, T. E., et al. 2020, Nat. Methods, 17, 261
Walter, F., Brinks, E., de Blok, W. J. G., et al. 2008, AJ, 136, 2563
Wang, J., Koribalski, B. S., Serra, P., et al. 2016, MNRAS, 460, 2143
Warren, S. R., Skillman, E. D., Stilp, A. M., et al. 2012, ApJ, 757, 84
White, S. D. M., & Frenk, C. S. 1991, ApJ, 379, 52
Wolfire, M. G., Hollenbach, D., McKee, C. F., Tielens, A. G. G. M., & Bakes, E. L. O. 1995, ApJ, 443, 152
Wolfire, M. G., McKee, C. F., Hollenbach, D., & Tielens, A. G. G. M. 2003, ApJ, 587, 278
Wong, T., Blitz, L., & Bosma, A. 2004, ApJ, 605, 183

[1] Argelander-Institut für Astronomie, Universität Bonn, Auf dem Hügel 71, 53121 Bonn, Germany
e-mail: eibensteiner@astro.uni-bonn.de
[2] Department of Astronomy, The Ohio State University, 4055 McPherson Laboratory, 140 West 18th Ave, Columbus, OH 43210, USA
[3] Center for Astrophysics, Harvard & Smithsonian, 60 Garden St., 02138 Cambridge, MA, USA
[4] Dept. of Physics, University of Alberta, Edmonton, Alberta T6G 2E1, Canada
[5] Max Planck Institute for Astronomy, Königstuhl 17, 69117 Heidelberg, Germany
[6] Sterrenkundig Observatorium, Universiteit Gent, Krijgslaan 281 S9, 9000 Gent, Belgium
[7] Netherlands Institute for Radio Astronomy (ASTRON), Oude Hoogeveensedijk 4, 7991 PD Dwingeloo, The Netherlands
[8] Kapteyn Astronomical Institute, University of Groningen, PO Box 800, 9700 AV Groningen, The Netherlands
[9] Department of Astronomy, University of Cape Town, Private Bag X3, 7701 Rondebosch, South Africa
[10] Department of Physics & Astronomy, Bloomberg Center for Physics and Astronomy, Johns Hopkins University, 3400 N. Charles Street, Baltimore, MD 21218, USA
[11] Department of Astronomy, University of Cape Town, Private Bag X3, Rondebosch 7701, South Africa
[12] Department of Physics and Astronomy, West Virginia University, White Hall, Box 6315, Morgantown, WV 26506, USA
[13] Center for Gravitational Waves and Cosmology, West Virginia University, Chestnut Ridge Research Building, Morgantown, WV 26505, USA
[14] National Radio Astronomy Observatory, 1003 Lopezville Road, Socorro, NM 87801, USA
[15] European Southern Observatory, Karl-Schwarzschild Straße 2, 85748 Garching bei München, Germany
[16] Observatorio Astronómico Nacional (IGN), C/ Alfonso XII, 3, 28014 Madrid, Spain
[17] Univ Lyon, Univ Lyon1, ENS de Lyon, CNRS, Centre de Recherche Astrophysique de Lyon UMR5574, 69230 Saint-Genis-Laval, France
[18] National Radio Astronomy Observatory, 520 Edgemont Rd, Charlottesville, VA 22903, USA
[19] Institüt für Theoretische Astrophysik, Zentrum für Astronomie der Universität Heidelberg, Albert-Ueberle-Strasse 2, 69120 Heidelberg, Germany
[20] Research School of Astronomy and Astrophysics, Australian National University, Canberra, ACT 2611, Australia
[21] Astrophysics Research Institute, Liverpool John Moores University, 146 Brownlow Hill, Liverpool L3 5RF, UK
[22] Department of Physics & Astronomy, University of Wyoming, Laramie, WY 82071, USA
[23] Cosmic Origins Of Life (COOL) Research DAO, Munich, Germany
[24] Departamento de Fisica de la Tierra y Astrofisica & IPARCOS, Facultad de CC Fisicas, Universidad Complutense de Madrid, 28040 Madrid, Spain
[25] Astronomisches Rechen-Institut, Zentrum für Astronomie der Universität Heidelberg, Mönchhofstraße 12-14, 69120 Heidelberg, Germany
[26] Sub-department of Astrophysics, Department of Physics, University of Oxford, Keble Road, Oxford OX1 3RH, UK
[27] Max-Planck-Institut für Radioastronomie, Radioobservatorium Effelsberg, Max-Planck-Strasse 28, Munich, Germany

Appendix A: Image Combination

Similar to the procedure described in the appendix of Koch et al. (2018), itself based on Chapter 3 of Stanimirovic et al. (1999), we analyzed the effects of combining the (i) VLA data with single dish (ii) Green Bank Telescope (GBT; project GBT11A-055) observations. (i) The VLA observation has an angular resolution of 21″ (∼ 500 pc) and a spectral resolution of 5.0 km s^{-1} . (ii) The GBT observation has an angular resolution of 523″ (∼ 12.13 kpc) and a spectral resolution of 5.15 km s^{-1} (see Figure A.1, panel 1a).

We used a distribution-based method on the $u-v$-amplitudes where the spatial coverage of the VLA and single dish data overlap to quantify the scaling factor. We used the `uvcombine` package (Koch & Ginsburg 2022) and examined the distributions of the single dish amplitudes, the VLA amplitudes, and their ratio across all channels. The amplitudes of the single dish and VLA in the overlap regions are well described by normal distributions, and as such, the ratio of the log-amplitude follows a Cauchy distribution (Koch et al. 2018). We fit a Cauchy distribution and used the location of the peak of the distribution as the scale factor. In Figure A.1, panel 1c, we show the distribution of the amplitudes across all channels and the best-fit Cauchy distribution.

Adopting a maximum-likelihood approach and using the ratios from all channels, we found a scaling factor of 0.982±0.003 for the GBT data. Because we expected the absolute flux uncertainties to be ∼10%, the scaling factor from the distribution fit is consistent with one, and thus we did not apply a scaling factor to the GBT data before feathering.

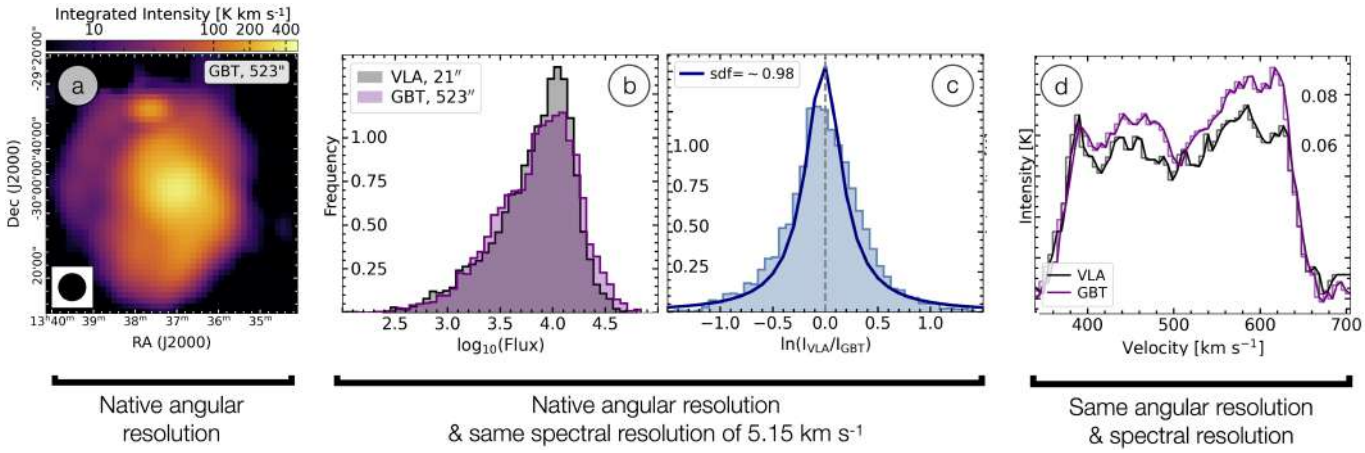

Fig. A.1. Image combination. **(a)** We show the integrated intensity maps of the GBT observation at native angular resolution. **(b)** Shows the distribution of the flux of the single dish (SD) and VLA data at matched spectral resolution (i.e. we regridded the VLA to the GBT spectral resolution). **(c):** We used the `uvcombine` python package to find the single dish scaling factor (sdf; blue line). The ratio of the low-res and high-res observations result in a Cauchy distribution. We fit the log of the ratio to a Cauchy distribution (blue histogram) and its mean is then an estimate for the scaling factor. **(d)**: The spectra of the VLA and GBT observation at matched angular and spectral resolution (i.e. we gaussian convolve and regridded the VLA to the GBT angular and spectral resolution).

Appendix B: Ten mosaic pointing and channel maps

Table B.1. The coordinates of the 10-point mosaic of our VLA observation that are shown in Figure B.1.

#	ID	RA	Dec
0	M83-S	13:37:30.0	-30.19.48.7
1	M83-SE	13:38:00.0	-30.06.02.5
2	M83-SW	13:36:24.4	-30.06.02.5
3	M83-W	13:35:47.9	-29.46.00.0
4	M83-C	13:37:01.2	-29.52.16.3
5	M83-E	13:38:45.0	-29.52.16.3
6	M83-NE	13:38:51.0	-29.34.00.0
7	M83-NC	13:37:37.8	-29.34.00.0
8	M83-NW	13:36:24.6	-29.34.00.0
9	M83-N	13:37:01.2	-29.20.00.0

Notes. # 0-9 corresponds to the numbers associated with each individual pointing shown in Figure B.1.

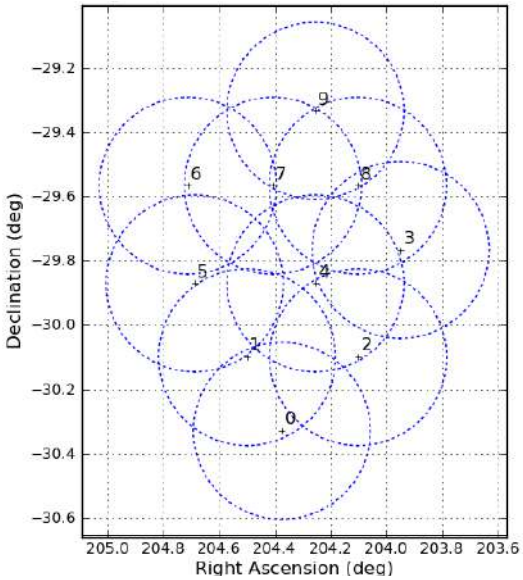

Fig. B.1. The position for the extended (~1.5^2 deg) 10-point mosaic of our VLA observation.

Figure B.1 shows the ten mosaic pointing for our VLA observation. We show the positions and their corresponding coordinates.

In Eq. (B.2) we show all channels (contrary to the overview shown in Figure 2, where we took every third 5.0 km s^{-1} channel) of our imaged data set. During the imaging procedure, we chose a spectral resolution of $\Delta_v = 5.0\,\mathrm{km\,s^{-1}}$ to increase the S/N of our observations.

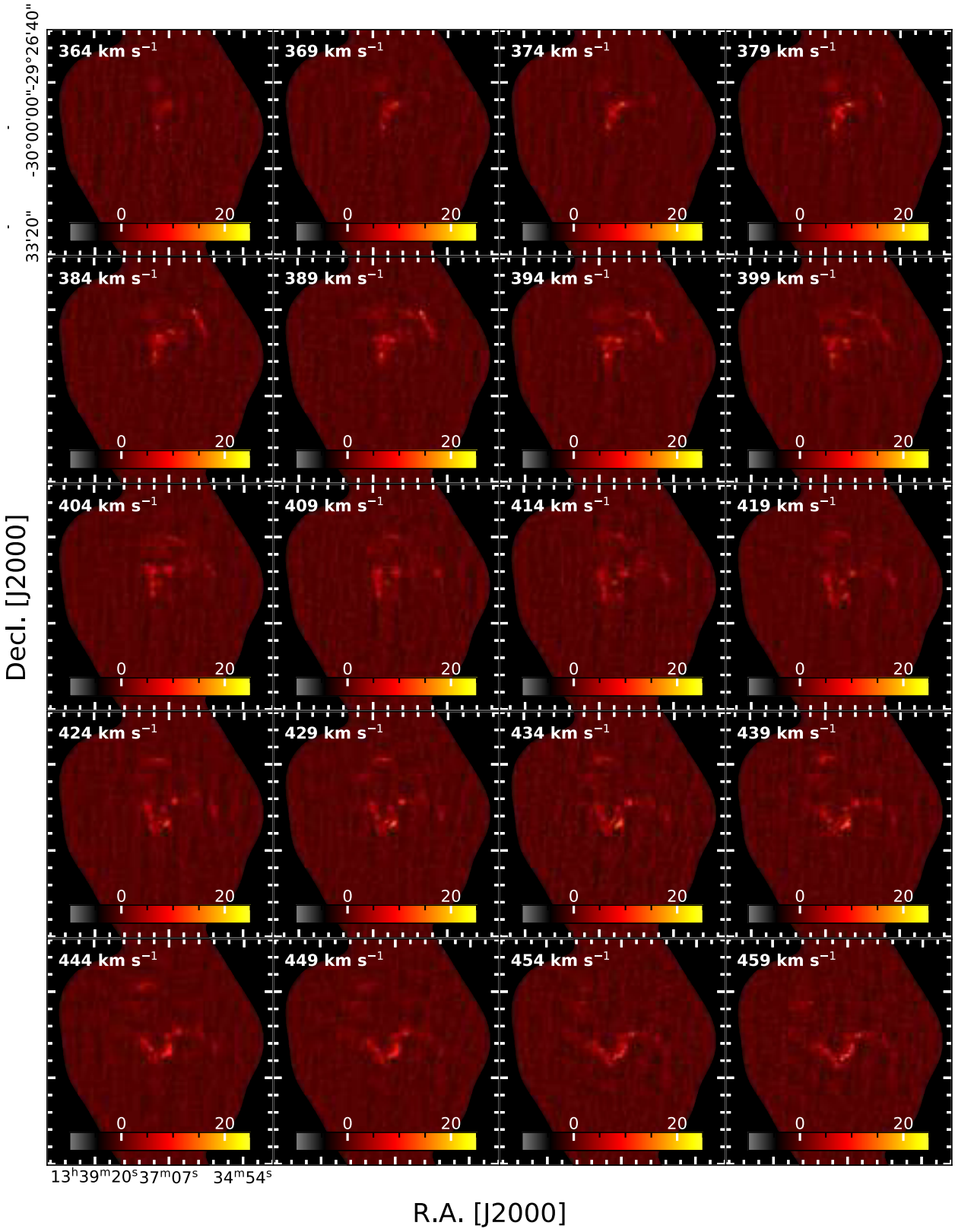

Fig. B.2. Channel maps of our VLA+GBT data. Here we show now every 5.0 km s^{-1} channel. The line-of-sight velocity of the shown channels is displayed on the upper left corner of each panel.

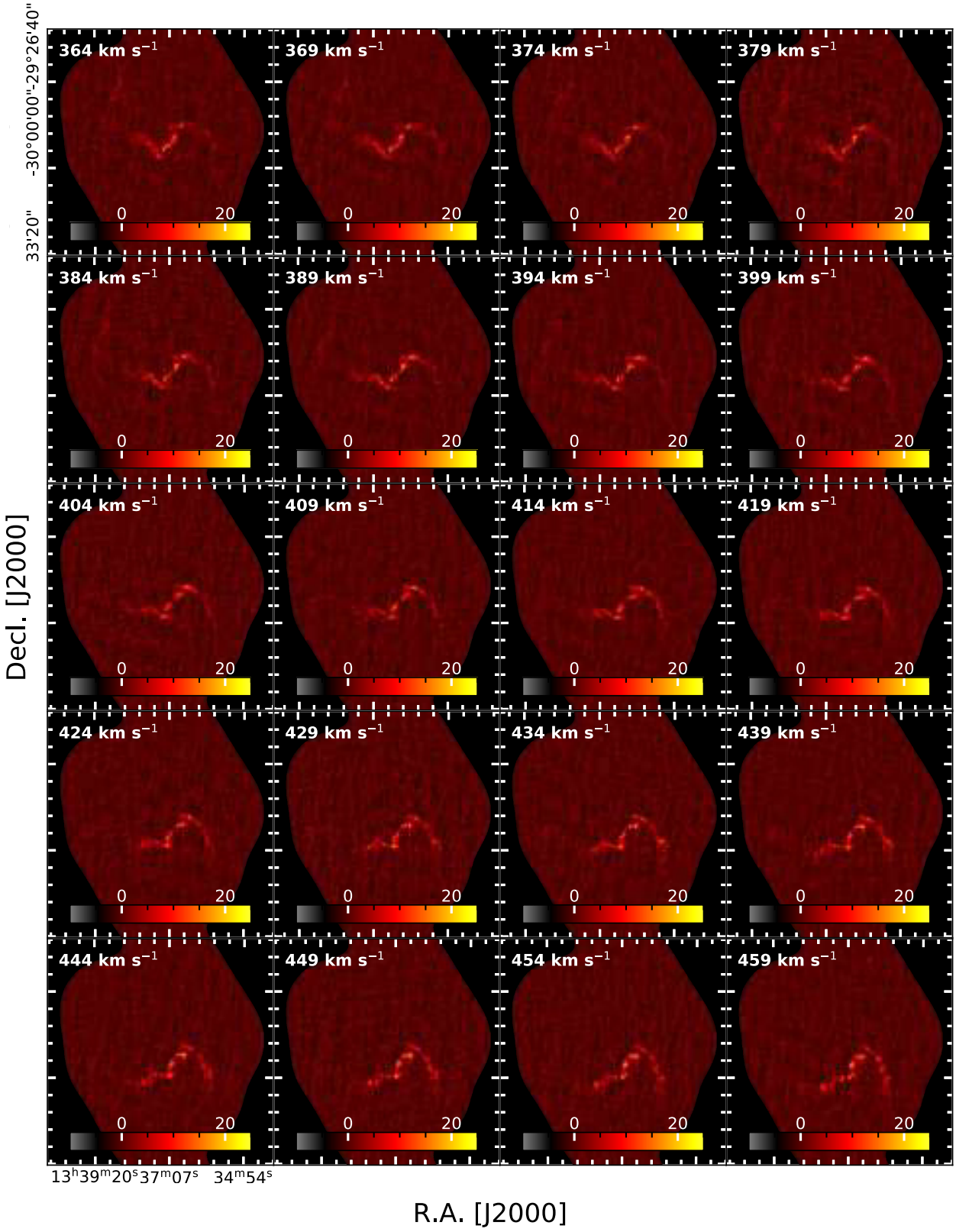

Fig. B.2. Continued.

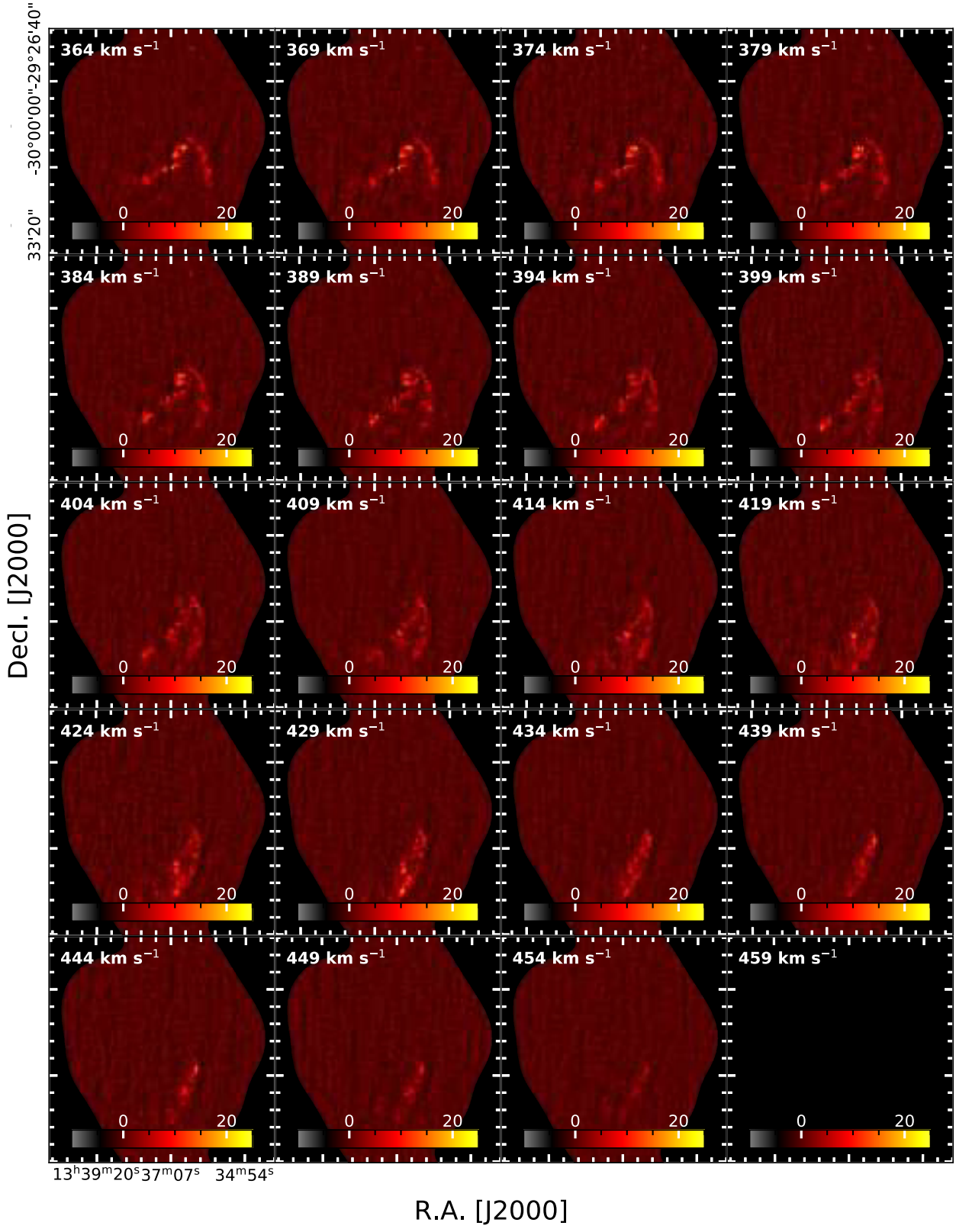

Fig. B.2. Continued.

Appendix C: Green Bank Telescope observation

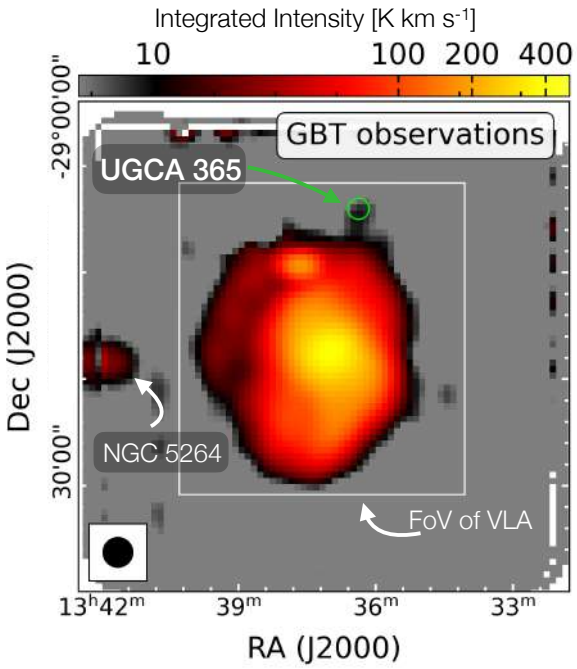

Fig. C.1. Integrated intensity map of the GBT observation. The white contours show the field of view of the VLA observation. We denote the companion galaxies UGCA 365 and NGC 5264. The H I emission of UGCA 365 is faint relative to M 83 (~10 K km s^{-1} compared to ~400 K km s^{-1}).

We show in Figure C.1 the integrated intensity map of the GBT observation with an angular resolution of 523″ together with the field of view of the VLA observation and the location of UGCA 365. The H I emission of UGCA 365 is faint relative to M 83 (~10 K km s^{-1} compared to ~400 K km s^{-1}).

Appendix D: Multiple velocity components

In Section 4.1 we mentioned that some of our sightlines show non-Gaussian or multiple velocity components. We show four examples in Eq. (D.1). We show in the left panels the velocity dispersion calculated with Eq. (5) and show the hexagon in green, of which we show the spectrum on the right. These spectra represent the multicomponent behavior of the spectrum of individual lines of sight in the ring region.

We looked into individual regions and compared the two approaches discussed in this paper to derive the velocity dispersion (i.e., $\sigma_{\rm eff}$ and $\sigma_{\sqrt{\rm mom2}}$) in Figure D.2. In the figure, we show linear regression fits in the form of $\log(y) = \beta \times \log(x) + \alpha$. We found for the central disk and ring region a moderate[12] linear correlation between $\sigma_{\rm eff}$ and $\sigma_{\sqrt{\rm mom2}}$. For all the other regions, we found a weak, approximately linear correlation. We observed the highest scatter in $\sigma_{\sqrt{\rm mom2}}$ in the ring region of ~2.5 dex, followed by a scatter of ~2.0 dex toward the central disk and southern area. These scatters most likely highlight the multicomponent and/or wider components of a spectrum. In the first panel of Figure D.2, where we show the x and y axis in linear scales, the velocity dispersions over ~20 km s^{-1} are likely to represent a multicomponent spectrum.

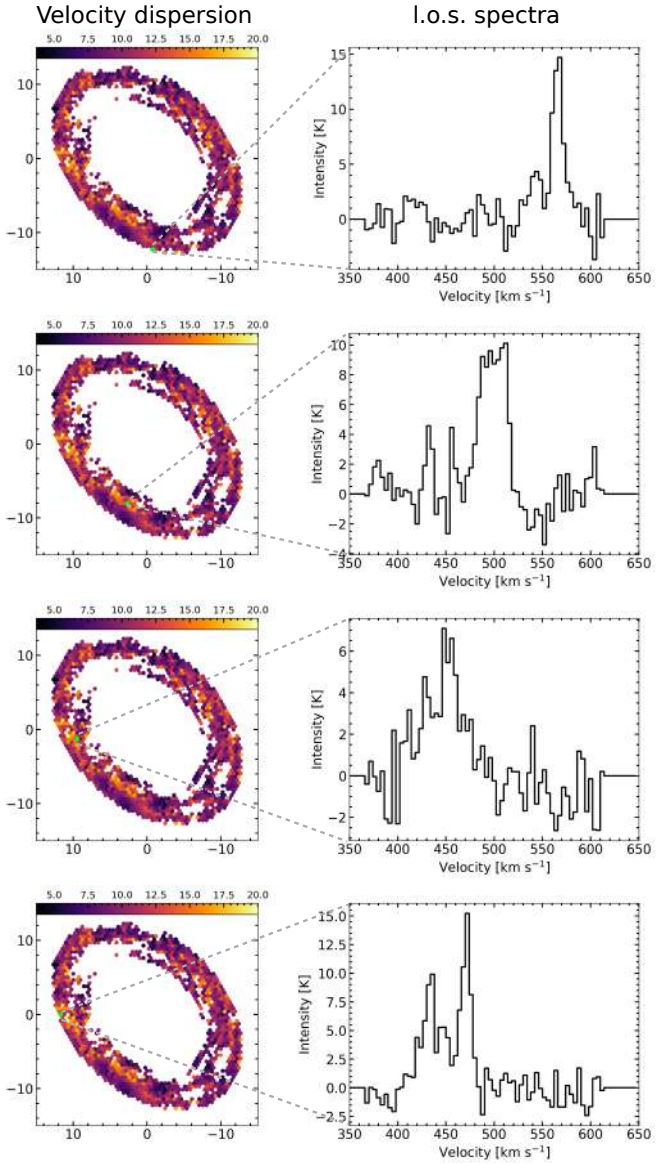

Fig. D.1. Examples of four spectra of individual line of sights that show higher values in the velocity map. These show the multi-component behavior of the spectra.

[12] Here we refer to a moderate correlation if ρ lies in the range of 0.5-0.7.

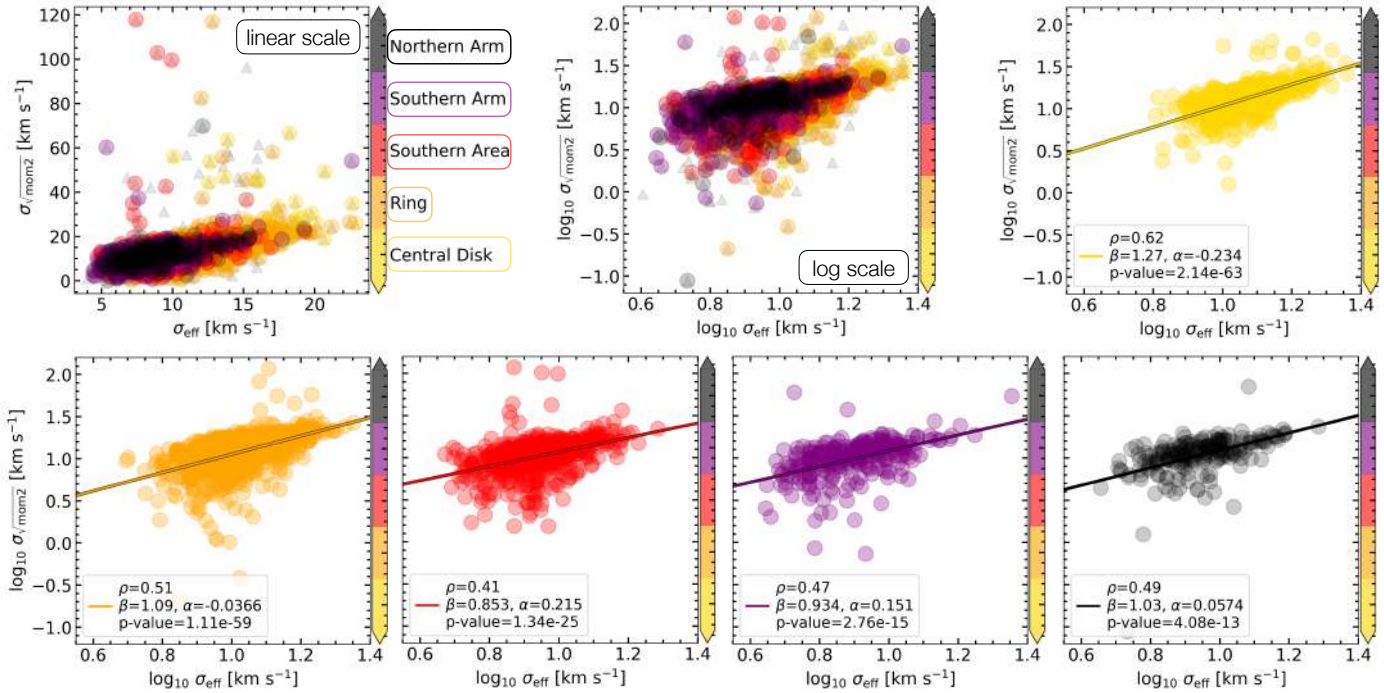

Fig. D.2. Comparison of two approaches to determine the velocity dispersion. In all panels, the y-axes show the $\sigma_{\sqrt{\text{mom2}}}$ and the x-axes the σ_{eff} values colored by the regions defined within this work (see the mask in Figure 5). Only the upper left panel shows the x and y axes in linear scale, all the others are in log scale. We show linear regression fits between $\sigma_{\sqrt{\text{mom2}}}$ and σ_{eff} for the central disk (yellow), ring (orange), southern area (red), southern arm (purple), and northern arm (black). We see the highest scatter in $\sigma_{\sqrt{\text{mom2}}}$ in the ring region of ∼2.5dex. This is likely to represent a multi-component spectrum.

Appendix E: Orbital time and free fall time

In Section 5.3 we assumed that t_{orb}∼6 t_{ff}. Here, we show the derivation of that result. We assumed that the material is distributed like a uniform density sphere. Then t_{ff} at some radius R within that mass distribution is:

$$t_{\text{ff}} = \sqrt{\frac{3\pi}{32\, G\, \rho}}, \tag{E.1}$$

where ρ = M / ((4 π R^3)/3) and where M is the mass enclosed within R and can also be expressed in terms of rotational velocities v_{rot}:

$$M = \frac{R\, v_{\text{rot}}^2}{G}. \tag{E.2}$$

The orbital time t_{orb} is defined as:

$$t_{\text{orb}} = 2\pi \sqrt{\frac{R^3}{G\, M}}. \tag{E.3}$$

As a result we get:

$$t_{\text{ff}} = \frac{1}{2\sqrt{8}}\, t_{\text{orb}} \tag{E.4}$$

or

$$t_{\text{orb}} \sim 6\, t_{\text{ff}}. \tag{E.5}$$

This, however, does not imply that material will undergo free fall to the center since there is a lot of kinetic energy and angular momentum that will prevent it. It nevertheless serves as a good estimate.

Bibliography

Aalto, S., A. G. Polatidis, S. Hüttemeister and S. J. Curran (2002), *CN and HNC line emission in IR luminous galaxies*, A&A **381** 783.

Anand, G. S., L. Rizzi and R. B. Tully (2018), *A Robust Tip of the Red Giant Branch Distance to the Fireworks Galaxy (NGC 6946)*, AJ **156**, 105 105.

Anand, G. S. et al. (2021), *Distances to PHANGS galaxies: New tip of the red giant branch measurements and adopted distances*, MNRAS **501** 3621.

Atkins, P. W. and R. S. Friedman (2011), *Molecular quantum mechanics*, Oxford university press.

Baan, W. A., C. Henkel, A. F. Loenen, A. Baudry and T. Wiklind (2008), *Dense gas in luminous infrared galaxies*, A&A **477** 747.

Barnes, A. T. et al. (2022), *Linking stellar populations to H II regions across nearby galaxies. I. Constraining pre-supernova feedback from young clusters in NGC 1672*, A&A **662**, L6 L6.

Bayet, E., Z. Awad and S. Viti (2010), *Deuterated Species in Extragalactic Star-forming Regions*, ApJ **725** 214.

Belfiore, F. et al. (2023), *Calibration of hybrid resolved star formation rate recipes based on PHANGS-MUSE Hα and Hβ maps*, A&A **670**, A67 A67.

Bennett, J. O. (2010), *Astronomie: die kosmische Perspektive*, Pearson Deutschland GmbH.

Benson, P. J., P. Caselli and P. C. Myers (1998), *Dense Cores in Dark Clouds. XI. A Survey for N_2H^+, C_3H_2, and CCS*, ApJ **506** 743.

Bergin, E. A. and M. Tafalla (2007), *Cold Dark Clouds: The Initial Conditions for Star Formation*, ARA&A **45** 339.

Bešlić, I. et al. (2021), *Dense molecular gas properties on 100 pc scales across the disc of NGC 3627*, MNRAS **506** 963.

Bigiel, F. et al. (2008), *The Star Formation Law in Nearby Galaxies on Sub-Kpc Scales*, AJ **136** 2846.

Bigiel, F. et al. (2010a), *Extremely Inefficient Star Formation in the Outer Disks of Nearby Galaxies*, AJ **140** 1194.

Bigiel, F. et al. (2010b), *Tightly Correlated H I and FUV Emission in the Outskirts of M83*, ApJ **720** L31.

Bigiel, F. et al. (2016), *The EMPIRE survey: systematic variations in the dense gas fraction and star formation efficiency from full-disk mapping of M51*, The Astrophysical Journal Letters **822** L26.

Blitz, L. and E. Rosolowsky (2004), *The Role of Pressure in Giant Molecular Cloud Formation*, ApJ **612** L29.

– (2006), *The Role of Pressure in GMC Formation II: The H_2-Pressure Relation*, ApJ **650** 933.

Braun, R. and R. A. M. Walterbos (1985), *A solution to the short spacing problem in radio interferometry.*, A&A **143** 307.

Bruzual, G. and S. Charlot (2003), *Stellar population synthesis at the resolution of 2003*, MNRAS **344** 1000.

Buat, V. (1992), *Global recent star formation in normal galaxies from a multiwavelength study. Comparison with their gas content.*, A&A **264** 444.

Calzetti, D. (2013), "Star Formation Rate Indicators", *Secular Evolution of Galaxies*, ed. by J. Falcón-Barroso and J. H. Knapen 419.

Caselli, P., C. M. Walmsley, M. Tafalla, L. Dore and P. C. Myers (1999), *CO Depletion in the Starless Cloud Core L1544*, ApJ **523** L165.

Caselli, P. and C. Ceccarelli (2012), *Our astrochemical heritage*, A&ARv **20**, 56 56.

Cerviño, M., D. Valls-Gabaud, V. Luridiana and J. M. Mas-Hesse (2002), *Confidence levels of evolutionary synthesis models. II. On sampling and Poissonian fluctuations*, A&A **381** 51.

Chabrier, G. (2003), *Galactic Stellar and Substellar Initial Mass Function*, PASP **115** 763.

Cheung, A. C., D. M. Rank, C. H. Townes, D. D. Thornton and W. J. Welch (1968), *Detection of NH_3 Molecules in the Interstellar Medium by Their Microwave Emission*, Phys. Rev. Lett. **21** 1701.

Combes, F. et al. (2014), *ALMA reveals the feeding of the Seyfert 1 nucleus in NGC 1566*, A&A **565**, A97 A97.

Cormier, D. et al. (2018), *Full-disc ^{13}CO(1-0) mapping across nearby galaxies of the EMPIRE survey and the CO-to-H_2 conversion factor*, MNRAS **475** 3909.

Cornwell, T. J. (2008), *Multiscale CLEAN Deconvolution of Radio Synthesis Images*, IEEE Journal of Selected Topics in Signal Processing **2** 793.

Dartois, E. (2005), "Dust Formation, Composition and Evolution", *The Cool Universe: Observing Cosmic Dawn*, ed. by C. Lidman and D. Alloin, vol. 344, Astronomical Society of the Pacific Conference Series 113.

Davis, T. A. (2014), *Systematic variation of the ^{12}CO/^{13}CO ratio as a function of star formation rate surface density*, MNRAS **445** 2378.

de Blok, W. J. G. et al. (2016), "An Overview of the MHONGOOSE Survey: Observing Nearby Galaxies with MeerKAT", *MeerKAT Science: On the Pathway to the SKA* 7 7.

Della Bruna, L. et al. (2022), *Stellar feedback in M83 as observed with MUSE – I. Overview, an unprecedented view of the stellar and gas kinematics and evidence of outflowing gas*, arXiv e-prints, arXiv:2202.01738 arXiv:2202.01738.

den Brok, J. S. et al. (2021), *New constraints on the ^{12}CO(2-1)/(1-0) line ratio across nearby disc galaxies*, MNRAS **504** 3221.

Di Teodoro, E. M. and J. E. G. Peek (2021), *Radial Motions and Radial Gas Flows in Local Spiral Galaxies*, ApJ **923**, 220 220.

Dickinson, D. F., E. N. Rodriguez Kuiper, A. S. C. Dinger and T. B. H. Kuiper (1980), *Shock enhancement of HCO/+/*, ApJ **237** L43.

Dobbs, C. L. et al. (2014), "Formation of Molecular Clouds and Global Conditions for Star Formation", *Protostars and Planets VI*, ed. by H. Beuther, R. S. Klessen, C. P. Dullemond and T. Henning 3.

Draine, B. T. (2011), *Physics of the Interstellar and Intergalactic Medium*, Princeton University Press.

Eibensteiner, C. et al. (2022), *A 2-3 mm high-resolution molecular line survey towards the centre of the nearby spiral galaxy NGC 6946*, A&A **659**, A173 A173.

Eibensteiner, C. et al. (2023), *Kinematic analysis of the super-extended HI disk of the nearby spiral galaxy M83*, arXiv e-prints, arXiv:2304.02037 arXiv:2304.02037.

Einstein, A. (1917), *Kosmologische Betrachtungen zur allgemeinen Relativitätstheorie*, Sitzungsberichte der Königlich Preussischen Akademie der Wissenschaften 142.

Elmegreen, B. G. (1989), *A Pressure and Metallicity Dependence for Molecular Cloud Correlations and the Calibration of Mass*, ApJ **338** 178.

Emsellem, E. et al. (2022), *The PHANGS-MUSE survey. Probing the chemo-dynamical evolution of disc galaxies*, A&A **659**, A191 A191.
Fathi, K. et al. (2008), *Spiral Inflow Feeding the Nuclear Starburst in M83, Observed in Hα Emission with the GHαFaS Fabry-Perot Interferometer*, ApJ **675** L17.
Field, G. B., D. W. Goldsmith and H. J. Habing (1969), *Cosmic-Ray Heating of the Interstellar Gas*, ApJ **155** L149.
Gallagher, M. J. et al. (2018a), *Dense gas, dynamical equilibrium pressure, and star formation in nearby star-forming galaxies*, The Astrophysical Journal **858** 90.
Gallagher, M. J. et al. (2018b), *Do Spectroscopic Dense Gas Fractions Track Molecular Cloud Surface Densities?*, The Astrophysical Journal Letters **868** L38.
Gao, Y. and P. M. Solomon (2004), *HCN survey of normal spiral, infrared-luminous, and ultraluminous galaxies*, The Astrophysical Journal Supplement Series **152** 63.
Garcia-Ruiz, I. (2001), *Warps in disk galaxies*.
Ginsburg, A. et al. (2016), *Dense gas in the Galactic central molecular zone is warm and heated by turbulence*, A&A **586**, A50 A50.
Goddard, Q. E., N. Bastian and R. C. Kennicutt (2010), *On the fraction of star clusters surviving the embedded phase*, MNRAS **405** 857.
Goldsmith, P. F., W. D. Langer, J. Ellder, E. Kollberg and W. Irvine (1981), *Determination of the HNC to HCN abundance ratio in giant molecular clouds*, ApJ **249** 524.
Gorski, M. et al. (2017), *Survey of Water and Ammonia in Nearby Galaxies (SWAN): Resolved Ammonia Thermometry, and Water and Methanol Masers in the Nuclear Starburst of NGC 253*, ApJ **842**, 124 124.
– (2018), *Survey of Water and Ammonia in Nearby Galaxies (SWAN): Resolved Ammonia Thermometry and Water and Methanol Masers in IC 342, NGC 6946, and NGC 2146*, ApJ **856**, 134 134.
Goulding, A. D. and D. M. Alexander (2009), *Towards a complete census of AGN in nearby Galaxies: a large population of optically unidentified AGN*, MNRAS **398** 1165.
Graninger, D. M., E. Herbst, K. I. Öberg and A. I. Vasyunin (2014), *The HNC/HCN Ratio in Star-forming Regions*, ApJ **787**, 74 74.
Groves, B. et al. (2023), *The PHANGS-MUSE nebular catalogue*, MNRAS **520** 4902.
Hacar, A., A. D. Bosman and E. F. van Dishoeck (2020), *HCN-to-HNC intensity ratio: a new chemical thermometer for the molecular ISM*, A&A **635**, A4 A4.
Hartwick, F. D. A. (1971), *On the Rate of Star Formation in M31*, ApJ **163** 431.
Heald, G. et al. (2016), *Neutral hydrogen and magnetic fields in M83 observed with the SKA Pathfinder KAT-7*, MNRAS **462** 1238.
Helou, G. et al. (2004), *The Anatomy of Star Formation in NGC 300*, ApJS **154** 253.
Henshaw, J. D. et al. (2022), *Star Formation in the Central Molecular Zone of the Milky Way*, arXiv e-prints, arXiv:2203.11223 arXiv:2203.11223.
Herbst, E., R. Terzieva and D. Talbi (2000), *Calculations on the rates, mechanisms, and interstellar importance of the reactions between C and NH_2 and between N and CH_2*, MNRAS **311** 869.
Ho, P. T. P. and C. H. Townes (1983), *Interstellar ammonia.*, ARA&A **21** 239.
Hodge, J. A. and E. da Cunha (2020), *High-redshift star formation in the Atacama large millimetre/sub-millimetre array era*, Royal Society Open Science **7**, 200556 200556.
Högbom, J. A. (1974), *Aperture Synthesis with a Non-Regular Distribution of Interferometer Baselines*, A&AS **15** 417.

Holdaway, M. A. (1999), "Mosaicing with Interferometric Arrays", *Synthesis Imaging in Radio Astronomy II*, ed. by G. B. Taylor, C. L. Carilli and R. A. Perley, vol. 180, Astronomical Society of the Pacific Conference Series 401.

Hoyle, F. and G. R. A. Ellis (1963), *On the Existence of an Ionized Layer about the Galactic Plane*, Australian Journal of Physics **16** 1.

Huettemeister, S. et al. (1995), *Dense gas in nearby galaxies. IX. A survey for HNC.*, A&A **295** 571.

Huggins, W. and M. Huggins (1889), *On the Spectrum, Visible and Photographic, of the Great Nebula in Orion*, Proceedings of the Royal Society of London Series I **46** 40.

Huggins, W. and W. A. Miller (1864), *On the Spectra of Some of the Fixed Stars*, Philosophical Transactions of the Royal Society of London Series I **154** 413.

Ianjamasimanana, R. et al. (2015), *The Radial Variation of H I Velocity Dispersions in Dwarfs and Spirals*, AJ **150**, 47 47.

James, T. A., S. Viti, J. Holdship and I. Jiménez-Serra (2020), *Tracing shock type with chemical diagnostics. An application to L1157*, A&A **634**, A17 A17.

Jansky, K. G. (1933), *Electrical phenomena that apparently are of interstellar origin*, Popular Astronomy **41** 548.

Jeffreson, S. M. R., J. M. D. Kruijssen, B. W. Keller, M. Chevance and S. C. O. Glover (2020), *The role of galactic dynamics in shaping the physical properties of giant molecular clouds in Milky Way-like galaxies*, MNRAS **498** 385.

Jenkins, L. P. et al. (2011), *Investigating the Nuclear Activity of Barred Spiral Galaxies: The Case of NGC 1672*, ApJ **734**, 33 33.

Jiménez-Donaire, M. J. et al. (2019), *EMPIRE: The IRAM 30 m Dense Gas Survey of Nearby Galaxies*, ApJ **880**, 127 127.

Jonas, J. and MeerKAT Team (2016), "The MeerKAT Radio Telescope", *MeerKAT Science: On the Pathway to the SKA* 1 1.

Józsa, G. I. G., F. Kenn, U. Klein and T. A. Oosterloo (2007), *Kinematic modelling of disk galaxies. I. A new method to fit tilted rings to data cubes*, A&A **468** 731.

Karachentsev, I. D. et al. (2007), *The Hubble Flow around the Centaurus A/M83 Galaxy Complex*, The Astronomical Journal **133** 504, ISSN: 1538-3881, URL: http://dx.doi.org/10.1086/510125.

Kennicutt Robert C., J. (1989), *The Star Formation Law in Galactic Disks*, ApJ **344** 685.

– (1998), *The Global Schmidt Law in Star-forming Galaxies*, ApJ **498** 541.

Kennicutt, R. C. and N. J. Evans (2012), *Star Formation in the Milky Way and Nearby Galaxies*, ARA&A **50** 531.

Kepley, A. A. et al. (2020), *Auto-multithresh: A General Purpose Automasking Algorithm*, PASP **132**, 024505 024505.

Kereš, D., N. Katz, D. H. Weinberg and R. Davé (2005), *How do galaxies get their gas?*, MNRAS **363** 2.

Kim, C.-G., W.-T. Kim and E. C. Ostriker (2011), *Regulation of Star Formation Rates in Multiphase Galactic Disks: Numerical Tests of the Thermal/Dynamical Equilibrium Model*, ApJ **743**, 25 25.

Kim, C.-G., E. C. Ostriker and W.-T. Kim (2013), *Three-dimensional Hydrodynamic Simulations of Multiphase Galactic Disks with Star Formation Feedback. I. Regulation of Star Formation Rates*, ApJ **776**, 1 1.

Klessen, R. S. and S. C. O. Glover (2016), *Physical Processes in the Interstellar Medium*, Saas-Fee Advanced Course **43** 85.

Koch, E. and A. Ginsburg (2022), *uvcombine: Combine images with different resolutions*, Astrophysics Source Code Library, record ascl:2208.014.

Koch, E. W. et al. (2018), *Kinematics of the atomic ISM ifigun M33 on 80 pc scales*, MNRAS **479** 2505.
Koda, J. et al. (2020a), *Systematic Variations of CO J = 2-1/1-0 Ratio and Their Implications in The Nearby Barred Spiral Galaxy M83*, ApJ **890**, L10 L10.
– (2020b), *Systematic Variations of CO J = 2-1/1-0 Ratio and Their Implications in The Nearby Barred Spiral Galaxy M83*, ApJ **890**, L10 L10.
Koribalski, B. S. and Á. R. López-Sánchez (2009), *Gas dynamics and star formation in the galaxy pair NGC1512/1510*, MNRAS **400** 1749.
Koribalski, B. S. et al. (2018), *The Local Volume H I Survey (LVHIS)*, MNRAS **478** 1611.
Kormendy, J. and J. Kennicutt Robert C. (2004), *Secular Evolution and the Formation of Pseudobulges in Disk Galaxies*, ARA&A **42** 603.
Kroupa, P. (2001), *On the variation of the initial mass function*, MNRAS **322** 231.
Krumholz, M. and A. Burkert (2010), *On the Dynamics and Evolution of Gravitational Instability-dominated Disks*, ApJ **724** 895.
Krumholz, M. R. (2015), *Notes on Star Formation*, arXiv e-prints, arXiv:1511.03457 arXiv:1511.03457.
Krumholz, M. R., B. Burkhart, J. C. Forbes and R. M. Crocker (2018), *A unified model for galactic discs: star formation, turbulence driving, and mass transport*, MNRAS **477** 2716.
Kwon, K.-A. et al. (2013), *High-speed camera characterization of voluntary eye blinking kinematics*, Journal of the Royal Society Interface **10** 20130227.
Lang, P. et al. (2020), *PHANGS CO Kinematics: Disk Orientations and Rotation Curves at 150 pc Resolution*, ApJ **897**, 122 122.
Langer, W. D. and A. A. Penzias (1990), *12C/ 13C Isotope Ratio across the Galaxy from Observations of 13C 18O in Molecular Clouds*, ApJ **357** 477.
Lebrón, M. et al. (2011), *Dense gas in nearby galaxies. XVII. The distribution of ammonia in NGC 253, Maffei 2, and IC 342*, A&A **534**, A56 A56.
Lee, H. .-., R. P. A. Bettens and E. Herbst (1996), *Fractional abundances of molecules in dense interstellar clouds: A compendium of recent model results.*, A&AS **119** 111.
Lee, J. C. et al. (2009), *Comparison of Hα and UV Star Formation Rates in the Local Volume: Systematic Discrepancies for Dwarf Galaxies*, ApJ **706** 599.
Lee, J. C. et al. (2022), *The PHANGS-HST Survey: Physics at High Angular Resolution in Nearby Galaxies with the Hubble Space Telescope*, ApJS **258**, 10 10.
Lee, J. C. et al. (2023), *The PHANGS-JWST Treasury Survey: Star Formation, Feedback, and Dust Physics at High Angular Resolution in Nearby GalaxieS*, ApJ **944**, L17 L17.
Lehmensiek, R. and I. P. Theron (2014), "Minimizing the MeerKAT system noise temperature", *2014 XXXIth URSI General Assembly and Scientific Symposium (URSI GASS)* 1.
Leitherer, C. et al. (1999), *Starburst99: Synthesis Models for Galaxies with Active Star Formation*, ApJS **123** 3.
Leroy, A. K. et al. (2008), *The Star Formation Efficiency in Nearby Galaxies: Measuring Where Gas Forms Stars Effectively*, AJ **136** 2782.
Leroy, A. K. et al. (2009), *Heracles: The HERA CO Line Extragalactic Survey*, AJ **137** 4670.
Leroy, A. K. et al. (2013), *Molecular Gas and Star Formation in nearby Disk Galaxies*, AJ **146**, 19 19.
Leroy, A. K. et al. (2016), *A Portrait of Cold Gas in Galaxies at 60 pc Resolution and a Simple Method to Test Hypotheses That Link Small-scale ISM Structure to Galaxy-scale Processes*, ApJ **831**, 16 16.
Leroy, A. K. et al. (2017), *Millimeter-wave Line Ratios and Sub-beam Volume Density Distributions*, ApJ **835**, 217 217.
Leroy, A. K. et al. (2019), *A z = 0 Multiwavelength Galaxy Synthesis. I. A WISE and GALEX Atlas of Local Galaxies*, ApJS **244**, 24 24.

Leroy, A. K. et al. (2021a), *PHANGS-ALMA Data Processing and Pipeline*, ApJS **255**, 19 19.
Leroy, A. K. et al. (2021b), *PHANGS-ALMA: Arcsecond CO(2-1) Imaging of Nearby Star-forming Galaxies*, ApJS **257**, 43 43.
Leroy, A. K. et al. (2022), *Low-J CO Line Ratios from Single-dish CO Mapping Surveys and PHANGS-ALMA*, ApJ **927**, 149 149.
Li, J., J. Wang, Q. Gu, Z.-y. Zhang and X. Zheng (2012), *Large-scale Kinematics, Astrochemistry, and Magnetic Field Studies of Massive Star-forming Regions through HC_3N, HNC, and C_2H Mappings*, ApJ **745**, 47 47.
Linden, S. T. et al. (2020), *The Star Formation in Radio Survey: 3-33 GHz Imaging of Nearby Galaxy Nuclei and Extranuclear Star-forming Regions*, ApJS **248**, 25 25.
Loenen, A. F., M. Spaans, W. A. Baan and R. Meijerink (2008), *Mechanical feedback in the molecular ISM of luminous IR galaxies*, A&A **488** L5.
Lucas, R. and H. Liszt (1996), *The Plateau de Bure survey of galactic λ3mm HCO+âbsorption toward compact extragalactic continuum sources.*, A&A **307** 237.
Lundgren, A. A., H. Olofsson, T. Wiklind and G. Rydbeck (2004), *Molecular gas in the galaxy M 83. II. Kinematics of the molecular gas*, A&A **422** 865.
Makarov, D., P. Prugniel, N. Terekhova, H. Courtois and I. Vauglin (2014), *HyperLEDA. III. The catalogue of extragalactic distances*, A&A **570**, A13 A13.
Maloney, P. R., D. J. Hollenbach and A. G. G. M. Tielens (1996), *X-Ray–irradiated Molecular Gas. I. Physical Processes and General Results*, ApJ **466** 561.
Mangum, J. G. et al. (2013), *Ammonia Thermometry of Star-Forming Galaxies*, ApJ **779**, 33 33.
Mangum, J. G. et al. (2019), *Fire in the Heart: A Characterization of the High Kinetic Temperatures and Heating Sources in the Nucleus of NGC 253*, ApJ **871**, 170 170.
Martin, D. C. et al. (2005), *The Galaxy Evolution Explorer: A Space Ultraviolet Survey Mission*, ApJ **619** L1.
Martın, S. et al. (2015), *Multimolecule ALMA observations toward the Seyfert 1 galaxy NGC 1097*, A&A **573**, A116 A116.
McKee, C. F. and J. P. Ostriker (1977), *A theory of the interstellar medium: three components regulated by supernova explosions in an inhomogeneous substrate.*, ApJ **218** 148.
McKee, C. F. and E. C. Ostriker (2007), *Theory of Star Formation*, ARA&A **45** 565.
Meier, D. S. and J. L. Turner (2005), *Spatially Resolved Chemistry in Nearby Galaxies. I. The Center of IC 342*, ApJ **618** 259.
– (2012), *Spatially Resolved Chemistry in nearby Galaxies. II. The Nuclear Bar in Maffei 2*, ApJ **755**, 104 104.
Meier, D. S., J. L. Turner and R. L. Hurt (2008), *Nuclear Bar Catalyzed Star Formation: ^{13}CO, $C^{18}O$, and Molecular Gas Properties in the Nucleus of Maffei 2*, ApJ **675** 281.
Meijerink, R. and M. Spaans (2005), *Diagnostics of irradiated gas in galaxy nuclei. I. A far-ultraviolet and X-ray dominated region code*, A&A **436** 397.
Meijerink, R., M. Spaans and F. P. Israel (2007), *Diagnostics of irradiated dense gas in galaxy nuclei. II. A grid of XDR and PDR models*, A&A **461** 793.
Meijerink, R., M. Spaans, A. F. Loenen and P. P. van der Werf (2011), *Star formation in extreme environments: the effects of cosmic rays and mechanical heating*, A&A **525**, A119 A119.
Menten, K. M. and C. M. Walmsley (1985), *Ammonia observations of L 1551.*, A&A **146** 369.
Mogotsi, K. M. et al. (2016), *H I and CO Velocity Dispersions in Nearby Galaxies*, AJ **151**, 15 15.

Müller, H. S. P., F. Schlöder, J. Stutzki and G. Winnewisser (2005), *The Cologne Database for Molecular Spectroscopy, CDMS: a useful tool for astronomers and spectroscopists*, Journal of Molecular Structure **742** 215.

Murphy, E. J. et al. (2011), *Calibrating Extinction-free Star Formation Rate Diagnostics with 33 GHz Free-free Emission in NGC 6946*, ApJ **737**, 67 67.

Oh, S.-H., S. Kim, B.-Q. For and L. Staveley-Smith (2022), *Kinematic Decomposition of the H I Gaseous Component in the Large Magellanic Cloud*, ApJ **928**, 177 177.

Ostriker, E. C., C. F. McKee and A. K. Leroy (2010), *Regulation of Star Formation Rates in Multiphase Galactic Disks: A Thermal/Dynamical Equilibrium Model*, ApJ **721** 975.

Ott, J., C. Henkel, J. A. Braatz and A. Weiß (2011), *Ammonia as a Temperature Tracer in the Ultraluminous Galaxy Merger Arp 220*, ApJ **742**, 95 95.

Ott, J., A. Weiss, C. Henkel and F. Walter (2005), *The Temperature Distribution of Dense Molecular Gas in the Center of NGC 253*, ApJ **629** 767.

Padoan, P. et al. (2014), "The Star Formation Rate of Molecular Clouds", *Protostars and Planets VI*, ed. by H. Beuther, R. S. Klessen, C. P. Dullemond and T. Henning 77.

Papadopoulos, P. P. (2007), *HCN versus HCO^+ as Dense Molecular Gas Mass Tracers in Luminous Infrared Galaxies*, ApJ **656** 792.

Peñaloza, C. H., P. C. Clark, S. C. O. Glover and R. S. Klessen (2018), *CO line ratios in molecular clouds: the impact of environment*, MNRAS **475** 1508.

Pettini, M. and B. E. J. Pagel (2004), *[OIII]/[NII] as an abundance indicator at high redshift*, MNRAS **348** L59.

Pety, J. et al. (2017), *The anatomy of the Orion B giant molecular cloud: A local template for studies of nearby galaxies*, A&A **599**, A98 A98.

Pickett, H. M. et al. (1998), *Submillimeter, millimeter and microwave spectral line catalog.*, J. Quant. Spectrosc. Radiative Transfer **60** 883.

Pineda, J. E., P. Caselli and A. A. Goodman (2008), *CO Isotopologues in the Perseus Molecular Cloud Complex: the X-factor and Regional Variations*, ApJ **679** 481.

Querejeta, M. et al. (2016), *AGN feedback in the nucleus of M 51*, A&A **593**, A118 A118.

Relaño, M., A. Monreal-Ibero, J. M. Vılchez and R. C. Kennicutt (2010), *Spatially resolved study of the physical properties of the ionized gas in NGC 595*, MNRAS **402** 1635.

Reynolds, R. J. (1989), *The Column Density and Scale Height of Free Electrons in the Galactic Disk*, ApJ **339** L29.

Rickard, L. J., P. Palmer, M. Morris, B. Zuckerman and B. E. Turner (1975), *Detection of extragalactic carbon monoxide at millimeter wavelengths.*, ApJ **199** L75.

Romeo, A. B. and K. M. Mogotsi (2017), *What drives gravitational instability in nearby star-forming spirals? The impact of CO and H I velocity dispersions*, MNRAS **469** 286.

Rosolowsky, E. and A. Leroy (2006), *Bias-free Measurement of Giant Molecular Cloud Properties*, PASP **118** 590.

Roy, N., N. Kanekar and J. N. Chengalur (2013), *The temperature of the diffuse H I in the Milky Way - II. Gaussian decomposition of the H I-21 cm absorption spectra*, MNRAS **436** 2366.

Sagan, C. (1986), *Dragons of Eden: Speculations on the evolution of human intelligence*, Ballantine Books.

Saintonge, A. and B. Catinella (2022), *The Cold Interstellar Medium of Galaxies in the Local Universe*, ARA&A **60** 319.

Saito, T. et al. (2017), *Merger-induced Shocks in the Nearby LIRG VV 114 through Methanol Observations with ALMA*, ApJ **834**, 6 6.

Salim, S., M. Boquien and J. C. Lee (2018), *Dust Attenuation Curves in the Local Universe: Demographics and New Laws for Star-forming Galaxies and High-redshift Analogs*, ApJ **859**, 11 11.
Salim, S. et al. (2007), *UV Star Formation Rates in the Local Universe*, ApJS **173** 267.
Salim, S. et al. (2016), *GALEX-SDSS-WISE Legacy Catalog (GSWLC): Star Formation Rates, Stellar Masses, and Dust Attenuations of 700,000 Low-redshift Galaxies*, ApJS **227**, 2 2.
Salo, H. et al. (2015), *The Spitzer Survey of Stellar Structure in Galaxies (S^4G): Multi-component Decomposition Strategies and Data Release*, ApJS **219**, 4 4.
Sánchez, S. F. et al. (2014), *A characteristic oxygen abundance gradient in galaxy disks unveiled with CALIFA*, A&A **563**, A49 A49.
Sánchez, S. F. et al. (2019), *The SAMI galaxy survey: exploring the gas-phase mass-metallicity relation*, MNRAS **484** 3042.
Sancisi, R., F. Fraternali, T. Oosterloo and T. van der Hulst (2008), *Cold gas accretion in galaxies*, A&ARv **15** 189.
Sandstrom, K. M. et al. (2013), *The CO-to-H_2 Conversion Factor and Dust-to-gas Ratio on Kiloparsec Scales in Nearby Galaxies*, ApJ **777**, 5 5.
Sanduleak, N. (1969), *Correlation of the Distributions of Young Stars and Neutral Hydrogen in the Small Magellanic Cloud*, AJ **74** 47.
Sault, R. J., L. Staveley-Smith and W. N. Brouw (1996), *An approach to interferometric mosaicing.*, A&AS **120** 375.
Schilke, P. et al. (1992), *A study of HCN, HNC and their isotopometers in OMC-1. I. Abundances and chemistry.*, A&A **256** 595.
Schinnerer, E., T. Böker, E. Emsellem and D. Downes (2007), *Bar-driven mass build-up within the central 50 pc of NGC 6946*, A&A **462** L27.
Schinnerer, E., T. Böker, E. Emsellem and U. Lisenfeld (2006), *Molecular gas dynamics in NGC 6946: a bar-driven nuclear starburst "Caught in the Act"*, The Astrophysical Journal **649** 181.
Schmidt, M. (1959), *The Rate of Star Formation.*, ApJ **129** 243.
Schneider, P. (2006), *Einführung in die extragalaktische Astronomie und Kosmologie*, Springer-Verlag.
Schruba, A., S. Bialy and A. Sternberg (2018), *The Metallicity Dependence of the H I Shielding Layers in Nearby Galaxies*, ApJ **862**, 110 110.
Schruba, A. et al. (2011), *A Molecular Star Formation Law in the Atomic-gas-dominated Regime in Nearby Galaxies*, AJ **142**, 37 37.
Schwarz, U. J. (1978), *Mathematical-statistical Description of the Iterative Beam Removing Technique (Method CLEAN)*, A&A **65** 345.
Seifried, D., W. Schmidt and J. C. Niemeyer (2011), *Forced turbulence in thermally bistable gas: a parameter study*, A&A **526**, A14 A14.
Selina, R. J. et al. (2018), "The ngVLA Reference Design", *Science with a Next Generation Very Large Array*, ed. by E. Murphy, vol. 517, Astronomical Society of the Pacific Conference Series 15.
Sheth, K. et al. (2010), *The Spitzer Survey of Stellar Structure in Galaxies (S4G)*, PASP **122** 1397.
Shirley, Y. L. (2015), *The Critical Density and the Effective Excitation Density of Commonly Observed Molecular Dense Gas Tracers*, PASP **127** 299.
Solomon, P. M. and R. de Zafra (1975), *Carbon monoxide in external galaxies.*, ApJ **199** L79.
Spitzer Lyman, J. (1942), *The Dynamics of the Interstellar Medium. III. Galactic Distribution.*, ApJ **95** 329.
Sternberg, A., F. Le Petit, E. Roueff and J. Le Bourlot (2014), *H I-to-H_2 Transitions and H I Column Densities in Galaxy Star-forming Regions*, ApJ **790**, 10 10.
Sun, J. et al. (2018), *Cloud-scale Molecular Gas Properties in 15 Nearby Galaxies*, ApJ **860**, 172 172.

Sun, J. et al. (2020a), *Dynamical Equilibrium in the Molecular ISM in 28 Nearby Star-forming Galaxies*, ApJ **892**, 148 148.
Sun, J. et al. (2020b), *Molecular Gas Properties on Cloud Scales across the Local Star-forming Galaxy Population*, ApJ **901**, L8 L8.
Sun, J. et al. (2022), *Molecular Cloud Populations in the Context of Their Host Galaxy Environments: A Multiwavelength Perspective*, AJ **164**, 43 43.
Tafalla, M., P. C. Myers, P. Caselli, C. M. Walmsley and C. Comito (2002), *Systematic Molecular Differentiation in Starless Cores*, ApJ **569** 815.
Talbi, D., Y. Ellinger and E. Herbst (1996), *On the HCN/HNC abundance ratio: a theoretical study of the H+CNH<->HCN+H exchange reactions.*, A&A **314** 688.
Tamburro, D. et al. (2009), *What is Driving the H I Velocity Dispersion?*, AJ **137** 4424.
Terwisscha van Scheltinga, J. et al. (2021), *The TW Hya Rosetta Stone Project. II. Spatially Resolved Emission of Formaldehyde Hints at Low-temperature Gas-phase Formation*, ApJ **906**, 111 111.
Thilker, D. A. et al. (2005), *Recent Star Formation in the Extreme Outer Disk of M83*, ApJ **619** L79.
Thompson, A. R., J. M. Moran and G. W. Swenson (2017), *Interferometry and synthesis in radio astronomy*, Springer Nature.
Tielens, A. G. G. M. (2010), *The Physics and Chemistry of the Interstellar Medium*.
Turner, B. E. (1995), *The Physics and Chemistry of Translucent Molecular Clouds. IV. HCO + and N 2H +*, ApJ **449** 635.
– (1998), *The Physics and Chemistry of Small Translucent Molecular Clouds. XI. Methanol*, ApJ **501** 731.
Turner, B. E., H.-H. Lee and E. Herbst (1998), *The Physics and Chemistry of Small Translucent Molecular Clouds. IX. Acetylenic Chemistry*, ApJS **115** 91.
Turner, B. E., L. Pirogov and Y. C. Minh (1997), *The Physics and Chemistry of Small Translucent Molecular Clouds. VIII. HCN and HNC*, ApJ **483** 235.
Unsöld, A., B. Baschek and W. J. Duschl (2002), *Der neue Kosmos: Einführung in die Astronomie und Astrophysik*, Springer.
Usero, A. et al. (2015), *Variations in the star formation efficiency of the dense molecular gas across the disks of star-forming galaxies*, The Astronomical Journal **150** 115.
van Cittert, P. (1934), *Die Wahrscheinliche Schwingungsverteilung in Einer von Einer Lichtquelle Direkt Oder Mittels Einer Linse Beleuchteten Ebene*, Physica **1** 201, ISSN: 0031-8914, URL: https://www.sciencedirect.com/science/article/pii/S0031891434900264.
van Dishoeck, E. F. (2014), *Astrochemistry of dust, ice and gas: introduction and overview*, Faraday Discussions **168** 9.
Veilleux, S., R. Maiolino, A. D. Bolatto and S. Aalto (2020), *Cool outflows in galaxies and their implications*, A&ARv **28**, 2 2.
Viti, S. et al. (2011), *L1157-B1: Water and Ammonia as Diagnostics of Shock Temperature*, ApJ **740**, L3 L3.
Walmsley, C. M. and H. Ungerechts (1983), *Ammonia as a molecular cloud thermometer.*, A&A **122** 164.
Walter, F. et al. (2008), *THINGS: The H I Nearby Galaxy Survey*, AJ **136** 2563.
Wang, J. et al. (2016), *New lessons from the H I size-mass relation of galaxies*, MNRAS **460** 2143.
Watanabe, N., T. Shiraki and A. Kouchi (2003), *The Dependence of H_2CO and CH_3OH Formation on the Temperature and Thickness of H_2O-CO Ice during the Successive Hydrogenation of CO*, ApJ **588** L121.

Wilson, R. W., K. B. Jefferts and A. A. Penzias (1970), *Carbon Monoxide in the Orion Nebula*, ApJ **161** L43.

Wilson, T. L., K. Rohlfs and S. Hüttemeister (2013), *Tools of Radio Astronomy*.

Wolfire, M. G., D. Hollenbach and C. F. McKee (2010), *The Dark Molecular Gas*, ApJ **716** 1191.

Wolfire, M. G., C. F. McKee, D. Hollenbach and A. G. G. M. Tielens (2003), *Neutral Atomic Phases of the Interstellar Medium in the Galaxy*, ApJ **587** 278.

Wolfire, M. G., L. Vallini and M. Chevance (2022), *Photodissociation and X-Ray-Dominated Regions*, ARA&A **60** 247.

Wong, T. and L. Blitz (2002), *The Relationship between Gas Content and Star Formation in Molecule-rich Spiral Galaxies*, ApJ **569** 157.

Woon, D. E. (2002), *Modeling Gas-Grain Chemistry with Quantum Chemical Cluster Calculations. I. Heterogeneous Hydrogenation of CO and H_2CO on Icy Grain Mantles*, ApJ **569** 541.

Wootten, A. (1981), *A dense molecular cloud impacted by the W28 supernova remnant*, ApJ **245** 105.

Wright, E. L. et al. (2010), *The Wide-field Infrared Survey Explorer (WISE): Mission Description and Initial On-orbit Performance*, AJ **140** 1868.

Yajima, Y. et al. (2021), *CO Multi-line Imaging of Nearby Galaxies (COMING). IX. $^{12}CO(J = 2\text{-}1)/^{12}CO(J = 1\text{-}0)$ line ratio on kiloparsec scales*, PASJ.

Zernike, F. (1938), *The concept of degree of coherence and its application to optical problems*, Physica **5** 785, ISSN: 0031-8914, URL: https://www.sciencedirect.com/science/article/pii/S0031891438802032.

List of Figures

List of Tables

Acronyms

AG	**A**tomic **G**as
AGN	**A**ctive **G**alactic **N**ucleus
ALMA	**A**tacama **L**arge **M**illimetre/submillimetre **A**rray
CASA	**C**ommon **A**stronomy **S**oftware **A**pplications
CGM	**C**ircum **G**alactic **M**edium
CMZ	**C**entral **M**olecular **Z**one
CNM	**C**old **N**eutral **M**edium
DE	**D**ynamical **E**quilibrium (-Pressure)
DF	**D**ynamical **F**eautures
DGTs	**D**ense **G**as **T**racers
EMPIRE	**E**MIR **M**ultiline **P**robe of the **I**SM **R**egulating Galaxy **E**volution Survey
FIR	**F**ar-**I**nfra**R**ed
FoV	**F**ield-**o**f-**V**iew
FT	**F**ourier **T**ransform
FWHM	**F**ull-**W**idth at **H**alf **M**aximum
GALEX	**GAL**axy **E**volution E**X**plorer
GBT	**G**reen **B**ank **T**elescope
GMC	**G**iant **M**olecular **C**loud
HERA	**HE**terodyne **R**eceiver **A**rray
HERACLES	The **HERA** **C**O-**L**ine **E**xtragalactic **S**urvey
HIM	**H**ot **I**onized **M**edium
HPBW	**H**alf **P**ower **B**eam **W**idth
IF	**I**ntermediate **f**requency
IRAM	**I**nstitut de **R**adio**a**stronomie **M**illimètrique
ISM	**I**nter**S**tellar **M**edium
ISRF	**I**nter**S**tellar **R**adiation **F**ield
JWST	**J**ames **W**ebb **S**pace **T**elescope
KS	**K**ennicutt-**S**chmidt
LO	**L**ocal **O**scillator
LOS	**L**ine **O**f **S**ight
LSR	**L**ocal **S**tandard of **R**est
LTE	**L**ocal **T**hermodynamic **E**quilibrium

MeerKAT	**M**ore of **K**aroo **A**rray **T**elescope
MG	**M**olecular **G**as
Mom	**Mom**ent (as for e.g. Moment map)
MUSE	**M**ulti **U**nit **S**pectroscopic **E**xplorer
MW	**M**ilky **W**ay
NBE	**N**orthern inner **B**ar **E**nd
ngVLA	**n**ext **g**eneration **V**ery **L**arge **A**rray
NIR	**N**ear-**I**nfra**R**ed
NUC	**NUC**lear region
NOEMA	**NO**rthern **E**xtended **M**illimeter **A**rray
NRAO	**N**ational **R**adio **A**stronomy **O**bservatory
PdBI	**P**lateau **d**e **B**ure **I**nterferometer
PDF	**P**robability **D**ensity **F**unction
PDR	**P**hoto**D**issociation **R**egions
PHANGS	**P**hysics at **H**igh **A**ngular resolution in **N**earby **G**alaxie**S**
PI	**P**rinciple **I**nvestigator
PSF	**P**oint **S**pread **F**unction
RFI	**R**adio **F**requency **I**nterference
rms	**r**oot-**m**ean-**s**quared
SBE	**S**outhern inner **B**ar **E**nd
SD	**S**ingle **D**ish
SDSS	**S**loan **D**igital **S**ky **S**urvey
SFR	**S**tar **f**ormation **r**ate
SFE	**S**tar-**f**orming **e**fficiency
SKA	Square **K**ilometre **A**rray
SSC	**S**hort-spacing **c**orrection
SSP	**S**hort-spacing **p**roblem
S/N	**S**ignal-to-**n**oise
THINGS	**T**he **HI** **N**earby **G**alaxy **S**urvey
TIR	**T**otal **i**nfra**r**ed
UV	**U**ltra **v**iolet
VLA	**V**ery **L**arge **A**rray
WIM	**W**arm **I**onised **M**edium
WISE	**W**ide-field **I**nfrared **S**urvey **E**xplorer
WNM	**W**arm **N**eutral **M**edium
XDR	**X**-ray **D**ominated **R**egion
XUV	E**X**tended **UV** disk

Molecules

CO	Carbon Monoxide
CS	Carbon Monosulfide
CH_3OH	Methanol
C_2H	Ethynyl
HI	Neutral Atomic Hydrogen
H_2	Molecular Hydrogen
HCN	Hydrogen Cyanide
HCO^+	Formylium Ion
HNC	Hydrogen Iso-Cyanide
HC_3N	Cyanoacetylene
H_2CO	Formaldehyde
N_2H^+	Diazenylium
NH_3	Ammonia

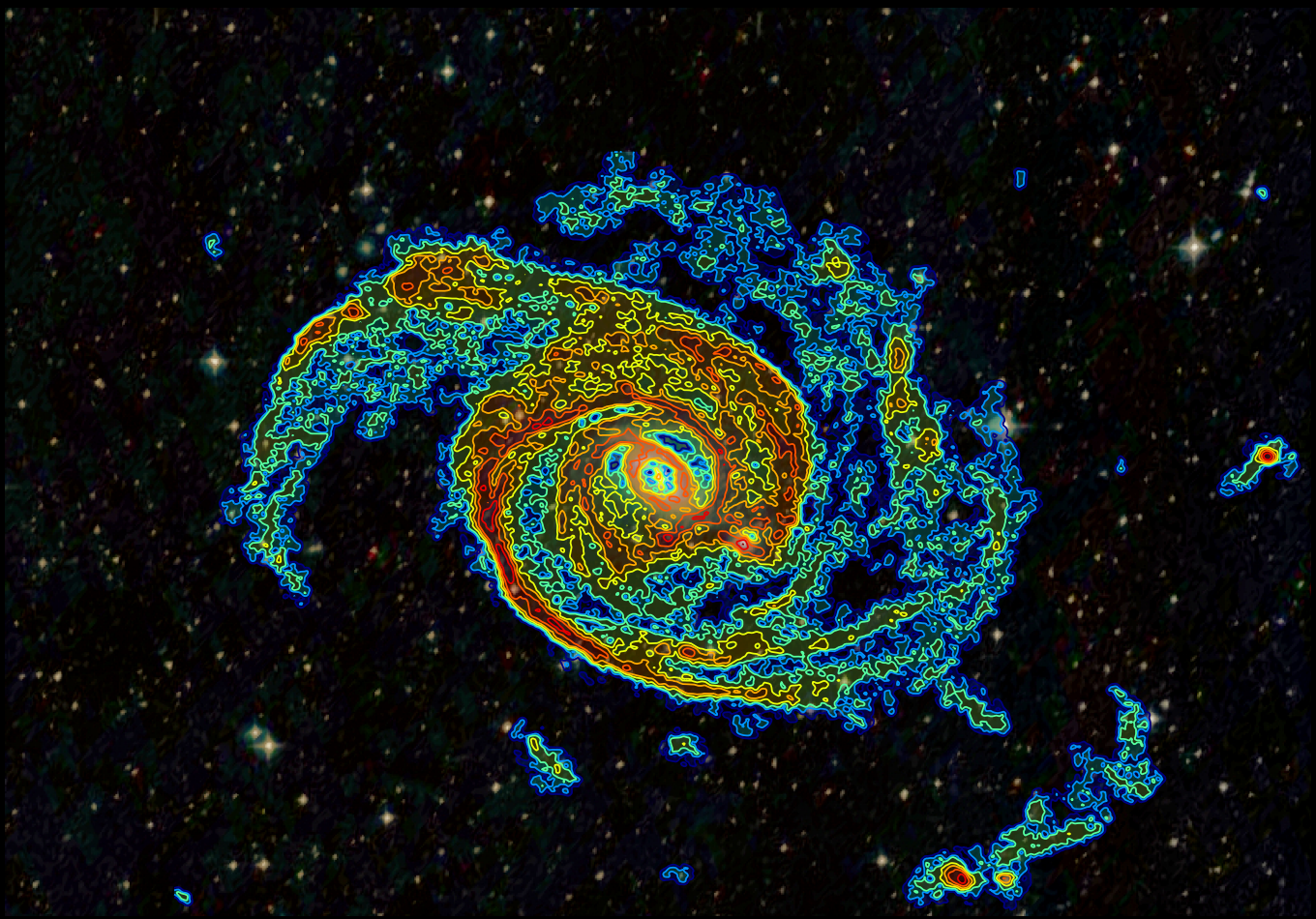

Front cover: Galaxy M 83 with HI contours over optical image (credit: CTIO/NOIRLab/DOE/NSF/AURA)
& Center of Galaxy NGC 6946 with CO (2-1) contours over optical image (credits: NASA, ESA, STScI, and the Subaru Telescope
Contours are from observations with the *Karl G. Jansky Very Large Array* (VLA) and *IRAM Plate de Bure Interferometer* (PdBI)

Back Cover: *(Top)* Galaxie NGC 1512 and dwarf galaxy NGC 1510 (credit: DSS2) *(Bottom)* with HI contours over optical image
Contours are from observations with the *More of Karoo Array Telescope* (MeerKAT)